J.-C.G. Bünzli and V.K. Pecharsky
Editors

HANDBOOK ON THE PHYSICS AND CHEMISTRY OF RARE EARTHS

Volume 44

Including Actinides

North-Holland

Handbook on the Physics and Chemistry of Rare Earths

Including Actinides

Volume 44

HANDBOOK ON THE PHYSICS AND CHEMISTRY
OF RARE EARTHS

Including Actinides

Handbook on the Physics and Chemistry of Rare Earths

Including Actinides

Volume 44

Editors

Jean-Claude G. BÜNZLI
Swiss Federal Institute of Technology, Lausanne (EPFL)
Institute of Chemical Sciences and Engineering
BCH 1402
CH-1015 Lausanne
Switzerland

Vitalij K. PECHARSKY
The Ames Laboratory, U.S. Department of Energy, and
Department of Materials Science and Engineering
Iowa State University
Ames, Iowa 50011-3020
USA

ELSEVIER
Amsterdam • Boston • Heidelberg • London • New York • Oxford
Paris • San Diego • San Francisco • Singapore • Sydney • Tokyo
North-Holland is an imprint of Elsevier
N·H

North-Holland is an imprint of Elsevier
Radarweg 29, PO Box 211, 1000 AE Amsterdam, The Netherlands
The Boulevard, Langford Lane, Kidlington, Oxford OX5 1GB, UK

British Library Cataloguing in Publication Data
A catalogue record for this book is available from the British Library

Library of Congress Cataloging-in-Publication Data
A catalog record for this book is available from the Library of Congress

ISBN: 978-0-444-62711-7
ISSN: 0168-1273

For information on all North-Holland publications
visit our website at store.elsevier.com

Printed and Bound in Great Britain

14 15 16 13 12 11 10 9 8 7 6 5 4 3 2 1

Preface

Jean-Claude G. Bünzli and Vitalij K. Pecharsky

> *These elements perplex us in our reaches [sic], baffle us in our speculations, and haunt us in our very dreams. They stretch like an unknown sea before us—mocking, mystifying, and murmuring strange revelations and possibilities.*
>
> Sir William Crookes (February 16, 1887)

Volume 44 of the *Handbook on the Physics and Chemistry of Rare Earths* adds four chapters to the series which span a broad range of subjects, from catalysis to molten salts, solar energy conversion, and intermetallic compounds R_5T_4 (T = Si, Ge, Sn) best known for giant magnetocaloric effect. The volume is therefore in tune with some of the global concerns about building a sustainable world.

The first chapter (Chapter 259) is devoted to a fairly new aspect of lanthanide catalysts, namely the use of borohydride complexes in polymerization of polar monomers. Borohydride catalysts were proposed about a decade ago for the ring-opening polymerization (ROP) of cyclic esters and the review presents extensive data about the exact experimental conditions, molecular characteristics, and performances of these catalysts. Emphasis is given to the strategies adopted by chemists to improve the steric control of the polymerization in relationship with tailored rare-earth ligands. The following review (Chapter 260) deals with melts of rare-earth inorganic salts. These liquids are known for a long time, but deciphering their exact structure is still a challenging problem. Major instrumental techniques to deal with this problem are X-ray and neutron diffraction. The author therefore first focuses on the definition of the radial distribution function and on the various data treatments leading to estimates of the coordination numbers of the first and second coordination sphere. The formation of polymers and clusters is carefully assessed with respect to their influence on coordination numbers. Potential contribution of rare-earth materials to solar energy conversion is critically evaluated in Chapter 261. Light-to-electricity conversion by semiconductors suffers from a major problem, namely spectral mismatch between the solar emission spectrum and the conversion yield versus wavelength. To rectify the situation, rare earth containing wavelength-converting materials are proposed which transform too energetic or insufficiently energetic photons into photons with optimum conversion wavelength. In this way, a few welcome percent can be added to the conversion efficiencies of solar cells. The final chapter (Chapter 262) describes rare-earth R_5T_4 intermetallic compounds (T is Si, Ge, Sn, Ga, P, Sb, Bi, or mixtures thereof). These compounds have very interesting fundamental science and, in addition, a giant magnetocaloric effect was reported for $Gd_5Si_2Ge_2$ in 1997, which paved the way for magnetic refrigeration applications near room temperature. The comprehensive review deals with composition–structure–property relationships and highlights the above-mentioned effect and other properties such as colossal magnetostriction, spontaneous generation of voltage, pressure enhancement of magnetocaloric effect, unconventional magnetic glass state, spin-flop transition, magnetic deflagration, or short-range order magnetic correlations.

CHAPTER 259. CATALYTIC BEHAVIOR OF RARE-EARTH BOROHYDRIDE COMPLEXES IN POLYMERIZATION OF POLAR MONOMERS

By SOPHIE M. GUILLAUME, LAURENT MARON, and PETER W. ROESKY
Université de Rennes 1, France, Université de Toulouse, France, and Karlsruher Institut für Technologie (KIT), Germany

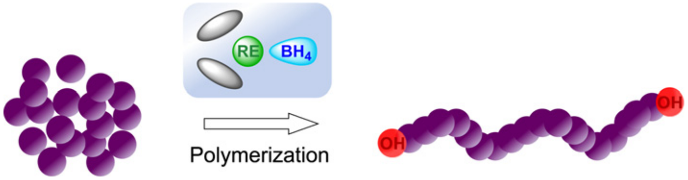

Rare-earth borohydride complexes have been used in polymerization for just over a decade. Significant achievements in the synthesis of such organometallic complexes have greatly contributed to their applications as valuable initiators in various polymerization reactions. The chapter focuses on the polymerization of polar monomers. The reader is first introduced to a brief summary of the synthesis and characterization of the rare-earth borohydride complexes that have revealed activity in such polymerizations. Advances in polymerization are then addressed from an experimental approach completed by mechanistic insights through computational density-functional investigations. The catalytic behavior of rare-earth borohydride complexes in ring-opening polymerization (ROP) of cyclic esters including various lactones, lactides, trimethylene carbonate, and α-aminoacid *N*-carboxyanhydrides, and in the polymerization of methylmethacrylate, is then comprehensively reviewed. The chapter is unique in that several tables gather the most significant features of the experimental conditions for the synthesis of the polymers, and of their molecular characteristics such as molar mass, dispersity values, and tacticity. Special emphasis is given to the strategies improving the control and the livingness of the polymerization. These strategies lead to tailor-made ligands with adequate properties and, additionally, allow access to original well-defined end-functionalized (co)polymers. Beyond the key reducing ability of the borohydride anion toward the formation of α,ω-dihydroxytelechelic polymers, the implication of the rare-earth ancillary ligand(s) is also highlighted. The review will be useful as a reference material for researchers active in rare-earth-promoted polymerization, in ROP, in hydroxytelechelic polymers and for other polymer communities as well.

CHAPTER 260. STRUCTURES AND PROPERTIES OF RARE-EARTH MOLTEN SALTS

By YASUHIKO IWADATE
Chiba University, Japan

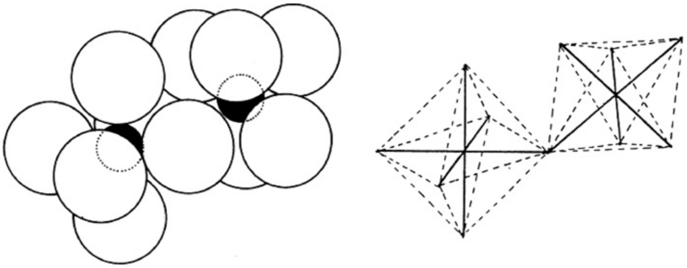

There is a definite overlap between the concepts of molten salts and ionic liquids since the former can be defined as high-temperature ionic liquids; however, the present tendency is to use the term “molten salts” to characterize melts of purely inorganic compounds. If theoretical modeling of ionic crystals is relatively easy to achieve, for instance making use of X-ray diffraction data, in view of the periodic arrangements of ions in the structure, it becomes a much more involved process when molten salts are considered because of interparticle interactions due to collisions. A single experimental technique usually gives partial reporting of the situation only so that a multiple-technique approach has to be used. For instance, X-ray diffraction, vibrational spectroscopy, density measurements, molecular dynamics, and Monte Carlo calculations are commonly combined to gain an objective representation of the ionic liquid state. The review first focuses on the definition of the radial distribution function and on the various ways prevailing to the estimate of coordination numbers in both the first and second shell from this function. The state of knowledge pertaining to melts of rare earth and alkali halides and salts with polyatomic anions is then critically detailed. An important point is the penetration of ions from the second into the first coordination sphere and its effect on coordination numbers. Finally, the formation of polymeric ions and their clustering is considered in the context of conciliating experimental data with the stoichiometry of the salts. The review is aimed at inorganic chemists and materials scientists dealing with electrolytes and their applications.

CHAPTER 261. LANTHANIDES IN SOLAR ENERGY CONVERSION

By JEAN-CLAUDE G. BÜNZLI and ANNE-SOPHIE CHAUVIN
École Polytechnique Fédérale de Lausanne (EPFL), Switzerland

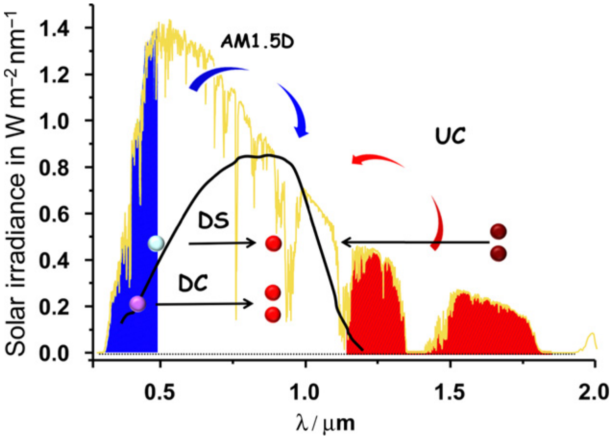

Solar energy represents an abundant (1000 W m^{-2}) and seemingly cheap source of energy. One way to tap it is to transform light into electricity with photovoltaic devices. Single-junction solar cells presently reach 32% conversion yield under 1-sun illumination while multijunction devices irradiated by concentrated light can reach 44%. One major problem encountered when trying to increase the conversion efficiency lies in the mismatch between the absorption spectrum of the semiconductor and the solar emission spectrum. As a remedy, wavelength-converting materials are being developed, and because solar cells perform best in a relatively narrow spectral range that depends on their bandgap energy, lanthanide luminescent divalent and trivalent ions are particularly well suited for this purpose. In addition, nonluminescent ions feature special crystallographic and conduction properties that make them invaluable in lattice-matched multijunction devices. In this chapter, the performances of rare-earth ions in downconverting, downshifting, and upconverting materials embedded into the architecture of luminescent solar concentrators, silicon solar cells, semiconductor photovoltaic devices, and dye-sensitized solar cells (DSSCs) are comprehensively and critically reviewed. Other contributions, for example, as scattering layers and as modifiers of the bandgap of titanium oxide in DSSCs, or to the powering of *in vivo* nanorobots, are likewise described. Finally, a general assessment is made and improvements on the order of +5 absolute% in conversion yields are predicted provided fully optimized materials can be created. The review will help scientists and materials engineers planning wavelength-converting materials for photovoltaic uses and, also, represents a welcome introductory text for anyone interested in the field.

CHAPTER 262. R_5T_4 COMPOUNDS: AN EXTRAORDINARY VERSATILE MODEL SYSTEM FOR THE SOLID STATE SCIENCE

By YAROSLAV MUDRYK, VITALIJ K. PECHARSKY, and KARL A. GSCHNEIDNER Jr.

Ames Laboratory, Iowa State University, USA

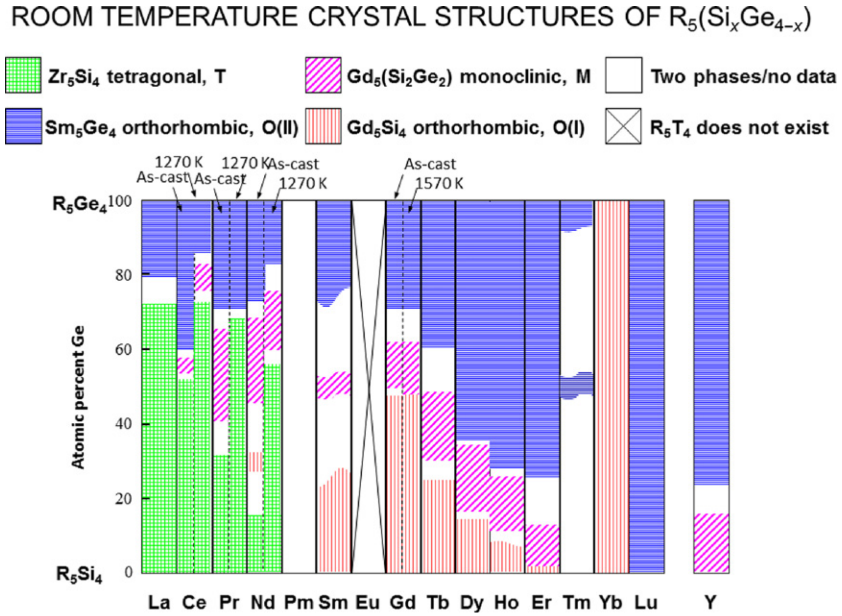

Rare-earth metals form intermetallic compounds with most of the metallic and semi-metallic elements in the periodic table. Due to chemical similarities among 16 of the 17 rare-earth elements (Sc frequently stands apart), they often form families of either isostructural or closely related compounds. Despite a long history of research in a broad field of intermetallics, a general theory that enables one to clearly relate composition and structure with physical properties of a multicomponent alloy is still lacking. The review describes a family of intermetallic materials formed by the rare-earth metals (R) and Group 14 elements (T, which can also include certain quantities of Group 13 and Group 15 elements substituted for Group 14 elements) at the R_5T_4 stoichiometry. The uniqueness of these compounds lies in their distinctly layered crystallography that can be judiciously controlled by chemistry, processing, and a variety of external triggers including temperature, pressure, and magnetic field. The materials exhibit a host of physical effects related to magnetic and structural transformations that can occur separately or simultaneously. Unlike many other extended families of intermetallic materials, present-day understanding of the composition–structure–physical property relationships of R_5T_4 compounds approaches predictive power, and in this chapter, examples of how one can predict some of the interesting physics based on the knowledge of chemical composition and crystal structure of these materials are shown. This review will be useful for researchers in the field of intermetallic compounds and materials engineers seeking materials that exhibit sharp changes of physical properties associated with first-order phase transitions.

Contents

Contents of Volumes 1–43

VOLUME 1: Metals

1978, 1st repr. 1982, 2nd repr. 1991; ISBN 0-444-85020-1

VOLUME 2: Alloys and intermetallics

1979, 1st repr. 1982, 2nd repr. 1991; ISBN 0-444-85021-X

VOLUME 3: Non-metallic compounds – I

1979, 1st repr. 1984; ISBN 0-444-85215-8

VOLUME 4: Non-metallic compounds – II

VOLUME 5

VOLUME 6

VOLUME 11: Two-hundred-year impact of rare earths on science

1988; ISBN 0-444-87080-6

VOLUME 12

1989; ISBN 0-444-87105-5

VOLUME 13

1990; ISBN 0-444-88547-1

VOLUME 14

VOLUME 15

CUMULATIVE INDEX, Vols. 1–15

VOLUME 16

VOLUME 17: Lanthanides/Actinides: Physics – I

VOLUME 18: Lanthanides/Actinides: Chemistry

1994; ISBN 0-444-81724-7

VOLUME 19: Lanthanides/Actinides: Physics – II

1994; ISBN 0-444-82015-9

VOLUME 20

VOLUME 21

VOLUME 22

VOLUME 23

VOLUME 24

VOLUME 25

VOLUME 26

VOLUME 27

VOLUME 28

VOLUME 29: The role of rare earths in catalysis

VOLUME 30: High-Temperature Superconductors – I

VOLUME 31: High-Temperature Superconductors – II

VOLUME 32

2001; ISBN 0-444-50762-0

VOLUME 33

2003; ISBN 0-444-51323-X

VOLUME 34

2004; ISBN 0-444-51587-9

VOLUME 35
2005; ISBN 0-444-52028-7

VOLUME 36
2006; ISBN 0-444-52142-9

VOLUME 37: Optical Spectroscopy
2007; ISBN 978-0-444-52144-6

VOLUME 38
2008; ISBN 978-0-444-52143-9

VOLUME 43

Index of Contents of Volumes 1–44

Chapter 259

Catalytic Behavior of Rare-Earth Borohydride Complexes in Polymerization of Polar Monomers

Sophie M. Guillaume[*], **Laurent Maron**[†] **and Peter W. Roesky**[‡]

[*]*Institut des Sciences Chimiques de Rennes, CNRS – Université de Rennes 1 (UMR 6226), Organometallics: Materials and Catalysis, Campus de Beaulieu, Rennes Cedex, France*

[†]*Laboratoire de Physique et Chimie de Nano-Objets, Université de Toulouse, INSA and CNRS, UMR5626 (IRSAMC), Toulouse, France*

[‡]*Institut für Anorganische Chemie and Helmholtz Research School: Energy-Related Catalysis, Karlsruher Institut für Technologie (KIT), Karlsruhe, Germany*

Chapter Outline

Handbook on the Physics and Chemistry of Rare Earths, Vol. 44.
http://dx.doi.org/10.1016/B978-0-444-62711-7.00259-0

1. HISTORICAL INTRODUCTION

1.1. General Context of the Use of Rare-Earth Complexes in Polymerization

Rare-earth[1] complexes, both divalent and trivalent ones, have been investigated in polymerization for over two decades. In the early 1990s, MacLain revealed the potential of rare-earth alkoxide compounds, namely $[R_5(\mu\text{-O})(OiPr)_{13}]$ ($R = Y$, La, Sm, Dy, Er, Yb) (Kritikos et al., 2001; Poncelet et al., 1989) and $[Y(OCH_2CH_2OEt)_3]$, in the ring-opening polymerization (ROP) of lactones (δ-valerolactone (VL), ε-caprolactone (CL)) and diesters (glycolide, D-Lactide, L-Lactide) (McLain and Drysdale, 1991, 1992; McLain et al., 1992, 1994). Within the same period of time, Yasuda reported the first investigations on the living polymerization of polar and nonpolar monomers promoted by discrete organometallic rare-earth initiators. In particular, $[(Cp^*)_2RMe(THF)]$ complexes ($R = Y$, Sm, Yb, Lu; $Cp^* = \eta^5\text{-}C_5Me_5$) (Evans et al., 1986, 1998; Schumann et al., 1995; Watson, 1983), enabled the living polymerization of lactones such as VL and CL affording polyesters of molar mass values ($\overline{M}n$) up to 50,000 g mol^{-1} with dispersity values ($Đ_M$, $\overline{M}w/\overline{M}n$) below 1.07 (Yamashita et al., 1996; Yasuda et al., 1993a). The same complexes also allowed the first living, highly syndiospecific ($rr > 90\%$) polymerization of methylmethacrylate (MMA) affording poly(methylmethacrylate) (PMMA) featuring $\overline{M}n = 65{,}000 - 120{,}000\,g\,mol^{-1}$ with $\overline{M}w/\overline{M}n = 1.03 - 1.05$ (Yasuda et al., 1992). In addition, rare-earth metal hydrides exhibiting high activity and unique behavior in various catalytic processes, among which polymerization reactions, were already the focus of much attention at that time. Thus, $[\{(Cp^*)_2SmH\}_2]$ ($Cp = \eta^5\text{-}C_5H_5$) (Evans et al., 1983; Jeske et al., 1985; Schumann et al., 1995) initiated the ROP of CL ($\overline{M}n \leq 142{,}200\,g\,mol^{-1}$-uncorrected $\overline{M}n_{SEC}$ value, $\overline{M}w/\overline{M}n = 1.05$) yet with a lower efficiency than its alkyl homologue

---

[1] Rare-earth metals herein symbolized by "R" refer to group III metals including in addition to scandium and yttrium, the fifteen lanthanide elements from lanthanum to lutetium.

(Yamashita et al., 1996). Also, this samarium metallocene hydride was shown to afford at 0 °C high molar mass PMMA ($\overline{M}n \leq 563{,}000\,g\,mol^{-1}$) with $\overline{M}w/\overline{M}n$ values in the 1.02–1.05 range, with a high activity and with a syndiotacticity exceeding 95% (Yasuda et al., 1992, 1993a,b). Taking advantage of the living polymerization process, random, and AB or ABA block copolymers of acrylates and/or lactones were next prepared from these trivalent organolanthanide complexes (Ihara et al., 1995; Tanabe et al., 2002; Yasuda et al., 1993b). These pioneering investigations, on both alkoxide, alkyl and hydride derivatives of rare-earth metal initiators, in the challenging field of living polymerizations, then revealed valuable results. All subsequent studies on the polymerization of polar and nonpolar monomers catalyzed by rare-earth metal-based systems were then inspired by these original works.

Ensuing advances were later reviewed, especially by Yasuda (Yasuda and Ihara, 1997; Yasuda and Tamai, 1993, 2000, 2002) and Okuda (Arndt et al., 2002; Okuda et al., 2001). Typical examples of organolanthanide complexes reported as initiators in the polymerization of polar and nonpolar monomers include metallocenes hydride and alkyl derivatives, including heterobimetallic species, such as for instance the above-mentioned [$\{(Cp^*)_2RH\}_2$] (R=La, Nd, Sm, Lu) and [$(Cp^*)_2RMe(THF)$] (R=Y, Sm, Yb, Lu), and [$\{(Cp)_2YbMe\}_2$] [$(Cp)_2YbMe(THF)$], [$\{(Cp)_2RMe\}_2$] (R=Y, Yb), [$(Cp^*)_2R(CHTMS_2)$] (R=Y, Sm), [$(Cp^*)La(CHTMS_2)_2$], [$\{(\eta^5{:}\eta^1\text{-}C_5Me_4SiMe_2NCMe_3)R(\mu\text{-}H)(THF)\}_2$] (R=Y, Lu), [$(Cp^*)_2R(\mu\text{-}Me)_2AlMe_2$] (R=Y, Sm, Yb, Lu), and [$Me_2Si\{[2,4\text{-}(TMS)_2C_5H_2][3,4\text{-}(TMS)_2\text{-}C_5H_2]\}Sm(THF)_2$] (Fig. 1; Schumann et al., 1995). Whereas CL and MMA have been, at the early stage, the most studied monomers, other polar as well as nonpolar monomers have been considered next, especially lactones (β-propiolactone (PL), VL), carbonates (trimethylene carbonate (TMC), dimethyl-TMC), oxiranes (ethylene oxide, propylene oxide, epichloridrin), alkyl (methyl, ethyl, isopropyl, *t*-butyl) (meth)acrylates, as well as olefins (ethylene, 1-hexene, styrene), conjugated dienes (butadiene, isoprene), or acetylene derivatives. The latest

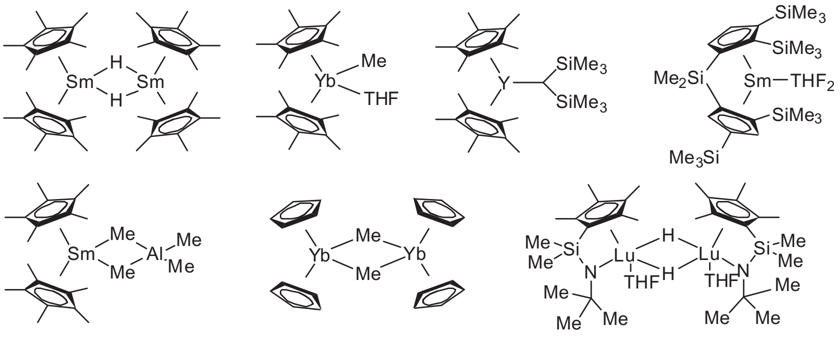

FIGURE 1 First typical organolanthanide complexes used as initiators in the polymerization of polar and nonpolar monomers.

contributions, in particular from Hou (Hou and Nishiura, 2010; Hou and Wakatsuki, 2002; Hou et al., 2006), Endo (Nomura and Endo, 1998), Agarwal and Greiner (Agarwal and Greiner, 2002; Agarwal et al., 2000), Kerton (Kerton et al., 2004), or Edelmann (Edelmann, 2009, 2010, 2011), have addressed more specific domains. Following the developments in organometallic synthesis of rare-earth complexes, original neutral or cationic initiators, either mono- or bicomponent catalytic systems, showed novel activity and regio- and/or stereo-selectivity in (co)polymerization; these include half-metallocene complexes bearing mixed Cp*-monodentate anionic ligands or cyclopentadienyl (Cp)-amido and -phosphido linked ligands, as well as Cp-free complexes such as [(COT)RCl] (COT = cyclooctatetraenyl). Alongside hydrides, alkyls, alkoxides or aryloxides, amides and halogenides, like in $[R(NTMS_2)_3]$ and $[SmI_2]$, were also introduced as active function. Indeed, although highly efficient in polymerization, hydride complexes of the rare-earth metals are, in comparison to other species, more sensitive and require good expertise for their isolation and subsequent handling (Ephritikhine, 1997; Konkol and Okuda, 2008; Schumann et al., 1995). This is one of the reasons that explain the burst of the investigations of non-hydride rare-earth complexes in polymerization catalysis. Note that among these latter, alkoxide or aryloxide derivatives have stimulated many efforts since they are the most easily prepared.

Tetrahydroborate -namely tetrahydridoborato, commonly referred to as borohydride -complexes of transition metals, including of f-elements, have not been that extensively studied as reflected by the limited number of reviews dedicated to this topic (Makhaev, 2000; Marks and Kolb, 1977; Visseaux and Bonnet, 2011; Xhu and Lin, 1996) or addressing it within a more general context of the related hydride complexes (Arndt and Okuda, 2002; Edelmann, 2009; Ephritikhine, 1997). Indeed, the chemistry of transition metal borohydride species has been essentially pursued to provide reactive hydride compounds. Rare-earth borohydride complexes, have been first synthesized as the inorganic compounds $[R(BH_4)_3]$ (Zange, 1960) and as solvates, $[R(BH_4)_3(THF)_3]$ (**1**; Gmelin Handbook, 1991; Mirsaidov et al., 1976, 1986b). However, it is only many years later that this chemistry has been revisited to the profit of organometallic rare-earth complexes (Cendrowski-Guillaume et al., 1998, 2000, 2002, 2003; Palard et al., 2005; Richter and Edelmann, 1996; Schumann et al., 1998). This whole pioneering work, up to the late 1990s, has really launched the organometallic chemistry of rare-earth borohydrides, as recently reviewed (Visseaux and Bonnet, 2011).

1.2. Significant Features and Advantages of the Borohydride Ligand

The tetrahydroborate ion, BH_4^-, the simplest known anionic boron hydride, is usually covalently coordinated to transition metal atoms through a B–H–metal three center-two electron bridging bond in an η^1, η^2, or η^3 mode

(Makhaev, 2000; Marks and Kolb, 1981; Parry and Kodama, 1993; Xhu and Lin, 1996). In most of the rare-earth borohydride complexes, the borohydride ligand is di- or tri-hapto bonded to a unique metal center (terminal BH_4^-), or bridging two metals in various ligation modes, $(\mu_2\text{-H})_3BH$ (Skvortsov et al., 2007a), $(\mu_2\text{-H})_2BH(\mu_3\text{-H})$ (Skvortsov et al., 2007a), $(\mu_2\text{-H})_2B(\mu_2\text{-H})_2$ (Khvostov et al., 1998; Visseaux et al., 2010), or $(\mu_2\text{-H})_2B(\mu_3\text{-H})_2$ (Cendrowski-Guillaume et al., 1998; Jaroschik et al., 2010). This unique mono-, bi-, or tri-dentate configuration of the bridging hydrogen atoms may be related to important species in catalytic transformations as a reminiscence of the reactivity of hydride homologues. Of high significance in rare-earth borohydride chemistry, tetrahydroborate complexes reacting with acidic substrates are valuable selective reducing agents, and also often play a major role as catalysts in reactions such as hydrogenation.

More importantly to the present considerations, BH_4^- features several advantages over other anionic ligands. On one hand, the borohydride ligand is isoelectronic with methane thus serving as a structural model in the C–H activation of saturated hydrocarbons (Makhaev, 2000). On the other hand, BH_4^- is considered as a pseudo halide. It is isosteric with Cl^-, yet it is much more electron donating (Cendrowski-Guillaume et al., 2000; Xhu and Lin, 1996). This highly valuable characteristic has been exploited for the isolation of otherwise inaccessible discrete 4f-element species that thus feature a higher degree of covalence. Furthermore, owing to the lower propensity of BH_4^- to form bridging compounds in comparison to the corresponding halide and alkoxide ligands, and thanks to the larger ionic radius (and therefore wider coordination sphere) of rare-earth metals, well-defined non-aggregated 4f-element derivatives thus become accessible with borohydride ligand(s). Clusters -often encountered in rare-earth alkoxide species- are therefore avoided. All these properties impart greater solubility to rare-earth complexes in nonpolar solvents. Last, but not least, formation of *ate* species is hence much less favored in borohydride chemistry, one reason being also the lower solubility of alkali metal borohydride salts which are thereby more easily removed by-products. Discrete neutral rare-earth borohydride complexes are thus quite (yet not always) readily accessible (Ephritikhine, 1997; Makhaev, 2000; Marks and Kolb, 1977; Visseaux and Bonnet, 2011; Xhu and Lin, 1996).

Also, borohydride species are rather attractive given that the presence and the structure of the borohydride ligand(s) can be easily assessed analytically. ^1H and ^{11}B NMR spectroscopies allow the detection of the borohydride ligand upon displaying a typical pattern in the ^1H NMR spectrum consisting of a broad quartet ($J_{BH} = 80\text{–}90$ Hz) arising from the quadrupolar ^{11}B nucleus (nuclear spin quantum number of 3/2). However, the rapid interchange of the bridging and terminal hydrogen atoms precludes distinguishing the exact structure between bidentate and tridentate coordination. Nevertheless, FTIR spectroscopy has demonstrated that these two coordination modes display quite distinct and characteristic B–H vibrational bands (Ephritikhine, 1997;

Makhaev, 2000; Marks and Kolb, 1977). Ultimately, X-ray analysis nowadays allows the ligation mode to be unambiguously determined as hinted by the R—B bond distance(s), and ideally by the location of the refined hydrogen atoms (Ephritikhine, 1997; Makhaev, 2000; Marks and Kolb, 1977; Xhu and Lin, 1996). These molecular spectroscopic tools provide a highly valuable "handle" for both the characterization of borohydride reaction products and the *in situ* monitoring of experiments, thus allowing identification of relevant intermediates leading to the clarification of reaction mechanisms.

Making the parallel between the bridging hydrogen atoms within the bonding mode of the BH_4^- ligand and those within discrete rare-earth hydride compounds (Arndt and Okuda, 2002; Makhaev, 2000; Marks and Kolb, 1977; Xhu and Lin, 1996), while further taking into account the high performances of the rare-earth hydride species in polymerization as mentioned above, exploring the ability of rare-earth borohydrides to promote polymerization thus appeared appealing. In light of the originality and versatility of this unusual anionic BH_4^- ligand featuring a hydridic character, well-defined rare-earth borohydride complexes have thus been developed to be used as initiators in the polymerization of polar monomers, and especially of cyclic esters and MMA (Fig. 2), as well as of nonpolar monomers. Expansion of these polymerization studies reciprocally impacted the growth of organometallic chemistry of rare-earth borohydride derivatives. The synthesis and characterization of inorganic and organometallic borohydride rare-earth complexes has been previously addressed (Arndt and Okuda, 2002; Ephritikhine, 1997; Makhaev, 2000; Marks and Kolb, 1977; Schumann et al., 1998; Visseaux and Bonnet, 2011; Xhu and Lin, 1996) and some aspects of the catalytic behavior of rare-earth borohydrides in polymerization have been recently reviewed by Visseaux and Bonnet (2011).

1.3. Scope of the Review

The present chapter is focusing on the most recent achievements (up to the early beginning of 2013) in the synthesis of rare-earth borohydride complexes designed for the polymerization of polar monomers. The synthesis and characterization of inorganic and organometallic rare-earth borohydride

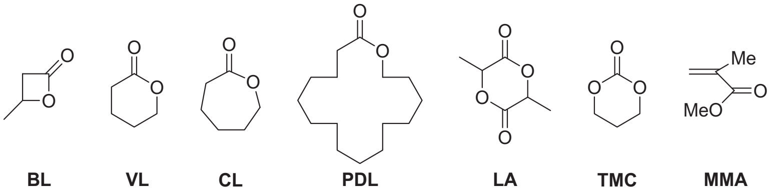

FIGURE 2 Typical polar and nonpolar monomers investigated in polymerization initiated by rare-earth complexes.

complexes is first presented in the following section, in light of the latest advances and in relevance to the compounds used as initiators in polymerization reactions described in the third section. Special emphasis is given to the strategies followed to improve the control and the livingness of the polymerization especially in terms of tailor-made ligands, and in turn, to access to original well-defined end-functionalized (co)polymers. Progress in understanding and tuning their mechanistic behavior as (pre)initiators in polymerization catalysis, both from an experimental approach combined with computational insights, is assessed. Efforts are also paid to demonstrate that theoretical DFT calculations are nowadays an essential tool to better understand and model polymerization mechanisms. Up-to-date experimental and computational advances of the past decade are comprehensively covered in the present tutorial review.

2. SYNTHESIS OF RARE-EARTH BOROHYDRIDE COMPLEXES

The general aspects of the synthesis and characterization of rare-earth borohydride complexes have been recently described (Visseaux and Bonnet, 2011) and only some essential features are addressed here for the understanding of the review. Thus, we do not present a full account of rare-earth element borohydride complexes but we rather focus only on those which are relevant as initiators for the polymerization of polar monomers.

2.1. Inorganic Borohydride Complexes

The trisborohydrides of the rare-earth elements $[R(BH_4)_3]$ (R = Y, Sm, Eu, Gd, Tb, Dy, Ho, Er, Tm, Yb, Lu) were initially prepared in 1960 by Zange upon reacting rare-earth metal alkoxides $[R(OCH_3)_3]$ with B_2H_6 (Zange, 1960). In the 1970s and 1980s Mirsaidov and coworkers reported in several publications a more convenient approach to the solvates $[R(BH_4)_3(THF)_3]$ (**1R**) by starting from RCl_3 and $NaBH_4$ (Scheme 1) (Mirsaidov and Kurbonbekov, 1985; Mirsaidov and Rakhimova, 1978; Mirsaidov et al., 1976, 1978, 1982, 1986a,b). A similar, yet optimized, synthetic protocol was also published by Ephritikhine and coworkers (Cendrowski-Guillaume et al., 2000). In contrast to the other rare-earth compounds, the scandium borohydride $[Sc(BH_4)_3(THF)_2]$ (**1Sc′**) (Lappert et al., 1983; Lobkovski et al., 1977) features only 2 equiv of THF coordinated to the central metal.

The divalent bisborohydride complexes $[R(BH_4)_2(THF)_2]$ (**2R**) (R = Sm, Eu, Yb) were originally reported in 1999 (Makhaev and Borisov, 1999).

$$RCl_3 + 3\ NaBH_4 \xrightarrow{THF} [R(BH_4)_3(THF)_3] + 3\ NaCl$$

1R

SCHEME 1 General synthesis of $[R(BH_4)_3(THF)_3]$ (**1**).

At that time, they were prepared from $[NaR(BH_4)_4(DME)_4]$ (R = Sm, Eu, Yb) by thermal reduction at 150–200 °C in vacuum. Unfortunately, the characterization was incomplete. Recently, Nief and Visseaux reported a more convenient approach to $[Sm(BH_4)_2(THF)_2]$ (**2Sm**), which was obtained from $[Sm(BH_4)_3(THF)_3]$ (**1Sm**) and Sm metal (Scheme 2) (Jaroschik et al., 2010). The complex was then fully characterized including its solid-state structure featuring an infinite monodimensional polymer with two tridentate BH_4^- in the bridging position between two six-coordinated Sm atoms. $[Yb(BH_4)_2(THF)_2]$ (**2Yb**) is accessible in a similar way (Marks et al., 2012) while $[Eu(BH_4)_2(THF)_2]$ (**2Eu**) was prepared by two synthetic pathways. Compound **2Eu** can either be obtained in a reductive pathway from $EuCl_3$ and $NaBH_4$ in a high yield or by a salt metathesis from $[EuI_2(THF)_2]$ and $NaBH_4$ (Scheme 2) (Marks et al., 2012).

The divalent thulium compound $[Tm(BH_4)_2(DME)_2]$ (**2Tm′**) was only prepared recently upon reduction of $[Tm(BH_4)_3(THF)_3]$ (**1Tm**) with C_8K or via salt metathesis from TmI_2 and KBH_4 in DME (Momin et al., 2011) (Scheme 2). The solid-state structure displays a discrete molecule with two DME ligands bonded to Tm^{II}.

The monocationic trivalent rare-earth metal borohydrides $[R(BH_4)_2(THF)_5][BPh_4]$ (**3R**) were obtained by Okuda and coworkers upon protonation of $[R(BH_4)_3(THF)_3]$ (**1R**, R = Y, La, Nd, Sm) with 1 equiv of the Brønsted acid $[NEt_3H][BPh_4]$ in THF (Robert et al., 2008), as sketched in Scheme 3.

2.2. Organometallic Borohydride Complexes

Although several synthetic routes to lanthanide borohydride derivatives have been described (Visseaux and Bonnet, 2011), the most popular way remains,

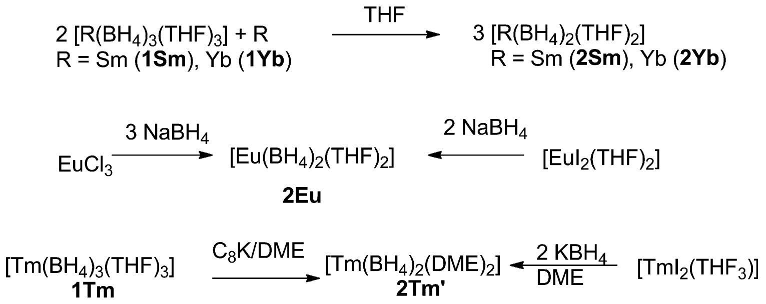

SCHEME 2 Synthesis of $[R(BH_4)_2(THF)_2]$ (**2R**) and $[Tm(BH_4)_2(DME)_2]$ (**2Tm′**).

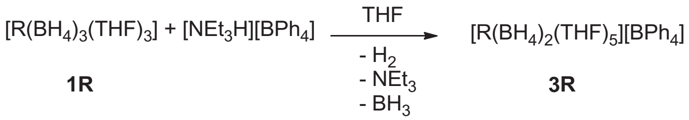

SCHEME 3 Synthesis of $[R(BH_4)_2(THF)_2][BPh_4]$ (**3R**).

$$[R(BH_4)_3(THF)_3] + ML \longrightarrow [(L)R(BH_4)_2] + MBH_4$$

$$[R(BH_4)_3(THF)_3] + 2\ ML \longrightarrow [(L)_2R(BH_4)] + 2\ MBH_4$$

M = alkali metal; L = ligand

SCHEME 4 General synthesis of organometallic rare-earth borohydride complexes.

$$\underset{\mathbf{2Sm}}{[Sm(BH_4)_2(THF)_2]} + KCp^* \xrightarrow[-\ KBH_4]{THF} \underset{\mathbf{4Sm}}{[\{(Cp^*)Sm(\mu\text{-}BH_4)(THF)_2\}_2]}$$

SCHEME 5 Synthesis of the monocyclopentadienyl complex $[\{Cp^*Sm(\mu\text{-}BH_4)(THF)_2\}_2]$ (**4Sm**).

by far, the salt metathesis reaction of an alkali metal derivative of a given ligand with $[R(BH_4)_3(THF)_3]$ (**1R**) (Scheme 4).

The long-time most popular ligand in organometallic chemistry of the rare-earth elements is the pentamethylcyclopentadienyl (C_5Me_5, Cp*) ligand and its related derivatives. In divalent rare-earth element chemistry, the monocyclopentadienyl complex $[\{(Cp^*)Sm(\mu\text{-}BH_4)(THF)_2\}_2]$ (**4Sm**) was only reported recently. It was synthesized by Nief, Visseaux, and coworkers in 43% yield from $[Sm(BH_4)_2(THF)_2]$ (**2Sm**) with KCp* in THF in a 1:1 ratio (Scheme 5) (Jaroschik et al., 2010).

The metallocene complexes of the trivalent rare-earth elements have been prepared in different ways, for example $[(Cp^*)_2Sm(BH_4)(THF)]$ (**5Sm**) was obtained either from $[SmCl_3(THF)_2]$, NaCp*, and $NaBH_4$ in THF (Schumann et al., 1998), or from $[Sm(BH_4)_3(THF)_3]$ and NaCp* (Palard et al., 2004). In a similar approach, metallocenes with a different substitution pattern on the five-membered ring were synthesized. Metallocenes with the bulkier cyclopentadienyl ligands $[(Cp^{*Pr})_2Nd(BH_4)(THF)]$ (**6Nd**), $[(Cp^{Ph3})_2Sm(BH_4)(THF)]$ (**7Sm**), and $[(Cp^{iPr4})_2Sm(BH_4)]$ (**8Sm**) ($Cp^{*Pr}=C_5Me_4(^nPr)$, $Cp^{Ph3}=C_5H_2Ph_3$-1,2,4, $Cp^{iPr4}=C_5H^iPr_4$) were prepared from the corresponding potassium cyclopentadienyls (KCp^{*Pr}, KCp^{Ph3}, KCp^{iPr4}) and $[R(BH_4)_3(THF)_3]$ (**1R**) (Barbier-Baudry et al., 2006). Only $[(Cp^{Ph3})_2Sm(BH_4)(THF)]$ (**7Sm**) was isolated.

Although metallocenes of the rare-earth elements are usually much more common than monocyclopentadienyl complexes, the latter class of compounds was well investigated and used as catalysts in the ROP of polar monomers. Thus, a significant number of monocyclopentadienyl bisborohydride compounds were prepared in which different substitution patterns on the five-membered ring have been achieved. In this context, the samarium complex $[(Cp^{Ph3})Sm(BH_4)_2(THF)_2]$ (**9Sm**) was prepared by Visseaux and coworkers upon reaction of $[Sm(BH_4)_3(THF)_3]$ (**1Sm**) with the appropriate amount of KCp^{Ph3} (Barbier-Baudry et al., 2006). The isopropyl substituted

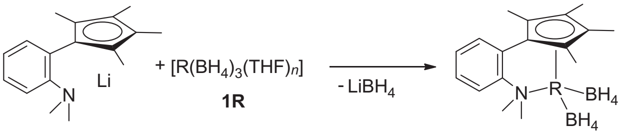

R = Sc (**11Sc**), Sm (**11Sm**)

SCHEME 6 Synthesis of the linked half-sandwich complexes [(C_5Me_4-C_6H_4-*o*-NMe_2)R$(BH_4)_2$] (R = Sc (**11Sc**), Sm (**11Sm**)).

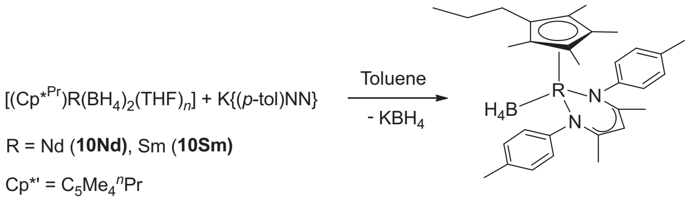

R = Nd (**12Nd**), Sm (**12Sm**)

SCHEME 7 Synthesis of heteroleptic β-diketiminate lanthanide complexes.

$$[\mathrm{MeY(THF)_6}][\mathrm{BPh_4}]_2 + \mathrm{NaBH_4} \xrightarrow[\text{- NaBPh}_4]{\text{THF}} [\mathrm{MeY(BH_4)(THF)_5}][\mathrm{BPh_4}]$$

14Y

SCHEME 8 Synthesis of the ionic species [MeY$(BH_4)(THF)_5$][BPh_4] (**14Y**).

compounds [(Cp^{*Pr})Nd$(BH_4)_2(THF)_2$] (**10Nd**), [(Cp^{*Pr})Sm$(BH_4)_2(THF)_2$] (**10Sm**) (Bonnet et al., 2004a) and linked half-sandwich complexes [(C_5Me_4-C_6H_4-*o*-NMe_2)R$(BH_4)_2$] (R = Sc (**11Sc**), Sm (**11Sm**)) (Jian et al., 2010) reported by Cui and coworkers, were all obtained in a similar way (Scheme 6).

Visseaux and coworkers reported on the heteroleptic β-diketiminate lanthanide complexes [(Cp^{*Pr}){(*p*-Tol)NN}R(BH_4)] ((*p*-Tol)NN = (*p*-$CH_3C_6H_4$)NC(Me)CHC(Me)N, R = Nd (**12Nd**), Sm (**12Sm**)) (Scheme 7) (Bonnet et al., 2004b). The complexes were prepared from the direct metathesis reaction of their monocyclopentadienyl precursors, [(Cp^{*Pr})Sm$(BH_4)_2(THF)_2$] (**10Sm**) and [(Cp^{*Pr})Nd$(BH_4)_2(THF)_2$] (**10Nd**), respectively, with K{(*p*-Tol)NN} in good yields (Scheme 7). The corresponding triphenyl derivative [(Cp^{Ph3}){(*p*-Tol)NN}Sm(BH_4)] (**13Sm**) was obtained in a one-pot reaction from [Sm$(BH_4)_3(THF)_3$] (**1Sm**), KCp^{Ph3}, and {(*p*-Tol)NN}K (Barbier-Baudry et al., 2006).

An non-cyclopentadienyl but organometallic ionic species, [MeY$(BH_4)$$(THF)_5$][$BPh_4$] (**14Y**), was synthesized in moderate yield by Okuda and coworkers upon reaction of the dicationic methyl complex [MeY$(THF)_6$][BPh_4]$_2$ with 1 equiv $NaBH_4$ (Scheme 8) (Kramer et al., 2008). The starting material $[MeY(THF)_6][BPh_4]_2$ was generated by protonation of $[Li_3YMe_6(THF)_n]$ with $[NEt_3H][BPh_4]$, a typical reagent used for the synthesis of cationic rare-earth species (Cendrowski-Guillaume et al., 1998, 2002).

2.3. Post-Metallocene Borohydride Complexes

Post-metallocene complexes of di- and trivalent rare-earth element compounds were synthesized. The divalent thulium trispyrazolylborate compound $[(Tp^{tBu,Me})Tm(BH_4)(THF)]$ (**15Tm**) ($Tp^{tBu,Me}$ = tris(2-*t*Bu-4-Me)pyrazolylborate) was obtained by Bonnet, Nief, and coworkers from $[Tm(BH_4)_2(DME)_2]$ (**2Tm′**) and ($KTp^{tBu,Me}$) (Momin et al., 2011). Another popular non-cyclopentadienyl ligand is the amidopyridine (Ap*) ligand developed by Kempe and coworkers. Salt elimination of Ap*K {Ap*H = (2,6-diisopropyl-phenyl)-[6-(2,4,6-triisopropyl-phenyl)-pyridin-2-yl]-amine} with $[YbI_2(THF)_3]$ leads to the ytterbium aminopyridinato complex $[(Ap^*)YbI(THF)_2]_2$ (**16Yb**) (Scott and Kempe, 2005) which was treated with $NaBH_4$ to give *in situ* the corresponding borohydride complex (Guillaume et al., 2007). The same groups also similarly generated *in situ* the trivalent borohydride derivatives of $[(Ap^*)LaBr_2(THF)_3]$ (**17La**) and $[(Ap^*)LuCl_2(THF)_2]$ (**18Lu**) (Scheme 9).

A very simple approach was reported by Yuan and coworkers (Scheme 10). They prepared the aryloxide lanthanide borohydrides $[(ArO)R(BH_4)_2(THF)_2]$ (Ar = C_6H_2-*t*-Bu_3-2,4,6; R = Er (**19Er**), Yb (**19Yb**)), simply by a “one-pot” reaction of RCl_3, $NaBH_4$, and ArONa in THF in low yield (Yuan et al., 2006a).

The bisborohydride complexes of the bisphosphiniminomethanide ligand developed by Roesky and coworkers, $[\{CH(PPh_2NTMS)_2\}La(BH_4)_2(THF)]$ (**20La**) and $[\{CH(PPh_2NTMS)_2\}R(BH_4)_2]$ (R = Y (**20Y**), Lu (**20Lu**)), were synthesized by two different synthetic routes (Scheme 11). The lanthanum and lutetium complexes were prepared from $[R(BH_4)_3(THF)_3]$ (**1R**) and

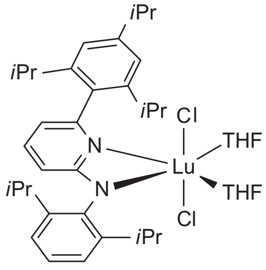

$[Ap^*LuCl_2(THF)_2]$
(18Lu)

SCHEME 9 Amidopyridinato complexes exemplified with $[(Ap^*)LuCl_2(THF)_2]$ (**18Lu**).

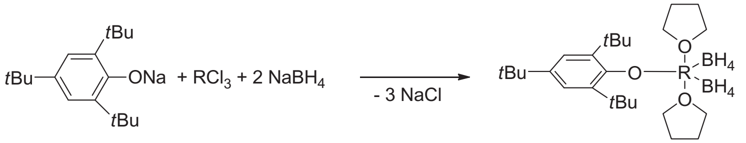

R = Er (**19Er**), Yb (**19Yb**)

SCHEME 10 Synthesis of the aryloxide lanthanide borohydrides [(ArO)R$(BH_4)_2(THF)_2$].

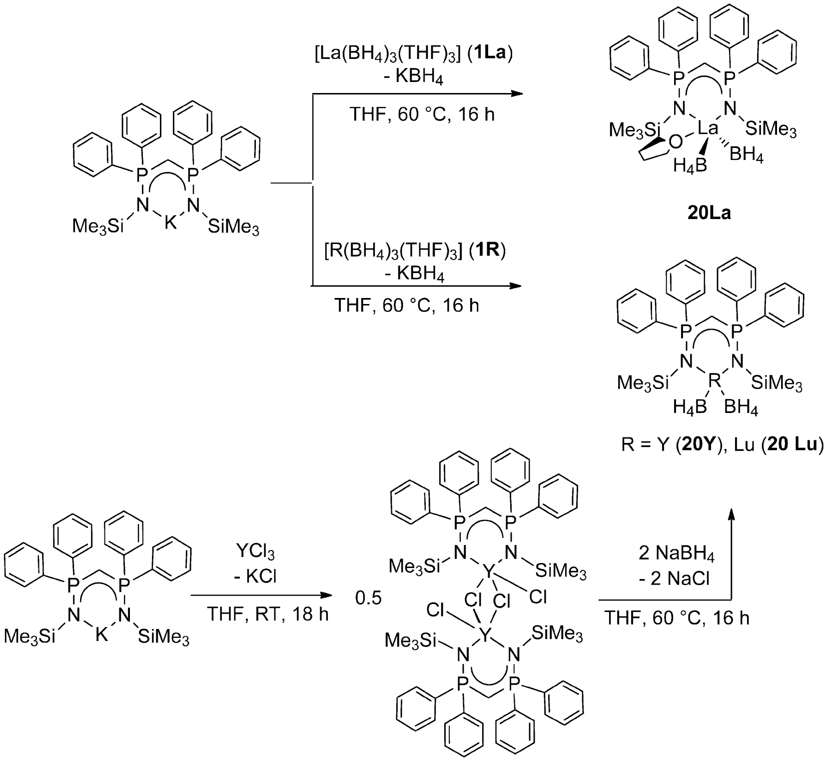

SCHEME 11 Different approaches for the synthesis of bisphosphiniminomethanide complexes.

K{CH$(PPh_2NTMS)_2$} in moderate to good yields, whereas the yttrium analogue was obtained from *in situ* prepared [{CH$(PPh_2NTMS)_2$}$YCl_2]_2$ and $NaBH_4$ (Jenter et al., 2010).

Amidinates and guanidinates are among the most popular ligands in post-metallocene chemistry of the rare-earth elements (Edelmann et al., 2002). Not surprisingly, these classes of compounds have been studied as initiators in the ROP of polar monomers. The guanidinate complexes [{$(TMS)_2NC(NCy)_2$}R$(BH_4)_2(THF)_2$] (R = Er (**21Er**) Yb (**21Yb**)) were synthesized in moderate yields by Yuan and coworkers from [R$(BH_4)_3(THF)_3$] (**1R**) with the sodium guanidinate [{$(TMS)_2NC(NCy)_2$}Na] in a 1:1 molar ratio in THF (Yuan et al., 2006b).

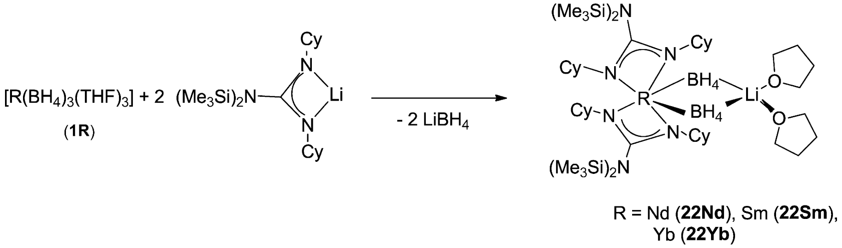

SCHEME 12 Synthesis of some selected guanidinate complexes.

By using the corresponding lithium salt [{(TMS)$_2$NC(NCy)$_2$}Li] instead of the sodium salt, the related *ate* complexes [{(TMS)$_2$NC(NCy)$_2$}$_2$R (μ-BH$_4$)$_2$Li(THF)$_2$] (R = Nd (**22Nd**), Sm (**22Sm**), Yb (**22Yb**)) were formed (Scheme 12) (Skvortsov et al., 2007b). The analogous isopropyl compounds [{(TMS)$_2$NC(N*i*Pr)$_2$}$_2$R(BH$_4$)$_2$Li(THF)$_2$] (R = Nd (**23Nd**), Sm (**23Sm**)) were synthesized by treatment of [R(BH$_4$)$_3$(THF)$_3$] (**1R**) with lithium *N*,*N*′-diisopropyl-*N*′-bis(trimethylsilyl)guanidinate in toluene (Skvortsov et al., 2007a).

The Mountford group reported on a number of polydentate nitrogen-based ligands. Thus, reaction of [Sm(BH$_4$)$_3$(THF)$_3$] (**1Sm**) with diamide–diamine ligands (2-C$_5$H$_4$N)CH$_2$N(CH$_2$CH$_2$NTMS)$_2$ (N$_2$NN^{TMS}) and (2-C$_5$H$_4$N)CH$_2$N (CH$_2$CH$_2$NMes)$_2$ (N$_2$NN^{Mes}) gave the dimeric compounds [{(N$_2$NN^{TMS})Sm (BH$_4$)}$_2$] (**24Sm**) and [{(N$_2$NN^{Mes})Sm(BH$_4$)$_2$Li}$_2$] (**25Sm**) (Scheme 13) (Bonnet et al., 2005b). In a similar way the diaminobis(phenoxide) ligand O$_2$NN^{py} (H$_2$O$_2$NN^{py} = (2-C$_5$H$_4$N)CH$_2$N{2-HO-3,5-C$_6$H$_2$^{t}Bu$_2$}$_2$) was coordinated to the various rare-earth metals to afford complexes of composition [{(O$_2$NN^{py})R(μ-BH$_4$)(THF)$_n$}$_2$] [R = Y, *n* = 0.5 (**26Y**); Nd, *n* = 1 (**26Nd**); Sm, *n* = 0 (**26Sm**)] (Scheme 13) (Bonnet et al., 2005a). Monomeric samarium borohydride complexes [(O$_2$N^L)Sm(BH$_4$)(THF)] (O$_2$N^L = R′CH$_2$N(CH$_2$-2-*o*-3,5-C$_6$H$_2$^{t}Bu$_2$)$_2$ where R′ = CH$_2$OMe, CH$_2$NMe$_2$, (2-C$_5$H$_4$N), or Et, with L = OMe (**27Sm**), NMe$_2$ (**28Sm**), py (**29Sm**)), and [(O$_2$N^{nPr})Sm(BH$_4$) (THF)$_2$] (**30Sm**) with the same and related bis(phenolate)amine ligands were obtained from [(BH$_4$)$_3$Sm(THF)$_3$] (**1Sm**) and Na$_2$O$_2$N^L (L = py, OMe, NMe$_2$, ^{n}Pr) (Scheme 13) (Dyer et al., 2010).

A similar approach was recently published by Trifonov, Carpentier, and coworkers. By using the diaminobis(phenolate) ligands [O$_2$N$_2$]^1 ({CH$_2$N (Me)CH$_2$-3,5-Me,*t*Bu-C$_6$H$_2$O}$_2$) and [O$_2$N$_2$]^2 (C$_5$H$_4$NCH$_2$N{CH$_2$-3,5-Me, *t*Bu-C$_6$H$_2$O}$_2$) the heterobimetallic borohydrido neodymium complexes [{(O$_2$N$_2$)^{1}Nd(BH$_4$)(μ-BH$_4$)Li(THF)}$_2$] (**31Nd**) and [(O$_2$N$_2$)^{2}Nd(BH$_4$)(μ-BH$_4$) Li(THF)$_2$] (**32Nd**) (Scheme 14) were synthesized from the lithium salts of the ligands and [Nd(BH$_4$)$_3$(THF)$_3$] (**1Nd**) (Sinenkov et al., 2011). Also, Sun and coworkers reported on tetrahydrosalen supported rare-earth metal complexes. They reacted the sodium salt of the ligand 6,6′-[ethane-1,2-diyl-bis(methylazanediyl)]bis(methylene)bis(2,4-di-tert-butylphenolate) (N$_2$O$_2$) with the lanthanide trichlorides RCl$_3$ (R = Er, Yb) in DME to form the

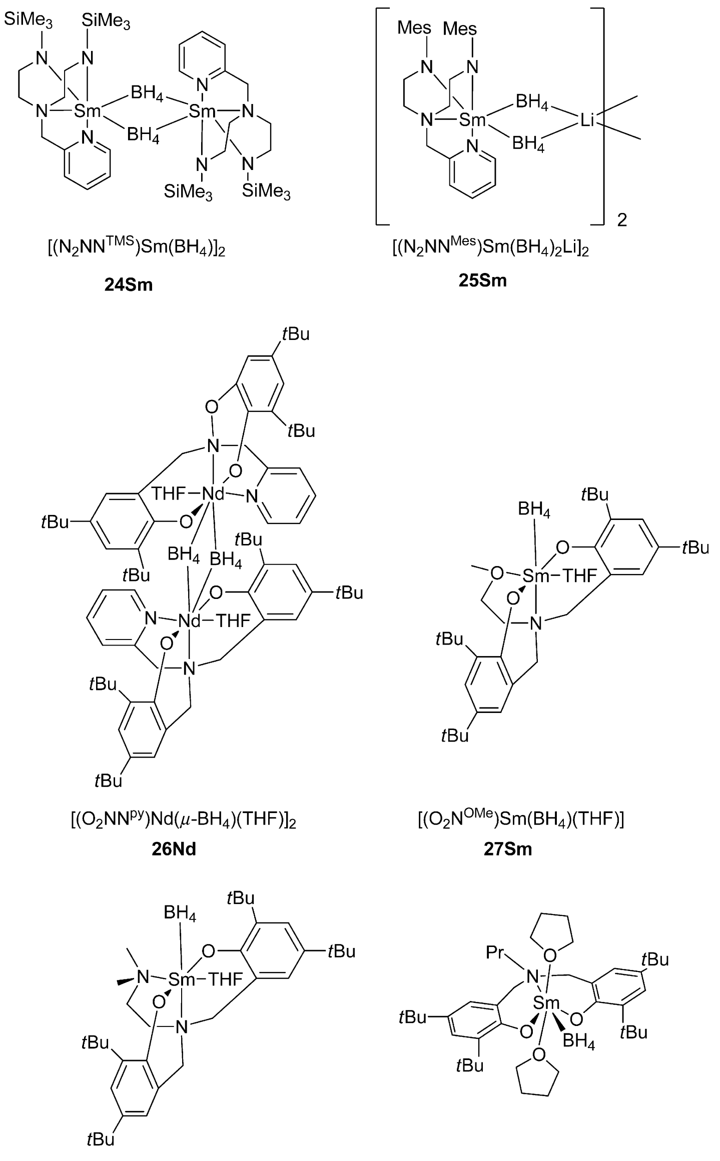

$[(N_2NN^{TMS})Sm(BH_4)]_2$

24Sm

$[(N_2NN^{Mes})Sm(BH_4)_2Li]_2$

25Sm

$[(O_2NN^{py})Nd(\mu\text{-}BH_4)(THF)]_2$

26Nd

$[(O_2N^{OMe})Sm(BH_4)(THF)]$

27Sm

$[(O_2N^{NMe2})Sm(BH_4)(THF)]$

28Sm

$[(O_2N^{nPr})Sm(BH_4)(THF)_2]$

30Sm

SCHEME 13 Polydentate nitrogen- and oxygen-based compounds as ligands for neodymium and samarium borohydrides.

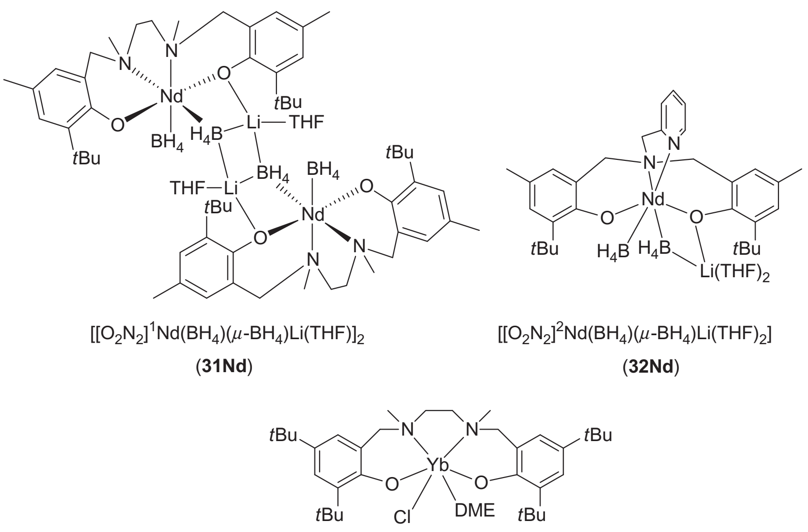

$[[O_2N_2]^1Nd(BH_4)(\mu\text{-}BH_4)Li(THF)]_2$
(**31Nd**)

$[[O_2N_2]^2Nd(BH_4)(\mu\text{-}BH_4)Li(THF)_2]$
(**32Nd**)

$[(N_2O_2)YbCl(DME)]$
(**33Yb**)

SCHEME 14 Polydentate nitrogen- and oxygen-based compounds as ligands for lanthanide borohydrides.

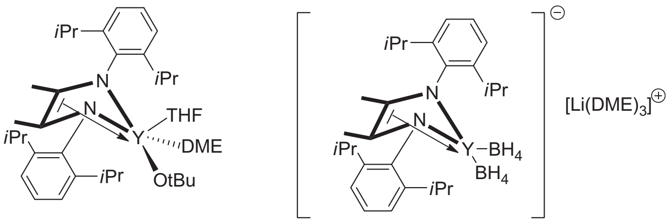

$[(DAB)Y(OtBu)(THF)(DME)]$
(**34Y**)

$[\{(DAB)Y(BH_4)_2\}\ Li(DME)_3]$
(**35Y**)

SCHEME 15 Some diazabutadiene yttrium complexes.

corresponding complexes $[(N_2O_2)RCl(DME)_n]$ (R = Er (**33Er**), Yb (**33Yb**)) (Scheme 14). These compounds were treated with $NaBH_4$ *in situ* to give the corresponding borohydrides (Wu et al., 2009).

The research groups of Carpentier and Trifonov used the chelating dianionic bis(amide) ligand (DAB^{2-}) ($((2,6\text{-}C_6H_3{}^iPr_2)NC(Me){=}C(Me)N(2,6\text{-}C_6H_3{}^iPr_2)^{2-}$) to prepare the yttrium complexes $[(DAB)Y(O^tBu)(THF)(DME)]$ (**34Y**) and $[\{(DAB)Y(BH_4)_2\}\{Li(DME)_3\}]$ (**35Y**) (Scheme 15). For the preparation of the borohydride, *in situ* generated $(DAB)Li_2$ was reacted with equimolar amounts of $[Y(BH_4)_3(THF)_3]$ (**1Y**) to give **35Y** in 52% yield (Mahrova et al., 2009).

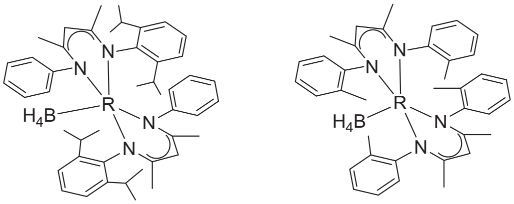

R = Y (**36Y**), Yb (**36Yb**) R = Y (**37Y**), Yb (**37Yb**)

SCHEME 16 Bis(β-diketiminate) rare-earth borohydride complexes.

Bis(β-diketiminate) rare-earth borohydride complexes were reported by Shen (Shen et al., 2012). Reaction of RCl_3 (Ln = Y, Yb) with the sodium salts of the β-diketiminate afforded the bis(β-diketiminate) rare-earth chlorides. According to the ligand system used, these chloride complexes were either isolated or prepared *in situ*. Reaction of these latter compounds with 1 equiv of $NaBH_4$, afforded the bis(β-diketiminate) monoborohydride complexes $[\{(2,6\text{-}i\text{Pr}_2C_6H_3)NC(Me)CHC(Me)N(C_6H_5)\}_2RBH_4]$ (R = Y (**36Y**), Yb (**36Yb**)) and $[(\{N(2\text{-}MeC_6H_4)C(Me)\}_2CH)_2RBH_4]$ (R = Y (**37Y**), Yb (**37Yb**)) (Scheme 16).

Recently the lanthanide borohydride complexes $[R(BH_4)_3(THF)_3]$ (R = La (**1La**), Nd (**1Nd**)) were grafted onto non-porous silica dehydroxylated at 700 °C, resulting in the bis(borohydride) surface species $[(@SiO)R(BH_4)_2(THF)_{2.2}]$ (R = La (**38La**), Nd (**38Nd**)) (Ajellal et al., 2010b). The monoborohydride grafted on silica $[(@SiO)La(BH_4)]$ (**39La**) was also discussed (Del Rosa et al., 2011a,b, 2012).

3. RARE-EARTH BOROHYDRIDE INITIATORS IN THE POLYMERIZATION OF POLAR MONOMERS

> Note that the terms related to polymers and polymerization used in the following section have been recently defined by the polymer division commission on macromolecular nomenclature subcommittee on macromolecular terminology and subcommittee on polymer terminology of the *International Union of Pure and Applied Chemistry* (Hiorns et al., 2012; Penczek and Moad, 2008).

For the sake of clarity, literature data on the polymerization of polar monomers are gathered in Tables 1–5 according to the monomer, namely lactones, lactides, carbonates, α-amino acid *N*-carboxyanhydrides, and methylmethacrylate, respectively.

In light of the remarkable performances of $[\{(Cp^*)_2SmH\}_2]$ in the polymerization of polar monomers (Yamashita et al., 1996), one would have expected further studies on rare-earth hydrides used as initiators in the ROP of polar monomers. Whereas the dimeric hydrido complex

$[\{(\eta^5{:}\eta^1\text{-}C_5Me_4SiMe_2NCMe_3)Y(THF)(\mu\text{-}H)\}_2]$ was demonstrated as being a single-site, single-component catalyst for the polymerization of ethylene, *tert*-butyl acrylate, and acrylonitrile (Arndt et al., 2002; Okuda et al., 2001), the only, to our knowledge, other rare-earth hydride complexes investigated in polymerization, namely the tetrasubstituted guanidinato yttrium and lutetium complexes, $[\{[TMS_2NC(NiPr)_2]_2R(\mu\text{-}H)\}_2]$ ($R = Y$, Lu), evaluated in the ROP of CL, displayed some activity but no control ($\overline{Mn}_{SEC} \leq 79{,}000\,g\,mol^{-1}$, $1.8 < \overline{Mw}/\overline{Mn} < 3.5$; Lyubov et al., 2008).

3.1. ROP of Lactones and Lactides, and α-Amino Acids *N*-Carboxyanhydrides

3.1.1. *Trivalent Inorganic Rare-Earth Borohydride Initiators*

3.1.1.1. ε-Caprolactone

The homoleptic rare-earth trisborohydride complexes $[R(BH_4)_3(THF)_3]$ (R = Y (**1Y**), La, (**1La**), Nd (**1Nd**), Sm (**1Sm**)) were the real first transition metal borohydride derivatives to be investigated in the ROP of a polar monomer, namely of CL, by Guillaume and coworkers in the early 2000s (Scheme 17; Guillaume et al., 2003; Palard et al., 2004, 2005, 2006) (Table 1). ROP of CL proceeded rapidly in THF, DCM, or DCM/toluene at room temperature in a controlled process. As many as 377 CL units per metal-BH_4 could be converted within 10 min using the samarium initiator **1Sm** providing PCL of molar mass up to $\overline{Mn}_{SEC} = 39{,}600\,g\,mol^{-1}$. The molar mass values $\overline{Mn}_{SEC}$ varied linearly with the feed ratio highlighting a "living" process. However, at $[CL]_0/[BH_4]_0 > 150$, assuming three growing polymer chains per metal, $\overline{Mn}_{SEC}$ deviated to lower values relative to $\overline{Mn}_{theo}$ indicating the presence of some transfer reactions. The fairly narrow dispersity values ($\overline{Mw}/\overline{Mn}_{La,Nd,Sm}$ *ca.*1.3) similarly suggested the occurrence of side reactions, yet to some minor extent. In ROP of cyclic esters, such undesirable reactions involve the typical inter- or intra-molecular transesterifications, that is, reshuffling or backbiting processes respectively, or other transfer reactions (Albertsson and Varma, 2003). Intra-molecular transesterification reactions lead to the formation of cyclic polymers (alongside linear ones), ultimately reducing the molar mass of the polymer. Intermolecular transesterification reactions, or intermolecular chain transfer reactions, induce the broadening of the dispersity. The moderate dispersity can also be attributed to a rate of

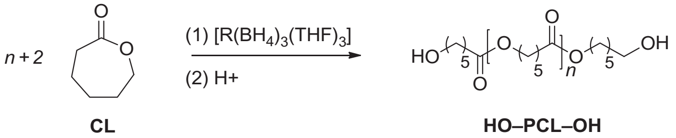

SCHEME 17 Synthesis of HO–PCL–OH from the ROP of CL initiated by $[R(BH_4)_3(THF)_3]$ (**1R**).

TABLE 1 Rare-Earth Borohydride Complexes Used as Initiators in the (Co)Polymerization of Lactones and Experimental Data

Rare-earth borohydride complex	Lactone ([Lactone]$_0$/[BH$_4$]$_0$ highest value)[a]	Solvent Temp. (°C)	Reaction time Conv.[b]	$\overline{M}n_{max}$[c] ($\overline{M}n_{theo}$)[a,d] g mol^{-1}	$Đ_M$[e]	Polymer Tacticity (%)	Copolymer
Divalent complex							
$[Sm(BH_4)_2(THF)_2]$ (**2Sm**, Scheme 2)	CL (232) (Jaroschik et al., 2010)	THF 25 °C	5 min 100%	24,600 (13,250)	1.59		
$[\{(Cp^*)Sm(BH_4)(THF)_2\}_2]$ (**4Sm**, Scheme 5)	CL (234) (Jaroschik et al., 2010)	THF 25 °C	3 min 84%	20,400 (22,400)	1.36		
$[Tm(BH_4)_2(DME)_2]$ (**2Tm′**, Scheme 2)	CL (233) (Momin et al., 2011)	THF 25 °C	19 min 74%	12,400 (19,600)	1.34		
$[(Tp^{tBu,Me})Tm(BH_4)(THF)]$[f] (**15Tm**)	CL (100)[f] (Momin et al., 2011)	THF 25 °C	3 min 100%	5700[f] (11,400)	1.44[f]		
$[(Ap^*)YbI(THF)_2]_2$ (**16Yb**)/$NaBH_4$[g]	CL (568) (Guillaume et al., 2007)	THF 23 °C	4 h 98%	43,600 (63,400)	1.56		
Trivalent complex							
$[Y(BH_4)_3(THF)_{2.5}]$[f] (**1Y′**, Scheme 1)	VL(200)[f] (Nakayama et al., 2009)	THF 60 °C	60 min 3.3%[f]	4300[f] (660)[h]	1.6[f]		
$[Y(BH_4)_3(THF)_3]$[f] (**1Y**, Scheme 1)	PDL (50)[f] (Nakayama et al., 2011)	THF 60 °C	1 min 66%[f]	11,000[f] (7920)[h]	1.9[f]		
$[R(BH_4)_2(THF)_5][BPh_4]$ R = Y (**3Y**), La (**3La**), Nd (**3Nd**), Sm (**3Sm**) (Scheme 3)	CL (250) (Robert et al., 2008)	THF 19 °C	30 s 100%	17,400 (28,500)	1.33		

$[\{CH(PPh_2NTMS)_2\}Y(BH_4)_2]$ (**20Y**, Scheme 11)	CL (150) (Jenter et al., 2010)	THF, Tol 20 °C	1 min 92%	15,700 (16,200)	1.38		
$[(^iPr(TMS)NC(N^iPr)N(CH_2)_3NC$ $(NiPr)N(TMS)^iPr)R(BH_4)(DME)]$ R = Y, Nd, Yb	CL (5000) (Zhang et al., 2012)	Tol 20 °C	5 min 100%	22,800 (45,800)	1.45		
$[\{(O_2NN^{py})Y(BH_4)(THF)_{0.5}\}_2]$[f] (**26Y**, Scheme 13)	CL (290) (Bonnet et al., 2005a)	Tol/THF 25 °C	2 min 84%[f]	24,700[f] (27,800)	1.74[f]		
$[\{(DAB)Y(BH_4)_2\}\{Li(DME)_3\}]$ (**35Y**, Scheme 25)	*rac*-BL(250) (Mahrova et al., 2009)	THF, Tol 20 °C	48 h 14%	4600 (3530)	1.23	Atactic PHB	
$[La(BH_4)_3(THF)_3]$[f] (**1La**, Scheme 1)	*rac*-BL (33) (Ajellal et al., 2010b)	Tol 20 °C	24 h 91%[f]	2700[f] (2610) [h]	1.75[f]	*P*m 50	
$[La(BH_4)_3(THF)_3]$[f] (**1La**, Scheme 1)	*rac*-BL (300) (Guillaume et al., 2013)	Tol 25 °C	92 h 31%	8500 (8000)	1.08	*P*m 56	
$[La(BH_4)_3(THF)_3]$ (**1La**, Scheme 1)	VL (300) (Nakayama et al., 2009)	THF, Tol 60 °C	30 min 94%	15,000 (16,200)[h]	1.43		PLLA-*co*-PVL PCL-*co*-PVL (Nakayama et al., 2009)
$[La(BH_4)_3(THF)_3]$ (**1La**, Scheme 1)	CL (251) (Palard et al., 2005, 2006)	THF 21 °C	15 min 100%	24,450 (28,610)	1.16		PCL-*co*-PVL (Nakayama et al., 2009)
$[La(BH_4)_3(THF)_3]$ (**1La**, Scheme 1)	PDL (50) (Nakayama et al., 2011)	THF 60 °C	1 min 83%	14,000 (2880)[h]	2.8		
$[(Ap^*)LaBr_2(THF)_3]$ (**17La**, Scheme 24)/$NaBH_4$[g]	CL (450) (Guillaume et al., 2007)	THF 23 °C	4 h 99%	46,300 (50,800)	1.45		
$[\{CH(PPh_2NTMS)_2\}$ $La(BH_4)_2(THF)]$ (**20La**, Scheme 11)	CL (150) (Jenter et al., 2010)	THF, Tol 20 °C	1 min 98%	13,400 (16,800)	1.34		

Continued

TABLE 1 Rare-Earth Borohydride Complexes Used as Initiators in the (Co)Polymerization of Lactones and Experimental Data—Cont'd

Rare-earth borohydride complex	Lactone ($[Lactone]_0/[BH_4]_0$ highest value)[a]	Solvent Temp. (°C)	Reaction time Conv.[b]	$\overline{M}n_{max}$[c] ($\overline{M}n_{theo}$)[a,d] $g\ mol^{-1}$	$Đ_M$[e]	Polymer Tacticity (%)	Copolymer
$[Pr(BH_4)_3(THF)_2]$[f] (**1Pr′**, Scheme 1)	VL (200)[f] (Nakayama et al., 2009)	THF 60 °C	60 min 55%[f]	8100[f] (11,000)[h]	1.4 [f]		
$[Nd(BH_4)_3(THF)_3]$[f] (**1Nd**, Scheme 1)	*rac*-BL (33) (Ajellal et al., 2010b)	Tol 20 °C	24 h 100%[f]	3100[f] (2900)[h]	1.83[f]	*P*m 50	
$[Nd(BH_4)_3(THF)_3]$[f] (**1Nd**, Scheme 1)	*rac*-BL (300) (Guillaume et al., 2013)	Tol 25 °C	92 h 31%	9700 (8000)	1.06	*P*m 54	
$[Nd(BH_4)_3(THF)_3]$ (**1Nd**, Scheme 1)	VL (200)[f] (Nakayama et al., 2009)	THF 60 °C	60 min 55%[f]	7300[f] (10,960)[h]	1.5[f]		
$[Nd(BH_4)_3(THF)_3]$ (**1Nd**, Scheme 1)	CL (221) (Guillaume et al., 2003; Palard et al., 2005, 2006)	THF, DCM 21 °C	15 min 100%	17,000 (25,200)	1.29		PCL-*b*-PBLG PBLG-*b*-PCL-*b*-PBLG (Schappacher et al., 2006) PCL-*co*-PLLA (Nakayama et al., 2007)
$[Nd(BH_4)_3(THF)_3]$ (**1Nd**, Scheme 1)/aldehyde, ketone	CL (157) (Wu et al., 2008)	THF/acetone 60 °C	14 min 90%	21,100 (nd)[h]	1.48		
$[Nd(BH_4)_3(THF)_3]$ (**1Nd**, Scheme 1)	PDL (200) (Nakayama et al., 2011)	THF 60 °C	8 h 87%	39,000 (41,760)[h]	1.53		

$[\{(O_2NN^{py})Nd(BH_4)(THF)\}_2]$[f] (**26Nd**, Scheme 13)	CL (275) (Bonnet et al., 2005a)	Tol/THF 25 °C	0.5 min 89%[f]	24,000[f] (27,900)	1.57		PCL-*b*-PLLA[f] PCL-*b*-PLA[f] (Bonnet et al., 2005a)
$[\{(O_2N_2)^1Nd(BH_4)_2Li(THF)\}_2]$ (**31Nd**, Scheme 14)	*rac*-BL (50) (Sinenkov et al., 2011)	THF Tol 20 °C	12 h 61%	5000 (2625)	1.09	Atactic PHB	
$[(O_2N_2)^2Nd(BH_4)_2Li(THF)_2]$ (**32Nd**, Scheme 14)	*rac*-BL (50) (Sinenkov et al., 2011)	THF, Tol 20 °C	12 h 24%	2500 (1050)	1.11	Atactic PHB	
$[Sm(BH_4)_3(THF)_3]$[f] (**1Sm**, Scheme 1)	*rac*-BL (300) (Guillaume et al., 2013)	Tol 25 °C	72 h 22%	8300 (5700)	1.05	*P*m 52	
$[Sm(BH_4)_3(THF)_3]$ (**1Sm**, Scheme 1)	CL (377) (Palard et al., 2004, 2005, 2006)	THF, DCM, DCM/Tol 21 °C	10 min 96%	39,600 (41,500)	1.24		PCL-*b*-PMMA PMMA-*b*-PCL-*b*-PMMA (Schappacher et al., 2007)
$[Sm(BH_4)_3(THF)_3]$ (**1Sm**, Scheme 1)	VL (200) (Nakayama et al., 2009)	THF 60 °C	60 min 26%[f]	4800[f] (5140)[h]	1.5[f]		
$[(Cp^*)_2Sm(BH_4)(THF)]$ (**5Sm**)	CL (565) (Palard et al., 2004, 2006)	THF 21 °C	30 min 99%	39,150 (63,850)	1.43		
$[\{(N_2NN^{TMS})Sm(BH_4)\}_2]$[f] (**24Sm**, Scheme 13)	CL (250)[f] (Bonnet et al., 2005b)	Tol/THF 25 °C	1 min 96%[f]	24,000[f] (27,400)	1.17[f]		

Continued

TABLE 1 Rare-Earth Borohydride Complexes Used as Initiators in the (Co)Polymerization of Lactones and Experimental Data—Cont'd

Rare-earth borohydride complex	Lactone ($[\text{Lactone}]_0/[BH_4]_0$ highest value)[a]	Solvent Temp. (°C)	Reaction time Conv.[b]	$\overline{M}n_{max}$[c] ($\overline{M}n_{theo}$)[a,d] g mol^{-1}	$Đ_M$[e]	Polymer Tacticity (%)	Copolymer
$[\{(O_2NN^{py})Sm(BH_4)\}_2]$[f] (**26Sm**, Scheme 13)	CL (275) (Bonnet et al., 2005a)	Tol/THF 25 °C	0.5 min 90%[f]	26,920[f] (28,250)	1.76[f]		
$[(O_2N^L)Sm(BH_4)(THF)]$ L = OMe (**27Sm**), NMe_2 (**28Sm**), py (**29Sm**), (Scheme 13) $[(O_2N^{nPr})Sm(BH_4)(THF)_2]$ (**30Sm**, Scheme 13)	CL (275) (Dyer et al., 2010)	Tol/THF RT	2 min 100%	28,400 (31,381)	1.83		
$[(N_2O_2)Er(Cl)(DME)]/NaBH_4$[g] (**33Er**, Scheme 14)	CL (1500) (Wu et al., 2009)	Tol/Hexane 65 °C	120 min 95%	33,300 (nd)[h]	1.43		
$[Yb(BH_4)_3(THF)_3]$[f] (**1Yb**, Scheme 1)	VL (200)[f] (Nakayama et al., 2009)	THF 60 °C	60 min 0%[f]	–[f]	–[f]		
$[(N_2O_2)Yb(Cl)(DME)_2]/NaBH_4$[g] (**33Yb**, Scheme 14)	CL (1000) (Wu et al., 2009)	Tol/Hexane 65 °C	120 min 96%	36,400 (nd)[h]	1.33		
$[(Ap^*)LuCl_2(THF)_2]$ (**18Lu**)/$NaBH_4$[g]	CL (450) (Guillaume et al., 2007)	THF 23 °C	4 h 99%	45,600 (50,800)	1.53		

[{CH($PPh_2NTMS)_2$}Lu($BH_4)_2$] (**20Lu**, Scheme 11)	CL (150) (Jenter et al., 2010)	THF, Tol 20 °C	0.5 min 95%	15,800 (16,400)	1.41	
[{(2,6-*i*$Pr_2C_6H_3$)NC(Me)CHC(Me)N(C_6H_5)}$_2RBH_4$] R = Y (**36Y**), Yb (**36Yb**) [({N(2-MeC_6H_4)C(Me)}$_2CH)_2RBH_4$] R = Y (**37Y**), Yb (**37Yb**) (Scheme 16)	CL (1000) (Shen et al., 2012)	Tol 20 °C	3 min (98%)	9870 (11,170)	1.35	
Supported complex						
[(@SiO)La($BH_4)_2$(THF)$_{2.2}$][f] (**38La**)	*rac*-BL (50) (Ajellal et al., 2010b)	Tol 20 °C	24 h (9%)[f]	600[f] (400)[h]	1.79[f]	*P*m 50 [f]
[(@SiO)Nd($BH_4)_2$(THF)$_{2.2}$] (**38Nd**)	*rac*-BL (100) (Ajellal et al., 2010b)	Tol 20 °C	24 h (75%)	11,500 (6450) [h]	1.61	*P*m 85

[a] *Note that the [lactone]$_0$/[BH_4]$_0$ ratio is different from the [lactone]$_0$/[initiator/catalyst]$_0$ value, the former being used in the calculation of the theoretical molar mass ($\overline{M}n_{theo}$) assuming one growing chain per BH_4^- group.*

[b] *Monomer conversion determined by ^1H NMR or by gravimetry and corresponding to the highest [lactone]$_0$/[BH_4]$_0$ value reported.*

[c] *Number average molar mass (maximum value) determined by SEC–MALLS or by SEC versus polystyrene standards and corrected by a factor of 0.56 for CL (Save et al., 2002) and uncorrected for PHB.*[2]

[d] *Theoretical molar mass calculated from [lactone]$_0$/[BH_4]$_0$ × monomer conversion × $M_{lactone}$, assuming one growing chain per BH_4 group, with M_{BL} = 86 g mol^{-1}, M_{VL} = 100 g mol^{-1}, M_{CL} = 114 g mol^{-1}, and M_{PDL} = 240 g mol^{-1}; note that a discrepancy between $\overline{M}n_{theo}$ and $\overline{M}n_{SEC}$ may be indicative of a number of growing polymer chains different from the number of BH_4^- groups in the initiating complex.*

[e] *Calculated average dispersity value as reported from SEC traces.*

[f] *Only a single experiment is reported.*

[g] *Prepared* in situ.

[h] *Value not reported by the authors.*

propagation which is faster than the rate of initiation (Penczek and Moad, 2008). The best control in terms of experimental and calculated molar mass agreement, and narrow dispersity was achieved with the largest metal, La > Sm > Nd. The quasi "living" character of the ROP process was later further demonstrated with the successful synthesis of block copolymers prepared by sequential copolymerization, poly(ε-caprolactone)-*b*-poly(trimethylene carbonate), PCL-*b*-PTMC (Section 3.5.1; Table 1). The studies on the influence of solvent revealed the detrimental effect on the polymerization rate of a coordinative polar solvent such as THF, in comparison to non-coordinative DCM or apolar toluene. Indeed, it is assumed that THF, because of its high affinity toward oxophilic rare-earth metals, competes with the polar CL monomer for coordination onto the metal center. This trend was later often observed in the ROP of cyclic esters promoted by rare-earth borohydride complexes, yet with some exception, as for instance with the higher CL polymerization rate reported in THF than in toluene using diaminobis(phenoxide)monoborohydride complexes (Bonnet et al., 2005a). The polyester recovered were established, based on extensive investigations by ^{1}H and ^{13}C NMR, FTIR, Matrix-Assisted Laser Desorption/Ionization-Time-of-Flight Mass Spectrometry (MALDI-ToF MS) and elemental analyses, as α,ω-dihydroxytelechelic PCL (Scheme 17). Note that dihydroxytelechelic polymers herein referred to as HO-polymer-OH are formally H-polymer-OH (Guillaume, 2013). Formation of such HO–PCL–OH, initially not foreseen, resulted from the reduction of the carbonyl group of the first inserted CL molecule (see below, Scheme 26, Section 3.1.4). This behavior is certainly distinct from that observed with the more common rare-earth alkoxide initiators which provide α,ω-hydroxyalkoxytelechelic (see below, Scheme 27, Section 3.1.4; Palard et al., 2006). Detailed FTIR investigations revealed that the terminal -OBH_2 group of the growing polymer was involved in van der Waals interactions leading to the cohesion of the experimentally observed "physical" gel. This route from rare-earth borohydride initiators represents a valuable strategy for the synthesis of highly desirable dihydroxytelechelic macroinitiators (*vide infra*; Section 3.1.5; Guillaume, 2013). Interestingly, the residual amount of metal present in the recovered PCL samples was measured around 0.26–0.63% of the initial loading in metal (Palard et al., 2005). This issue is relevant considering the potential application of PCL in the biomedical field. Subsequent investigations on the *in vitro* cytotoxicity of PCL samples prepared from various metal derivatives, including the rare-earth trisborohydride complexes, were carried out by Guillaume and coworkers (Schappacher et al., 2010). The results revealed the absence of toxic influence of the polyesters on human osteoprogenitor cells, making these polymers valuable candidates as biomaterials to be in contact with living human cells. Besides, the absence of toxicity of the residual rare-earth metal remaining in the isolated PCL was also demonstrated.

Following their interest in cationic rare-earth organometallic species, Okuda and coworkers investigated the first ROP of a cyclic ester using a cationic borohydride rare-earth complex, $[R(BH_4)_2(THF)_5][BPh_4]$ (R = Y (**3Y**); La (**3La**), Nd (**3Nd**), Sm (**3Sm**)) (Robert et al., 2008) (Table 1). All initiators featured a higher activity toward the ROP of CL ($\overline{M}n < 17{,}400\,g\,mol^{-1}$ with $1.25 < \overline{M}w/\overline{M}n < 1.38$) than the parent neutral complexes $[R(BH_4)_3(THF)_3]$ (R = Y (**1Y**), La (**1La**), Nd (**1Nd**), Sm (**1Sm**); 100% conversion within 15 min; Palard et al., 2005), with a complete CL conversion reached in 30s whichever the metal ($[CL]_0/[BH_4]_0$ *ca.* 250). However, the number of growing chains per metal center always exceeded two (as anticipated from such bisborohydride initiators), presumably due to rapid gelation of the reaction mixture involving chain transfer reactions. These preliminary results next prompted theoretical investigations by Okuda, Maron, and coworkers on the ROP of CL initiated by $[MeY(BH_4)(THF)_5][BPh_4]$ (**14Y**; Susperregui et al., 2011; see below Section 4 and Table 6).

As an extension of these studies on homoleptic rare-earth borohydride initiators, Sun and coworkers developed an elegant approach toward the synthesis of related end-capped PCLs (Wu et al., 2008) (Table 1). The so-called one-pot reduction/initiation strategy was successfully extended to the reduction (up to 90% within 14 min at 60 °C), by the rare-earth borohydride complexes $[R(BH_4)_3(THF)_3]$ (R = Y (**1Y**), Nd (**1Nd**)), of the carbonyl group of an exogenous aldehyde or ketone RC(O)R′ (R = alkyl, aryl, R′ = H, alkyl; see below, Scheme 28, Section 3.1.4). The resulting rare-earth alkoxide $[R(OCHRR')_3]$ then triggered the ROP of CL with high efficiency, ultimately affording HO–PCL–OCHRR′ as evidenced by ^1H NMR and FTIR analyses ($2{,}650 < \overline{M}n < 21{,}100\,g\,mol^{-1}$ with $1.25 < \overline{M}w/\overline{M}n < 1.76$). Double or multi carbonyl-containing reagents similarly gave α,ω-hydroxyalkoxytelechelic PCLs. While the reduction reactivity of aliphatic aldehydes is prior to that of ketones, the polymerization process from aliphatic aldehydes was less efficient than others.

3.1.1.2. δ-Valerolactone

The ROP of the one-carbon smaller lactone, δ-valerolactone (VL) was investigated by Nakayama, Shiono, and coworkers at 60 °C in THF or toluene from $[R(BH_4)_3(THF)_x]$ (R = Y, $x = 2.5$ (**1Y′**); La, $x = 3$ (**1La**); Pr, $x = 2$ (**1Pr′**); Nd, $x = 3$ (**1Nd**); Sm, $x = 3$ (**1Sm**); Yb, $x = 3$ (**1Yb**)) with various metal centers (Nakayama et al., 2009) (Table 1). The catalytic activities observed were in the same order as the ionic radii of the ions $La \geq Pr \geq Nd > Sm > Y > Yb$ (Shannon, 1976), and better in toluene as opposed to THF. The linear variation of $\overline{M}n$ values with the PVL yields along with $\overline{M}w/\overline{M}n$ *ca.* 1.43 indicated a rather controlled polymerization in the case of **1La**. In comparison to CL, the ROP of VL in THF was considerably slower (30 min for 81% conversion at $[VL]_0/[BH_4]_0 = 200$) as expected for a less strained VL ring (Saiyasombat et al., 1998). ^1H NMR and MALDI-ToF MS analyses supported the formation of α,ω-dihydroxytelechelic

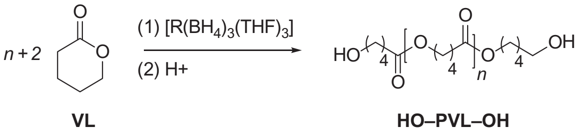

SCHEME 18 Synthesis of HO–PVL–OH from the ROP of VL initiated by $[R(BH_4)_3(THF)_3]$ (**1R**).

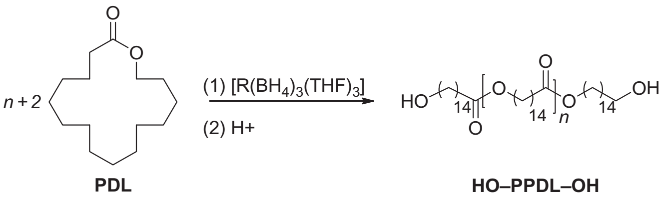

SCHEME 19 Synthesis of HO–PPDL–OH from the ROP of PDL initiated by $[R(BH_4)_3(THF)_3]$ (**1R**).

PVLs ($\overline{M}n$ up to 15,000 g mol^{-1} with $1.3 < \overline{M}w/\overline{M}n < 1.7$) following the same mechanism as that established for CL (Scheme 18).

3.1.1.3. ω-Pentadecalactone

In the $[R(BH_4)_3(THF)_3]$ (R = Y (**1Y**), La (**1La**), Nd (**1Nd**)) series, the neodymium complex was the most efficient (83% in 1 min at $[PDL]_0/[BH_4]_0 = 50$) toward the ROP of ω-pentadecalactone (PDL) at 60 °C, as established by Nakayama et al. (2011) (Table 1). The molar mass of the polymer synthesized from **1Nd** increased with the yield ($\overline{M}n$ up to 39,000 g mol^{-1} with $\overline{M}w/\overline{M}n$ *ca.* 1.4) featuring a quite good control. The resulting polyesters were shown by ^1H NMR and MALDI-ToF MS analyses as being α,ω-dihydroxytelechelic PPDL, HO–PPDL–OH, thereby assuming a mechanism similar to that of CL (Scheme 19).

3.1.1.4. Lactide

The series of complexes $[R(BH_4)_3(THF)_x]$ (R = Y, $x = 2.5$ (**1Y′**); La, $x = 3$ (**1La**); Pr, $x = 2$ (**1Pr′**); Nd, $x = 3$ (**1Nd**); Sm, $x = 3$ (**1Sm**); Yb, $x = 3$ (**1Yb**)) were also shown by Nakayama, Shiono, and coworkers to be active in the ROP of *racemic*-lactide (*rac*-LA, Nakayama et al., 2009) (Table 2). The same trend in catalytic activity related to the metal center ($La \geq Pr \geq Nd > Sm > Y > Yb$) or solvent polarity (ROP proceeded slower in THF as compared to in toluene) was observed, as for VL (*vide supra*). No stereoselectivity data have been reported for PLA ($3{,}800 < \overline{M}n < 30{,}100$ g mol^{-1} with $1.2 < \overline{M}w/\overline{M}n < 1.7$). The ROP of (*S*,*S*)-lactide (L-lactide, LLA), initiated by **1Nd** at $[LLA]_0/[BH_4]_0 = 50$, reached 76% in 30 min at 60 °C, affording highly crystalline PLLA ($Tm = 162$ °C, $\overline{M}n \leq 16{,}500$ g mol^{-1}) with $1.2 < \overline{M}w/\overline{M}n < 1.6$ suggesting the absence of

TABLE 2 Rare-Earth Borohydride Complexes Used as Initiators in the (Co)Polymerization of Lactides and Experimental Data

Rare-earth borohydride complex	Lactide ($[Lactide]_0/[BH_4]_0$ highest value)[a]	Solvent Temp. (°C)	Reaction time Conv.[b]	$\overline{Mn}_{max}$[c] ($\overline{Mn}_{theo}$)[a,d] g mol^{-1}	$Đ_M$[e]	Polymer Tacticity (%)	Copolymer
Trivalent complex							
$[Y(BH_4)_3(THF)_{2.5}]$[f] (**1Y′**, Scheme 1)	*rac*-LA(133)[f] (Nakayama et al., 2009)	THF 60 °C	60 min 24%[f]	3800[f] (4550)[g]	1.7[f]	nd[g]	
$[\{(O_2NN^{py})Y(BH_4)(THF)_{0.5}\}_2]$ (**26Y**, Scheme 13)	*rac*-LA (200) (Bonnet et al., 2005a)	THF, 25 °C Tol, 70 °C	60 min 72%	10,600 (18,300)	1.52	*Pr* 87	
$[\{(O_2NN^{py})Y(BH_4)(THF)_{0.5}\}_2]$ (**26Y**, Scheme 13)	LLA (200)[f] (Bonnet et al., 2005a)	THF 25 °C	180 min 28%[f]	3850 (7780)	1.37[f]	Isotactic PLLA	
$[\{(DAB)Y(BH_4)_2\}\{Li(DME)_3\}]$ (**35Y**, Scheme 25)	*rac*-LA (75) (Mahrova et al., 2009)	THF, Tol 20 °C	4 h 92%	13,400 (9950)	1.21	Atactic PLA	
$[La(BH_4)_3(THF)_3]$ (**1La**, Scheme 1)	*rac*-LA (200) (Nakayama et al., 2009)	THF 60 °C	60 min 90%	30,100 (17,625)[g]	1.33	nd[g]	PLLA-*co*-PVL (Nakayama et al., 2009)
$[Pr(BH_4)_3(THF)_2]$[f] (**1Pr′**, Scheme 1)	*rac*-LA (133)[f] (Nakayama et al., 2009)	THF 60 °C	60 min 65%[f]	12,700[f] (12,500)[g]	1.3[f]	nd[g]	
$[Nd(BH_4)_3(THF)_3]$ (**1Nd**, Scheme 1)	*rac*-LA (133)[f] (Nakayama et al., 2009)	THF 60 °C	60 min 64%[f]	12,200[f] (12,300)[g]	1.4[f]	nd[g]	
$[Nd(BH_4)_3(THF)_3]$ (**1Nd**, Scheme 1)	LLA (200) (Nakayama et al., 2007)	THF 60 °C	3 h 76%	16,500 (22,000)	1.2	Isotactic PLLA	PCL-*co*-PLLA (Nakayama et al., 2007)

Continued

TABLE 2 Rare-Earth Borohydride Complexes Used as Initiators in the (Co)Polymerization of Lactides and Experimental Data—Cont'd

Rare-earth borohydride complex	Lactide ($[\text{Lactide}]_0/[\text{BH}_4]_0$ highest value)[a]	Solvent Temp. (°C)	Reaction time Conv.[b]	$\overline{\text{Mn}}_{\text{max}}$[c] ($\overline{\text{Mn}}_{\text{theo}}$)[a,d] g mol^{-1}	$Đ_M$[e]	Polymer Tacticity (%)	Copolymer
$[\{(\text{TMS})_2\text{NC}(\text{N}^i\text{Pr})_2\}_2\text{Nd}(\text{BH}_4)_2\text{Li}(\text{THF})_2]$[f] (**22Nd**, Scheme 12)	*rac*-LA (200) (Skvortsov et al., 2007a)	THF, Tol 20 °C	60 min >98%	52,000 (28,220)	1.68	Atactic PLA	
$[\{(\text{TMS})_2\text{NC}(\text{N}^i\text{Pr})_2\}_2\text{Nd}(\text{BH}_4)_2\text{Li}(\text{THF})_2]$[f] (**22Nd**, Scheme 12)	LLA (100) (Skvortsov et al., 2007a)	THF 20 °C	60 min 98%	17,300 (14,100)	1.54	Isotactic PLA	
$[1,8\text{-C}_{10}\text{H}_6\{\text{NC}(^t\text{Bu})\text{N-2,6-Me}_2\text{-C}_6\text{H}_3\}_2]\text{R}(\text{BH}_4)_2\text{Li}(\text{THF})_2]$ R = Nd, Sm	*rac*-LA (250) (Yakovenko et al., 2012)	THF, Tol 20 °C	18 h 97%	18,700 (36,000)	1.57	*Pr* 62	
$[(^i\text{Pr}(\text{TMS})\text{NC}(\text{N}^i\text{Pr})\text{N}(\text{CH}_2)_3\text{NC}(\text{NiPr})\text{N}(\text{TMS})^i\text{Pr})\text{R}(\text{BH}_4)(\text{DME})]$ R = Y, Nd, Yb	*rac*-LA (1000) LLA (3000) (Zhang et al., 2012)	THF, Tol 20 °C	3–15 h 78%	30,500 (33,700)	1.55	*Pr* 72	
$[\{(\text{O}_2\text{NN}^{\text{py}})\text{Nd}(\text{BH}_4)(\text{THF})\}_2]$ (**26Nd**, Scheme 13)	*rac*-LA (200) (Bonnet et al., 2005a)	THF, 25 °C Tol, 70 °C	120 min 33%	4800 (9500)	1.57	*Pr* 64	PCL-*b*-PLA[f] (Bonnet et al., 2005a)
$[\{(\text{O}_2\text{NN}^{\text{py}})\text{Nd}(\text{BH}_4)(\text{THF})\}_2]$ (**26Nd**, Scheme 13)	LLA (200)[f] (Bonnet et al., 2005a)	THF 25 °C	180 min 34%[f]	6330 (9790)	1.31[f]	Isotactic PLLA	PCL-*b*-PLLA[f] (Bonnet et al., 2005a)

$[\{(O_2N_2)^1Nd(BH_4)_2Li(THF)\}_2]$ (**31Nd**, Scheme 14)	*rac*-LA(100) (Sinenkov et al., 2011)	THF, Tol 20 °C	12 h >99%	22,800 (13,700)	1.21	Atactic PLA
$[(O_2N_2)^2Nd(BH_4)(BH_4)Li(THF)_2]$ (**32Nd**, Scheme 14)	*rac*-LA (250) (Sinenkov et al., 2011)	THF, Tol 20 °C	12 h 99%	15,000 (29,900)	1.60	Atactic PLA
$[Sm(BH_4)_3(THF)_3]$[f] (**1Sm**, Scheme 1)	*rac*-LA (133)[f] (Nakayama et al., 2009)	THF 60 °C	60 min 59%[f]	12,100[f] (11,400)[g]	1.3 [f]	nd [g]
$[\{(TMS)_2NC$ $(NCy)_2\}_2Sm(BH_4)_2Li(THF)_2]$ (**22Sm**, Scheme 12)	*rac*-LA (200) Skvortsov et al., 2007a)	THF, Tol 20 °C	16.5 h 95%	23,500 (13,820)	2.10	Atactic PLA
$[\{(TMS)_2NC$ $(NCy)_2\}_2Sm(BH_4)_2Li(THF)_2]$ (**22Sm**, Scheme 12)	LLA (100)[f] (Skvortsov et al., 2007a)	THF 20 °C	60 min 12%	2200 (1700)	1.56	Isotactic PLA [f]
$[\{(O_2NN^{py})Sm(BH_4)\}_2]$ (**26Sm**, Scheme 13)	*rac*-LA (200) (Bonnet et al., 2005a)	THF 25 °C Tol 70 °C	60 min 66%	15,700 (18,000)	1.53	*Pr* 71.5
$[\{(O_2NN^{py})Sm(BH_4)\}_2]$ (**26Sm**, Scheme 13)	LLA (200)[f] (Bonnet et al., 2005a)	THF 25 °C	45 min 74%[f]	15200[f] (14,400)	1.63[f]	Isotactic PLLA
$[(O_2N^L)Sm(BH_4)(THF)]$ L = OMe (**27Sm**), NMe_2 (**28Sm**), py (**29Sm**) (Scheme 13) $[(O_2N^{nPr})Sm(BH_4)(THF)_2]$ (**30Sm**, Scheme 13)	*rac*-LA (200) (Dyer et al., 2010)	THF RT	30 min 92%	21,700 (26,520)	1.58	*Pr* 84
$[Yb(BH_4)_3(THF)_3]$[f] (**1Yb**, Scheme 1)	*rac*-LA (133)[f] (Nakayama et al., 2009)	THF 60 °C	60 min 0%[f]	–[f]	–[f]	nd[g]

Continued

TABLE 2 **Rare-Earth Borohydride Complexes Used as Initiators in the (Co)Polymerization of Lactides and Experimental Data—Cont'd**

Rare-earth borohydride complex	Lactide ($[Lactide]_0/[BH_4]_0$ highest value)[a]	Solvent Temp. (°C)	Reaction time Conv.[b]	$\overline{M}n_{max}$[c] ($\overline{M}n_{theo}$)[a,d] $g\ mol^{-1}$	$Đ_M$[e]	Polymer Tacticity (%)	Copolymer
$[\{(TMS)_2NC(N^iPr)_2\}_2Yb(BH_4)_2Li(THF)_2]$ (**22Yb**, Scheme 12)	*rac*-LA, LLA (200) (Skvortsov et al., 2007a)	Tol 20 °C	16.5 h 94%	15,500 (13,700)	1.72	Atactic PLA PLLA	
$[\{(2,6\text{-}i\text{Pr}_2C_6H_3)NC(Me)CHC(Me)N(C_6H_5)\}_2RBH_4]$ R = Y (**36Y**), Yb (**36Yb**) (Scheme 16)$[(\{N(2\text{-}MeC_6H_4)C(Me)\}_2CH)_2RBH_4]$R = Y (**37Y**), Yb (**37Yb**) (Scheme 16)	LLA (1000) (Shen et al., 2012)	Tol 20 °C	4 min (96)	12,660 (13,760)	1.36	PLLA	

[a] *Note that the $[lactide]_0/[BH_4]_0$ ratio is different from the $[lactide]_0/[initiator/catalyst]_0$ value, the former being used in the calculation of the theoretical molar mass ($\overline{M}n_{theo}$) assuming one growing chain per BH_4^- group.*

[b] *Monomer conversion determined by ^1H NMR or by gravimetry and corresponding to the highest $[lactide]_0/[BH_4]_0$ value reported.*

[c] *Number average molar mass (maximum value) determined by SEC–MALLS or by SEC versus polystyrene standards and corrected by a factor of 0.58 for PLA (Save et al., 2002).*

[d] *Theoretical molar mass calculated from $[lactide]_0/[BH_4]_0 \times$ monomer conversion $\times M_{lactide}$, assuming one growing chain per BH_4^- group, with $M_{LA} = 144\ g\ mol^{-1}$; note that a discrepancy between $\overline{M}n_{theo}$ and $\overline{M}n_{SEC}$ may be indicative of a number of growing polymer chains different from the number of BH_4 groups in the initiating complex.*

[e] *Calculated average dispersity value as reported from SEC traces.*

[f] *Only a single experiment is reported.*

[g] *Value not reported by the authors.*

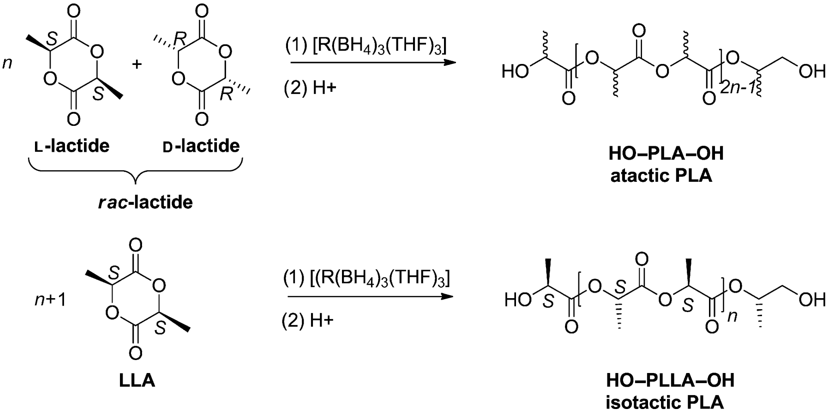

SCHEME 20 Synthesis of atactic and isotactic HO–PLA–OH from the (non)stereoselective ROP of *rac*-LA or LLA, respectively, initiated by [R$(BH_4)_3$$(THF)_3$] (**1R**).

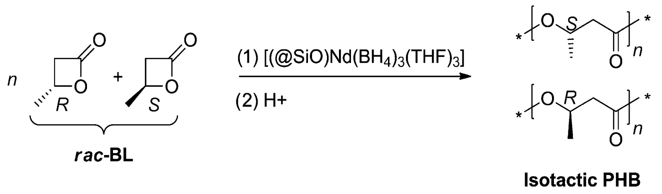

SCHEME 21 Stereoselective synthesis of isotactic PHB from the ROP of *rac*-BL initiated by [(@SiO)Nd$(BH_4)_2$$(THF)_{2.2}$] (**38Nd**).

epimerization, and possibly the occurrence of transesterification reactions (Nakayama et al., 2007). Formation of α,ω-dihydroxytelechelic PLLA was evidenced by MALDI-ToF MS (Scheme 20).

3.1.1.5. β-Butyrolactone

The ROP of *racemic* β-butyrolactone (*rac*-BL), a four-membered ring lactone known as a reluctant monomer to ring-open polymerize (Saiyasombat et al., 1998), was briefly studied by Thomas, Gauvin, and coworkers, using molecular [R$(BH_4)_3$$(THF)_3$] (**1La**, **1Nd**) and supported [(@SiO)R$(BH_4)_2$$(THF)_{2.2}$] (R = La (**38La**), Nd (**38Nd**)) rare-earth trisborohydride complexes (Scheme 21; Ajellal et al., 2010b) (Table 1). These supported complexes featured two BH_4^- ligands in line with the determined B/R ratio *ca.* 2 and with the carbon content. The molecular derivatives **1Nd** and **1La** successfully ring-open polymerized BL from both BH_4^- groups at 20 °C, with **1Nd** being more active than **1La** (results based on a unique experiment) and providing atactic (3-hydroxybutyrate) oligomers (PHB, $\overline{M}n \leq 3{,}100\,\text{g}\,\text{mol}^{-1}$).[2] Whereas the grafted lanthanum **38La** gave

---

[2] Note that in the case of PHBs, the molar mass values obtained from SEC: using a refractive index detector are uncorrected values because the difference in hydrodynamic radius of PHB versus the poly(styrene) standards used for calibration has not been established.

poor activity and atactic PHB, the grafted neodymium derivative **38Nd** exhibited the highest stereoselectivity for the isospecific polymerization of *rac*-BL (*P*m 85%), as determined from analysis of the carbonyl region of the $^{13}C\{^{1}H\}$ NMR spectrum of the PHB ($\overline{M}n \leq 11{,}500\,g\,mol^{-1}$; Scheme 21). These heterogeneous initiators **38La**, **38Nd** appeared comparatively less active than the non-supported analogues **1La**, **1Nd**. No further characterization of the PHB (chain-ends, thermal transition temperature of isotactic PHB) was reported. The effect of the grafting mode of a rare-earth borohydride complex onto a silica surface was next investigated from kinetic and thermodynamic parameters through DFT studies on the ROP of the larger lactone, namely CL, by Maron and coworkers (Del Rosa et al., 2011a,b).

Recently, Guillaume, Maron, Roesky, and coworkers showed the controlled ROP of *rac*-BL from **1La**, **1Nd**, and **1Sm** initiators (Guillaume et al., 2013). The ROP remained quite slow, as commonly observed with this β-lactone, and a better control was observed in the order Sm > Nd > La. Well-defined atactic α,ω-dihydroxytelechelic PHBs, with $\overline{M}n$ up to 7900 g mol^{-1} and dispersity values ≤1.10 were formed, in THF or toluene at 25 °C, as evidenced from combined NMR and MALDI-ToF analyses (Scheme 22). These findings were further supported by DFT calculations (*vide infra*).

3.1.1.6. γ-Benzyl-L-Glutamate *N*-Carboxyanhydride

Although α-amino acids *N*-carboxyanhydrides (NCAs), also known as Leuchs' anhydrides, are not cyclic esters, they are cyclic monomers which undergo ROP to afford the corresponding poly(α-amino acid)s. The trisborohydride complexes $[R(BH_4)_3(THF)_3]$ (R = Sc (**1Sc**), Y (**1Y**), La (**1La**), Dy (**1Dy**)) were thus investigated in the ROP of α-amino acids NCA, namely γ-benzyl-L-glutamate NCA, by Shen and coworkers (BLG; Peng et al., 2012a, 2012b) (Table 3). The molar mass values of the resulting poly(γ-benzyl-L-glutamate *N*-carboxyanhydride) (PBLG) prepared from **1Y** were controlled to some extent by the $[BLG]_0/[\mathbf{1Y}]_0$ ratio and increased with higher reaction temperatures, but were found larger than the calculated ones. The yttrium complex **1Y** always afforded higher molar mass ($\overline{M}n \leq 86{,}200\,g\,mol^{-1}$) than the other three rare-earth metal complexes, while **1Sc** gave the lowest $\overline{M}n$ values. Detailed MALDI-ToF and Electron-Spray Ionization MS analyses along with various NMR experiments (^{1}H, ^{13}C, COSY, HMQC) of a polymer sample prepared from the related L-alanine NCA (ALA) and **1Y** showed the

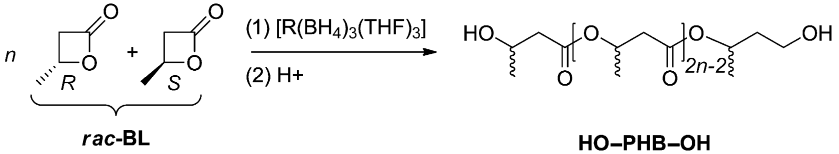

SCHEME 22 Synthesis of atactic PHB from the ROP of *rac*-BL initiated by $[R(BH_4)_3(THF)_3]$ (**1R**; R = La, Nd, Sm).

TABLE 3 Rare-Earth Borohydride Complexes Used as Initiators in the (Co)Polymerization of BLG–NCA and Experimental Data

Rare-earth borohydride complex	BLG ($[BLG]_0/[BH_4]_0$ highest value)[a]	Solvent Temp. (°C)	Reaction time Conv.[b]	$\overline{Mn}_{max}$[c] ($\overline{Mn}_{theo}$)[a,d] g mol^{-1}	$Đ_M$[e]	Polymer Tacticity (%)	Copolymer
Trivalent complex							
$[Sc(BH_4)_3(THF)_2]$ (**1Sc′**, Scheme 1)	BLG (73) (Peng et al., 2012a,b)	DMF 40 °C	24 h 98%	35,100 (15,700)	1.65		
$[Y(BH_4)_3(THF)_3]$ (**1Y**, Scheme 1)	BLG (388) (Peng et al., 2012a,b)	DMF 40 °C	24 h 92%	86,200 (78,100)	1.32		P(BLG-*b*-ALA) P(BLG-*b*/*co*-BLL) (Peng et al., 2012b)
$[La(BH_4)_3(THF)_3]$ (**1La**, Scheme 1)	BLG (69) (Peng et al., 2012a,b)	DMF 40 °C	24 h 90%	49,800 (13,500)	1.29		
$[Dy(BH_4)_3(THF)_3]$ (**1Dy**, Scheme 1)	BLG (59) (Peng et al., 2012a,b)	DMF 40 °C	24 h 90%	56,800 (11,500)	1.16		

[a] *Note that the $[BLG]_0/[BH_4]_0$ ratio is different from the $[BLG]_0/[initiator/catalyst]_0$ value, the former being used in the calculation of the theoretical molar mass ($\overline{Mn}_{theo}$) assuming one growing chain per BH_4^- group.*

[b] *Monomer conversion determined by ^1H NMR or by gravimetry and corresponding to the highest $[BLG]_0/[BH_4]_0$ value reported.*

[c] *Number average molar mass (maximum value) determined by SEC–MALS in DMF/LiBr.*

[d] *Theoretical molar mass calculated from $[BLG]_0/[BH_4]_0 \times$ BLG conversion $\times M_{BLG}$, assuming one growing chain per BH_4^- group, with $M_{BLG} = 219$ g mol^{-1}; note that a discrepancy between $\overline{Mn}_{theo}$ and $\overline{Mn}_{SEC}$ may be indicative of a number of growing polymer chains different from the number of BH_4 groups in the initiating complex.*

[e] *Calculated average dispersity value as reported from SEC traces.*

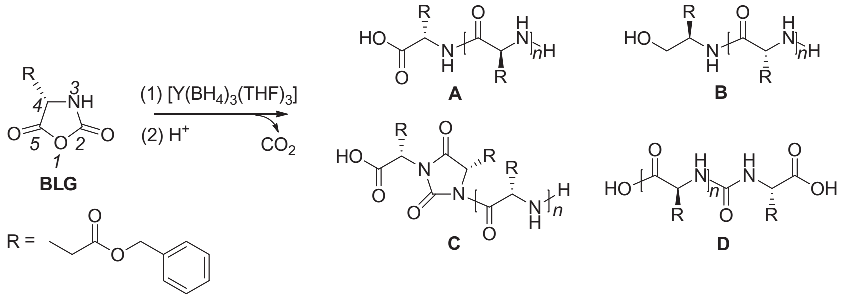

SCHEME 23 Synthesis of PBLG from the ROP of BLG initiated by $[Y(BH_4)_3(THF)_3]$ (**1Y**).

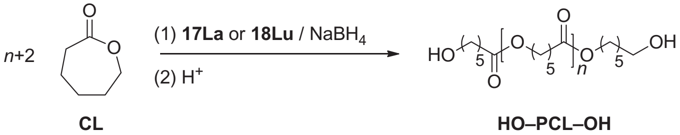

SCHEME 24 Synthesis of HO–PCL–OH from the ROP of CL initiated by the rare-earth borohydride complexes generated *in situ* from $[(Ap^*)RBr_2(THF)_3]$ (R = La (**17La**), Lu (**18Lu**))/$NaBH_4$.

formation of an α-carboxylic-ω-aminotelechelic polypeptide chain (**A**) and an α-hydroxyl,ω-aminotelechelic polymer (**B**), as the two major products. Two other minor compounds were identified as an α-amino,ω-hydantoinic (**C**), and an α-carboxylic,ω-hydantoic acid (**D**) end-functionalized poly(ALA) (Scheme 23; see also Schemes 29 and 30 in Section 3.1.4).

3.1.2. *Trivalent Organometallic Rare-Earth Borohydride Initiators*

3.1.2.1. ε-Caprolactone

***3.1.2.1.1. Trivalent Rare-Earth Borohydride Initiators Made* in Situ** In a recent study, Kempe, Guillaume, and coworkers pioneered the *in situ* synthesis of a rare-earth borohydride initiator from the salt metathesis reaction between $NaBH_4$ and the aminopyridinato rare-earth halides $[(Ap^*)LaBr_2(THF)_3]$ (**17La**) or $[(Ap^*)LuCl_2(THF)_2]$ (**18Lu**), in the ROP of CL (Scheme 24; Guillaume et al., 2007) (Table 1). Whereas no polymer was obtained in the absence of $NaBH_4$, dihydroxytelechelic PCLs were formed from such bicomponent initiating systems, **17La**,**18Lu**/$NaBH_4$, thus demonstrating the successful *in situ* generation of the rare-earth borohydride preinitiating species (*vide infra*). Fairly large CL loadings ($[CL]_0/[BH_4]_0 \leq 450$) were quantitatively converted within 4 h at 23 °C affording quite high molar mass PCLs ($\overline{M}n$ up to 46,300 g mol^{-1}) with $\overline{M}w/\overline{M}n$ *ca.* 1.49. This attractive strategy, using a borohydride alkali metal salt combined to a rare-earth halide as a precursor to the rare-earth borohydride initiator, has later been only rarely applied in the ROP of cyclic esters to make PCL: examples are the tetrahydrosalen-backboned rare-earth complexes reported by Shen and coworkers $[(N_2O_2)R(Cl)(DME)_n]$ (R = Er, $n = 1$ (**33Er**), Yb, $n = 2$ (**33Yb**))/$NaBH_4$ (Wu et al., 2009) (Scheme 14) and the related $[\{CH(PPh_2NTMS)_2\}R(\eta^5\text{-}C_5Me_5)Cl]$/HOiPr (R = Y, Sm, Yb), (Gamer et al., 2007) combination. Such an approach generating the active borohydrido species *in situ* avoids the prior synthesis and isolation of the complex, which represents a significant advantage. Yet it remains largely under-exploited in comparison to the use of discrete rare-earth borohydride polymerization initiators.

3.1.2.1.2. *Discrete Trivalent Rare-Earth Borohydride Initiators*

The catalytic behavior of $[(Cp^*)_2Sm(BH_4)(THF)]$ (**5Sm**) was studied in the ROP of CL by Guillaume and coworkers as the first organometallic rare-earth borohydride evaluated in the ROP of a cyclic ester (Palard et al., 2004) (Table 1). Quantitative CL conversions were easily reached within 30 min even at higher monomer loadings ($[CL]_0/[BH_4]_0 = 565$), affording quite high molar mass ($\overline{M}n$ up to 39,150 g mol^{-1} with $\overline{M}w/\overline{M}n$ *ca.* 1.43). A linear dependence of the experimental molar mass on the $[CL]_0/[BH_4]_0$ ratio was observed with a small deviation at higher monomer loadings resulting from side reactions. Use of this single-site initiator enabled to better understand the ROP mechanism of a cyclic ester promoted by a borohydride initiator, especially in providing solubility to key intermediates such as $[(Cp^*)_2Sm(BH_4)(CL)]$ (see Scheme 26, Section 3.1.4). The contribution of the ancillary Cp* ligands was highlighted by comparison with the performances of the homoleptic complex $[Sm(BH_4)_3(THF)_3]$ (**1Sm**). The favorable steric hindrance of the Cp* versus BH_4^- ligand limited the side reactions whereas the greater electron-donating ability of Cp* versus BH_4^- slowed down the rate of polymerization by a factor of six, thereby enabling a better control of the ROP of CL with the metallocene initiator.

The ROP of CL from the samarium borohydride complexes of the diamide–diamine ligand, $[\{(N_2NN^{TMS})Sm(BH_4)\}_2]$ (**24Sm**) and $[\{(N_2NN^{Mes})Sm(BH_4)_2Li\}_2]$ (**25Sm**), were briefly described by Mountford and coworkers (Bonnet et al., 2005b). This latter species was found, under the same conditions, half as active as the former one (96% yield in 1 min of 25 CL equivs by **24Sm**), possibly as a result of the greater steric hindrance of the mesityl groups.

3.1.2.2. ε-Caprolactone and Lactide

The post-metallocene complexes $[\{(O_2NN^{py})R(\mu\text{-}BH_4)(THF)_n\}_2]$ [R = Y, $n = 0.5$ (**26Y**); Nd, $n = 1$ (**26Nd**); Sm, $n = 0$ (**26Sm**)] were shown by Bonnet, Mountford, and coworkers as being very effective initiators (up to 90% conversion of 275 CL units in 0.5 min) in the ROP of CL at 25 °C (Bonnet et al., 2005a) (Table 1). While a fair control of the molar mass ($\overline{M}n \leq 26{,}920$ g mol^{-1}) was observed, dispersity values were rather large ($1.57 < \overline{M}w/\overline{M}n < 1.76$). The slightly lower activity of the yttrium complex was attributed to its smaller radius. ROP of lactides initiated by a rare-earth borohydride complex was first reported with the evaluation of this same series of initiators (Bonnet et al., 2005a) (Table 2). The ROP of L-lactide (LLA) in THF (25 °C) or toluene (70 °C) showed, under similar conditions ($[\text{LLA}]_0/[\mathbf{26R}]_0=200$), the samarium complex (**26Sm**) to be the most active (74% of isotactic PLLA in 45 min) and the only one to enable a good control, yet only in THF. As for the ROP of CL, the occurrence of transesterification reactions or a slow initiation step compared to propagation rationalized both the deviation of the molar mass values measured experimentally ($\overline{M}n \leq 15{,}200\,\text{g}\,\text{mol}^{-1}$) from the expected values, and the large dispersity values of the PLLA ($1.31<\overline{M}w/\overline{M}n<1.73$). High $[\text{LLA}]_0/[\text{initiator}]_0$ ratios and/or the use of toluene as solvent at 70 °C afforded a poorer control of the molar mass, assuming one growing chain per metal center. The O_2NN^{py} complexes of Y (**26**Y), Nd (**26Nd**), and Sm (**26Sm**) were also all active in the ROP of *rac*-LA in THF (25 °C) or toluene (7 °C), with again a "living" polymerization with limited chain transfer demonstrated in the case of the samarium initiator (Table 2). Heterotactic enriched PLAs (up to P_r 87% for **26Y**) were obtained from the ROP of *rac*-LA in THF ($\overline{M}n \leq 15{,}700\,\text{g}\,\text{mol}^{-1}$), whereas the reaction in toluene provided atactic polymers. No NMR details on the microstructure of the formed polylactides and especially on the nature of the chain-ends, nor on the ROP mechanism of lactides, were reported. FTIR υ(OH) stretching bands between 3650 and 3200 cm^{-1} were attributed to end-functionalities.

As an extension of these studies, the solvated samarium borohydride complexes supported by the bis(phenolate)amine ligands, $[(O_2N^L)Sm(BH_4)(THF)]$ (L = OMe (**27Sm**), NMe_2 (**28Sm**), py (**29Sm**)), and $[(O_2N^{Pr})Sm(BH_4)(THF)_2]$ (**30Sm**) (Scheme 13), were further reported in the ROP of CL and *rac*-LA by Duchateau, Maron, Mountford, and coworkers (Dyer et al., 2010) (Tables 1 and 2). All samarium complexes were efficient initiators (full conversion within 2 min) for the ROP of CL ($[\text{CL}]_0/[\mathbf{27\text{–}29R}]_0=275$) affording, based on ^{1}H NMR and MALDI-ToF MS analyses, linear α,ω-dihydroxytelechelic PCLs ($\overline{M}n \leq 31{,}400\,\text{g}\,\text{mol}^{-1}$) contaminated by some cyclic polymers. Both the dispersity –ranging from 1.4 to 2.5– and the control depended on the O_2N^L ligand pendant arm, with $[(O_2N^{OMe})Sm(BH_4)(THF)]$ (**27Sm**) being the best, especially in terms of PCL molar mass agreement. In the ROP of *rac*-LA, only the complexes with the tetradentate O_2N^L ligand were active, the one without a pendant donor group, that is, the tridentate $[(O_2N^{Pr})Sm(BH_4)(THF)_2]$ (**30Sm**) compound, being totally inactive. The pendant arm effect was reflected by the following increasing order of activity toward *rac*-LA: $O_2N^{OMe} \approx O_2N^{py} < O_2NN^{Me2}$. Heterotactic enriched α,ω-dihydroxytelechelic PLAs ($\overline{M}n \leq 26{,}500\,\text{g}\,\text{mol}^{-1}$) were always obtained (*Pr* 78–84%). Poly(*rac*-LA) formed from $[(O_2N^L)Sm(BH_4)(THF)]$ (L = OMe, py), showed by MALDI-ToF analyses, in addition to the —C(O)CH(Me)OH chain-end arising from the protonolysis of the metal–oxygen bond, the presence of a —$OCH(Me)CH_2OH$ end-group originating from the insertion of the first LA unit into the Sm–BH_4 moiety accompanied by carbonyl reduction by Sm–BH_4. In contrast, with O_2N^{NMe2}, a mixed α-hydroxy,ω-aldehyde-terminated PLA displaying both —C(O)CH(Me)OH and —CH(Me)CHO end-groups was obtained. All the MALDI-ToF spectra also evidenced the presence of cyclic PLAs along with these linear polymers. These experimental findings were next supported by DFT calculations which pointed to α,ω-dihydroxy-terminated PLAs as being the most favored polymers.

The series of bis(phosphinimino)methanide complexes of the rare-earth elements developed by Roesky and coworkers were first evaluated in the ROP of CL from the *in situ* prepared alkoxide initiators (Gamer et al., 2007) (Table 1). The promising results including a living polymerization along with well-defined PCL featuring controlled molecular features (end-groups and $\overline{M}n$ fidelity, very narrow dispersity values $1.06 < \overline{M}w/\overline{M}n < 1.20$) prompted further studies from the corresponding borohydride complexes $[\{CH(PPh_2NTMS)_2\}La(BH_4)_2(THF)]$ (**20La**) and $[\{CH(PPh_2NTMS)_2\}R(BH_4)_2]$, (R = Y (**20Y**), Lu (**20Lu**)) (Scheme 11), by Roesky, Guillaume, Maron, and coworkers (Jenter et al., 2010). The ROP of CL proceeded smoothly at 20 °C with complete conversion ($[CL]_0/[\mathbf{20Y/Lu}]_0 \leq 150$) being achieved within a few minutes in THF or toluene. With respect to the $\overline{M}w/\overline{M}n$ values, the ROP appeared slightly less controlled in toluene, whereas lowering of the reaction temperature from 23 to 0 °C resulted in a significantly improved control and activity of the catalyst. Indeed, at 0 °C, the dispersity determined ($1.06 < \overline{M}w/\overline{M}n < 1.11$ for all three metal complexes) was lower than that from room temperature ($1.16 < \overline{M}w/\overline{M}n < 1.49$). Noteworthy, these $\overline{M}w/\overline{M}n$ data are, to our knowledge, the narrowest values ever obtained for the ROP of CL initiated by rare-earth borohydride complexes (Table 1). All three catalysts were highly active without any significant difference arising from the metal center. Thus, the ancillary ligand in this latter case, as well as the bis(phosphinimino)methanide, most likely significantly and positively influenced the control of the ROP of CL. The unique role played by the ligand itself in the ROP process was later substantiated by DFT insights by the same groups (Barros et al., 2008a; Jenter et al., 2010) (Table 6; *vide infra*).

The bis(β-diketiminate) rare-earth borohydride complexes, $[\{(2,6\text{-}iPr_2C_6H_3)NC(Me)CHC(Me)N(C_6H_5)\}_2RBH_4]$ (R = Y (**36Y**), Yb (**36Yb**)) and $[(\{N(2\text{-}MeC_6H_4)C(Me)\}_2CH)_2RBH_4]$ (R = Y (**37Y**), Yb (**37Yb**)), were recently reported by Shen to be active in the ROP of CL and LA using high monomer loadings (up to 1000 equiv) (Shen et al., 2012). The efficieny of the initiating complexes depended on both the ligand and the metal with **36R** being more effective than **37R**. A good control of the PCL molecular features (molar mass and dispersity values) was achieved at room temperature within 3 min, in particular with **37Yb**; it was also found better for polymerizations ran in toluene as compared to THF, and at 20 °C rather than at 10 or 40 °C. Similarly, the best control in the ROP of LLA was obtained for

37Yb with evidences of a living feature being reported (linear variation of the molar mass with monomer conversion) and dispersity around 1.35, yet suggesting the occurrence of some transesterifications. Dihydroxytelechelic PCLs were obtained while PLLAs were end-capped by a —CH_2OH and a —CHMeOH groups, as evidenced by ^{1}H NMR spectra. Sucessful immortal ROP (Ajellal et al., 2010a; Guillaume and Carpentier, 2012) was also perfomed with ^{i}PrOH (up to 200 equiv) at 20–60 °C. In these cases, the PLLA featured a —O^{i}Pr and a —CHMeOH end-capping units.

Finally, the group of Shen recently reported bridged bis(guanidinate) monoborohydride complexes [(^{i}Pr(TMS)NC(N^{i}Pr)N(CH_2)$_3$NC(N^{i}Pr)N(TMS)^{i}Pr)R(BH_4)(DME)] R = Y, Nd, Yb in the ROP of CL, *rac*-LA and LLA (Zhang et al., 2012) (Tables 1 and 2). Whereas a significant metal effect was observed in the ROP of CL, *rac*-LA, and LLA, the neodymium derivatives revealed the most efficient (Nd ≫ Yb > Y) in terms of activity and molar mass control whichever the monomer. Very high loadings of CL (up to 5000 equiv) or LLA (up to 3000 equiv) afforded PCLs and PLAs with $\overline{M}n_{PCL}$ up to 22,800 g mol^{-1} and $\overline{M}n_{PLLA}$ up to 30,500 g mol^{-1}, yet with rather large dispersities ($\overline{M}w/\overline{M}n$ 1.31–1.81). A double LLA addition experiment showed the expected increase in PLA molar mass values. Slightly heterotactic PLAs were formed from *rac*-LA ($Pr < 72\%$). The authors evidenced the formation of PCL diols as expected, and observed the characteristic quartet for the —C*H*Me(OH) end-group, yet without mentioning whether only one type of chain-end group was observed.

3.1.2.3. Lactide

Lanthanide borohydride complexes of the bulky guanidinate ligands, [{$(TMS)_2$NC(NCy)$_2$}$_2$R(μ-BH_4)$_2$Li(THF)$_2$] (R = Nd (**22Nd**), Sm (**22Sm**), Yb (**22Yb**)), initiated the ROP of *rac*-LA and LLA as reported by Carpentier, Trifonov, and coworkers (Skvortsov et al., 2007a) (Table 2). Assuming only one growing polymer chain per metal center (instead of the two expected for a bisborohydride initiator), the overall control (Nd ≫ Yb > Sm) over the PLA molar mass ($\overline{M}n \leq 52{,}000\,g\,mol^{-1}$) and dispersity values ($1.09 < \overline{M}w/\overline{M}n < 2.99$) revealed better than that observed in the polymerization of MMA (Skvortsov et al., 2007c, *vide infra*; Table 5). The detrimental effect of THF versus apolar non-coordinating toluene on the rate of the ROP of LA was evidenced, in agreement with most common (see the above-mentioned study on CL, Palard et al., 2005), yet not systematic (Bonnet et al., 2005a), literature findings. Whichever the reaction solvent, the observed order of decreasing activity was Nd ≫ Yb > Sm. Whereas atactic PLA was formed, the ROP of LLA afforded isotactic microstructures, as evaluated by analyses of the methine region of the decoupled ^{1}H NMR spectra (Kasperczyk, 1995). The polymers were clearly end-capped by a —CH(Me)OH group indicative of a classical coordination–insertion mechanism with an oxygen-acyl bond cleavage, as observed with the homoleptic trisborohydride complexes **1R** (Nakayama et al., 2007). However, the other chain-end group could not be unambiguously identified. Finally, these same groups reported the ROP of *rac*-LA promoted by the moderately active heterobimetallic *ansa*-bis(amidinate) lanthanide borohydrides featuring a conformationally rigid naphthalene linker $[1,8\text{-}C_{10}H_6\{NC(^tBu)N\text{-}2,6\text{-}Me_2\text{-}C_6H_3\}_2R(BH_4)_2Li(THF)_2]$ (R = Nd Sm) (Yakovenko et al., 2012) (Table 2). Slightly heterotatic PLAs (*P*r 54–62%) were prepared in THF or toluene at room temperature, with controlled molar mass for lower monomer loadings (≤120 equiv) and relatively large dispersity values ($1.47 < \overline{M}w/\overline{M}n < 1.67$).

3.1.2.4. Lactide and β-Butyrolactone

The yttrium borohydride complex supported by chelating diamido ligand, $[\{(DAB)Y(BH_4)_2\}\{Li(DME)_3\}]$ (**35Y**, Scheme 15), initiates the ROP of *rac*-LA and *rac*-BL at 20 °C in toluene providing atactic polymers ($\overline{M}n \leq 13{,}400\,g\,mol^{-1}$, $1.15 < \overline{M}w/\overline{M}n < 1.30$), as briefly shown by Trifonov, Carpentier, and coworkers (Scheme 25; Mahrova et al., 2009) (Tables 1 and 2). A quite good control of the molar mass (assuming two growing polymer chains per metal center) and dispersity values were obtained. Higher reaction rates were observed in an apolar solvent such as toluene compared to THF. The nature of PHB chain-ends were not discussed.

Similarly, these authors reported that the neodymium complexes supported by diaminobis(phenoxide) ligands ($(O_2N_2)^1 = \{CH_2N(Me)CH_2\text{-}3,5\text{-}Me,^t\text{-}Bu\text{-}C_6H_2O\}_2$; $(O_2N_2)^2 = C_5H_4NCH_2N\text{-}\{CH_2\text{-}3,5\text{-}Me,^tBu\text{-}C_6H_2O\}_2$), $[\{(O_2N_2)^1Nd(BH_4)(\mu\text{-}BH_4)Li(THF)\}_2]$ (**31Nd**), and $[(O_2N_2)^2Nd(BH_4)(\mu\text{-}BH_4)Li(THF)_2]$ (**32Nd**; Scheme 14), provided atactic PLA ($\overline{M}n \leq 22{,}800\,g\,mol^{-1}$, $1.15 < \overline{M}w/\overline{M}n < 1.82$) and atactic PHB ($\overline{M}n \leq 5{,}000\,g\,mol^{-1}$, $1.07 < \overline{M}w/\overline{M}n < 1.12$) based on NMR analyses (Sinenkov et al., 2011) (Tables 1 and 2). The solvent effect was more pronounced in the case of *rac*-LA than of *rac*-BL, with ROP in THF being faster than in toluene. The data suggested that only one BH_4^- group initiated the ROP of *rac*-BL, and that with *rac*-LA, a single BH_4^- group initiated polymerization in the case of **31Nd**, and that both BH_4^- groups within **32Nd** were active. ^1H NMR spectra of low molar mass PLA samples showed the characteristic quartet (δ 4.33 ppm) for the —$CH(CH_3)OH$ terminal group whereas the exact nature of all termini could not be unambiguously determined. No noticeable

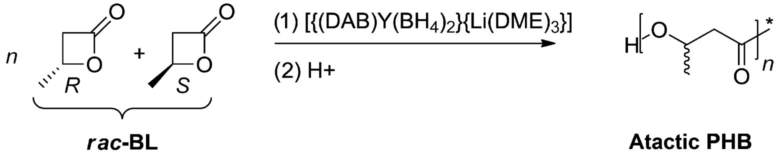

SCHEME 25 Nonstereoselective synthesis of atactic PHB from the ROP of BL initiated by $[\{(DAB)Y(BH_4)_2\}\{Li(DME)_3\}]$ (**35Y**).

influence of the ancillary ligand could be evidenced. The behavior of all these (DAB) and (O_2N_2) compounds is reminiscent to that of the above lanthanide borohydride *ate* complexes bearing guanidinate ligands, **22 Nd**, **22 Sm**, **22 Yb**.

3.1.3. Divalent Rare-Earth Borohydride Initiators

As a result of their higher sensitivity, with respect to their marked tendency to oxidize to the more stable trivalent state, divalent rare-earth borohydride complexes have only been rarely and lately studied as initiators in the polymerization of a polar monomer, namely of (only) CL (Guillaume et al., 2007; Iftner et al., 2011; Jaroschik et al., 2010; Momin et al., 2011) (Table 1).

3.1.3.1. Divalent Rare-Earth Borohydride Initiators Made *in Situ*

Kempe, Guillaume, and coworkers were the first to evaluate a divalent rare-earth borohydride initiating species in the ROP of a cyclic ester (Guillaume et al., 2007). The aminopyridinato ligand (Scott and Kempe, 2005) allowed stabilization and isolation of the mono-ancillary ytterbium(II) halide complex $[(\mathrm{Ap^*})\mathrm{YbI}(\mathrm{THF})_2]_2$ (**16Yb**). The pre-initiating ytterbium species formed *in situ* from the combination of **16Yb** and $NaBH_4$ (1–2 molar equiv) afforded high molar mass PCLs ($\overline{M}n \leq 47{,}500\,\mathrm{g\,mol^{-1}}$; $\overline{M}w/\overline{M}n$ *ca.* 1.56), yet with a control of the polymer features not as good as that obtained with the trivalent alike initiating systems **17La**, **18Lu**/$NaBH_4$ (Scheme 9) (Table 1). Indeed, the larger trivalent lanthanum bromide based initiating system **17La**/$NaBH_4$ afforded the best defined PCLs (*vide supra*). This whole study allowed evaluation, on a given –namely aminopyridinato– series of rare-earth derivatives, of the metal, of the oxidation state, and of the halide substituent effects, as rarely exemplified. Noteworthy, no oxidation of the divalent complex was observed during the ROP of CL, as opposed to the behavior of the samarium $[\mathrm{Sm(BH_4)_2(THF)_2}]$ (**2Sm**) and $[\{(\mathrm{Cp^*})\mathrm{Sm(BH_4)(THF)_2}\}_2]$ (**4Sm**) or thulium $[\mathrm{Tm(BH_4)_2(DME)_2}]$ (**2Tm′**) and $[(\mathrm{Tp}^{t\mathrm{Bu,Me}})\mathrm{Tm(BH_4)(THF)}]$ (**15Tm**) complexes described by Nief and Visseaux (Iftner et al., 2011; Jaroschik et al., 2010; Momin et al., 2011; *vide infra*).

3.1.3.2. Discrete Divalent Rare-Earth Borohydride Initiators

Of note, compounds based on $\mathrm{Tm^{II}}$ –the divalent lanthanide exhibiting the largest reducing power ($\mathrm{Tm^{II}} > \mathrm{Sm^{II}} > \mathrm{Yb^{II}} > \mathrm{Eu^{II}}$)– as later developed by Bonnet, Visseaux, Nief, and coworkers, $[\mathrm{Tm(BH_4)_2(DME)_2}]$ (**2Tm′**) and $[(\mathrm{Tp}^{t\mathrm{Bu,Me}})\mathrm{Tm(BH_4)(THF)}]$ (**15Tm**), were found active in the ROP of CL at 25 °C (Momin et al., 2011) (Table 1). However, assuming one growing PCL chain per R-BH_4, the control over the PCL molar mass and dispersity values remained limited, in comparison to the $\mathrm{Sm^{II}}$ initiator $[\{(\mathrm{Cp^*})\mathrm{Sm(BH_4)(THF)_2}\}_2]$ (**4Sm**) ($\overline{M}n$ up to 20,400 g $\mathrm{mol^{-1}}$ with $1.28 < \overline{M}w/\overline{M}n < 1.36$; Jaroschik et al., 2010; Iftner et al., 2011) (Table 1). With all four divalent initiators $[\mathrm{Sm(BH_4)_2(THF)_2}]$ (**2Sm**), **2Tm′**, **4Sm**, and **15Tm**, the metal was oxidized during the polymerization leading to a $\mathrm{R^{III}}$ active species, as hinted by the observed (from a dark to a light) color change of the reaction solution. The oxidation of the Tm^{II} center seemed faster than that of Sm^{II}. The monosubstituted complexes **4Sm** and **15Tm** seemed to display a higher activity in comparison to the homoleptic analogues **2Sm** and **2Tm′**, reflecting the influence of the ancillary ligand, Cp* and $Tp^{tBu,Me}$, respectively, in making the complex more readily oxidizable. Two different mechanisms, involving either monoelectronic transfer (favored at low $[CL]_0/[Sm]_0$ ratios = 116) or insertion into the Sm^{II}–BH_4 bond (favored at higher $[CL]_0/[Sm]_0$ ratios = 465), were suggested from the experimental results on the samarium complexes (Jaroschik et al., 2010), and next investigated computationally by Maron and coworkers (*vide infra*; Iftner et al., 2011).

3.1.4. Mechanistic Insights from Analytical Studies on the ROP of Lactones, Lactides, and α-Amino Acids N-Carboxyanhydrides Initiated by Rare-Earth Borohydride Complexes

3.1.4.1. ROP of Lactones and Lactides

The rare-earth borohydride complex used in the ROP of a polar monomer is herein commonly referred to as the initiator or as the catalyst. More precisely, it does act as a pre-initiator as described thereafter.

The ROP mechanism of a lactone initiated by a rare-earth borohydride complex has been first described by Guillaume and coworkers on the basis of comprehensive investigations (Guillaume et al., 2003; Palard et al., 2004, 2005). Detailed NMR, FTIR, MALDI-ToF MS, and elemental analyses, including in particular the monitoring of the stoichiometric reaction of $[La(BH_4)_3(THF)_3]$ (**1La**, a diamagnetic complex facilitating NMR understanding) and $[(Cp^*)_2Sm(BH_4)(THF)]$ (**5Sm**, an organometallic complex providing better solubility and featuring the Cp* as diagnostic group for NMR and MS investigations –and thus identification– of resulting intermediates) with CL, all the way to the hydrolysis products, allowed identification of several key intermediates which were isolated and fully characterized. As depicted in Scheme 26, during the initiation step, the first three incoming CL molecules displace the coordinated THF from the metal in $[Nd(BH_4)_3(THF)_3]$ (**1Nd**) to form the adduct $[Nd(BH_4)_3(CL)_3]$ (**i**). Subsequently, these first CL molecules insert into each of the Nd-HBH_3 bonds with a C(O)—O (oxygen-acyl) bond cleavage to give the intermediate $[Nd\{O(CH_2)_5C(O)H{\cdot}BH_3\}_3]$ (**ii**) (most likely solvated by a Lewis base). The displaced BH_3 group then immediately reduces the adjacent aldehyde to form a $—CH_2OBH_2$ function thereby generating the alkoxyborane derivative $[Nd\{O(CH_2)_5CH_2OBH_2\}_3]$ (**iii**). Ensuing propagation into the Nd—O bond of this active species gives the living polymer $[Nd[\{O(CH_2)_5C(O)\}_{n+1}O(CH_2)_6OBH_2]_3]$ (**iv**). Finally, upon termination –that is, quenching and deactivation– hydrolysis of both the R—O and $CH_2O—BH_2$ bonds of **iv** generates an hydroxyl end-group at each chain-end ($\delta_{1H/13C}$ 3.71/59.9 ppm) giving $HO(CH_2)_5C(O)\{O(CH_2)_5C(O)\}_nO(CH_2)_6OH$, HO–PCL–OH (**v**). Direct experimental evidence was provided

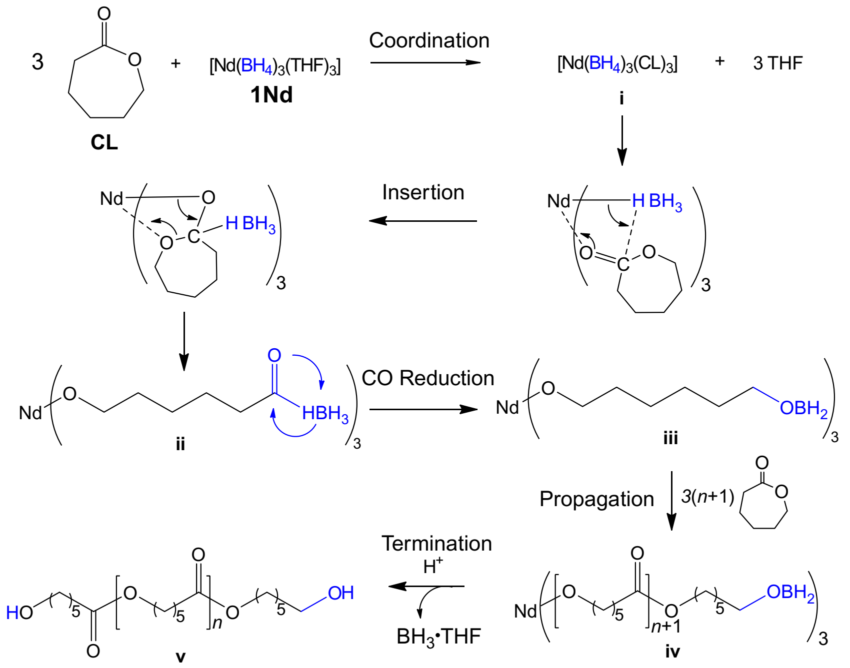

SCHEME 26 Proposed general mechanism for the ROP of CL initiated by a rare-earth borohydride complex illustrated with $[Nd(BH_4)_3(THF)_3]$.

for species of the type **i**, **iii**, **iv**, and **v** from both mono- and tris(borohydride) catalytic systems (Guillaume et al., 2003; Palard et al., 2004). Additional support of the presence of —CH_2OBH_2 groups (which lead to the formation of a "physical gel") during the polymerization process was obtained from FTIR investigations which unambiguously showed the presence of B–H unit(s) in the relevant intermediates depicted in Scheme 26 (Palard et al., 2005).

From these observations, the *pseudo* anionic coordination–insertion mechanism illustrated in Scheme 26 for the neodymium complex, involving in particular the carbonyl reduction by the reactive —HBH_3 group and common to all borohydride initiators $[(L)_xR(BH_4)_{3-x}(THF)]$ ("L_x" = ancillary ligand, for example, Cp^*_2; $x = 1–2$), was suggested to rationalize the formation of α,ω-hydroxytelechelic PCL. Finally, this mechanism has been corroborated by detailed DFT investigations by Maron and coworkers on both trisborohydride and single-site monoborohydride organometallic complexes (Barros et al., 2008a; *vide infra*) (Table 6). This mechanism is similarly taking place during the ROP of lactones (BL, Guillaume et al., 2013; CL, Guillaume et al., 2003; VL, Nakayama et al., 2009; PDL, Nakayama et al., 2011) or lactides (Dyer et al., 2010; Nakayama et al., 2007) initiated by trivalent rare-earth borohydride complexes.

The divalent samarium borohydride complex [$Sm(BH_4)_2(THF)_2$] (**2Sm**) has been suggested by Nief, Visseaux, and coworkers to operate through a similar coordination–insertion mechanism thereby affording α,ω-dihydroxytelechelic PCL (Jaroschik et al., 2010). A different monoelectronic oxidative process, with the polymerization induced by the oxidation of Sm^{II} then involving two samarium centers, was proposed to rationalize the single growing PCL chain per two metal ions and the observed chain-ends. DFT investigations computed this oxidative route through radical species to be favorable, but the study showed that it does not occur experimentally unless one considers transfer reactions with the solvent (*vide infra*; Iftner et al., 2011).

Therefore, in the ROP of a polar monomer promoted by a rare-earth borohydride complex, during the initiation step, the rare-earth borohydride complex reacts with the first incoming monomer molecule to form a complex then featuring a metal–oxygen bond, which is the real active species. In the ROP of cyclic esters and acrylates such as lactones, lactides or carbonates and methyl methacrylate (MMA), the complex formed from the equimolar mixture of the rare-earth borohydride and the first monomer moiety added, results in the formation of a rare-earth alkoxide/enolate (*vide infra*) as the real initiating and propagating species. Consequently, when using a rare-earth borohydride in the polymerization of a polar monomer, the propagation will always take place in a metal–oxygen (and not in a metal–HBH_3) bond. Also, the number of growing polymer chains is given, in a controlled “living” ROP process, by the number of R-BH_4 unit.

In such a coordination–insertion mechanism, the larger size of the metal center should accelerate the monomer coordination by providing less steric hindrance in a wider coordination sphere. However, as exemplified above in several series of rare-earth borohydride complexes, this trend does not always apply experimentally. Also, the potential coordination of a solvent or another substrate molecule onto the metal center may similarly impact the rate of polymerization. This reveals the significant role played by the ancillary(ies) in providing, along with the metal itself, a delicate balance of steric and electronic parameters. As demonstrated by the DFT investigations discussed below, thermodynamic as well as kinetic factors also significantly contribute to the whole energetic reaction profile.

Finally, we note that using rare-earth borohydride complexes rather than alkoxide ones as initiators does present the significant advantage of affording directly α,ω-dihydroxytelechelic polymers instead of α-alkoxy,ω-hydroxytelechelic analogues (Scheme 27; Palard et al., 2006). Whereas any initiator will always generate one hydroxyl chain-end upon hydrolysis of the metal–oxygen bond during termination, only borohydride complexes will concomitantly lead to a second alike —OH end-capping function thanks to the reduction of the cyclic ester carbonyl by the BH_3 group (Barros et al., 2008a; Palard et al., 2006). The potential ring-opening of the cyclic ester through a O—C (oxygen-alkyl) bond cleavage that may occur besides the

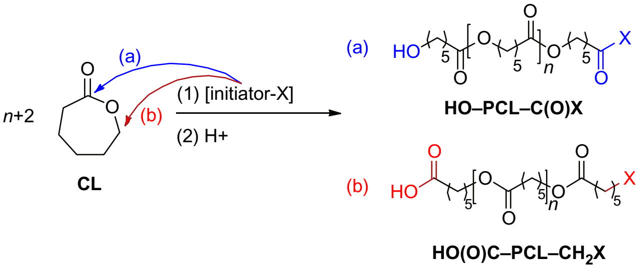

SCHEME 27 Synthesis of α,ω-functionalized PCL from the ROP of CL illustrating the two possible monomer openings, the O—C(O) oxygen-acyl (blue) and the O—C oxygen-alkyl (red) bond cleavages.

O—C(O) (oxygen-acyl) bond rupture, as in the case of cationic initiators and more often with the small four-membered ring β-lactones such as BL or propiolactone (Scheme 27), has been disclaimed in these mechanistic studies from polymer chain-end analyses.

In the related synthesis of end-capped PCLs through the reduction of an exogenous aldehyde or ketone R′C(O)R″ (R′ = alkyl, aryl, R″ = H, alkyl; Scheme 28) by the homoleptic rare-earth trisborohydride complexes **1R**, Sun and coworkers envisaged two possible mechanisms (Wu et al., 2008). Two concomitant reduction pathways involving either the active alkoxide complexes [R(OCHR′R″)$_3$] in the case of aromatic aldehydes or ketones (path A), or the BH_3·THF active byproduct in the case of substrates such as propanal and butanal with limited steric effect and high reactivity (path B), are proposed to account for the incomplete control of the polymerization observed experimentally (Scheme 28).

3.1.4.2. ROP of α-Amino Acids *N*-Carboxyanhydrides

The ROP of α-amino acids *N*-carboxyanhydrides studied experimentally with (γ-benzyl-L-glutamate *N*-carboxyanhydride) (BLG) has been investigated analytically by Shen, Ling, and coworkers in an effort to understand the polymerization mechanism (Peng et al., 2012a,b) (Table 3). In particular NMR and MS analyses of a polymer sample (no NMR data are, however, reported) prepared from the related L-alanine NCA (ALA) revealed an α-carboxylic-ω-aminotelechelic polypeptide chain (**A**) as the major product (Scheme 29). An activated monomer mechanism (typical tertiary amine NCA ROP mechanism; reaction pathway **A** in Scheme 29) was proposed to explain its formation. In this route, the *N*-yttrium metallated NCA (**i**) formed upon 3-NH deprotonation, attacks the second incoming ALA at the 5-CO leading to dimer (**ii**) featuring a highly electrophilic *N*-acyl NCA end-group and a nucleophilic carbamate end-group. Further chain growth then proceeds through the carbamate end by attack at the 5-CO of another NCA or of **i**, or through the

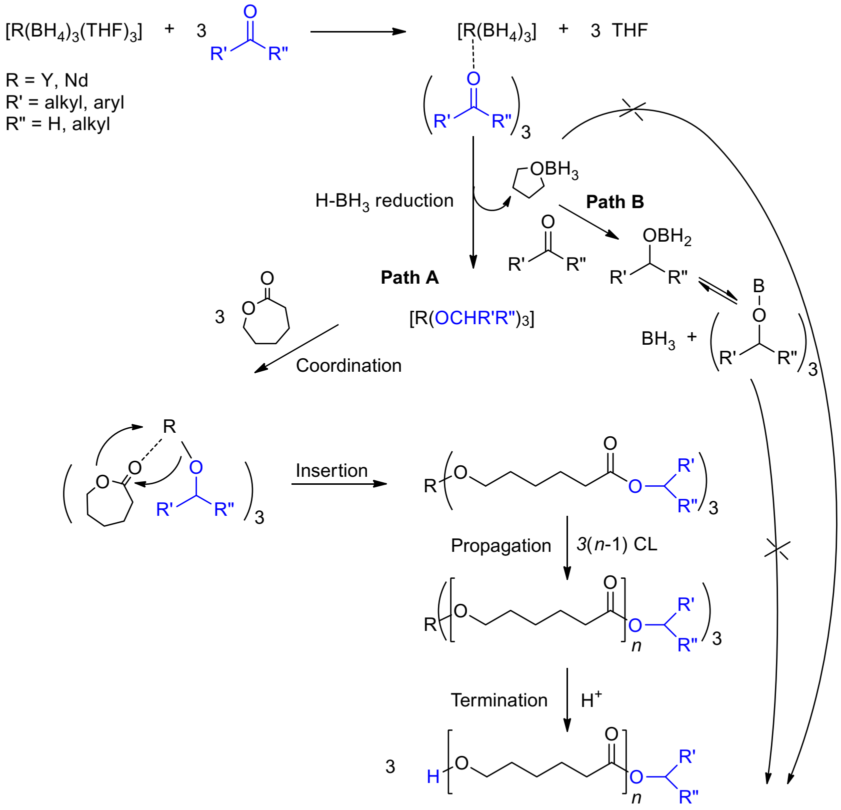

SCHEME 28 Proposed mechanism for the ROP of CL initiated by a rare-earth alkoxide generated *in situ* from **1**/R′R″C(O).

electrophilic *N*-acyl NCA end attacked by **i** or by the carbamate end of another **ii**. The COOH end-group is then generated during the precipitation upon 5-CO attack of *N*-acyl NCA end-group by H_2O and release of a molecule of CO_2. The (other) amino end-group arises from hydrolysis of the active yttrium carbamate group followed by release of one CO_2 molecule. The second major distribution of peaks was assigned to α-hydroxyl, ω-aminotelechelic polymer (**B**) formed via a nucleophilic ring-opening initiation and chain growth process (known as the normal amine mechanism; reaction pathway **B** in Scheme 29). The ALA attacks at 5-CO by $[Y(BH_4)_3(THF)_3]$, ring-opens and inserts into the Y—HBH_3 bond to give the intermediate (**iv**), in which the immediate interaction of the HBH_3 group with the α-carbonyl results in the formation of the corresponding yttrium alanine carbamate derivative (**v**). The ROP of ALA by **v** then proceeds through attack at its 5-CO by the yttrium carbamate with the (1-oxygen)-(5-acyl) bond cleavage, and subsequent release of one molecule of CO_2. Water termination/hydrolysis of the $[—NHCH(CH_3)CH_2(OBH_2)]$

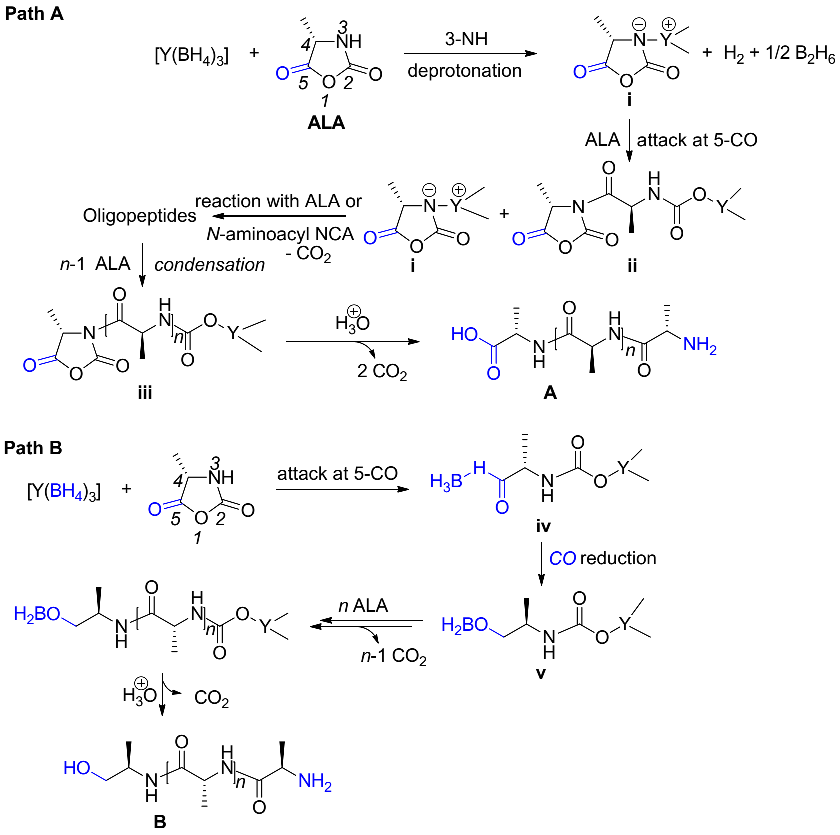

SCHEME 29 Postulated major mechanisms for the ROP of BLG initiated by [$Y(BH_4)_3(THF)_3$], **1Y**.

chain-end generates the hydroxyl end-group, while hydrolysis of the active yttrium carbamate group and release of CO_2 generate the amino group of the resulting α-hydroxyl,ω-aminotelechelic poly(ALA) chains (**B**). The swift back and forth switching between these two mechanisms afforded monomodal SEC traces and partial control of the polypeptide molar mass.

Both an amino and hydantoic (**C**, Scheme 30), and a carboxylic and hydantoic acid (**D**, Scheme 30) end-functionalized poly(ALA) were finally identified as minor products in the MALDI-ToF mass spectrum. The formation of product **C** is closely related to species **i**. After formation of the dimer **ii**, both cyclization and propagation competitively take place. The cyclized 3-(yttrium carboxylate) hydantoin product **iv** attacks the 5-CO of *N*-acyl NCA end-group of a polymer chain (**iii**), thus giving **C**. Also, the addition of a propagating nucleophilic carbamate end-group onto the yttrium α-isocyanato carboxylate that arises from the rearrangement of **i** is postulated to result in the formation of product **D** (Peng et al., 2012a,b).

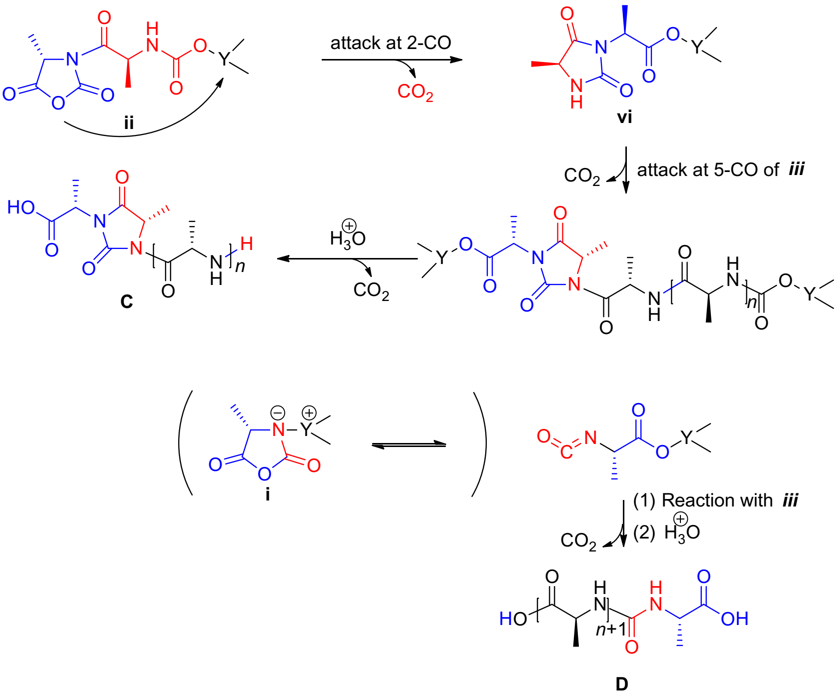

SCHEME 30 Proposed side reactions of the ROP of BLG initiated by $[Y(BH_4)_3(THF)_3]$, **1Y**.

3.1.5. Valuable α,ω-Dihydroxytelechelic Polyesters

The most significant advantage of using rare-earth borohydride complexes as initiators in the ROP of cyclic esters is the resulting *direct* formation of α,ω-dihydroxytelechelic polyesters which are not accessible from the more common alkoxide initiators (Scheme 27; Palard et al., 2006). Indeed, no chemical modification of a chain-end is required to generate the second OH group, the first one being necessarily created within the termination step upon hydrolysis of the active metal–oxygen bound into an OH (*vide supra*). Hydroxytelechelic polymers are indeed highly desirable and valuable since they provide easy access to copolymers which are otherwise not so straightforwardly prepared, or to original (multi-)block (co)polymers (*vide infra*, Section 3.5.2; Guillaume, 2013).

3.2. ROP of Trimethylene Carbonate

Given the reactivity of the BH_4^- group with the carbonyl of the first inserted lactone or diester monomer unit, the ROP of a carbonate monomer was foreseen as promising. However, in contrast to the ROP of lactones or lactides which have been comparatively quite investigated with a variety of inorganic and organometallic complexes (Table 1), studies on the ROP of a cyclic

TABLE 4 Rare-Earth Borohydride Complexes Used as Initiators in the (Co)Polymerization of Trimethylene Carbonate (TMC) and Experimental Data

Rare-earth borohydride complex	TMC ($[TMC]_0/[BH_4]_0$ highest value)[a]	Solvent Temp. (°C)	Reaction time Conv.[b]	$\overline{M}n_{max}$[c] ($\overline{M}n_{theo}$)[a,d] g mol^{-1}	$Đ_M$[e]	Copolymer
Trivalent complex						
$[\{CH(PPh_2NTMS)_2\}Y(BH_4)_2]$ (**20Y**, Scheme 11)	(250) (Guillaume et al., 2012)	Tol 20 °C	2 min 26%	8000 (6600)	1.29[f]	
$[\{CH(PPh_2NTMS)_2\}La(BH_4)_2(THF)]$ (**20La**, Scheme 11)	(250) (Guillaume et al., 2012)	Tol 20 °C	2 min 42%	11,300 (13,300)	1.47	
$[Sm(BH_4)_3(THF)_3]$ (**1Sm**, Scheme 1)	(345) (Palard et al., 2007)	THF, DCM 21 °C	4 h 74%	27,050 (26,050)	1.32	PTMC-*b*/*co*-PCL (Palard et al., 2007)
$[\{CH(PPh_2NTMS)_2\}Lu(BH_4)_2]$ (**20Lu**, Scheme 11)	(250) (Guillaume et al., 2012)	Tol 20 °C	5 min 47%	12,100 (12,000)	1.42	

[a] *Note that the* $[TMC]_0/[BH_4]_0$ *ratio is different from the* $[TMC]_0/[initiator/catalyst]_0$ *value, the former being used in the calculation of the theoretical molar mass* ($\overline{M}n_{theo}$) *assuming one growing chain per* BH_4^- *group.*

[b] *Monomer conversion determined by* ^1H *NMR or by gravimetry and corresponding to the highest* $[TMC]_0/[BH_4]_0$ *value reported.*

[c] *Number average molar mass (maximum value) determined by SEC versus polystyrene standards and corrected by a factor of 0.73 for TMC (Palard et al., 2004).*

[d] *Theoretical molar mass calculated from* $[TMC]_0/[BH_4]_0 \times$ *TMC conversion* $\times M_{TMC}$, *assuming one growing chain per* BH_4^- *group, with* $M_{TMC} = 102$ g mol^{-1}; *note that a discrepancy between* $\overline{M}n_{theo}$ *and* $\overline{M}n_{SEC}$ *may be indicative of a number of growing polymer chains different from the number of* BH_4^- *groups in the initiating complex.*

[e] *Calculated average dispersity value as reported from SEC traces.*

carbonate monomer are limited to trimethylene carbonate, TMC, and to just a couple of rare-earth borohydride initiators (Table 4).

3.2.1. Inorganic Rare-Earth Borohydride Initiators

To this end, poly(trimethylene carbonate), PTMC, was synthesized by Guillaume and coworkers from the ROP of TMC promoted by [$Sm(BH_4)_3(THF)_3$], **1Sm**, under mild conditions (Palard et al., 2007) (Table 4). Polycarbonates with quite high molar mass ($\overline{M}n_{SEC}$ up to 27,000 g mol^{-1}) were obtained in high yields, with a linear dependence of $\overline{M}n_{SEC}$ with the $[TMC]_0/[BH_4]_0$ ratio. Remarkably, the ROP proceeded without decarboxylation (no ether linkages observed in the NMR spectra of the polycarbonates) as otherwise commonly observed with other catalytic systems. The ROP of TMC (81% in 90 min at $[TMC]_0/[BH_4]_0 = 86$) was found, under similar operating conditions ($[\text{initiator}]_0$ *ca.* 4.5 mmol L^{-1}), to be slower than that of CL (100% in 5 min at $[CL]_0/[BH_4]_0 = 87$; Table 1). The dispersity values of PTMC ($\overline{M}w/\overline{M}n$ *ca.* 1.3) were quite narrow in comparison with PTMC samples prepared from other non-borohydride rare-earth initiators, and hardly larger than the ones measured for other polyesters- such as PCLs or PLAs- prepared from rare-earth borohydride complexes. Note that the correction factor applied to PTMC samples analyzed by SEC against polystyrene standards to correct for the hydrodynamic radius difference between such two distinct polymers was established in this original work from comparative MALDI-ToF MS, viscosimetry, and NMR investigations. Detailed ^{1}H and ^{13}C, 1D and 2D NMR and MALDI-ToF MS analyses revealed the formation of α-hydroxy,ω-formatetelechelic PTMC, the first example of formate end-functionalized PTMC (Scheme 31).

3.2.2. Organometallic Rare-Earth Borohydride Initiators

The unique study on the ROP of TMC promoted by an organometallic rare-earth borohydride complex involves the bis(phosphinimino)methanide bisborohydride complexes of lanthanum, yttrium, and lutetium, [{$CH(PPh_2NTMS)_2$}$La(BH_4)_2(THF)$] (**20La**) and [{$CH(PPh_2NTMS)_2$}$R(BH_4)_2$] (R = Y (**20Y**), Lu (**20Lu**)) reported by Guillaume et al. (2012) (Table 4). The ROP proceeded rapidly in toluene at 20 °C with quantitative TMC conversion reached within 2 min at $[TMC]_0/[\mathbf{20Y,La,Lu}]_0 = 100$ (TOF = 3000 $mol_{TMC}\ mol_{Y,La,Lu}\ h^{-1}$). At larger monomer loadings (500 equivs), this high activity was maintained or improved (TOF up to

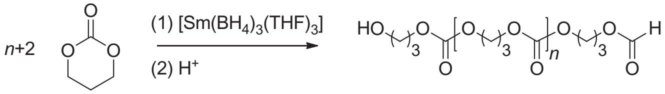

SCHEME 31 Synthesis of HO–PTMC–OC(O)H from the ROP of TMC initiated by [$Sm(BH_4)_3(THF)_3$], **1Sm**.

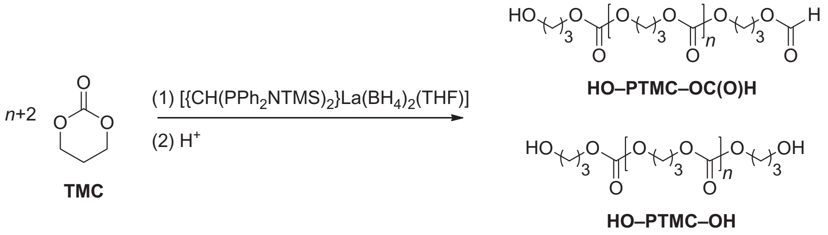

SCHEME 32 Synthesis of HO–PTMC–OC(O)H and HO–PTMC–OH from the ROP of TMC initiated by $[\{CH(PPh_2NTMS)_2\}La(BH_4)_2(THF)]$, **20La**.

6300 $mol_{TMC}\,mol_{La}\,h^{-1}$). Changing the solvent to THF was found to inhibit the polymerization. A good control of the PTMC molar mass was obtained up to $\overline{M}n_{SEC} \approx \overline{M}n_{NMR} \approx \overline{M}n_{theo} = 10{,}000\,g\,mol^{-1}$. Although the SEC traces remained unimodal, the $\overline{M}w/\overline{M}n$ values around 1.42 indicated the occurrence of transcarbonatation reactions as commonly encountered in the ROP of carbonates. ^1H NMR analyses of the PTMC samples only showed the presence of both hydroxy and formate end-groups, featuring a HO—C*H*$_2$— and —$CH_2OC(O)$*H* intensity ratio of generally 2:1. The concomitant formation of α-hydroxy,ω-formate telechelic PTMC (*vide infra*, Scheme 34 path A) and of α,ω-dihydroxytelechelic PTMC (*vide infra*, Scheme 34 path B), displaying a common —C*H*$_2$OH ^1H NMR signal, was also likely and could not be ruled out from the experimental data (Scheme 32). *In silico* investigations of the mechanism next revealed the formation of the latter heterofunctionalized α-hydroxy, ω-formatetelechelic PTMCs to be slightly preferred computationally. Also, these DFT insights highlighted the valuable role of the bis(phosphinimino)methanide ligand (*vide infra*).

3.2.3. Mechanistic Insights from Analytical Studies on the ROP of TMC Initiated by Rare-Earth Borohydride Complexes

Given the ROP mechanism of the related CL, initiated by rare-earth borohydride complexes, the mechanism of the ROP of TMC has been similarly investigated from detailed NMR, FTIR, and MALDI-ToF MS analyses. In particular, the (soluble) $[Sm(BH_4)_3(EtOC(O)OEt)_3]$ intermediate was successfully isolated and characterized, thus demonstrating the initial displacement of THF from the Sm coordination sphere by the incoming (non polymerizable) Et_2CO_3 carbonate molecules (Palard et al., 2007). The initiation step of the polymerization of TMC promoted by $[Sm(BH_4)_3(THF)_3]$ (**1Sm**) thus involves the substitution of the coordinated THF by the first three incoming carbonate molecules to give $[Sm(BH_4)_3(TMC)_3]$ (**i**) (Scheme 33). The nucleophilic attack of **i** on the carbon atom of the TMC carbonyl function was followed by the carbonate insertion into the Sm—HBH_3 bond with an oxygen-acyl bond cleavage to form $[Sm\{O(CH_2)_3OC(O)HBH\}_3]$, (**ii**). Indeed careful analysis of the polymer chain-ends by ^1H and ^{13}C NMR did not show the

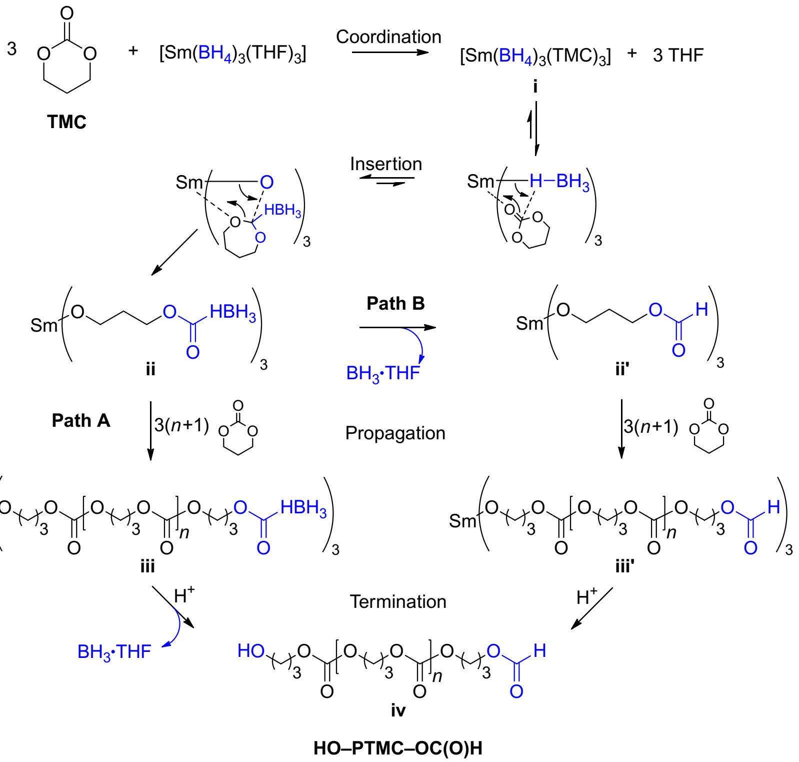

SCHEME 33 Proposed mechanism for the ROP of TMC initiated by a rare-earth borohydride initiator illustrated with $[Sm(BH_4)_3(THF)_3]$, **1Sm**.

terminal specific HOC(O)O— and —CH_2CH_3 groups arising from an oxygen-alkyl (OC(O)O—CH_2) bond breakage, but clearly evidenced the $HOCH_2$— and —OC(O)H protons and carbons at δ 3.71/59.9 and 8.03/161.8 ppm, respectively. At this stage, it appeared experimentally, from the NMR spectra of the analogous lanthanum species which display the —O*C*(O)H signals, that the C(O) of the inserted carbonate of **ii** would not undergo reduction by the adjacent H–BH_3 group, unlike in the case of CL. However, elimination of the $BH_3 \cdot THF$ adduct from **ii** (Scheme 33 path **B**) or later on upon hydrolysis from **iii** (Scheme 33 path **A**), could not be established from experimental data. Propagation then proceeds from the active samarium alkoxide species **ii**/**ii**′ into the active polymer $[Sm\{O(CH_2)_3OC(O)\}_{n+1}\{O(CH_2)_3OC(O)HBH_3\}_3]$, (**iii**), or the BH_3-free analogue $[Sm\{O(CH_2)_3OC(O)\}_{n+1}\{O(CH_2)_3OC(O)H\}_3]$ (**iii**′), respectively. Termination upon acidic hydrolysis of the Sm—O and possibly of the $OC(O)HBH_3$ bond(s) (path A), gives the α-hydroxy,ω-formatetelechelic PTMC, $HO(CH_2)_3OC(O)\{O(CH)_3OC(O)\}_nO(CH)_3OC(O)H$, HOPTMC—OC(O)H, (**iv**) (Scheme 33). This is the first *pseudo* anionic coordination–insertion type process fully detailed for the ROP of a carbonate initiated by a rare-earth complex. It is also different from the cationic process described for the ROP of TMC initiated by rare-earth trishalides (Shen et al., 1997), which proceeds through an oxygen-alkyl bond scission of the monomer leading to a high concentration of ether segments, not observed in this study.

Interestingly, the use of the organometallic bis(phosphinimino)methanide bisborohydride rare-earth complexes $[\{CH(PPh_2NTMS)_2\}R(BH_4)_2(THF)]$ (R = La (**20La**), Y (**20Y**), Lu (**20Lu**)) by Guillaume et al. (2012), raised the question of the carbonyl reduction by the BH_3 function leading to the formation of a putative α-hydroxy,ω-hemiacetaltelechelic PTMC (Scheme 34). The latter species, $[H\{O(CH_2)_3OC(O)\}_{n+1}O(CH_2)_3OCH_2OH]$ (**ii′**) would be formed after the coordination–insertion of the first incoming TMC molecules to **20La** (in)to $[\{CH(PPh_2NTMS)_2\}La\{O(CH_2)_3OC(O)HBH_3\}]$ (**i**), followed by the reduction of the adjacent carbonyl group of **i** by the terminal BH_3 into

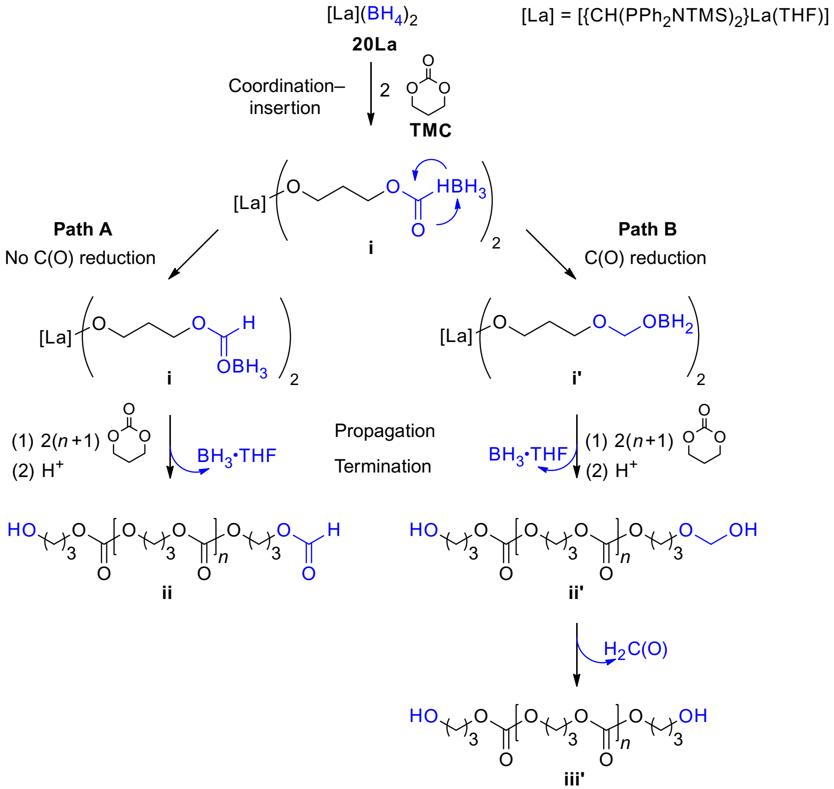

SCHEME 34 Proposed mechanism for the ROP of TMC initiated by $[\{CH(PPh_2NTMS)_2\}La(BH_4)_2(THF)]$, **20La**.

[{CH($PPh_2NTMS)_2$}La{O($CH_2)_3OCH_2OBH_2$}] (**i**′) and then by the propagation (Scheme 34 path **B**), as observed with the ROP of CL (Scheme 26). However, no evidence of **ii**′ could be detected by ^{1}H NMR most likely because the unstable hemiacetal chain-end evolved toward an —OH group with liberation of formaldehyde, thus affording the α,ω-dihydroxytelechelic PTMC, [H{O($CH_2)_3$OC(O)}$_n$O($CH_2)_3$OH] (**iii**′) (Scheme 34 path **B**). The hydroxyl chain-ends of **iii**′ would then be identical to the one of the α-hydroxy,ω-formatetelechelic PTMC (**ii**), the latter being formed via the ROP mechanism which does not involve the carbonyl reduction (Scheme 34 path **A**), as previously described for the ROP of TMC from trisborohydride complexes and illustrated in Scheme 33 with [Sm($BH_4)_3$($THF)_3$] (**1Sm**). DFT studies next showed that these two mechanisms (Scheme 34 path **A** and **B**) were computationally feasible (*vide infra*).

3.3. Concluding Remarks on the ROP of Polar Monomers Initiated by Rare-Earth Borohydride Complexes

The molar mass of the polymers formed from the controlled ROP of a polar cyclic (non-acrylate) monomer generally remains smaller than 50,000 g mol^{-1}; yet, higher molar mass values have not necessarily been targeted (Tables 1–4). Note that a difference between the experimental molar mass value ($\overline{M}n_{SEC}$), and the one calculated ($\overline{M}n_{theo}$) assuming that all BH_4^- groups participate in the ROP, suggested either a poor control of the catalytic system, or a number of initiating BH_4^- functions different from expected (Penczek and Moad, 2008).

It is noteworthy that regarding polylactones and polylactides, the narrowest dispersity values ($\overline{M}w/\overline{M}n < 1.06$) were obtained for the ROP of CL initiated by the bisphosphiniminomethanide complexes [{CH($PPh_2NTMS)_2$}La($BH_4)_2$(THF)] (**20La**) and [{CH($PPh_2NTMS)_2$}R($BH_4)_2$] (R = Y (**20Y**), Lu (**20Lu**)), reported by Roesky, Guillaume, Maron, and coworkers (Jenter et al., 2010), or with the synthesis of PHB promoted by the diaminobis(phenoxide) complexes [{($O_2N_2)^1$Nd($BH_4)_2$Li(THF)}$_2$] (**31Nd**) and [($O_2N_2)^2$Nd($BH_4)_2$Li($THF)_2$] (**32Nd**) reported by Carpentier, Trifonov, and coworkers (Sinenkov et al., 2011), or by the homoleptic rare-earth trisborohydride complexes [R($BH_4)_3$($THF)_3$] (R = La (**1La**), Nd (**1Nd**), Sm (**1Sm**)) as found by Guillaume et al. (2013), thus suggesting a well-controlled ROP process in these cases (Tables 1 and 2). The $\overline{M}w/\overline{M}n$ values recorded for poly(lactide)s prepared from rare-earth borohydride catalysts were larger than the ones commonly obtained from a well-controlled ROP process involving the more common alkoxide initiators. In comparison to polylactones, the dispersity values usually obtained for PTMC ($\leq$1.3) samples were generally higher as a result of a larger extent of transcarbonatation side reactions versus transesterification ones (Tables 1–4).

The activities of the rare-earth borohydrides investigated in the ROP of polar monomers (under the operating conditions reported, that is, reaction times not necessarily optimized) including lactones, lactides, *N*-carboxyanhydrides, and carbonates can be estimated from data gathered in Tables 1–4. The comparison shows the highest activity of up to $TOF = 34{,}200\ mol_{CL}\ mol_{Lu}\ h^{-1}$, recorded with bis(phosphinimino)methanide borohydride complexes $[\{CH(PPh_2NTMS)_2\}La(BH_4)_2(THF)]$ (**20La**) and $[\{CH(PPh_2NTMS)_2\}R(BH_4)_2]$ (R = Y (**20Y**), Lu (**20Lu**)), by Roesky, Guillaume, Maron, and coworkers (Jenter et al., 2010), to be in the same range as those obtained with the rare-earth cationic bisborohydride complexes $[R(BH_4)_2(THF)_5][BPh_4]$ (R = Y (**6Y**); La (**6La**), Nd (**6Nd**), Sm (**6Sm**)) ($TOF = 30{,}000\ mol_{CL}\ mol_{Y,La,Nd,Sm}\ h^{-1}$) by Okuda and coworkers (Robert et al., 2008), or with the bridging monoborohydride diaminobis(phenoxide) derivatives $[\{(O_2NN^{py})R(\mu\text{-}BH_4)(THF)_n\}_2]$ (R = Y, $n = 0.5$ (**26Y**), Nd, $n = 1$ (**26Nd**), Sm, $n = 0$ (**26Sm**)) ($TOF = 29{,}700\ mol_{CL}\ mol_{Sm}\ h^{-1}$) reported by Mountford (Bonnet et al., 2005a). Remarkably, these activities are, to our knowledge, the highest values reported for rare-earth borohydride initiators promoting either a cyclic polar monomer or an acrylate (*vide infra*) polymerization (Tables 1–4).

Although within a given series of rare-earth complexes, a direct correlation of the polymerization activity with the ionic radii of the metal centers is often observed, this trend cannot be taken as a general rule throughout the rare-earth series. Indeed, subtle parameters often related to the steric and electronic contribution of the ancillary molecule(s), and most significantly to the nature of the ligand itself as well as to the presence of the "non-spectator" BH_4^- ligand, have to be taken into account. This can be assessed through DFT investigations as elegantly exemplified with the interaction of the bisphosphiniminomethanide ligand with the borohydride ligand.

The mechanism for the ROP of cyclic lactones, lactides, carbonates, and α-amino acid *N*-carboxyanhydrides, based on experimental investigations, are now well established and recognized. However, the exact nature of the polymer end-capping functions has not yet been systematically investigated or evidenced. Whereas α,ω-dihydroxytelechelic PHB, PCL, PVL, PPDL, PLA, PLLA, PTMC are formed, other end-functionalized PTMCs and PBLGs have also been obtained, thus underlying the singularity of both carbonate and α-amino acid NCA monomers. As addressed thereafter, DFT input has been a determining factor to support (some of) the mechanisms proposed and to provide other energetic information otherwise inaccessible.

Regarding the ROP of cyclic carbonates or α-amino acid *N*-carboxyanhydrides, the investigations remain quite rare in comparison to other cyclic esters (lactones and lactides) and limited to TMC and BLG monomers. The concomitant occurrence of several possible ROP pathways, as evidenced experimentally and especially from mechanistic insights, may be a limiting factor.

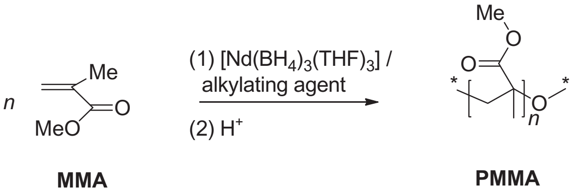

SCHEME 35 Synthesis of PMMA from the polymerization of MMA initiated by $Nd(BH_4)_3(THF)_3$ (**1Nd**).

3.4. Polymerization of Methyl Methacrylate

3.4.1. Inorganic and Organometallic Rare-Earth Borohydride Initiators

Using $Nd(BH_4)_3(THF)_3$ (**1Nd**) as a pre-initiator, in association with variable amounts of an alkylating agent as co-catalyst such as Mg^nBu_2, ^{n}BuLi or $[(2,6\text{-}^t\text{Bu-4-Me-}C_6H_3O)_2AlEt]$, poly(methyl methacrylate) (PMMA) with different tacticities depending on the solvent, was prepared at −40/0 °C in yields up to 95% by Visseaux and coworkers (Scheme 35; Barbier-Baudry et al., 2006) (Table 5). Highly syndiotactic PMMA (rr up to 75%) was formed from all reactions performed in THF, whereas only the use of **1Nd**/BuLi in toluene led to an isotactic enriched PMMA (mm up to 93%). No mechanistic information was reported.

The polymerization of methyl methacrylate (MMA) initiated by the rare-earth borohydride complexes $[R(BH_4)_3(THF)_3]$ (R = Nd (**1Nd**), Sm (**1Sm**)) or $[(Cp^*)_2Sm(BH_4)(THF)]$ (**5Sm**) proceeded in various solvents (THF, DCM, toluene) at ambient temperature to give rather syndiotactic (rr up to 67%) poly(methyl methacrylate) as reported by Maron, Guillaume, and coworkers (Barros et al., 2008b) (Table 5). Lowering the temperature from 25 to −10 °C improved the conversion of MMA from 10% in 24 h to 35% in 4 h when using **1Nd**/DCM. Use of the metallocene complex **5Sm** enabled to reach quantitative MMA conversion and significantly enhanced both the activity (TOF up to $111\ \text{mol}_{\text{MMA}}\ \text{mol}_{\text{Sm}}\ \text{h}^{-1}$) and the productivity (up to 221 turnover numbers in 2 h). However, the experimental molar mass values were generally much higher than expected and quite broad dispersities ($1.2 < \overline{M}w/\overline{M}n < 2.7$) were obtained, suggesting poor initiation efficiency. DFT investigations by Maron, Guillaume, and coworkers of MMA polymerization reactions using $[(Cp)_2Eu(BH_4)]$ as model initiator in comparison to $[(Cp)_2Eu(H)]$ (related to Yasuda's work on $[\{(Cp^*)_2Sm(H)\}_2]$) rationalized these experimental data, and allowed a ROP mechanism to be established (*vide infra*, Barros et al., 2008b). In particular, in the reaction of $[(Cp)_2Eu(BH_4)]$ with MMA, the most likely among all possible computed products was the exergonic borate $[(Cp)_2Eu\ \{(OBH_3)(OMe)C{=}C(Me)_2\}]$ complex, which was formed via the enolate $[(Cp)_2Eu\ \{O\ (OMe)C{=}C(Me)_2\}]$ (Scheme 36).

TABLE 5 Rare-Earth Borohydride Complexes Used as Initiators in the (Co)Polymerization of Methylmethacrylate (MMA) and Experimental Data

Rare-earth borohydride complex	MMA ($[MMA]_0/[BH_4]_0$ highest value)[a]	Solvent Temp. (°C)	Reaction time Conv.[b]	$\overline{\mathrm{Mn}}_{\mathrm{max}}$[c] ($\overline{\mathrm{Mn}}_{\mathrm{theo}}$)[a,d] g mol^{-1}	$Đ_M$[e]	Polymer Tacticity (%)	Copolymer
Trivalent complex							
$[(C_5Me_4—C_6H_4\text{-}o\text{-}NMe_2)Sc(BH_4)_2]$(**11Sc**, Scheme 6)	(250) (Jian et al., 2010)	Benz, THF 20 °C	2 h Benz: TOF = 13 THF: TOF = 70	16,600 (nd)[f]	1.59	mm/mr/rr Benz: 80/14/6 THF: 2/24/74	
$[(C_5Me_4—C_6H_4\text{-}o\text{-}NMe_2)Sc(BH_4)_2]$(**11Sc**, Scheme 6)/ Mg^nBu_2, ^nBuLi[g]	(250) (Jian et al., 2010)	Benz, THF 20 °C	THF: 2.5 min TOF = 15	190,000 (nd)[f]	2.16	THF: mm/mr/rr 0/20/80	
$[\{CH(PPh_2NTMS)_2\}Y(BH_4)_2]$ (**20Y**, Scheme 11)	(400) (Guillaume et al., 2011)	THF, Tol 23 °C	24 h <5%	nd[f,h]	nd[f,h]	mm/mr/rr 25/31/44	
[{CH(PPh2NTMS)2}La(BH4) 2(THF)](**20La**, Scheme 11)	(400) (Guillaume et al., 2011)	THF, Tol 23 °C	2 h 9%	nd[f,h]	nd[f,h]	mm/mr/rr 29/40/31	
$[Nd(BH_4)_3(THF)_3]$ (**1Nd**, Scheme 1)	(130) (Barros et al., 2008b)	THF, DCM, Tol 25 °C	4 h THF: 22%	31,500 (680)	2.1	mm/mr/rr 16/27/57	

[Nd$(BH_4)_3(THF)_3$] (**1Nd**, Scheme 1)/Mg^{n}Bu$_2$, ^{n}BuLi, [(2,6-^{t}Bu-4-Me-$C_6H_3O)_2$AlEt][g]	(167) (Barbier-Baudry et al., 2006)	THF, Tol −40 °C	THF: 23 h, 81% Tol: 3 h, 95%	110,000 (13,500)[f]	2.46	mm/mr/rr THF: 3/22/75 Tol: 93/6/1, 1/18/81	
[$(Cp^{*Pr})_2$Nd(BH_4)(THF)] (**6Nd**)/Mg^{n}Bu$_2$, ^{n}BuLi[g]	(500) (Barbier-Baudry et al., 2006)	THF, Tol 0 °C	15 h 100%	31,000 (44,500)[f]	2.85	mm/mr/rr 4/18/78, 77/11/12	
[(Cp^{*Pr})Nd$(BH_4)_2(THF)_2$] (**10Nd**, Scheme 7)/^{n}BuLi[g,i]	(250) (Barbier-Baudry et al., 2006)	THF, Tol 0 °C	19 h 92%[i]	21,400[i] (23,000)[f] Tol: BM[i,j]	2.0[i]	mm/mr/rr THF: 0/27/73[i] Tol: 94/5/1[i]	
[(Cp^{*Pr})\{(*p*-Tol)NN\}R(BH_4)] R = Nd (**12Nd**), Sm (**12Sm**) (Scheme 7)/BuLi[g,i]	(500) (Barbier-Baudry et al., 2006)	Tol 0 °C	16 h Nd: 100%[i] Sm: 59%[i]	1,000,000[i] (50,000)[f] or BM[j]	1.5[i]	mm/mr/rr 96/3/1[i]	
[\{$(TMS)_2$NC$(NCy)_2$\}$_2$Nd$(BH_4)_2$Li$(THF)_2$] (**22Nd**, Scheme 12)	(775) (Skvortsov et al., 2007c)	Tol 21 °C	8 h 39%	615,050 (30,550)[f]	2.72	mm/mr/rr 31/34/35	
[\{$(TMS)_2$NC$(N^iPr)_2$\}$_2$Nd$(BH_4)_2$Li$(THF)_2$][i] (**23Nd**)	(250) (Skvortsov et al., 2007b)	Tol, RT	3 h 52%[i]	8500[i] (13,000)[f]	2.52[i]	mm/mr/rr 44/41/15[i]	
[Sm$(BH_4)_3(THF)_3$] (**1Sm**, Scheme 1)	(125) (Barros et al., 2008b)	THF, DCM, Tol 25 °C	24 h Tol: 7%	30,000 (880)	2.2	mm/mr/rr 24/20/56	PCL-*b*-PMMA PMMA-*b*-PCL-*b*-PMMA (Schappacher et al., 2007)

Continued

TABLE 5 Rare-Earth Borohydride Complexes Used as Initiators in the (Co)Polymerization of Methylmethacrylate (MMA) and Experimental Data—Cont'd

Rare-earth borohydride complex	MMA ($[MMA]_0/[BH_4]_0$ highest value)[a]	Solvent Temp. (°C)	Reaction time Conv.[b]	$\overline{Mn}_{max}$[c] ($\overline{Mn}_{theo}$)[a,d] g mol^{-1}	$Đ_M$[e]	Polymer Tacticity (%)	Copolymer
[(Cp*)$_2$Sm(BH$_4$)(THF)] (**5Sm**)	(320) (Barros et al., 2008b)	THF, DCM, Tol 25 °C	20 h THF: 100%[i]	378,000[i] (22,140)	2.1	mm/mr/rr 18/15/67	
[(Cp^{Ph3})$_2$Sm(BH$_4$)(THF)][i] (**7Sm**)	(500)[i] (Barbier-Baudry et al., 2006)	Tol 0 °C	16 h 90%[i]	418,000[i] (45,000)[f]	2.5[i]	mm/mr/rr 0/18/82[i]	
[(Cp^{Ph3})$_2$Sm(BH$_4$)(THF)] (**7Sm**)/^{n}BuLi[g,i]	(500)[i] (Barbier-Baudry et al., 2006)	THF 0 °C	23 h 67%[i]	31,500[i] (33,500)[f]	2.1[i]	mm/mr/rr 2/28/70[i]	
[(Cp^{iPr4})$_2$Sm(BH$_4$)][i] (**8Sm**)	(50)[i] (Barbier-Baudry et al., 2006)	Tol 25 °C	4 h 100%[i]	540,000[i] (5000)[f]	1.45[i]	mm/mr/rr –/–/68	
[(Cp^{iPr4})$_2$Sm(BH$_4$)] (**8Sm**)/Mg^{n}Bu$_2$,[g,i] ^{n}BuLi[g]	(500) (Barbier-Baudry et al., 2006)	Tol 0 °C	20 h 45%	BM[j]	BM[j]	mm/mr/rr 85/11/4	
[(Cp^{Ph3})Sm(BH$_4$)$_2$(THF)$_2$] (**9Sm**)/Mg^{n}Bu$_2$, ^{n}BuLi[g,i]	(250) (Barbier-Baudry et al., 2006)	Tol 0 °C	16 h Mg: 70%[i] Li: 23%[i]	BM[j]	BM[j]	mm/mr/rr Mg: 17/18/65[i] Li: 84/7/9[i]	

$[(\mathrm{Cp}^{*\mathrm{Pr}})\mathrm{Sm}(\mathrm{BH}_4)_2(\mathrm{THF})_2]$ (**10Sm**)/$\mathrm{Mg}^n\mathrm{Bu}_2$[g]	(250) (Barbier-Baudry et al., 2006)	Tol 0 °C	6 h 45%	nd[f]	nd[f]	mm/mr/rr 41/19/40
$[(\mathrm{C}_5\mathrm{Me}_4\text{—}\mathrm{C}_6\mathrm{H}_4\text{-}o\text{-}\mathrm{NMe}_2)\mathrm{Sm}(\mathrm{BH}_4)_2]$(**11Sm**, Scheme 6)	(250) (Jian et al., 2010)	Benz, THF 20 °C	Benz: 2.5 h TOF = 4 THF: 1 h TOF = 42	21,600 (nd)[f]	1.51	mm/mr/rr Benz: 43/37/20 THF: 9/33/58
$[(\mathrm{C}_5\mathrm{Me}_4\text{—}\mathrm{C}_6\mathrm{H}_4\text{-}o\text{-}\mathrm{NMe}_2)\mathrm{Sm}(\mathrm{BH}_4)_2]$(**11Sm**, Scheme 6)/$^n\mathrm{BuLi}$[g]	(250) (Jian et al., 2010)	THF 20 °C	1 h TOF = 40	246,300 (nd)[f]	1.90	mm/mr/rr 4/24/72
$[(\mathrm{Cp}^{\mathrm{Ph3}})\{(p\text{-Tol})\mathrm{NN}\}\mathrm{Sm}(\mathrm{BH}_4)]$ (**13Sm**)/BuLi[g,i]	(500) (Barbier-Baudry et al., 2006)	THF, Tol −10 °C	THF: 24 h 79%[i] Tol: 3 h 68%[i]	36,400 (39,500)[f,i] Tol: BM[i,j]	2.4[i]	mm/mr/rr THF: 1/24/75[i] Tol: 93/5/2[i]
$[\{(\mathrm{TMS})_2\mathrm{NC}(\mathrm{NCy})_2\}_2\mathrm{Sm}(\mathrm{BH}_4)_2\mathrm{Li}(\mathrm{THF})_2]$ (**22Sm**, Scheme 12)	(775) (Skvortsov et al., 2007c)	Tol 21 °C	8 h 62%	58,000 (48,300)[f]	1.53	mm/mr/rr 51/12/37
$[\{(\mathrm{TMS})_2\mathrm{NC}(\mathrm{N}^i\mathrm{Pr})_2\}_2\mathrm{Sm}(\mathrm{BH}_4)_2\mathrm{Li}(\mathrm{THF})_2]$[i] (**23Sm**)	(250) (Skvortsov et al., 2007b)	Tol RT	3 h 77%[i]	199,900[i] (19,250)[f]	9.95[i]	mm/mr/rr 22/31/47[i]
$[\{(\mathrm{N}_2\mathrm{NN}^{\mathrm{TMS}})\mathrm{Sm}(\mathrm{BH}_4)\}_2]$ (**24Sm**, Scheme 13)	(200) (Bonnet et al., 2005b)	Tol/THF 25 °C	3 h 50%	35,660[i] (10,000)[f]	1.21[i]	mm/mr/rr 27/38/35[i]

Continued

TABLE 5 Rare-Earth Borohydride Complexes Used as Initiators in the (Co)Polymerization of Methylmethacrylate (MMA) and Experimental Data—Cont'd

Rare-earth borohydride complex	MMA ($[MMA]_0/[BH_4]_0$ highest value)[a]	Solvent Temp. (°C)	Reaction time Conv.[b]	$\overline{M}n_{max}$[c] ($\overline{M}n_{theo}$)[a,d] $g\ mol^{-1}$	$Đ_M$[e]	Polymer Tacticity (%)	Copolymer
$[\{(N_2NN^{Mes})Sm(BH_4)_2Li\}_2]$ (**25Sm**, Scheme 13)[i]	(100)[i] (Bonnet et al., 2005b)	Tol/THF 25 °C	12 h 26%[i]	12,400[i] (2600)[f]	1.64[i]	mm/mr/rr 25/40/35[i]	
$[(ArO)Er(BH_4)_2(THF)_2]$ (**19Er**, Scheme 10)	(100) (Yuan et al., 2006a)	Tol 0 °C	1.5 h 58%	96,500 (4150)[f]	nd[f]	mm/mr/rr 6/34/60	
$[\{(TMS)_2NC(NCy)_2\}Er(BH_4)_2(THF)_2]$(**21Er**)	(300) (Yuan et al., 2006b)	Tol 0 °C	2.5 h 28%	25,800 (7100)[f]	2.45	nd[f]	
$[(ArO)Yb(BH_4)_2(THF)_2]$ (**19Yb**, Scheme 10)	(100) (Yuan et al., 2006a)	Tol 0 °C	1.5 h 60%	98,000 (4710)[f]	nd[f]	mm/mr/rr 7/34/59	
$[\{(TMS)_2NC(NCy)_2\}Yb(BH_4)_2(THF)_2]$(**21Yb**)	(150) (Yuan et al., 2006b)	Tol 0 °C	1.5 h 41%	15,100 (6150)[f]	2.05	nd[f]	
$[\{(TMS)_2NC(NCy)_2\}_2Yb(BH_4)_2Li(THF)_2]$ (**22Yb**, Scheme 12)	(775) (Skvortsov et al., 2007c)	Tol 21 °C	8 h 32%	57,700 (24,900)[f]	1.63	mm/mr/rr 52/32/16	

[{CH(PPh_2NTMS)$_2$}Lu(BH_4)$_2$] (**20Lu**, Scheme 11)	(400) (Guillaume et al., 2011)	THF, Tol 23 °C	24 h 11%	nd[f,h]	nd[f,h]	mm/mr/rr 12/27/61
[{(2,6-*i*$Pr_2C_6H_3$)NC(Me) CHC(Me)N(C_6H_5)}$_2$RBH_4] R = Y (**36Y**), Yb (**36Yb**) (Scheme 16) [({N(2-MeC_6H_4)C(Me)}$_2$CH)$_2$ RBH_4]R = Y (**37Y**), Yb (**37Yb**) (Scheme 16)	(2500) (Shen et al., 2012)	Tol 0 °C	2 h 100%	72,090 (nd)	1.62	mm/mr/rr 0/21/80
Supported complex						
[(@SiO)Nd(BH_4)$_2$(THF)$_{2.2}$] (**38Nd**)	(500) (Del Rosa et al., 2012)	–[f]	9 h (40%)	42,200 (nd) [f]	4.2	mm/mr/rr 69/15/16

[a] *Note that the $[MMA]_0/[BH_4]_0$ ratio is different from the $[MMA]_0/[initiator/catalyst]_0$ value, the former being used in the calculation of the theoretical molar mass ($\overline{M}n_{theo}$) assuming one growing chain per BH_4 group.*

[b] *MMA conversion determined by ^1H NMR or by gravimetry and corresponding to the highest $[MMA]_0/[BH_4]_0$ value reported; TOF values given in $mol_{MMA}\ mol_{complex}\ h^{-1}$.*

[c] *Number average molar mass (maximum value) determined by SEC–MALLS or by SEC versus polystyrene standards and corrected by a factor of 1.0 for PMMA.*

[d] *Theoretical molar mass calculated from $[MMA]_0/[BH_4]_0 \times$ MMA conversion $\times M_{MMA}$, assuming one growing chain per BH_4^- group, with $M_{MMA} = 100\ g\ mol^{-1}$; note that a discrepancy between $\overline{M}n_{theo}$ and $\overline{M}n_{SEC}$ may be indicative of a number of growing polymer chains different from the number of BH_4^- groups in the initiating complex.*

[e] *Calculated average dispersity value as reported from SEC traces.*

[f] *Value not reported by the authors.*

[g] *Prepared* in situ.

[h] *Polymer insoluble in THF.*

[i] *Only a single experiment is reported.*

[j] *Bimodal (BM) SEC traces.*

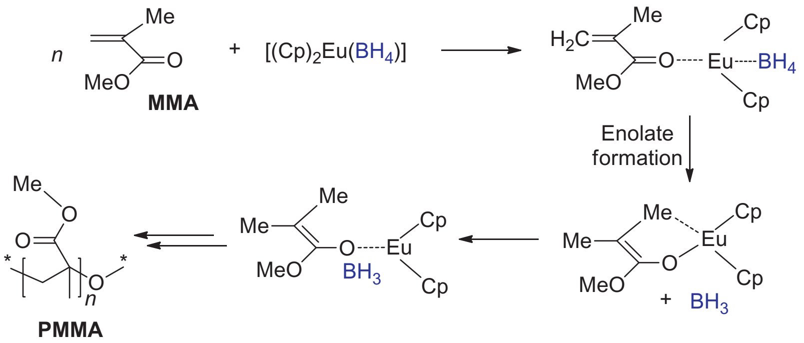

SCHEME 36 Synthesis of PMMA from the polymerization of MMA initiated by [$(Cp)_2Eu(BH_4)$].

The polydentate diamide–diamine supported samarium monoborohydride complex [$\{(N_2NN^{TMS})Sm(BH_4)\}_2$] (**24Sm**) developed by Mountford and coworkers enabled the polymerization of MMA providing polymers with a microstructure depending on the reaction temperature: the syndiotacticity reached 65% at −78 °C while rather atactic PMMA (mm/mr/rr *ca.* 25/38/35%) were obtained at 25 °C (Bonnet et al., 2005b) (Table 5). Although high molar mass PMMA formed ($\overline{M}n = 52{,}800\,g\,mol^{-1}$) with quite narrow $\overline{M}w/\overline{M}n$ values (*ca.* 1.23), no further investigations from **24Sm** but these few experiments were reported. The comparatively less efficient (26% in 12 h at 25 °C) lithiated analogous complex, [$(N_2NN^{Mes})Sm(BH_4)_2Li]_2$ (**25Sm**) similarly gave atactic PMMA (mm/mr/rr 25/40/35%). These preliminary data first exemplified the polymerization of MMA by a rare-earth borohydride complex. In comparison, the compounds [$\{(O_2N^{py})R(\mu\text{-}BH_4)(THF)_n\}_2$] (R = Y, $n = 0.5$ (**26Y**); Nd, $n = 1$ (**26Nd**); Sm, $n = 0$ (**26Sm**)) were ineffective for the polymerization of MMA (Bonnet et al., 2005a).

The borohydride metallocene and half-metallocene systems reported by Visseaux and coworkers derived from substituted cyclopentadienyl rare-earth complexes [$(Cp^{Ph3})_2Sm(BH_4)(THF)$], (**7Sm**), [$(Cp^{Ph3})Sm(BH_4)_2(THF)_2$] (**9Sm**), [$(Cp^{*Pr})R(BH_4)_2(THF)_2$] (R = Nd (**10Nd**), Sm, (**10Sm**)), [$(Cp^{iPr4})_2Sm(BH_4)$] (**8Sm**), and/or diketiminate [$(Cp^{Ph3})\{(p\text{-Tol})NN\}Sm(BH_4)$] (**13Sm**), [$(Cp^{*Pr})\{(p\text{-Tol})NN\}R(BH_4)$] (R = Nd (**12Nd**), Sm (**12Sm**)), and $(p\text{-Tol})NN = [(p\text{-}CH_3C_6H_4)N(CH_3)C]_2CH$ combined (or not) to Mg^nBu_2 or ^nBuLi gave highly syndiotactic (rr 82%) or highly isotactic (mm 96%) PMMAs, depending on the ancillary ligand, the alkylating agent and the polarity of the reaction medium (Barbier-Baudry et al., 2006) (Table 5). While an electron-withdrawing ligand like Cp^{Ph3} (rr 82%) or the use of THF (rr *ca.* 74%) seemed to favor syndiotacticity, ^nBuLi rather provided isotactic PMMA (mm *ca.* 89%) in apolar solvent. However, regardless of the nature of the ancillary ligand and the operating conditions, the control of the polymerization was not always satisfactory with these initiating systems, most likely as a result of propagation faster than initiation, often providing bi/multi-modal SEC traces.

The aryloxide rare-earth bisborohydride complexes, $[(ArO)R(BH_4)_2(THF)_2]$ (R = Er (**19Er**), Yb (**19Yb**)), of Yuan and coworkers were found moderately active in the polymerization of MMA at −30 to 40 °C, and most active at 0 °C (Yuan et al., 2006a) (Table 5). Rising the temperature from 0 to 25 °C significantly decreased the yield of PMMA obtained from the erbium and ytterbium compounds from 58–60% down to 14–13%, respectively. Mainly syndiotactic (rr *ca.* 60%) PMMA was formed regardless of the initiator and reaction conditions. However, the polymerization was not controlled in terms of molar mass values ($\overline{M}w/\overline{M}n$ not reported).

The same group also reported the neutral monoguanidinate rare-earth bisborohydride complexes, $[\{(TMS)_2NC(NCy)_2\}R(BH_4)_2(THF)_2]$ (R = Er (**21Er**), Yb (**21Yb**)), as active (Er > Yb) in the polymerization of MMA (Yuan et al., 2006b) (Table 5). The homoleptic guanidinate parent compounds were inert toward MMA thus highlighting the required presence of the BH_4^- group. The complexes were more active at 0 °C due to their deactivation at higher temperature. However, the polymerization was not controlled in terms of molar mass and dispersity values ($\overline{M}w/\overline{M}n$ *ca.* 2.45). No tacticity data were given.

The bis(β-diketiminate) ytterbium borohydride complex $[\{(2,6\text{-}i\text{Pr}_2C_6H_3)NC(Me)CHC(Me)N(C_6H_5)\}_2YbBH_4]$ (**36Yb**) reported by Shen was found to polymerize MMA (Shen et al., 2012). The highest activity (quantitative monomer conversion) was reached within 2 h in toluene at 0 °C at $[MMA]_0/[\mathbf{36Yb}]_0$ of 1000, affording syndiotactic PMMA (*ca.* 80%) with molar mass up to $\overline{M}n = 72{,}100\,\text{g mol}^{-1}$, and $1.45 < Đ_M < 1.81$ suggesting a poor control.

As later reported by Trifonov and coworkers, the corresponding anionic *N*,*N*′-diisopropyl-*N*′-bis(trimethylsilyl) guanidinate rare-earth borohydride complexes, $[\{(TMS)_2NC(N^iPr)_2\}_2R(BH_4)_2Li(THF)_2]$ (R = Nd (**23Nd**), Sm (**23Sm**)), and $[\{(TMS)_2NC(NCy)_2\}_2R(BH_4)_2Li(THF)_2]$ (R = Nd (**22Nd**), Sm (**22Sm**), Yb (**22Yb**)) did allow the polymerization of MMA in toluene with a different level of control according to the metal (Skvortsov et al., 2007b, c) (Table 5). The PMMA thus formed was characterized by NMR analysis as heterotactic with a slight predominance of isotactic (**23Nd**, **22Nd**, **22Sm**, **22Yb**) or syndiotactic triads (**23Sm**). The catalytic activity which remained moderate, decreased within the series according to Sm > Nd > Yb. However, the polymerization was generally uncontrolled in terms of molar mass (assuming two BH_4^- initiating groups per metal center) and dispersity values, with the exception of **22Sm**.

The group of Cui used the linked half-sandwich bisborohydride complexes $[(C_5Me_4{-}C_6H_4\text{-}o\text{-}NMe_2)R(BH_4)_2]$ (R = Sc (**11Sc**), Sm (**11Sm**)) which showed high isoselectivity at 20 °C (mm 80%) when the polymerization of MMA was carried out in benzene, and alternatively syndio-enriched PMMA (rr 74%) was formed in THF at −20 °C (Jian et al., 2010). The related two component initiating systems $[(C_5Me_4—C_6H_4\text{-}o\text{-}NMe_2)R(BH_4)_2]$ (R = Sc (**11Sc**), Sm (**11Sm**))/Mg^{n}Bu$_2$,^{n}BuLi also favored the formation of syndiotactic PMMA (rr up to 80% at −40 °C) in THF. Activation with an alkylating agent generally improved the activity regardless of the metal center. An extremely high activity for the synthesis of syndio-enriched PMMA (rr 75%) was claimed (TOF = 1200 mol_{MMA} mol_{Sc} h^{-1}) from **11Sc**/^{n}BuLi at −20 °C.

Investigations of the ability of bis(phosphinimino)methanide rare-earth metal borohydrides, $[\{CH(PPh_2NTMS)_2\}Y(BH_4)_2]$ (**20Y**), $[\{CH(PPh_2NTMS)_2\}La(BH_4)_2(THF)]$ (**20La**), and $[\{CH(PPh_2NTMS)_2\}Lu(BH_4)_2]$ (**20Lu**) to polymerize MMA, have been reported both experimentally and computationally by Guillaume et al. (2011) (Table 5). Both the lanthanum and lutetium complexes polymerized MMA to some extent (yield < 11%) at 23 °C whereas the yttrium derivative was hardly active, whichever the operating conditions (solvent, reaction time). The overall control was quite poor providing PMMA insoluble in THF (*i.e.*, suggesting the formation of polymers with high molar mass). Rather atactic PMMA was obtained from **20La** and **20Y**, whereas **20Lu** afforded slightly syndio-enriched PMMA (rr up to 61%). Similarly, the analogous (phosphinimino)methanide chloro complexes combined with the amido ligand, $[\{CH(PPh_2NTMS)_2\}R\{(Ph_2P)_2N\}Cl]$ (R = Y, La), were not very efficient, although more active in presence of an alkylating co-catalyst, and afforded atactic PMMA (Gamer et al., 2005). DFT insights highlighted the beneficial influence of the phosphiniminomethanide ligand, in particular its significant steric, electronic, and energetic contributions to the polymerization process in trapping the liberated BH_3 group (Guillaume et al., 2011). Also, in the case of yttrium, steric considerations, in addition to energetically comparable barriers for the first and second MMA insertions, support the experimentally observed difficulty to polymerize MMA (Section 4; *vide infra*).

3.4.2. Concluding Remarks on the Polymerization of MMA Initiated by Rare-Earth Borohydride Complexes

All rare-earth borohydride initiators, whether in the presence of an alkylating agent or not and regardless of the solvent, were (in comparison to the ROP of cyclic esters, *vide supra*) generally poorly active in the polymerization of MMA (non-optimized TOF values generally ≤ 120 mol_{MMA} $mol_{rare\text{-}earth}$ h^{-1}) with one exception claimed (≤11,120 mol_{MMA} mol_{Sc} h^{-1}, Jian et al., 2010). Higher reaction temperatures appeared to lower the yield of PMMA in agreement with thermally-activated chain termination steps. Although good data were sparingly obtained (duplicate experiments were not always reported) especially with complexes in which the metal center bears (a) polydentate ancillary ligand(s) (metallocene or non-metallocene type), the control in terms of molar mass (again assuming one growing PMMA chain per each BH_4^- group) and dispersity values was, in general, not good. The experimental

$\overline{Mn}$ values most often largely exceeded the expected ones, and $\overline{Mw}/\overline{Mn}$ were typically in the 1.2–2.7 range, with some PMMA even featuring bi- or multi-modal SEC traces. Both highly syndio- (rr up to 82%) and iso-enriched (mm up to 96%) PMMAs were obtained depending on the initiating system (Barbier-Baudry et al., 2006) (Table 5). To date, a rare-earth borohydride initiating system well established as nicely active and productive in the polymerization of MMA, thus still remains to be unveiled.

3.5. Copolymers of Polar Monomers (Cyclic Esters, γ-Benzyl-L-Glutamate *N*-Carboxyanhydrides, Methyl Methacrylate)

The "living" character of the ROP of polar monomers promoted by rare-earth borohydride complexes being established within most of these homopolymerization studies, prompted copolymerization processes to be considered.

3.5.1. Copolymers of Cyclic Esters (Including Carbonates)

3.5.1.1. Copolymers of ε-Caprolactone and Lactides

Compound [{(O$_2$NN^{py})Nd(μ-BH$_4$)(THF)}$_2$] (**26Nd**) reported by Bonnet, Mountford, and coworkers enabled the preparation of a CL/LLA (23/77 mol%/mol%) block copolymer ($\overline{Mn}$ = 14,400 g mol^{-1}, $\overline{Mw}/\overline{Mn}$ = 1.85), provided the CL was added first in a controlled amount (≤62 equiv) (Scheme 37; Bonnet et al., 2005a) (Tables 1 and 2). Both the sequential copolymerization by addition of LLA first, and the random *ca.*1:1 CL/LLA mixture copolymerization, only gave PLLA. The copolymerization of CL with

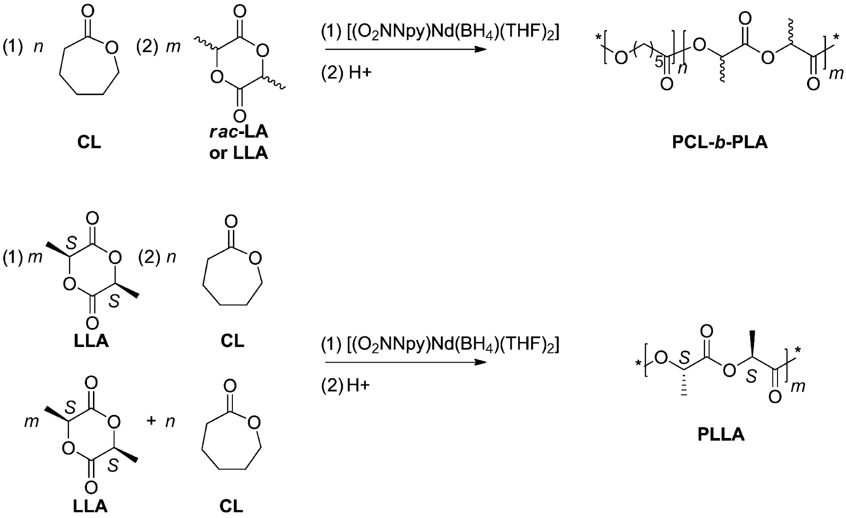

SCHEME 37 Synthesis of PCL-*b*-PLA from the sequential copolymerization of CL/*rac*-LA or LLA initiated by[(O$_2$NN^{py})Nd(μ-BH$_4$)(THF)]$_2$.

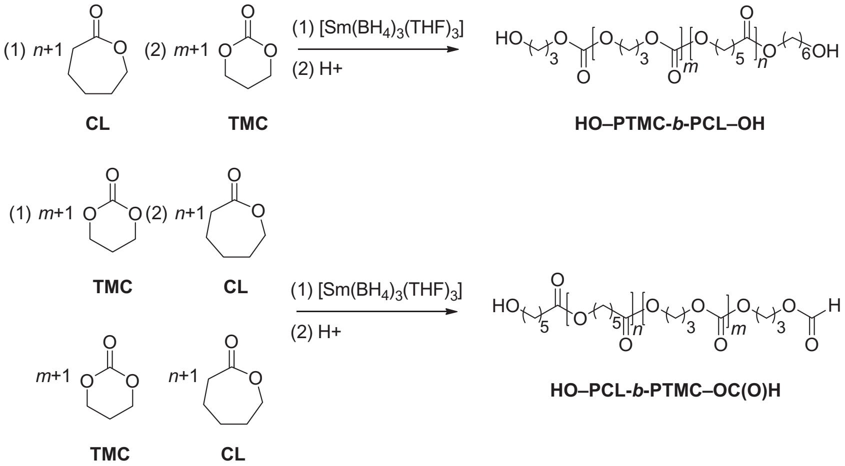

SCHEME 38 Synthesis of PTMC-*b*/*co*-PCL from the sequential/simultaneous copolymerization of TMC/CL initiated by $[Sm(BH_4)_3(THF)_3]$ (**1Sm**).

rac-LA as the second monomer gave a mixture of the expected block copolymer PCL-*b*-PLA along with PLA. No further characterization was reported.

3.5.1.2. Copolymers of ε-Caprolactone and Trimethylene Carbonate

The sequential copolymerization of TMC and CL, as reported by Guillaume and coworkers, afforded block copolymers PTMC-*b*-PCL ($\overline{M}n \leq 11{,}200\,g\,mol^{-1}$, $\overline{M}w/\overline{M}n$ *ca.* 1.45), featuring different end-capping functions depending on the order of monomer addition (Scheme 38; Palard et al., 2007) (Tables 1 and 4). High TMC (≤98%) and CL (≤92%) conversion were obtained using **1Sm** as initiator whichever the order of monomer addition. Depending on the different ROP mechanisms of a carbonate or a lactone promoted by a rare-earth borohydride complex, which generate either a hydroxyl and a formate terminal functions on a polycarbonate or two hydroxyl end-groups on a polylactone (*vide supra*), α-hydroxy,ω-formatetelechelic or α,ω-dihydroxytelechelic PTMC-*b*-PCL were generated upon introduction of TMC or CL first, respectively, as evidenced by ^1H NMR analyses (Scheme 38). The copolymers composition in both the carbonate or ester segments (40–60% in either block) faithfully reflected the initial feed. Interestingly, NMR analysis also showed signals corresponding to adjacent TMC and CL units. No decarboxylation (ether segments) was observed from ^1H NMR spectra. Correspondingly, DSC thermograms of these PTMC-*b*-PCL exhibited two *T*gs (−60 °C, −16 °C) corresponding to each block (CL and TMC, respectively), along with a *T*m (64 °C) arising from the PCL segment.

Also, the same authors reported that TMC/CL random copolymers, poly(trimethylene carbonate)-*co*-poly(ε-caprolactone), PTMC-*co*-PCL ($\overline{M}n$ *ca.* $8700\,g\,mol^{-1}$, $\overline{M}w/\overline{M}n = 1.48$), can be successfully prepared in high yields from $[Sm(BH_4)_3(THF)_3]$ (**1Sm**) at ambient temperature in THF or DCM, upon simultaneous addition of TMC and CL (Palard et al., 2007) (Tables 1 and 4). Given the established difference in reactivity between a carbonate and a lactone, careful analysis of the copolymer chain-ends by NMR showing both a formate and a hydroxyl end-groups, revealed that a carbonate unit is inserted first into the Sm—HBH_3 bond (Scheme 38). The quasi-quantitative conversion of the monomers, *ca.* 96%, in TMC versus only *ca.* 81% in CL also showed that TMC reacted faster whichever the feed ratio ($[TMC]_0/[CL]_0 = 28/80$ to 80/20). This reactivity ratio is reversed in comparison to the corresponding homopolymerization behaviors in which CL homopolymerized faster than TMC. DSC analysis of the copolymers revealed a *T*g (−35 °C) intermediate between those of each homopolymer, and a *T*m (48 °C) lower than that of PCL, thereby supporting its random nature.

3.5.1.3. Copolymers of δ-Valerolactone and ε-Caprolactone or Lactides

The effectiveness of $[La(BH_4)_3(THF)_3]$ (**1La**) in the ROP of CL, VL, and LLA prompted copolymerization studies of these monomers (Nakayama et al., 2007, 2009) (Tables 1 and 2). The random copolymerization of VL and LLA resulted in little incorporation of VL (<6%) in PLLA ($\overline{M}n \leq 11{,}900\,g\,mol^{-1}$, $\overline{M}w/\overline{M}n = 1.3$) as observed with the CL/LLA couple which leveled off at 8% of CL incorporated in the growing PLLA chain ($\overline{M}n \leq 8300\,g\,mol^{-1}$, $\overline{M}w/\overline{M}n = 1.53$). Sequential copolymerization of VL and then LLA resulted in too slow polymerization of LLA. Random copolymerization of CL and VL using **1La**, proceeded at a rate slower than in the respective homopolymerization leading (up to 50% yield) to copolymers ($\overline{M}n \leq 13{,}300\,g\,mol^{-1}$, $\overline{M}w/\overline{M}n = 1.5$) with slightly lower CL contents than VL contents. All these copolymers have not been further characterized (Nakayama et al., 2009).

3.5.2. Copolymers of ε-Caprolactone and γ-Benzyl-L-Glutamate N-Carboxyanhydride or Methyl Methacrylate

As mentioned above, α,ω-dihydroxytelechelic polyesters are highly valuable polymers. Indeed, they can act as macroinitiators toward the synthesis of various copolymers (Guillaume, 2013). First, the —OH terminated polymer can be used as a macro-alcohol allowing the preparation of polyester–polyester or polyester–polycarbonate block copolymers (Guerin et al., 2013; Guillaume, 2013; Helou et al., 2009). Alternatively, upon chemical modification of the terminal OH group(s) of a polyester, formed from the ROP of a cyclic ester promoted by a rare-earth borohydride complex, into an amino- or a bromo-function, one can further initiate the polymerization of a second co-monomer requiring a distinct polymerization mechanism. As detailed thereafter, the combination of two mechanistically distinct polymerization techniques such as the ROP of a cyclic ester, the ROP of an α-amino acid NCA, the radical polymerization of a methacrylate, represents a two-step alternative to the unsuccessful (direct) copolymerization of such monomers. It is noteworthy that whereas PTMC diols can be used toward the synthesis of polyurethanes, via reaction with a diisocyanate (Loh et al., 2012), the chemical modification of the hydroxyl end-capping groups of an α,ω-dihydroxytelechelic PTMC (Ajellal et al., 2010a; Guillaume, 2013; Guillaume and Carpentier, 2012; Helou et al., 2009) into cyclic carbonate units, allowed the synthesis, upon polycondensation with a diamine, of the highly valuable non-isocyanate poly(urethane)s, known as NIPUs (Guillaume, 2013; Helou et al., 2011).

Following this strategy, analogous diblock and triblock polyester–polypeptide copolymers of PCL and PBLG have thus been synthesized by Guillaume and coworkers from the ROP of ε-caprolactone followed by the ROP of γ-benzyl-L-glutamate (BLG, Scheme 39; Schappacher et al., 2006) (Tables 1 and 3). In this approach the corresponding mono- or dihydroxy end-functionalized PCL were first chemically modified into the analogous mono- or diamino end-capped analogous polyesters, which were subsequently used as macroinitiators for the ROP of the BLG monomer.

Note that block and random copolypeptides of BLG and ALA or ε-carboxbenzoxy-L-lysine (BLL), PBLG-*b*-PALA, and PBLG-*b*/*co*-PBLL have

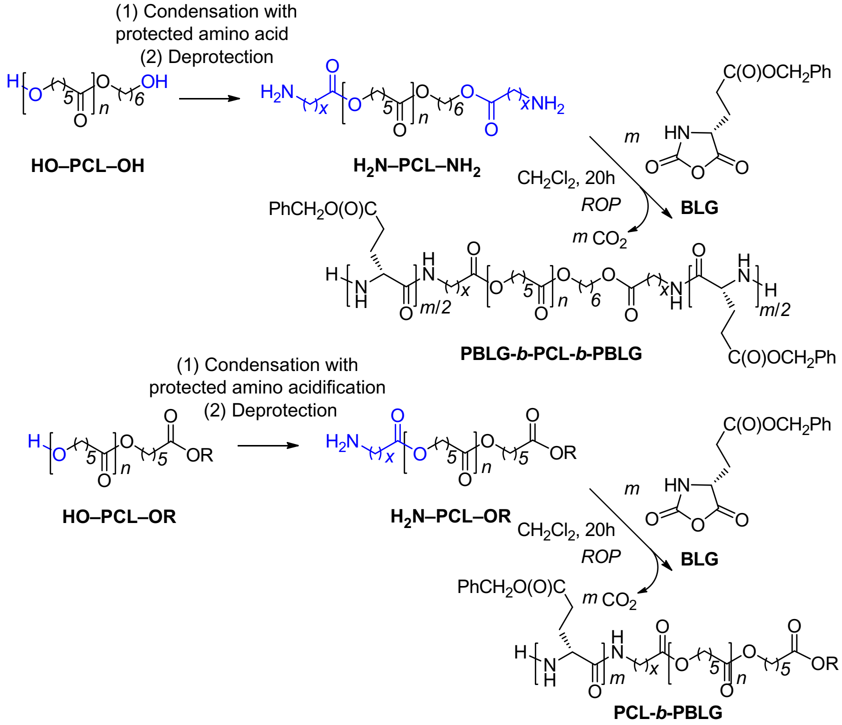

SCHEME 39 Synthesis of PCL-*b*-PBLG and PBLG-*b*-PCL-*b*-PBLG upon ROP of BLG using mono- or di-amino end-capped PCL macroinitiators.

been prepared from **1Y** within a few days (Peng et al., 2012b) (Table 3). ^{1}H NMR analyses showed that all PBLG chains initiated the ALA/BLL NCA polymerization and that the calculated molar ratio of monomers was close to the feed ratio. The control of the molar mass ($\overline{M}n_{theo}$ *vs* $\overline{M}n_{SEC} < 39{,}000\,g\,mol^{-1}$) was not always good while $\overline{M}w/\overline{M}n$ remained below 1.30.

Also, rare-earth borohydride complexes generally appeared as poorly active in the homopolymerization of MMA. Similarly, they basically failed to copolymerize MMA with CL or TMC as co-monomer, as reported with the trisborohydrides [Nd $(BH_4)_3(THF)_3$] (**1Nd**) (Barros et al., 2008b) or with the phosphiniminomethanide borohydride complex [{$CH(PPh_2NTMS)_2$}Lu $(BH_4)_2$] (**20Lu**) (Guillaume et al., 2011), respectively. These results also revealed that polyester–polyacrylate copolymers could not be prepared, under the reported operating conditions, from the sequential copolymerization of a lactone or a carbonate with a methacrylate by using these rare-earth borohydride initiators. Such copolymers have, however, been successfully synthesized by Guillaume and coworkers from a combined ROP/radical polymerization approach (Scheme 40) (Tables 1 and 5). The synthetic route

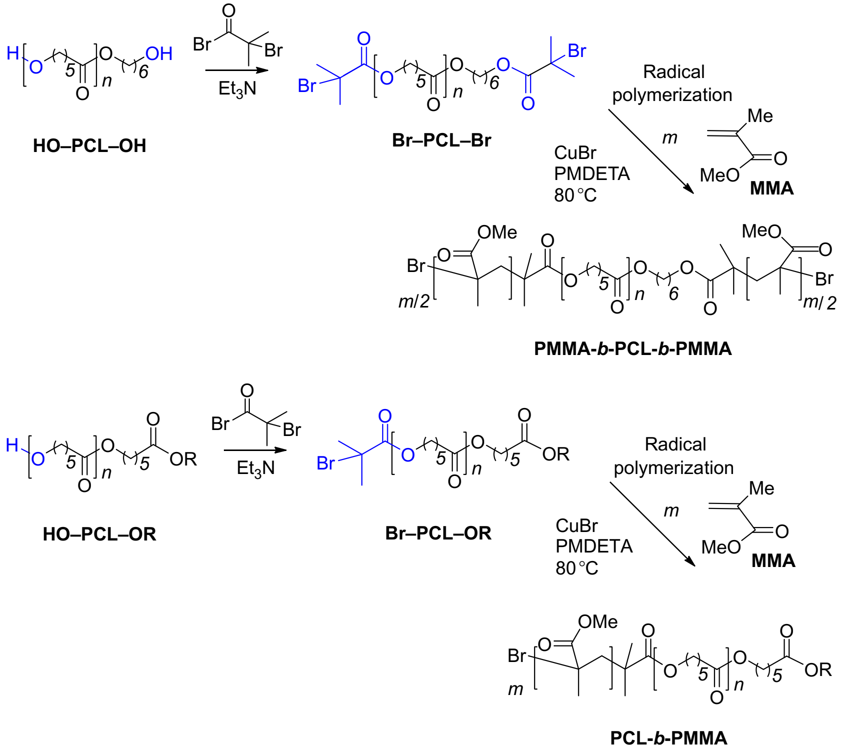

SCHEME 40 Synthesis of PCL-*b*-PMMA and PMMA-*b*-PCL-*b*-PMMA upon radical polymerization of MMA using mono- or di-bromo end-capped PCL macroinitiators.

consisted in using bromo-functionalized PCLs–prepared from the mono- or dihydroxyfunctionalized PCLs upon esterification by 2-bromoisobutyryl bromide–as macroinitiators for the polymerization of MMA (Scheme 40, Schappacher et al., 2007). This approach allowed the preparation of both analogous diblock PCL-*b*-PMMA and triblock PMMA-*b*-PCL-*b*-PMMA copolymers, as opposed to the previous MMA/CL sequential copolymerization route developed by Yasuda and coworkers from $[(Cp^*)_2Sm(Me)(THF)]$ which only gave the diblock copolymers (Yamashita et al., 1996).

Interestingly, the synthesis of PCL-*b*-PBLG and PBLG-*b*-PCL-*b*-PBLG (Schappacher et al., 2006), as well as of PCL-*b*-PMMA and PMMA-*b*-PCL-*b*-PMMA (Schappacher et al., 2007), using the appropriate macroinitiator derived from α,ω-dihydroxytelechelic PCL as instigated by Guillaume and coworkers, remains the only pathway established so far toward the preparation of such analogous diblock and triblock polyester/polypeptide and polyester/polyacrylate copolymers.

4. COMPUTATIONAL STUDIES: DFT INPUT INTO THE MECHANISM OF THE POLYMERIZATION OF POLAR MONOMERS

Since the so-called DFT revolution, theoretical methods have been extensively used to determine the profile of reactions involving transition metals. However, much less has been reported on the theoretical investigations of the mechanism of polymerization of polar monomers. The first *in silico* report by Guillaume, Maron, and coworkers in 2008 addressed the polymerization of methylmethacrylate catalyzed by the rare-earth borohydride complexes $[Eu(BH_4)_3]$ and $[(Cp)_2Eu(BH_4)]$ (Barros et al., 2008b). Since then, several computational investigations have been undertaken dealing with other monomers and alike metallic borohydride complexes, indicating that each catalytic system is different. However, the number of studies remained rather limited and mainly involves ε-caprolactone (Table 6).

4.1. ROP of ε-Caprolactone and Lactide

The first theoretical investigations on the ROP of CL reported by Guillaume, Mountford, and Maron involved the comparison of the metallocene $[(Cp)_2Eu(BH_4)]$ and the post-metallocene diamide–diamine $[(N_2NN')Eu(BH_4)]$ catalytic systems (Barros et al., 2008a). These models were selected to mimic the experimental behavior of the related derivatives, namely of $[(Cp^*)_2Sm(BH_4)(THF)]$ (**5Sm**) (Palard et al., 2004) and $[\{(N_2NN^{TMS})Sm(BH_4)\}_2]$ (**24Sm**) (Bonnet et al., 2005b), respectively (Table 6). Only the first CL insertion was considered in order to explain the experimentally observed formation of α,ω-dihydroxytelechelic PCL (Guillaume et al., 2003, 2007; Palard et al., 2004, 2005, 2006). The reaction with $[(Cp)_2Eu(BH_4)]$ or $[(N_2NN')Eu(BH_4)]$

TABLE 6 Relevant Data on the DFT Mechanistic Investigations of the Polymerization of Polar Monomers Promoted by Rare-Earth Borohydride Complexes

Rare-earth borohydride complex	Monomer	Most significant features
Divalent complex		
[Sm(BH$_4$)$_2$(THF)$_2$] (**2Sm**, Scheme 2)	CL (Iftner et al., 2011)	No oxidation of the metal center during the ROP Formation of α,ω-dihydroxytelechelic PCL
Trivalent complex		
[MeY(BH$_4$)(THF)$_5$][BPh$_4$] (**14Y**, Scheme 8)	CL (Susperregui et al., 2011)	Methyl and BH$_4^-$ ligands are active in the ROP process (telomerization is possible) Formation of α,ω-dihydroxytelechelic PCL
[{CH(PPh$_2$NTMS)$_2$}Y(BH$_4$)$_2$] (**20Y**, Scheme 11)	CL (Jenter et al., 2010)	Highly efficient catalyst because of the low coordination strength of BH$_4^-$ to Y Formation of α,ω-dihydroxytelechelic PCL
[Eu(BH$_4$)$_3$] (**1Eu′**)	CL (Barros et al., 2008a)	Two consecutive B–H activations Formation of α,ω-dihydroxytelechelic PCL
[(Cp)$_2$Eu(BH$_4$)]	CL (Barros et al., 2008a)	Similar features as for [Eu(BH$_4$)$_3$]
[(O$_2$N^L)Sm(BH$_4$)(THF)] L=OMe (**27Sm**), NMe$_2$ (**28Sm**), py (**29Sm**) (Scheme 13) [(O$_2$N^{nPr})Sm(BH$_4$)(THF)$_2$] (**30Sm**, Scheme 13)	*rac*-LA (Dyer et al., 2010)	Possible formation of either α,ω-dihydroxytelechelic or ketone-terminated PLA
[{CH(PPh$_2$NTMS)$_2$}Y(BH$_4$)$_2$] (**20Y**, Scheme 11)	TMC (Guillaume et al., 2012)	Formation of α,ω-dihydroxy telechelic or α-hydroxy,ω-formatetelechelic PTMC
[{CH(PPh$_2$NTMS)$_2$}R(BH$_4$)$_2$] (R=Y, La; **20Y**, **20La**, Scheme 11)	MMA (Guillaume et al., 2011)	PMMA formation is possible because of the efficient trapping of BH$_3$ by the nitrogen of the ligand yielding to the enolate formation. This trapping does not affect the subsequent insertion to form a keto-enolate complex

Continued

TABLE 6 Relevant Data on the DFT Mechanistic Investigations of the Polymerization of Polar Monomers Promoted by Rare-Earth Borohydride Complexes—Cont'd

Rare-earth borohydride complex	Monomer	Most significant features
$[Eu(BH_4)_3]$ (**1Eu′**)	MMA (Barros et al., 2008b)	No PMMA formation because of the lack of formation of the enolate Critical importance of the BH_3 trapping
$[(Cp)_2Eu(BH_4)]$	MMA (Barros et al., 2008b)	Similar features as for $[Eu(BH_4)_3]$ but even less efficient
Supported complex		
$[(@SiO)Nd(BH_4)_2(THF)_{2.2}]$ (**38Nd**)	MMA (Del Rosa et al., 2012)	Isotactic PMMA formation due to the trapping of BH_3 by the surface allowing formation of the enolate
$[(@SiO)La(BH_4)]$ (**39La**)	CL (Del Rosa et al., 2011a,b)	Enhanced reactivity due to the presence of the silica surface Possibility of trapping of BH_3 by the surface Formation of α,ω-dihydroxytelechelic PHB

was shown to occur in two steps corresponding to two successive B–H activations (Fig. 3). The first step involves the nucleophilic attack of one of the hydrides of the BH_4^- ligand on the ketonic carbon of the CL, which is concomitant with the trapping of BH_3 by the exocyclic oxygen of the coordinated CL. Interestingly, the borohydride never decoordinates the metal center during this step. The second step consisting in the ring-opening of the CL is induced by the hydrogen transfer from the trapped BH_3 to the ketonic carbon (the same as in the first step). The ketone is then reduced affording, after hydrolysis, α,ω-dihydroxytelechelic PCL, in agreement with the experimental findings (Scheme 26). For this system, the ring-opening step was found to be an equilibrium thereby providing a better control of the polymerization process. The calculated free-energy profile for the reaction of CL with the metallocene $[(Cp)_2Eu(BH_4)]$, depicting these first and second steps and depicting the optimized structures of the various intermediates as determined from DFT calculations, is illustrated on Fig. 3. It exemplifies the typical reaction profile commonly obtained for the ROP of lactones promoted by a rare-earth catalyst. In comparison to the ring-opening/initiation reaction computed from

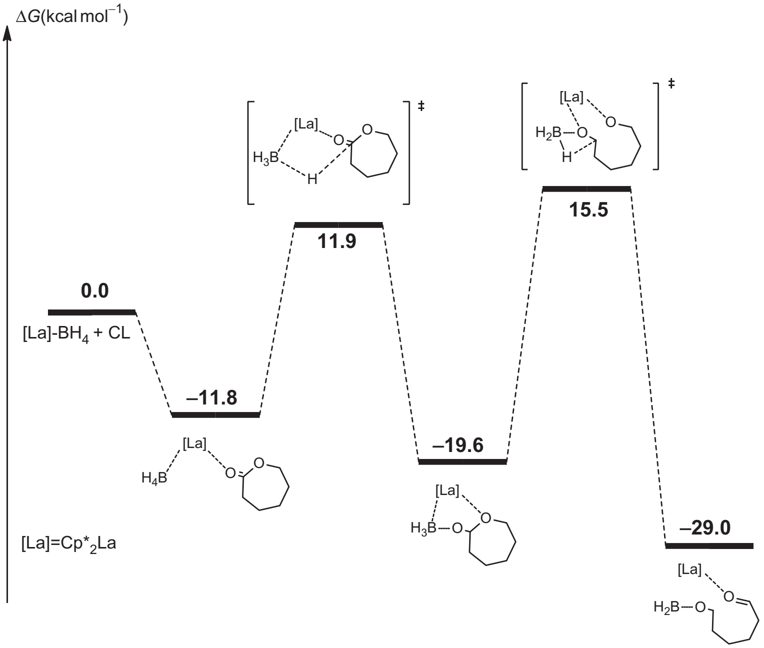

FIGURE 3 Calculated free-energy profile for the reaction of CL with [(Cp)$_2$Eu(BH$_4$)], **37Eu**, depicting the structure of the intermediates as determined by DFT.

the related [(Cp)$_2$Eu(H)] (Yamashita et al., 1996), it is more easily thermodynamically controlled with the borohydride derivative because no quasi-equilibrium is involved. In both hydride and borohydride cases, it was evidenced that the ring-opening proceeds through the oxygen-acyl bond cleavage, as observed experimentally. Note that this hydride catalyst was indeed found from this DFT study to afford an alkoxy-aldehyde initiating species, [(Cp)$_2$Eu{O(CH$_2$)$_5$C(O)H}], which would ultimately lead, via [(Cp*)$_2$SmO(CH$_2$)$_6$OSm(Cp*)$_2$], to α,ω-dihydroxytelechelic PCL.

Subsequently, Mountford, Maron, and coworkers reported the first DFT study of *rac*-lactide polymerization using the bisphenolate derivatives [(O$_2$N$'^{\mathrm{NMe2}}$)Eu(BH$_4$)] (O$_2$N$'^{\mathrm{NMe2}}$ = O$_2$N$^{\mathrm{NMe2}}$ with the ^{t}Bu groups removed) as model of [(O$_2$N$^{\mathrm{NMe2}}$)Sm(BH$_4$)(THF)] (**27Sm**) (Dyer et al., 2010) (Table 6). Again, the aim being the investigation of the nature of the polymer chain-end (controlled by the first insertion), the calculations were restricted to the first insertion. Both the reaction profiles leading to either α,ω-dihydroxytelechelic PCL or α-hydroxy,ω-aldehyde-terminated PCL were computed and compared. Each of these two reaction mechanism profiles was slightly different from the one reported for CL by Mountford, Guillaume, Maron, and coworkers (Barros et al., 2008a), as it involved three steps instead of two. Indeed, the first step involves the attack of the borohydride ligand that is decoordinated from the metal center, onto the ketonic carbon. This leads to an intermediate in which the formed BH_3 still interacts with the hydride and from which the trapping by the exocyclic oxygen of CL can thus occur. The formation of the two types of end-functionalized poly(lactide) from the latter species was predicted as being kinetically possible, yet with an obvious thermodynamic preference for the formation of α,ω-dihydroxytelechelic PCL. This results from the low kinetic stability of BH_3, that has to be efficiently trapped to allow the formation of the aldehyde-terminated PCL (for instance by a THF molecule). These investigations thus highlighted the significant influence of both the ligand and the monomer onto the overall reaction mechanism.

Further instigations developed by Okuda and Maron dealt with the ROP of CL catalyzed by the simple trivalent cation, $[MeY(BH_4)(THF)_5][BPh_4]$ (**14Y**) (Susperregui et al., 2011) (Table 6). As mentioned above in the computed ROP of LA catalyzed by $[(O_2N'^{NMe2})Eu(BH_4)]$ (Dyer et al., 2010), the reaction involves three steps. In the yttrium promoted ROP, only α,ω-dihydroxytelechelic PCL was predicted but the propagation can take place from either the borohydride or the methyl groups. Moreover, trans effect was also found quite important, as changing the trans ligand led to either an increase or a decrease of the overall energetic barrier.

Recently, theoretical studies were extended by Visseaux, Maron, and coworkers to a homoleptic borohydride of divalent samarium (Iftner et al., 2011). This was computationally challenging because the classical reactivity of the borohydride had to be compared with the mechanism involving the oxidation of the lanthanide center (from +II to +III). The computed reaction mechanism of the ROP of CL promoted by $[Sm(BH_4)_2(THF)_2]$ (**2Sm**) was shown not to involve any oxidation of the metal center, in excellent correlation with the experimental observations, and to lead to an α,ω-dihydroxytelechelic PCL. Moreover, the mechanism involves only two steps, as in the DFT study of the ROP of CL by the trivalent derivatives (Barros et al., 2008a).

Finally, Roesky, Guillaume, Maron, and coworkers computationally instigated the ROP of CL catalyzed by a bis(phosphinimino)methanide borohydride complex, $[\{CH(PMe_2NSiH_3)_2\}Y(BH_4)_2]$, which mimicked the complex used experimentally, $[\{CH(PPh_2NTMS)_2\}Y(BH_4)_2]$ (**20Y**) (Jenter et al., 2010) (Table 6). The originality of this organometallic catalyst lies in the two potential initiating BH_4^- sites. Also, the first B–H activation of BH_4^- is achieved in two distinct unprecedented steps in contrast to the unique step involved with monoborohydride complexes (Fig. 4). This first B–H activation involves the nucleophilic attack of one hydride on the carbon atom of the ketone with decoordination of BH_4^- from yttrium, followed by the trapping of BH_3 by the oxygen atom of the ketone. This specificity arises from the two BH_4^- groups along with the positive influence of greater electron-donating ability of the bis(phosphinimino)methanide ligand. The second B–H activation was classical for a rare-earth

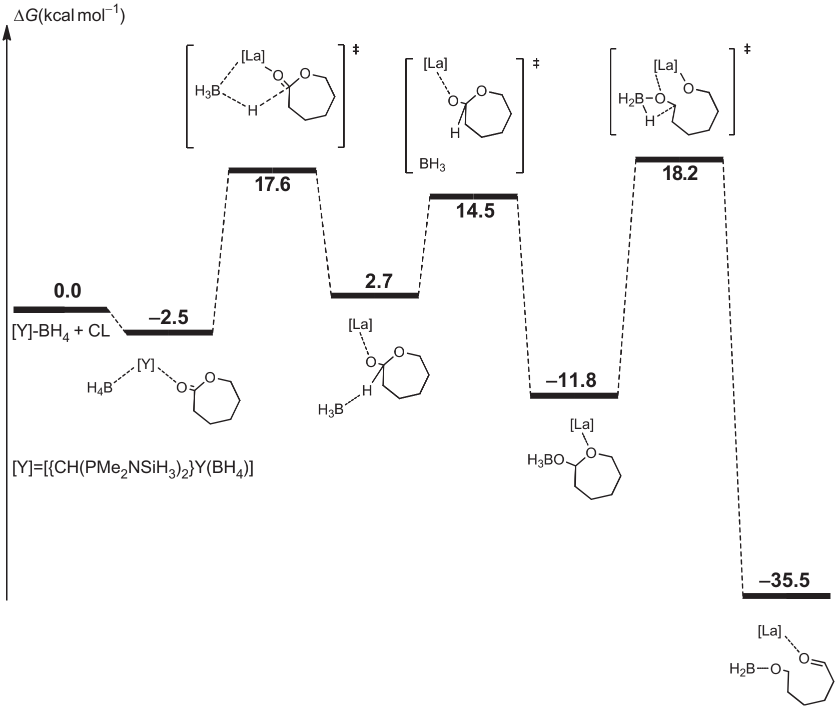

FIGURE 4 Calculated free-energy profile for the reaction of CL with [{CH(PMe$_2$NSiH$_3$)$_2$}Y(BH$_4$)$_2$], depicting the structure of the intermediates as determined by DFT.

borohydride catalyst. The three-step initiation mechanism found is similar to the one determined for the ROP of LA by [(O$_2$N$'^{NMe2}$)Eu(BH$_4$)] (Dyer et al., 2010), and also promotes the formation of HO–PCL–OH with an overall kinetically facile and thermodynamically favorable reaction. Interestingly, [{CH(PMe$_2$NSiH$_3$)$_2$}Y(BH$_4$)$_2$] is predicted to date, to be the most efficient catalyst investigated theoretically (lowest activation barrier of all investigated complexes). This is attributed to the fact that this organometallic complex is less sterically crowded than the metallocene complex [(Cp)$_2$Eu(BH$_4$)] (Barros et al., 2008a).

The effect of the ancillary ligand in rare-earth borohydride catalyzed polymerization was lately studied on silica-grafted homoleptic species, as reported by Maron and coworkers (Del Rosa et al., 2011a,b) (Table 6). The effect of grafting a borohydride complex onto a silica surface has been carefully considered in terms of the coordination mode and the effect of the coligand on the energetic parameters. The reaction mechanism is similar to the one reported for the ROP of lactide (Dyer et al., 2010; Susperregui et al., 2011). The formation of the CL adduct is predicted to be highly favorable and strongly exergonic because the grafting of the lanthanide complex onto the surface increased its Lewis acidity. Interestingly, despite the presence of surface oxygen, BH_3 is more efficiently trapped by the exocyclic oxygen of CL than by the surface. Thus, the formation of α,ω-dihydroxytelechelic PCL is more likely than the formation of aldehyde-terminated PCL. On the other hand, the nature of the grafting mode (mono-grafted or bi-grafted) is found to hardly affect the reactivity. This is an important outcome since the grafting mode of the complexes is very often not known experimentally. Thus, the catalysis of grafted complexes could be viewed as the combination of different simultaneously "operating" catalysts. Moreover, the grafted complexes were found among the most efficient catalysts compared to the other alike molecular catalysts reported in the literature (low activation barrier). The effect of the coligand was minor, mainly because the grafting mode imposes a cis conformation for the two ligands, reinforcing the importance of the trans effect proposed by Susperregui et al. (2011).

4.2. ROP of Trimethylene Carbonate

As already mentioned, while theoretical DFT investigations on the ROP mechanism remained rather limited to CL, a very recent study by Guillaume, Maron, Roesky, and coworkers addressed the reactivity of the bis(phosphinimino)methanide rare-earth complexes **20Y**, **20La**, **20Lu** in the ROP of TMC (Guillaume et al., 2012) (Tables 4 and 6). This work was similarly restricted to the first insertion in order to predict the nature of the chain-end of the polymer. Two kinetically and thermodynamically favorable pathways are accessible and gave two distinct end-functionalized PTMCs. Indeed, the carbonyl reduction could occur, or not, leading to either the "classical" α,ω-dihydroxy- or to the α-hydroxy,ω-formate telechelic PTMC, respectively. Although both profiles are very close in energy, the formation of the latter is predicted to be the most favorable (Fig. 5). Interestingly, the formation of this chain-end implies the trapping of the formed BH_3 molecule, as it cannot be used to reduce the carbonyl of the TMC. The reaction mechanism involves first the intermediate trapping of the BH_3 by the intracyclic oxygen of TMC rather than by the exocyclic one. Thus, a 1,2-shift of BH_3 occurs leading to the BH_3 trapping by the exocyclic oxygen of TMC (needed for the formation of the α,ω-dihydroxytelechelic PTMC). From this intermediate, either the reduction of the carbonyl can be achieved or an easy ring-opening process takes place with subsequent trapping of BH_3 by the nitrogen of the bis(phosphinimino)methanide ligand. The former leads to the formation of the α,ω-dihydroxytelechelic PTMC and the latter to an α-hydroxy, ω-formate telechelic PTMC. Moreover, this study demonstrated the importance of the ancillary ligand in this reaction process, while the calculations did not highlight any significant differences among all three complexes **20Y**, **20La**, or **20Lu**. This in-depth computational study remains, to date, the only one dealing with the ROP of a carbonate (Table 6).

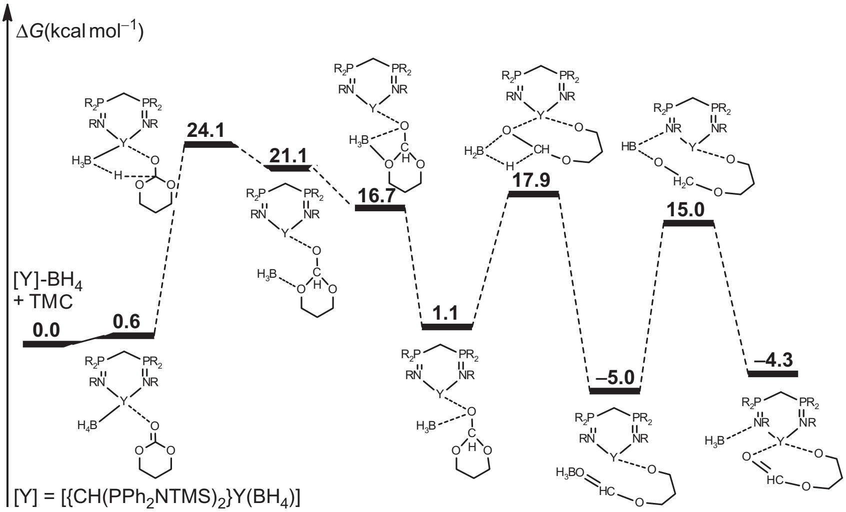

FIGURE 5 Calculated free-energy profile for the reaction of TMC with [{CH(PPh$_2$NTMS)$_2$}Y (BH$_4$)$_2$], **20Y**, depicting the structure of the intermediates as determined by DFT.

4.3. Polymerization of Methyl Methacrylate

Unlike the ROP of TMC, the polymerization of MMA has been slightly more theoretically investigated (Table 6). As stated above, the very first *in silico* study on polymerization promoted by rare-earth complexes was carried out by Maron, Guillaume, and coworkers on MMA (Barros et al., 2008b). This study was limited to the first insertion, using [(Cp)$_2$Eu(BH$_4$)] and [Eu(BH$_4$)$_3$] as model catalysts for [(Cp*)$_2$Sm(BH$_4$)(THF)] (**5Sm**) and [Sm(BH$_4$)$_3$(THF)$_3$] (**1Sm**), respectively. In particular, the formation of the enolate complex, initially proposed by Yasuda and coworkers as the key intermediate in the case of the corresponding rare-earth hydride catalysts ([{(Cp*)$_2$Sm(H)}$_2$]; Yasuda and Tamai, 2002), is found highly endergonic, mainly because of the already discussed BH$_3$ trapping. The only stable complex is a borate-type one where the BH$_3$ is trapped by the oxygen of the enolate, somewhat similar to the intermediate reported in the ROP of lactones. Insertion from this complex is difficult, rationalizing the experimental low efficiency of both catalysts in MMA polymerization. It was however calculated that the energetic profile for [Eu(BH$_4$)$_3$] (**1Eu′**) is more favorable than that of the corresponding organolanthanide catalyst. Moreover, all other investigated reactions, involving hydroboration or carboxylate formation, are discriminated either for kinetic (carboxylate) or thermodynamic reasons. Once again, the crucial importance of the BH$_3$ trapping was demonstrated in these DFT investigations.

This was further demonstrated by Guillaume et al. (2011) using the bis (phosphinimino)methanide borohydride complexes **20La** and **20Lu** already examined computationally in the ROP of CL (Jenter et al., 2010) and TMC

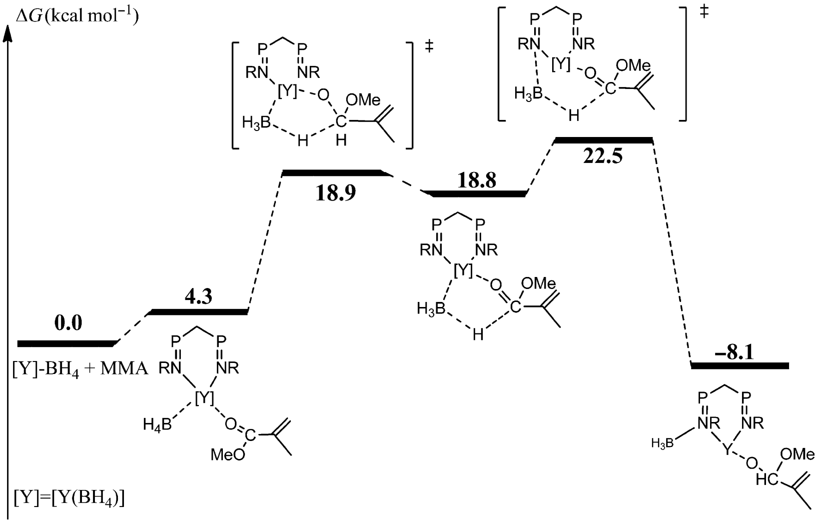

FIGURE 6 Calculated free-energy profile for the reaction of MMA with [{CH($PPh_2NTMS)_2$}Y$(BH_4)_2$], **20Y**, depicting the structure of the intermediates as determined by DFT.

(Guillaume et al., 2012) (Tables 4 and 6). Interestingly, unlike all other reports, both the first and the second insertions were taken into consideration (Fig. 6). Noteworthy, the formation of the enolate complex is determined exergonic, because the trapping of the BH_3 is ensured by the nitrogen of the bis(phosphinimino)methanide ligand, as similarly observed in the ROP of TMC (Guillaume et al., 2012). The trapping of the BH_3 molecule by the ligand is seen not to affect the activity of the complex, since the second insertion of the MMA molecule is found to be even more kinetically favorable than the first one. The activity of this complex in MMA polymerization was in agreement with the experimental observations.

Another demonstration of the importance of the BH_3 trapping was lately unveiled by Gauvin, Maron, Thomas, and coworkers in the polymerization of MMA from neodymium borohydride catalyst **1Nd** grafted on a silica surface ([(@SiO)Nd$(BH_4)_2(THF)_{2.2}$]; Del Rosa et al., 2012). The three first insertions are theoretically investigated in order to explain the propensity of the catalyst to experimentally form isotactic rather than the usual syndiotactic PMMA (Barros et al., 2008b). For the first MMA insertion, the BH_3 trapping by the surface oxygen leads to an exergonic enolate formation, allowing polymerization. The experimental preference for isotacticity was thus theoretically supported; it was explained by the number of oxygen–rare-earth stabilizing interactions –since the PMMA is acting as a chelating ligand– that are maximized in an isotactic enchainment. Noteworthy, this is, to date, the only theoretical investigation involving a rare-earth borohydride catalyst dealing with the tacticity of the resulting PMMA (Table 6).

4.4. Theoretical Investigations: An Essential Tool for Polymerization Catalysis

Theoretical methods are nowadays, mainly due to the efficiency of the new computers and the so-called DFT revolution, able to tackle problems as complicated as catalytic reactions such as polymerizations as well as stereoselectivity (in particular, the tacticity of polymers). Thus, *in silico* methods recently became an important and essential tool in polymerization catalysis. Indeed, understanding the key factors that govern the polymerization is crucial to design the best catalyst for a given polymerization, and DFT methods can provide accurate reaction pathways in agreement with experimental findings. For instance, in the specific case of borohydride catalysts, it was unambiguously theoretically demonstrated that the key issue, in order to be able to target well-defined polymers, is the trapping of the formed BH_3 molecule. If the BH_3 moiety is trapped by the carbonyl group, then only α,ω-dihydroxytelechelic polymers are obtained in the case of cyclic monomers, while a poor activity is obtained with MMA. On the other hand, if the BH_3 molecule can be efficiently trapped either by the solvent, the ancillary ligand or the surface, then one can access a greater diversity of polymers and subsequently, of polymer properties. In the same way, theoretical methods are able to accurately account for the tacticity of the polymer and the steric and electronic effects that control the selectivity. In that sense, theoretical investigations, when carried out in close combination with experimental studies, can be considered as an essential tool to understand and foresee the polymerization mechanism.

5. CONCLUSIONS AND OUTLOOKS

In the frame of this chapter, we have evidenced that rare-earth borohydride complexes constitute an attractive valuable class of catalysts for the polymerization of polar monomers. Throughout their evaluation in the ROP of cyclic esters such as lactones, lactides, carbonates, and even of α-amino acid NCAs, such complexes have often revealed unexpected and unique behaviors, as established experimentally. Computational DFT studies have further supported these findings while rationalizing the postulated polymerization mechanisms. Moreover, calculations have enabled to better understand the origin of the chain-ends of the observed α,ω-functionalized polymers, often unveiling unanticipated key intermediates. Whereas the intrinsic nature and reductive potential of the BH_4^- active function proved an essential factor in understanding the overall mechanism, other key parameters have been identified. Initial efforts to design and synthesize original discrete rare-earth organometallic post-metallocene borohydride derivatives have thus been deeply rewarding. Future research in the design of tuned and well-defined rare-earth borohydride, especially regarding their surrounding ancillary ligand(s), but also considering their oxido-reduction potential, thus remains highly promising. In particular, stereoselectivity issues of ROP involving chiral lactones still remain a largely unexplored domain. Similarly, the efficiency of chiral rare-earth complexes in selectively controlling polymerizations remains an open field of research. Factors governing the stereoselectivity of the polymerization of polar monomers still remain to be better understood so as to enable access to better controlled polymerization processes and in turn to more original polymers. The access to well-defined copolymers of controlled chemical structure from rare-earth borohydride catalysts has been demonstrated as feasible; yet it is hardly exploited and much remains to be studied especially regarding simultaneous copolymerization. Such fundamental experimental (synthetic organometallic and polymer chemistries) and theoretical investigations are thus a prerequisite for developing controlled polymerization processes and subsequently for allowing access to tailored functional (co) polymer materials.

ACKNOWLEDGMENTS

The authors gratefully acknowledge the coworkers whose names appear in the following references for their contribution to this research. S. M. G. most gratefully acknowledges Michèle Schappacher for her significant contribution to the pioneering investigations on the use of rare-earth borohydride catalysts in the ROP of cyclic esters. The authors are thankful to the Centre National de la Recherche Scientifique (CNRS) (S. M. G.), the Deutsche Forschungsgemeinschaft (DFG) (P. W. R.), and the Institut Universitaire de France (L. M.) for their continuous support.

LIST OF SYMBOLS, ABBREVIATIONS, AND ACRONYMS

ALA	L-alanine *N*-carboxyanhydride
Ap*H	(2,6-diisopropyl-phenyl)-[6-(2,4,6-triisopropyl-phenyl)-pyridin-2-yl]-amine
Ar	$(C_6H_2{}^tBu_3$-2,4,6)
Benz	benzene
***rac*-BL**	*racemic*-β-butyrolactone, (*S*,*S*/*R*,*R*)-β-butyrolactone
BLL	ε-carboxbenzoxy-L-lysine *N*-carboxyanhydride
BLG	γ-benzyl L-glutamate *N*-carboxyanhydride
CL	ε-caprolactone
COT	η^8-cyclooctatetraenyl (η^8-C_8H_8)
Cp	η^5-cyclopentadienyl (η^5-C_5H_5)
$\mathbf{Cp}^{i\mathbf{Pr4}}$	tetra-*iso*-propylcyclopentadienyl ($C_5H{}^iPr_4$)
$\mathbf{Cp}^{\mathbf{Ph3}}$	1,2,4-triphenylcyclopentadienyl ($C_5H_2Ph_3$-1,2,4)
Cp*	η^5-pentamethylcyclopentadienyl (η^5-C_5Me_5)
$\mathbf{Cp}^{*\mathbf{Pr}}$	tetramethyl-*n*-propylcyclopentadienyl ($C_5Me_4{}^nPr$)
Cy	cyclohexyl (C_6H_{11})
$\mathbf{DAB}^{2-}$	$((2,6\text{-}C_6H_3{}^iPr_2)NC(Me){=}C(Me)N(2,6\text{-}C_6H_3{}^iPr_2))^{2-}$
DCM	dichloromethane (CH_2Cl_2)

DFT	density functional theory
$Đ_\mathrm{M}$	dispersity (molar mass distribution; $\overline{M}w/\overline{M}n$)
DME	1,2-dimethoxyethane ($MeO(CH_2)_2OMe$)
DSC	differential scanning calorimetry
FTIR	Fourier transform infrared spectroscopy
HO-polymer-OH	α,ω-hydroxytelechelic polymer
D-LA	D-lactide, (*R*,*R*)-lactide
LLA	L-lactide, (*S*,*S*)-lactide
***rac*-LA**	*racemic*-lactide, (D,L)-lactide, (*R*,*R*/*S*,*S*)-lactide
MALDI-ToF	matrix-assisted laser desorption/ionization- time-of-flight
Mes	mesityl ($C_6H_2Me_3$-2,4,6)
mm %	isotactic triad content
MMA	methyl methacrylate
$\overline{M}n$	number average molar mass
mr %	atactic triad content
MS	mass spectrometry
$\overline{M}w$	weight average molar mass
$\overline{M}w/\overline{M}n$	dispersity ($Đ_M$; molar mass distribution)
NCA	*N*-carboxyanhydride
nd	not determined
N_2NN'	$(2\text{-}C_5H_4N)CH_2N(CH_2\text{-}CH_2NMe)_2$
N_2NN^{Mes}	$(2\text{-}C_5H_4N)CH_2N(CH_2CH_2N(C_6H_2Me_3\text{-}2,4,6))_2$
N_2NN^{TMS}	$(2\text{-}C_5H_4N)CH_2N(CH_2CH_2N(SiMe_3))_2$
O_2N^L	$RCH_2N(CH_2\text{-}2\text{-}O\text{-}3,5\text{-}C_6H_2{}^tBu_2)_2$ where $R = CH_2OMe$, CH_2NMe_2, $(2\text{-}C_5H_4N)$, or Et for L = OMe, NMe_2, py, or ^{n}Pr, respectively
$(O_2N_2)^1$	$\{CH_2N(Me)CH_2\text{-}3,5\text{-}Me,{}^tBu\text{-}C_6H_2O\}_2$
$(O_2N_2)^2$	$C_5H_4NCH_2N—\{CH_2\text{-}3,5\text{-}Me,{}^tBu\text{-}C_6H_2O\}_2$
PBLG	poly(γ-benzyl L-glutamate *N*-carboxyanhydride)
PCL	poly(ε-caprolactone)
PCL-*b*-PTMC	poly(ε-caprolactone)-*b*-poly(trimethylene carbonate)
PCL-*co*-PTMC	poly(ε-caprolactone)-*co*-poly(trimethylene carbonate)
PDL	ω-pentadecalactone
PHB	poly(3-hydroxybutyrate)
PLA	poly(lactic acid), poly(lactide)
PLLA	poly(L-lactic acid), poly(L-lactide)
***P*m**	probability of *meso* linkages between monomer units
PMMA	poly(methyl methacrylate)
***P*r**	probability of *racemic* linkages between monomer units
PTMC	poly(trimethylene carbonate)
py	pyridine (C_5H_5N)
ROP	ring-opening polymerization

rr %	syndiotactic triad content
RT	room temperature
SEC	size exclusion chromatography
@SiO	silica grafted
$Sn(Oct)_2$	stannous(2-ethylhexanoate)
tetrahydrosalen	$[(2\text{-OH—}C_6H_2{}^tBu_2\text{-}3,5)CH_2N(CH_3)CH_2]_2$
***T*g**	glass transition temperature
THF	tetrahydrofuran
***T*m**	melting temperature
TMC	trimethylene carbonate (3-dioxan-2-one)
TMS	trimethylsilyl ($SiMe_3$)
TOF	turn over frequency, activity
***p*-Tol**	*para*-tolyl ($p\text{-}CH_3{=}C_6H_4$)
(*p*-Tol)NN	$[(p\text{-}CH_3C_6H_4)N(CH_3)C]_2CH$
$Tp^{tBu,Me}$	tris(2-*t*-butyl-4-methyl)pyrazolylborate
VL	δ-valerolactone

REFERENCES

Agarwal, S., Greiner, A., 2002. J. Chem. Soc Perkin Trans. 1, 2033–2042.

Agarwal, S., Mast, C., Dehnicke, K., Greiner, A., 2000. Macromol. Rapid Commun. 21, 195–212.

Ajellal, N., Carpentier, J.-F., Guillaume, C., Guillaume, S.M., Helou, M., Poirier, V., Sarazin, Y., Trifonov, A., 2010a. Dalton Trans. 39, 8363–8376.

Ajellal, N., Durieux, G., Delevoye, L., Tricot, G., Dujardin, C., Thomas, C.T., Gauvin, R.M., 2010b. Chem. Commun. 46, 1032–1034.

Albertsson, A.-C., Varma, I.K., 2003. Biomacromolecules 4, 1466–1486.

Arndt, S., Okuda, J., 2002. Chem. Rev. 102, 1953–1976.

Arndt, S., Beckerle, K., Hultzsch, K.C., Sinnema, P.-J., Voth, P., Spaniol, T.P., Okuda, J., 2002. J. Mol. Catal. A Chem. 190, 215–223.

Barbier-Baudry, D., Bouyer, F., Madureira, B.A.S., Visseaux, M., 2006. Appl. Organomet. Chem. 20, 24–31.

Barros, N., Mountford, P., Guillaume, S.M., Maron, L., 2008a. Chem. Eur. J. 14, 5507–5518.

Barros, N., Schappacher, M., Dessuge, P., Maron, L., Guillaume, S.M., 2008b. Chem. Eur. J. 14, 1881–1890.

Bonnet, F., Visseaux, M., Barbier-Baudry, D., Hafid, A., Vigier, E., Kubicki, M.M., 2004a. Inorg. Chem. 43, 3682–3690.

Bonnet, F., Visseaux, M., Barbier-Baudry, D., Vigier, E., Kubicki, M.M., 2004b. Chem. Eur. J. 10, 2428–2434.

Bonnet, F., Cowley, A.R., Mountford, P., 2005a. Inorg. Chem. 44, 9046–9055.

Bonnet, F., Hillier, A.C., Collins, A., Dubberley, S.R., Mountford, P., 2005b. Dalton Trans. 421–423.

Cendrowski-Guillaume, S.M., Nierlich, M., Lance, M., Ephritikhine, M., 1998. Organometallics 17, 786–788.

Cendrowski-Guillaume, S.M., Le Gland, G., Nierlich, M., Ephritikhine, M., 2000. Organometallics 19, 5654–5660.

Cendrowski-Guillaume, S.M., Le Gland, G., Lance, M., Nierlich, M., Ephritikhine, M., 2002. C. R. Chim. 5, 73–80.

Cendrowski-Guillaume, S.M., Le Gland, G., Nierlich, M., Ephritikhine, M., 2003. Eur. J. Inorg. Chem. 1388–1393.

Del Rosa, I., Poteau, R., Maron, L., 2011a. Dalton Trans. 40, 11211–11227.

Del Rosa, I., Poteau, R., Maron, L., 2011b. Dalton Trans. 40, 11228–11240.

Del Rosa, I., Tschan, M.J.-L., Gauvin, R.M., Maron, L., Thomas, C.M., 2012. Polym. Chem. 3, 1730–1739.

Dyer, H.E., Huijser, S., Susperregui, N., Bonnet, F., Schwarz, A.D., Duchateau, R., Maron, L., Mountford, P., 2010. Organometallics 29, 3602–3621.

Edelmann, F.T., 2009. Chem. Soc. Rev. 38, 2253–2268.

Edelmann, F.T., 2010. Struct. Bond. 137, 109–163.

Edelmann, F.T., 2011. Coord. Chem. Rev. 255, 1834–1920.

Edelmann, F.T., Freckmann, D.M.M., Schumann, H., 2002. Chem. Rev. 102, 1851–1896.

Ephritikhine, M., 1997. Chem. Rev. 97, 2193–2242.

Evans, W.J., Bloom, I., Hunter, W.E., Atwood, J.L., 1983. J. Am. Chem. Soc. 105, 1401–1403.

Evans, W.J., Dominguez, R., Hanusa, T.P., 1986. Organometallics 5, 263–270.

Evans, W.J., Chamberlain, L.R., Ulibarri, T.A., Ziller, J.W., 1998. J. Am. Chem. Soc. 110, 6423–6432.

Gamer, M.T., Rastätter, M., Roesky, P.W., Steffens, A., Glanz, M., 2005. Chem. Eur. J. 11, 3165–3172.

Gamer, M.T., Roesky, P.W., Palard, I., Le Hellaye, M., Guillaume, S.M., 2007. Organometallics 26, 651–657.

Gmelin Handbook, 1991. In: Gmelin Handbook of Inorganic and Organometallic Chemistry, RE Main vol. C 11 b. Springer-Verlag, Berlin, pp. 480–487.

Guerin, W., Helou, M., Carpentier, J.-F., Slawinski, M., Brusson, J.-M., Guillaume, S.M., 2013. Polym. Chem. 4, 1095–1106.

Guillaume, S.M., 2013. Eur. Polym. J. 49, 768–779.

Guillaume, S.M., Carpentier, J.F., 2012. Catal. Sci. Perspect. 2, 898–906.

Guillaume, S.M., Schappacher, M., Soum, A., 2003. Macromolecules 36, 54–60.

Guillaume, S.M., Schappacher, M., Scott, N.M., Kempe, R., 2007. J. Polym. Sci. A Polym. Chem. 45, 3611–3619.

Guillaume, S.M., Brignou, P., Susperregui, N., Maron, L., Kuzdrowska, M., Roesky, P.W., 2011. Polym. Chem. 2, 1728–1736.

Guillaume, S.M., Brignou, P., Susperregui, N., Maron, L., Kuzdrowska, M., Kratsch, J., Roesky, P.W., 2012. Polym. Chem. 3, 429–435.

Guillaume, S.M., Annunziata, L., Maron, L., Roesky, P.W., Schmid, M., 2013. Polym. Chem. 4, 3077–3087. http://dx.doi.org/10.1039/c3py00056g.

Helou, M., Miserque, O., Brusson, J.-M., Carpentier, J.-F., Guillaume, S.M., 2009. Macromol. Rapid. Commun. 30, 2128–2135.

Helou, M., Carpentier, J.-F., Guillaume, S.M., 2011. Green Chem. 13, 266–271.

Hiorns, R.C., Boucher, R.J., Duhlev, R., Hellwich, K.-H., Hodge, P., Jenkins, A.D., Jones, R.G., Kahovec, J., Moad, G., Ober, C.K., Smith, D.W., Stepto, R.F.T., Vairon, J.-P., Vohidal, J., 2012. Pure Appl. Chem. 84, 2167–2169.

Hou, Z., Nishiura, M., 2010. Bull. Chem. Soc. Jpn. 6, 595–608.

Hou, Z., Wakatsuki, Y., 2002. Coord. Chem. Rev. 231, 1–22.

Hou, Z., Luo, Y., Li, X., 2006. J. Organomet. Chem. 691, 314–3121.

Iftner, C., Bonnet, F., Nief, F., Visseaux, M., Maron, L., 2011. Organometallics 30, 4482–4485.

Ihara, E., Morimoto, M., Yasuda, H., 1995. Macromolecules 28, 7886–7892.

Jaroschik, F., Bonnet, F., Le Goff, X.-F., Ricard, L., Nief, F., Visseaux, M., 2010. Dalton Trans. 39, 6761–6766.

Jenter, J., Roesky, P.W., Ajellal, N., Guillaume, S.M., Susperregui, N., Maron, L., 2010. Chem. Eur. J. 16, 4629–4638.

Jeske, G., Lauke, H., Mauermann, H., Swepston, P.N., Schumann, H., Marks, T.J., 1985. J. Am. Chem. Soc. 107, 8091–8103.

Jian, Z., Zhao, W., Liu, X., Chen, X., Tang, T., Cui, D., 2010. Dalton Trans. 39, 6871–6876.

Kasperczyk, J.E., 1995. Macromolecules 30, 3937–3939.

Kerton, F.M., Witwood, A.C., Williams, C.K., 2004. Dalton Trans. 2237–2244.

Khvostov, A.V., Belsky, V.K., Sizov, A.I., Bulychev, B.M., Ivchenko, N.B., 1998. J. Organomet. Chem. 564, 5–12.

Konkol, M., Okuda, J., 2008. Coord. Chem. Rev. 252, 1577–1591.

Kramer, M.U., Robert, D., Arndt, S., Zeimentz, P.M., Spaniol, T.P., Yahia, A., Maron, L., Eisenstein, O., Okuda, J., 2008. Inorg. Chem. 47, 9265–9278.

Kritikos, M., Moustiakimov, M., Wijk, M., Westin, G., 2001. J. Chem. Soc. Dalton Trans. 1931–1938.

Lappert, M.F., Singh, A., Atwood, J.L., Hunter, W.E., 1983. J. Chem. Soc. Chem. Commun. 206–207.

Lobkovski, E.B., Kravchenko, S.E., Semenenko, K.N., 1977. Zh. Strukt. Khim. 18, 389–391.

Loh, X.J., Guerin, W., Guillaume, S.M., 2012. J. Mater. Chem. 22, 21249–21256.

Lyubov, D.M., Bubnov, A.M., Fukin, G.K., Dolgushin, F.M., Antipin, M.Y., Pelcé, O., Schappacher, M., Guillaume, S.M., Trifonov, A.A., 2008. Eur. J. Inorg. Chem. 2090–2098.

Mahrova, T.V., Fukin, G.K., Cherkasov, A.V., Trifonov, A.A., Ajellal, N., Carpentier, J.-F., 2009. Inorg. Chem. 48, 4258–4266.

Makhaev, V.D., 2000. Russ. Chem. Rev. 69, 727–746.

Makhaev, V.D., Borisov, A.P., 1999. Zh. Neorg. Khim. 44, 1489–1491.

Marks, T.J., Kolb, J.R., 1977. Chem. Rev. 77, 263–293.

Marks, T.J., Kolb, J.R., 1981. Inorg. Chem. 20, 297–299.

Marks, S., Heck, J.G., Habicht, M.H., Oña-Burgos, P., Feldmann, C., Roesky, P.W., 2012. J. Am. Chem. Soc. 134, 16983–16986.

McLain, S.J., Drysdale, N.E., 1991. (E.I. du Pont de Nemours and Co.). U. S. Patent 5028667.

McLain, S.J., Drysdale, N.E., 1992. Polym. Prepr. (Am. Chem. Soc. Div. Polym. Chem.) 33, 174–175.

McLain, S.J., Ford, T.M., Drysdale, N.E., 1992. Polym. Prepr. (Am. Chem. Soc. Div. Polym. Chem.) 33, 463–464.

McLain, S.J., Ford, T.M., Drysdale, N.E., Shreeve, J.L., Evans, W.J., 1994. Polym. Prepr. (Am. Chem. Soc. Div. Polym. Chem.) 35, 534–535.

Mirsaidov, U., Kurbonbekov, A., 1985. Dokl. Akad. Nauk Tadzh. SSR 28, 219–220.

Mirsaidov, U., Rakhimova, A.Z., 1978. Izv. Akad. Nauk Tadzh. SSR Otd. Fiz.-Mat. Geol.-Khim. Nauk 121.

Mirsaidov, U., Rotenberg, T.G., Dymova, T.N., 1976. Dokl. Akad. Nauk Tadzh. SSR 19, 30–33.

Mirsaidov, U., Kurbonbekov, A., Rotenberg, T.G., Dzhuraev, K., 1978. Izv. Akad. Nauk SSSR Neorg. Mater. 14, 1722–1725.

Mirsaidov, U., Kurbonbekov, A., Khikmatov, M., 1982. Zh. Neorg. Khim. 27, 2436–2439.

Mirsaidov, U., Boiko, G.N., Kurbonbekov, A., Rakhimova, A., 1986a. Dokl. Akad. Nauk Tadzh. SSR 29, 608–611.

Mirsaidov, U., Shaimuradov, I.B., Khikmatov, M., 1986b. Zh. Neorg. Khim. 31, 1321–1323 Russ. J. Inorg. Chem. 31, 753–754.

Momin, A., Bonnet, F., Visseaux, M., Maron, L., Takats, J., Ferguson, M.J., Le Goff, X.-F., Nief, F., 2011. Chem. Commun. 47, 12203–12205.

Nakayama, Y., Okuda, S., Yasuda, H., Shiono, T., 2007. React. Funct. Polym. 67, 798–806.

Nakayama, Y., Sasaki, K., Watanabe, N., Cai, Z., Shiono, T., 2009. Polymer 50, 4788–4793.

Nakayama, Y., Watanabe, N., Kusaba, K., Sasaki, K., Cai, Z., Shiono, T., Tsutsumi, C., 2011. J. Appl. Polym. Sci. 121, 2098–2103.

Nomura, R., Endo, T., 1998. Chem. Eur. J. 4, 1605–1610.

Okuda, J., Arndt, S., Beckerle, K., Hultzsch, K.C., Voth, P., Spaniol, T.P., 2001. Pure Appl. Chem. 73, 351–354.

Palard, I., Soum, A., Guillaume, S.M., 2004. Chem. Eur. J. 10, 4054–4062.

Palard, I., Soum, A., Guillaume, S.M., 2005. Macromolecules 38, 6888–6894.

Palard, I., Schappacher, M., Soum, A., Guillaume, S.M., 2006. Polym. Int. 55, 1132–1137.

Palard, I., Schappacher, M., Belloncle, B., Soum, A., Guillaume, S.M., 2007. Chem. Eur. J. 13, 1511–1521.

Parry, R.W., Kodama, G., 1993. Coord. Chem. Rev. 128, 245–260.

Penczek, S., Moad, G., 2008. Pure Appl. Chem. 80 (10), 2163–2193.

Peng, H., Ling, J., Shen, Z., 2012a. J. Polym Sci. Polym. Chem. 50, 1076–1085.

Peng, H., Ling, J., Zhu, Y., You, L., Shen, Z., 2012b. J. Polym Sci. Polym. Chem. 50, 3016–3029.

Poncelet, O., Sartain, W.J., Hubert-Pfalzgraf, L.G., Folting, K., Caulton, K.G., 1989. Inorg. Chem. 28, 263.

Richter, J., Edelmann, F.T., 1996. Eur. J. Solid State Inorg. Chem. 33, 1063–1069.

Robert, D., Kondracka, M., Okuda, J., 2008. Dalton Trans. 2667–2669.

Saiyasombat, W., Molloy, R., Nicholson, T.M., Johnson, A.F., Ward, I.M., Poshyachinda, S., 1998. Polymer 39, 5581–5585.

Save, M., Schappacher, M., Soum, A., 2002. Macromol. Chem. Phys. 203, 889–899.

Schappacher, M., Soum, A., Guillaume, S.M., 2006. Biomacromolecules 7, 1373–1379.

Schappacher, M., Fur, N., Guillaume, S.M., 2007. Macromolecules 40, 8887–8896.

Schappacher, M., Le Hellaye, M., Bareille, R., Durrieu, M.-C., Guillaume, S.M., 2010. Macromol. Biosci. 10, 60–67.

Schumann, H., Meese-Marktscheffel, J.A., Esser, L., 1995. Chem. Rev. 95, 865–986.

Schumann, H., Keitsch, M.R., Demtschuk, J., Mühle, S., 1998. Z. Anorg. Allg. Chem. 624, 1811–1818.

Scott, N.M., Kempe, R., 2005. Eur. J. Inorg. Chem. 1319–1324.

Shannon, R.D., 1976. Acta. Cryst. A32, 751–767.

Shen, Y., Shen, Z., Zhang, Y., Hang, Q., 1997. J. Polym. Sci. A 35, 1339–1352.

Shen, X., Xue, M., Jiao, R., Ma, Y., Zhang, Y., Shen, Q., 2012. Organometallics 31, 6222–6230.

Sinenkov, M.A., Fukin, G.K., Cherkasov, A.V., Ajellal, N., Roisnel, T., Kerton, F.M., Carpentier, J.-F., Trifonov, A.A., 2011. New J. Chem. 35, 204–212.

Skvortsov, G.G., Yakovenko, M.V., Castro, P.M., Fukin, G.K., Cherkasov, A.V., Carpentier, J.-F., Trifonov, A.A., 2007a. Eur. J. Inorg. Chem. 3260–3267.

Skvortsov, G., Yakovenko, M., Fukin, G., Baranov, E., Kurskii, Y., Trifonov, A., 2007b. Russ. Chem. Bull. 56, 456–460.

Skvortsov, G.G., Yakovenko, M.V., Fukin, G.K., Cherkasov, A.V., Trifonov, A.A., 2007c. Russ. Chem. Bull. Int. Ed. 56, 1742–1748.

Susperregui, N., Kramer, M.U., Okuda, J., Maron, L., 2011. Organometallics 30, 1326–1333.

Tanabe, M., Sugimura, T., Yasuda, H., 2002. React. Funct. Polym. 52, 135–141.

Visseaux, M., Bonnet, F., 2011. Coord. Chem. Rev. 255, 374–420.

Visseaux, M., Terrier, M., Mortreux, A., Roussel, P., 2010. Eur. J. Inorg. Chem. 18, 2867–2876.

Watson, P., 1983. J. Chem. Soc. Chem. Commun. 276–277.

Wu, G., Sun, W., Shen, Z., 2008. React. Funct. Polym. 68, 822–830.

Wu, G., Sun, W., Shen, Z., 2009. J. Appl. Polym. Sci. 112, 557–562.

Xhu, Z., Lin, Z., 1996. Coord. Chem. Rev. 156, 139–162.

Yakovenko, M.V., Trifonov, A.T., Kirillov, E., Roisnel, T., Carpentier, J.-F., 2012. Inorg. Chim. Acta 383, 137–142.

Yamashita, M., Takemoto, Y., Ihara, E., Yasuda, H., 1996. Macromolecules 29, 1798–1806.

Yasuda, H., Ihara, E., 1997. Adv. Polym. Sci. 133, 55–101.

Yasuda, H., Tamai, H., 1993. Prog. Polym. Sci. 18, 1097–1139.

Yasuda, H., Tamai, H., 2000. Prog. Polym. Sci. 25, 573–626.

Yasuda, H., Tamai, H., 2002. J. Organometallic. Chem. 647, 128–138.

Yasuda, H., Yamamoto, H., Yokota, K., Miyake, S., Nakamura, A., 1992. J. Am. Chem. Soc. 114, 4908–4910.

Yasuda, H., Yamamoto, H., Takemoto, Y., Miyake, S., Yamashita, M., Yokota, K., Miyake, S., Nakamura, A., 1993a. Makromol. Chem. Macromol. Symp. 67, 187–201.

Yasuda, H., Yamamoto, H., Yamashita, M., Yokota, K., Nakamura, A., Miyake, S., Kai, Y., Kanehisa, N., 1993b. Macromolecules 22, 7134–7143.

Yuan, F., Yang, J., Xiong, L., 2006a. J. Organomet. Chem. 691, 2534–2539.

Yuan, F., Zhu, Y., Xiong, L., 2006b. J. Organomet. Chem. 691, 3377–3382.

Zange, E., 1960. Chem. Ber. 93, 652–657.

Zhang, X., Wang, C., Xue, M., Zhang, Y., Yao, Y., Shen, Q., 2012. J. Organomet. Chem. 713, 182–188.

Chapter 260

Structures and Properties of Rare-Earth Molten Salts

Yasuhiko Iwadate
Department of Applied Chemistry and Biotechnology, Graduate School of Engineering,
Chiba University, Yayoi-cho 1-33, Inage-ku, Chiba, Japan

Chapter Outline

1. INTRODUCTION

Molten salts discussed in this chapter have been classified into high-temperature ionic liquids in the narrow sense until room-temperature ionic liquids appeared as relatively bulky but ionic organic solvents. As time goes by, definitions of both liquids tend to overlap with each other. Nowadays, the term of “molten salts” is usually used to express “melts of inorganic compounds” composed of cations

Handbook on the Physics and Chemistry of Rare Earths, Vol. 44.
http://dx.doi.org/10.1016/B978-0-444-62711-7.00260-7

and anions. In this chapter, the concept of "liquid" as one of the three states of matter is first defined and the following points are discussed: the general theory of liquids, structural features and properties of molten salts, and methodology of structural analyses. The present state of the art of works on structures and properties of rare-earth molten salts is outlined.

Apart from gaseous phase, particles such as molecules or ions are located very closely to each other and thus strong forces act between them in solid and liquid states. As atoms in solids are arranged properly in lines, their physicochemical properties are calculated with relative ease. In contrast, particles in liquids are mobile and get easily into contact; thus interparticle interactions are very difficult to model, which consequently delayed progress in the solid-state physics of liquids. A legitimate theory of liquid appeared in the 1930s by taking advantage of the analysis of atomic arrangement in liquids by X-ray diffraction (XRD).

The main differences between solids and liquids are that solids have short-range ordering as well as long-range ordering but liquids possess only the latter ordering; furthermore, liquids retain mobility but keep their density constant thanks to the cohesion among the constituent particles. Accordingly, molten salts happen to have the same features.

2. MOLTEN SALTS AS LIQUIDS

In order to make the concept of liquid clear, phase diagrams describing the relationship among pressure, volume, and temperature are briefly referred to. Figure 1 shows the states of pure matter at a given temperature and pressure (Nakamura, 1993). Three phases such as gas phase (G), liquid phase (L), and solid phase (S) coexist at the triple point $\mathrm{T_t}$. The critical temperature and the glass transition temperature are designated by T_c and T_g, respectively. The dotted line in Fig. 1 refers to supercooling. At atmospheric pressure, three different states of matter can occur, depending on the temperature. For further classification of liquids, the origins of interactions among constituent particles should be considered.

The liquids can be roughly divided into three types on the basis of intermolecular forces acting between particles. Type 1 corresponds to molecular liquids which can further be divided into four different categories: simple liquids (such as argon), nonpolar molecular liquids (*n*-hexane), polar molecular liquids (acetone), and hydrogen-bonded molecular liquids (water). Type 2 encompasses ionic liquids or molten salts such as sodium chloride melt, for instance. Liquid metals constitute type 3.

The averaged physical properties of type 1, 2, and 3 liquids near their melting points under ambient pressure are listed in Table 1, in which the values between parentheses correspond to those for crystals. The differences

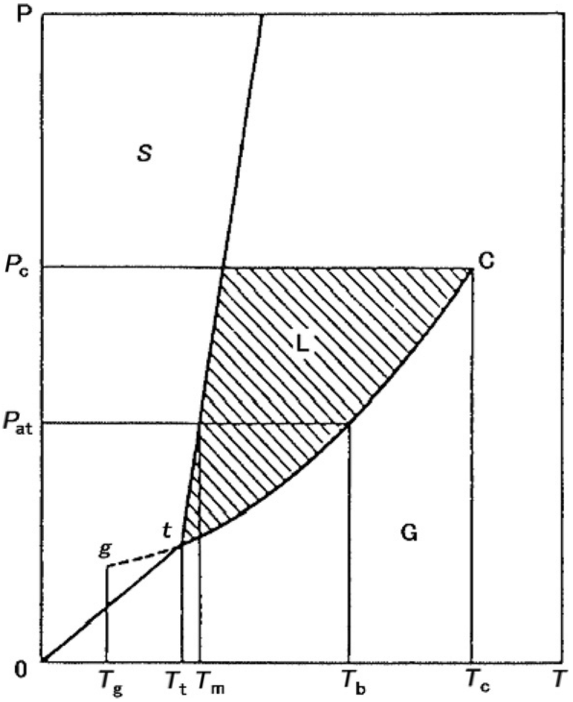

FIGURE 1 Phase diagram of pure matter. *Reproduced with permission from Nakamura (1993), © 1993 Ceramic Society of Japan.*

TABLE 1 Averaged Physical Properties of Liquids near the Melting Points Under Ambient Pressure (Nakamura, 1993)

Physical property	Molecular liquid	Liquid metal	Ionic melt
Ratio of fusion energy to cohesive energy	~10%	~5%	~5%
Volume change on melting	10–15%	2–5%	15~20%
Nr of nearest neighbors	~10(12)[a]	~10(12)[a]	4~5(6)[a]
Packing fraction	~0.45(0.74)[a]	~0.45(0.74)[a]	~0.35(0.52)[a]

[a] *For crystals.*

in cohesive energy and density between liquids and crystals are not so large. The packing fraction in closest-packed crystals is estimated at about 3/4 and that in liquids to about 1/2; this disparity is a fundamental factor leading to fluidity for liquids. The attractive force between molecules in molecular liquids is well expressed by a Van der Waals potential which varies as the inverse sixth power of the intermolecular distance *r*. A vibrating potential with an oscillatory form is known to be applicable to liquid metals (Egelstaff, 1967), while an electrostatic Coulombic potential is an important factor determining the structure and properties of ionic melts (molten salts).

3. DEFINITIONS OF MOLTEN SALTS

Salts are produced by the chemical reaction of acids and alkalis. Molten salts are understood to be liquefied by heating. It has been long pointed out that the oscillating amplitude between constituent ions reaches more than 10% of interionic distance near the melting point of an ionic crystal before fusion at the critical point (Lindemann, 1910). In principle, molten salts cover alkali halides and oxysalts such as nitrates and sulfates. Definition is often expanded to silicates, borates, and organic salts. As expected from the periodic table, candidate cations are more than 80 and counterpart anions over 30. Accordingly, the combinations of potential salts can reach over 2000. If binary and ternary systems are considered, this number is, in fact, quasi infinite.

Constituents consist of cations and anions being regarded as extremely concentrated solutions or solutes without solvents at elevated temperatures. In molten salts, long-ranged coulombic interactions predominantly determine the structure and properties of molten salts.

4. TYPICAL STRUCTURES OF MOLTEN SALTS

4.1. Methodology for Obtaining Structural Information

Physicochemical properties of molten salts closely ressemble those of liquid structures composed of mobile cations and anions at high temperatures. It is thus of much importance to determine structural information for understanding their systematic properties.

XRD and neutron diffraction (ND) have usually been employed to analyze the structure of molten salts. In order to comprehend the liquid structure quantitatively, a radial distribution function, $D(r)$ (RDF) and a correlation function, $G(r)$ (Fig. 2) of a given constituent ionic pair have to be estimated from diffraction data (Iwadate et al., 2005). The coordination numbers of individual atomic pairs may be estimated from Fig. 2 by deconvolution of $D(r)$ into respective peaks and by integration of each contribution over an interatomic distance *r*. The downward parabola of $D(r)$ or the solid straight line of $r^{-1}D$

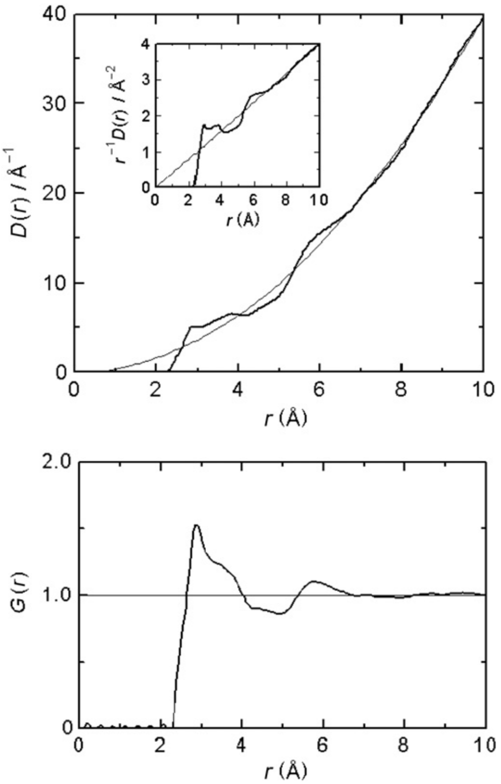

FIGURE 2 Distribition (Top) and Coorelation (bottom) functions for molten lead dichlorie. *Reproduced with permission from Iwadate et al. (2005), © 2005 Elsevier.*

(r) describes the average number density of the medium. The line $G(r)=1$ in Fig. 2 corresponds to the average number density distribution of atoms. The $G(r)$ function becomes attenuated with increasing r and reaches a value close to unity, which reflects that the atomic arrangement is getting less ordered.

4.2. Definition of Radial Distribution Function

In order to understand RDFs, some of their definitions are explained briefly here. The results of structural analyses are affected by not only the experimental techniques but also the definitions and calculation procedures of RDFs used.

4.2.1. Definition 1

The pair number density function $\rho(r)$ is related to coherent-scattered X-ray intensity $I^{\mathrm{coh}}(Q)$ in electron units as described by Eqs. (1)–(4) (Waseda, 1980a):

$$I^{\mathrm{coh}}(Q)=\langle f^2\rangle+\langle f\rangle^2\int_0^\infty 4\pi r^2[\rho(r)-\rho_0]\sin(Qr)\cdot(Qr)^{-1}\mathrm{d}r \tag{1}$$

$$\langle f^2\rangle=\sum_{i=1}^{n}c_if_i^2 \tag{2}$$

$$\langle f\rangle^2=\left(\sum_{i=1}^{n}c_if_i\right)^2 \tag{3}$$

$$\rho(r)=\sum_{i=1}^{n}\sum_{j=1}^{n}c_if_if_j\rho_{ij}(r)/\langle f\rangle^2 \tag{4}$$

where $Q=4\pi\ \sin\theta/\lambda$, λ is the wavelength of incident X-ray, 2θ the scattered angle, c_i and f_i the atomic fraction and scattering factor of atom i, respectively, and ρ_0 the mean number density. $\rho_{ij}(r)$ represents the number density function of atom j around atom i, the separation of which is defined as r. In conventional XRD experiments, the averaged density $\rho_{ij}(r)$ is obtained as $\rho(r)$. On the basis of Eq. (1), the structure factor of amorphous material, sometimes called the interference function, is defined by the following equation:

$$a(Q)=\left[I^{\mathrm{coh}}(Q)-\left(\langle f^2\rangle-\langle f\rangle^2\right)\right]/\langle f\rangle^2 \tag{5}$$

Accordingly, Fourier transformation of $a(Q)$ as explicitated in Eq. (6) gives the RDF

$$4\pi r^2[\rho(r)-\rho_0]=rG(r)=(2r/\pi)\int_0^\infty Q[a(Q)-1]\sin(Qr)\mathrm{d}Q \tag{6}$$

Further expansion of Eq. (6) produces the partial structure factor $a_{ij}(Q)$ as well as the partial pair distribution function (pdf) $g_{ij}(r)$ (Waseda, 1980a).

$$a_{ij}(Q)=1+\int_0^\infty 4\pi r^2\rho_0\left[g_{ij}(r)-1\right]\sin(Qr)\cdot(Qr)^{-1}\mathrm{d}r \tag{7}$$

$$4\pi r^2\rho_0\left[g_{ij}(r)-1\right]=rG_{ij}(r)=(2r/\pi)\int_0^\infty Q\left[a_{ij}(Q)-1\right]\sin(Qr)\mathrm{d}Q \tag{8}$$

where $g_{ij}(r)=\rho_{ij}(r)/(c_j\rho_0)$.

4.2.2. *Definition 2*

The pair function method developed by Mozzi and Warren is frequently used to analyze the structure of metal oxide melts and glasses as follows (Mozzi and Warren, 1969):

$$i(Q)=\left[I_{\mathrm{eu}}(Q)\Big/N-\sum_{\mathrm{uc}}f_i^2\right]\Big/f_{\mathrm{e}}^2 \tag{9}$$

$$f_{\mathrm{e}}=\sum_{\mathrm{uc}}f_{\mathrm{i}}\Big/\sum_{\mathrm{uc}}Z_{\mathrm{i}} \tag{10}$$

$$\mathrm{RDF}_{\mathrm{exp}}=2\pi^2r\rho_{\mathrm{e}}\sum Z_{\mathrm{i}}+\int_0^{Q_{\max}}Q\cdot i(Q)\exp\left[-a^2Q^2\right]\sin(Qr)\mathrm{d}Q \tag{11}$$

where $I_{\mathrm{eu}}(Q)/N$ is the scattered X-ray intensity per unit composition, Σ the summation over all atoms in unit composition, f_{e} the averaged scattering factor defined by Eq. (10), ρ_{e} the mean electron number density, and Z_{i} the atomic number.

The total RDF for the given i–j pairs with coordination numbers N_{ij} at distances r_{ij} calculated according to the pair function method is expressed in the following form:

$$\mathrm{RDF}_{\mathrm{cal}}=\sum\sum\left(N_{ij}/r_{ij}\right)\int_0^{Q_{\max}}f_if_j(f_{\mathrm{e}})^{-2}\exp\left[-a^2Q^2\right]\sin\left(Qr_{ij}\right)\sin(Qr)\mathrm{d}Q \tag{12}$$

4.2.3. *Definition 3*

Direct Fourier transformation of the scattered intensity leads to the pdf or RDF only for the systems composed of monoatomic liquids. In contrast, the distribution functions are not obtainable with a rigorous scientific definition, but approximated ones can be estimated for liquids consisting of polyatomic molecules.

As for monoatomic liquids, the structural contributions in the scattered intensity, $i(Q)=I_{\mathrm{coh}}(Q)-f(Q)^2$, are normalized by the square of the atomic scattering factor, being relevant to a unit pair, $f(Q)^2$, as shown in Eq. (13).

$$i(Q)=\left[I_{\mathrm{coh}}-f(Q)^2\right]/f(Q)^2 \tag{13}$$

The RDF is then expressed by the following form:

$$4\pi r^2\rho(r)=4\pi r^2\rho_0+(2r/\pi)\int_0^{\infty}Qi(Q)\sin(Qr)\mathrm{d}Q \tag{14}$$

Thus, the two-body density function is evaluated, from which the pair correlation function is obtained by using $\rho(r)=\rho_0g(r)$ with $\rho_0=N/V$. In connection with this relation, Narten et al. (1967) have carried out the following Fourier transformation for the diffraction data of polyatomic molecules by defining the modification function $M(Q)=1/\Sigma f_j(Q)^2$ (Levy et al., 1966; Narten et al., 1967),

$$4\pi r^2[\rho(r)-\rho_0]=(2r/\pi)\int_0^{Q_{\max}} Qi(Q)M(Q)\exp\left(-BQ^2\right)\sin(Qr)\mathrm{d}Q \tag{15}$$

where $Q_{\max}$ refers to the maximum value in the measured range of Q. The function $\exp(-BQ^2)$ is introduced to reduce the termination effect in Fourier transformation and the parameter B is usually set to satisfy the equation $\exp(-BQ^2_{\max})=0.1$. Ohtaki (1982) has proposed the relationship $\Sigma f_j(0)^2/\Sigma f_j(Q)^2=\Sigma Z_j^2/\Sigma f_j(Q)^2$ as a modification function, where Z_j is the electron number of atom j.

Furthermore, Narten (1972) has adapted the applicability of liquid structural models to real systems by defining the interference function $i(Q)$ in a reciprocal lattice space, see Eq. (16), where the atomic correlations in the r range longer than a given distance $r'_{\alpha\beta}$ are assumed to be distributed at mean atomic number density:

$$\begin{aligned} i(Q)=\Bigg[&\sum_{i=1}^{m}\sum_{k} N_{ik}\exp\left(-\sigma_{ik}Q^2\right)f_i f_k \sin(Qr_{ik})/(Qr_{ik}) \\ &+\sum_{\alpha=1}^{m}\sum_{\beta=1}^{m}\left[\exp\left(-\sigma'_{\alpha\beta}Q^2\right)f_\alpha f_\beta 4\pi\rho_0\left(Qr'_{\alpha\beta}\cos\left(Qr'_{\alpha\beta}\right)\right)\right. \\ &\left.-\sin\left(Qr'_{\alpha\beta}\right)\right]/Q^3\Bigg]\Big/ f_{\mathrm{e}}^2 \end{aligned} \tag{16}$$

4.2.4. Definition 4

Let m and n be the atoms at the origin of the coordinate axes and at a given point, respectively. In polyatomic liquids, the RDF cannot be directly calculated through Fourier transformation of the XRD intensity function since both $f_{\mathrm{m}}(Q)$ and $f_{\mathrm{n}}(Q)$ are functions of Q. But if estimated values of the effective scattered electron number of each atom, K_{m}, K_{n}, are introduced, an approximate solution of RDF is obtainable (Ohno et al., 1994; Warren et al., 1936).

$$i(Q)=\left[I_{\mathrm{eu}}^{\mathrm{coh}}(Q)-N\sum\left\{f_{\mathrm{m}}(Q)^2\right\}\right]\Big/N\sum\left\{f_{\mathrm{m}}(Q)^2\right\} \tag{17}$$

If Eq. (17) can be derived from diffraction experiments, the following form of RDF, namely, $D(r)$, is finally determined:

$$D(r)=4\pi r^2\left(\sum K_m\right)^2\rho_0+\sum(K_m)^2\frac{2r}{\pi}\int_0^{Q_{\max}} Q\cdot i(Q)\sin(Qr)\mathrm{d}Q \tag{18}$$

In practice, it is very important that appropriate substitution of the atomic scattering factors $f_i(Q)$ in the above equations by the scattering lengths b_i is valid for ND analyses, where attention should paid to the fact that b_is are independent of Q, that is constant. The absolute values b_is for all elements in the periodic table are almost of the same order of magnitude. This trend is quite different for $f_i(Q)$s. For more details, the reader is referred to the literature cited later. In practice, structural parameters such as interatomic distance r, coordination number (CN), and mean square displacement ($\langle \Delta r^2 \rangle$) for a particular atomic pair are to be evaluated from these functions.

Spectroscopic measurements have also been used for the same goal, in particular, for elucidating the short-range structure, that is, for identifying the chemical species in molten salts. It is noteworthy that both techniques are powerful and complementary tools.

Principles and calculation procedures of XRD are well described in several reviews (Furukawa, 1962; Gingrich, 1943; Karnicky and Pings, 1976; Kruh, 1962; Levy et al., 1966; Pings, 1968; Waseda and Ohtani, 1971a; Waseda and Ohtani, 1971b).

As for neutral diffraction data, literature provides us with fundamental and useful information (Adya, 2002; Adya, 2003; Enderby and Biggin, 1983). The above analytical procedures correspond to those carried out in real space. But for the analyses in reciprocal lattice space, the works of Narten et al. (Narten, 1972; Narten and Levy, 1969; Narten et al., 1967) based on the Debye scattering equation as well as the algorithm proposed by Busing and Levy (1962) are of great advantage and service.

4.2.5. Estimation of Nearest-Neighbor Coordination Number from RDF

The coordination number of nearest neighbor n_I provides important information on the structure of liquids. There are four methods commonly used for estimating n_1 (Pings, 1968; Mikolaj and Pings, 1968), which are labeled A–D in Fig. 3. These methods result in progressively higher numerical values in the order, $n_1^A < n_1^B < n_1^C < n_1^D$.

Method A—Symmetrical turn-in of D(r)/r

This method involves symmetrizing the first peak in the $D(r)/r$ function around a radius of symmetry.

Method B—Symmetrical turn-in of D(r)

This is based on the assumption that the coordination shells are symmetric about a radius which corresponds to the maximum in the $D(r)$ function.

Method C—Decomposition of D(r) into shells

The distance $r_{\max}$, giving the first maximum in $D(r)$, is taken as the mean radius of the first shell. Any particle at a distance less than $r_{\max}$ is counted as belonging to the first shell. As depicted in Fig. 3, a smooth extrapolation of the leading edge of the second shell followed by subtraction gives the outward portion of the first shell.

Method D—Integration to the first minimum in D(r)

n_1 is determined by integrating $D(r)$ up to a distance corresponding to the first minimum after the first peak.

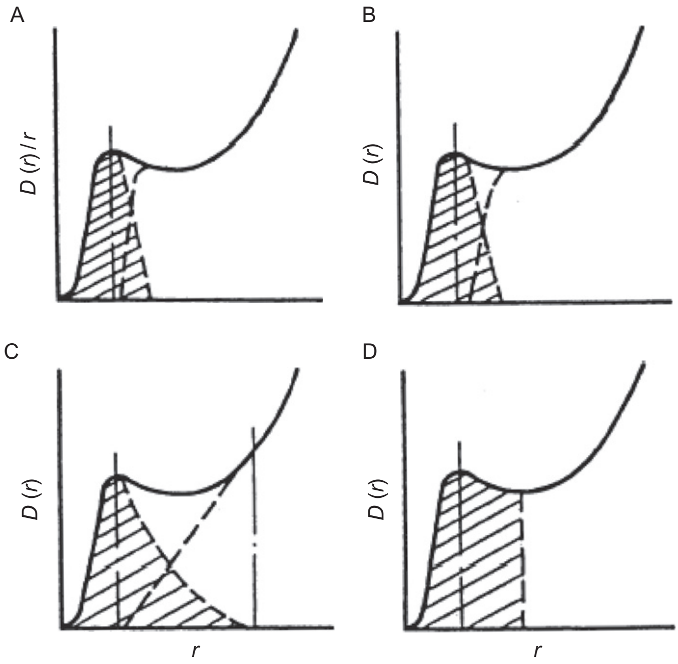

FIGURE 3 Calculation methods of the coordination number. *Reproduced with permission from Ohno et al. (1994), © 1994 Trans Tech Pub.*

Method A was proposed by Coulson and Rushbrooke (1939) under the assumption that $D(r)/r$ is, for each coordination shell, symmetrical around its mean radius for any Einstein model of a liquid. Since the radius of symmetry in $D(r)/r$ is less than r_{max}, this method will generally gives the smallest value of n_1. Although method B is perhaps one of the most common schemes in use, the $D(r)$ function is not really symmetric about the first peak. This fact is especially noticeable in the measurements made on high-density liquids near their melting points. As for method C, it is usually difficult to define the position of the second peak and to extrapolate the coordination number. This method tends to bear larger uncertainty than the other three methods. It is the advantage of method D, however, that the distance characteristic to the first minimum in $D(r)$ may be precisely determined and gives a plain value of n_1. It is therefore essential that the method used to evaluate n_1 and r_1 be precisely described in scientific reports. Moreover, it is indispensable to compare the observed values of n_1 and r_1 with those calculated by computer simulation (Sangster and Dixon, 1976; Woodcock and Singer, 1971).

4.2.6. Stability of Nearest-Neighbor Coordination Shell and Penetration Effect of Second Coordination Shell

As described in detail by Enderby and Biggin (1983), the partial structure factors S_{++}, S_{--}, and S_{+-} are related to the pair correlation functions $g_{\alpha\beta}(r)$s by

$$S_{\alpha\beta}(Q)=1+\frac{4\pi\rho}{Q}\int\left[g_{\alpha\beta}(r)-1\right]\cdot r\sin(Qr)\mathrm{d}r \tag{19}$$

where α and β refer to + and − corresponding to a cation and an anion, respectively, and ρ to the total density of ions. It is nowadays widely accepted that the most significant structural information about molten salts is contained in $S_{\alpha\beta}(Q)$. The pair correlation function, $S_{\alpha\beta}(Q)$, gives reach over a measure of the probability of finding a β-type particle at a distance r from an α-type particle placed at the origin. In other words, let us place an α-type particle at the origin and ask what is the average number of β-type particles which occupy a spherical shell of radius r and thickness dr at the same time. The number is given by:

$$\mathrm{d}n_r=4\pi\rho_\beta g_{\alpha\beta}(r)r^2\mathrm{d}r \tag{20}$$

where $\rho_\beta=N_\beta/V$ and N_β is the number of β species contained in the sample of volume V. A hypothetical $g(r)$ function for a simple liquid which contains a single chemical species is sketched in Fig. 4. Since the chance of finding two particles separated by a distance less than r_1 is negligible, r_1 becomes a measure for the closest distance of approach of two particles in the system. On the other hand, $\bar{r}$ giving the maximum $g(r)$ in the first coordination shell allows us to define the most probable separation of two atoms, and r_2 provides the range over which near-neighbor interactions are likely to be important. The definition of $g(r)$ given in Eq. (20) implies that the value of integral $4\pi\rho\int_0^{r_2}g(r)r^2\mathrm{d}r$ is the average number of near neighbors for one particle chosen to be at the origin. This number is often called the coordination number, n, although defined in several ways as indicated in the preceding section, which combined with the value of $\bar{r}$ allows us to build up a chemically plausible picture of the short-range order. The ratio h'/h is an important measure of the stability of the first coordination shell. If a distinct

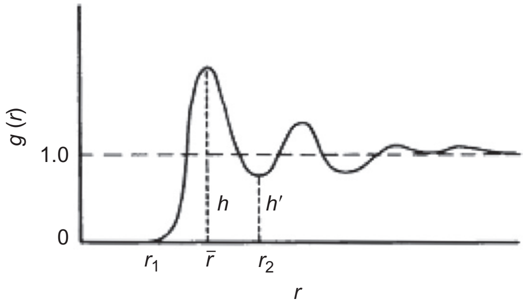

FIGURE 4 Hypothetical radial distribution function $g(r)$ for a simple liquid containing a single chemical species. *Reproduced with permission from Enderby and Biggin (1983), © 1983 Elsevier.*

and long-lived local geometry exists, h'/h tends to be small. For simple liquids in which there are no special chemical effects, h'/h is typically equal to about 1/4. If $g_{\alpha\beta}(r)$ functions are known with sufficient accuracy over a wide range of temperature T, pressure P, and concentration X, the thermodynamic properties relating to mixtures can, in principle, be deduced.

Enderby and Biggin (1983) have concluded that for systems in which the cation is small (e.g., Li^+, Na^+, Mg^{2+}, Zn^{2+}, and Mn^{2+}), calculation of the near-neighbor coordination number from $g(r)$ is satisfactory. The fundamental reason for this is the absence of significant penetration of similar ions into the first shell. This means that r_{+-} deduced from the total diffraction pattern should also be reliable, as emphasized by Ohno and Furukawa (1981). For large cations, in contrast, substantial penetration of the first shell by like ions results in an asymmetric first peak in $g(r)$. It is also important to realize that integrating up to the first minima in $g(r)$ or $r^2g(r)$ is unreliable since spurious peaks frequently occur in this region of the r-space. This results from the Fourier transformation of the S-space data. It therefore becomes difficult to locate the position of the minimum with confidence. Typical examples are depicted in Fig. 5, which clearly evidence the marked tendency for interpenetration of the first and second coordination shells for the larger cations.

The authors propose that another concept should be introduced to take the stability of the nearest coordination shell into account. When some penetration of the second coordination shell into the first coordination shell takes place, for example, in molten $SrCl_2$, this results in an overestimation of the number of chloride ions in the first coordination shell. As a consequence, the evaluation of the nearest-neighbor coordination number should rely on the integration of $g(r)$ or $g_{+-}(r)$ up to the cross point of $g_{+-}(r)$ and $g_{--}(r)$, or up to the first point where $g_{+-}(r)$ approaches unity from the origin. In any case, it is highly important to describe precisely in scientific reports which definition is employed for evaluating the nearest-neighbor coordination number.

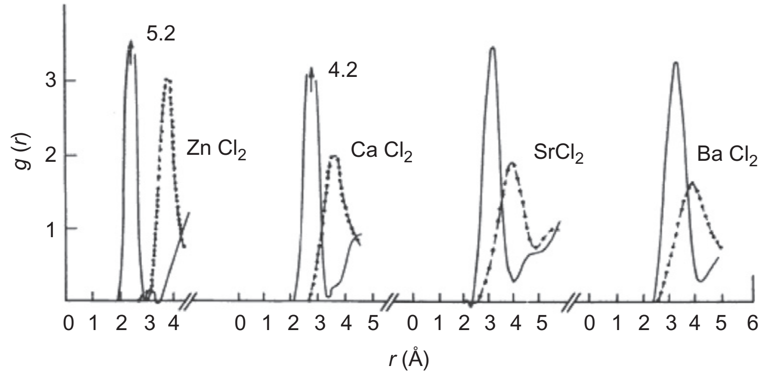

FIGURE 5 Increased penetration of the second into the first coordination sphere: solid line, $g_{+-}(r)$; dotted line, $g_{--}(r)$. *Reproduced with permission from Enderby and Biggin (1983), © 1983 Elsevier.*

4.3. Alkali Halide-Type Molten Salts Composed of Monoatomic Ions

The excess radial distribution of molten LiCl is shown in Fig. 6 (Marcus, 1977). The large peak at $r = 0.385$ nm corresponds to the contributions of pairs of same ions, mainly due to adjacent Cl^-–Cl^- pairs, while those from Li^+–Li^+ pairs are very small. At less than the above distance, there is a small peak in the XRD pattern. Simultaneously, a trough appears at around 0.245 nm since the scattering length of ^7Li for thermal neutron is negative (Sears, 1992). This peak is derived from the scattering of nearest-neighbor pairs, that is Li^+–Cl^- pairs, by taking into account the Coulomb forces acting in the melt. The other peaks are observed at $r = 0.70$ nm and 1.02 nm, perhaps being due to the Cl^-–Cl^- like ion pair. Over $r = 1.0$ nm, the assignments of the peaks are difficult and less reliable. Similar results have already been reported for the other alkali halide melts as listed in Table 2.

It is found from Table 2 that the nearest-neighbor coordination numbers of melts are always smaller than those of corresponding solids, for example, CN = 6 for NaCl-type solids and CN = 8 for CsCl-type solids. Due to the decrease in nearest-neighbor coordination number, nearest-neighbor interatomic distances in melts are reduced by as much as 5% on average in comparison with those in solids. The second-neighbor coordination numbers in liquids are usually smaller than those in solids, namely, 12. The second-neighbor interatomic distances increase by about 2% on average although there exist some exceptions. It is noteworthy that the peaks in RDFs are wide and the peak positions are no more than the mean values of individual distributions. As for the structures of molten alkali halides in the solid state and the liquid state just above their melting points, the following semi-empirical but quantitative equation is known to be applicable to real systems (Furukawa, 1961; Furukawa and Ohno, 1973),

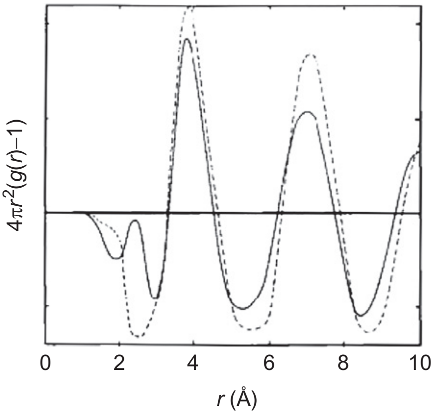

FIGURE 6 Excess radial distribution function of molten LiCl at 900 °C. *Reproduced with permission from Marcus (1977), © 1977 John Wiley & Sons.*

TABLE 2 Radial Distribution Analyses of Molten Alkali Halides by XRD, ND, and Computer Simulations (Ohno et al., 1994)[a]

Melt	r_1^s (nm)	n_1^s	r_1^1 (nm)	n_1^1	n_1^1 (cal)	r_2^s (nm)	n_2^s	r_2^l (nm)	$\Delta V_m/V_m^s$ (%)	Method	References	r_1^1 (nm)[b]	Method	References
LiI	0.312	6	0.285	5.6	3.9	0.441	12	0.445	20	XRD	1	0.26	MC	10
												0.273	MD	11
LiBr	0.285	6	0.268	5.2	4.0	0.403	12	0.412	22.4	XRD	1			
LiCl	0.266	6	0.255	4.1	4.2	0.376	12	0.39	26.2	XRD	2	0.240	MC	12
			0.247	4.0	3.9			0.385		XRD	1	0.200	MD	13
			0.245	3.5	3.7			0.38		ND	1	0.221	MD	14
			0.240	4.0	3.5			0.386		XRD	3	0.203	MD	15
			0.237	–						ND	4	0.23	MC	10
LiF	0.210	6	0.200	3.7	4.0	0.297	12	0.30	29.4	XRD	5	0.175	MD	16
	0.2013	6	0.185	3.1	–			0.302		XRD	6			
NaI	0.239		0.315	4.0	4.1	0.474	12	0.480	18.6	XRD	1	0.301	MD	17
												0.30	MD	18
NaCl	0.295		0.288	4.7	4.5	0.416	12	0.42	25.0	XRD	2	0.265	MD	19
			0.277	3.7	4.0			0.415		XRD	7	0.27	MD/MC	20
												0.26	MD	11
												0.265	MD	21
KBr	0.341	6	0.318	3.5	4.2			0.465	17	XRD	8			

NaF	0.250	6	0.230	4.1	4.1	0.330	12	0.35	27.4	XRD	5			
KCl	0.327	6	0.320	5.2	4.7	0.461	12	0.44	17.3	XRD	2	0.296	MC	22
			0.310	3.7	4.3			0.40–0.50		XRD	1	0.29	MC	23
			0.310	3.5	4.3					ND	1	0.295	MD	9
			0.305	3.6	4.4					XRD	9			
			0.301	–						ND	4			
CsCl	0.357	6	0.353	4.6	5.2	0.427	6	0.45–0.53	10.5	ND	1			
						(0.505)	(12)							
			0.342	–						ND	4			
KF	0.280	6	0.265	4.9	4.3	0.396	12	0.36–0.42	17.2	XRD	5	0.235–0.250	MC	24

1: Levy et al. (1960); 2: Zarzycki (1958); 3: Ohno et al. (1978a); 4: Miyamato et al. (1994); 5: Zarzycki (1957); 6: Vaslow and Narten (1973); 7: Ohno and Furukawa (1981); 8: Ohno and Furukawa (1983); 9: Takagi et al. (1979); 10: Lewis et al. (1975); 11: Michielsen et al. (1975); 12: Krogh-Moe et al. (1969); 13: Woodcock (1971); 14: Okada et al. (1980); 15: Takagi et al. (1975); 16: Sangster and Dixon (1976); 17: Dixon and Sangster (1976a); 18: Dixon and Sangster (1975); 19: Lantelme et al. (1974); 20: Lewis and Singer (1975); 21: Dixon and Sangster (1976b); 22: Woodcock and Singer (1971); 23: Romano and McDonald (1973); 24: Adams and McDonald (1974).

[a] *Key:* r_1*, nearest-neighbor interatomic distance;* n_1*, nearest-neighbor coordination number; cal, value calculated by Eq. (1);* r_2*, second-neighbor interatomic distance;* n_2*, second-neighbor coordination number; s, solid state; l, liquid state;* V_m*, molar volume;* ΔV_m*,* V^l_m-V^s_m*; MD, molecular dynamics simulation; MC, Monte Carlo simulation.*

[b] *Computer simulated.*

TABLE 3 **Coordination Numbers of Monovalent and Divalent Metal Chloride Melts at Respective Melting Points (Enderby and Biggin, 1983; Janz et al., 1968)**

Melt	Cationic radius (Å)	n_1 calc. from Eq. (1)	n_1 estimated from $g_{+-}(r)$	T (K)
$ZnCl_2$	0.74	3.5	4.3	548
NaCl	0.95	4.0	3.9	1073
$CaCl_2$	0.99	5.8	5.3	1055
$SrCl_2$	1.12	6.5	5.1	1148
KCl	1.33	4.1	4.1	1043
$BaCl_2$	1.35	7.5	6.4	1235
RbCl	1.47	3.8	3.5	988

$$V_\mathrm{m}^\mathrm{s}/V_\mathrm{m}^\mathrm{l} = \left(r_1^\mathrm{s}/r_1^\mathrm{l}\right)^3 \cdot \left(n_1^\mathrm{l}/n_1^\mathrm{s}\right) \tag{21}$$

The applicability of Eq. (21) to several melts is demonstrated in Table 3 (Enderby and Biggin, 1983), where $g_{+-}(r)$ refers to the partial pdf of dissimilar ion pairs. It is found that even for monovalent or divalent metal chloride melts, there is good or fairly good correspondence between observed and calculated coordination numbers of these ion pairs.

Equation (21) represents the melting phenomenon of ionic crystal and describes the volume change on melting from the viewpoints of changes in nearest-neighbor distance and coordination number. It is found from Tables 2 and 3 that melting of matter can be interpreted as follows: (1) the interatomic distance and the coordination number of a given nearest-neighbor pair in molten state become shorter and decrease, respectively, in comparison with those in solid state and (2) the second-neighbor interatomic distance in melt needs to be longer than that in solid so as to realize the thermal expansion on melting.

4.4. Cation–Polyatomic Anion Type Molten Salts

Another category of simple molten salts consists in salts built from metal cations and polyatomic anions such as nitrates, nitrites, carbonates, sulfates, and so on. The atomic arrangements of cations around a particular polyatomic anion in these melts are usually investigated by XRD, ND, XAFS, MD, Raman, and their combinations. Polyatomic anions such as NO_3^-, CO_3^{2-},

TABLE 4 **Interatomic Distances of N–O and O–O Pairs in NO_3^- Ions (Suzuki and Fukushima, 1977; Waseda, 1980b)**

	N–O (Å)		O–O (Å)	
System	*Liquid*	*Solid*	*Liquid*	*Solid*
$LiNO_3$	1.26	1.24	2.09, 2.21	2.15
$NaNO_3$	1.25	1.22	2.17	2.11
KNO_3	1.26	1.20, 1.22	2.17	2.09, 2.10
$RbNO_3$	1.25		2.17	
$CsNO_3$	1.26	1.22	2.18	2.12
$AgNO_3$	1.27		2.10, 2.22	
$TlNO_3$	1.25	1.23	2.14, 2.18	2.13
$Ca(NO_3)_2$	1.25	1.22	2.10, 2.20	2.12
$Ba(NO_3)_2$	1.24	1.24	2.09, 2.22	2.14

and SO_4^{2-} are rigid so that they suffer less structural changes and keep their internal structures even in molten salts at elevated temperatures as listed in Table 4 (Suzuki and Fukushima, 1977; Waseda, 1980b), provided that the polyatomic anions modify their internal structures with little distortion by interactions with coexisting cations.

4.5. Association in Molten Salts

It is well known that associated chemical species or network structures are formed in melts such as $BeCl_2$, $ZnCl_2$, SiO_2, and GeO_2. As a typical example, structural parameters of molten $ZnCl_2$ are listed in Table 5 (Enderby and Biggin, 1983). The coordination state in molten $ZnCl_2$ is not changed very much compared with that in solid, reflecting that molten $ZnCl_2$ possesses a large density comparable with its solid and a little thermal expansion appears to be detected on melting. There exist $ZnCl_4^{2-}$ complex ions with stable first coordination shell and their clustered species in the melt, which provide high viscosity and low conductivity.

Similar effects are expected to appear in molten salts composed of multivalent cations and halide anions. Description according to Eq. (21) is, however, difficult since there are not enough experimental data. Structural comprehension by invoking Eq. (21) is attempted as earlier. The structural parameters of the principal molten salt systems are listed in Tables 6–9. In particular, the short-range structures of molten lanthanide trihalides are discussed in detail later.

TABLE 5 Interionic Distances and Coordination Numbers *n* in Solid and Molten $ZnCl_2$ as Determined by X-Ray Diffraction, Unless Otherwise Stated (Enderby and Biggin, 1983)

Form of $ZnCl_2$	Zn–Zn		Cl–Cl		Zn–Cl	
	Distance Å	*Coord.* n	*Distance Å*	*Coord.* n	*Distance Å*	*Coord.* n
α solid	3.82	4	3.82	8	2.34	4
β solid	3.77	4	3.78	12	2.31	4
γ solid	3.70	4	3.70	8	2.27	4
δ solid	–	4	3.71	12	2.27	5.07
Liquid, 603 K (EXAFS)	–	–	–	–	2.35	4[a]
Liquid, 596 K (X-ray)	3.66[a]	4[a]	3.85[a]	12[a]	2.29[a]	4[a]
Liquid, 600 K	3.8±0.1	4.7±0.8	3.71±0.02	8.6±0.5	2.29±0.02	4.3±0.3

[a] *Values of the input parameters used in a nearest-neighbor model to give the best fit to the total X-ray pattern.*

TABLE 6 Interatomic Distances (*D* in nm) and Coordination Number (CN) of Molten Cupper Monohalides (Shirakawa et al., 1991)

Salt	*D*(Cu–X) (CN)[a]	*D*(Cu–Cu) (CN)		*D*(X–X) (CN)[a]
CuCl	0.234 (2.76)	0.321 (8.69)		0.382 (9.33)
CuBr	0.248 (3.03)	0.334 (5.14)	0.405 (10.06)	0.469 (15.99)
CuI	0.264 (3.36)	0.356 (4.61)	0.437 (6.41)	0.485 (14.97)

[a] *X = Cl, Br, I.*

5. CRYSTAL STRUCTURES OF RARE-EARTH HALIDES

Crystal structures of rare-earth trihalides at ambient temperature and pressure can be divided into seven classes on the basis of the elementary combinations of rare earths and halogens. Evolution of the crystal structures is due to the change in the ratio of ionic radii, $r(X^-)/r(Ln^{3+})$, where the ionic radii with sixfold coordination proposed by Shannon are generally employed (Shannon, 1976). Crystal types, lattice constants, and densities of rare-earth trichlorides and tribromides are summarized by Murase (1999a, 1999b) in Tables 10 and 11, respectively. As described in the previous section, very few papers

TABLE 7 Nearest-Neighbor Ag–Ag Interatomic Distances (*D* in nm) and Coordination Numbers (CN) of Molten Silver Monohalides (Inui et al., 1991)

Salt	*D*(Ag–Ag)	CN
AgCl	0.262	3.7
AgBr	0.272	3.9
AgI	0.290	4.6

TABLE 8 Interatomic Distances (*D* in nm) and Coordination Numbers (CN) of Molten Metal Dihalides (Iwadate, 2011)

Salt	Atomic pair	*D* (nm)	CN	References
$MgCl_2$	Mg–Cl	0.221	4	Takagi and Tomita (1993)
	Cl–Cl	0.353	n.a.	
	Mg–Mg	0.433	n.a.	
$MgCl_2$	Mg–Cl	0.242	4.3	Biggin et al. (1984)
	Cl–Cl	0.356	12	
	Mg–Mg	0.38	5	
$CaCl_2$	Ca–Cl	0.272	5.5	Iwamoto et al. (1982)
	Cl–Cl	0.355	7.4	
$CaCl_2$	Ca–Cl	0.278	5.4	Biggin and Enderby (1981)
	Cl–Cl	0.373	7.8	
	Ca–Ca	0.360	4.2	
$MnCl_2$	Mn–Cl	0.251	4	Ohno et al. (1978b)
	Cl–Cl	0.410	10	
	Mn–Mn	0.500	8	
$NiCl_2$	Ni–Cl	0.236	4.7	Newport et al. (1985)
	Cl–Cl	0.380	13.8	
	Ni–Ni	0.400	6.0	
$NiBr_2$	Ni–Br	0.247	4.7	Wood and Howe (1988)
	Br–Br	0.397	14.0	
	Ni–Ni	0.370	5.3	

Continued

TABLE 8 Interatomic Distances (*D* in nm) and Coordination Numbers (CN) of Molten Metal Dihalides (Iwadate, 2011)—Cont'd

Salt	Atomic pair	*D* (nm)	CN	References
NiI_2	Ni–I	0.260	4.2	Wood et al. (1988)
	I–I	0.410	13.1	
	Ni–Ni	0.460	5.3	
$ZnCl_2$	Zn–Cl	0.229	4.3	Biggin and Enderby (1981)
	Cl–Cl	0.371	8.6	
	Zn–Zn	0.380	4.7	
$ZnCl_2$	Zn–Cl	0.230	3.6	Iwadate et al. (2001a)
	Cl–Cl	0.370	9.0	
	Zn–Zn	0.432	4.0	
$ZnCl_2$	Zn–Cl	0.221	3.9	Fukushima et al. (2005)
	Cl–Cl	0.355	n.a.	
	Zn–Zn	0.427	3.8	
$ZnBr_2$	Zn–Br	0.240	3.4	Iwadate et al. (2001a)
	Br–Br	0.390	6.3	
	Zn–Zn	0.458	3.6	
$ZnBr_2$	Zn–Br	0.239	3.9	Iwadate et al. (2001b)
	Br–Br	0.385	6.2	
	Zn–Zn	0.450	3.9	
$ZnBr_2$	Zn–Br	0.243	3.9	Fukushima et al. (2005)
	Br–Br	0.387	n.a.	
	Zn–Zn	0.469	3.8	
$ZnBr_2$	Zn–Br	0.241	3.9	Allen et al. (1991)
ZnI_2	Zn–I	0.260	4.2	Allen et al. (1991)
$SrCl_2$[a]	Sr–Cl	0.29	6.7	Biggin and Enderby (1981)
	Cl–Cl	0.38	10.2	
	Sr–Sr	0.49	11.3	
$BaCl_2$	Ba–Cl	0.310	7.7	Biggin and Enderby (1981)
	Cl–Cl	0.386	7	
	Ba–Ba	0.49	14	

TABLE 8 Interatomic Distances (*D* in nm) and Coordination Numbers (CN) of Molten Metal Dihalides (Iwadate, 2011)—Cont'd

Salt	Atomic pair	*D* (nm)	CN	References
$CoCl_2$	Co–Cl	0.239	3.90	Takagi and Nakamura (1985)
	Cl–Cl	0.380	10.88	
	Co–Co	0.488	3.60	
	Co–Cl	0.556	10.90	
$PbCl_2$	Pb–Cl	0.280	4.0	Okamoto et al. (2005)
	Pb–Cl	0.320	2.5	
	Cl–Cl	0.366	9.6	
	Pb–Pb	0.483	10.5	
	Pb–Cl	0.610	22.5	
	Pb–Cl	0.284	4.0	Iwadate et al. (2005)
	Pb–Cl	0.340	1.9	
	Cl–Cl	0.369	6.1	
	Pb–Pb	0.445	9.0	
	Pb–Cl	0.576	15.1	
$PbBr_2$	Pb–Br	0.286	1.9	Iwadate et al. (2005)
	Pb–Br	0.315	1.9	
	Br–Br	0.364	6.8	
	Pb–Pb	0.442	8.8	
	Pb–Br	0.597	18.6	
BeF_2	Be–F	0.159	4.0	Vaslow and Narten (1973)
	F–F	0.254	6.0	
BeF_2	Be–F	0.158	4.0	Umesaki et al. (1991)
	F–F	0.258	4.0	
	Be–Be	0.306	6.0	

[a] *Simulated.*

TABLE 9 Interatomic Distances (*D* in nm) and Coordination Numbers (CN) of Molten Metal Halides of Trivalent Cations (Iwadate, 2011)

Salt	Atomic pair	*D* (nm)	CN	References
$LiAlCl_4$	Al–Cl	0.215	4	Takahashi et al. (1985a)
	Cl–Cl (intra)	0.350	3	
	Cl–Cl (inter)	0.350	3	
	$AlCl_4^- - AlCl_4^-$	0.675	4	
$NaAlCl_4$	Al–Cl	0.213	4	Takahashi et al. (1985b)
	Cl–Cl	0.348	3	
	Na–Cl	0.280	1	
	Na–Cl	0.473	2	
	Na–Cl	0.610	1	
	Na–Al	0.420	1	
	$NaAlCl_4$–$NaAlCl_4$	0.698	8	
$AlCl_3$	Al–Cl	0.211	4.0	Badyal et al. (1994)
$AlBr_3$	Al–Br	0.229	4.0	Saboungi et al. (1993)
	Br–Br	0.387	7.1	
	Al–Al	0.313	1.8	
$FeCl_3$	Fe–Cl	0.223	3.8	Badyal et al. (1997)
$GaBr_3$	Ga–Br	0.234	4.0	Saboungi et al. (1993)
	Br–Br	0.391	8.6	
	Ga–Ga	0.320	1.9	
GaI_3	Ga–I	0.254	3.75	Saboungi et al. (1993)
	I–I	0.435	11.1	
	Ga–Ga	0.328	1.5	
$ScCl_3$	Sc–Cl	0.248	4.8	Wasse and Salmon (1999a)
ScI_3	Sc–I	0.276	4.7	Wasse and Salmon (1999a)
$InCl_3$	In–Cl	0.235	5–6	Price et al. (1993)
$LaCl_3$	La–Cl	0.283	5.7	Mochinaga et al. (1991)
	Cl–Cl	0.401	8.3	
	La–La	0.525	4.5	

TABLE 9 Interatomic Distances (*D* in nm) and Coordination Numbers (CN) of Molten Metal Halides of Trivalent Cations (Iwadate, 2011)—Cont'd

Salt	Atomic pair	*D* (nm)	CN	References
$LaCl_3$[a]	La–Cl	0.269	6	Okamoto and Ogawa (1999b)
	Cl–Cl	0.37	n.a.	
	La–La	n.a.	n.a.	
$LaCl_3$[a]	La–Cl	0.281	6	Okamoto and Ogawa (1999a)
	Cl–Cl	0.380	8	
	La–La	0.500	5	
$LaBr_3$[a,c]	La–Br	0.295	6	Okamoto and Ogawa (1999a)
	Br–Br	0.375	8	
	La–La	0.510	5	
$CeCl_3$	Ce–Cl	0.284	5.6	Iwadate et al. (1992)
	Cl–Cl	0.405	11.3	Mochinaga et al. (1993a)
	Ce–Ce	0.521	6.5	
$PrCl_3$[a]	Pr–Cl	0.282	5.7	Mochinaga et al. (1991)
	Cl–Cl	0.414	11.0	
	Pr–Pr	0.514	4.8	
$NdCl_3$[a]	Nd–Cl	0.277	5.7	Igarashi et al. (1990)
	Cl–Cl	0.404	11.3	
	Nd–Nd	0.508	4.8	
$GdCl_3$	Gd–Cl	0.272	5.5	Mochinaga et al. (1991)
	Cl–Cl	0.388	10.9	Matsuoka et al. (1993)
	Gd–Gd	0.500	5.0	
$SmCl_3$	Sm–Cl	0.277	5.7	Mochinaga et al. (1991)
	Cl–Cl	0.398	9.0	
	Sm–Sm	0.506	4.8	
$TbCl_3$	Tb–Cl	0.272	6.3	Wasse and Salmon (1999b)
	Cl–Cl	0.358	8.1	
	Tb–Tb	n.a.	n.a.	
$DyCl_3$[b]	Dy–Cl	0.269	5.7	Mochinaga et al. (1991)
	Cl–Cl	0.382	8.9	Mochinaga et al. (1993b)
	Dy–Dy	0.490	4.5	

Continued

TABLE 9 Interatomic Distances (*D* in nm) and Coordination Numbers (CN) of Molten Metal Halides of Trivalent Cations (Iwadate, 2011)—Cont'd

Salt	Atomic pair	*D* (nm)	CN	References
$HoCl_3$	Ho–Cl	0.276	6.4	Wasse and Salmon (1999b)
	Cl–Cl	0.359	8.1	
	Ho–Ho	n.a.	n.a.	
$ErCl_3$	Er–Cl	0.263	5.8	Iwadate et al. (1994)
	Cl–Cl	0.375	8–9	
	Er–Er	0.405	1–2	
$ErCl_3$	Er–Cl	0.274	5.6	Wasse and Salmon (1999b)
	Cl–Cl	0.358	8.9	
	Er–Er	n.a.	n.a.	
YCl_3	Y–Cl	0.271	5.9	Saboungi et al. (1991)
	Cl–Cl	0.364	8.2	
	Y–Y	n.a.	n.a.	
YCl_3	Y–Cl	0.269	5.9	Okamoto et al. (1996)
	Cl–Cl	0.359	n.a.	
	Y–Y	n.a.	n.a.	
YCl_3	Y–Cl	0.272	5.7	Wasse and Salmon (1999b)
	Cl–Cl	0.355	7.8	
	Y–Y	n.a.	n.a.	
UCl_3[a]	U–Cl	0.284	6	Okamoto et al. (1998)
	Cl–Cl	0.402	8	
	U–U	0.520	5	
	U–Cl	0.580	8	

[a] *For $LaCl_3$, $PrCl_3$, $NdCl_3$, UCl_3, and $LaBr_3$ pure melts, each nearest-neighbor coordination number of RE has been reported to be about 6. See Okamoto et al. (1999).*

[b] *The nearest-neighbor coordination number of Dy has been calculated to be about 6 by MD simulation. See Takagi et al. (1999).*

[c] *For $LaBr_3$, $CeBr_3$, $DyBr_3$, and YBr_3 pure melts, nearest-neighbor coordination numbers of RE have been simulated at 7.1, 7.4, 6.2, and 6.2, respectively. See Hutchinson et al. (2000).*

have yet reported structural investigations of molten rare-earth fluorides and molten rare-earth iodides by diffraction techniques and thus the corresponding crystallographic data are not discussed here. Four types of crystal structures are known for rare-earth trichlorides. The crystals of $LaCl_3$ to $GdCl_3$ have hexagonal UCl_3-type structure, and those of YCl_3 and $DyCl_3$ to $LuCl_3$ possess monoclinic $AlCl_3$-type

TABLE 10 **Crystal Structures of Rare-Earth Trichlorides** (Murase, 1999a)

		Lattice constant				
$LnCl_3$	**Crystal type**	a (Å)	b (Å)	c (Å)	*Angle (°)*	*d* (g/cm^3)[a]
$ScCl_3$	BiI_3	6.979[b]			$\alpha=54.4$ [b]	2.39
		6.397[c]		17.82[c]		2.39
YCl_3	$AlCl_3$	6.920	11.94	6.44	$\beta=111.0$	2.61
$LaCl_3$	UCl_3	7.483		4.364		3.85
$CeCl_3$	UCl_3	7.454		4.312		3.94
$PrCl_3$	UCl_3	7.423		4.272		4.03
$NdCl_3$	UCl_3	7.400		4.240		4.14
$PmCl_3$	UCl_3	7.397		4.211		4.23
$SmCl_3$	UCl_3	7.380		4.169		4.33
$EuCl_3$	UCl_3	7.375		4.134		4.41
$GdCl_3$	UCl_3	7.363		4.105		4.54
$TbCl_3$	$PuBr_3$	3.860	11.71	8.48		4.60
$TbCl_3$[d]	(Hexagonal?)	6.425		11.771		4.60
$DyCl_3$	$AlCl_3$	6.91	11.97	6.4	$\beta=111.2$	3.59
$HoCl_3$	$AlCl_3$	6.85	11.85	6.39	$\beta=110.8$	3.69
$ErCl_3$	$AlCl_3$	6.80	11.79	6.39	$\beta=110.7$	3.77
$TmCl_3$	$AlCl_3$	6.75	11.73	6.39	$\beta=110.6$	3.83
$YbCl_3$	$AlCl_3$	6.73	11.65	6.38	$\beta=110.4$	3.94
$LuCl_3$	$AlCl_3$	6.72	11.60	6.39	$\beta=110.4$	3.98

[a] *Values calculated from lattice constants.*
[b] *Defined as rhombohedral.*
[c] *Defined as hexagonal.*
[d] *Over 520 °C.*

structure at room temperature. Only $TbCl_3$ crystallizes in an orthorhombic $PuBr_3$-type structure, and it transforms into an hexagonal high-temperature phase above 520 °C. The crystal structure of $ScCl_3$ is of hexagonal BiI_3-type.

As the ionic radius of Cl^- is larger than that of F^-, the coordination number of Cl^- around a rare-earth ion is not as large as that of F^-. The coordination numbers of Cl^-s are estimated at 9 for UCl_3, 8 for $PuBr_3$, and 6 for $AlCl_3$ crystals. The atomic arrangements (configurations) of UCl_3-, $PuBr_3$-, and $AlCl_3$-type unit cells are shown in Fig. 7, respectively, which were drawn by VESTA 3 (Momma and Izumi, 2011).

TABLE 11 Crystal Structures of Rare-Earth Tribromides (Murase 1999b)

		Lattice constant				
LnBr$_3$	Crystal type	a *(Å)*	b *(Å)*	c *(Å)*	*Angle* α(°)	*d* (g/cm^3)[a]
ScBr$_3$	BiI$_3$	7.352[b]			53.83[b]	3.91
		6.665[c]		18.838[c]		
YBr$_3$	BiI$_3$	7.575[b]			55.67[b]	3.95
		7.072[c]		19.150[c]		
LaBr$_3$	UCl$_3$	7.971		4.522		5.07
CeBr$_3$	UCl$_3$	7.952		4.444		5.18
PrBr$_3$	UCl$_3$	7.939		4.389		5.28
NdBr$_3$	PuBr$_3$	4.115	12.659	9.158		5.35
PmBr$_3$	PuBr$_3$	4.08	12.650	9.12		5.45
SmBr$_3$	PuBr$_3$	4.042	12.706	9.124		5.59
EuBr$_3$	PuBr$_3$	4.015	12.638	9.099		5.63
GdBr$_3$	BiI$_3$	7.633[b]			56.40[b]	4.57
		7.216[c]		19.189[c]		
TbBr$_3$	BiI$_3$	7.608[b]			56.13[b]	4.66
		7.159[c]		19.163[c]		
DyBr$_3$	BiI$_3$	7.592[b]			55.83[b]	4.78
		7.107[c]		19.161[c]		
HoBr3	BiI$_3$	7.576[b]			55.67[b]	4.86
		7.072[c]		19.150[c]		
ErBr3	BiI$_3$	7.568[b]			55.47[b]	4.93
		7.045[c]		19.148[c]		
TmBr$_3$	BiI$_3$	7.540[b]			55.36[b]	5.02
		7.005[c]		19.092[c]		
YbBr$_3$	BiI$_3$	7.540[b]			55.17[b]	5.11
		6.973[c]		19.086[c]		
LuBr$_3$	BiI$_3$	7.527[b]			55.00[b]	5.17
		6.950[c]		19.109[c]		

[a] *Values calculated from lattice constants.*
[b] *Defined as rhombohedral.*
[c] *Defined as hexagonal.*

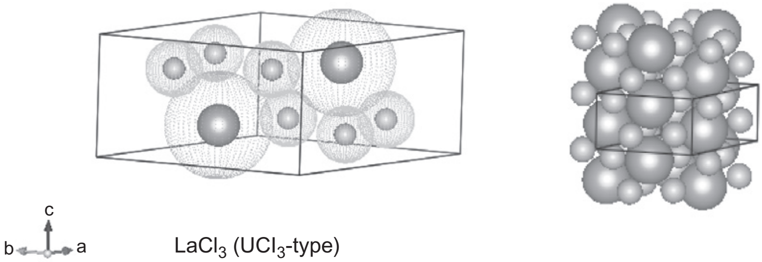

LaCl$_3$ (UCl$_3$-type)

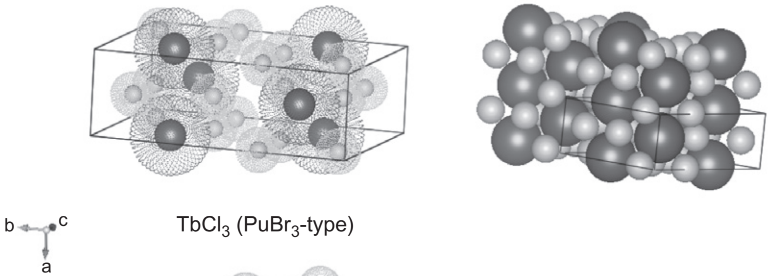

TbCl$_3$ (PuBr$_3$-type)

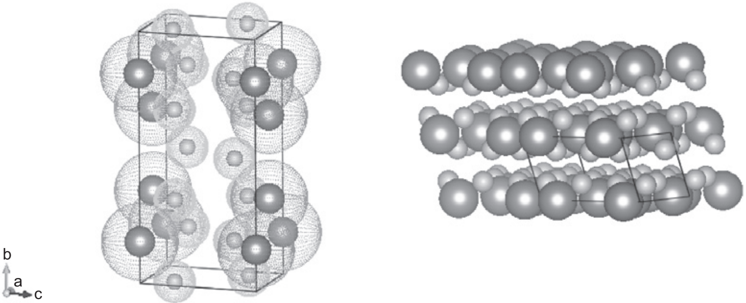

YCl$_3$ (AlCl$_3$-type)

FIGURE 7 Atomic arrangements in UCl$_3$-, PuBr$_3$-, and AlCl$_3$-type unit cells. *Redrawn from VESTA 3 (Momma and Izumi, 2011), © 2011 International Union of Crystallography.*

As given in Table 11, crystal structures of rare-earth tribromides at ambient temperature and pressure are classified into three types. The crystals of LaBr$_3$ to PrBr$_3$ are of UCl$_3$-type; those of NdBr$_3$ to EuBr$_3$ have a PuBr$_3$-type structure; and finally, ScBr$_3$, YBr$_3$, and GdBr$_3$ to LuBr$_3$ possess BiI$_3$-type structure. No structural phase change has been observed for rare-earth tribromides except for ScBr$_3$.

6. DENSITY OF RARE-EARTH HALIDES IN SOLID AND MOLTEN STATES

Density is one of the most significant thermophysical properties characterizing matters and materials, and thus, acquisition of accurate data is required as the most important parameter for not only industrial designing but also theoretical examinations on structures of molten salts, derivation of other thermodynamic properties, and correlation of various thermophysical properties. A fairly large number of density data are available for molten salts, but there are plenty of problems to be solved with respect to data reliability and ranges of temperature and pressure.

In general, the density ρ is approximated as a linear function of temperature as described in Eq. (22). This is a rule of thumb with no theoretical basis. The molar volume V_m is calculated from the density data according to Eq. (23), and the coefficient of expansion β is derived by using Eq. (24).

$$\rho = a - bT \tag{22}$$

$$V_\mathrm{m} = \frac{M}{\rho} \tag{23}$$

$$\beta = \frac{1}{V} \cdot \left(\frac{\partial V}{\partial T} \right)_\mathrm{p} = \frac{b}{\rho} \tag{24}$$

where M is the molar mass, T the temperature, a and b the least-squares fitted constants.

The molar volumes of rare-earth halides in solid and molten states are estimated from their respective density data, leading to the volume changes upon melting. This property is very fundamental and plays a crucial role in understanding the structure of molten salts, as is described in details in subsequent sections. The principles pertaining to density measurement of molten salts are quite simple and an instrumental prototype is sketched in Fig. 8 (Janz et al., 1972).

Two techniques of density measurement, such as the Archimedes method and the dilatometric method, have been employed at elevated temperatures. The former makes use of the principle that the upthrust experienced by a body wholly or partially immersed in a fluid is equal to the weight of fluid displaced. In studies of molten salts, a plummet of platinum or gold–palladium alloy suspended from a balance pan by a thin platinum wire has frequently been utilized. A typical apparatus of this kind is shown, complete with furnace, in Fig. 8. The Archimedes method has the advantage of applicability to temperatures higher than 1270 K and to more corrosive melts. The adhesion of melt to and the condensation of vapor on the suspending wire are potential difficulties which must be closely watched (Bell and Flengas, 1964; Bloom et al., 1953; Edwards et al., 1952; Neithamer and Peake, 1961; Peake and Bothwell, 1954; Spooner and Wetmore, 1951).

Dilatometers made of glassy materials have been used below 820 K (Pyrex) or 1020 K (silica); an apparatus of this type is also illustrated in Fig. 8. An alternative is the approach by Husband (Husband, 1958) and by the groups of Frame and Gebhardt (Frame et al., 1959; Gebhardt and Becker, 1943) who

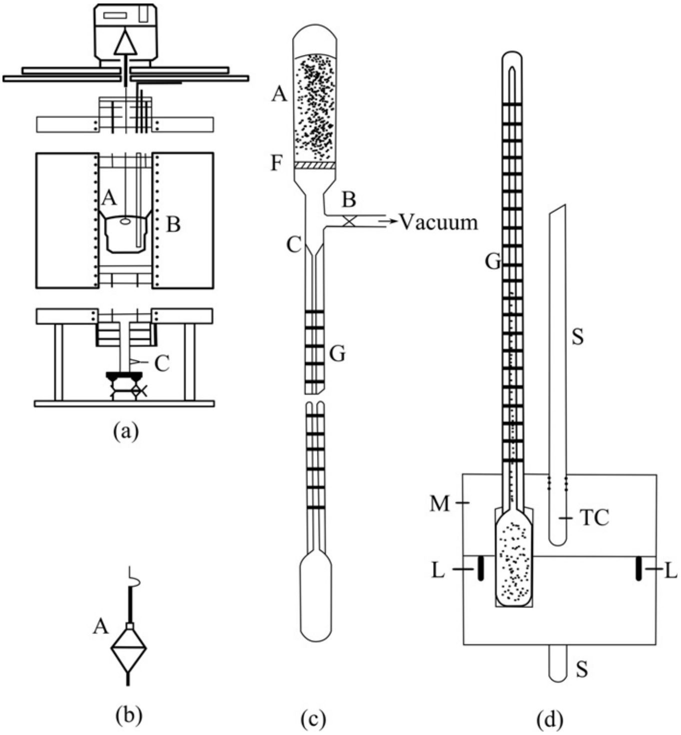

FIGURE 8 Experimental techniques for the measurement of density. (a) Archimedes apparatus: A, density plummet; B, thermocouple; C, inlet for controlled atmospheres. (b) Density plummet design: (The tip is designed to known dimensions for surface tension measurements using the detachment technique.) (c) Dilatometer and loading tube: A, loading tube filled with salt and sealed; B and C, constrictions for vacuum seals; F, fritted disk; G, graduated dilatometer stem. (d) Dilatometer and support assembly: G, dilatometer stem; L, locking pins in aluminum block; M, aluminum block (two sections); S, support rods (hollow); TC, thermocouple well. *Reproduced with permission from Janz et al. (1972), © 1972 American Institute of Physics.*

used the manometric technique in which one measures the pressure of an inert gas required to bring about a known difference in height between two columns of the liquid. A difficulty encountered in dilatometry is the maintenance of constant temperature over a relatively great length of the furnace core. Both this problem and that of corrosion become more serious at higher temperatures.

For molten pure rare-earth halides, a limited number of data are available (Janz et al., 1968; Janz et al., 1975), since there are many problems with respect to their reliability due to hygroscopy of rare-earth chlorides and their reactions with water content to produce oxychlorides at elevated temperatures as well as the maintenance of constant temperature in the long furnace. The volume change on melting is subsequently easily evaluated from the above molar volumes of solid and melt. This change is expected to reflect the melt structure very well, as described in Table 1 as well as Eq. (21) for alkali halides. The empirical density equations of molten rare-earth trihalides are tabulated in Table 12, from which the densities at 1100 K are estimated for comparison by interpolation or extrapolation. At first approximation and except for fluorides, the ρ values increase with increasing atomic weights of constituent ions, as a first approximation. The irregularity of molten fluorides

TABLE 12 **Recommended Density Equations for Molten Rare-Earth Halides (ρ and T are in g cm^{-3} and K, respectively)**

	$\rho = a - bT$				
Salt	**a**	**b × 10^3**	**Temperature range**	**ρ(1100 K) (g cm^{-3})**	**References**
LaF_3	5.793	0.682	1750–2450	5.793	Kirshenbaum et al. (1960)
CeF_3	6.253	0.936	1700–2200	5.223	Kirshenbaum et al. (1960)
$ScCl_3$	$\rho = 1.67$		1213 K	n.a.	Klemm (1926)
	$\rho = 1.63$		1273 K	n.a.	
YCl_3	3.007	0.50	998–1118	2.457	Klemm (1926)
$LaCl_3$	4.0895	0.7774	1146–1246	3.2344	Yaffe and van Artsdalen (1956)
$CeCl_3$	4.248	0.920	1123–1223	3.236	Mellors and Senderoff (1960)
$PrCl_3$	4.0120	0.74165	1120–1250	3.196	Cho et al. (1972)
$NdCl_3$	4.2642	0.93014	1090–1270	3.2410	Cho et al. (1972)
$GdCl_3$	4.1491	0.67139	940–1280	3.4106	Cho et al. (1972)
$DyCl_3$	4.2668	0.6821	980–1260	3.5165	Cho et al. (1972)
$LaBr_3$	5.0351	0.096	1069–1185	4.9295	Yaffe and van Artsdalen (1956)
$NdBr_3$	4.9750	0.7779	968–1133	4.119	Yaffe and van Artsdalen (1956)
LaI_3	5.4581	1.1109	1124–1182	4.2361	Kutscher and Schneider (1974)
NdI_3	5.4069	1.0701	1111–1193	4.2298	Kutscher and Schneider (1974)
GdI_3	5.2097	0.9086	1254–1306	4.2102	Kutscher and Schneider (1974)

might be due to good packing of ions, complex ions, and/or clusters in the melts, reflecting the very high melting points.

In many practical cases, molten salts are utilized under the form of multi-component mixed melts. When the densities of pure melts are known, those of their mixtures can be evaluated on the assumption that the additivity rule is applicable to the molar volume. The density of a mixed melt ρ_m is formulated as follows,

$$\rho_m = \frac{\sum x_i M_i}{\sum x_i V_i} = \frac{\sum x_i M_i}{\sum x_i \frac{M_i}{\rho_i}} \tag{25}$$

where x_i refers to the mole fraction, V_i is the molar volume, and M_i the molar mass of the *i*th pure melt, respectively.

As for the densities of molten mixtures of rare-earth trihalides with alkali halides, there have been plenty of data collected up to now; they are listed in Tables 13–21 under the form of a linear function of temperature, $\rho_m = a - bT$.

For a mixed melt having interionic interactions similar to those in pure melts, the additivity rule holds well enough to estimate the density or the molar volume of the mixture. Unfortunately, such ideal mixtures are rarely found in real systems. This might be due to transformations occurring in the melt upon mixing, for instance, the formation of complex species. In many cases, complex formation occurs easily in mixed melts composed of multivalent cations and halide anions as central ions and ligands, respectively (Nakamura, 1983). One has so far been inclined to consider whether observation of deviations between the measured molar volumes of the mixture melts and the additivity rule offers or not a useful criterion for unraveling

TABLE 13 Density of Molten LiCl–$LaCl_3$ System Versus Composition and Temperature (Kim et al., 1987)

$LaCl_3$ (mol%)	ρ_m (g cm^{-3})	*T* range (K)
12.0	$2.476 - 5.311 \times 10^{-4}T$	840–1211
24.0	$2.917 - 6.324 \times 10^{-4}T$	1008–1217
35.5	$3.251 - 6.987 \times 10^{-4}T$	993–1217
56.0	$3.671 - 7.798 \times 10^{-4}T$	1109–1215
61.0	$3.727 - 7.713 \times 10^{-4}T$	1031–1218
81.5	$3.953 - 7.850 \times 10^{-4}T$	1088–1215
86.0	$4.011 - 8.091 \times 10^{-4}T$	1102–1218
100.0	$4.154 - 8.326 \times 10^{-4}T$	1146–1218

TABLE 14 Density of Molten NaCl–$LaCl_3$ System Versus Composition and Temperature (Kim et al., 1987)

$LaCl_3$ (mol%)	ρ_m (g cm^{-3})	T range (K)
11.5	$2.599–6.579 \times 10^{-4}T$	1028–1221
24.5	$2.944–6.926 \times 10^{-4}T$	890–1196
36.5	$3.226–7.373 \times 10^{-4}T$	1059–1221
49.5	$3.450–7.497 \times 10^{-4}T$	1091–1221
62.0	$3.658–7.734 \times 10^{-4}T$	1119–1221
76.0	$3.857–7.947 \times 10^{-4}T$	1089–1221
87.0	$3.995–8.125 \times 10^{-4}T$	1109–1221

TABLE 15 Density of Molten KCl–$LaCl_3$ System Versus Composition and Temperature (Kim et al., 1987)

$LaCl_3$ (mol%)	ρ_m (g cm^{-3})	T range (K)
11.5	$2.418–6.057 \times 10^{-4}T$	978–1204
24.5	$2.711–6.461 \times 10^{-4}T$	909–1213
38.0	$2.941–6.394 \times 10^{-4}T$	970–1216
50.5	$3.306–7.622 \times 10^{-4}T$	1115–1202
63.5	$3.563–7.908 \times 10^{-4}T$	1139–1203
76.0	$3.783–8.129 \times 10^{-4}T$	1141–1210
88.0	$3.966–8.159 \times 10^{-4}T$	1110–1218

the existence of complex ions as well as for estimating their stabilities. The final decision concerning the formation of complicated species such as complex ions, clustered ions, molecules, and so on in the melts should be made according to direct observations of near-neighbor structures, namely, diffraction works and Raman spectroscopic measurements as will be described later.

7. STRUCTURES OF RARE-EARTH HALIDE MELTS

Physical and chemical properties of rare-earth compounds have usually been thought to be similar, since there are very small differences in ionic radii.

TABLE 16 **Density of Molten CsCl–$LaCl_3$ System Versus Composition and Temperature (Kim et al., 1987)**

$LaCl_3$ (mol%)	ρ_m (g cm^{-3})	T range (K)
12.0	$3.708–9.726\times10^{-4}T$	908–1213
25.0	$3.714–9.377\times10^{-4}T$	1072–1219
40.0	$3.753–9.064\times10^{-4}T$	1015–1217
51.5	$3.849–9.198\times10^{-4}T$	875–1208
64.0	$3.918–8.911\times10^{-4}T$	1148–1215
77.5	$4.053–9.107\times10^{-4}T$	1090–1112
90.5	$4.127–8.826\times10^{-4}T$	1113–1217

TABLE 17 **Density of Molten NaCl–$CeCl_3$ System Versus Composition and Temperature (Sato and Yamamura, 1992)**

$CeCl_3$ (mol%)	ρ_m (g cm^{-3})	T range (K)
12.0	$2.564–6.047\times10^{-4}$ T	1023–1134
24.5	$2.945–6.826\times10^{-4}$ T	910–1137
37.0	$3.276–7.625\times10^{-4}$ T	986–1138
50.0	$3.508–7.764\times10^{-4}$ T	989–1143
61.5	$3.715–8.067\times10^{-4}$ T	1010–1131
73.0	$3.875–8.237\times10^{-4}$ T	1019–1136
85.0	$3.972–8.001\times10^{-4}$ T	1042–1135
100.0	$4.012–7.183\times10^{-4}$ T	1046–1145

As mentioned in Sections 5 and 6, some differences which could not be disregarded are really found even in the crystal structures of rare-earth halides and in their densities in solid and molten states. Accordingly, local or short-range structures of rare-earth halides have to be clarified in the first place. Up to now, numerous works have been published which report the structure of aqueous solutions containing rare-earth ions, but the number of works on the melt structures is quite limited to halides. As for the techniques to investigate the local structure of melt, potential tools can be divided broadly into three categories. The first is comprised of diffraction methods such as XRD

TABLE 18 Density of Molten NaCl–$NdCl_3$ System Versus Composition and Temperature (Janz, 1988)

$NdCl_3$ (mol%)	ρ_m (g cm^{-3})	T range (K)
12.5	$2.522-5.37 \times 10^{-4}T$	1131–1284
26.2	$3.032-6.92 \times 10^{-4}T$	1093–1283
39.3	$3.351-7.20 \times 10^{-4}T$	1016–1283
55.3	$3.703-7.83 \times 10^{-4}T$	1023–1282
68.5	$3.930-8.57 \times 10^{-4}T$	1005–1281
85.0	$4.120-8.43 \times 10^{-4}T$	1021–1273

TABLE 19 Density of Molten NaCl–$SmCl_3$ System Versus Composition and Temperature (Sato and Yamamura, 1992)

$SmCl_3$ (mol%)	ρ_m (g cm^{-3})	T range (K)
11.5	$2.597-6.227 \times 10^{-4}T$	1002–1147
23.0	$2.959-6.790 \times 10^{-4}T$	915–1148
34.5	$3.273-7.379 \times 10^{-4}T$	915–1157
51.5	$3.639-7.929 \times 10^{-4}T$	919–1155
58.5	$3.773-8.062 \times 10^{-4}T$	905–1152
73.0	$3.983-8.188 \times 10^{-4}T$	935–1146
90.5	$4.154-7.854 \times 10^{-4}T$	917–1155
100.0	$4.205-7.472 \times 10^{-4}T$	925–1146

and ND, the second is Raman spectroscopy, and the third gathers X-ray absorption fine structure (XAFS) and computer-aided calculations. Hereafter, the structures of rare-earth halide melts obtained by the three categories of methods are described in due order.

7.1. Structures from Diffraction Experiments

Structural analyses have been continuously carried out since the 1960s so as to comprehend physicochemical properties of molten salts. At the beginning, laboratory-scale X-ray diffractometers and less stable neutron source-detector systems were, however, compelled to be used at the sacrifice of data accuracy. Since electronics, mechanical devices, and the detector systems have gradually and continuously been developed, this has resulted in substantial improvements

TABLE 20 Density of Molten LiF–YF_3 System Versus Composition and Temperature (Janz, 1988)

YF_3 (mol%)	ρ_m (g cm^{-3})	T range (K)
0.0	$2.074–3.321 \times 10^{-4}T$	1140–1340
19.0	$3.254–5.595 \times 10^{-4}T$	980–1340
30.0	$3.695–6.672 \times 10^{-4}T$	1080–1340
40.0	$3.902–6.154 \times 10^{-4}T$	1080–1340
50.0	$4.287–7.216 \times 10^{-4}T$	1120–1340
60.0	$4.174–5.065 \times 10^{-4}T$	1220–1340

TABLE 21 Density of Molten LiF–LaF_3 System Versus Composition and Temperature (Janz, 1988)

LaF_3 (mol%)	ρ_m (g cm^{-3})	T range (K)
5.0	$2.491–3.648 \times 10^{-4}T$	1140–1350
10.0	$2.799–3.118 \times 10^{-4}T$	1180–1350
15.0	$3.500–6.658 \times 10^{-4}T$	1110–1350
20.0	$3.737–6.486 \times 10^{-4}T$	1130–1350
25.0	$3.799–5.507 \times 10^{-4}T$	1130–1350

in the apparatuses. Examples of new and performing setups are the high-energy monochromatic X-ray beam line with a diffractometer at SPring-8 (synchrotron radiation facility "Super Photon ring-8 GeV") and the pulsed neutron sources with high-precision detectors at KEK (High Energy Accelerator Research Organization) or J-Parc (Japan Proton Accelerator Research Complex) in Japan. Therefore, accurate measurements of the melt structures are now within feasibility. Similar apparatuses are also operating at ESRF and ILL (Institut Laue–Langevin) in France, APS (advanced photon source) and SNS (spallation neutron source) in the United States, ISIS (centre for research at the Rutherford Appleton Laboratory; pulsed neutron and muon source) in the United Kingdom, and in several other countries.

Pioneering works on the structures of molten rare-earth chlorides have been done by Saboungi et al. (1991) and Mochinaga et al. (1991) in the early 1990s. The former researchers have reported a ND study of the liquid structure of YCl_3 and combined the structural data with macroscopic melting and transport data to compare the behavior of this molten salt with those of

$SrCl_2$, $ZnCl_2$, and $AlCl_3$ as prototypes of different melting mechanisms for ionic materials. $DyCl_3$, $HoCl_3$, and $ErCl_3$ melts have very similar structure to YCl_3, thus confirming the earlier suggestion of a similarity of structural behavior for these systems in the liquid phase. A novel melting mechanism for trivalent metal chlorides, leading to a loose disordered network of edge-sharing octahedral units in the liquid phase, has been thereby established. The various melting behaviors were related to bonding character with the help of Pettifor's phenomenological chemical scale (Pettifor, 1986). These findings were in good agreement with Papatheodorou's suggestion obtained from an extensive Raman scattering study of YCl_3 that the structure of the melt may be a network of distorted chlorine-sharing octahedra (Papatheodorou, 1977). In the first place, this suggestion emerged from a comparison of the Raman spectra of pure liquid and solid YCl_3 as well as from a series of measurements on mixtures of YCl_3 and alkali chlorides, in which Raman modes of YCl_6 octahedra were observed in stoichiometric mixed crystals at room temperature and monitored first up to and across melting and then as a function of the YCl_3 content in the liquid mixture up to the pureYCl_3 melt.

In the latter report (Mochinaga et al., 1991), the structures of a series of $LaCl_3$, $CeCl_3$, $PrCl_3$, $NdCl_3$, $GdCl_3$, $DyC1_3$, and $SmCl_3$ pure melts were systematically studied with a laboratory-scale X-ray diffractometer. In these rare-earth chloride melts, the existence of six chloride ions as the nearest neighbors surrounding a rare-earth cation was deduced from the interatomic distance ratio of $r(\text{Cl–Cl})/r(\text{R–Cl})$; interatomic distances as well as the coordination numbers of the rare-earth ions are listed in Table 9. Interpretation of Raman spectra also showed in the same report that the chloride ions and the rare-earth cations form octahedral complex anions $RCl_6{}^{3-}$ (R = La, Ce, Pr, Nd, Gd, Dy, and Sm). Taking account of the low equivalent electrical conductivities and the separation between the nearest cations R^{3+}–R^{3+} in the results of X-ray analysis of these melts, the existence of dimers or more polymeric complex anions may be alleged. As an example, parameters obtained from XRD data of pure $DyCl_3$ melt are shown in Figs. 9–11. The calculation procedure is the same as described before. The three nearest-neighbor ion pairs R^{3+}–Cl^-, R^{3+}–R^{3+}, and Cl^-–Cl^- were assumed to follow a Gaussian distribution with a mean square displacement $2b_{ij}$ from the peak positions r_{ij}, and the quantities n_{ij}, r_{ij}, and b_{ij} could be obtained by least-squares fitting of Debye equation for the reduced intensity function $S \cdot i(S)$.

We also briefly describe results obtained by other experimental techniques. The Raman spectra of pure molten YCl_3, $DyCl_3$, $GdCl_3$, $PrCl_3$, and $LaCl_3$ are illustrated in Fig. 12. The normal modes of vibration of octahedral XY_6-type chemical species are schematically presented in Fig. 13, where only the vibrational modes ν_1, ν_2, and ν_5 are Raman active (Nakamoto, 1978). The typical Raman peaks on the Rayleigh wings for the respective melts are observed in the wavenumber range of about 140 to 300 cm^{-1}, corresponding to the stretching vibration mode, ν_1, of octahedral XY_6 species. The weak bending modes are barely detectable at lower wavenumbers.

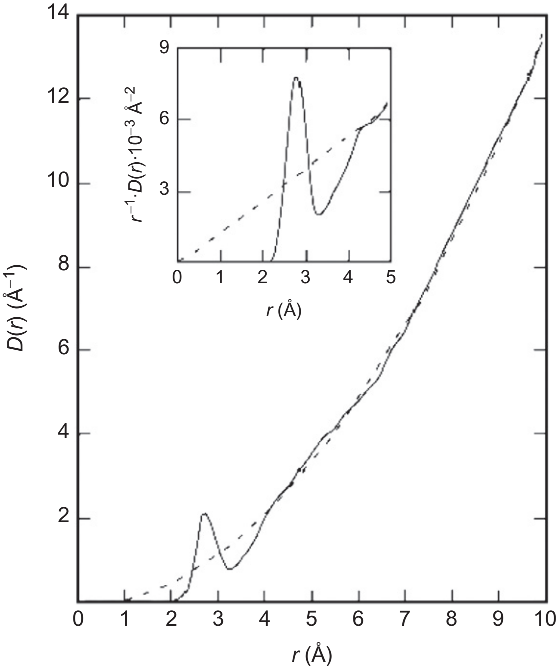

FIGURE 9 Radial distribution function $D(r)$ for $DyCl_3$ melt. *Reproduced with permission from Mochinaga et al. (1991), © 1991 Trans Tech Pub.*

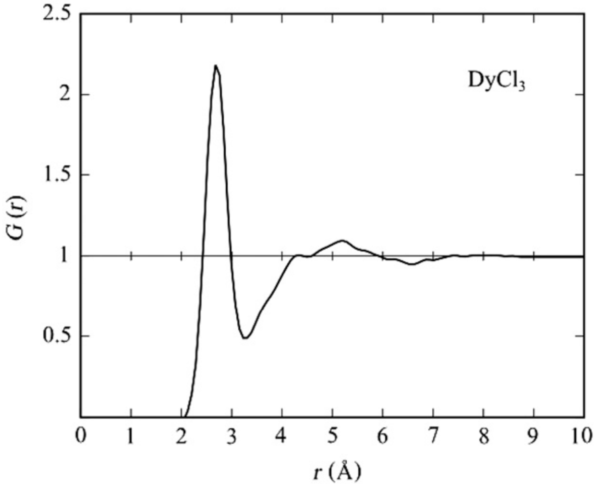

FIGURE 10 Correlation function $C(r)$ for $DyCl_3$ melt. *Reproduced with permission from Mochinaga et al. (1991), © 1991 Trans Tech Pub.*

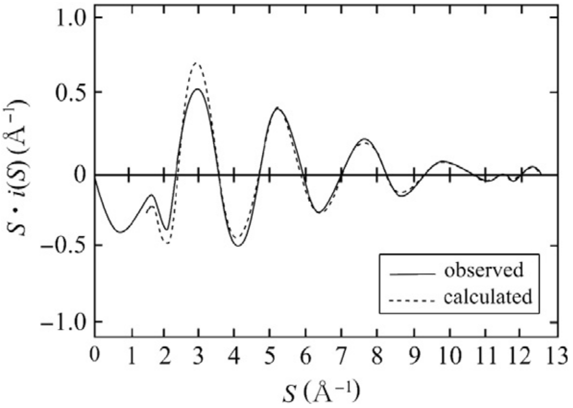

FIGURE 11 Reduced intensity function $S \cdot i(S)$ for $DyCl_3$ melt. *Reproduced with permission from Mochinaga et al. (1991), © 1991 Trans Tech Pub.*

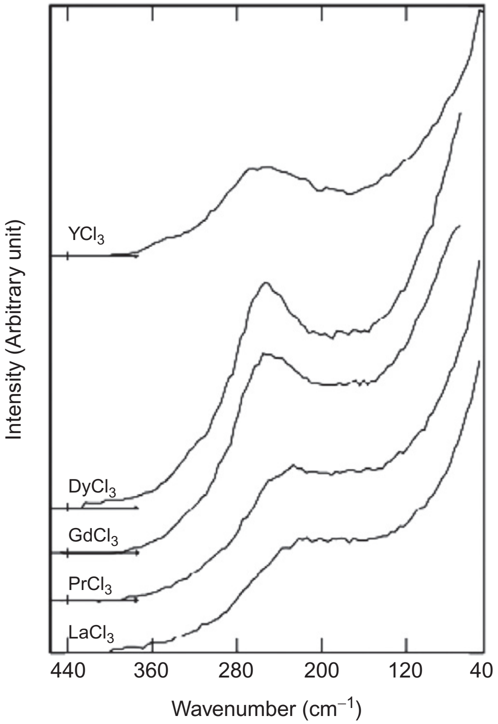

FIGURE 12 Raman spectra of several rare-earth chloride melts. *Reproduced with permission from Mochinaga et al. (1991), © 1991 Trans Tech Pub.*

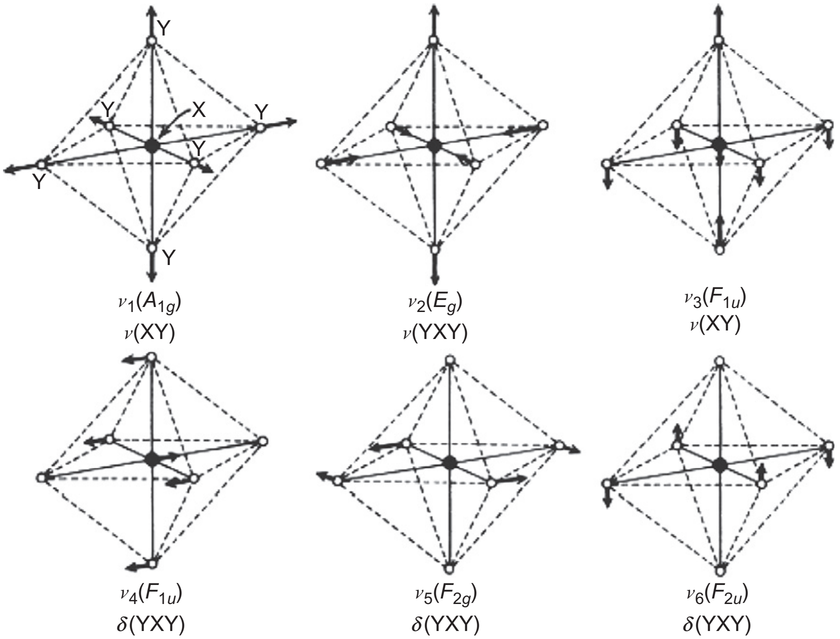

FIGURE 13 Normal modes of vibrations of octahedral XY_6-type chemical species. *Reproduced with permission from Nakamoto (1978), © 1978 John Wiley & Sons.*

Conventional molecular dynamics simulation was also carried out to investigate the local structure of molten $DyCl_3$, using the simple Born–Mayer–Huggins-type potentials in which parameters were determined so as to reproduce the interference function $S \cdot i(S)$ of the melt. The octahedral coordination of the cations was ascertained from the angular distribution of $\angle Cl^-–Dy^{3+}–Cl^-$, in which strong correlations were obtained at about $\theta = 90°$ and 180° as given in Fig. 14. The distances between the nearest-neighbor cations, $r(R^{3+}–R^{3+})$, in Table 9 are commonly less than twice the distance of $r(R^{3+}–Cl^-)$. Under the assumption that the octahedral species are linked through at least one or two Cl^- ions, that is corner- or edge-sharing, with each other, the above facts are consistent with this geometry and the $\angle R^{3+}–Cl^-–R^{3+}$ angles listed in Table 22 indicate bent, not linear, configurations of the octahedra. These data are in line with the possibility that clusters consisting of dimeric or more polymeric complex anions $RCl_6{}^{3-}$ exist in pure RCl_3 melts. The most probable model is illustrated in Fig. 15.

As a consequence, the formation of clusters determines the physicochemical properties of molten rare-earth halides. As a typical example, the electrical conduction of molten chlorides is briefly discussed. The molar conductivities, formerly called equivalent electrical conductivities, of KCl, NaCl, $CaCl_2$, $ZnCl_2$, and RCl_3 melts so far measured are shown in Fig. 16 (Janz et al., 1968). The molar conductivities of RCl_3 melts are much smaller than that

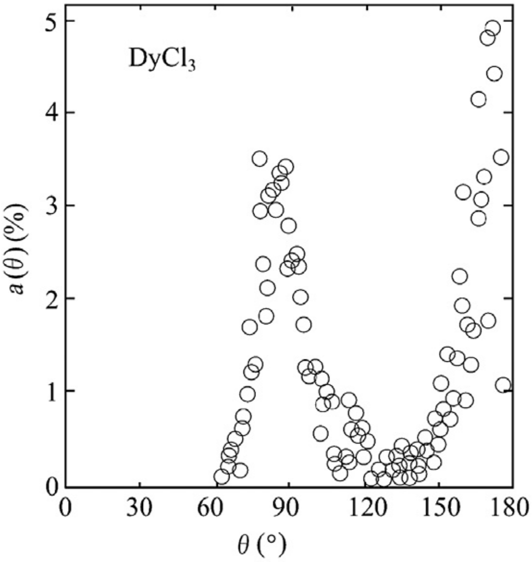

FIGURE 14 Angular distribution of the $Cl^-–Dy^{3+}–Cl^-$ angle simulated by molecular dynamics. *Reproduced with permission from Mochinaga et al. (1991), © 1991 Trans Tech Pub.*

TABLE 22 Average Angles $R^{3+}–Cl^-–R^{3+}$ estimated from XRD data (Mochinaga et al., 1991)

RCl_3 melt	$\angle R^{3+}–Cl^-–R^{3+}$(°)
$LaCl_3$	135
$CeCl_3$	130
$PrCl_3$	128
$NdCl_3$	133
$GdCl_3$	134
$DyCl_3$	131
$SmCl_3$	132

of the $CaCl_2$ melt in which similar octahedral complex anions $CaCl_6{}^{4-}$ exist. $ZnCl_2$ has a highly developed network structure in the molten state, and thus, its electrical conductivity is known to be very low. The electrical conductivities of RCl_3 melts are in the middle range between those of low-conductive $ZnCl_2$ and high-conductive KCl and NaCl melts.

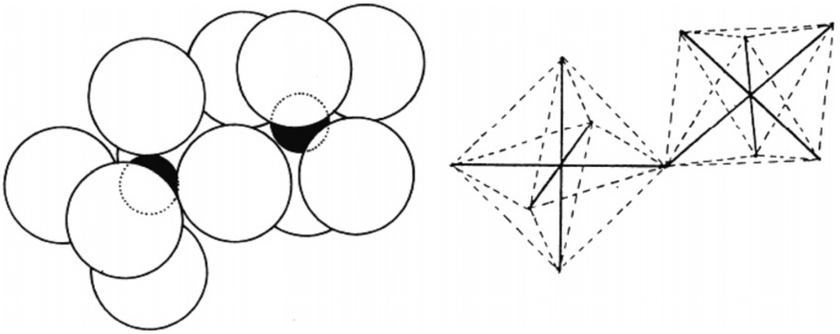

FIGURE 15 Most probable model for dimeric ions $R_2Cl_{11}^{5-}$. Black circles: R; empty circles: Cl. *Reproduced with permission from Mochinaga et al. (1991), © 1991 Trans Tech Pub.*

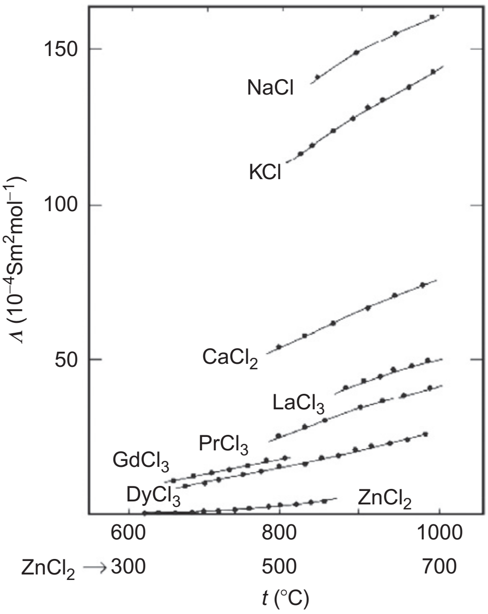

FIGURE 16 Molar conductivities of several molten salts. *Reproduced with permission from Mochinaga et al. (1991), © 1991 Trans Tech Pub.*

After confirmation from Raman scattering experiments on molten $CeCl_3$ that octahedral $CeCl_6^{3-}$ exists, a somewhat detailed discussion has been made on the medium range structure of this melt (Iwadate et al., 1992). The density of molten $CeCl_3$ dilatometrically measured at 1143 K amounts to 3.193 g cm^{-3}, corresponding to a molar volume of 77.19 cm^3 mol^{-1}. Assuming that the Ce^{3+} ions are homogeneously distributed in the melt, the mean interionic Ce^{3+}–Ce^{3+}distance is calculated to be 5.04 Å. But the most

TABLE 23 Coordination Numbers n_{ik}, Interionic Distances r_{ik}, and Root-Mean Square Displacements $\langle \Delta r_{ik}^2 \rangle^{1/2}$ for Molten $CeCl_3$ (Iwadate et al., 1992)

i	k	n_{ik}	r_{ik} (Å)	$\langle \Delta r_{ik}^2 \rangle^{1/2}$ (Å)
Ce^{3+}	Cl^-	5.6	2.84	0.249
Cl^-	Cl^-	11.3	4.05	0.573
Ce^{3+}	Ce^{3+}	6.5	5.21	0.660

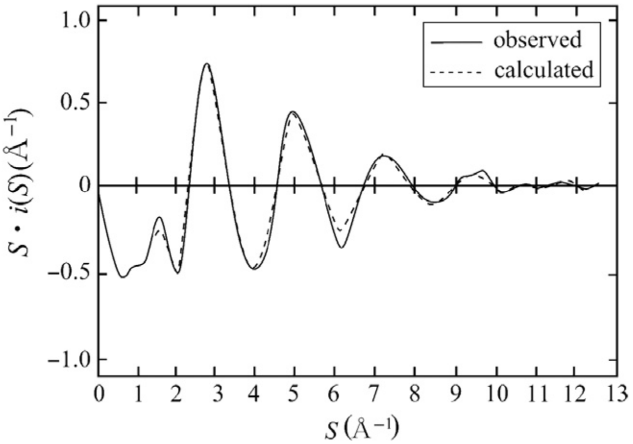

FIGURE 17 Reduced intensity function $S \cdot i(S)$ for molten $CeCl_3$. *Reproduced with permission from Iwadate et al. (1992), © 1992 Chiba University.*

probable interionic distance for Ce^{3+}–Ce^{3+} pairs reported in Table 23 is 5.21 Å, that is about 3.4% larger. This fact indicates that there is some special interaction between $CeCl_6^{3-}$ complex ions.

When two discrete $CeCl_6^{3-}$ ions approach each other as closely as possible, the shortest Ce^{3+}–Ce^{3+} distance is estimated to 6.04 Å by considering the steric hindrance of Cl^- ions and the equality of intraionic and interionic Cl^-–Cl^- distances, both of which are undistinguishable in the modeling of the $S \cdot i(S)$ function (see Fig. 17). Therefore, the real medium range melt structure is probably not composed of discrete $CeCl_6^{3-}$ octahedra.

Another model was therefore considered, named edge-sharing model and in which two octahedra share two Cl^- ions and form, for example, $Ce_2Cl_{10}^{4-}$ dinuclear decahalides. From short-range XRD analysis and Raman spectra, the Cl^-–Ce^{3+}–Cl^-angles and the Ce^{3+}–Cl^- and Cl^-–Cl^- distances were calculated to be 90°, 2.84 Å, and 4.05 Å, respectively. The Ce^{3+}–Ce^{3+}

distance should be, thus, close to 4.0 Å, but the observed value is 5.21 Å, indicating that the edge-sharing model is also not a good approximation for the $CeCl_3$ melt.

In the third, corner-sharing model, two octahedra share one Cl^- ion and form a $Ce_2Cl_{11}{}^{5-}$ ion. When the Ce^{3+}–Cl^-–Ce^{3+} configuration is linear, the interionic Ce^{3+}–Ce^{3+} distance is the same as the sum of the respective ionic radii, 5.64 Å according to Shannon (1976). This value is indeed greater than 5.21 Å, but if the Ce^{3+}–Cl^-–Ce^{3+} angle is set to 133.1°, the corner-sharing model becomes valid as shown in Fig. 15. In the same manner, trimer, tetramer, and larger polymeric ions, denoted $Ce_nCl_{(5n+1)}{}^{(2n+1)-}$, may exist in the melt. As can be seen from the general form of the polymer, a linear configuration does not satisfy the $CeCl_3$ stoichiometry and values of the Cl/Ce ratio approach 5 when linear polymerization occurs. Therefore, clustering of octahedra as predicted by the corner-sharing model and the existence of polymeric ions seem to be needed in order to reduce the Cl/Ce ratio down to the stoichiometric ratio 3 and to reconcile the structural model with the whole set of experimental data. Additionally, this type of ionic bond has been thought to be not necessarily rigid, that is, to break and form again in a kinetic process. It may be concluded from the above discussion and in view of other physicochemical data that polymeric ions and their clustering exist in the $CeCl_3$ melt.

Tosi et al. have published a series of excellent papers titled *Ordering in Metal Halide Melts* (Tosi et al., 1993), *Melting and Liquid Structure of Polyvalent Metal Halides* (Tosi, 1994a), *Structure of Covalent Liquids* (Tosi, 1994b), and *The Molten State of Trivalent Metal Halides and Oxides: Recent Progress* (Akdeniz et al., 1998). In particular, the ordering of trihalide melts and the network formation are mentioned in these reviews. As stated before, several research groups interested in molten salts have carried out determinations of liquid structures for several trivalent metal halides based on measurements of total X-ray and ND patterns. They focus on two main themes: (i) the trend from cation-dominated Coulomb ordering to loose network structures across the series of sixfold-coordinated rare-earth chlorides, including YCl_3 and (ii) the competition between network formation and stabilization of molecular-type liquid structures with strong intermolecular correlations, as in associated molecular liquids. The overall structural evolution as the trivalent metal ion is changed is governed by the increasing weight of covalency versus ionicity. The macroscopic properties reported for trichlorides reflect melting mechanisms that are consistent with the observed liquid structures. Progressive network formation in the melt from $LaCl_3$ to YCl_3 is signaled by decreasing values of ΔS, $\Delta V/V_l$ and σ, where ΔS is the entropy change, $\Delta V/V_l$ gives the relative difference between the volume V_l of the liquid at T_m and that of the solid at room temperature, and σ is the electric conductivity.

Regarding network formation, the following conclusion has been drawn on the basis of liquid structure data available from XRD for $LaCl_3$, $CeCl_3$, $PrCl_3$,

$NdCl_3$, $SmCl_3$, $GdCl_3$, and $DyCl_3$ (Mochinaga et al., 1991) as well as from ND for molten $NdCl_3$ (Saboungi et al., 1990). These compounds have the UCl_3 structure in their high-temperature crystal phase, except for $DyCl_3$, which transforms into the $AlCl_3$ structure before melting. The UCl_3 structure is hexagonal, with each metal cation (M) surrounded by six chlorides on the corners of a trigonal prism and further coordinated by three coplanar chlorides at somewhat larger distance (Wyckoff, 1964). The structure can be built by stacking into a chain MCl_3 units shaped as trigonal pyramids with M at the apices and the three chlorides in the base of each pyramid being equally shared between two M to form the trigonal prism around each M, and then packing these chains so as to give three coplanar interchain M–Cl bonds for each M. Evidently, a molecular-type crystal structure results if each M is brought closer to one of the two triplets of chlorides forming each prism. The $AlCl_3$ structure can also be built from MCl_3 pyramidal units, arranged in layers so as to yield a slightly distorted cubic close packing of chlorides inside which planes of octahedral sites are alternately either occupied by M or empty (Templeton and Carter, 1954). Each layer of the $AlCl_3$ structure can almost be viewed as a hexagonal planar lattice of M sandwiched between two triangular lattices of chlorides having the phase relationship of adjacent (111) planes in the face-centered cubic lattice, as shown in Fig. 18. In this figure, the lower cluster shows the octahedral coordination of the metal ion in the crystal, which is basically preserved in molten YCl_3. The upper cluster shows an Al_2C1_6 unit, which, through the displacement of the two metal ions as indicated by arrows, yields an Al_2C1_6 molecule on melting of $AlCl_3$.

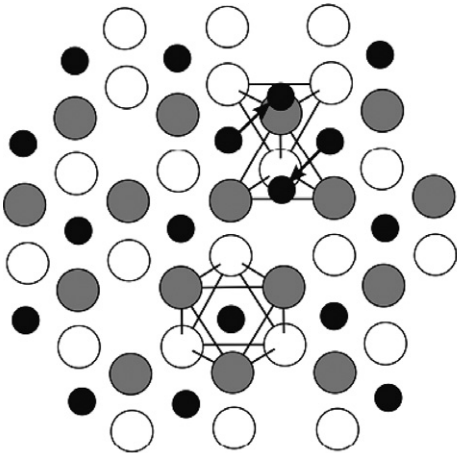

FIGURE 18 Schematic illustration of a layer in the $AlCl_3$, crystal structure and of melting in YCl_3 and $AlCl_3$. The black spheres represent a plane of trivalent metal ions, and the gray and white spheres represent planes of chlorines above and below the plane of metal ions, respectively. *Reproduced with permission from Price et al. (1992), © 1992 Electrochemical Society.*

All rare-earth trichlorides listed above have similar structural characteristics in the melt. The first-neighbor coordination number of the metal ions is 5.6–5.7 and the R–Cl bond length lies in the range 2.69–2.87 Å. The second-neighbor bond lengths are r(R–R) = 4.9–5.2 Å and r(Cl–Cl) = 3.8–4.1 Å, indicating a Coulomb ordering primarily determined by the repulsion between the polyvalent cations, as discussed earlier for molten $SrCl_2$. Yet the ionic conductivity in the melt decreases steadily through the series of compounds from $LaCl_3$ to $DyCl_3$, and Raman-scattering data show that a high-frequency spectral shoulder in $LaCl_3$ rises to become a very well-defined peak in $DyCl_3$ (Mochinaga et al., 1991). This suggests that the essentially six-fold coordination of the metal ions becomes progressively more stable through the series, leading to a liquid structure that resembles a loose network of distorted Cl-sharing octahedra. The ND pattern of molten $NdCl_3$ shows a relatively weak and broad structure in the region of the first sharp diffraction peak, FSDP (Saboungi et al., 1990).

$DyCl_3$ and YCl_3 are structurally isomorphous before melting and melt with similarly low values of ΔS and $\Delta V/V_l$. In a ND experiment on molten YCl_3 (Saboungi et al., 1991), the Faber–Ziman structure factor exhibited a well-defined FSDP at $k = 0.95$ Å^{-1}, giving unambiguous evidence of intermediate-range order. The average coordination number of the metal ions is 5.9, which confirms the Raman-scattering finding (Papatheodorou, 1977) of rather long-lived octahedral coordination of the metal ions, though in detail the octahedra in the liquid are somewhat expanded and distorted. The octahedral network must be relatively loose on a time scale longer than the period of the breathing mode of the octahedron at $\nu = 260$ cm^{-1}, to be compatible with the value of the ionic conductivity of molten YCl_3 (Akdeniz and Tosi, 1992; Janz et al., 1968). The second-neighbor C1–C1 coordination is approximately 8.2, somewhat lower than the value of 9 for intralayer Cl–Cl correlations in the crystal.

The structural trend represented by increasing connectivity of highly coordinated local structures from $LaCl_3$ to YCl_3 can be reproduced within a purely ionic model (Tatlipinar et al., 1992). This model relates the appearance and growth of intermediate-range order in a 3:1 liquid to the decrease in the radius R_M of the metal ion. Figure 19 shows the evolution of the theoretical partial structure factors from $LaCl_3$ through YCl_3 and $AlCl_3$ at constant density. As R_M decreases, Coulomb ordering becomes stronger, as indicated by the alignment of peaks in the R–R and Cl–Cl structure factors with the valley in the R–Cl structure factor. At the same time, the main peak associated with cation ordering in $LaCl_3$ evolves into the FSDP in $AlCl_3$. When the fluid with $R_M = 0.82$ Å is allowed to expand to densities appropriate to real $AlCl_3$ at standard pressure, the model suggests stabilization of dimeric bound states.

As mentioned above, the main features of the local structures adopted by molten rare-earth halides have been elucidated during the 1990s by Tosi and coworkers (Akdeniz et al., 1998; Tosi, 1994a; Tosi, 1994b; Tosi et al., 1993).

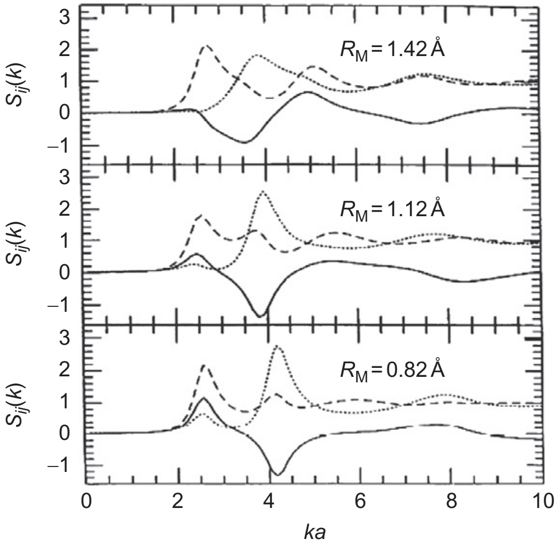

FIGURE 19 Partial structure factors as functions of scaled wave vector in liquid MCl_3 at fixed density, for three values of the metal ion radius R_M corresponding to La^{3+}, Y^{3+}, and $A1^{3+}$ (from top to bottom). (Dotted lines) $S_{ClCl}(k)$, (dashed lines) $S_{MM}(k)$, (solid lines) $S_{MCl}(k)$. *Reproduced with permission from Tatlipinar et al. (1992), © 1992 IOP Pub.*

In the diffraction studies, the CN of the first M–Cl correlation has been consistently evaluated to be about 6 for the pure melts, except for molten $ScCl_3$, for instance, by Wasse and Salmon (1998), Okamoto and Ogawa (1999a, 1999b), and Okamoto et al. (1999). However, another structural interpretation has been proposed on the basis of ND and molecular dynamics (MD) data. Wasse and Salmon (1999c) reported from systematic ND studies of molten rare-earth trichlorides that the CN of the first M–Cl correlation is not always equal to 6; for example, that of molten $LaCl_3$ is 8.2. Hutchinson et al. (1999, 2001) have obtained MD simulation results of some rare-earth trichloride melts by using a PIM, which reproduces well the ND results obtained by Wasse and Salmon. The CN was estimated to be 7.9 for molten $LaCl_3$. These ND and MD works concluded that the CN changes with cation size in the pure melts. The results of simulation works will be described afterwards.

We now introduce and discuss typical structures of molten rare-earth trihalides analyzed by ND. The structure of molten lanthanum and cerium trihalides using the method of isomorphic substitution in ND has been carried out by Wasse and Salmon (1999d). The total structure factors of molten RX_3, where R denotes La or Ce and X denotes Cl, Br, or I, have been measured by using ND. Difference function methods were then applied on assuming that the LaX_3 and CeX_3 melts are isomorphic for a given halide ion. The results which follow from this assumption show that the FSDP in the measured total structure factors arises from cation correlations and its shift to lower scattering vector values with increasing anion size is consistent with an enhanced separation in real space of cation-centered polyhedra. Upon melting, the RX_3 salts exhibit a decrease in the coordination number of both the cations and anions. In the liquid state, the R–X coordination environment is asymmetric with R–Cl, R–Br, and R–I nearest-neighbor distances of 2.93(2) Å, 3.01(2) Å, 3.18(2) Å, respectively, and R–Cl, R–Br, and R–I coordination numbers of 8.2(2), 7.4(2), 6.7(2), respectively. The Cl–Cl, Br–Br, and I–I nearest-neighbor distances are 3.58(3) Å, 3.76(3) Å, 4.13(2) Å, respectively, and there is a significant penetration of the X–X partial pdf into the first peak of the M–X partial pdf for all three anions. The Cl–Cl, Br–Br, and I–I coordination numbers are 9.2(2), 8.7(2), and 8.2(2), respectively, if the R–R coordination number is set to two.

The structure of molten $ScCl_3$ and ScI_3 has also been studied with the same experimental techniques (Wasse and Salmon, 1999a). The structure of the salts ScX_3, where X denotes Cl or I, was investigated by using ND. On heating $ScCl_3$, a phase transition from the $FeCl_3$-type crystal structure to possibly the YCl_3-type crystal structure is observed, whereas ScI_3 remains in its room-temperature $FeCl_3$-type crystal structure up to the melting point. On melting, there is a reduction in the Sc–X coordination number from 6 to 4.8 (2) for $ScCl_3$ and from 6 to 4.7(2) for ScI_3 and the Sc–Cl and Sc–I nearest-neighbor distances in the liquid are 2.48(2) Å and 2.76(2) Å, respectively. The measured total structure factors of molten $ScCl_3$ and ScI_3 each have a prominent FSDP at a scattering vector value of 0.75(5) $Å^{-1}$. The results are discussed in the context of those available for several other trivalent metal halide systems which also melt from the closely related YCl_3-type and $FeCl_3$-type crystal structures.

In the same way, the structure of molten trivalent metal chlorides such as $TbCl_3$, YCl_3, $HoCl_3$, and $ErCl_3$ has been investigated and the total structure factors measured. (Wasse and Salmon, 1999b). All four salts melt with a volume change of 65% from structures comprising $RCl_6{}^{3-}$ octahedra to form liquids which show intermediate-range ionic ordering as manifested by a FSDP at about 1 $Å^{-1}$ which moves to smaller scattering vector values with decreasing cation size. In the liquid, R–Cl distances are comparable with the sum of the ionic radii and the results are consistent with the existence of distorted $RCl_6{}^{3-}$ octahedral units.

Furthermore, ND measurements were performed to determine the structure of molten trivalent rare-earth bromides such as $DyBr_3$, YBr_3, $HoBr_3$, and $ErBr_3$ (Wasse et al., 2000). Upon heating $DyBr_3$, YBr_3, and $HoBr_3$, a phase transition from the $FeCl_3$-type crystal structure to possibly the YCl_3-type crystal structure is observed. The liquids were studied at the total structure factor level, and difference function methods were also applied to $DyBr_3$ and YBr_3 by assuming isomorphous structures. The melts are found to comprise distorted $RBr_6{}^{3-}$ octahedra with R–Br distances comparable to the sum of the ionic radii, and there is evidence for a substantial number of edge-sharing configurations. The octahedra pack to give intermediate-range ionic ordering as manifested by the appearance of a FSDP at 0.79(2)–0.87(2) Å^{-1} which is associated with cation correlations.

The structural information obtained by the research group of Wasse and Salmon includes molecular dynamics simulations in order to give a detailed description of molten rare-earth halides. Selected examples are described here. For instance, the structure of molten $DyCl_3$ and $DyNa_3Cl_6$ has been simulated with polarizable- and rigid-ion models (PIM and RIM) (Takagi et al., 1999). In these simulations, the Born–Mayer–Huggins potential was employed with the same potential parameters for both models. In the PIM, the polarization of the chloride ions was taken into account. Although the partial RDFs between Dy and Cl, and between Cl and Cl are very similar for the two models, the RDF between Dy and Dy is quite different. The RDF between Dy and Dy experimentally determined by the isotope substitution method is well reproduced by PIM simulations. The strong Coulomb interaction between Dy^{3+} cations is screened by the polarization of Cl^- ions, and the interaction distance between Dy^{3+} cations becomes smaller than that given by the RIM. MD simulations for $DyNa_3Cl_6$ were made similarly. The PIM also reproduces the experimental total structure factor very well. It is concluded that strong Coulomb interaction between Dy^{3+} cations is screened by the polarization of Cl^- ions. On the other hand, MD simulation of $DyNa_3Cl_6$ with the PIM shows that the most prominent peak of $g_{\mathrm{Dy-Dy}}(r)$ is at a much larger separation. It would appear that the polarization effects promote the break-up of the network and the formation of discrete ${DyCl_6}^{3-}$ molecular units.

Short- and intermediate-range orders in molten metal tribromides have been studied in terms of a molecular dynamics simulation (Hutchinson et al., 2000). Calculations were performed on four molten metal tribromides, RBr_3 with R = La, Ce, Y, and Dy. The many-body (polarizable-ion) simulation potentials were constructed from metal trichloride potentials using physically transparent scaling arguments to account for the change in anion size and polarizability. Comparison was made with neutron scattering results by constructing the total structure factors from the simulated partial functions. In addition, difference functions, which exploit the proposed isomorphous nature of the (Dy, Y) and (La, Ce) pairs, were constructed and compared with experimental data. The authors proposed that the structures of the trihalide melts fall into three distinct structure classes, depending on the ratio of cation and anion radii and independent of the specific cation and anion involved. For a large radius ratio, a (7–8)-coordinate cation is found and the relative arrangements of the coordination polyhedra around neighboring cations show no particular pattern; the polyhedra seem simply to pack together. The systems which form these liquids exhibit the nine-coordinate UCl_3 structure in the solid phase. For a wide range of intermediate radius ratios, a family of structures based upon more-or-less six-coordinate cations arises. These approximately octahedral units exhibit a marked tendency to edge-share so

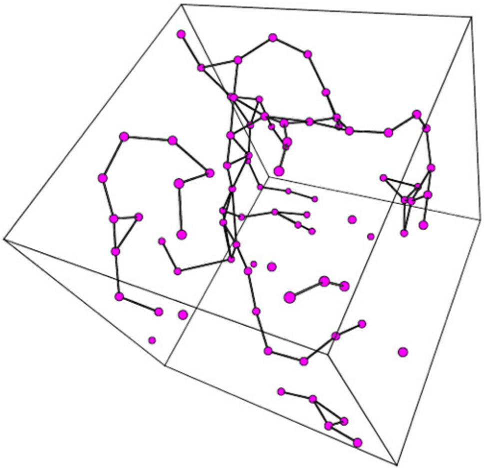

FIGURE 20 A molecular graphics "snapshot" of the edge-sharing units in a single YBr_3 configuration highlighting the chain-like nature of the inherent structure. *Reproduced with permission from Hutchinson et al. (2000), © 2000 IOP Pub.*

as to form extended and cross-linked chains, as demonstrated in Fig. 20. This structural motif seems quite stable against variations in the actual mean coordination number from about 6.5 to 5.5. Most systems within this class exhibit the six-coordinate YCl_3 (or BiI_3) crystal structure, but some systems melt into it from higher-coordinate crystal structures, like the (8 + 1)-coordinate $PuBr_3$ structure. For still smaller radius ratios, quasi-molecular fluids based on four-coordinate cations are found, as in $AlCl_3$.

Efforts similar to those described above have been made with the goal of obtaining a unified description of $MC1_3$ systems with a simulation model including polarization (Hutchinson et al., 2001). Calculations were performed to substantially improve the agreement with experiments for $LaC1_3$, $TbC1_3$, $YC1_3$, and $AlCl_3$, and simulation results were presented for the first time for $ScC1_3$, which was shown to exhibit a fascinating cross-linked network structure. Table 24 lists values for the average numbers of coordinated anions around cations for each of the simulations with the optimum potentials.

Coordination numbers are obtained by *integrating the cation–anion pdfs up to the position of the first minimum* and are compared with the results from ND studies. Surprisingly, good agreement is found, considering the different shapes of the first peaks, their pdfs, and the ND patterns. Furthermore, in the ND data, the first peak (due to M–Cl correlations) and the second (due to Cl–Cl correlations) of the neutron RDF overlap rather strongly, but their analysis (based simply on the simulated MCl partial distribution functions and partial structure factors) supports the neutron values.

TABLE 24 Temperatures and Densities Used in the Simulations of the $MC1_3$ Liquids Along with Simulated and Experimental Cation–Anion Coordination Numbers (Hutchinson et al., 2001)

System	Temperature (K)	Density (g cm^{-3})	CN (sim.)	CN (exp.)
$LaC1_3$	1178	3.174	7.9	8.2
$CeC1_3$	1108	3.234	–	–
$TbC1_3$	900	3.580	7.2	7.5
YCl_3	1033	2.492	6.6	6.2
$ScCl_3$	1253	1.643	5.6	5.2
$AlC1_3$	600	1.277	4.0	4.0

The results for the coordination numbers of the larger cation systems, which show values of about 8, are controversial. Raman studies of these systems suggest octahedral coordination, even in the pure melt. Also, older X-ray studies were interpreted in terms of octahedral coordination (Mochinaga et al., 1991). A full resolution of this controversy will probably await the separation of partial pdfs using isotopic substitution methods. To date, such studies have been made only for the intermediate-size cation Dy^{3+} (Takagi et al., 1999), which, according to all studies, is basically octahedrally coordinated (Dy^{3+} is very similar to Y^{3+}, both experimentally and in our simulation models). Ongoing efforts are being made to reconcile results from ND, X-ray, and EXAFS studies with computer simulations, which hopefully will lead to a consensus.

For intermediate-size cations, ranging from about Y^{3+} (or Dy^{3+}) to Sc^{3+}, the chloride melts are predominantly octahedrally coordinated, with average coordination numbers slightly higher than for the larger members and lower for the smaller. The coordination polyhedra are linked together into a network, with a considerable degree of edge-sharing. A snapshot of the instantaneous structure of the $ScC1_3$ melt is shown in Fig. 21.

Only a slice of the simulated cell is shown so that there are a number of ions which are disconnected from their actual neighbors. Nevertheless, the picture shows five- and six-coordinate Sc^{3+} linked together with a very high degree of edge-sharing to form a cross-linked network. The structure features a number of voids, and intervoid correlations are responsible for the prominent, low k prepeak in the structure factor (Wilson and Madden, 1998).

7.2. Structural Approaches from Raman Spectroscopy

A series of pioneering studies on high-temperature Raman spectroscopy of molten rare-earth halides were commenced in the 1970s in order to prove

FIGURE 21 Molecular graphics snapshot of the liquid $ScC1_3$ showing the edge-linked chain structural motif. The large circles represent the Cl^- anions and the smaller circles the Sc^{3+} cations. *Reproduced with permission from Hutchinson et al. (2001), © 2001 Taylor & Francis.*

and establish the presence of associated species in binary charge-unsymmetrical fused-salt system as well as to characterize them from a structural viewpoint, since the thermodynamics of $LaC1_3$–AC1 (A = Li, Na, K, Rb, or Cs) melts by calorimetric and electromotive-force methods implied the presence of complex species (Papatheodorou and Østvold, 1974). Early works dealt with $LaC1_3$–KC1 melts (Maroni et al., 1974) and $Cs_2NaLaCl_6$, Cs_3LaCl_6, and K_3LaCl_6 in molten and solid states (Papatheodorou, 1975); efforts were made to surmount technical problems such as the unwanted fluorescence and the residual background extending almost to 2000 cm^{-1} which created difficulties in the determination of a reliable baseline, and to establish experimental and computational procedures. The above systematic studies were expanded into high-temperature Raman investigations of molten salts by Papatheodorou (Papatheodorou, 1977). The Raman spectra of molten YCl_3–ACl (A = Cs, K, Li) mixtures have been reported for different compositions and temperatures up to 890 °C in a paper entitled *Raman Spectroscopic Studies of Yttrium (III) Chloride–Alkali Metal Chloride Melts and of* Cs_2NaYCl_6 *and* YCl_3 *Solid Compounds*. The Raman spectra of polycrystalline Cs_2NaYCl_6 and YCl_3 were also measured from 25 °C to temperatures above melting. Factor-group analysis of crystalline Cs_2NaYCl_6 was used to identify the three Raman active modes (ν_1, ν_2, ν_5) of octahedral $YCl_6{}^{3-}$. For liquid mixtures rich in alkali halide, the predominant features of the spectra are characterized by a polarized and a depolarized band with frequencies close to the ν_1 and ν_2 frequencies of octahedral $YCl_6{}^{3-}$, which thus indicates the existence of such a species in the melt. In melts containing more than 25% YCl_3, a new polarized band D appears which shifts continuously and rapidly to higher energies with increasing YCl_3 concentration. The frequency shift is attributed to a continuous distortion mechanism of the YCl_6^{3-} octahedra by the neighboring yttrium ions. This shift and a comparison of the liquid and solid Raman spectra of yttrium chloride suggest the existence of lattice-type modes in these melts. Typical spectra and a structural model are depicted in Figs. 22 and 23, respectively.

This methodology has been applied to the ScI_3–CsI system to determine its phase diagram and to establish the existence of two solid compounds, Cs_3ScI_6

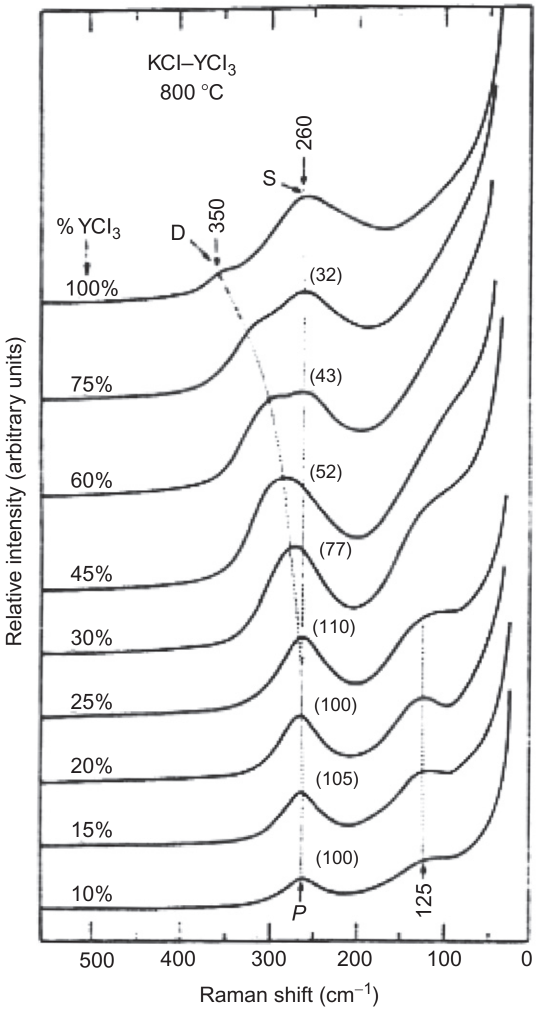

FIGURE 22 Raman spectra of molten KCl–YCl_3 mixture at 800 °C versus increasing concentration of YCl_3. *Reproduced with permission from Papatheodorou (1977), © 1977 American Institute of Physics.*

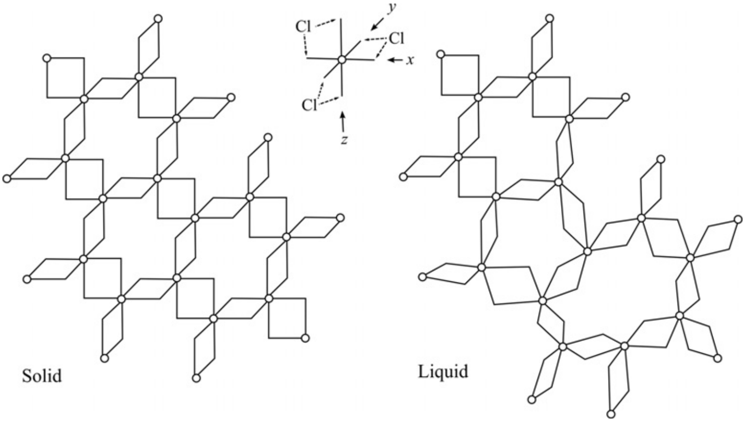

FIGURE 23 Structural skeletons for crystalline and liquid $YC1_3$. *Reproduced with permission from Papatheodorou (1977), © 1977 American Institute of Physics.*

and $Cs_3Sc_2I_9$ (Metallinou et al., 1991). The data are discussed in terms of the possible species formed in the melt mixtures. It is suggested that two predominant ionic species are in equilibrium in the melt, $ScI_6^{3-} \rightleftharpoons ScI_4^- + 2I^-$. The Raman frequencies attributed to the ionic species are as follows: for ScI_6^{3-}, $\nu_1 = 119 \pm 1\ cm^{-1}$, $\nu_2 = 67 \pm 2\ cm^{-1}$, ($\nu_5 = 80\ cm^{-1}$); for ScI_4^-, $\nu_1 = 129 \pm 1\ cm^{-1}$, $\nu_2 = 37 \pm 3\ cm^{-1}$, $\nu_4 = 54 \pm 3\ cm^{-1}$. A third dinuclear Sc species is also present in vapors at high ScI_3 concentrations.

Further attempts have been made to extend Raman spectroscopy to a variety of rare-earth compounds in different states. Raman spectra of liquids and glasses in the $RC1_3$–$AlC1_3$ (R = Nd, Gd) systems were measured by Murase et al. (1994). The existence of stable glass-forming liquid mixtures in the $RC1_3$–$AlC1_3$ (R = Nd, Gd) binary systems is established. Based on Raman spectroscopic measurements, a structural model is proposed for these glasses where the main participating units are "$AlC1_4$" and, partially, "$A1_2C1_7$". The coordination of the lanthanide is ninefold for neodymium and eightfold for gadolinium.

Vibrational modes and structure of rare-earth halide/alkali halide binary melts have been discussed in a series of papers for YBr_3–ABr (A = Li, K, Cs) and YF_3–KF (Dracopoulos et al., 1997), for LnF_3–KF (Ln = La, Ce, Nd, Sm, Dy, Yb) (Dracopoulos et al., 1998), and for $LnBr_3$–KBr (Ln = La, Nd, Gd) and $NdCl_3$–ACl (A = Li, Na, K, Cs) (Photiadis et al., 1998). It was found from the Raman spectra of YBr_3–ABr (A = Li, K, Cs) and YF_3–KF melts that the octahedral YX_6^{3-} anions (X = F, Br) are the predominant species in mixtures rich in alkali halide, and the trends of the YX_3–KX spectra in going from bromide to chloride and fluoride melts suggest that pure molten YF_3 is likely to possess a loose "network" structure of edge-bridged distorted octahedra as in the case of molten YCl_3 and YBr_3.

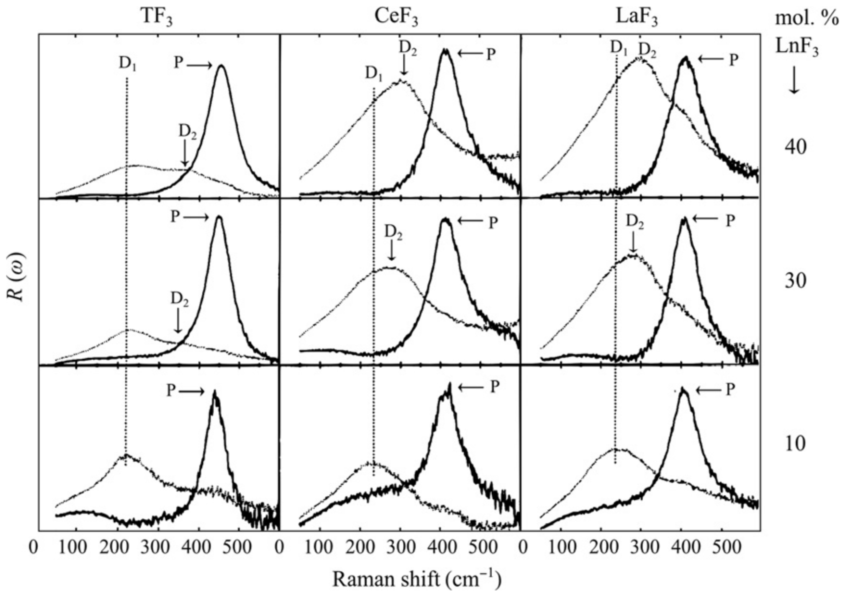

FIGURE 24 Composition dependence of the reduced isotropic (solid line) and anisotropic (dotted line) Raman spectra of the molten LnF_3–KF (Ln = Y, Ce, La) at 1000 °C. *Reproduced with permission from Dracopoulos et al. (1998), © 1998 Royal Society of Chemistry.*

As for LnF_3–KF (Ln = La, Ce, Nd, Sm, Dy, Yb) melts, the data indicate that at mole fractions $x(LnF_3) \leqq 0.25$ the LnF_6^{3-} octahedra are the predominant species, and at mole fractions $x(LnF_3) > 0.25$ one polarized and two depolarized bands (designated as P and D in Fig. 24) appear in the spectra which are interpreted as corresponding to distorted LnF_6^{3-} octahedra bound by common fluorides (edge-sharing). The anisotropic scattering intensity increases, relative to the isotropic intensity, with increases in both the size and mole fraction of the lanthanide cation. This unusual effect is attributed to dipole-induced-dipole interactions between cations in the melt and its variation from system to system is related to the size and polarizability of the Ln^{3+} cation and its relative shielding by the F^- anions.

From Raman spectra of $LnBr_3$–KBr (Ln = La, Nd, Gd) and $NdCl_3$–ACl (A = Li, Na, K, Cs) melts, the following phenomena and interpretations were obtained. In molten mixtures rich in alkali halide with lanthanide halide mole fractions less than 0.25, the predominant species are the octahedral LnX_6^{3-} anions giving rise to two main bands P_1 (polarized) and D_1 (depolarized) which are assigned to the v_1 and v_5 modes, respectively. In molten mixtures rich in LnX_3, the spectra are characterized by the P_1 and D_1 bands plus two new bands D_2 (depolarized) and P_2 (polarized). The P_2 band shifts continuously to higher frequencies with increasing LnX_3 content. These four bands are attributed to the D_3 distortions of the LnX_6^{3-} octahedra bound by edges.

The room temperature Raman spectra of the LnX_3 solid compounds are characterized by bands due to the vibrational modes of the different crystalline structures: hexagonal for $LaBr_3$ and $NdCl_3$, orthorhombic for $NdBr_3$, and rhombohedral for $GdBr_3$ having the Ln^{3+} coordination number 9, 8, and 6, respectively. With increasing temperature, the spectra of the $GdBr_3$ solid become dominated by six Raman bands which are assigned to the vibrational modes of a triple layer of ions consisting of distorted octahedra $GdBr_6^{3-}$ (CN = 6) which share edges with neighboring octahedra. Upon melting, the molar volume of $GdBr_3$ does not change much and the spectra are characterized by the above-mentioned P_1, P_2, D_1, and D_2 bands and can be correlated to the triple layer modes of the solid. The high-temperature spectra of hexagonal $LaBr_3$, $NdCl_3$, and orthorhombic $NdBr_3$ show that the structure and CN remain the same up to melting. However, upon melting, the compact orthorhombic (CN = 8) and hexagonal (CN = 9) forms increase drastically their molar volume and give spectra similar to those of molten $GdBr_3$, YBr_3, and YCl_3 where the Ln^{3+} is in a sixfold coordination. It appears that the structures of all the LnX_3 melts are similar and independent of the structure of the solids; fast exchange of ions leads to short lifetimes for the octahedra and weak intralayer interactions. Accordingly, schematic diagrams of phase transitions of rare-earth trihalides upon melting are proposed as can be seen in Fig. 25.

The next Raman studies on molten rare-earth halides have turned to the scandium(III) systems which feature the smallest ionic radius in the rare-earth series and high melting points. Zissi and Papatheodorou (1999) have measured

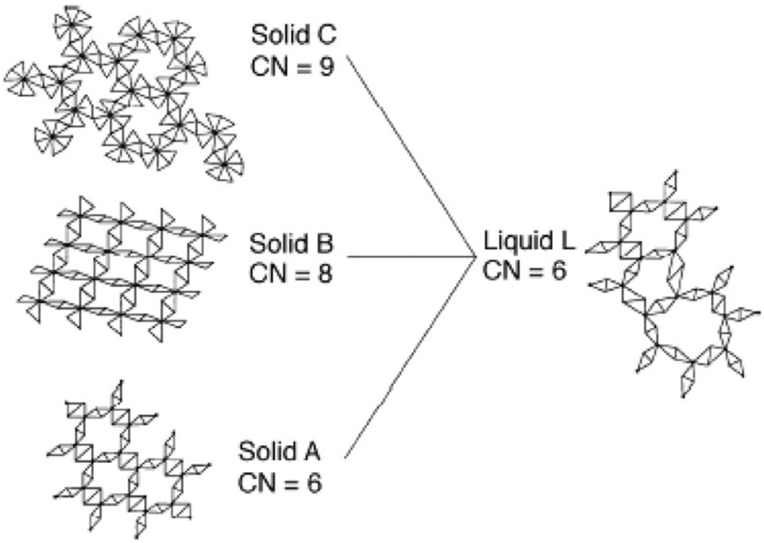

FIGURE 25 Schematic structures of solid and molten rare-earth trihalides; solid A: monoclinic or rhombohedral; solid B: orthorhombic; solid C: hexagonal. *Reproduced with permission from Photiadis et al. (1998), © 1998 Royal Society of Chemistry.*

Raman spectra of $Cs_2NaScCl_6$, Cs_3ScCl_6, $Cs_3Sc_2Cl_9$, and $ScCl_3$ compounds from 258 °C to temperatures above their melting points. The vibrational modes of the discrete species $ScCl_6^{3-}$ and $Sc_2Cl_9^{3-}$ in the solids are transferred upon melting into the liquid and reflect an equilibrium involving $ScCl_4^-$, that is, $2Sc_2Cl_9^{3-} \leftrightharpoons ScCl_6^{3-} + 3ScCl_4^-$. The spectra of solid $ScCl_3$ are dominated by the vibrational modes of a triple layer of ions consisting of edge-sharing $ScCl_6^{3-}$ octahedra.

The aforenamed researchers have discovered an interesting phenomenon in the spectra of molten $ScCl_3$–CsCl mixtures in the range of 600–900 °C (Zissi and Papatheodorou, 2002). The intensity changes of the H and P_1 bands with composition (see Fig. 26) imply that an equilibrium: $ScCl_7^{4-} \leftrightharpoons ScCl_6^{3-} + Cl^-$, is established and that the structure of melts dilute in $ScCl_3$ is dominated by six- and seven-coordinated scandium species. Figure 27 also indicates that the seven-coordinated species predominates in the melt structure at lower temperatures while the six-coordinated species is favored at higher temperatures.

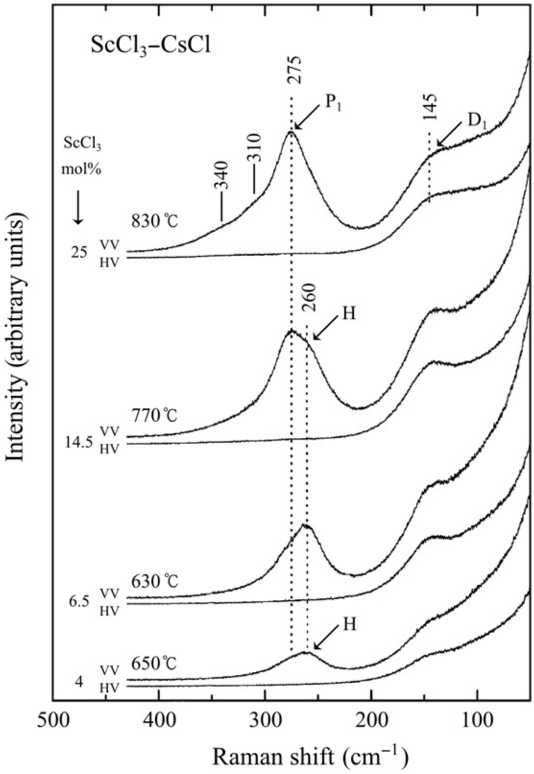

FIGURE 26 Composition dependence of the Raman spectra of xScCl$_3$–$(1-x)$ CsCl $(0<x<0.25)$ molten mixtures at a few degrees above the binary liquidus temperature. *Reproduced with permission from Zissi and Papatheodorou (2002), © 2002 Royal Society of Chemistry.*

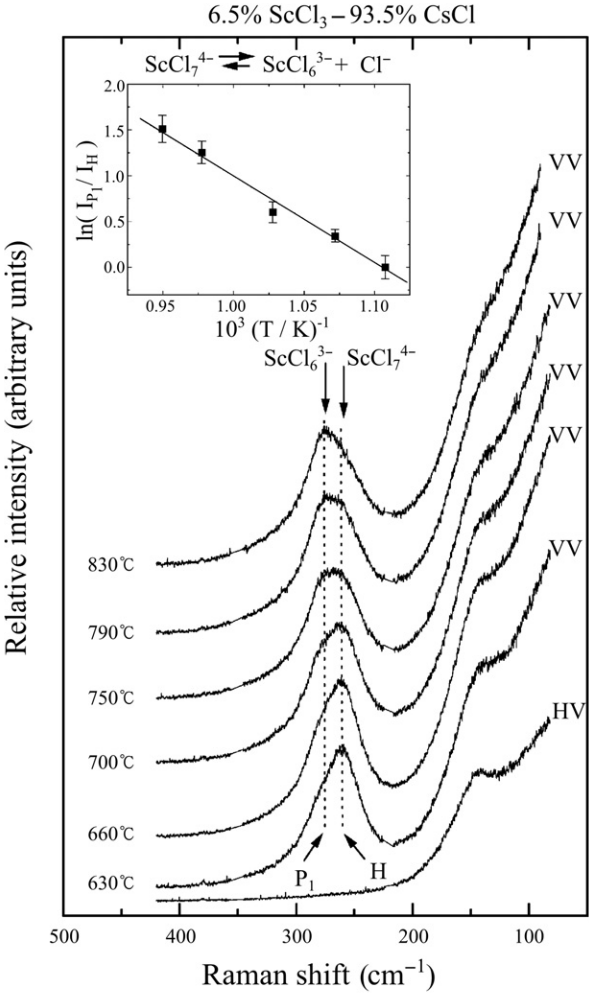

FIGURE 27 Evolution of the Raman spectra with temperature for molten 0.065$ScCl_3$–0.935CsCl mixture. *Reproduced with permission from Zissi and Papatheodorou (2002), © 2002 Royal Society of Chemistry.*

These studies have been expanded in order to unravel the composition- and temperature-induced changes on the structure of molten $ScCl_3$–CsCl mixtures (Zissi and Papatheodorou, 2004) in comparison with the results of molecular dynamics simulations, using a polarizable ion model (PIM) reported by Madden et al. (2004). The following conclusions concerning the structure of molten $ScCl_3$–CsCl mixtures were reached:

(i) Contrary to other trivalent systems, the composition of solutions dilute in $ScCl_3$ is dominated by two species in equilibrium: $ScCl_7^{4-} \leftrightharpoons ScCl_6^{3-} + Cl^-$. The octahedral $ScCl_6^{3-}$ species overcome the seven-coordinated species at high temperatures and at composition above ~20 mol% $ScCl_3$.

(ii) At $ScCl_3$ mole fractions between ~25 and ~50 mol%, an equilibrium is established where a dimer of the "octahedral" species bridged by a face dissociates into a "tetrahedral" and an "octahedral" species: $2Sc_2Cl_9^{3-} \rightleftarrows 3ScCl_4^- + ScCl_6^{3-}$.

(iii) A loose network structure of bridged "octahedra" appears to form in melts rich in $ScCl_3$. Two main bands are seen in the isotropic Raman spectra at these compositions; the P_1 and P_2 bands whose position and relative intensities behave in a manner analogous to that found for other lanthanide halide systems. The origin of the P_2 band is assigned to a distortion of the bridged octahedra, in accordance with the γ-polarizable mechanism scheme proposed by computer simulation studies. Both schemes require that the IR active T_{1u} mode of the octahedra becomes Raman active and that its intensity and frequency increase with increasing $ScCl_3$ content.

(iv) A cluster model is proposed for pure molten $ScCl_3$. Each cluster is composed of a central fragment of a limited network of bridged "octahedra" (i.e., an YCl_3-like network structure) and is terminated on the "surface" with chlorides bridged to tetrahedrally coordinated scandium having also (nonbridged) terminal chlorides. The cluster model implies (a) an average scandium coordination number less than six and (b) a partial molecular-like character and an electronic conductivity arising from self-ionization. Furthermore, the model is in accordance with the Raman spectra, the coordination number, and network structure proposed by the computer simulations and with some physicochemical properties of this melt.

Two years later, vibrational modes and structure of the $LaCl_3$–CsCl melts have been reported by Zissi et al. (2006). Detailed Raman spectroscopic measurements of the $LaCl_3$–CsCl melt mixtures at different temperatures and compositions show a spectral behavior "isomorphous" to that observed for a large number of LnX_3–AX systems with small or large rare-earth cations. "Isolated" octahedral $LaCl_6^{3-}$ ions are definitely formed in CsCl-rich melts, which with increasing $LaCl_3$ mole fraction share chlorides forming a loose network of coordination polyhedra in $LaCl_3$-rich melts. The systematics of the "isomorphous" spectra in all these binary mixtures suggest that the coordination of La^{3+} is more likely to be octahedral at all compositions.

In order to confirm conclusions drawn from Raman spectra, the electronic absorption spectra of the f←f hypersensitive transitions $Ho(^5G_6 \leftarrow {}^5I_8)$ and $Nd(^4G_{5/2} \leftarrow {}^4I_{9/2})$ have been measured in molten LiCl–KCl eutectic and in $LaCl_3$–KCl molten mixtures by Chrissanthopoulos and Papatheodorou (2006). The ligand-field components of the above transitions in octahedral symmetry have been identified, and the molar absorptivity changes with temperature and composition have been measured. The spectra are discussed in terms of the coordination geometries of the probe cations Ho^{3+} and Nd^{3+}. The Boltzmann thermal factor appears to be partially responsible for the variation of the "hot" band intensities. The data suggest that the predominant factors affecting the oscillator strength of the Ho^{3+} and Nd^{3+} hypersensitive transitions is the degree of octahedral distortions in conjunction with the overall charge asymmetry around the $LnCl_6^{3-}$ anions (Ln = Ho, Nd). It appears that no drastic changes occur in the coordination of the probe cations

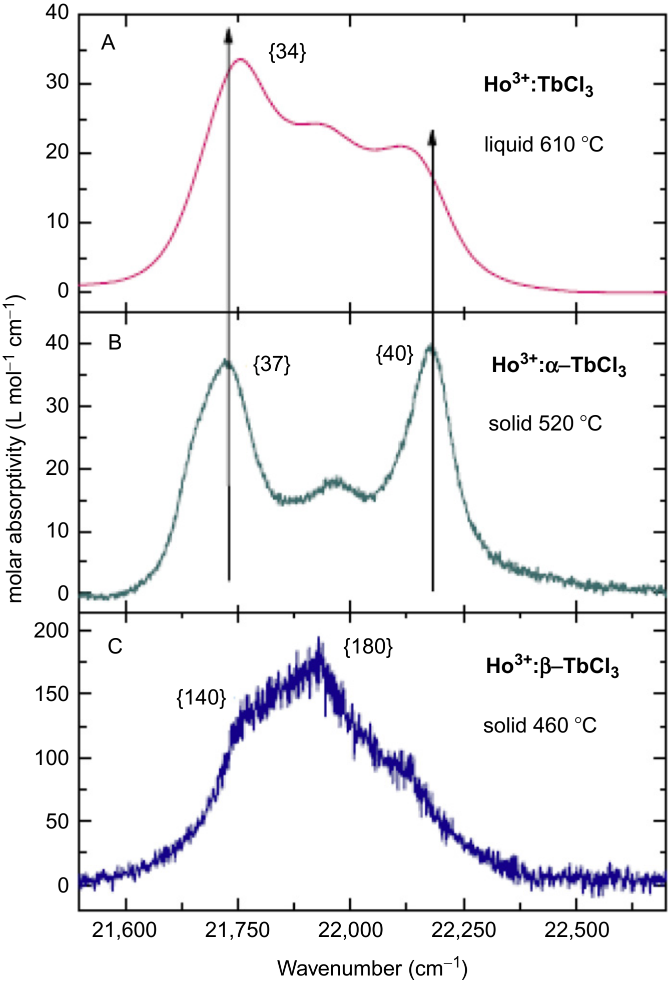

FIGURE 28 Electronic absorption spectra of Ho^{3+} in the region of the $^5G_6 \leftarrow {}^5I_8$ transition: (A) in liquid $TbCl_3$; (B and C) in the two allotropic crystalline α- and β-forms of $TbCl_3$, respectively. *Reproduced with permission from Chrissanthopoulos and Papatheodorou (2008), © 2008 Elsevier.*

in going from dilute solutions in $LaCl_3$ to pure $LaCl_3$ melts; this suggests that the coordination of La^{3+} is more likely to be sixfold in the host melt. Further evidence for sixfold coordination is given by the Judd–Ofelt parameters of Nd^{3+} in both molten $NdCl_3$ and $La(Nd)Cl_3$. All these data are considered as a further and strong indication that the coordination of La^{3+} in all $LaCl_3$–KCl melt compositions and in pure molten $LaCl_3$ is predominantly sixfold.

Using the same technique, absorption spectra of the hypersensitive transition $Ho(^5G_6 \leftarrow {}^5I_8)$ have been measured in different chloride coordination environments (Chrissanthopoulos and Papatheodorou, 2008). Drastic changes of the molar absorptivity of the Ho^{3+} probe have been observed during the $\alpha \rightarrow \beta$ solid phase transition of $TbCl_3$ during which the coordination is altered from six- to eightfold, as depicted in Fig. 28. In contrast, rather smooth and continuous changes occur upon melting of $Y(Ho)Cl_3$ and $Tb(Ho)Cl_3$. The data indicate that the distorted octahedral coordination of Ho^{3+} in these solids is preserved in the liquid. Furthermore, it was established that the molar absorptivity of the Ho^{3+} probe remains practically invariant in liquid rare-earth chlorides RCl_3 with either large (e.g., La) or small (e.g., Y) cations. For the same group of chlorides, the Raman spectra were found to be rather isomorphous, implying that the vibrational modes in these liquids arise from similar

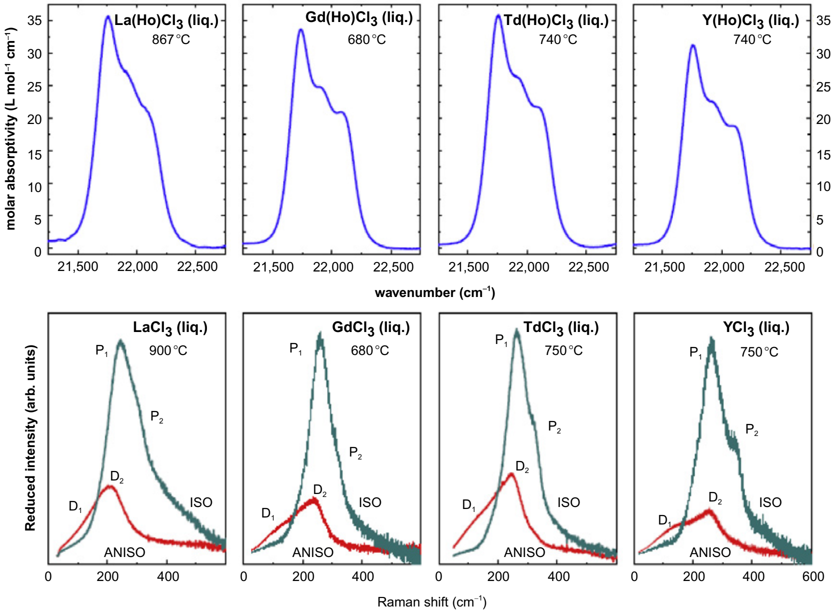

FIGURE 29 Systematics of absorption (top) and Raman (bottom) spectra in the rare-earth chloride series. Upper set of figures: Molar absorptivity of the Ho^{3+} hypersensitive transition $^5G_6 \leftarrow {}^5I_8$ in molten RCl_3. Lower set of figures: reduced Raman spectra of molten RCl_3. *Reproduced with permission from Chrissanthopoulos and Papatheodorou (2008), © 2008 Elsevier.*

coordination geometries. These findings in conjunction with an almost identical molar volume for all RCl_3 liquids suggest similar liquid structures which are dominated by coordination polyhedra having the R^{3+} cation in distorted octahedral geometries, as can be seen in Fig. 29 where the definitions of reduced Raman spectra are given in the literature (Dracopoulos et al., 1997). The present method is quite useful in understanding the reliability of high-temperature Raman spectroscopy of molten salts.

7.3. Approaches from Other Techniques

When a variety of physicochemical properties of solids are correlated with crystal structures, it is necessary to identify specific crystal directions, because many properties are directional. As for isotropic liquids, it is of no need to consider such a situation. Instead, much attention must be paid to ionic species, complexation, and clustering in the molten salts. In physics and chemistry of molten salts with multivalent cations and univalent anions, novel developments are progressing smoothly, typical examples of which are molecular dynamics simulations of structures (Wilson and Madden, 1993) and Raman spectra (Pavlatou et al., 1997) interpreted on the basis of the polarizable-ion model.

Liquid structure of lanthanide trichlorides has been studied in some detail by XRD and/or Raman spectroscopy, for instance, pure $CeCl_3$ with hexagonal UCl_3-type crystal structure (Mochinaga et al., 1993a) and $ErCl_3$ with monoclinic $AlCl_3$-type (Iwadate et al., 1994). These results indicate that the nearest-neighbor chloride coordination number of Ce^{3+} ions decrease from 9 in the crystal to 6 in the melt and that CN for Er^{3+} ions remains unchanged to 6 in both crystal and melt, in any event, allowing for octahedral geometry around the lanthanide ions. Some difference in bond nature is, however, predictable from Ce–Ce and Er–Er distances as well as from volume increases on melting. Consequently, there appear to exist corner-sharing linkage of octahedra in molten $CeCl_3$ and edge-sharing combination of octahedra in molten $ErCl_3$, in the sense of “most probable type of linkage.” This finding may characterize the melting behavior of a series of lanthanide trichloride crystals (Iwadate et al., 1995). Little is, however, known about the structure of molten lanthanide trichlorides mixed with alkali chlorides. The short-range structure of molten $SmCl_3$–LiCl, $SmCl_3$–NaCl, and $SmCl_3$–KCl systems at different compositions and temperatures has been preliminarily analyzed by Raman spectroscopy and XRD (Iwadate et al., 1998). According to these works, the octahedral $SmCl_6{}^{3-}$ complex anions are found to exist indeed not only in the pure melt but also in the mixtures. In particular, peak splitting in the isotropic Raman component is clearly identified in the reduced Raman spectra of mixtures, probably, with increasing fraction of distorted $SmCl_6{}^{3-}$ species and bridged octahedra. This hypothesis is confirmed for the molten $SmCl_3$–NaCl system by conventional molecular dynamics simulation in relationship with ND experiments on YCl_3 melt by Saboungi et al. (1991) and in a report on melting and liquid structure of polyvalent metal halides by Tosi (1994a). Furthermore, another aim of this work is to investigate the ionic arrangements in molten $SmCl_3$–NaCl system as a prototype of lanthanide trichlorides/alkali chlorides mixtures.

As demonstrated in Section 4, computer-aided simulations such as the molecular dynamics method and the Monte Carlo method (MC) have made essential contributions to physics and chemistry of molten salts for more than four decades. Therefore, the author's research group has applied MD to the structural analysis of molten $SmCl_3$–NaCl system (Iwadate et al., 1999). The MD calculations were carried out as follows: 800 or 840 particles corresponding to the melt compositions ($SmCl_3$ mol%: 100, 75, 50, and 25) were randomly located in a basic cubic cell, the length of which ranged from 2.908 to 2.967 nm, reflecting the measured molar volumes of the melt mixtures (Fukushima et al., 1997).

The Born–Mayer–Huggins-type potential described by Eq. (26) was assumed to be applicable to *i*–*j* pairs of particles, but parameters C_{ij} and D_{ij} for dipole–dipole and dipole–quadrupole interactions, respectively, were disregarded in this work.

$$\varphi_{ij}(r) = \left(Z_i Z_j e^2/r\right) + A_{ij} b \exp\left[\left(\sigma_i + \sigma_j - r\right)/\rho\right] - \left(C_{ij}/r^6\right) - \left(D_{ij}/r^8\right) \quad (26)$$

$$A_{ij} = 1 + (Z_i/n_i) + \left(Z_j/n_j\right) \quad (27)$$

where Z_i is the electric charge of the *i*th ion, *e* the elementary electric charge, *r* the interionic separation, A_{ij} the Pauling factor defined by Eq. (27) with n_i the number of electrons in the outer shell, *b* the repulsive parameter (0.338×10^{-19}J), σ_i the size parameter relative to the ionic radius, ρ the softness parameter. The parameters were determined after repeated trial and error cycles so as to reproduce the reduced XRD intensity function $Q \cdot i(Q)$ as closely as possible. The predictor–corrector method (Gear, 1971) was used as an algorithm for the calculation of particle coordinates and the Ewald method for Coulomb forces. A total of 10,000 steps (time step $\Delta t = 2$ fs), extending up to 20 ps, were accumulated at constant temperature according to Nosé's method (Nosé, 1984). The coincidence of interference functions $Q \cdot i(Q)$s derived from XRD and MD for $SmCl_3$(25 mol%)–NaCl(75 mol%) melt at 903 K are displayed in Fig. 30, expressing the validity of the pair potential used.

According to statistical data on particle position and velocity simulated using the following pair potential parameters $Z_{Sm} = 3$, $Z_{Na} = 1$, $Z_{Cl} = -1$, $\sigma_{Sm} = 0.120$ nm, $\sigma_{Na} = 0.105$ nm, $\sigma_{Cl} = 0.175$ nm, and $\rho = 0.025$ nm, the pair correlation function $g_{ij}(r)$ and the running coordination number $N_{ij}(r)$ are defined by Eqs. (28) and (29), respectively.

$$g_{ij}(r) = \left\{V/\left(N_i N_j\right)\right\} \sum_{j}^{Nj} n_{ij}(r - \Delta r/2; r + \Delta r/2)/\left(4\pi r^2 \Delta r\right) \quad (28)$$

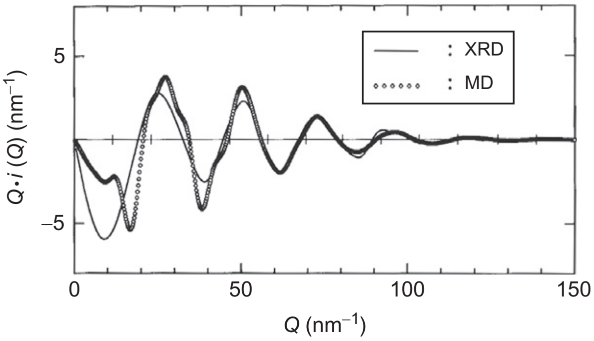

FIGURE 30 Interference function $Q \cdot i(Q)$ for molten $SmCl_3$(25mol%)–NaCl(75mol%). *Reproduced with permission from Iwadate et al. (1999), © 1999 Elsevier.*

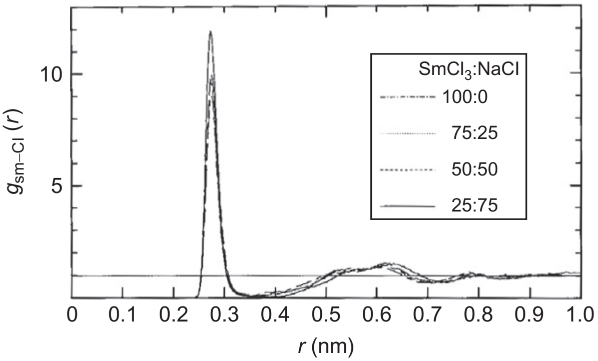

FIGURE 31 Pair correlation function $g_{\mathrm{Sm-Cl}}(r)$. *Reproduced with permission from Iwadate et al. (1999), © 1999 Elsevier.*

$$N_{ij}(r) = \int_0^r 4\pi \rho_j r'^2 \, g_{ij}(r) dr' \tag{29}$$

where Ni and Nj are the numbers of ions i and j, respectively, $n_{ij}(r - \Delta r/2;\ r + \Delta r/2)$ the number of ions j in the spherical shell of a radius range from $r - \Delta r/2$ to $r + \Delta r/2$ with ion i being at the origin, and ρj the average number density of ion j. In estimating coordination numbers, integration was made up to the second point at which $g_{ij}(r)$ becomes unity, not the first minimum. A sample of the $g_{ij}(r)$s and $N_{ij}(r)$s obtained from MD calculations at 953 K is shown in Figs. 31 and 32, and the first peak positions in $g_{ij}(r)$s for several pair correlations are given in Table 25.

As for pure $SmCl_3$ melt, the first peak positions in $g_{ij}(r)$s occur at 0.529 nm, 0.275 nm, and 0.359 nm for Sm–Sm, Sm–Cl, and Cl–Cl pair correlations, respectively. It is evident from the first two distances that one Sm^{3+} ion is not in direct contact with the other (no Sm–Sm bonding) and that some

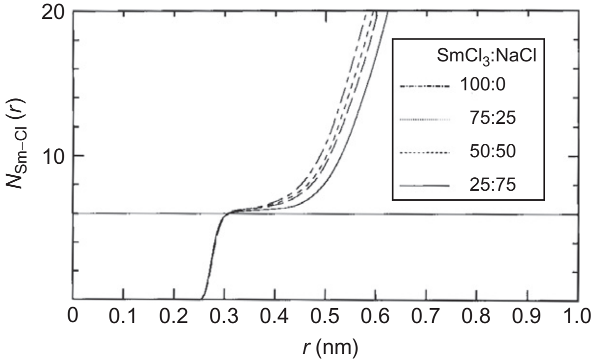

FIGURE 32 Running coordination number $N_{Sm-Cl}(r)$. *Reproduced with permission from Iwadate et al. (1999), © 1999 Elsevier.*

TABLE 25 First Peak Positions in $g_{ij}(r)$s for the Molten $SmCl_3$–NaCl System at 953 K (Iwadate et al., 1999)

$SmCl_3$ (mol%)	100	75	50	25
r_{Sm-Sm} (nm)	0.529	0.531	0.529	0.535
r_{Sm-Cl} (nm)	0.275	0.273	0.275	0.273
r_{Cl-Cl} (nm)	0.359	0.363	0.367	0.379

Cl^- ions are always inserted between the two Sm^{3+} ions. The distance ratio r_{Cl-Cl}/r_{Sm-Cl} amount to 1.305, which is roughly equal to $\sqrt{2}$, and, furthermore, the running coordination number $N[Sm–Cl(r)]$ reaches a plateau in the range $0.3 \leqq r/\text{nm} \leqq 0.4$, the magnitude of which is about 6. These findings indicate that six Cl^- ions are octahedrally coordinated to a Sm^{3+} ion. In conjunction with Raman spectroscopic data (Iwadate et al., 1998), it was confirmed that octahedral complex ions of the type $SmCl_6^{3-}$ exist in the melt. Regarding $SmCl_3$–NaCl mixture melts, $g_{Sm-Cl}(r)$ and $N_{Sm-Cl}(r)$ at $SmCl_3$ concentrations of 50 and 75 mol% behave similarly as in the case of pure $SmCl_3$ melt. But at 25 mol% composition, the first peak in $g_{Sm-Cl}(r)$ becomes more intense, the other peak position shifts to the right, and the plateau in $N_{Sm-Cl}(r)$ becomes longer, as illustrated in Figs. 31 and 32. In the same way, it was found from the first peak in $g_{Cl-Cl}(r)$ that the nearest-neighbor Cl–Cl distance is lengthened with decreasing $SmCl_3$ concentration and therefore that the ratio of the first peak position in $g_{Cl-Cl}(r)$ to that in $g_{Sm-Cl}(r)$ approaches $\sqrt{2}$, a value corresponding to octahedral geometry. Other features reveal that the octahedra are less distorted with decreasing $SmCl_3$ concentration and this trend appears strongly at 25 mol% of $SmCl_3$, the concentration of which corresponds to the point for which the local composition of ($3Na^+ + SmCl_6{}^{3-}$) is identical to the stoichiometry of the mixed melt.

The location of Na^+ ions was determined from Sm–Na, Na–Cl, and Na–Na correlations. In comparison with the first peak positions in the $g_{ij}(r)$ functions of these three distinct correlations, Na–Cl correlation possesses a sharp peak at $r = 0.29$ nm, independent of $SmCl_3$ concentration. But for Sm–Na and Na–Na correlations, only broad peaks appears in the r-range between 0.42 and 0.57 nm as well as between 0.35 and 0.50 nm, respectively. It is therefore natural that $N_{\mathrm{Sm-Na}}(r)$ decreases with increasing $SmCl_3$ concentration; more interestingly, the mode of the first peak in $g_{\mathrm{Sm-Na}}(r)$, statistically defined, is situated around $r_{\mathrm{Sm-Na}} = 0.5$ nm at $SmCl_3$ concentrations between 25 and 50 mol%. In contrast, the corresponding value is quite shortened, 0.46 nm, at 75 mol%. This fact is tentatively ascribed to the fact that the linkages between $SmCl_6{}^{3-}$ units are broken by addition of NaCl and thus that the Na^+ ions enter into the gap shaped between the newly formed octahedra.

In MD simulation, the coordinates of all particles were calculated at every step and thus the distribution of the number of coordinated Cl^- ions around a Sm^{3+} ion could be studied in detail. At this stage, it is of high importance to determine the range of the first coordination shell. The limiting distance of the first coordination shell (LDFCS) defining the dimension of the shell is defined in the following ways; it corresponds to (1) the second point at which $g_{\mathrm{Sm-Cl}}(r)$ becomes unity, r_1 and (2) the first minimum in $g_{\mathrm{Sm-Cl}}(r)$ just after the first peak, r_2. The values of LDFCSs are tabulated in Table 26. It should be stressed that coordinative bond formation between Sm^{3+} and Cl^- depends on the magnitude of LDFCS.

Under these conditions, the number of Cl^- ions surrounding a given Sm^{3+} ion is counted up to the distance r_1 or r_2. The results are depicted in Figs. 33 and 34, respectively.

In the first case, most of the Sm^{3+} ions are found to be coordinated by six Cl^- ions at every concentration of $SmCl_3$ (Fig. 33). On the contrary, if the distribution of coordination numbers is still centered at six in Fig. 34, a marked shoulder points to a nonnegligible quantity of ions displaying CN = 7. If this

TABLE 26 Limiting Distances of First Coordination Shell (LDFCS) in Pair Correlation Function $g_{\mathrm{Sm-Cl}}(r)$ for Molten $SmCl_3$–NaCl System (Iwadate et al., 1999)

$SmCl_3$ (mol%)	100	75	50			25
Temp. (K)	953	953	753	853	953	953
r_1 (nm)	0.304	0.307	0.311	0.308	0.307	0.305
r_2 (nm)	0.353	0.351	0.353	0.351	0.355	0.391

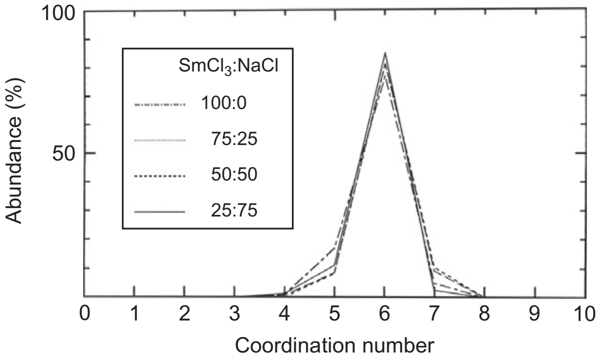

FIGURE 33 Distribution of coordination numbers for Sm–Cl pair in molten $SmCl_3$–NaCl system at 953 K: Integration up to the second point at which $g_{Sm-Cl}(r)$ become unity. *Reproduced with permission from Iwadate et al. (1999), © 1999 Elsevier.*

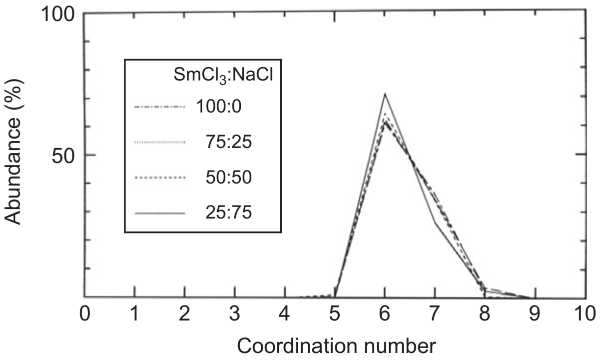

FIGURE 34 Distribution of coordination numbers for Sm–Cl pair in molten $SmCl_3$–NaCl system at 953 K: Integration up to the first minimum in $g_{Sm-Cl}(r)$. *Reproduced with permission from Iwadate et al. (1999), © 1999 Elsevier.*

were true (r_2 was used to test bond formation), it means that every Sm^{3+} ion is combined with another one through Cl^- bridging ions, leading to not only large polyatomic anions but also to a network structure. $SmCl_3$–NaCl mixture melts including pure $SmCl_3$ melt are much less viscous than network-forming $ZnCl_2$ melt. Raman data (Iwadate et al., 1998; Matsuoka et al., 1993) and XRD studies (Mochinaga et al., 1991) reported so far support the hypothesis of the presence of octahedral species with sixfold coordination, and therefore, it is rational to define the LDFCS with respect to r_1, not r_2. As a consequence, fivefold or sevenfold coordination appear to be virtually impossible.

The following conclusions can be drawn from detailed analyses of the pair correlation and running coordination functions.

(I) Octahedral complex species of the type $SmCl_6^{3-}$ exist, as deduced from Raman and XRD data.

(II) Rational estimates of the important parameter LDFCS point to bond formation between Sm^{3+} and Cl^{-}.

Many novel details and suggestions for the structure of molten rare-earth halides have been gained from advanced simulations different from the conventional ones presented earlier (Hutchinson et al., 1999). For instance, simulations using a polarizable, formal charge ionic interaction model are reported for a range of RX_3 molten salts. The $LaCl_3$, $TbCl_3$, and YCl_3 systems studied span a range of cation sizes and the interaction model is a “generic” one, in the sense that the cation size is the only parameter in the interaction potential which distinguishes one system from another. The liquid structures predicted from the simulations are compared with recently obtained ND data. Excellent agreement is found, except that the first coordination shell seems to be too tightly bound in the theoretical model. The cation in $LaCl_3$ is found to be seven- to eightfold coordinate, and the coordination number drops to 6 for the smallest cation considered (Y^{3+}) so that the coordination number in these systems does not change substantially on melting, in contrast to earlier reports. The polarization effects promote a significant degree of edge-sharing between these coordination polyhedra relative to predictions from a simple ionic pair potential model. Associated with these changes is a shift to smaller scattering vectors of the prepeak in the structure factor and an increase in the fluidity.

MD simulations have been performed with another goal of reproducing not only experimental structural but also vibrational data for ionic rare-earth chloride melts. Pavlatou et al. have reported simulations of the short-time, vibrational dynamics of the network-forming ionic melts $LaCl_3$, and its mixtures with network-breaking alkali halides. In the mixtures, high-frequency peaks in the vibrational density of states are describable in terms of the normal coordinates of the vibrations of transient molecular ion species, like $LaCl_6^{3-}$ (Pavlatou et al., 1997). Concretely speaking, the densities of states (DOS) of the Cl^{-}, La^{3+}, and K^{+} ions were obtained for the $LaCl_3$–4KCl solution where the DOS spectrum of the K^{+} cations was characterized by a single band centered at about 50 cm^{-1}, while the corresponding spectra of the Cl^{-} and La^{3+} ions were more “structured.” This structure might be associated with vibrational motions of the $LaCl_6^{3-}$ ions evident from the snapshots (see Fig. 35). In the same way, the snapshots of the structure of pure $LaCl_3$ melt indicates that La^{3+} ions remain predominantly six coordinate in the melt but that the octahedral units are linked together, building a network. The implication of this for the vibrational dynamics is that the vibrations of the individual octahedral units are somewhat coupled.

Interpretation of Raman spectra by computer simulation has been extended to the complex-forming $ScCl_3$ melt, again using the polarizable-ion interaction model (Madden et al., 2004). Their final conclusions are summarized in the paper titled *Raman Spectra of Ionic Liquids: A Simulation Study of* $LaCl_3$ *and Its Mixtures with Alkali Chlorides* (Glover and Madden, 2004) in which

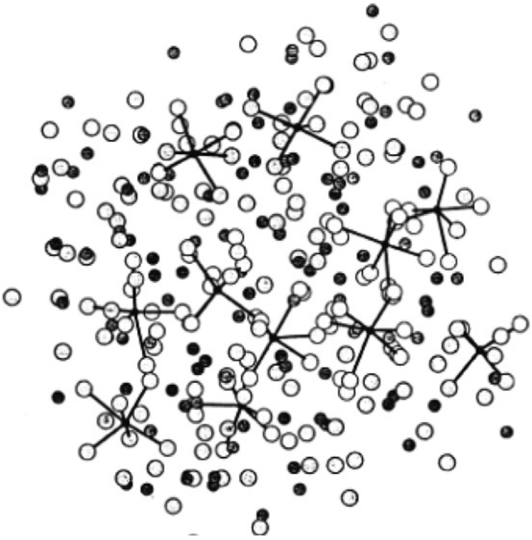

FIGURE 35 Molecular graphics "snapshots" of molten $LaCl_3$–4KCl. The large spheres are the Cl^- ions, the medium the K^+, and the smallest the La^{3+}. "Bonds" are drawn between La–Cl pairs at separations of less than 3.3 Å. *Reproduced with permission from Pavlatou et al. (1997), © 1997 American Institute of Physics.*

Raman spectra of $Cs_2NaLaC1_6$ and of $LaC1_3$ and its mixtures with NaCl and CsCl are calculated. These calculations are much more extensive than previous ones and allow a systematic exploration of the spectra for this all range of systems. Although there is a systematic overestimation of the vibrational frequencies, the pattern of the spectra and their evolution with mixture composition match experimental results very well. For crystals, a clear link between the predicted spectral bands and the measured vibrational DOS of the $LaC1_6{}^{3-}$ coordination centers is seen. In the molten mixtures, bands are seen at similar frequencies, *despite the fact that 6-coordination is no longer predominant according to* Madden et al. (2004), except in dilute solutions. The coordination number of the La^{3+} ions increases from 6 in dilute solution to between 7 and 8 for the pure melt. This increase appears to occur when the coordination centers begin to cross-link. CsCl appears to be a much better structure breaker than NaCl so that the coordination units consist of long-lived, isolated $LaC1_6{}^{3-}$ anions for $LaCl_3$ concentrations below 25%.

In the early 1970s, Sayers et al. (1971) have succeeded in applying Fourier analysis to their point-scattering theory of XAFS to formally transform experimental data into a radial structure function with determinable parameters of distance from the absorbing atom, number of atoms, and widths of coordination shells for the evaporated and crystalline Ge systems. With the advent of large-scale synchrotron radiation facilities in the late 1990s, this technique proved to produce excellent results on the local structure around rare-earth cations in several states.

The coordination environment around Gd^{3+} ions in $GdAl_3Cl_{12}$ glass and supercooled liquid has been studied using Gd L_{III}-edge EXAFS spectroscopy (Sen et al., 2000). The Gd coordination environment in the glass is found to be similar to that in the $GdAl_3Cl_{12}$ crystal with eight Cl^- nearest neighbors and four Al^{3+} next-nearest neighbors. The Gd–Cl distance in the glass is the same as in the crystal (~2.8 Å) although the Gd–Al distance in the glass (~3.85 Å) is longer compared to the crystal (~3.7 Å), indicating a less dense structure with a larger Gd–Cl–Al bond angle in the glass. The Gd–Cl distance and coordination number remain unchanged in the supercooled liquid at 60 °C as demonstrated from EXAFS spectra (Fig. 36). However, the absence of any Gd–Al second-neighbor shell in the EXAFS spectra of the liquid indicates substantial increase in static disorder in the spatial distribution of $AlCl_4$ tetrahedra around Gd in the liquid. Such temperature-dependent structural changes are probably responsible for the marked fragility of this liquid.

In line with the increasing use of XAFS spectroscopy for elucidating the nearest-neighbor structure in condensed phases, XAFS spectra of $NdCl_3$ and $DyCl_3$ in both solid and liquid phases have been measured at the Nd and Dy L_{III} absorption edges on beam line BM29 of the European Synchrotron Radiation Facility (ESRF) (Matsuura et al., 2001). The Fourier-transformed radial structure functions $\varphi(r)$ show that the prominent peaks corresponding to R–Cl (R = Nd, Dy) first shell contributions are shifted to shorter distances in the liquid melts as compared to those found in the corresponding solids. A similar behavior has been observed with other diffraction techniques in typical ionic melts such as NaCl. The temperature dependence of the radial

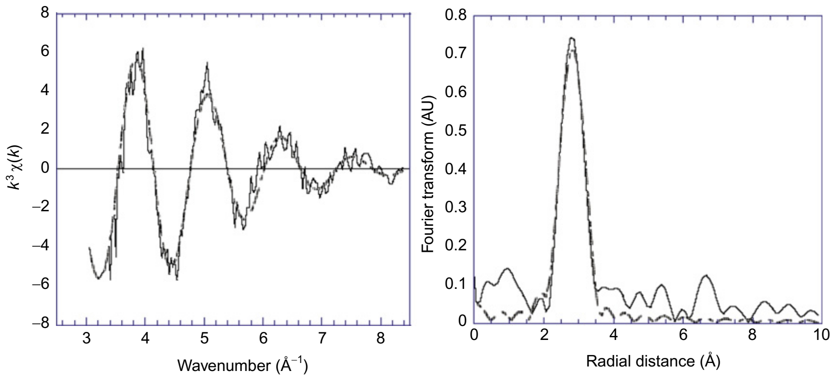

FIGURE 36 (Left) k^3-weighted Gd L_{III}-edge EXAFS and (right) the corresponding Fourier-transformed partial radial distribution function for Gd^{3+} ions at 60 °C in the $GdAl_3Cl_{12}$ supercooled liquid. Solid lines represent experimental data and dashed lines correspond to least-squares fits. *Reproduced with permission from Sen et al. (2000), © 2000 IOP Pub.*

structure functions clearly point to the change in the M–Cl distance upon melting being much larger for $NdCl_3$ compared to $DyCl_3$.

The local structure and structural changes in molten YCl_3–LiCl–KCl and YBr_3–LiBr systems have been investigated by using a high-temperature extended X-ray absorption fine structure (EXAFS) technique (Okamoto et al., 2001). Octahedral coordination of halide ions around the Y^{3+} ion has been studied by EXAFS of the Y^{3+} K-absorption edge. The nearest Y^{3+}–Cl^- and Y^{3+}–Br^- distances and the coordination numbers of halide ions around the Y^{3+} ion do not change by mixing with the alkali halides. Stabilization of the octahedral $[YCl_6]^{3-}$ and $[YBr_6]^{3-}$ anions upon addition of alkali halides was suggested from the decrease in the Debye–Waller factor and the anharmonicity of the nearest Y^{3+}–Cl^- and Y^{3+}–Br^- interactions. The bridging structure of the $[YBr_6]^{3-}$ octahedra sharing a Br^- ion in the molten YBr_3–LiBr system was studied by EXAFS of the Br K-absorption edge. The number of coordinated Y^{3+} around the Br^- ion decreases from 2 in the pure melt to almost unity in the 30 and 15 mol% YBr_3 melts. This suggests that the bridging is almost broken and that stable octahedra exist freely in the LiBr-rich melts. Schematic diagrams of isolated and bridged species found in the melts are presented in Fig. 37. Improvements of the sample cell and furnace led to better measurement accuracy, but the above conclusions were not altered (Okamoto et al., 2002).

As for the local structure of molten $LaCl_3$, the nearest-neighbor La–Cl distance and coordination number of La^{3+} were estimated from the radial distribution analysis of XRD to be about 0.28 nm and nearly equal to 6, respectively. On the other hand, according to the La–L_{III} absorption-edge XAFS technique, the number of coordinated Cl^- around La^{3+} was evaluated to be around 7. As a result, the local structure of molten $LaCl_3$ was described as an octahedral-like coordination scheme where La^{3+} is surrounded by six or seven chloride anions. This implies the presence of octahedral complex ions, $[LaCl_6]^{3-}$, in agreement with Raman data reported by other authors. The La–La distance was evaluated at about 0.5 nm from the position of a weak and broad second peak in the correlation function $g(r)$, suggesting that a distorted corner-sharing connection of two octahedral complex species was predominant in the melt. The difference between the numbers of nearest-neighbor Cl^- around La^{3+} obtained by X-ray and XAFS measurements could not be explained in a paper in which a new method for correcting diffraction data was proposed to prevent the coordination number from being reduced in real space (Iwadate et al., 2006).

Rollet et al. (2004) have developed a cell for high-temperature X-ray absorption measurements in both solid and molten lanthanide fluorides. Two plates of pyrolitic boron nitride are fixed hermetically together around the sample in order to avoid any evaporation and interaction with the atmosphere. EXAFS spectra of molten mixtures of LiF–LaF_3 measured at the La–L_{III} absorption-edge are reported up to 900 ºC and show the tightness of this cell which allows data acquisition during a long time, thereby improving the signal-to-noise ratio.

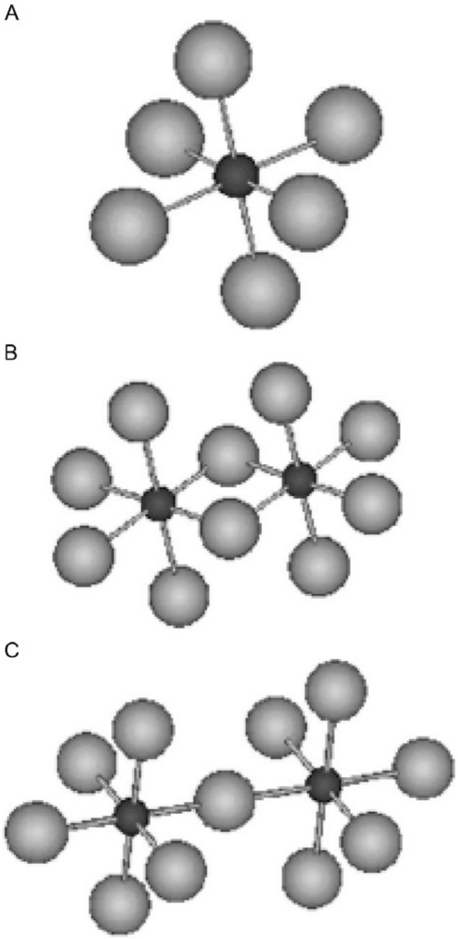

FIGURE 37 Models of local structures for molten rare-earth trihalides. (A) Octahedral coordination $[MX_6]^{3-}$, (B) edge-sharing model, (C) corner-sharing model. Small ball, metal ion M^{3+}; large ball, halide ion X^-. *Reproduced with permission from Okamoto et al. (2001), © 2001 International Union of Crystallography.*

The above work should stimulate future XAFS researches on molten alkali metal fluoride systems including rare-earth fluorides, in which the numbers of coordinated fluorides were reported to be in the wide range of 3 to 10 (Matsuura et al., 2009; Numakura et al., 2010; Watanabe et al., 2006). Though XAFS has become a very powerful tool due to improvements of high-energy synchrotron radiation facilities, it is of importance to bear in mind that the accuracy in coordination number is of the order of ±10% only, making precise evaluation of coordination numbers quite difficult.

8. CONCLUDING REMARKS

The present review has outlined the major structural properties of rare-earth molten salts as unraveled from several experimental techniques. Some systematic and common trends have been obtained. However, there is no common understanding of the structural characteristics of molten rare-earth halides such as fluorides, bromides, and iodides. Moreover, discrepancies in structural information about molten rare-earth chlorides still exist, particularly with respect to coordination numbers, despite more than 20 years of heated discussions.

The crystal structure of rare-earth trichlorides can be divided broadly into two categories, one concerning light rare earths (La–Gd) and the other the heavier ones (Y, Dy–Lu, but excluding Tb). The crystal structure of light rare-earth chlorides is of UCl_3-type in which the metal cation is surrounded by three chlorides forming a triangle and six chlorides at the corners of a hexagonal prism, resulting in a ninefold coordination. The crystal structure of heavy rare-earth chlorides is, in contrast, of $AlCl_3$-type in which the metal cation is octahedrally coordinated by six chlorides. Incidentally, $TbCl_3$ is out of the above crystal scheme, the structure of which is orthorhombic and of $PuBr_3$-type. Each Tb possesses eight nearest Cl neighbors at an average distance of 2.81 Å (Forrester et al., 1964).

Akdeniz and Tosi (1992) have declared that there also exist two structure categories for molten rare-earth trichlorides. During the phase transition from solid to liquid, the molar volume of a typical light rare-earth chloride decreases by as much as 20% while that of a heavy rare-earth chloride hardly changes ca. 0–5% at most. This conclusion has proved valid and was confirmed in a subsequent paper (Iwadate et al., 1995), see Table 27. The entropy change of a light rare-earth chloride on melting is therefore larger than that of a heavy rare-earth chloride.

As mentioned thus far, the melting behavior has been explained in terms of structural information obtained from experimental techniques such as XRD, ND as well as from molecular dynamics simulations. Iwadate et al. (1995) have obtained the nearest-neighbor distances and coordination numbers of several ion pairs by model fitting of the XRD structure factors. From these studies, it has been suggested that each rare-earth cation is coordinated to six chloride ions in the melt. Further suggested is that the local octahedral units, $[RCl_6]^{3-}$ are linked to each other through apexes of octahedra in light rare-earth chloride melts, while they share edges of octahedra in heavy rare-earth chloride melts.

Some research groups have proposed a slightly different picture for pure melts of light rare-earth chlorides (not for mixtures) on the basis of ND data and MD simulations. For example, Wasse and Salmon (1999d) have reported from pdfs that integration of the first peak over the range $2.50 \leqq r(\text{Å}) \leqq 3.37$ to the first shoulder gives a number of coordinated Cl^- around La^{3+} equal to 6.7,

TABLE 27 Molar Volume Changes on Melting (Iwadate et al., 1995)

System	$LaCl_3$	$CeCl_3$	$PrCl_3$	$NdCl_3$	$SmCl_3$	$GdCl_3$	$DyCl_3$	$HoCl_3$	$ErCl_3$	YCl_3
T_m (K)	1150	1095	1059	1029	935	875	928	993	1046	987
V_s ($cm^3\ mol^{-1}$)	63.90	62.42	61.40	60.47	59.23	58.03	74.38	73.02	72.11	74.83
V_m ($cm^3\ mol^{-1}$)	76.30	76.06	74.30	73.65	73.73	73.34	74.62	74.00	75.65	75.17
$100(V_m - V_s)V_s^{-1}$ (%)	19.1	21.9	21.0	21.8	24.5	26.4	0.3	1.3	4.9	0.5

while integration to the first minimum at 3.86 Å gives 8.2 as the corresponding coordination number, and the authors think that the latter value is preferable. But such a large CN requires the presence of many anion–anion "contacts" in the melt, as pointed out by Hutchinson et al. (1999), which does not seem to be logical. With the help of MD calculation and the structure factors reported by Wasse and Salmon (1999d), Madden et al. (2004) have simulated similar data for the number of coordinated Cl^- around La^{3+} by integrating the La–Cl pdf up to the first minimum. The experimental results are thought to be quite reliable and the calculation procedures are correct, within the definitions of CN used. However, we would like to draw the attention of the readers on the conclusions of Sections 4.2.5 and 4.2.6. The values of CNs are directly influenced by the definitions adopted for CN, the integration range, and whether penetration of the coordination shell of Cl–Cl pairs into that of La–Cl pairs occurs or not. The simulated pdfs of molten $LaCl_3$ and molten YCl_3 suggest the importance of the integration range in the evaluation of the nearest-neighbor CN (Hutchinson et al., 1999), as illustrated in Fig. 38. In fact, the first coordination shell of Cl–Cl pairs penetrates deeply

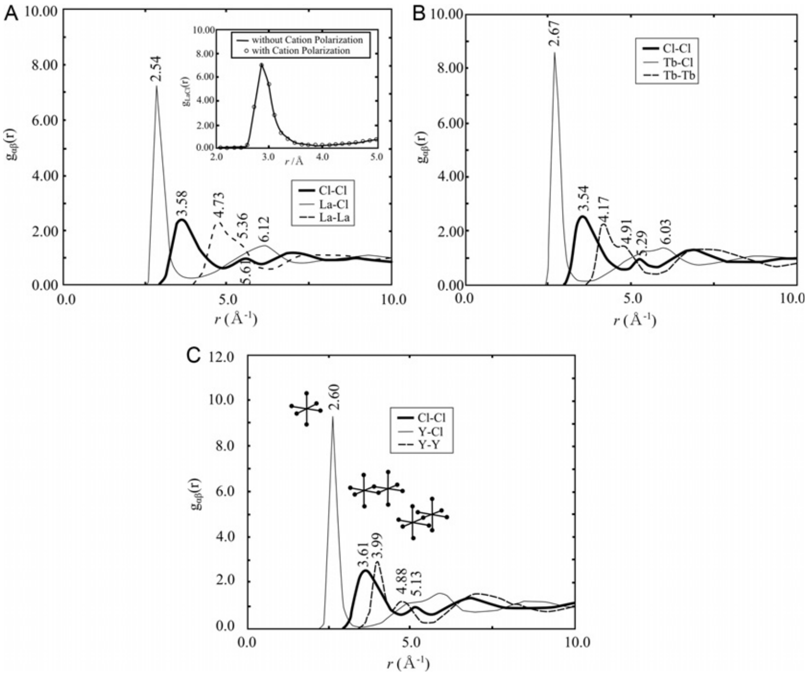

FIGURE 38 Partial pair distribution functions for (A) $LaCl_3$. [The inset shows the effect of including cation polarization on $g_{LaCl}(r)$.] (B) $TbCl_3$ and (C) YCl_3 with peak positions displayed. In (C), molecular models are given for YCl_3, showing several of the Y–CI, Y–Y, and Cl–Cl interionic distances corresponding to the various peaks (bold lines). *Reproduced with permission from Hutchinson et al. (1999), © 1999 American Institute of Physics.*

into that of La–Cl pairs in comparison with the case of molten YCl_3; moreover, the first coordination shell of La–Cl pairs possesses a long tail extending up to the first minimum of the pdf, at which the value of the pdf is much larger than in molten YCl_3. This situation tends to lead to overestimation of CNs. Therefore, the author thinks that integration of the first coordination shell of La–Cl pairs up to the point where the first coordination shells of La–Cl pairs and Cl–Cl pairs cross each other is a better procedure. Alternatively, integration can be carried out up to the second point at which $g_{\mathrm{La\text{–}Cl}}(r)$ becomes unity as described in MD simulations for $SmCl_3$–NaCl system (Iwadate et al. (1999)). As for higher CNs such as 7 or 8 obtained by extending the integration range up to the first minimum of the pdf, they can be explained without invoking the existence of $[LaCl_7]^{4-}$ or $[LaCl_8]^{5-}$ species. They arise because the separations among the central La^{3+} cations and the Cl^- ligands are not necessarily isotropic, as hinted by the long-tail of the first peak before the first minimum in $g_{\mathrm{La\text{–}Cl}}(r)$. The Raman spectra reported by Zissi et al. (2006) only feature the vibrational modes of octahedral species, meaning that $[LaCl_6]^{3-}$ exists as a chemical species in pure $LaCl_3$ melt. The variation in CN during the melting process of $LaCl_3$, from 9 to 8, is, however, regarded to be too small in comparison with a ~20% volume change (see data in Sections 4 and 6). If we consider all the reported data and interpret them according to the above context, we have to admit that some discrete Cl^- ions surround the octahedral species $[LaCl_6]^{3-}$ locally and induce ligand exchange with $[LaCl_6]^{3-}$ at short intervals as well as some clustering among octahedra by bridging through one or two chlorides. This is probably the real situation in the $LaCl_3$ melt. In other words, this means that different authors see the same data but analyze them with different models and definitions and, therefore, derive different conclusions.

Consequently, it is concluded from the discussion up to this point that polyhedral-type complex ions are formed in the molten salt systems including multivalent cations, which are further linked each other, building up clusters. The structure of molten $ZnCl_2$ illustrated in Fig. 39 represents such an example. Two tetrahedral $ZnCl_4{}^{2-}$ complex ions are linked through a common Cl^- (corner-sharing) and form clusters of higher order, which causes high viscosity and wide temperature range of supercooling phenomena for this melt. The Zn–Cl–Zn angle is estimated at about 140° in the melt, which is larger than the corresponding angle in crystals, 109°. The clustering of complex ions takes more complicated aspects with increasing valence of the central metal ion such as rare-earth cations, as demonstrated in Fig. 40. The La^{3+} ion is located at the center of the octahedron and surrounded by six Cl^- ions. There exist discrete octahedra and corner-shared clusters in low concentrations of $LaCl_3$, the abundance of edge-shared clusters may increase with increasing $LaCl_3$ concentration. Such a structural complexity is responsible for the diversity observed in physicochemical properties of molten rare-earth compounds.

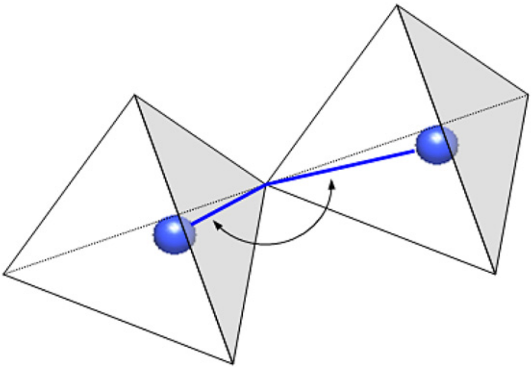

FIGURE 39 Tetrahedral complex ions and clustering in molten $ZnCl_2$. *Reproduced with permission from Iwadate et al. (2004), © 2004 Elsevier.*

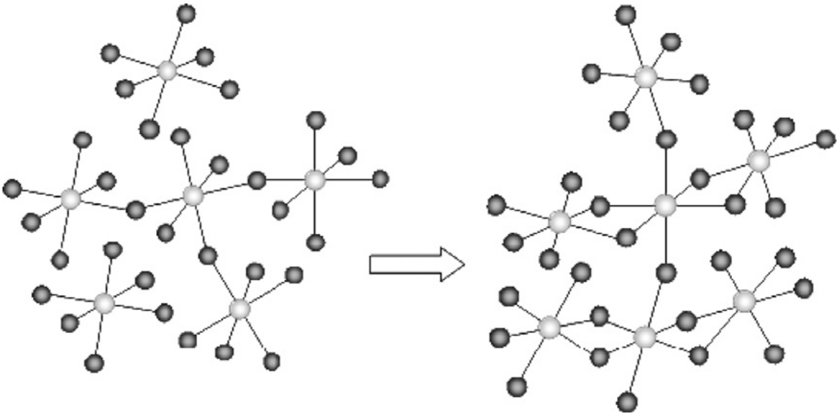

FIGURE 40 Conceptual diagram of high-ordered clustering of octahedral units in the $LaCl_3$ mixture melt ($LaCl_3$ concentration: low ⇒ high); white balls: La^{3+}; gray balls: Cl^-. *Reproduced from Photiadis et al. (1998), © 1998 Royal Society of Chemistry and Iwadate et al. (2009), © 2009 Electrochemical Society of Japan.*

In summary, we have tried to comprehend the structures and properties of rare-earth molten salts by critically discussing the following points. (1) Definitions of molten salts as liquids; (2) crystal structures of rare-earth halides; (3) melt structure of rare-earth halides analyzed by diffraction, Raman spectroscopy, and other techniques; (4) methodology for obtaining structural information from diffraction experiments: definition of the RDF, estimation of nearest-neighbor coordination number from RDF, stability of the nearest-neighbor coordination shell, and penetration effect of the second coordination shell; (5) density of rare-earth halides in solid and molten states. The properties listed above are static properties and represent merely half of all properties of the melts. Dynamic properties of rare-earth compounds in solid and molten states, such as diffusion, viscous flow, electrical conduction, thermal conduction, ligand exchange, are largely unexplored and should be investigated. Experimental techniques are presently available, for instance, high-temperature NMR which has been developed in recent years. Acquiring both dynamic and static properties of molten rare-earth compounds will benefit their global understanding. Moreover, macroscopic properties permit the discussion of microscopic properties and the reverse procedure should be implemented too. Therefore, correct application of theory to the real systems is highly desirable.

ACKNOWLEDGMENTS

The author would like to express my sincere gratitude to Professor Karl A. Gschneidner, Jr. for giving me the opportunity to write for the *Handbook on the Physics and Chemistry of Rare Earths*. The author would particularly like to thank Professor Gin-ya Adachi and Professor Jean-Claude Bünzli for their arrangements, encouragements, and patience in the course of publication. My deepest appreciation also goes to the members of "Molten salt committee, The Electrochemical Society of Japan" for discussions, in particular, to Professor Junichi Mochinaga. Finally, special thanks would be dedicated to Kato Foundation for Promotion of Science, Japan for financial supports making possible part of our experiments.

LIST OF ACRONYMS

CN	coordination number
DOS	density of states
ESRF	European Synchrotron Radiation Facility
EXAFS	extended X-ray absorption fine structure
FSDP	first sharp diffraction peak
LDFCS	limiting distance of the first coordination shell
MC	Monte Carlo simulation
MD	molecular dynamics simulation
ND	neutron diffraction
pdf	pair distribution function
PIM	polarizable ion model
Raman	Raman spectroscopy
RDF	radial distribution function
RE	rare-earth element
RIM	rigid ion model
XAFS	X-ray absorption fine structure
XRD	X-ray diffraction

REFERENCES

Adams, D.J., McDonald, I.R., 1974. J. Phys. C: Solid State Phys. 7, 2761.

Adya, A.K., 2002. In: Gaune-Escard, M. (Ed.), Molten Salts: From Fundamentals to Applications. Kluwer Academic Publishers, London, p. 107.

Adya, A.K., 2003. In: Proceedings of International Symposium on Ionic Liquids in Honour of Marcelle Gaune-Escard, June 26-28, 2003. Carry le Rouet, France, 411.

Akdeniz, Z., Tosi, M.P., 1992. Proc. R. Soc. Lond. Ser. A 437, 85.

Akdeniz, Z., Price, D.L., Saboungi, M.-L., Tosi, M.P., 1998. Plasmas & Ions 1, 3.

Allen, D.A., Howe, R.A., Wood, N.D., Howells, W.S., 1991. J. Chem. Phys. 94, 5071.

Badyal, Y.S., Allen, D.A., Howe, R.A., 1994. J. Phys. Condens. Matter 6, 10193.

Badyal, Y.S., Saboungi, M.-L., Price, D.L., Haeffner, D.R., Shastri, S.D., 1997. Europhys. Lett. 39, 19.

Bell, M.C., Flengas, S.N., 1964. J. Electrochem. Soc. 569–575, 111.

Biggin, S., Enderby, J.E., 1981. J. Phys. C: Solid State Phys. 14, 3577.

Biggin, S., Gay, M., Enderby, J.E., 1984. J. Phys. C 17, 977.

Bloom, H., Knaggs, I.W., Molloy, J.J., Welch, D., 1953. Trans. Faraday Soc. 49, 1458.

Busing, W.R., Levy, H.A., 1962. Oak Ridge Natl. Lab. Rept. ORNL-TM-271.

Cho, K., Irisawa, K., Mochinaga, J., Kuroda, T., 1972. Electrochim. Acta 17, 1821.

Chrissanthopoulos, A., Papatheodorou, G.N., 2006. J. Mol. Struct. 782, 130.

Chrissanthopoulos, A., Papatheodorou, G.N., 2008. J. Mol. Struct. 892, 93.

Coulson, C.A., Rushbrooke, G.S., 1939. Phys. Rev. 56, 1239.

Dixon, M., Sangster, M.J.L., 1975. J. Phys. C: Solid State Phys. 8, L8.

Dixon, M., Sangster, M.J.L., 1976a. J. Phys. C: Solid State Phys. 9, 909.

Dixon, M., Sangster, M.J.L., 1976b. J. Phys. C: Solid State Phys. 9, L5.

Dracopoulos, V., Gilbert, B., Børrensen, B., Photiadis, G.M., Papatheodorou, G.N., 1997. J. Chem. Soc. Faraday Trans. 93, 3081.

Dracopoulos, V., Gilbert, B., Papatheodorou, G.N., 1998. J. Chem. Soc. Faraday Trans. 94, 2601.

Edwards, J.D., Taylor, C.S., Russell, A.S., Maranville, L.F., 1952. J. Electrochem. Soc. 99, 527.

Egelstaff, P.A., 1967. An Introduction to the Liquid State. Academic Press, London p. 46.

Enderby, J.E., Biggin, S., 1983. In: Mamantov, G., Mamantov, C.B. (Eds.), Advances in Molten Salt Chemistry5, Elsevier, Amsterdam, p. 1.

Forrester, J.D., Zalkin, A., Templeton, D.H., Wallmann, J.C., 1964. Inorg. Chem. 3, 185.

Frame, J.P., Rhodes, E., Ubbelohde, A.R., 1959. Trans. Faraday Soc. 55, 2039.

Fukushima, K., Koseki, S., Wakabayashi, K., Yamane, S., Iwadate, Y., 1997. J. Alloys Compd. 261, 198.

Fukushima, K., Okamoto, Y., Iwadate, Y., 2005. J. Phys. Chem. Solids 66, 414.

Furukawa, K., 1961. Discuss. Faraday Soc. 32, 53.

Furukawa, K., 1962. Rep. Prog. Phys. 34, 395.

Furukawa, K., Ohno, H., 1973. Bussei Kenkyu 19, 1335.

Gear, G.W., 1971. Numerical Initial Value Problems in Ordinary Differential Equations. Prentice Hall, Englewood Cliffs, NJ.

Gebhardt, E., Becker, M., 1943. Z. Metallkunde 39, 314.

Gingrich, N.S., 1943. Rev. Mod. Phys. 15, 90.

Glover, W.J., Madden, P.A., 2004. J. Chem. Phys. 121, 7293.

Husband, L.J.B., 1958. J. Sci. Instrum. 35, 300.

Hutchinson, F., Rowley, A.J., Walters, M.K., Wilson, M., Madden, P.A., Wasse, J.C., Salmon, P.S., 1999. J. Chem. Phys. 111, 2028.

Hutchinson, F., Wilson, M., Madden, P.A., 2000. J. Phys. Condens. Matter 12, 10389.

Hutchinson, F., Wilson, M., Madden, P.A., 2001. Mol. Phys. 99, 811.

Igarashi, K., Kosaka, M., Ikeda, M., Mochinaga, J., 1990. Z. Naturforsch. 45a, 623.

Inui, M., Takeda, S., Shirakawa, Y., Tamaki, S., Waseda, Y., Yamaguchi, Y., 1991. J. Phys. Soc. Jpn. 60, 3025.

Iwadate, Y., 2011. In: Adachi, G. (Ed.), Rare Metal Binran, Maruzen, Tokyo, II-376.

Iwadate, Y., Fukushima, K., Igarashi, K., Mochinaga, J., 1992. J. Fac. Eng. Chiba Univ. 44, 31.

Iwadate, Y., Iida, T., Fukushima, K., Mochinaga, J., Gaune-Escard, M., 1994. Z. Naturforsch. 49a, 811.

Iwadate, Y., Okako, N., Koyama, Y., Kubo, H., Fukushima, K., 1995. J. Mol. Liq. 65/66, 369.

Iwadate, Y., Yamoto, H., Fukushima, K., 1998. Molten Salt Forum 5–6, 193.

Iwadate, Y., Yamoto, H., Fukushima, K., Takagi, R., 1999. J. Mol. Liq. 83, 41.

Iwadate, Y., Seki, Y., Fukushima, K., Misawa, M., Fukunaga, T., 2001a. J. Phys. Soc. Jpn. 70 (Suppl. A), 359.

Iwadate, Y., Kenmotsu, H., Mori, T., Fukushima, K., Misawa, M., Fukunaga, T., 2001b. J. Non-Crystal. Solids 293–295, 586.

Iwadate, Y., Fukushima, K., Seki, Y., Itoh, K., Fukunaga, T., Misawa, M., Matsuura, H., Kajinami, A., Ohtori, N., Umesaki, N., Kofuji, H., Myochin, M., 2004. Sci. Technol. Adv. Mater. 5, 683.

Iwadate, Y., Seki, Y., Fukushima, K., Misawa, M., Fukunaga, T., Itoh, K., Nakazawa, T., Okamoto, Y., Matsuura, H., Kajinami, A., Ohtori, N., Umesaki, N., 2005. J. Phys. Chem. Solids 66, 433.

Iwadate, Y., Suzuki, K., Onda, N., Fukushima, K., Watanabe, S., Kajinami, A., Takase, K., Ohtori, N., Umesaki, N., Kofuji, H., Myochin, M., 2006. J. Alloys Compd. 408–412, 248.

Iwadate, Y., Matsuura, H., Kajinami, A., Takase, K., Ohtori, N., Umesaki, N., Fujita, R., Mizuguchi, K., Kofuji, H., Myochin, M., 2009. Electrochemistry 77, 736.

Iwamoto, N., Umesaki, N., Asahina, T., Kosaka, M., 1982. Nippon Kinzoku Gakkaishi 46, 920.

Janz, G.J., 1988. J. Phys. Chem. Ref. Data 17 (Suppl. 2).

Janz, G.J., Dampier, F.W., Lakshminarayanan, G.R., Lorenz, P.K., Tomkins, R.P.T., 1968. Electrical Conductance, Density, and Viscosity Data. NSRDS-NBS 15 (National Standard Reference Data Series-National Bureau of Standards 15). Molten SaltsVol. 1. U.S. Government Printing Office, Washington, DC.

Janz, G.J., Krebs, U., Siegenthaler, H.F., Tomkins, R.P.T., 1972. J. Phys. Chem. Ref. Data 1, 581.

Janz, G.J., Tomkins, R.P.T., Allen, C.B., Downey Jr., J.R., Gardner, G.L., Krebs, U., Singer, S.K., 1975. J. Phys. Chem. Ref. Data 4, 871.

Karnicky, J.F., Pings, C.J., 1976. In: Prigogine, I., Rice, S.A. (Eds.), Advances in Chemical Physics, vol. 34. John Wiley and Sons, New York, p. 159.

Kim, K., Sato, Y., Shimakage, K., Ejima, T., 1987. J. Japan Inst. Metals 51, 630.

Kirshenbaum, A.D., Cahill, J.A., Stokes, C.S., 1960. J. Inorg. Nucl. Chem. 15, 297.

Klemm, W., 1926. Z. Anorg. Chem. 235–295, 152.

Krogh-Moe, K., Ostvolt, T., Førland, T., 1969. Acta Chem. Scand. 23, 2421.

Kruh, R.F., 1962. Chem. Rev. 62, 395.

Kutscher, J., Schneider, A., 1974. Z. Anorg. Allg. Chem. 408, 121.

Lantelme, F., Turq, P., Quentrec, B., Lewis, L.W., 1974. Mol. Phys. 28, 1537.

Levy, H.A., Agron, P.A., Bredig, M.A., Danford, M.D., 1960. Ann. N. Y. Acad. Sci. 79, 762.

Levy, H.A., Danford, M.D., Narten, A.H., 1966. Oak ridge national laboratory report 3960.

Lewis, L.W., Singer, K., 1975. J. Chem. Soc. Faraday Trans. II 71, 41.

Lewis, L.W., Singer, K., Woodcock, L.V., 1975. J. Chem. Soc. Faraday Trans. II 71, 301.

Lindemann, F.A., 1910. Z. Phys. 11, 609.

Madden, P.A., Wilson, M., Hutchinson, F., 2004. J. Chem. Phys. 120, 6609.

Marcus, Y., 1977. Introduction to Liquid State Chemistry. John Wiley & Sons, London, p.122.

Maroni, V.A., Hathaway, E.J., Papatheodorou, G.N., 1974. J. Phys. Chem. 78, 1134.

Matsuoka, A., Fukushima, K., Igarashi, K., Iwadate, Y., Mochinaga, J., 1993. Nippon Kagaku Kaishi 471.

Matsuura, H., Adya, A.K., Bowron, D.T., 2001. J. Synchrotron Rad. 8, 779.

Matsuura, H., Watanabe, S., Akatsuka, H., Okamoto, Y., Adya, A.K., 2009. J. Fluorine Chem. 130, 53.

Mellors, G.W., Senderoff, S., 1960. J. Phys. Chem. 64, 294.

Metallinou, M.M., Nalbandian, L., Papatheodorou, G.N., Voigt, W., Emons, H.H., 1991. Inorg. Chem. 30, 4260.

Michilsen, J., Wörlee, P., Graaff, F.V.d., Ketelaar, J.A.A., 1975. J. Chem. Soc. Faraday Trans. II 71, 1730.

Mikolaj, P.G., Pings, C.J., 1968. Phys. Chem. Liq. 1, 93.

Miyamato, Y., Okazaki, S., Odawara, O., Okada, I., Misawa, M., Fukunaga, T., 1994. Mol. Phys. 82, 887.

Mochinaga, J., Iwadate, Y., Fukushima, K., 1991. Mater. Sci. Forum 73–75, 147.

Mochinaga, J., Ikeda, M., Igarashi, K., Fukushima, K., Iwadate, Y., 1993a. J. Alloys Compd. 193, 36.

Mochinaga, J., Miyagi, Y., Igarashi, K., Fukushima, K., Iwadate, Y., 1993b. Nippon Kagaku Kaishi 459.

Momma, K., Izumi, F., 2011. J. Appl. Crystallogr. 44, 1272.

Mozzi, R.L., Warren, B.E., 1969. J. Appl. Crystallogr. 2, 164.

Murase, K., 1999a. In: Adachi, G. (Ed.), Kidorui-no-kagaku (Science of Rare Earths). Kagakudojin, Kyoto, p. 322.

Murase, K., 1999b. In: Adachi, G. (Ed.), Kidorui-no-kagaku (Science of Rare Earths). Kagakudojin, Kyoto, p. 323.

Murase, K.A., Adachi, G., Zissi, G.D., Boghosian, S., Papatheodorou, G.N., 1994. J. Non-Crystal. Solids 180, 88.

Nakamoto, K., 1978. Infrared and Raman Spectra of Inorganic and Coordination Compounds, 3rd ed. John Wiley & Sons, New York p. 153.

Nakamura, T., 1983. Molten Salt 26, 181.

Nakamura, Y., 1993. Ceramics 28, 1221.

Narten, A.H., 1972. J. Chem. Phys. 56, 1905.

Narten, A.H., Levy, H.A., 1969. Science 165, 447.

Narten, A.H., Danford, M.D., Levy, H.A., 1967. Discus Faraday Soc. 43, 97.

Neithamer, R.W., Peake, J.S., 1961. J. Chem. Eng. Data 6, 197.

Newport, R.J., Howe, R.A., Wood, N.D., 1985. J. Phys. C 18, 5249.

Nosé, S., 1984. J. Chem. Phys. 81, 511.

Numakura, M., Okamoto, Y., Yaita, T., Shiwaku, H., Akatsuka, H., Nezu, A., Tajima, K., Shimohara, Y., Bessada, C., Pauvert, O., Zanghi, D., Chamelot, P., Matsuura, H., 2010. J. Fluorine Chem. 131, 1039.

Ohno, H., Furukawa, K., 1981. J. Chem. Soc. Faraday Trans. I 77, 1981.

Ohno, H., Furukawa, K., 1983. J. Chem. Soc. Faraday Trans. II 79, 463.

Ohno, H., Yoroki, M., Furukawa, K., Takagi, Y., Nakamura, T., 1978a. J. Chem. Soc. Faraday Trans. I 74, 1861.

Ohno, H., Furukawa, K., Tanemoto, K., Takagi, Y., Nakamura, T., 1978b. J. Chem. Soc. Faraday Trans. I 74, 804.

Ohno, H., Igarashi, K., Umesaki, N., Furukawa, K., 1994. X-ray Diffraction Analysis of Ionic Liquids. Trans Tech Publications, Zürich.

Ohtaki, H., 1982. Rev. Inorg. Chem. 4, 103.

Okada, I., Takagi, R., Kawamura, K., 1980. Z. Naturforsch. 35a, 493.

Okamoto, Y., Ogawa, T., 1999a. Z. Naturforsch. 54a, 91.

Okamoto, Y., Ogawa, T., 1999b. Z. Naturforsch. 54a, 599.

Okamoto, Y., Hayashi, H., Ogawa, T., 1996. J. Non-Crystal. Solids 205–207, 139.

Okamoto, Y., Kobayashi, F., Ogawa, T., 1998. J. Alloys Compd. 271–273, 355.

Okamoto, Y., Hayashi, H., Ogawa, T., 1999. Jpn. J. Appl. Phys. 38 (Suppl. 38–1), 156.

Okamoto, Y., Akabori, M., Motohashi, H., Shiwaku, H., Ogawa, T., 2001. J. Synchrotron Rad. 8, 1191.

Okamoto, Y., Akabori, M., Motohashi, H., Itoh, A., Ogawa, T., 2002. Nucl. Instrum. Meth. Phys. Res. A 487, 605.

Okamoto, Y., Iwadate, Y., Fukushima, K., Matsuura, H., Minato, K., 2005. J. Phys. Chem. Solids 66, 452.

Papatheodorou, G.N., 1975. Inorg. Nucl. Chem. Lett. 11, 483.

Papatheodorou, G.N., 1977. J. Chem. Phys. 66, 2893.

Papatheodorou, G.N., Østvold, T., 1974. J. Phys. Chem. 78, 181.

Pavlatou, E.A., Madden, P.A., Wilson, M., 1997. J. Chem. Phys. 107, 10446.

Peake, J.S., Bothwell, M.R., 1954. J. Am. Chem. Soc. 76, 2653.

Pettifor, D.G., 1986. J. Phys. C 19, 285.

Photiadis, G.M., Børresen, B., Papatheodorou, G.N., 1998. J. Chem. Soc. Faraday Trans. 94, 2605.

Pings, C.J., 1968. In: Temperly, H.N.V., Rowlinson, J.S., Rushbrooke, G.S. (Eds.), Physics of Simple Liquids. North Holland Publishing Co., Amsterdam Chapter 10.

Price, D.L., Saboungi, M.-L., Hashimoto, S., Moss, S.C., 1992. In: Gale, R.J., Blomgren, G., Kojima, H. (Eds.), Proceedings of the 8th International Symposium on Molten Salts, Electrochem. Soc., 199214.

Price, D.L., Saboungi, M.-L., Howells, W.S., Tosi, M.P., 1993. In: Proceedings of the International Symposium on Molten Salt Chemistry and Technology, May 16-21, 1993. Hawaii, PV93-91.

Rollet, A.-L., Bessada, C., Auger, Y., Melin, P., Gailhanou, M., Thiaudiere, D., 2004. Nucl. Instrum. Meth. Phys. Res. B 226, 447.

Romano, S., McDonald, I.R., 1973. Physica 67, 625.

Saboungi, M.-L., Howe, M.A., Price, D.L., 1990. In: Proceedings of the Seventh International Symposium on Molten Salts, May 6-11, 1990. Electrochem. Soc., Montreal, p. 8.

Saboungi, M.-L., Price, D.L., Scamehorn, C., Tosi, M.P., 1991. Europhys. Lett. 15, 283.

Saboungi, M.-L., Howe, M.A., Price, D.L., 1993. Mol. Phys. 79, 847.

Sangster, M.L.J., Dixon, M., 1976. Adv. Phys. 25, 247.

Sato, Y., Yamamura, T., 1992. Met. Rev. MMIJ 9, 100.

Sayers, D.E., Stern, E.A., Lytle, F.W., 1971. Phys. Rev. Lett. 27, 1204.

Sears, V.F., 1992. Neutron News 3, 26.

Sen, S., Zissi, G.D., Papatheodorou, G.N., 2000. J. Phys. Condens. Matter 12, 2885.

Shannon, R.D., 1976. Acta Crystal. A32, 751.

Shirakawa, Y., Saito, M., Tamaki, S., lnui, M., Takeda, S., 1991. J. Phys. Soc. Jpn. 60, 2678.

Spooner, R.C., Wetmore, F.E.W., 1951. Can. J. Chem. 29, 777.

Suzuki, K., Fukushima, Y., 1977. Z. Naturforsch. 32a, 1438.

Takagi, Y., Nakamura, T., 1985. Phil. Mag. 51, L43.

Takagi, R., Tomita, M., 1993. Z. Naturforsch. 48a, 1239.

Takagi, R., Okada, I., Kawamura, K., 1975. Bull. Tokyo Inst. Technol. 127, 45.

Takagi, R., Ohno, H., Furukawa, K., 1979. J. Chem. Soc. Faraday Trans. I 75, 1477.

Takagi, R., Hutchinson, F., Madden, P.A., Adya, A.K., Gaune-Escard, M., 1999. J. Phys. Condens. Matter 11, 645.

Takahashi, S., Koura, N., Muneta, T., Ohno, H., 1985a. J. Chem. Soc. Faraday Trans. II 81, 319.

Takahashi, S., Muneta, T., Koura, N., Ohno, H., 1985b. J. Chem. Soc. Faraday Trans. II 81, 1107.

Tatlipinar, H., Akdeniz, Z., Pastore, G., Tosi, M.P., 1992. J. Phys. Condens. Matter 4, 8933.

Templeton, D.H., Carter, G.F., 1954. Acta Crystallogr. 58, 940.

Tosi, M.P., 1994a. Z. Phys. Chem. 184, S121.

Tosi, M.P., 1994b. J. Phys. Condens. Matter 6, A13.

Tosi, M.P., Price, D.L., Saboungi, M.-L., 1993. Annu. Rev. Phys. Chem. 44, 173.

Umesaki, N., Ohno, H., Iwamoto, N., 1991. In: Doyama, M., Suzuki, T., Kihara, J., Yamamoto, R. (Eds.), Computer Aided Innovation of New Materials. Elsevier Science Publishing, BV, Amsterdam, pp. 911–914.

Vaslow, F., Narten, A.H., 1973. J. Chem. Phys. 59, 4949.

Warren, B.E., Krutter, H., Morningstar, O., 1936. J. Am. Ceram. Soc. 19, 202.

Waseda, Y., 1980a. The Structure of Non-Crystalline Materials. McGraw-Hill, New York p. 41.

Waseda, Y., 1980b. The Structure of Non-Crystalline Materials. McGraw-Hill, New York p. 188.

Waseda, Y., Ohtani, M., 1971a. Senkenshu 27, 117.

Waseda, Y., Ohtani, M., 1971b. Senkenshu 27, 127.

Wasse, J.C., Salmon, P.S., 1998. Phys. B 241–243, 967.

Wasse, J.C., Salmon, P.S., 1999a. J. Phys. Condens. Matter 11, 2171.

Wasse, J.C., Salmon, P.S., 1999b. J. Phys. Condens. Matter 11, 9293.

Wasse, J.C., Salmon, P.S., 1999c. J. Phys. Condens. Matter 11, 13.

Wasse, J.C., Salmon, P.S., 1999d. J. Phys. Condens. Matter 11, 1381.

Wasse, J.C., Salmon, P.S., Delaplane, R.G., 2000. J. Phys. Condens. Matter 12, 9539.

Watanabe, S., Adya, A.K., Okamoto, Y., Umesaki, N., Honma, T., Deguchi, H., Horiuchi, M., Yamamoto, T., Noguchi, S., Takase, K., Kajinami, A., Sakamoto, T., Hatcho, M., Kitamura, N., Akatsuka, H., Matsuura, H., 2006. J. Alloys Compd. 408–412, 71.

Wilson, M., Madden, P.A., 1993. J. Phys. Condens. Matter 5, 6833.

Wilson, M., Madden, P.A., 1998. Phys. Rev. Lett. 80, 532.

Wood, N.D., Howe, R.A., 1988. J. Phys. C 21, 3177.

Wood, N.D., Howe, R.A., Newport, R.J., Faber Jr., J., 1988. J. Phys. C 21, 669.

Woodcock, L.V., 1971. Chem. Phys. Lett. 10, 257.

Woodcock, L.V., Singer, K., 1971. Trans. Faraday Soc. 67, 12.

Wyckoff, R.W.G., 1964. Crystal Structures. vol. 2. Interscience, New York p. 45.

Yaffe, I.S., van Artsdalen, E.R., 1956. Chemistry division semiannual progress report, oak ridge national laboratory, ORNL-2159, p.77

Zarzycki, J., 1957. J. Phys. Rad. Suppl. Phys. Appl. 18, 65A.

Zarzycki, J., 1958. J. Phys. Rad. Suppl. Phys. Appl. 19, 13A.

Zissi, G.D., Papatheodorou, G.N., 1999. Chem. Phys. Lett. 308, 51.

Zissi, G.D., Papatheodorou, G.N., 2002. J. Chem. Soc. Dalton Trans. 2599.

Zissi, G.D., Papatheodorou, G.N., 2004. Phys. Chem. Chem. Phys. 6, 4480.

Zissi, G.D., Chrissanthopoulos, A., Papatheodorou, G.N., 2006. Vibration. Spectrosc. 40, 110.

Chapter 261

Lanthanides in Solar Energy Conversion

Jean-Claude G. Bünzli[*,†] **and Anne-Sophie Chauvin**[†]

[*]*Department of Materials Chemistry, WCU Center for Next Generation Photovoltaic Systems, Korea University, Sejong Campus, Sejong-si, Republic of Korea*

[†]*Swiss Federal Institute of Technology Lausanne (EPFL), Institute of Chemical Sciences and Engineering, Lausanne, Switzerland*

Dedicated to Professor Renata Reisfeld for her pioneering work in photovoltaics

Chapter Outline

Handbook on the Physics and Chemistry of Rare Earths, Vol. 44.
http://dx.doi.org/10.1016/B978-0-444-62711-7.00261-9

1. INTRODUCTION

1.1. The Challenges

Simple in its principle, solar energy conversion encounters difficult technical problems related to various aspects. The first difficulty lies in the spectral distribution of solar energy and its variation with the degree of cloudiness, the time of the day and of the year, as well as the latitude. For instance, the total available power may vary by as much as a factor 6 between clear and overcast sky. Variations between summer and winter may represent far larger differences, up to a ratio of about 30. Furthermore, the relative proportions between ultraviolet (UV), visible, and near-infrared (NIR) light also depend on the meteorological conditions. The standard solar spectrum is generally given as AM1.5G, where G stands for global sun, that is including both direct and diffuse light, and AM for air mass (Fig. 1); the latter is the ratio of the effective solar irradiation path length (L_S) in the atmosphere over that corresponding to a vertical position of the sun (thickness of the atmosphere, L_A); for an incident angle θ relative to the normal of the earth's surface and an irradiation flux of 1000 W m^{-2} ($\equiv$100 mW cm^{-2} or 1 sun), one has:

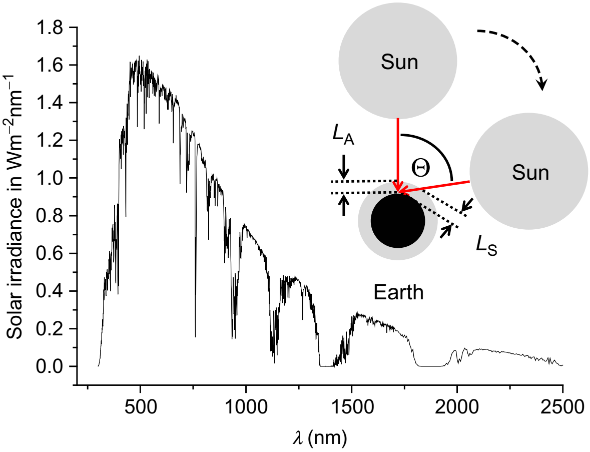

FIGURE 1 Air-Mass 1.5G (AM1.5G) solar irradiance spectrum and sketch showing definitions for parameters used in Eq. (1).

$$\frac{L_S}{L_A} = \frac{1}{\cos\theta} \tag{1}$$

The AM coefficient varies with latitude and with the time of the day and of the year. AM1.5 corresponds to an angle of 48.2°, characteristic of temperate latitudes where most of the world urban populations live. It is the standard when evaluating the performances of solar panels. AM0 describes the solar spectrum outside the atmosphere, which is the irradiance of a 5800-K black body; it is about 28% more intense than AM1.5G. For solar concentrator work, only direct irradiation is taken into account and the corresponding spectrum is AM1.5D, about 10% less intense than AM1.5G.

Photovoltaic cells all work according to the same basic principle: (i) absorption of light generates electron–hole pairs in a semiconductor material and (ii) the charge carriers are separated and extracted into an external circuit, generating electricity in it. The most widespread semiconductors are silicon, cadmium telluride, gallium arsenide, and titanium dioxide. Therefore, the second problem in solar energy conversion arises from the spectral mismatch between the energy-converting material and the solar emission spectrum. For instance, silicon absorbs at most only about 48% of the total solar emission (Fig. 2). Moreover, not all of the absorbed light is converted into electrical power. For example, reflection losses, lattice thermalization, recombination, junction, and contact voltage losses reduce the overall efficiency of silicon-based solar cells to a theoretical limit of about 31%, named Shockley–Queisser limit (Shockley and Queisser, 1961), while practical devices have

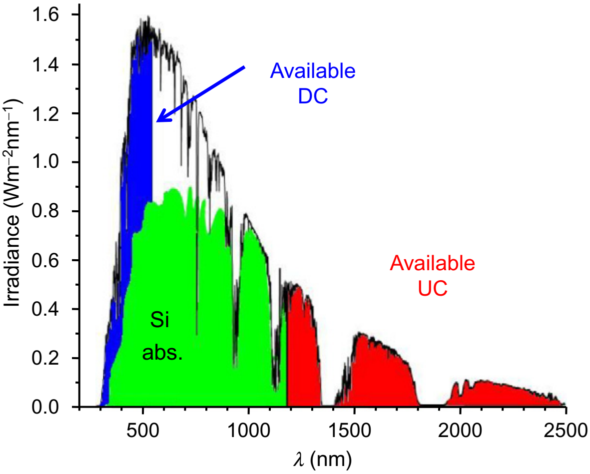

FIGURE 2 Air-Mass 1.5G (AM1.5G) solar irradiance spectrum along with fractions absorbed by a thick silicon wafer (about 48%) and available for down- (DC, about 16% up to 500 nm) and upconversion (UC, about 17%, in the 1.2–2.5 μm range). *Redrawn from Richards (2006a).*

reached 25% with single crystalline silicon (c-Si). Cheaper polycrystalline silicon (p-Si) gives inferior results (15–17%) although new fabrication techniques have now boosted the efficiency of commercial panels up to 21%. Slightly better yields are obtained with the so-called III–V cells featuring, for instance, gallium arsenide (27.6%) or with multijunction devices such as GaInP/GaAs/Ge displaying 32% yield (Green et al., 2012). The situation seems to be less bright for dye-sensitized solar cells (DSSCs) which presently reach only12% efficiency (Kalyanasundaram, 2010a; Yella et al., 2011), but these devices present nevertheless definite advantages over Si or semiconductor cells. For instance, contrary to other photovoltaic (PV) cells, they feature separation of the two essential processes: light harvesting/charge generation and charge transport. This is not the case for silicon-based cells, which imposes harsh requirements on the purity of Si and, consequently, considerably increases the cost of Si-based cells. For the time being, commercial DSSC submodules having overall efficiency close to 10% are available (Green et al., 2012).

One way toward improving the light-to-electricity conversion yield is to concentrate the solar light on the photovoltaic devices so as to reach higher surface powers and, consequently, better conversion. Presently, the record of these "concentrator cells" is held by the multijunction, lattice-matched GaInP/GaAs/GaInNAs–GaAs cell with 43.5% conversion efficiency under illumination equivalent to 418 suns (Herb, 2012). Alternatively, a spectral-splitting module comprising a pair of two-cell stacks (GaInP/GaAs and GaInAsP/GaInAs) reached a photovoltaic efficiency of 38.5% under 20-sun irradiation; in this design, a dichroic reflector is used to split the light beam into two subbeams which are focused on the two different cell stacks (Green et al., 2012).

The other avenue for improving the conversion yield of solar cells derives from the fact that these cells perform best under monochromatic light with a wavelength λ_{opt} (in nm) given by the following equation:

$$\lambda_{\mathrm{opt}} = \frac{1240}{E_{\mathrm{g}}}(\mathrm{nm}) \qquad (2)$$

where the band gap energy E_{g} is in eV and 1240 is a unit conversion factor (1 cm^{-1} corresponds to 1.24×10^{-4} eV). This corresponds, for instance, to 1127 nm for c-Si ($E_{\mathrm{g}} \sim 1.1$ eV) or to 690 nm for amorphous silicon (a-Si, $E_{\mathrm{g}} \sim 1.8$ eV). Therefore, concentrating the 300- to 1500-nm solar emission spectrum into a single narrow band spectrum corresponding to λ_{opt} would lead to theoretical efficiencies close to 80% (van Sark et al., 2010). The present state of the art is still far from this idealized goal, and the solution is approached stepwise by introducing wavelength-converting layers responsive to specific portions of the solar spectrum (Figs. 2 and 3).

For instance, the UV part of the solar spectrum can be harvested by luminescent compounds which then emit at a longer wavelength: the process is

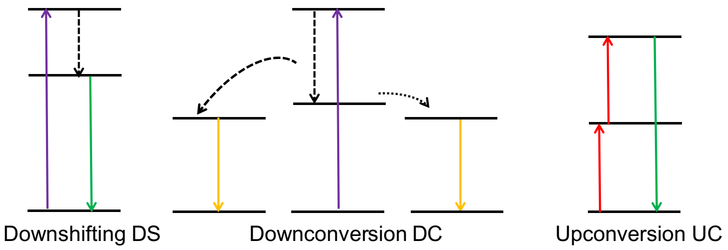

FIGURE 3 Schematic representation of downshifting, downconversion, and upconversion mechanisms.

known as wavelength downshifting (DS). Alternatively, a more complex mechanism is downconversion (DC), or quantum cutting, in which the material absorbs an energetic photon and emits two photons of lower energy.

In turn, the NIR portion of the spectrum can be harvested and two (or more) low-energy photons transformed into one shorter wavelength photon by upconversion (UC). Since upconversion is at least a two-photon process, relatively large excitation powers are required, which explains why attempted applications to solar energy conversion are relatively recent (Shalav et al., 2003, 2007; Trupke et al., 2002b). Pairs of lanthanide ions involving a sensitizer and a luminescent ion provide efficient upconversion systems, for instance, Yb^{III}/Er^{III} or Yb^{III}/Tm^{III} (Auzel, 2004). For Si cells, however, upconverting systems featuring the sole Er^{III} ion are more adequate (Marques-Hueso et al., 2011). Some transition metal ions, quantum dots (QDs) (de Wild et al., 2011), and organic dyes (Cheng et al., 2012; Schulze et al., 2012) are also prone to upconversion (Strümpel et al., 2007). Theoretical calculations show that adding an upconversion layer to semiconductor multijunction cells could increase the absolute external quantum efficiency (EQE) from about 40% to 50% under AM1.5G illumination (Trupke et al., 2006).

When it comes to devices, the wavelength-converting materials can be incorporated into either the solar cell architecture (Fig. 4) or a luminescent solar concentrator (LSC, Fig. 5). Downshifting and downconversion materials are usually doped into thin layers grown on the top of the solar cell (Fig. 4A), while upconverting layers are positioned at the bottom of the solar cell and the emitted light is reflected toward the top of the cell by an additional reflection layer (Fig. 4B). Both designs generate inconveniencies. The DS and DC layers are often highly reflective so that reflection losses increase. In the case of upconversion, NIR light may be absorbed by the top layers, leading to a warming of the solar cell and diminished performances. An elegant solution consists in splitting the solar light into two different beams with a dichroic mirror (Fig. 4C) and to focus the two beams on two adequately tailored solar cells. This design has been used in the spectral-splitting concentrator module mentioned earlier. In the case of DSSCs, the wavelength-converting materials

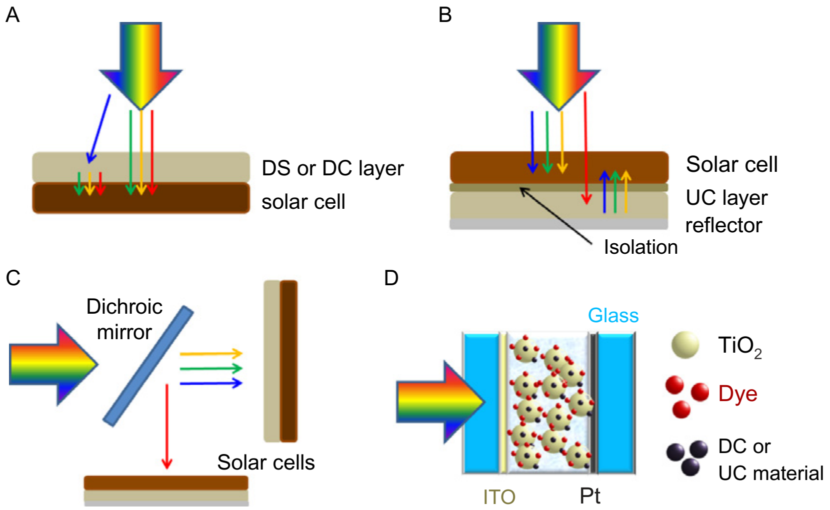

FIGURE 4 Introduction of wavelength-converting materials into the architecture of solar cells: (A) front downshifting or downconverting layer; (B) back upconverting layer; (C) removal of the IR light for specific conversion; (D) introduction of downshifting material in a dye-sensitized cell. ITO, indium tin oxide.

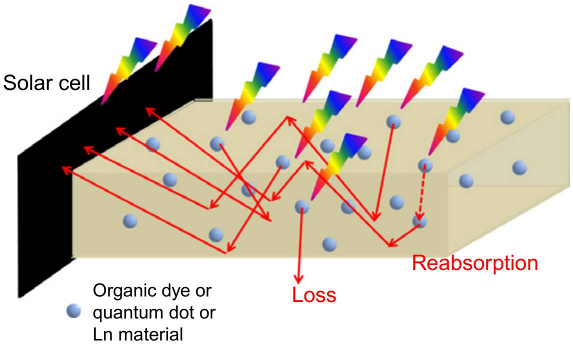

FIGURE 5 Principle of a luminescent solar concentrator.

can be co-doped with the organic dye on titanium oxide particles (Fig. 4D) or, possibly, in the electrolyte, which minimizes the problem of reflection losses.

1.2. Role of Rare Earths in Photovoltaic Systems

Various properties of rare-earth elements and compounds are of interest in solar energy conversion. For instance, it was discovered that insertion of a thin insulating layer made up of rare-earth metals between the semiconductor (e.g., silicon) and the metal of a Schottky contact improves greatly the photovoltaic yield; scandium, yttrium, samarium, ytterbium, and lutetium were tested as solar cell barrier metals and Sc and Lu performed particularly well (Munz and Bucher, 1982). This was the first application of these elements to solar energy conversion. Moreover, rare-earth oxides have structural properties which are helpful in lattice-matched multilayer semiconductor cells while their conductivity properties are used to enhance conduction between the semiconductor layer and the electrode in silicon cells (Takei, 2011). In addition, cerium oxide displays photoelectric properties similar to those of titanium oxide (Turkovic and Orel, 1997) and rare-earth oxides are helpful in lattice-matched multijunction cells (Clark et al., 2010). But by far, the main applications of lanthanides in photovoltaics stem from the luminescent properties of their divalent and trivalent ions.

Indeed the electronic configurations $4f^n$ (Ln^{III}) and $4f^{n-1}5d^1$ (Ln^{II}) generate a wealth of electronic levels which are particularly suitable for acting as wavelength-converting entities. As a matter of fact, an early application of luminescent lanthanide ions to solar energy conversion was their introduction as downshifting materials into LSCs (Reisfeld, 1983, 1987). The Ln^{III} ions also perform well in downconversion. This phenomenon was predicted in 1957 (Dexter, 1957) but only demonstrated two decades later with a single Ln^{III} ion, Pr^{III} doped into yttrium fluoride, absorbing at 185 nm and emitting two visible photons at 408 and 620 nm with a quantum yield up to 140% (Piper et al., 1974). Much better quantum yields have then been obtained, close to 200%, with systems featuring different Ln^{III} ions, such as Gd^{III} and two Eu^{III}, for instance (Wegh et al., 1999). Finally, lanthanide ions are ubiquitous in upconversion (Auzel, 2004); for instance, the $NaYF_4$:Yb(18%), Er(2%) material is finding applications in fields as diverse as counterfeiting tags, security inks, bioimaging of live animals, time-resolved luminescence immunoassays, and solar cells (Tan, 2012).

In this chapter, we concentrate on the use of rare-earth compounds as wavelength-converting materials in LSCs and various types of solar cells. The burgeoning field of lanthanide-containing photocatalysts for water splitting or water decontamination (Weber et al., 2012) is not included in the present work. With the exception of review papers and of Section 3.2 in which prospective materials for downconversion are described, the chapter presents and critically assesses works in which experiments with solar concentrators or solar cells are presented and not those claiming "potential applications." This considerably limits the size of the cited literature, which is covered until the end of 2012.

2. LUMINESCENT SOLAR CONCENTRATORS

2.1. Definitions and Basic Properties

Luminescent solar concentrators offer a cheap solution to solar energy conversion in that they concentrate photoluminescence on the expensive surface of solar cells, the light emitted by the dopant being kept inside the layer by total internal reflection (TIR, Fig. 5). They collect diffuse light very well and consequently eliminate the need for tracking systems which orientate Si solar cells in the most favorable position with respect to sunlight.

These devices are highly transparent glass plates or polymer sheets doped with luminescent materials featuring high quantum yields and, ideally, emission bands having little overlap with absorption bands. Solar light is absorbed by the dopant and the reemitted radiation concentrates at the end edge of the thin plate thanks to TIR. Total internal reflection occurs when light impinges the LSC/air boundary with angles larger than the critical angle θ_c (Rowan et al., 2008):

$$\theta_c = \sin^{-1}\left(\frac{1}{n}\right) \tag{3}$$

n is the refractive index of the LSC layer and the fraction of photoluminescent light which will be totally internally reflected is given by:

$$F_{\mathrm{TIR}} = \frac{(n^2-1)^{1/2}}{n} \tag{4}$$

For $n=1.5$, which is a common refractive index value for glasses, F_{TIR} will be around 75%, which means that a quarter of the luminescence intensity is lost. Moreover, if the solar concentrator is not coated with an antireflection layer, part of the sunlight impinging on the surface will be reflected back (Fresnel reflection). Assuming vertical incidence, the reflected fraction will be (Goetzberger and Greubel, 1977):

$$R = \frac{(n-1)^2}{(n+1)^2} \tag{5}$$

The fraction of light entering the collector is $(1-R)$ so that if η_{PL} is the photoluminescence quantum yield of the dopant, the loss due to the luminescence and TIR processes can be written as:

$$L_{\mathrm{L}} = (1-R)(1-F_{\mathrm{TIR}})\eta_{\mathrm{PL}} \tag{6}$$

Finally, the total loss will be:

$$L_{\mathrm{tot}} = (1-R)(1-F_{\mathrm{TIR}})\eta_{\mathrm{PL}} + R \tag{7}$$

which translates into the following expression if η_{PL} is set to 1:

$$L_{\mathrm{tot}} = 1 - \frac{4(n-1)^{1/2}}{(n+1)^2} \tag{8}$$

The graph of L_{tot} versus n depicted in Fig. 6 presents a broad minimum for $n=2.0$ for which the total loss is 23%. At this stage, we make two remarks.

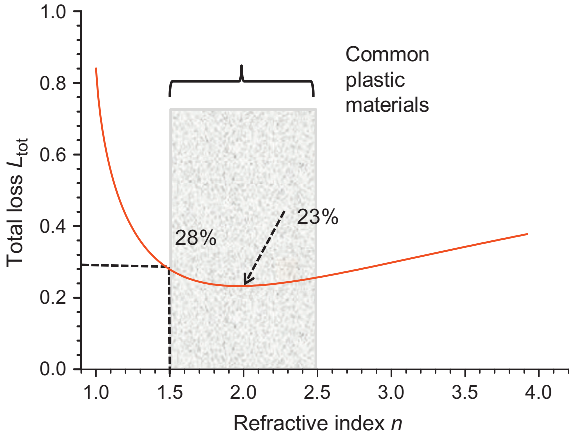

FIGURE 6 Total loss due to reflection and incomplete light refraction, according to Eq. (8), with the hypotheses that light incidence is vertical and $\eta_{PL} = 1$. *Redrawn from Goetzberger and Greubel (1977).*

The first one is that under the given hypotheses, Fresnel reflection loss does not add much to the total loss since the loss due to incomplete TIR, as expressed by Eq. (8), amounts to 25%, as compared to 28% for the total loss when $n = 1.5$. The second remark is that the curve is fairly flat in the range $1.5 < n < 2.5$ so that common plastic materials (e.g., polymethylmethacrylate, PMMA), glasses, or organic–inorganic hybrids with refractive indices in the range of 1.5–1.6 are well suited for LSCs.

Luminescent solar concentrators present the following advantages: (i) both direct and diffuse light is collected, (ii) heat generated by unused energy is well dissipated into the large area of the collector plate so that light reaching the photovoltaic cell is “cold” minimizing heating of the device. In addition, the luminescent material can be chosen to match the maximum sensitivity of the photovoltaic cell. Therefore, cheap LSCs can concentrate light on the small areas of expensive solar cells. Present interest for these devices is large because of their ability to collect the often sizeable diffuse component of solar irradiation, particularly in Northern countries. Commercial exploitation of this technology seems to be close (Chatten et al., 2010), but we note with some concern that a similar statement was already made in 1977 (Goetzberger and Greubel, 1977). In fact, it is thought that 30% efficiency would be needed to make LSCs commercially viable (Sholin et al., 2007), whereas today the largest yield is estimated to be ≈7% (Currie et al., 2008).

Three types of LSCs have been proposed. One design makes use of organic dyes, which have large quantum yields (near unity) and are available in a wide range of colors. However, reabsorption (i.e., overlap between absorption and emission spectra) is a problem, as well as their poor thermal and photo stabilities under solar irradiance; for instance, rhodamine B doped in PMMA sustains up to 20–37% thermal degradation upon heating in the temperature range of 45–94 °C (Meseguer et al., 1981). Despite these drawbacks, a practical LSC made up of two organic dyes doped in PMMA was shown to have a power conversion efficiency of 7.1% when linked with four GaAs solar cells connected in parallel (Slooff et al., 2008). Theoretical modeling has been attempted to maximize the light output of LSCs (Earp et al., 2004b) and efficiencies of up to 9.1% with an InGaP cell or 14.5% with a Cu(In,Ga)Se_2 cell are predicted (van Sark, 2013). Moreover, a practical lighting (not energy-converting) device was fabricated consisting of three different layers of LSC (violet, green, and pink) and having an overall efficiency of about 50% (Earp et al., 2004a). This type of device can be adapted for photovoltaics by inserting spectral-matched solar cells at the end of each LSC stack (Rowan et al., 2008).

QDs, for example PbS or CdSe nanoparticles, represent the second alternative. They offer several improvements over organic dyes: (i) their absorption spectra are much broader and extend into the UV, (ii) absorption properties can be tuned by modulating the size of the QDs, (iii) their thermal and photo stabilities are better compared to organic dyes but still are not quite sufficient, although it has been shown that QDs recover their absorption properties after a prolonged dark cycle (Hyldahl et al., 2009), and (iv) the shift between absorption and luminescence is related to the spread of the QD sizes, a parameter that can be mastered during the growth process. On the other hand, their quantum yield is often smaller compared with organic dyes; they are more expensive; they still have nonnegligible absorption/emission overlap; they are quite sensitive to water, ions, and oxygen; and one may have some concern about toxicity of lead and cadmium (van Sark et al., 2008).

All of this explains why lanthanide complexes and lanthanide-containing upconverting nanoparticles (UCNPs) have also been probed as a third alternative and are presently the subject of a renewed interest which started around 2009 (see below).

Assessment of the various solutions for the design of LSCs has been presented in recent review articles (Reisfeld, 2010; Rowan et al., 2008) in which the authors conclude that a combination of organic and inorganic materials (hybrid materials) might be the panacea. Data pertaining to the case of an LSC coupled to a silicon solar cell are listed in Table 1. Plasmonics may contribute too (see Section 3.4.5): introduction of silver nanoparticles into luminescent plates increases their luminescent efficiency by as much as 12% (Reisfeld, 2010).

2.2. Downshifting into the NIR Spectral Range

The concept of downshifting for improving the performances of LSCs was revived by Weber and Lambe in 1976 (Weber and Lambe, 1976) followed 1 year later by the fabrication of a practical device (Levitt and Weber, 1977)

TABLE 1 Assessment of Luminescent Materials for a LSC Coupled to a Si Solar Cell with Respect to Four Criteria

Property	Organic dye	Quantum dots[a]	Ln materials	Hybrid materials[b]
Absorb all light <950 nm	×	√	×	√
No reabsorption	×	×	√	√
Quantum yield >90%	√	×	≈	√
Stable >10 years	≈	≈	√	√

[a] *PbS QD.*
[b] *See text and Section 2.5.*
Adapted from Rowan et al. (2008).

consisting in a thin layer (1.2 mm) of Nd^{III} laser glass containing 3 wt% of Nd_2O_3 and having an area of 100 cm^2. Upon pumping at 577 nm, a voltage gain of ≈6 could be obtained (30% from 880-nm emission and 70% from 1060-nm emission). Lanthanide-containing LSCs have long-term photostability, but the low absorptivity of Ln^{III} ions due to the parity-forbidden f-f transitions is a definite drawback. This may be overcome by introducing a sensitizer, although at the cost of larger complexity.

Most of the work on lanthanide-containing LSCs has been performed in conjunction with silicon solar cells. For maximizing the performances of the tandem LSC-Si cell, the luminescent material should absorb all wavelengths shorter than 950 nm and emit a single band in the range of 950–1100 nm, which corresponds to the maximum response of a c-Si cell. NIR-emitting organic dyes having low quantum efficiencies, lanthanide ions such as Nd^{III} (emission at 880 and 1060 nm) and Yb^{III} (emission at 980 nm) have been tested. Indeed, quantum yields can reach 80–90% in glass matrices. Unlike Yb^{III} which only absorbs at 970–980 nm, Nd^{III} has several absorption bands in the visible and NIR ranges and it is one of the lanthanide ions having the largest molar absorption coefficients (10–15 M^{-1} cm^{-1}). An LSC glass substrate combining these two ions effectively absorbs about 20% of the solar light in the 440–980 nm range, and since the Nd-to-Yb energy transfer is quite efficient, this combination leads to a single emission peak in the range of 900–1100 nm with a maximum close to 1000 nm (Reisfeld, 1983). To compensate for the still low absorptivity of lanthanide ions, energy transfer from a better absorbing species may be required. One of the first donors tested was Cr^{III} which has two broad absorption bands and which transfers energy to Nd^{III} and Yb^{III} with an efficiency close to 90% in lithium lanthanum phosphate glass (Reisfeld, 1983). An alternative sensitizer is uranyl: an LSC containing 18 wt% of uranyl and 9–10 wt% Nd^{III} ions and with an aluminum antireflection coating led to an apparent 40% increase in the solar-to-electrical energy conversion of the attached Si cell (Sytko and Pershina, 1995). Not much further work has been described on these systems until 2011 when nanocrystals of Nd^{III}- and Yb^{III}-doped yttrium aluminum garnet (YAG) or gadolinium gallium garnet (GGG, $Ga_3Ga_5O_{12}$) or simple yttrium sesquioxide have been incorporated into PMMA in which efficient Nd-to-Yb transfer was demonstrated (≈78%). However, the LSCs were not coupled to solar cells to evaluate their performances (Kozlowska et al., 2011). A final option for sensitizing Ln^{III} NIR emission is to resort to organic ligands, which have intense absorption bands in the UV–vis and transfer energy efficiently onto the metal ion; the shortcoming here is the presence of high-energy vibrations, for example, C-H oscillators, which effectively deactivate the Ln^{III} excited states. For instance, $[Yb(OPyr)_3(Phen)]$ (Scheme 1) has a quantum yield of 2.3% in CCl_4 which decreases to only 1% when inserted into a transparent PMMA stab at 0.001% concentration (Sanguineti et al., 2012).

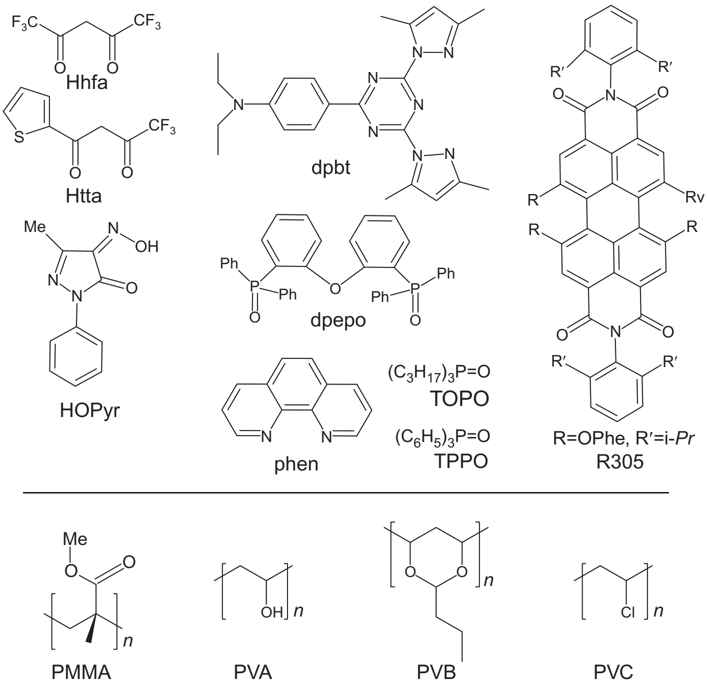

SCHEME 1 (Top panel), left: diketone and pyrazolone ligands (L); middle: ancillary ligands L′ for ternary complexes $[Eu(L)_3L']$; right: organic dye R305 used for reabsorption study. (Bottom panel) Some polymers used as matrices.

2.3. Downshifting into the Visible Spectral Range

Other devices concentrate on converting the UV portion of the solar spectrum into red light. This is a relatively recent development, the first report having been published in 2000 (Machida et al., 2000). In most studies, europium is chosen as the dopant luminescent ion (main emission lines at 590–620 and 690 nm). Either simple coordination compounds or inorganic–organic hybrids have been tested to this end. Ternary complexes of *tris*(β-diketonates) have received special attention since they are among the most luminescent europium complexes with organic ligands, quantum yields reaching 80–85% (Bünzli and Eliseeva, 2013; Malta et al., 1998; Moudam et al., 2009; Zucchi et al., 2011). One advantage of lanthanide complexes compared to all-organic dyes is very limited reabsorption due to the excitation into the ligand levels, which generates large Stokes' shifts. This has been firmly established by comparing an organic dye, R305 (Scheme 1), having a photoluminescence quantum yield close to 100%, with the highly emitting [Eu(hfa)$_3$(dpepo)] complex (Scheme 1, QY = 80% both in solution and in PMMA) (Wilson et al., 2010). The organic dye has a 23-nm Stokes' shift while the shift for [Eu(hfa)$_3$(dpepo)] amounts to 300 nm (Fig. 7). R305 was subjected to a detailed investigation of the reabsorption losses versus the dye concentration in PMMA (5–1574 ppm) and the excitation wavelength. Experimental results

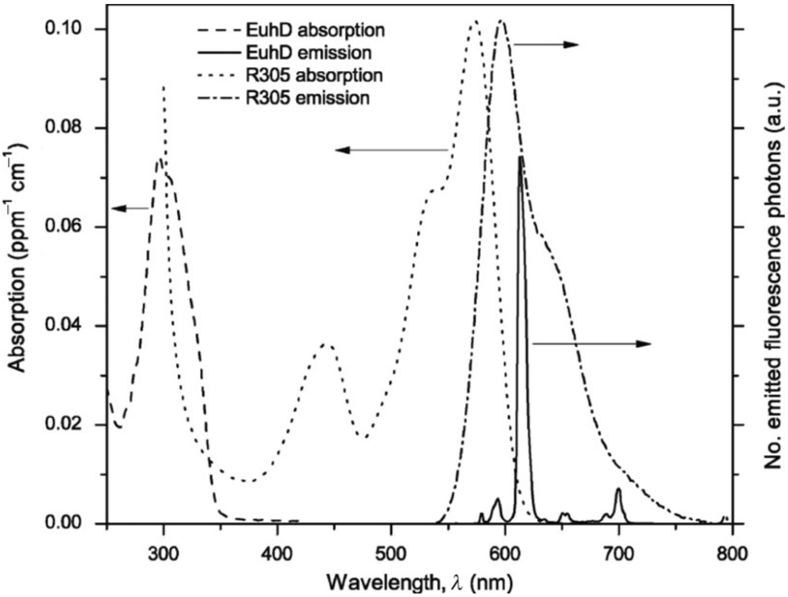

FIGURE 7 Absorption and normalized emission spectra of R305 and [Eu(hfa)$_3$(dpepo)] (λ_{ex} = 530 and 320 nm, respectively). *Reproduced with permission from Wilson et al. (2010) © 2010 The Optical Society of America.*

were in good agreement with Monte Carlo simulations of photon transport inside the LSC devices. LSCs were cut from the doped 3-mm thick PMMA sheets. The optical efficiency of the LSC defined as the number of photons emitted at the edges divided by the number of photons absorbed over the surface, η_{opt}, was found to be 50% for a 10×10-cm^2 sheet doped with 210 ppm R305 while this efficiency increased to 64% for the Eu$^{\text{III}}$ complex under the same conditions. The larger efficiency of the lanthanide-doped LSC despite the lower quantum yield of the metal complex can be entirely traced back to the absence of reabsorption losses.

Another comparative study focused on [Eu(tta)$_3$(phen)] and [Eu(tta)$_3$(dpbt)] (Scheme 1) doped at 1.6 wt% into polyvinyl butyral (PVB) with a refractive index of 1.51 (Wang et al., 2011d). This concentration was chosen since it ensured total absorption of light (transmission $<1\%$). The doped PVB solution was cast onto a 7.8×7.8-cm^2 glass with 3-mm thickness (Fig. 8, right). Three edges were coated with black masks and a c-Si cell was attached onto the last one; [Eu(tta)$_3$(dpbt)] absorption has better match with the solar spectrum, compare Fig. 8 with Fig. 2. The authors estimate that [Eu(tta)$_3$(dpbt)] absorbs 7.6% of the solar spectrum, compared to 2.6% for [Eu(tta)$_3$(phen)]. The EQE of the LSCs depends on the wavelength and is maximum for the absorption maxima at 330 (L = phen) and 420 nm (L = dpbt), reaching 24–25%. It is expressed by the following equation (Wang et al., 2011c):

$$\eta_{\text{EQE}} = \eta_{\text{Q}} \times \eta_{\text{abs}} \times \eta_{\text{G}} \times \frac{\eta_{\text{PL}} \times \eta_{\text{TIR}}(1-r)}{1 - r \times \eta_{\text{PL}} \times \eta_{\text{TIR}}} \tag{9}$$

which reduces to the following simplified expression if r (reabsorption probability) is set to 0:

$$\eta_{\text{EQE}} = \eta_{\text{Q}} \times \eta_{\text{abs}} \times \eta_{\text{PL}} \times \eta_{\text{TIR}} \times \eta_{\text{G}} \tag{10}$$

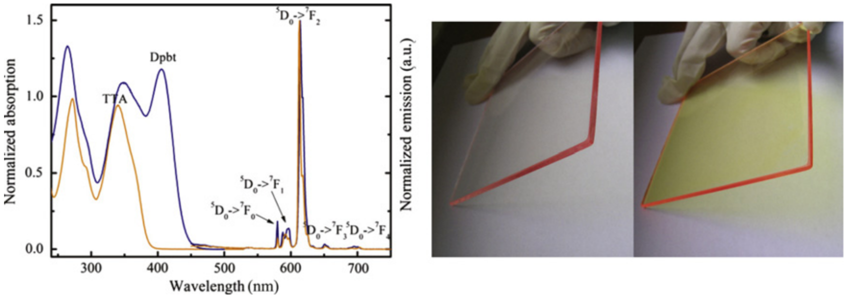

FIGURE 8 (Left) Absorption and luminescence spectra of the [Eu(tta)$_3$L] complexes doped in PMMA. (Right) Photograph of the two LSCs under natural daylight (left: L = phen; right: L = dpbt). *Reproduced with permission from Wang et al. (2011d) © 2011 Elsevier B.V.*

in which η_Q is the quantum efficiency of the c-Si cell at 613 nm (76%), η_{abs} is set to 1 (see above), F_{TIR} is 75% according to Eq. (4), and η_G, the geometry efficiency of the host material related to its absorption, is also set to 1 (no absorption). Since the quantum yields of the complexes doped in PVB, η_{PL}, is estimated to be 44% at the wavelength maxima of the absorption spectra, η_{EQE} reaches ~25%.

These numbers seem interesting. However, when the cell is put under simulated solar illumination (AM1.5G), the overall power conversion efficiency η_P remains small, 0.044 (L = phen) and 0.05% (L = dpbt) for one edge. The power conversion efficiency is given by (Wang et al., 2011d):

$$\eta_P = \frac{P_{out}}{P_{in}} = \frac{V_{OC} \times J_{SC} \times \mathrm{FF}}{P_{in}} \tag{11}$$

with V_{OC} being the open-circuit voltage (≈0.47 V), J_{SC} the short-circuit current density (0.15, L = phen, and 0.17, L = dpbt, mA cm^{-2}), and FF the fill factor (≈0.63). If one multiplies this result by 4 (assuming that the three black masks are substituted by mirrors), one gets η_P(total) = 0.18 and 0.20% only. That is, replacing phen with dpbt only leads to an 11% increase in power conversion efficiency despite the much better absorptivity of $[\mathrm{Eu(tta)_3(dpbt)}]$. This remains unexplained.

A similar study by the same group (Wang et al., 2011c) deals with $[\mathrm{Eu(tta)_3(TOPO)_2}]$ in PMMA (Scheme 1) which has η_{PL} = 73% (Teotonio et al., 2008). The LSC was fabricated by dip-coating a solution of PMMA containing 10 wt% of the complex onto a 10 × 10-cm^2 glass plate of thickness 3 mm and refractive index 1.52. First, the authors demonstrate that η_{EQE} of the LSC remains constant around 50% with variation of the geometric gain of the LSC (ratio of the area of the LSC divided by the area of the attached solar cell) between 0 (no LSC) and 10, contrary to an LSC containing an organic dye which exhibits the efficiency decreasing by a factor 5 due to reabsorption. The performance of the LSC is summarized by η_P(total) = 0.28%, V_{OC} = 0.51 V, J_{SC} = 0.828 mA cm^{-2}, and FF = 0.66, that is substantially better than the previously described LSCs (see Fig. 9). But the main point of the paper is the study of the current–voltage performance with an attached Si cell under AM1.5G irradiation: both η_P and J_{SC} decrease 10 times slower in function the irradiated surface with $[\mathrm{Eu(tta)_3(TPPO)_2}]$ compared with a dye-based LSC (Wang et al., 2011c).

Triazine-based ligands have excellent sensitization properties for the luminescence of europium up to 400–410 nm (Xue et al., 2010) and some of them display sizeable two-photon absorption cross-sections (Lo et al., 2011) so that in addition to dpbt (Scheme 1) several triazinyl ligands have been tested for use in LSCs (Scheme 2) (Katsagounos et al., 2011). Thin 40-nm thick layers of $[\mathrm{Eu(NO_3)_3(trz}i)_2]$ (i = 1, 3), $[\mathrm{Eu(NO_3)_3(trz2)(H_2O)_2}]$, and $[\mathrm{Eu(NO_3)_2(trz4)_2}]^+$ complexes were spin coated from dichloromethane solutions onto a quartz plate

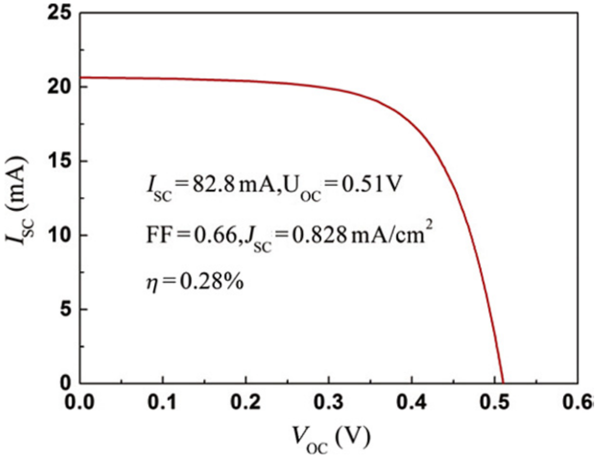

FIGURE 9 Current–voltage performance of the [Eu(tta)$_3$(TOPO)$_2$]-doped LSC under AM1.5G illumination. See text for definitions of variables. *Reproduced with permission from Wang et al. (2011c). © 2011 Elsevier B.V.*

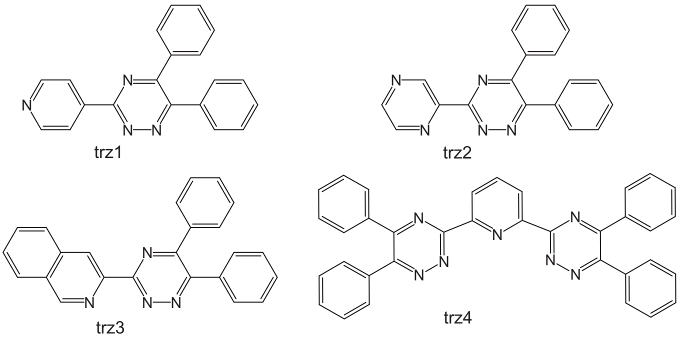

SCHEME 2 Triazinyl derivatives (Katsagounos et al., 2011).

to one end of which a multicrystalline silicon (m-Si) solar cell with 15% conversion yield was attached. No quantitative data on the photophysical properties of the metal complexes are given, but [Eu(NO$_3$)$_3$(trz1)$_2$] appears to be the most luminescent and it is also the most effective in LSCs. For an initial concentration of 14.8 mM of the spin-coated solution, a 15% increase in photocurrent and 7.5% increase in photovoltage were observed for a monolayer (area ratio G of the LSC with respect to the solar cell ≈3) while these figures rise to 26% and 8%, respectively, for three layers (G≈9). Translated in terms of overall cell efficiency, this represents increases of 17% and 28%, respectively. A qualitative assessment rates the photostability of these LSCs as being good (no luminescence loss over several months). The reported large increases in performances are, however, surprising: the thin films absorbs only up to about 400 nm and in the 280–400 nm range, about 3.4% only of the sun irradiance are available. Given the above evaluation ($\eta_{EQE}=0.25$ for $\eta_{PL}=0.44$, see Eq. (10)), one would have predicted adding +1.7 to +3.4 absolute% to the overall cell efficiency for quantum yields of the luminescent complex equal to 44% and 88%, respectively, whereas +2.6% is reported for the one-layer LSC; quantum yields of the complexes are not given.

Terbium emission matches well the spectral response of AlGaAs so that application of terbium salicylate doped in polyvinyl alcohol (PVA) or PMMA (Scheme 1) to LSCs has been assessed. Upon UV excitation around 300 nm, both salicylate and Tb^{III} emit, but quantum efficiencies, were found to be too low for practical purposes despite the calculated optical conversion of 8.8% at 542 nm (Misra and Mishra, 2008).

Another way of designing LSCs is to introduce the luminescent dopant directly into inorganic matrices (e.g., glass). Siloxane- or silicate-based inorganic–organic hybrids present several advantages. They are synthesized by sol-gel methods under mild conditions, which protects the fragile organic molecules from decomposition while dispersion into the inorganic matrix avoids aggregation detrimental to photophysical properties. In addition, many precursors are commercially available and the hybrids are versatile in their composition, processing, and optical properties (Reisfeld, 2010).

Transparent organically modified silicates (ORMOSIL) films prepared from sol-gel processes have been doped with a simple phenanthroline complex $[Eu(phen)_2]^{3+}$ featuring a sizeable quantum yield of 56% (QY = 80% with respect to YPO_4:Eu having QY of 70%) (Giaume et al., 2005). The thickness of the film was 300 nm, and an LSC was made by coating a quartz plate with this film. When coupled with a c-Si solar cell, the device increased the photovoltaic current by 10–15% (Machida et al., 2000). Luminescent Eu^{III}-bridged silsesquioxanes obtained from the organosilane precursors P1 (5,5′ isomer) and P2 (6,6′ isomer) depicted in Scheme 3 have been considered for LSCs too (Graffion et al., 2011). In particular, the material based on the P2 isomer exhibits a sizeable quantum yield of 34% when processed under the form of a thin film with thickness of 54 nm, and an optical conversion

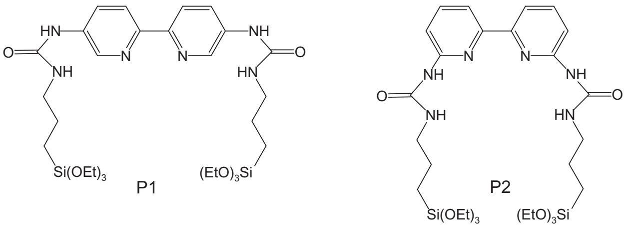

SCHEME 3 Organosilane precursors (Graffion et al., 2011).

efficiency of 4% was obtained. When corrected for losses (see Eqs. (4)–(8)), the effective optical efficiency dropped to 1.7%.

2.4. Other Rare-Earth Materials for LSCs

A proof of principle has been made on the use of ITO electrodes co-doped with Eu^{III} and Y^{III} ions. Co-doping Y^{III} increases the photoluminescence yield compared to an electrode containing only the luminescent ion and, provided that the doping concentrations are precisely controlled (0.1–0.5%), there is no deterioration of the conductivity. When such electrodes are introduced into solar cells, they play a dual role as LSCs and transparent conductive electrode (Ting and Tsai, 2009).

2.5. What's Next?

Improvement of LSCs efficiencies with lanthanide materials is still in its infancy, and although the concept was laid out about 25 years ago, the field started to gain some momentum only during the past 5 years during which a dozen of papers appeared on the subject (or mentioning the subject). There is presently much intellectual excitement about the idea, especially within the context of the current large interest for rare earths in high technology (Eliseeva and Bünzli, 2011). Rare-earth materials have certainly some inimitable advantages such as high photostability and very little reabsorption losses, but they have disadvantages too, the more detrimental one being the very small absorption coefficients which necessitate sensitization of the Ln^{III} luminescence by organic ligands, inorganic matrices through LMCT transitions, or d-transition metal ions. Another pathway is to pump energy into 4f5d states. One example is SrB_4O_7:Sm^{II}(5%), Eu^{II}(5%) which displays broad absorption in the range of 300–600 nm and emits in the NIR range of 650–850 nm with an external quantum efficiency of 90% (de Boer et al., 2011). If, in addition, cholesteric filters are provided to prevent escape of emitted light, this phosphor could help increasing the efficiency of LSCs (de Boer et al., 2012); an experimental efficiency of 2.5% has been obtained when coupled to a c-Si cell (Desmet et al., 2012). Other drawbacks of Ln-based materials are quantum yields which are not always large enough and the high price of some photonic lanthanides. Setting aside these detrimental considerations, it seems, however, that a reasonable view would be to see rare-earth materials help boosting the efficiency of LSCs in a range where practical applications become feasible, particularly if hybrid materials combining inorganic and organic sensitizers are considered. Finally, many engineering efforts are deployed to minimize losses by using 3D photonic materials (Goldschmidt et al., 2010; Gutmann et al., 2011).

An insistent wish is that more precise quantitative data should be reported so that intercomparison between the proposed systems becomes feasible and helps designing better devices.

3. SILICON-BASED SOLAR CELLS

3.1. General Considerations

Light-to-electricity conversion is based on the photoelectric effect discovered by H. Hertz in 1887 and has deep roots in the past with names of eminent scientists, including A. E. Becquerel, C. Fritts, A. Stoletov, A. Einstein, and R. Ohl, associated with its practical implementation. The first solar cells used selenium, but their yield was rather low (<1%). The real start of the field is the seminal paper by researchers from Bell Laboratories in 1954 which briefly describes (the letter is less than one page long!) a new silicon p–n junction converting 6% of the sunlight; the authors predict that a conversion efficiency of 22% could be reached (Chapin et al., 1954). The bandgap of the silicon used was a little over 1 eV so that photons with wavelengths shorter than about 1200 nm could theoretically trigger the conversion.

The commercial production of Si-based solar panels has been intimately linked to the developments of the semiconductor industry and, as a matter of fact, started by using wafers rejected by this industry since the purity requirements for solar cells are somewhat less stringent than for semiconductors. As a result, the price could be reduced from about 100 US$/W to a present value of about 2.1 US$/W. The estimated "grid parity" price is 1 US $/W and present technology is close to it, with multijunction panels nearing 1.3 US$/W. There are three generations of Si cells: (i) wafers using crystalline or multicrystalline Si (c-Si or m-Si) with thickness of about 100–300 μm, which account presently for more than 75% of the market, (ii) thin films based on amorphous Si (α-Si or a-Si), which are much cheaper but have lower conversion efficiency, and (iii) advanced thin films which are thinner and hydrogenated or doped with carbon, nitrogen, or germanium, for the purpose of modulating the bandgap. The most sophisticated and best performing cells are multijunction devices in which the various components have different bandgaps in order to harvest the largest portion possible of the sun emission.

In Si cells, the absorbed photons generate electron–hole pairs (excitons) which have to be separated before being extracted into an external circuit to generate electric current. They are characterized by their overall conversion efficiency which in turn can be broken down into the product of reflection, thermodynamic, charge carrier separation, and conduction efficiencies. Reflection losses can be as large as 30% so that Si cells are usually coated with an antireflection layer. The thermodynamic efficiency depends on the bandgap energy and the wavelength of the impinging photons (Shockley–Queisser limit). On a practical level, the solar cell efficiency (or EQE) is determined by measuring the maximum cell power output, P_m (W), and dividing it by the surface input power P_S (W m^{-2}) and the cell area A (m^2):

$$\mathrm{EQE} = \frac{P_m}{P_S \times A} \tag{12}$$

P_m corresponds to the load that maximizes the output voltage. Measurements have to be conducted under standard test conditions (STC): 25 °C, 1000 W m^{-2} irradiance with an AM 1.5 global spectrum. Characteristic parameters are (i) the quantum efficiency η_Q which is governed by the charge production and separation efficiency as well as by the conduction efficiency, (ii) the open-circuit voltage V_{OC} (V), (iii) the short-circuit current I_{SC} (A), and (iv) the fill factor (Fig. 10); they are related by the following relationship, equivalent to Eq. (11):

$$\mathrm{FF} = \frac{P_m}{V_{OC} \times I_{SC}} = \frac{\eta_Q \times P_S \times A}{V_{OC} \times I_{SC}} \tag{13}$$

Academic laboratories try hard to maximize EQE but in practice, the power-to-cost ratio is more important. There are several ways of maximizing EQE: (i) minimizing reflection losses, (ii) concentrating the irradiation, (iii) using multijunction cells, and (iv) trying to downconvert/downshift (Klampaftis et al., 2009; Richards, 2006a,b; Richards and Shalav, 2005; Strümpel et al., 2007; van der Ende et al., 2009a; Zhou et al., 2010b) and/or upconvert (Fischer et al., 2012b; Richards, 2006a; Richards and Shalav, 2005; Shalav et al., 2007; Strümpel et al., 2007) the portions of the solar spectrum not matched by the bandgap material. In the following, we concentrate on the latter two aspects, with reference to Ln-containing materials.

Downconversion, or quantum cutting, refers to a system in which an energetic photon is absorbed and two photons of lower energy emitted (Fig. 3), with a quantum yield which can theoretically reach 200% (Wegh et al., 1999). In Ln-containing materials, the intermediate level (IL) needed is an f-level, whereas in other compounds, it is materialized by an impurity. Quantum cutting

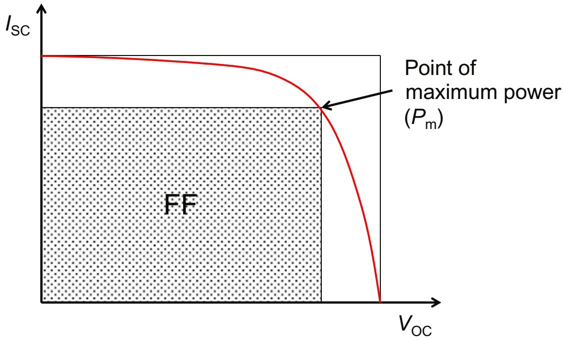

FIGURE 10 Schematic representation of the fill factor FF.

in lanthanide-doped materials proceeds according to three different mechanisms. (i) Generation of two electron–hole (e–h) pairs in the Si lattice, which requires an energy of at least 2.6 eV, so that the expected increase in EQE is small (<5% for $\lambda = 350$ nm). (ii) Production of two visible photons by a single Ln^{III} ion, for example, Pr^{III} which emits blue (405 nm) and red (620 nm) photons upon excitation at 185 nm with an efficiency of 140% (Piper et al., 1974). (iii) Downconversion in systems containing two different lanthanide ions; a wealth of such systems are presently investigated (see below). We have to mention here another process induced by QDs with composition PbS, PbSe, PbTe, or CdSe: multiexciton generation (MEG) in which one photon with energy $h\nu \geq E_g$ yields n e-h pairs (Lohse and Murphy, 2012; Richards, 2006b).

When an energetic photon is simply converted into a longer-wavelength photon by a single Ln^{III} ion, the correct denomination is downshifting, but downconversion is also often used in the literature. An intermediate case is when the excitation photons are converted into both visible and NIR photons, emitted, for instance, by the matrix and the Ln^{III} active ion, respectively. In the reported examples, the mechanism is likely to be a double downshifting process and not a cooperative energy transfer (CET).

In optimizing wavelength-converting materials, one has to keep in mind the sun spectrum and the spectral response of the solar cell. Indeed, Fig. 2 shows the absorption of a c-Si cell, but when one looks into the conversion efficiency of c-Si versus wavelength (Fig. 11), one realizes that the best conversion improvement one could get is when downconversion/downshifting, or

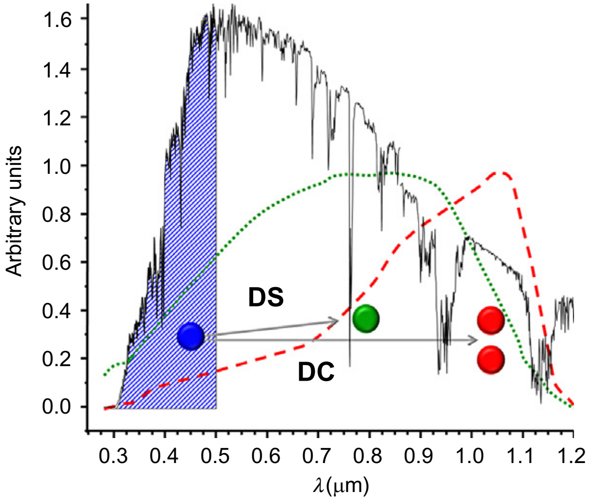

FIGURE 11 Normalized spectral responses of m-Si (dotted line) and c-Si (dashed line) compared to the solar spectrum AM1.5G and definitions of downshifting (DS) and downconversion (DC). *Redrawn from Zhou et al. (2010b) and Katsagounos et al. (2011).*

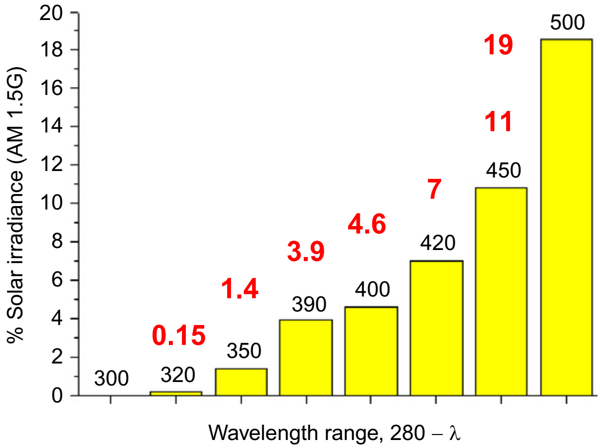

FIGURE 12 Calculated percentages of the AM1.5G solar spectrum emitted between 280 nm and wavelength λ.

upconversion, produces photons in the wavelength range of 850–1100 nm, with 1050 nm being optimum (Zhou et al., 2010b). With respect to c-Si cells, the wavelength range of 300–500 nm is well suited for downconversion and it represents ~19% of the sun total illumination (Fig. 12), while wavelengths larger than ~1150 nm are appropriate for upconversion. This demonstrates that processes, which produce photons in the range of 400–750 nm, are not ideal with respect to c-Si response. On the other hand, they are well suited for m-Si cells. Additionally, one has to take into account the fact that if one converts one 300–500 nm photon into a single 850–1100 nm photon, there will be a large energy loss (10,000–25,000 cm^{-1}, or 1.2–3.1 eV) which will translate in heating of the cell. Therefore in theory, one would have to look for downconversion (possibly "double downshifting") rather than for downshifting of a single photon.

3.2. Downconverting Materials

3.2.1. Prospective Studies

A theoretical background for downconversion in solar cells, which has been published in 2002 and was based on the hypothesis that no recombination losses occur, has probed both the effect of the converter layer and its position, either at the front or at the back of the cell under STC (Trupke et al., 2002a). The left part of Fig. 13 displays the energy scheme of a device with front location of the downconverter and for the ideal case for which (i) $E_g(\mathrm{DC}) = 2\,E_g(\mathrm{Si})$ and (ii) the IL lies at the center of the downconverter bandgap $E_g(\mathrm{DC})$. Taking a refractive index of 3.6, which is typical for Si or GaAs

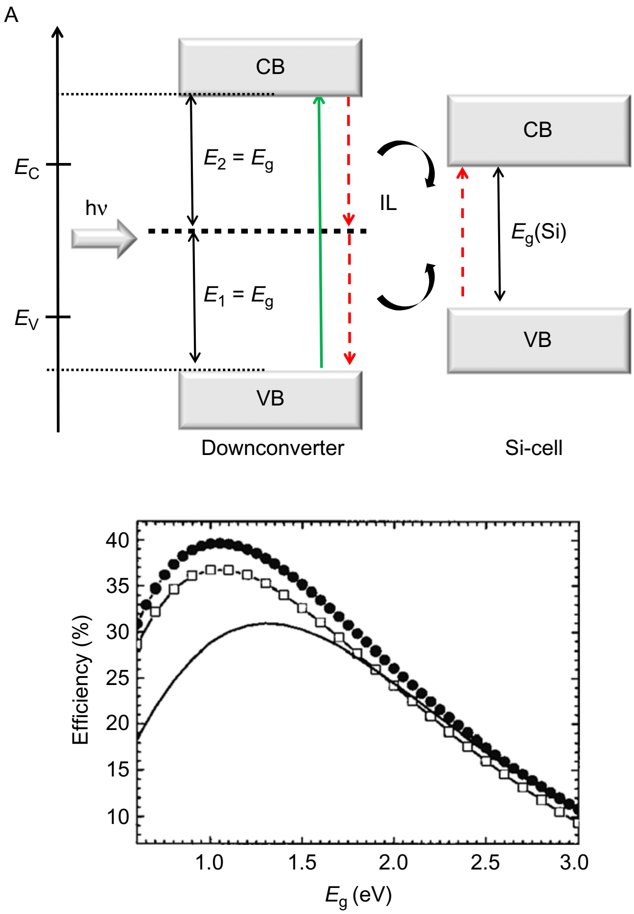

FIGURE 13 (A) Schematic energy diagram for a c-Si cell fitted with a downconverter layer in the ideal case for which the energy of the IL lies in the center of the bandgap of the converter and $E_g(\mathrm{DC}) = 2\ E_g(\mathrm{Si})$. (B) Efficiencies versus bandgap energy, Shockley–Queisser limit (solid line), downconverter at the front (empty squares), and downconverter at the rear (solid circles). *(A) Adapted from Trupke et al. (2002a). (B) Reproduced with permission from Trupke et al. (2002a), © 2002 American Institute of Physics.*

materials, and assuming nonconcentrated irradiation from a 6000-K sun, an optimum efficiency of 39.6% may be obtained when the bandgap is 1.05 eV (c-Si) and the converter positioned at the rear. If the converter is placed at the front, the Shockley–Queisser limit (30.9%) is still largely overcome, but the maximum efficiency is smaller, 36.8% for a bandgap of 1.1 eV (Fig. 13, right). As downconversion layer, the authors suggest the use of III–V compounds, for example, AlAs or GaP doped with lanthanide "impurities." The results obtained by Trupke et al. were corroborated by another model study including both upconversion and MEG, and which calculated that efficiencies up to 49% could be obtained (Shpaisman et al., 2008). The enhancement potential of downconversion in the absence of sun concentration has also been modeled by Abrams et al. (2011), who carefully took into account all effects, including losses. They confirm the above conclusions by calculating that DC can add, in an ideal system, a maximum of 7 absolute % to the cell efficiency. Improvement essentially arises from an increase in photocurrent, while the photovoltage remains the same as in the absence of DC.

In fact, the increase in efficiency depends largely on the type of illumination: a similar theoretical study of anm-Si cell fitted with a top upconversion layer made up of QDs emitting at 603 nm concluded that the increase in short-circuit current is 6.3%, 9.6%, and 28.6% under direct, global (AM1.5G), and diffuse irradiation (van Sark, 2005). Further modeling taking into account more realistic irradiation patterns (as measured by a Dutch meteorological station on a yearly basis) shows that the improvement in I_{SC} varies between 7% and 23% and is linearly related to the average photon energy (van Sark, 2008). In any case, when applying downconverting layers to solar cells, one has to realize that the NIR photons are not necessarily emitted in the direction of the semiconductor. Depending on the refractive index of the converter, up to half of the photons can be lost in the sun direction. Simply increasing the refractive index n(DC) to match that of silicon might unfortunately not be the right solution because of greater reflection at the air–converter interface. An antireflection layer has therefore to be added between air and the converter. If it is difficult to modify n(DC), a second antireflection layer should then be introduced between the converter and the semiconductor; in this case, the efficiency of the device becomes independent of n(DC). This points to the necessity of carefully considering light trapping issues when optimizing solar cells (De Vos et al., 2009).

In two other prospective papers, B.S. Richards has examined which Ln-containing systems could be envisaged for downconversion (Richards, 2006a,b). The practical relevance of quantum cutting is, in fact, very limited. Indeed, both in one-ion or two-ion systems, absorption is usually either in the vacuum UV (Strümpel et al., 2007), for example, the Pr(4f-5d) transition at 185 nm or the Gd($^6G_J \leftarrow {}^8S_{7/2}$) transition at 202 nm, or in the UV (300–360 nm), that is in a spectral range where there is no or very little sun emission (Fig. 12). Some potential systems are however worth discussing even though they have not been directly coupled with solar cells.

3.2.2. Prospective Systems with Narrow-Band Absorption

Several systems have been investigated. For instance, excitation of the $^1G_4$ level of Tm^{III} in $Cs_2LiTmCl_6$:Nd at 476.5-nm followed by deactivation to $^3H_5$ and energy transfer onto the Nd($^2H_{9/2}$) level; then relaxation to Nd($^4F_{3/2}$) leads to emission around 900 nm. Tm^{III} emits simultaneously in the range of 800–840 nm, and other mechanisms are also operating so that the quantum yield could not been determined (Tanner et al., 2002). Some other papers deal with downconversion to $\mathrm{Er^{III}}$; however, the emission of this ion in the range of 1520–1560 nm is not suited for silicon but, rather, for germanium which has a bandgap corresponding to about 1700 nm (Chen et al., 2012d; Timmerman et al., 2008; Zhou et al., 2010a,c). $\mathrm{Er^{III}}$ and $\mathrm{Nd^{III}}$ ions are much more sensitive to nonradiative deactivation as compared to $\mathrm{Yb^{III}}$. The latter includes the $^2F_{5/2}\rightarrow{}^7F_{7/2}$ transition in the range of 950–1150 nm, usually peaking around 980 nm, and featuring extended longer-wavelength crystal-field and vibronic structures. This emission is ideal because it is only slightly more energetic than the c-Si bandgap (see Fig. 11), which will minimize thermal losses. $\mathrm{Yb^{III}}$ can be excited by a wealth of other $\mathrm{Ln^{III}}$ ions, and the relevant works are briefly discussed here because they contributed to extendour knowledge of $\mathrm{Ln^{III}}$ spectroscopy and energy-transfer processes. It is worth mentioning that the host matrix has to be chosen with care since it not only influences some of the energy migration paths but, more importantly, it may induce multiphonon nonradiative deactivations. Selected phosphors involving $\mathrm{Yb^{III}}$ are reported in Table 2. The downconversion efficiency η_{DC} is calculated as (Ueda and Tanabe, 2009):

$$\eta_{\mathrm{DC}} = \eta_{\mathrm{D}}(1-\eta_{\mathrm{CET}}) + 2\eta_{\mathrm{CET}} \times \eta_{\mathrm{Yb}} \tag{14}$$

where η_{D} and η_{Yb} are the quantum yields of the donor and of the acceptor ($\mathrm{Yb^{III}}$), respectively, under direct excitation (intrinsic quantum yields) and η_{CET} is the efficiency of the CET:

$$\eta_{\mathrm{CET}} = 1 - \frac{\tau_{\mathrm{D}}(\mathrm{obs})}{\tau_{\mathrm{D}}(0)} \tag{15}$$

with $\tau_{\mathrm{D}}(\mathrm{obs})$ and $\tau_{\mathrm{D}}(0)$ being the observed lifetimes of the donor in the presence and in the absence of the acceptor, respectively.

In Eq. (15), lifetimes may be replaced with integrated emission intensities. Surprisingly, η_{Yb} is rarely determined and simply set to 1 because the matrices used have usually low phonon energies, minimizing nonradiative deactivations. However, if the $\mathrm{Yb^{III}}$ concentration becomes large, cross-relaxation may considerably reduce the quantum yield: in YAG, for instance, η_{Yb} is reduced from 96% for a concentration between 2% and 6% to 70% for a concentration equal to 10% (Ueda and Tanabe, 2009). Downconverting systems are often characterized by η_{DC} only, but much as for luminescent compounds, it is the product of η_{DC} by the absorptivity of the materials in the excitation range used which should be considered. This is rarely done quantitatively. Furthermore, if coupled with a Si cell, this product should then be further multiplied by the conversion efficiency at the emitted wavelength to give an objective description of the overall efficiency of the downconverting layer.

TABLE 2 Selected $\mathrm{Yb^{III}}$-Containing Downconversion Systems Based on f-f Excitation and Studied as Potential Candidates for Increasing the Efficiency of Si Solar Cells

No.	Sensitizer (mol%)	Emitter (mol%)	Host lattice	λ_{exc} (nm)	λ_{em} (nm)	η_{DC} (%)	References
1	Pr(0.1)	Yb(0.1–1.5)	β-YF_3	482	976	194	Chen et al. (2008a)
2	Pr(0.05–0.3)	Yb(0.5–17)	SrF_2	441	980	140	van der Ende et al. (2009b)
3	Pr(1)	Yb(1–30)	$NaYF_4$	443	977	134	Chen et al. (2009b)
4	Pr(0.5)	Yb(2–40)	$LiYF_4$	481	990	Small	van Wijngaarden et al. (2010)
5	Pr(0.1)	Yb(0.1–1.5)	Oxyfluoride glass[a]	470	976	153	Chen et al. (2012b)
6	Nd(0.5)	Yb(2–10)	YF_3	350	986	140	Meijer et al. (2010)
7	Tb[b]	Yb[b]	$KYb(WO_4)_2$	308	980	n.a.	Strek et al. (2001)
8	Tb(1)	Yb(5–99)	$YbPO_4$	488	1000	188	Vergeer et al. (2005)
9	Tb(1)	Yb(1–99)	$GdAl_3(BO_3)_4$	485	1000	196	Zhang et al. 2007)
10	Tb(0.5)	Yb(1–15)	Borate glass[c]	330	976	174	Chen et al. (2008b)
11	Tb(1)	Yb(1–25)	$LaBaB_9O_{16}$	481	980	153	Wang et al. (2009)
12	Tb(1)	Yb(1–15)	Zn_2SiO_4 thin film	485	980	154	Huang and Zhang (2009)
13	Tb(1)	Yb(1–30)	$GdBO_3$	486	970	191	Huang et al. (2009)
14	Ce(1),Tb(5)	Yb(1–10)	$GdBO_3$	360(320–390)[d]	970	[e]	Huang et al. (2009)

15	Tb(10)	Yb(10–20)	$LaBGeO_5$	484/300–490[f]	1020	146	Liu et al. (2009a)
16	Er(1)	Yb(5–30)	$NaYF_4$	380	650/980	Small	Aarts et al. (2009)
17	Er(0.5)	Yb(3)	NGC[g]	350–415[h]	990/1540	199	Rodriguez et al. (2010)
18	Er(1)	Yb(15)	$Cs_3Y_2Br_9$	490/300–380[i]	999	>195	Eilers et al. (2010)
19	Tm[h]	Yb[h]	Oxyfluoride glass[j]	468	1016	144–162	Ye et al. (2008a)
20	Tm(1)	Yb(5–50)	YPO_4	474	970–1010	173	Xie et al. (2009)

[a] *Glass composition:* $45SiO2–25Al_2O_3–10Na_2O–20CaF_2–0.1PrF_3–xYbF_3$ *(x = 0.1, 0.3, 0.5, 1.0, and 1.5).*

[b] *Doping rate not available.*

[c] *Glass composition:* $B_2O_3–BaO–CaO–La_2O_3$*.*

[d] *4f-5d transition of* Ce^{III}*.*

[e] *Not available, but Yb emission is 30 times stronger than in the doubly doped (Tb, Yb) material.*

[f] *f-f transitions to excited* Tb^{III} *levels.*

[g] *Oxyfluoride nanostructured glass ceramic with optimized composition* $32SiO_2–9AlO_{1.5}–31.5CdF_2–18.5PbF_2–5.5ZnF_2{:}3.5LnF_3$ *mol% and a Yb/Er ratio equal to 6.*

[h] *f-f transitions to* $^2H_{9/2}$, $^4G_{11/2}$, *and* $^2G_{7/2}$ *excited levels of* Er^{III}*.*

[i] *The excitation spectrum of Yb emission also shows a broad* Br^-*-to-*Yb^{3+} *charge transfer band between 300 and 380 nm.*

[j] *Glass composition:* $45SiO_2–12Na_2O–23Al_2O_3–20LaF_3–0.5Tm^{3+}–xYb^{3+}$ *(x = 0, 4, 8).*

3.2.3. Prospective Systems with Broad-Band Absorption

The systems listed in Table 2 rely on f-f absorptions as excitation so that they present limited interest for solar energy conversion because the total amount of light which can be absorbed is small despite some impressive quantum yields. This is exemplified by $GdBO_3$:Tb(1%),Yb(x%) (Table 2, entry 13) with downconversion efficiency of 191% for $x=30$, but which only emits very weakly despite a very efficient $Tb(^5D_4) \rightarrow Yb(^2F_{5/2})$ transfer reaching 91% (Huang et al., 2009). The luminescence intensity of the phosphor is, however, considerably increased when broad-band absorbing Ce^{III} is added (Table 2, entry 14), 30-fold with respect to $GdBO_3$:Tb,Yb. This is because this ion has a strong allowed 4f-5d absorption in the range of 320–380 nm and, also, because energy transfer from the Ce(5d) excited level to $Tb(^5D_3)$ is very efficient (98%) as is the Tb-to-Yb transfer; in fact, the luminescence intensity of the ternary phosphor is fourfold greater compared to $GdBO_3$:Ce,Yb (Huang et al., 2009). The main observed mechanism is a CET and energy migration pathways are sketched on Fig. 14.

As a matter of fact, broad-band excitation seems to be the only feasible alternative. It can be achieved through the lattice, through charge-transfer transitions, or through 4f-5d transitions. The energy of the latter two can be largely tuned by changing the metal ion environment (i.e., the lattice). Surprisingly, fewer broad-band excitation systems have been studied compared to the less

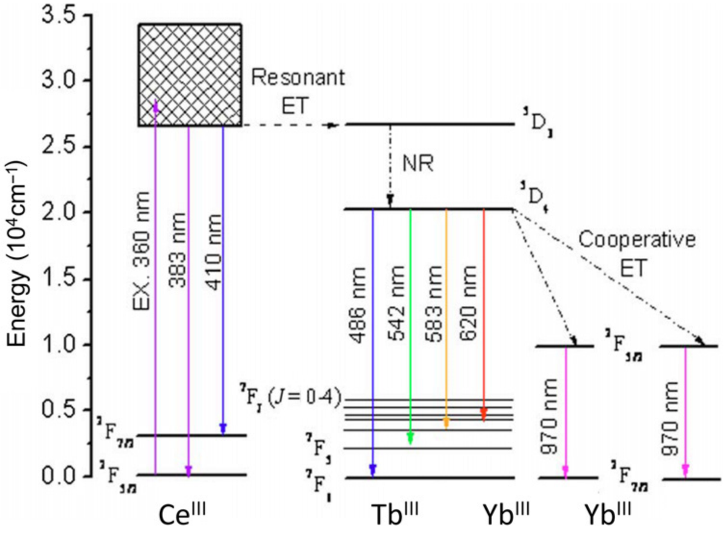

FIGURE 14 Schematic energy-level diagram of the ternary phosphor $GdBO_3$:Ce,Tb,Yb. Dotted arrows denote either nonradiative or energy-transfer processes. *Reproduced with permission from Huang et al. (2009), © 2009 American Institute of Physics.*

efficient f-f excitation. The $Cs_3Y_2Br_9$ host (Table 2, entry 18) which has very low phonon energies ($\sim$180 cm^{-1}) allows both f-f and broad-band excitation, but its hygroscopic nature hampers application to solar cells (Eilers et al., 2010). Selected examples involving Yb^{III} as emitter and broad-band sensitizers are listed in Table 3. The downconversion efficiencies are similar to those reported in Table 2, but the absorptivity of the phosphors is larger. As stated above, there is, however, no quantitative data to assess this aspect.

The tunability of the 4f-5d transition by the lattice is illustrated by Ce^{III}. When embedded into YAG, this ion displays two 4f → 5d transitions owing to the splitting of the 5d orbital by the crystal field generated by the garnet, one centered at 350 nm extending from 300 to 370 nm and another one, much more intense, with a maximum around 450 nm and stretching from 400 to about 500–550 nm. On the other hand, the charge transfer (CT) band of Yb^{III} lies in the UV ($\sim$250–260 nm) and is not of any help for solar energy conversion.

Striking are the large differences in η_{DC} depending on the composition of the downconverting phosphor, from 96% (Table 3, entry 5) to 175% (entry 6). Now if Ce^{III} is doped into a borate glass, the energy of the 4f-5d transition is considerably blue-shifted to $\sim$330 nm (Table 3, entry 4) which is detrimental since solar emission is not intense in the range of 300–380 nm. Introduction of an additional ion such as Tb^{III} in a Ca_2BO_3Cl matrix, for instance (entry 2), has been attempted, and the excitation spectrum contains additional bands from Tb^{III} f-f transitions; in turn, this necessitates a double energy-transfer Ce-to-Tb-to-Yb; it seems, nevertheless, that the corresponding phosphor is much brighter than the $GdBO_3$ downconverters listed in Table 2 (entries 9, 10, 13, 14).

The divalent ions Eu^{II} and Yb^{II} have also adequate spectroscopic properties for harvesting part of the UV solar spectrum. For instance, NIR emission of Yb^{III} occurs after CET from the Eu^{II}($4f^6 5d^1$) level centered at 404 nm (emission range 350–500 nm) to Yb^{III}($^2F_{5/2}$) in borate glass (Zhou et al., 2009). The excitation spectrum displays the O^{2-}-to-Yb^{III} CT band at 262 nm (range 220–350) nm and the Eu^{II}(5d←4f) transition at 320 nm (range 260–400 nm). The latter is the most efficient in harvesting solar light. Upon addition of increasing amounts of Yb^{III}, the Eu^{II}($4f^6 5d^1 \rightarrow 4f^7$) emission is quenched and the intensity of the Yb^{III}($^2F_{5/2} \rightarrow {}^2F_{7/2}$) fluorescence increases. This intensity is temperature independent, which points to CET being the operative mechanism. The composition maximizing CET and minimizing Yb^{III} cross-relaxation is 0.5 mol% Eu^{II} and 3 mol% Yb^{III}. The same authors have sintered a mixture of $CaCO_3$, Al_2O_3, and Yb_2O_3 under reducing atmosphere (8% H_2/92% N_2) which resulted in a mixed valence compound with about 40% of the Yb content reduced to Yb^{II} (Teng et al., 2010). The corresponding Yb^{II}(5d ← 4f) transition occurs at 310 nm (range 230–360 nm, including the Yb^{III} CT transition mentioned above). No luminescence is usually observed at room temperature from the $4f^{12}5d^1$ state, but in the presence of Yb^{III}, the luminescence of the latter is enhanced. A log–log plot of the

TABLE 3 **Selected Yb^{III}-Containing Downconversion Systems Based on Broad-Band Excitation (4f-5d or Charge-Transfer Transitions) and Studied as Potential Candidates for Boosting the Efficiency of Si Solar Cells**[a]

No.	Sensitizer (mol%)	Emitter (mol%)	Host lattice	λ_{exc}(nm transition)	η_{DC} (%)	References
1	$Ce^{III}(1)Tb^{III}(4)$	Yb(2)	Borate glass[b]	304 (250–350) Ce(4f-5d)350–400, 484 Tb (f-f)	n.a.	Zhou et al. (2010d)
2	$Ce^{III}(1)Tb^{III}(4)$	Yb(2)	Ca_2BO_3Cl	315 (280–340), 369 (330-400)	n.a.[c]	Zhang et al. (2009)
3	$Ce^{III}(0.5)$	Yb(5)	Borate glass[d]	330 (250–380) Ce(4f-5d)	174	Chen et al. (2008b)
4	$Ce^{III}(3)$	Yb(6.7)	YAG	470 (400–520) Ce(4f-5d)	153	Liu et al. (2009b)
5	$Ce^{III}(0.5)$	Yb(5)	YAG	440 (400–500) Ce(4f-5d)	96	Ueda and Tanabe (2009)
6	$Ce^{III}(1)$	Yb(25)	YAG	467 (400–500) Ce(4f-5d)	175	Lin et al. (2010)
7	$Eu^{II}(0.5)$	Yb(1–15)	Borate glass[b]	262 (220–350) Yb^{III}(CT)/320 (260–400) Eu(5d←4f)	164	Zhou et al. (2009)
8	$Yb^{II}(1.6)$	Yb(2.4)	$CaAl_2O_4$	310 (230–360) Yb^{II}(4f-5d)	n.a.	Teng et al. (2010)
9	$Bi^{III}(1)$	Yb(5–15)	Gd_2O_3	347 (300–400) $Bi(^3P_1\leftarrow{}^1S_0)$	174[e]	Huang and Zhang (2010)
10	Si–O defects	Yb(2)	STS glass[f]	310 (250–350) Si–O defects	n.a.[g]	Ye et al. (2008b)
11	Li defects	Yb(1)	$ZnO:LiYbO_2$	395 (350–450) Li defects in ZnO	n.a.	Ye et al. (2010)
12	$VO_4{}^{3-}$	Yb(1)	SiO_2/YVO_4 bilayer film	320 (300–360) $O^{2-}V^{5+}$ CT	n.a.[h]	Peng et al. (2011)

[a] *NIR emission maxima are in the range of 975–1030 nm.*
[b] *Glass composition:* $15Na_2O–5Al_2O_3–80B_2O_{316}$.
[c] *NIR emission is 10 and 2.8 times larger than for* $Gd_{0.89}Tb_{0.01}Yb_{0.10}BO_3$ *(see Table 2, entries 9, 10, 13) upon excitation at 315 and 369 nm, respectively.*
[d] *Glass composition:* $B_2O_3–BaO–CaO–La_2O_3$.
[e] *Assuming both* η_{Bi} *and* η_{Yb} *being equal to 1.*
[f] *Glass composition:* $40SrO–20TiO_2–40SiO_2–xYb_2O_3$.
[g] *One visible photon (550 nm) emitted by the glass and one NIR photon by* Yb^{III}*; energy-transfer efficiency: 56% for* $x = 12$ *mol%.*
[h] *The antireflective bilayer displays a transmission of 95% at 550 nm.*

emitted intensity versus excitation power yields a straight line with a slope 0.43 ± 0.03. The expected value for CET transfer onto two Yb^{III} ions would be 0.5; if phonon assisted (to degrade the remaining energy), the process would need 8 phonons (the aluminate matrix has phonon energy of about $1000\ cm^{-1}$) which is large. Consequently, the authors suggest that part of the $(Yb^{II})^*$ energy is dissipated via CET to three Yb^{III} ions (the slope of the log–log plot for such a process would be 0.33), although they admit that such a mechanism has low probability. The idea is partially supported by the fact that Yb^{III} luminescence is almost temperature independent in the range of 15–350 K.

Ions other than lanthanides have absorption in the range of 300–400 nm and Bi^{III} $(6s^2)$ is one of them. The $^3P_1 \leftarrow {}^1S_0$ transition is centered at 347 nm and $^3P_1$ transfers energy onto $Yb^{III}(^2F_{5/2})$ levels in doped Gd_2O_3 with an efficiency varying between 34% and 74% for Yb^{III} concentrations between 5 and 15 mol%, respectively (Table 3, entry 9). Under the assumption that η_{Bi} and η_{Yb} are both equal to unity, η_{DC} is calculated to reach 174% (see Eq. (14); Huang and Zhang, 2010). Similar observations are reported for Y_2O_3 doped with 1% Bi^{III} and 2% Yb^{III} (Huang et al., 2011). Silicon defects in $Ba_2TiSi_2O_8$ crystals doped with Yb^{III} also act as sensitizers for this ion although they absorb in a slightly less favorable spectral range, 250–350 nm (Ye et al., 2008b). More interesting are ZnO hybrid phosphors, for instance, $ZnO{:}LiYbO_2$(1 mol%): excitation into Li defects of ZnO (350–450 nm, maximum at 395 nm) results in intense Yb^{III} fluorescence in addition to self-activated emission from ZnO peaking at 520 nm but extending from 450 to 650 nm; this can be considered as being a double downshifting process (Ye et al., 2010).

3.2.3.1. Trivalent Holmium as Downconverting Ion

Yttrium vanadate is an alternative host for Ln^{III} ions which displays a CT absorption band at 328 nm (range: 250–360 nm) and emits a broad band at 450 nm (370–670 nm). When 2 mol% of Ho^{III} is doped into YVO_4, energy transfer occurs and strong Ho^{III} luminescence bands at 550 ($^5S_4$, $^5F_2 \rightarrow {}^5I_8$), 650 ($^5F_5 \rightarrow {}^5I_8$), 975 ($^5F_5 \rightarrow {}^5I_7$), 1015 ($^5S_4$, $^5F_2 \rightarrow {}^5I_6$), 1150 and 1190 ($^5I_6 \rightarrow {}^5I_8$) nm appear, while the CT luminescence is almost completely quenched (Yu et al., 2012a). The process can be interpreted as being a sequential two-step downconversion mechanism yielding two NIR photons; the corresponding transitions are numbered ① and ② in Fig. 15. The same host was chosen to develop an antireflective bilayer film for c-Si cells comprising SiO_2 and doped YVO_4 layers that displays downconversion upon excitation into the vanadate CT band at 320 nm; a highly transparent device was obtained with transmission up to 95% at 550 nm (Peng et al., 2011).

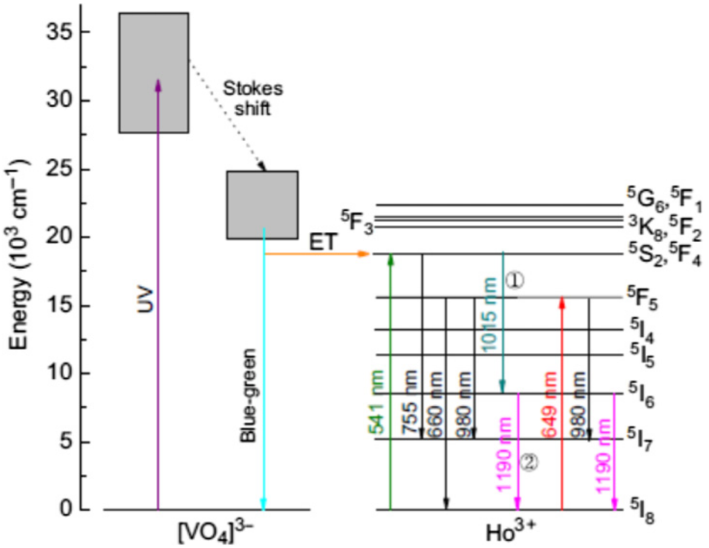

FIGURE 15 Energy-level diagram for the energy migration processes occurring in YVO_4: Ho(2%) after excitation into the CT band of VO_4^{3-}; energy transfer on Ho^{III} generates the two NIR transitions labeled ① and ②; direct excitation into Ho^{III} levels $^5S_4$, $^5F_2$, or $^5F_5$ and subsequent luminescence transitions are also shown. *Reproduced with permission from Yu et al. (2012a), © Elsevier B.V. 2012.*

3.2.4. Practical Systems for Downconversion

Until now, very few papers report successful downconversion experiments with actual solar cells. One Chinese patent mentions transparent oxyfluoride microcrystalline glasses containing 1–40 mol% of Ln^{III} ions and featuring quantum yields larger than 1 (Chen et al., 2009a). In a recent paper, authors report that a c-Si cell fitted with an oxyfluoride glass layer (2×2 cm^2 $\times$ 2 mm) with composition 60 SiO_2–20 Al_2O_3–20 CaF_2: 0.4Pr^{III}, Yb^{III} (0–4 mol%) has lower EQE compared to the cell without the downconverting layer despite a DC quantum yield of 158%. Two reasons may explain this deceptive result: reflection losses due to the added layer and, possibly, a smaller real quantum yield than calculated (Zhou et al., 2012). Finally, the performances of a c-Si cell have been evaluated with the photovoltaic simulation program PC1D; the simulated conversion efficiency increases from 12.3% to 14.9% (+22 relative%) upon incorporation of a 3-mm thick fluoride glass co-doped with Pr^{III} (1.7×10^{25} ions/m^3) and Yb^{III} (3.6×10^{26} ions/m^3). The quantum yield of the downconversion system amounts to 186% (Song and Jiang, 2012).

On the other hand, downshifting materials have been tested and they are described in the following sections.

3.3. Downshifting Materials

There are two types of downshifting materials: fluorescent organic dyes and transition metal (mainly 4f) phosphors and complexes. As will be described below, it seems that approximately 1% can be added to the efficiency of modules with overall efficiencies of 10–15% by using a downshifting layer. For instance, c-Si cells encapsulated into PMMA containing a LUMOGEN® dye (570, 083, or 300) from BASF display an increase in EQE below 400 nm from near zero up to 40%, and the subsequent rise in photocurrent induces a +1% increase in total efficiency (McIntosh et al., 2009). The fluorescent organic dyes suffer from the same drawbacks as those described for LSCs, particularly poor photostability, henceforth the idea to replace them with Ln^{III} compounds which are less prone to photobleaching and reabsorption. The downshifting process is easier to put into practice than downconversion because there is no need to precisely match transition energies in the donor and acceptor ions. That is, broad-band excitation can be used routinely, either by antenna effect in coordination complexes or 4f-5d transitions for inorganic materials containing divalent (e.g., Eu^{II}) or trivalent (e.g., Ce^{III}) ions.

3.3.1. *Complexes with Organic Ligands*

To our knowledge, the first demonstration of downshifting increasing the efficiency of both crystalline and amorphous Si solar cells dates back to 1997. Hybrid Si polyvinyl chloride (PVC) cells were coated with an ORMOSIL containing 1–3 mol% of $[EuCl_3(phen)_2]$ or $[TbCl_3(bpy)_2]$ complexes (Scheme 4). A relative increase in the conversion efficiency of 15% was observed under

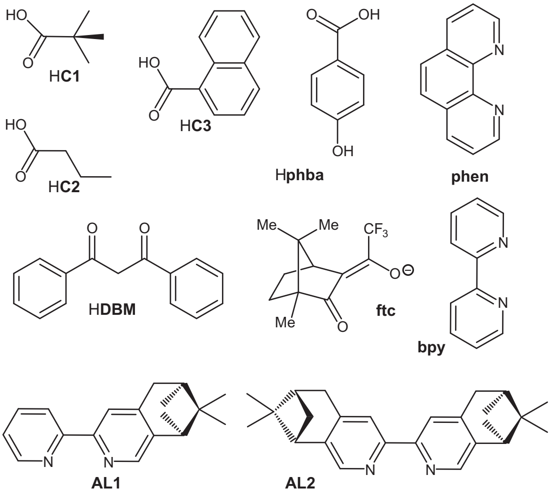

SCHEME 4 Carboxylate ligands, dibenzoylmethane, camphorate, and ancillary ligands mentioned in Section 3.3.1.

AM1.5G illumination for the c-Si PVC cell coated with the ORMOSIL–Eu^{III} complex, while the Tb^{III} coating was detrimental. In order to lower the amount of light scattered by the ORMOSIL–Eu^{III} complex coating, a silica gel layer was added and the increase in efficiency went up to 18%. The final absolute efficiency of the commercially available solar cell was 9.1%. Conversely, the efficiency of the hybrid a-Si PVC cell was increased by 8% when an ORMOSIL–Tb^{III} complex layer was added (Jin et al., 1997). These results were confirmed 3 years later by the same authors in a slightly different way. The ORMOSIL–$EuCl_3(phen)_2$ (3 mol%) solution was dip-coated onto a quartz plate until a 300-nm thick film was obtained. A LSC was then assembled from three such plates with Ag paste and coupled to commercially available c-Si PVC hybrid cells (with absolute yield between 6% and 8.5%). The photovoltaic output of the composite device increased by 10–15% with respect to the uncoupled cell, that is adding about 1% to the absolute external quantum efficiency (Machida et al., 2000). This is in fact a good performance because the absorption spectrum of the Eu^{III} complex only marginally overlaps with the solar spectrum in the range of 300–390 nm, which represents merely 3.9% of the solar spectrum; this means that the reported overall downshifting process has an efficiency of about 26%. A later investigation confirmed the usefulness of such coatings. For instance, a c-Si cell was fitted with a layer of PVA containing 10% of $[Eu(NO_3)_3(phen)_2]$ (absorbing >90% of the high-energy tail of the solar spectrum; quantum yield 40%) and between 0.8% to 1% was added to the overall efficiency of the cell (the efficiency itself was not given). However, we note that this experiment has been conducted under AM 0 illumination which delivers about twice as much photons in the 300–390 nm range than AM 1.5 (Marchionna et al., 2006).

Highly luminescent Eu^{III}β-diketonates have the same effect. For instance, films containing an equimolar (0.5 mol%/0.5 mol%) mixture of europium *tris* (thenoyltrifluoro acetylacetonate) (Scheme 1) and terbium *p*-hydroxybenzoate (Scheme 4) and dip-coated on c-Si commercial cells (yield not known) are reported to increase the conversion efficiency by 15% but no details are given (Li and Xianping, 2008). In another attempt, 2 wt% of $[Eu(tta)_3(phen)]$ microparticles (mean diameter 20 μm) encapsulated into silicate glass by a sol-gel procedure resulted in a 1-mA cm^{-2} increase in the short-circuit current density of a c-Si cell (yield not given) (Fukuda et al., 2009). A PVA coating doped with 2 wt% of $[Eu(dbm)_3(phen)]$ increases the measured maximum power of a 13%-efficiency c-Si module (147×68 cm^2) by 2.7 ± 0.1 relative % (standard deviation for 15 I–V measurements) and its short-circuit current by 1.1 ± 0.1 relative %, under AM 1.5G conditions. A similar enhancement is obtained by co-doping minute quantities of $[Eu(dbm)_3(phen)]$, 0.0015 wt% and of the camphorate $[Eu(tfc)_3]$ complex (Scheme 4), 0.003 wt% (Le Donne et al., 2009). When the module is equipped with a protective glass cover, these numbers decrease to 0.81 ± 0.1% and 0.65 ± 0.1%, respectively; however, a calculation shows that despite the additional cost of the doped PVA coating (estimated to

2.2€), the cost per watt produced decreases by about 10%. A patent by Japanese scientists proposes to incorporate simple neutral Eu^{III} complexes [Eu(C$_n$)$_3$] (n = 1, 2), [Eu(C$_1$)$_3$(bpy)], [Eu(C$_3$)$_3$(phen)], or [Eu(dbm)$_3$(phen)] (Scheme 4) in the resin used as sealing material in solar cells and modules. The Eu-content is between 0.1 and 1 wt%, and an increase in the efficiency of Si solar modules from 14.5% to 15.5% is reported (Kanesato et al., 2010). More recently, several diketonate ternary complexes, [Eu(DBM)(phen) and [Eu(tta)L] (L = bipy, phen, AL1, AL2 Scheme 4), have been tested as downshifting materials. They were doped into PVA and the best result is with [Eu(tta)(AL2)] at 1 wt%: the photocurrent increases from 35.7 to 36.4 mA cm^{-2} and the conversion yield from 16.1% to 16.4% corresponding to + 2 rel% (Liu et al., 2013). We note that lanthanide complexes with dbm (Ln = Pr, Sm, Eu, Tb) have also been proposed as electron acceptors in organic photovoltaic devices (OPVs) (Si et al., 2007).

The work of Katsagounos et al. (2011) is also worth mentioning. These authors put an m-Si cell with initial quantum efficiency of 15% into contact with 1 and 3 LSC layers doped with [Eu(NO$_3$)$_3$(trz1)] (Scheme 2) and achieved improvements reaching 17% and 28%, respectively, corresponding to absolute 2.5% and 4.2% increases (see Section 2.3). This is the largest enhancement obtained since all other experiments reported to date and involving simple Eu^{III} complexes converge toward an improvement of 0.5–1% in the absolute external quantum efficiency of Si cells. Although modest, this is by no way negligible, provided that the added cost and induced extra engineering is not too large.

3.3.2. *Inorganic Materials*

An isolated report published in 1998 claimed that implanting europium ions (2.5×10^{11} ions/cm^2) into the antireflection glass of an a-Si cell improved its characteristics (I vs. V and P vs. V) by as much as 58% under 240 lx irradiation (AM1.5G); the reason invoked is wavelength conversion by Eu^{III} ions (Diaw, 1998). However, the luminescence spectrum shown displays a broad shoulder around 500 nm and no typical emission bands from trivalent europium at 590/620 nm. These data would be more in line with Eu^{II} emission. Moreover, absorption of the ions has a maximum around 370 nm, a spectral range in which little sun irradiance occurs. There has been no direct follow up to this work until 2009 when Eu^{III} ions were introduced into a silica film by a sol-gel method and the film was deposited onto an optical glass antireflective substrate by dip-coating. Characteristic Eu^{III} emission spectra were obtained upon excitation into the $^5L_6 \leftarrow {}^7F_{0,1}$ transition at 396 nm, and the efficiency of an a-Si cell increased from 11.0% to 12.0% when a 0.5M Eu^{III} solution was used in the sol-gel synthesis. Further increase in the Eu^{III} concentration led to concentration quenching (Cheng et al., 2009). These data seem reasonable since one may calculate from Fig. 1 that the spectral range of 385–405 nm ($^5L_6 \leftarrow {}^7F_{0,1}$ transition) contains 1.7% of the sun emission, and if considering other excitation paths for Eu^{III}, the 300–405 nm range corresponds to 5.2% of sunlight.

With respect to inorganic compounds, early experiments took advantage of the known red phosphors Y_2O_3:Eu^{III} and Y_2O_2S:Eu^{III} which were dispersed in PVA/water mixtures and spin-coated onto epoxy-encapsulated Si cells. Under UV excitation (250–400 nm), improved conversion was obtained but the conversion yield decreased substantially under visible excitation, due to the coatings inducing light scattering (Chung et al., 2007). Other phosphors perform better. For instance, KCaGd$(PO_4)_2$:Eu^{III} (% Eu not given) dispersed in PMMA was screen-printed on the top of the Si_3N_4 reflective layer of c-Si cells to form a 3–4-μm thick film. Thus, the efficiency of the solar cells increased by 0.5% to 16.0% due to the conversion of 350–400 nm photons into red photons (580–710 nm) and to a lower reflectivity (Chen et al., 2011). Screen-printed c-Si cells are drawing attention and downshifting has also been applied in an effort to improve their overall efficiency. Since lanthanide-doped inorganic phosphors are difficult to disperse in solvents, investigators have turned to yttrium hydroxide nanotubes doped with 5 mol% Eu^{III}. This nanomaterial can be conveniently synthesized via the hydrothermal route at low temperature (180 °C) and is then spin cast on the front face of the cell. The authors claim that under AM1.5G illumination the yield of the cell increases from 15.2% to 17.2% upon adding the downshifting layer (Cheng and Yang, 2012), an amazing +2 absolute%. Indeed, since the system relies on f-f transitions of Eu^{III} in the range of 300–400 nm (4.6% of the solar irradiance), this would mean that the efficiency of the downshifting layer is close to 44%. Moreover, the authors report that neither the open-circuit voltage nor the series resistance of the cells change. Finally, the ICPE curve of the modified cell only exceeds that of the reference cell by 3.5% in the range of 450–700 nm and does not display a marked increase at 620 nm where the most intense emission of Eu^{III} occurs. There is little doubt that these results will have to be confirmed in an independent experiment. On the other hand, an 8.5–9.2-μm thick PMMA film doped with YVO_4:Bi (3.6–15 mol/%), Eu(36 mol%) position on the top of a c-Si module with Al tape as side mirrors and a refractive-index matching oil resulted in a decrease in the conversion efficiency by 1–2% (Iso et al., 2012).

ZBLAN glasses containing chloride and doped with Eu^{II}, $48ZrF_4$–$10BaF_2$–$10BaCl_2$–20NaCl–$3.5LaF_3$–$3AlF_3$–$0.5InF_3$–5EuF, show Eu^{II} luminescence under UV excitation (280 nm) only; but after oxidation, typical emission bands from Eu^{III} develop upon excitation in the range of 300–400 nm. When fitted on the top of a conventional c-Si cell, the short-circuit current increases considerably in this spectral range, up to a factor of 6 at 360 nm, as depicted on Fig. 16 (Schweizer et al., 2010).

Another ion worth of interest is divalent europium with two 4f-5d absorption bands centered at 215 and 335 nm and an broad emission band at 425 nm, which can be displaced by modifying the chemical environment of the ion. This ion has therefore been doped into a crystal of CaF_2 itself used as replacement for the antireflection coating of an a-Si commercial cell. An optimized

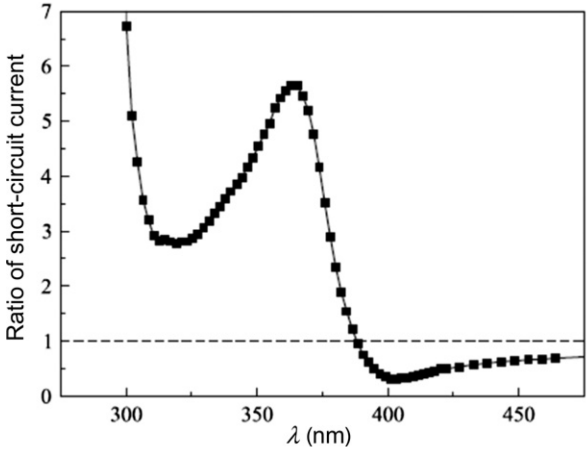

FIGURE 16 Short-circuit current ratio between a conventional c-Si cell with a glass ceramic cover made of ZBLAN glass containing 5% $\mathrm{Eu^{III}}$ and a cell without glass cover. *Reproduced with permission from Schweizer et al. (2010), © 2010, SPIE.*

0.05 mol% doping yields substantial improvements in the cell efficiency which depends on the intensity of the irradiation: for an illumination of 9×10^4 lx, +10% is recorded while this figure goes up to 50% (EQE increasing from 10% to 15%) for 1×10^4 lx (Kawano et al., 1997a,b). A later determination yielded +8% and +45%, respectively (Kawano et al., 2009).

Inorganic nanoglasses have also been proposed (Chen et al., 2012a), for instance, nanoglass ceramics containing $\mathrm{YF_3}$:Dy,Tb in which dysprosium efficiently transfers energy onto $\mathrm{Tb^{III}}$ (Santana-Alonso et al., 2011) and gadolinium oxide co-doped with $\mathrm{Bi^{III}}$ (0.5%) and $\mathrm{Nd^{III}}$(2%). The first material presents the inconvenience of relying on weak f-f transitions, while the second is more interesting because it displays a broad and intense absorption band between 320 and 400 nm and the bismuth-to-neodymium energy transfer reaches 64% (Liu et al., 2011a). However, none of these nanoglasses has actually been coupled to solar cells.

3.4. Upconverting Materials

In a seminal paper, Trupke and coworkers (Trupke et al., 2002b) have analyzed the influence of adding a rear upconverting layer to solar cells. The idea is to convert the NIR light unabsorbed by the cell photomaterial into light with shorter wavelength which, after reflection by a mirror can be absorbed by the semiconductor (Fig. 4B). The solar cell C1 (Fig. 17) is electronically insulated from the converter and absorbs sunlight with energies larger than the bandgap E_g. The upconverter absorbs energies lower than the bandgap and can be represented by three cells C2, C3, and C4 which are connected in series. The cell C2 represents the band–band transition and cells C3 and

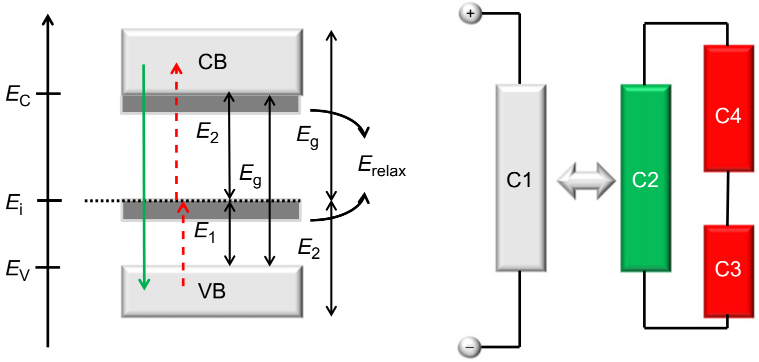

FIGURE 17 Scheme of a solar cell fitted with an upconverting rear layer: energy levels (left) and equivalent circuit (right). *Redrawn from Trupke et al. (2002b).*

C4 the two intermediate transitions. The upconverting material ideally has a band gap matching the one of the solar cell but possesses an IL with energy E_1 above the valence-band edge; additionally, the energy difference between the lower valence-band edge and the upper conduction-band edge should be equal to $E_g + E_2$. The two sequential transitions result in the creation of electrons in the conduction band (CB) and holes in the valence band (VB). A fraction of these electron–hole pairs then recombine in a radiative band-to-band transition, and since the solar cell and the upconverting material are assumed to have similar E_g values, the generated photons are reabsorbed by the solar cell.

The overall conversion yield of the cell fitted with the upconverting layer depends on several factors, namely, E_g, E_1, the illumination (nonconcentrated or concentrated light, incidence angle), and the relaxation of the electrons in the intermediate state (thermalization, dark gray bands in the energy scheme of Fig. 17). With this model, the authors calculate an upper limit of efficiency for idealized 6000-K blackbody spectrum of 47.6% taking the following values of the parameters into account: $E_g = 2$ eV, $E_1 = 0.94$ eV, $E_2 = 1.39$ eV, and $E_{relax} = 0.33$ eV. For concentrated illumination, this value goes up to ≈60%. When the more realistic terrestrial sun spectrum AM1.5G is used, with the same refractive index of 3.6, the yield reaches 50.7% for a 2-eV bandgap (Trupke et al., 2006). The theoretical maximum efficiency versus E_g is visualized in Fig. 18.

This model has been later refined by taking into account refractive indices of the cell and the upconverter and by considering an alternate set-up with the upconverting layer in front of the cell. The main conclusions are that the efficiency increases if refractive indices increase and that no improved conversion efficiency is obtained by inserting the upconverting layer in front of the cell (Badescu and Badescu, 2009). A practical calculation for c-Si cells

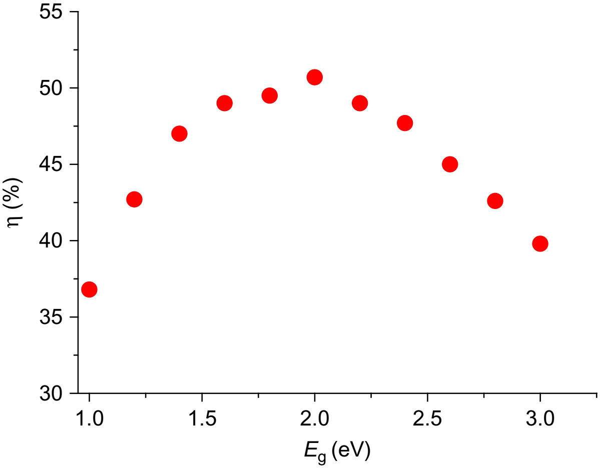

FIGURE 18 Theoretical maximum efficiency η of an upconversion-fitted semiconductor solar cell versus the bandgap E_g of the semiconductor material (refractive index set to $n=3.6$). *Redrawn from data reported in Trupke et al. (2006).*

($E_g = 1.1$ eV, $n = 3.4$) without and with the rear upconverting layer ($n = 3.4$) does not show any improvement under nonconcentrated illumination, while under 1000 suns irradiation, the conversion efficiency is increased by ≈20% with respect to a cell without converter. The absolute calculated yields differ considerably from those reported by Trupke et al. (Trupke et al., 2002b): 21% and 31%, respectively, because the band gap (1.1 eV vs. 2 eV) and the refractive index (3.4 vs. 3.6) used in the second work are different, and because refractive losses have been taken into account.

This points to theoretical models being still insufficiently accurate to predict the exact effect of upconverting layers taking all parameters into consideration. But the perspective of boosting the yield of solar cells by upconversion has stirred a lot of attention, even for Si cell for which the overall yield is already sizeable, and several review and perspective articles have tackled the problem (de Wild et al., 2011; Fischer et al., 2012b; Reisfeld, 2010; Richards, 2006a; Shalav et al., 2007; Strümpel et al., 2007; van der Ende et al., 2009a; van Sark et al., 2010; Wang et al., 2011a,b). A good upconverter for c-Si cells should meet the following requirements (Strümpel et al., 2007):

- Absorption in the range $\lambda > \sim 1100$ nm (corresponding to $E_g < \sim 1.12$ eV)
- Emission at $\lambda < 1100$ nm
- High upconversion yield at low power excitation
- High transmittance of the upconverted light

The wavelength limits given above depend on the bandgap of the semiconductor. Moreover, thin film a-Si cells display relatively low absorption in

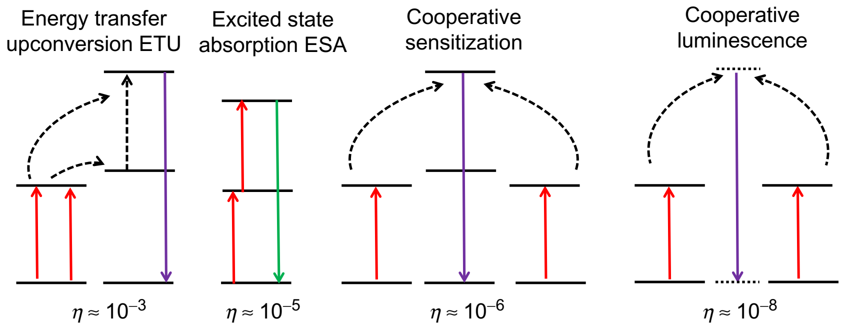

FIGURE 19 Upconversion mechanisms and estimated relative efficiencies according to Auzel (2004). Note that the second mechanism, ESA, is more precisely described as GSA–ESA, ground state absorption followed by excited state absorption.

the range of 950–1100 nm so that an upconverter absorbing in this range might also be useful. Upconversion is different from two-photon absorption in that it requires a real intermediate electronic level (Fig. 19), whereas in two-photon absorption, the IL is a virtual level. The upconversion yield is a real concern in that it rarely exceeds 10%. The reason lies in the upconversion mechanisms which require sequential multiphoton absorption and, therefore, are less efficient compared to common one-photon excitation. The main upconversion mechanisms which may play a role are schematically depicted in Fig. 19. Energy-transfer upconversion (ETU) has the highest probability. When the upconverted emission intensity is plotted against the excitation power in a log–log graph, the slope of the resulting linear correlation indicates how many photons are involved ($n = 2$ for the mechanisms described in Fig. 19). However, the experimentally determined numbers are often smaller and noninteger due to cross-relaxation and nonradiative losses.

The various mechanisms can take place simultaneously, but one is usually dominant. For instance, for doping concentrations larger than 2% and relatively low excitation powers (<200 mW cm^{-2}), ETU is the main mechanism. Several experimental techniques are available to assess which mechanism governs the UC process, in particular when it comes to distinguishing between ETU and ESA (Shalav et al., 2007). Indeed, the luminescence decay profile for ground state absorption (GSA)-ESA and ETU mechanisms are different. Excitation in the first case only occurs during the light pulse and the luminescence intensity decreases exponentially after illumination is switched off. On the other hand, in the case of ETU energy transfer occurs as long as the IL is populated, that is, even after the end of the light pulse so that the decays are not exponential. Excitation spectra are also useful in that their crystal-field structure narrows with the number of photons needed to reach the final excited state (Auzel, 2004).

The cell architecture, especially the position of the upconversion layer, is equally important. From a theoretical study (Badescu and Badescu, 2009), as well as from the experimental results described below, the best design is to position the upconverting layer at the rear of the cell, with a mirror layer (often Al, playing the additional role of electrode) sending the upconverted photons into the Si layers.

When looking at Fig. 2, one realizes that 7% of the sun irradiance is emitted between 1.4 and 1.9 μm so that this spectral range has been a main target for developing upconverting solar materials. One lanthanide ion of choice is undoubtedly Er^{III} since it absorbs in the range of 1460–1580 nm (2.8% of solar emission) and emits at 980 nm, an ideal wavelength with respect to the c-Si band-gap. Additionally, it can also absorb at 980 nm (or be excited through energy transfer from Yb^{III}) and emit green (540 nm) and red (620 nm) light. Other ions of interest include Nd^{III} (Ahrens et al., 2008), Ho^{III} (Chen and Chen, 2011; Lahoz, 2008), Yb^{III} (Lahoz et al., 2011), and, possibly, Tm^{III} (Strümpel et al., 2007).

3.4.1. Erbium-Based Upconverters

The $4f^{11}$ electronic structure of Er^{III} generates 364 electronic levels and its spectroscopy is quite intricate. A partial diagram is shown below (Fig. 20). The main transitions of interest for our purpose are the ones involving the ^4I_J ($J = 9/2$, 11/2, 13/2, and 15/2) levels. Transitions leading to green and red emission from the $^4S_{3/2}$, $^4F_{9/2}$ levels are better suited for upconversion in DSSCs (see Section 5.6).

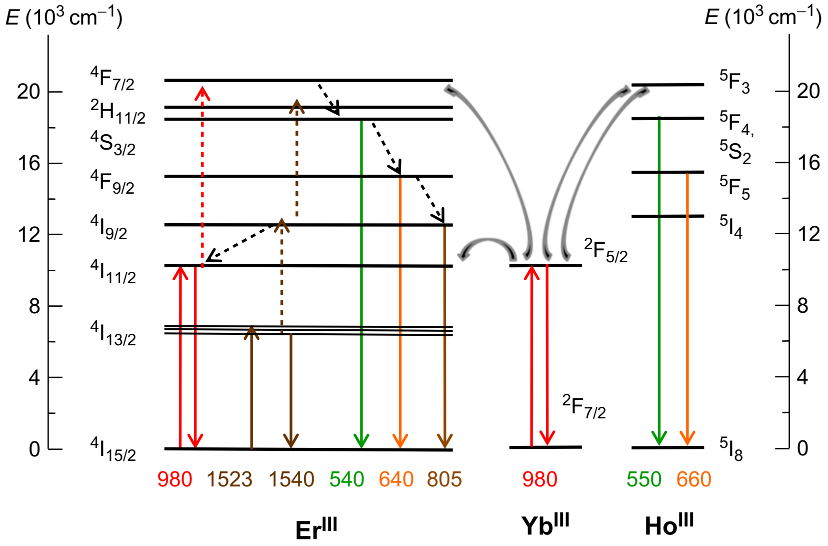

FIGURE 20 Partial energy level diagrams of Er^{III}, Yb^{III}, and Ho^{III} with main absorption, emission, and upconversion transitions (wavelengths given in nm) and showing the sensitizer role of Yb^{III}. *Energy levels are taken from Carnall (1979).*

The host into which the optically active ion is embedded is of utmost importance, particularly with reference to preventing nonradiative deactivations. In this respect, chloride and bromide hosts, with phonon energies of 260 and 175 cm^{-1}, appear to be ideal. However, they generate weak crystal-field splitting, and as a consequence, the absorption range is reduced, as exemplified in Fig. 21. Additionally, these hosts are often hygroscopic and therefore unstable inambient atmosphere. Another point to note here is that population of some excited levels, for example, $\mathrm{Er}(^4\mathrm{I}_{11/2})$, the most significant level contributing to the total upconversion yield, is phonon assisted and low phonon energies result in smaller population. For these reasons, a majority of investigations rely on fluoride hosts (350 cm^{-1}), as can be seen from Table 4.

In particular, the β-phase of $\mathrm{NaYF_4}$ doped with 20% $\mathrm{Er^{III}}$ (or, for visible upconversion, 18% $\mathrm{Yb^{III}}$ and 2% $\mathrm{Er^{III}}$) proved to be an efficient upconverter, contrary to the α-phase; upconversion yields for the $\mathrm{Yb^{III}}$, $\mathrm{Er^{III}}$-doped microcrystalline powder can be as high as 5–6% upon laser excitation at 980 nm and 200 mW cm^{-2} (Hehlen et al., 2001) and newer designs considerably boost the UC yield (see Section 3.4.4).

When reporting an upconversion quantum yield, it is important to mention the excitation power since the yield (EQE) is proportional to $P_i^{(n-1)}$, where n

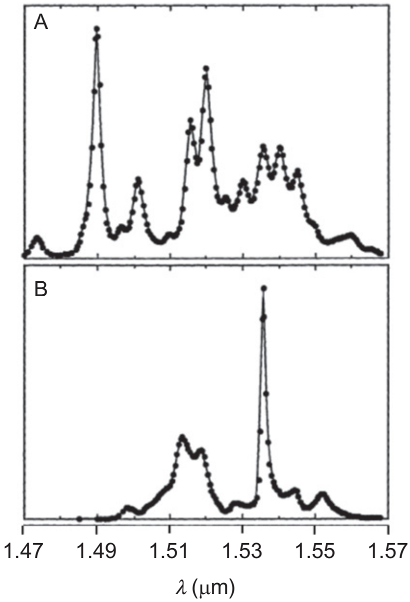

FIGURE 21 Excitation spectra of (A) $\mathrm{YF_3{:}Er(20\ mol\%)}$ and (B) $\mathrm{BaCl_2{:}Er(28\ mol\%)}$; $\lambda_{\mathrm{em}} = 550$ nm. *Adapted with permission from Ohwaki and Wang (1994), © 1994, Japan Society of Applied Physics.*

TABLE 4 Selected Ln^{III}-Based Upconverting Materials for Si Solar Cells

Upconverter	How introduced	Solar cell	Exc./Em. (nm)	Effect (excitation power P_{ex})	References
NaYF$_4$:Er(20%)	Acrylic adhesive gel on rear of cell in 3:2 wt% ratio, 0.5-mm thick	Bifacial c-Si ($\eta = 15\%$)	1480–1580/ 980–1020	EQE 1523 nm: 2.5% (5.1 mW) IQE = 3.8%	Shalav et al. (2003, 2005a,b)
NaYF$_4$:Er(20%)	White oil + rubberizer on rear of cell in 4:1 wt% ratio,1.6-mm thick	Bifacial c-Si ($\eta = 15\%$)	1480–1580/ 980–1020	EQE 1523 nm: 3.4% (6 mW or 2.4 W cm^{-2}) IQE = 5.7% IOE = 16.7% (2.4 Wcm^{-2})	Shalav et al. (2005b) and Richards and Shalav (2007)
NaYF$_4$:Er(20%)	Acrylic adhesive gel on rear of cell	Bifacial c-Si ($\eta = 15\%$)	1480–1580/ 980–1020	EQE 1550 nm: 0.6% (2000 Wm^{-2})	Trupke et al. (2006)
NaYF$_4$:Er(20%)	96 wt% in zapon varnish ($n = 1.50$) at rear of cell	Bifacial c-Si ($\eta = 19\%$)	1460–1580/ 980–1020	EQE 1522 nm: 0.34% (1090 Wm^{-2}) IQE 1.1% (440 Wm^{-2}) IOE 5.1% (1880 Wm^{-2})	Fischer et al. (2010)
NaYF$_4$:Er(20%)	98 wt% in zapon varnish ($n = 1.50$) at rear of cell (0.9-mm thick)	Bifacial Si ($\eta = 16.7\%$)	1460–1600/ 980–1020	EQE 1523 nm: 0.47% (1629 Wm^{-2}) EQE 1523 nm: 0.71% (2601 Wm^{-2}) EQE 1460–1600 nm: 1.07% (2601 Wm^{-2})	Goldschmidt et al. (2011)
NaYF$_4$:Er(2%)	0.75% in a spin-coated layer on a glass at rear of cell	Bifacial c-Si ($\eta = 7.7\%$)	1 sun, AM 0	Relative increase of 8.6% in η, from 7.7% to 8.3%	Chen et al. (2012c)
NaYF$_4$:Yb(18%), Er(2%)	Dissolved in PMMA and dropcast over ZnO:Al back contact	a-Si:H, single junction	980/400–700	EQE 980 nm: 0.01% (3 W cm^{-2})	de Wild et al. (2010a)
NaYF$_4$:Yb(18%), Er(2%)	In PMMA, at rear of cell	a-Si:H cell ($\eta = 8\%$)	981–986/650, 540, 522	Doubling of current density from 5 to 10 μA cm^{-2}	de Wild et al. (2010b)
NaYF$_4$:Yb(18%), Er(2%)	Front layer of NaYF$_4$:Yb, Er,Gd(30%) nanorods fitted with Au NPs or Au shells	a-Si:H cell	980 (1.1 W)/ 540, 660	16- (without Au) and 72-fold (with Au) increase in photocurrent (from 16 to 260 and 440 μA, respectively) EQE = 0.14% (with Au)	Li et al. (2012c)

Continued

TABLE 4 Selected Ln^{III}-Based Upconverting Materials for Si Solar Cells—Cont'd

Upconverter	How introduced	Solar cell	Exc./Em. (nm)	Effect (excitation power P_{ex})	References
$NaYF_4$:Yb(18%), Er(2%)	Dispersed into PDMS (conc. unknown)	a-Si (thin film)	1 sun	Current increases from 16 to 17 mA cm^{-2}; conversion yield increases from 5.7% to 6.0% (+5 rel%)	Zhang et al. (2010b)
Gd_2O_3:Er	250-nm film at front of cell as passivation layer	c-Si ($\eta \sim 11\%$)	1520–1560 1 sun	Increase in photocurrent 2.8 (n-type abs.) or 4% (p-type abs.) decrease in η	Sewell et al. (2009)
Gd_2O_2S:Er	Dissolved in PMMA and drop cast over ZnO:Al back contact	a-Si:H, single junction	980/400–700	EQE 980 nm: 0.05–0.09% depending on texture (0.6–3 W cm^{-2})	de Wild et al. (2010a)
Yb_2O_3:Er	250-nm film at front of cell as passivation layer	c-Si ($\eta \sim 11\%$)	1520–1560 1 sun	Increase in photocurrent 4.4% decrease in η(p-type abs.)	Sewell et al. (2009)
ZBLAN:Er(5%)[a]	2-mm thick glass plate on the top of cell	c-Si (η: n.a.)	1540	Increase in photocurrent	Passlick et al. (2010) and Schweizer et al. (2010)
ZBLAN:Er(2–14%)[a]	2-mm thick glass plate on the top of cell	c-Si (η: n.a)	1540	EQE = 1.6% (9.1% Er, 1 mW)	Henke et al. (2009)
$La_2Mo_2O_9$:Yb(18%), Er(2%)	10 wt% in PMMA, at rear of cell	Bifacial pc-Si ($\eta =$ 16.23%)	1 sun (AM: n.a.)	I_{SC}: +2.2%, η: +2.7% (16.67%)	Chen and Chen (2011)
	10 wt% in PMMA, at front of cell	Bifacial pc-Si ($\eta =$ 16.52%)		I_{SC}: +1.9%, η: +1.8% (16.81%)	
$La_2Mo_2O_9$:Yb(18%), Ho(2%)	10 wt% in PMMA, at front of cell	Bifacial pc-Si ($\eta =$ 16.53%)	1 sun (AM: n.a.)	I_{SC}: +1.6%, η: +1.5% (16.70%)	Chen and Chen (2011)

[a] *ZLAN:Er has composition* $48ZrF_4–20BaF_2–20NaF–3.5LaF_3–3AlF_3–0.5InF_3–5ErF_3$.

is the number of photons needed to excite the emissive level. Synthesizing the β-phase in pure form is difficult, but an efficient synthesis has been elaborated so that its availability is now common (Krämer et al., 2004). Despite that interest in this material for solar energy conversion started at the beginning of the century (Shalav et al., 2003), there are very few reports describing the effect of upconverting layers under full one-sun illumination, most of the investigations restricting themselves to proofs of concept under monochromatic illumination at either 1523 or 980 nm. An overview is presented in Table 4. Comparisons are not always straightforward since authors do not report the same parameters. In particular, three types of parameters (which are sometimes normalized) are used to determine the upconversion efficiency, and it is not always clear which definition is adopted in a given study:

- the external quantum efficiency EQE determined from electrochemical measurements at a given wavelength, see Eqs. (12) and (16);
- the internal quantum efficiency (IQE) which is equal to EQE corrected for absorption and reflection losses, see Eq. (17);
- the integrated optical efficiency, η_{UC} or IOE, determined by optical measurements; integration is over the entire emission spectral range.

A good summary of all parameters with their exact definitions is given in Fischer et al. (2010). We have to stress though that there are at least two different definitions of EQE, the one described by Eq. (12) and the following:

$$\mathrm{EQE} = \frac{I_{\mathrm{SC}}}{P_{\mathrm{in}}} \times \frac{hc}{\mathrm{e}\lambda} \tag{16}$$

where e is the electron charge and hc/λ the photon energy. Uncertainties are rarely mentioned, but it seems difficult to determine EQE with an accuracy better than 3% (Goldschmidt et al., 2011). A simulation of the expected increase in EQE and IQE versus phonon energy, doping concentration, and $\mathrm{Er^{III}}$ environment is described by S. Fischer and collaborators and shows large potential for improving UC properties for solar applications (Fischer et al., 2012b). In principle, $\mathrm{Er^{III}}$ alone is used for c-Si cells and $\mathrm{Yb^{III}}$, $\mathrm{Er^{III}}$ for a-Si cells since their bandgap is at the border of the visible range (≈690–700 nm).

In an early system, polycrystalline $\mathrm{NaYF_4{:}Er(20\%)}$ samples were adhered at the rear of a bifacial Si cell ($\eta = 15\%$ and 12% upon front and rear illumination, respectively) with a transparent acrylic and adhesive gel; a reflective white layer was painted at the rear of the system ($R > 80\%$ for IR photons). No attempt was made to measure the cell efficiency, but the EQE curve clearly showed a band in the range of 1480–1580, whereas the corresponding plot for the reference cell was flat. An EQE value of 2.5% was obtained upon 5.1 mW pump power which translates into 3.8% IQE when taking into account the reflection and absorption loss fraction (L) due to the added layer (Shalav et al., 2003):

$$\mathrm{IQE} = \frac{\mathrm{EQE}}{1 - L} \tag{17}$$

Although interesting, this yield is, however, insufficient to compensate for the deterioration of the rear reflectivity and for Si absorption losses (Shalav et al., 2003, 2005a). Later, the authors improved the cell by replacing the white reflective paint with evaporated silver and the acrylic adhesive with white oil mixed with a rubberizer. EQE up to 3.4% could be obtained under 6 mW illumination at 1523 nm (corrected for losses: IQE = 5.7%). Here, upconversion is a two-photon process, which most probably obeys the ETU mechanism, and EQE will be proportional to the input power. Since in the latest work the authors increased the excitation power from 5.1 to 6 mW, the real improvement is only 0.5 absolute %. They also demonstrated that the optimum concentration of $\mathrm{Er^{III}}$ is 20 mol% and that adding $\mathrm{Yb^{III}}$ does not lead to any improvements (Shalav et al., 2005b). The added external quantum efficiency of the $\mathrm{NaYF_4}$:Er(20%) doped layer is depicted in Fig. 22, right; note that the vertical scale is logarithmic. Subsequently, the authors analyzed in detail the origin of the losses and concluded that under illumination of 2.4 W cm^{-2} at 1523 nm, an optical efficiency of 16.7% is obtained for the upconversion mechanism. By scrutinizing the reflection losses at the various interfaces and those due to the less-than-unity conversion of Si at 980 nm, the authors further predict that an EQE of 14% should be obtainable under illumination corresponding to 1000 suns (Richards and Shalav, 2007).

Comparable experimental results were achieved by another group using a similar setup (Trupke et al., 2006): the obtained EQE was only 0.6% at 1550 nm, but if extrapolated at 1523 nm, it would be four times larger that is a value similar to the one reported in the 2003 study (Shalav et al., 2003).

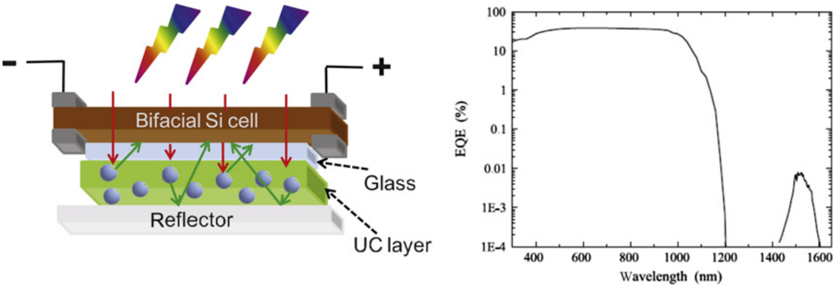

FIGURE 22 (Left) Scheme of an upconversion Si cell. (Right) External quantum efficiency of a bifacial Si cell fitted with an $\mathrm{NaYF_4}$:Er(20%)-doped upconversion layer upon constant photon flux of $1.6 \times 10^{23}\ \mathrm{m^{-2}s^{-1}}$. *(Left) Redrawn after Chen et al. (2012c). (Right) Reproduced with permission from Ahrens et al. (2008), © 2008 Wiley-VCH Verlag.*

A detailed electrochemical and photoluminescence study was undertaken by S. Fischer and collaborators on a similar bifacial Si cell with higher efficiency (19%). All parameters were carefully tested, including the nature of the upconverter binder (silicone vs. zapon varnish), the influence of incident power, and a detailed comparison between electrochemical and optical measurements (Fischer et al., 2010). The differences between IOE, IQE, and EQE are detailed in Fig. 23. The discrepancy between IOE and IQE is attributed to experimental errors and uncertainties in the estimates of some parameters.

All these investigations have tested the upconverter under monochromatic illuminations. The first comparison between monochromatic and broad-band excitation dates back to 2011 only (Goldschmidt et al., 2011); the authors demonstrate a better EQE, 1.07% versus 0.71% when 1523-nm (2601 W m^{-2}) irradiation is swapped for a 1460–1600 nm range illumination at the same power density. However, the improvement of the cell overall efficiency amounts to only 0.18% (absolute), and this is achieved under an irradiation corresponding to 732 ± 17 suns. Previously, Zhang et al. had demonstrated that NaYF$_4$:Yb(18%),Er(2%) dispersed into polydimethylsiloxane (PDMS) enhances the yield of a thin-film a-Si cell from 5.7% to 6.0% under AM 1.5G illumination (Zhang et al., 2010b); however, no reference cell with an undoped NaYF$_4$/PDMS layer has been measured.

A more comprehensive and innovative study is reported by researchers from the Shanghai Institute of Ceramics (Chen et al., 2012c). In this work, oleic acid-coated upconverting NaYF$_4$:Er(2 mol%) nanocrystals prepared through a solvothermal method (Wang and Li, 2006) are mixed with a solution of trialkoxysilane in hexane containing traces of acetic acid. This leads

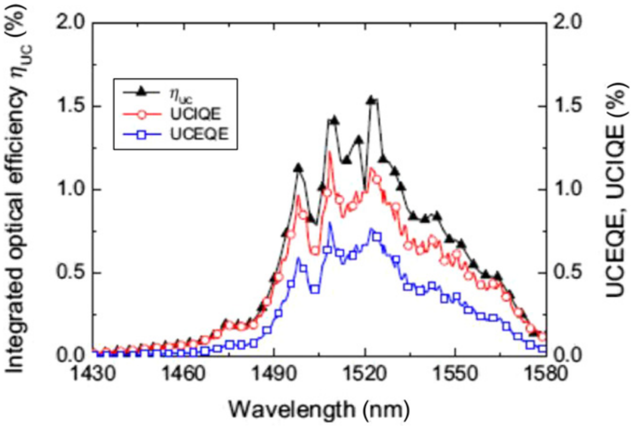

FIGURE 23 Differences between IOE (η_{UC} on the figure, scaled to an irradiance of 440 W m^{-2}), IQE (UCIQE), and EQE (UCEQE) for a bifacial Si cell fitted with a rear upconversion layer (96 wt% NaYF$_4$:Er(20%) in zapon varnish). *Reproduced with permission from Fischer et al. (2010), © 2010 American Institute of Physics.*

to exchanging oleic acid with silane groups, enabling fixation of the UCNPs on a $3 \times 3\ \mathrm{cm}^2$ borosilicate glass plate by spin-coating of a methanolic suspension of the ligand-exchanged nanoparticles. This plate is then fitted on a bifacial c-Si solar cell (Fig. 22, left) where the glass plate plays the role of insulator and corresponding V_{OC}, J_{SC}, FF, and η data are determined for AM0 illumination. Influence of the concentration of UCNPs in the methanolic suspension and of the spinning rate is described in Fig. 24 (solid squares). Improvement in the overall cell yield increases from 1.8 to 5.2 relative % by decreasing the UCNP concentration in the film from 3.5% to 0.75%. Further improvement, from 5.2 up to 8.6 relative % is obtained by increasing the spinning rate from 2000 to 3500 rev/s. The main contribution to the increase in η arises from an increase of 5.1% in J_{SC}, while V_{OC} and FF are improved by 1.7% and 1.6%, respectively. Interestingly, the authors have measured the cell parameters when the glass plate is coated with an undoped layer of $NaYF_4$. The effect is detrimental, but no clear correlation is observed between the decrease in η and both the NP concentration and spin rate. The loss in overall yield ranges from −3.2 to −6.2 relative% (solid circles, Fig. 23; average $-5 \pm 1\%$). The scatter of data may simply reflect experimental uncertainties, since a 3% experimental error in EQE determination was mentioned above (Goldschmidt et al., 2011). As a matter of fact, values ranging from −1.4 to −5.4 relative% were obtained for sample Nr. 4. The losses mainly arise from scattering and reflection from the added UC layer. Taking

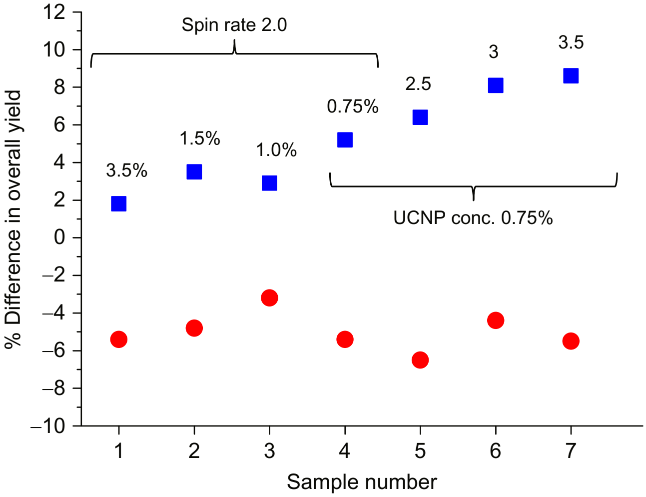

FIGURE 24 Change in overall yield of bifacial c-Si cells upon AM 0 irradiation. Blue squares: cell fitted with a glass plate coated with a film containing various amounts of $NaYF_4$:Er(2%); spin rate is given in 10^3 rev/s; initial yield of the reference cell: 7.7%. Red circles: same data for undoped $NaYF_4$ NPs; initial yield of the reference cell: 14.9%. *Drawn from data reported in Chen et al. (2012c).*

this into account, the upconversion layer therefore increases the overall efficiency of the cell by about 13 relative%, under AM0 illumination. The only questionable aspect of this study is that the cell used for determining the upconversion improvements has a small yield of 7.7%, while the effects of the undoped NC layers have been determined on a cell with twice the efficiency (14.9%); the authors do not comment on this in the paper, but when questioned about this fact, they answered that the commercial cell used has been damaged when wire electrodes were welded, which resulted in low FFs (~0.5) and consequently low yields.

Cubic rare-earth oxides are also convenient hosts for luminescent Ln^{III} ions despite featuring more energetic phonons. One advantage stems from the lattice parameter of these oxides being about twice that of silicon so that they are able to use the silicon lattice as a template for crystalline growth and can therefore be deposited directly on epitaxially grown silicon p–n structures. When illuminated under laser excitation in the range of 1520–1560 nm, upconverting layers of Ln_2O_3:Er (Ln = Gd, Yb; % Er not specified, but <10%) display a small short-circuit photocurrent density which is proportional to the laser power between 0.5 and 4.5 mW (990–8940 W m^{-2} nm^{-1}) and reaches 1.1 μA cm^{-2}. The corresponding slopes are 1.8 for Gd^{III} and 1.3 for Yb^{III}. This proves that upconversion generates the photocurrent. On the other hand, when these layers are fitted onto the Si cells, a decrease in overall efficiency is observed, −4.4% for Yb_2O_3:Er and between −2.8% and −4% for Gd_2O_3:Er, depending on the absorber, n-type or p-type (Sewell et al., 2009).

ZBLAN glasses with basic composition ZrF_4–BaF_2–LaF_3–AlF_3–NaF and doped with Er^{III} reach UC efficiency up to 12.7% (Ivanova and Pellé, 2009) and are potential candidates for UC layers. Upon irradiation at 1540 nm, they display both NIR emission at 980 nm (two-photon process) and visible luminescence at 550 nm and 660 nm (three-photon), in addition to weak four-photon excited emission at 420 nm (Ahrens et al., 2008). A proof of concept is provided by a glass modified with $BaCl_2$ and containing 5% Er^{III} which induces an increase in photocurrent when put onto a c-Si cell, without special optical coupling, under laser excitation at 1540 nm (Passlick et al., 2010; Schweizer et al., 2010). The maximum EQE obtained depends on the doping concentration and excitation power at 1540 nm: it stands at 1.6% for 9.1% Er^{III}; the 980-nm upconverted emission is the strongest for all excitation powers (1–17 mW) amounting to 90% at 1 mW and 70% at 10 mW, for instance (Fig. 25, left). The upconverted 540-nm light is visible on the right hand side of Fig. 25 (Henke et al., 2009).

The upconverting phosphor $NaYF_4$:Yb(18%),Er(2%) is not convenient for crystalline Si cells because the emitted light is in the visible (520, 540—main emission—and 650 nm) that is in a spectral range in which the light-to-electricity conversion efficiency of c-Si cell is not optimum. This has been verified by Shalav et al. (2005b). Despite this handicap, $La_2Mo_2O_9$:Yb(18%),Er(2%)

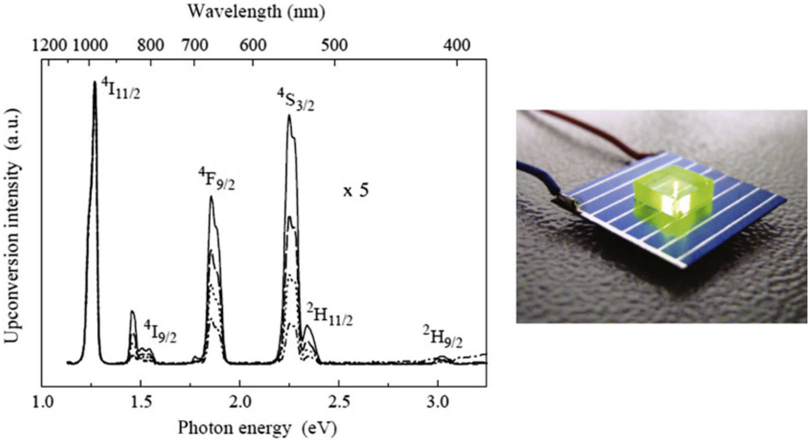

FIGURE 25 (Left) Upconverted spectrum from ZBLAN:Er(9.1%) glass under 1540-nm excitation with 17.2 (solid curve), 7.8 (dashed), 3.55 (dotted), and 1.15 mW power (dash-dotted). (Right) Monocrystalline c-Si cell (2 × 2 cm) with an upconversion Er-doped ZBLAN glass layer ($7 \times 7 \times 2$ mm^3). *Reproduced with permission from Henke et al. (2009), © 2009, SPIE.*

nanoparticles dispersed at 10% in PMMA have been tested on a c-Si cell with overall yield of 16.5% (Chen and Chen, 2011). When fitted at the rear of the cell, a relative improvement in η of 2.7% is observed, mainly due to an increase in photocurrent (+2.2%). When positioned at the front of the cell, the upconversion layer is less effective, leading to a 1.6–1.7% increase in η. A slightly smaller improvement is recorded (1.5%) when $\mathrm{Er^{III}}$ is replaced with $\mathrm{Ho^{III}}$, which emits upconverted light at 550 and 660 nm (see Fig. 25).

Amorphous silicon cells have much better conversion efficiency in the visible, with EQE peaking between 450 and 600 nm so that $\mathrm{NaYF_4}$:Yb(18%),Er(2%) UCNPs have been introduced into a PMMA layer at the rear of a standard p–i–n (p-type/intrinsic/n-type) a-Si cell with conversion efficiencies of 8% and 5% upon front (through the p-layer) and rear illumination, respectively (de Wild et al., 2010b). The cell was irradiated with a diode laser at 980 nm (10 mW) and compared to a reference cell without the upconversion layer, its photocurrent density doubles, from 5 to 10 μA cm^{-2}. A similar experiment with a hydrogenated a-Si:H cell, and an illumination at 980 nm of 28 mW gives an EQE of 0.03%, compared to 0.01% from direct absorption of sub-bandgap photons. This corresponds to an increase in photocurrent density of 6.4 μA cm^{-2}. The measured EQE of the cell at 540 nm, which is the wavelength of the strongest upconversion emission, amounts to 0.62% upon back side illumination (de Wild et al., 2010c). Better results are reported by Li et al. (2012c) who have coated $\mathrm{NaYF_4}$:Yb,Er,Gd nanorods (NR) with gold nanoparticles or a gold shell; a 16-fold increase in I_{SC} is found for the uncoated NRs which goes up to 64-fold improvement with the coated NRs, demonstrating the effect of plasmon resonance.

3.4.2. Other Systems

As briefly mentioned above, some authors have proposed to use Ho^{III} which absorbs in the range of 1130–1225 nm for exciting $Yb(^2F_{5/2})$ by both upconversion with the help of the $^5I_6 \leftarrow {}^5I_8$ transition and energy transfer from higher levels (Fig. 20); an estimated EQE of 10^{-3} has been calculated from photophysical data, and a suitable model has been suggested to account for the energy migration phenomena, but this system has not been applied to a solar cell (Lahoz et al., 2011).

Another proposed phosphor for upconversion in a-Si cells is the IR-detector Q42 from Lumitek®; its exact composition is not known, but it contains Ln^{III} oxysulfides in a calcium sulfide matrix. Both a UV and an IR photons are absorbed and emission occurs at 650 nm (Mawyin et al., 2008).

3.4.3. Perspectives

As can be inferred from the above description, there are only two fully tested systems demonstrating enhancement of light-to-electricity conversion by upconversion in silicon solar cells. The improvement is rather small, the UC layer adding 0.25–0.44% to cells with initial yields of 16.2–16.5% (Chen and Chen, 2011) under AM 1.5 illumination or 0.6% to cells with starting efficiencies of 7.7% under AM 0 illumination (Chen et al., 2012c). This is by far much less than the theoretical models predict, namely, an increase of the Shockley–Queisser limit up to 40% (Trupke et al., 2006). There are two reasons for this situation: the small yield of upconversion processes and the power dependence of the UC yield. Obvious fixes will therefore include concentrating the sun irradiation (up to 1000 sun equivalents), or increasing the UC yield either by clever design of the materials or by plasmonic effects. What is also clear is that $NaYF_4$ doped with Er^{III} only (and therefore absorption in the 1.5 μm region) is better than the classical $NaYF_4$:Yb,Er upconverting material for c-Si cells, see (de Wild et al., 2010a).

3.4.4. Enhancement of the Upconversion Yield

Upconversion quantum yields in bulk microcrystalline lanthanide materials are usually limited to 15–18% under illumination of a few $W\,cm^{-2}$ and are more commonly in the range of 1–5% (Fischer et al., 2012c). They are often much smaller for some nanoparticles. In addition, the absorptivity of Er^{III} or Yb^{III} is low so that the overall luminosity remains weak. Several innovative ways have been paved to circumvent the problem and to produce more luminescent UCNPs. Three of them are described here while metal-enhanced upconversion and photonic crystals are dealt with in the next sections.

The first solution proposed in 2007 consists in coating $NaYF_4$:Yb^{III},Ln^{III} NPs with a layer of undoped tetrafluoride itself fitted with an amphiphilic layer made of a mixture of octylamine and isopropylamine-modified poly (acrylic) acid. Enhancements of 7.4 and 29.6 times in the upconversion yields are reported for Ln = Er and Tm, respectively, which then reach about 60% of the bulk yield (Yi and Chow, 2007).

A second concept relies on broad-band excitation. Increasing the excitation bandwidth of $NaYF_4$:Er^{III} embedded into an oxyfluoride ceramic from 12 to 38 nm results in a 55-fold increase in upconverted emission (MacDougall et al., 2012) but much broader bandwidth can be achieved with organic chromophores. For instance, oleylamine-coated UCNPs have been coupled to a NIR-absorbing dye from the cyanine family; the chromophore absorbs in the range of 650–850 nm and emits a broad band with maximum at 806 nm, tailing off at around 930 nm, which generates enough overlap with Yb^{III} absorption spectrum for sizeable energy transfer to occur. Although the quantum yield of the coated UCNPs under 800-nm excitation is lower compared with the undoped material (0.12% vs. 0.3%), the total luminescence intensity is more than 3000 times larger (Zou et al., 2012). The concept is appealing but does not really match the needs of c-Si cells since the absorbed light is in a range in which silicon absorbs as well and has large light-to-current conversion efficiency.

Third, since upconversion is a nonlinear process, it was suggested to couple broad-band excitation with concentration of the light onto the active material by QDs or organic chromophores. One example are PbS/PbSe nanocrystal QDs which absorb in the range of 1.1–1.3 μm and emit around 1.3–1.5 μm (Goldschmidt et al., 2008). In turn, this emission is absorbed by Er^{III} ions which upconvert it to 980 nm. Since the QDs also absorb the radiation emitted by the upconverter, a special cell-upconverter–concentrator arrangement was designed (Fig. 26). The authors estimate a total system efficiency of up to 25% for an Er^{III}-containing upconverter and a c-Si cell.

Finally, theoretical considerations of the energy migration paths and associated rate constants and level populations can also help increasing the UC yields by adequate design of upconverting systems. Models have been proposed for theoretically investigating the energy-transfer mechanisms which enhance and suppress visible upconversion luminescence under near-infrared excitation, for instance, in oxyfluoride glass-ceramics co-doped with 3.45% Yb^{III} and 0.05% Er^{III} (Rodriguez et al., 2011). For another system, $NaYF_4$: Er(2%),Tm(2%), an experimentally validated population balance model and a path-tracing algorithm allow the authors to objectively identify transitions with the most significant contributions to the population of the desired excited level. Several pathways divert energy away from the green-emitting manifolds and concentrate it into the Tm^{III}($^3F_4$) manifold, which subsequently populates the red-emitting Er^{III}($^4F_{9/2}$), resulting in high quantum yield for the latter upconversion while green emission is 85% quenched (Chan et al., 2012).

In Fig. 27, the major pathways are photon absorption (980 nm, A), energy concentration and storage (B), population of the emitting manifold via

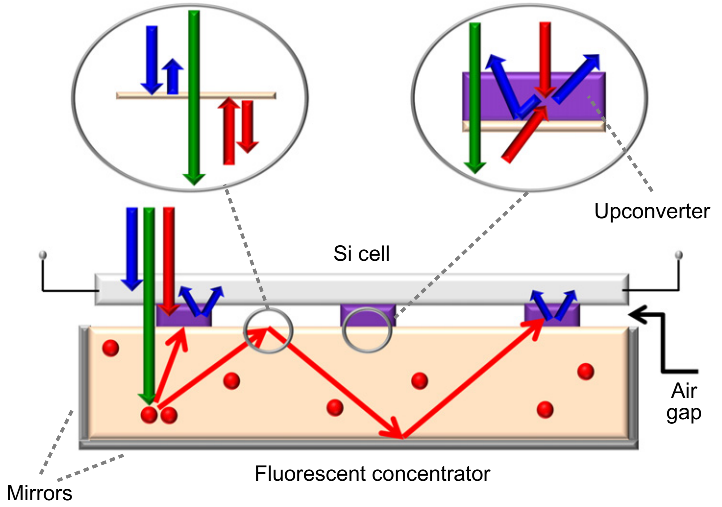

FIGURE 26 Proposed setup for an advanced upconverter for a c-Si solar cell. Blue arrows: light absorbed by the cell; green arrows: light absorbed by the concentrator; red arrows: light absorbed by the upconverter. *Redrawn from Goldschmidt et al. (2008).*

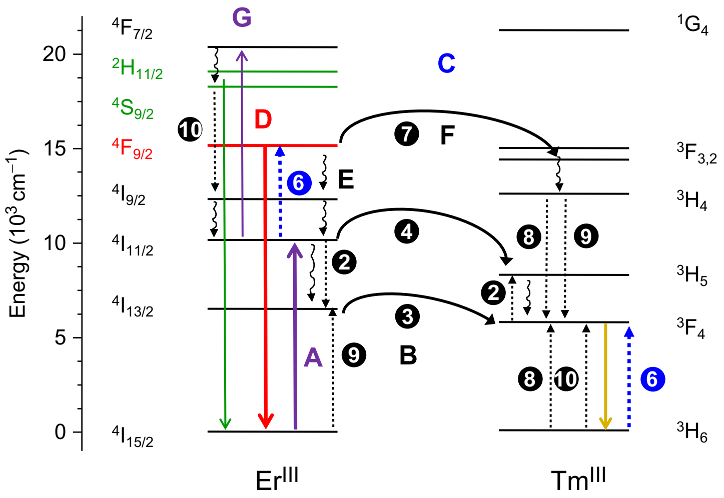

FIGURE 27 Energy level diagrams and major steady-state pathways (capital letters) and energy transfers (numbers) for NaYF$_4$:Er(2%),Tm(2%) nanocrystals; straight, plain arrows represent photon absorption and emission, curved and dotted arrows correspond to energy-transfer processes, and undulated arrows depict multiphonon relaxation. *Redrawn from Chan et al. (2012). See text for explanations.*

upconversion (C), red luminescence (660 nm, D), energy recycling via multiphonon relaxation (E) or via energy transfer/cross relaxation (F); finally, the minor pathway leading to Er^{III} green emission at 540 nm is schematized under (G). Emission at 1.5 μm arises essentially from the Tm($^3F_4 \rightarrow {}^3H_6$) transition. The Er($^4F_{9/2}$) level is almost exclusively populated by the ETU mechanism (C). Its rate is almost 60% of the rate of the GSA, Er($^4I_{11/2} \leftarrow {}^4I_{15/2}$), mainly because of two reasons: (a) the oscillator strengths of the Er($^4F_{9/2} \leftarrow {}^4I_{11/2}$) and Tm($^3F_4 \leftarrow {}^3H_6$) transitions are large, representing 90% of all oscillator strengths in their respective ions and (b) the steady-state population of the Tm($^3F_4$) level is high, being more than 25 times the population of any other excited level in the Er^{III}/Tm^{III} system.

3.4.5. *Plasmonic Enhancement of Photophysical Properties*

A way of enhancing luminescence is to bring the emitting moiety in close contact with a metallic surface or with small colloidal silver or gold islands/nanoparticles. The physics behind the phenomenon is rather complex and depending on the size of the metallic colloidal particles either luminescence quenching or enhancement can be generated (Lakowicz, 2005). Small colloids have the tendency to quench luminescence because light absorption is dominant over scattering while larger colloids are expected to enhance luminescence. The incident electric field from the electromagnetic wave is modified by interacting with the metal surface, resulting in strong coupling between the surface plasmons of the metal particles and the transition dipoles of the chromophore. The radiative lifetime is substantially decreased and, in parallel, luminescence intensity is enhanced. In practice, nanoparticles can be used for this purpose, for instance, Au-core/Ag-shell nanoparticles with size >50 nm (Xie et al., 2006). Since not only metal-enhanced luminescence is achieved but also reduction in photobleaching (Muthu et al., 2008), the technique is starting to find applications in biosciences (Bünzli, 2013), photocatalysis (Thomann et al., 2011), and photovoltaics (Giannini et al., 2011).

Present research in photovoltaics is focused on benefitting from the high near fields surrounding metallic nanostructures close to their surface plasmon resonance frequency and from light trapping in the active semiconductor layer to boost light absorption (Atwater and Polman, 2010; Green and Pillai, 2012; Schuller et al., 2010). Several light-trapping geometries have been proposed for thin-film solar cells: (i) metal nanoparticles at the surface, which trap light by scattering, (ii) metal NPs embedded into the semiconductor, which absorb light by localized plasmons, and (iii) metal/semiconductor interface which absorbs light by surface plasmon polaritons, and their relative properties modeled and discussed (Atwater and Polman, 2010). Optimization requires adjustment of the metallic nanostructure size, shape, and spacing, and this is unique to each specific solar-cell type (Catchpole and Polman, 2008). Such an optimization carried out for a thin-film Si cell results in enhancement in photocurrent up to 43% (Pala et al., 2009). To date, however, no plasmonic effects have been exploited for Si cells in conjunction with upconverting layers even if a potential system based on Nd^{III} has been prospected (Ahrens et al., 2008), nanometallic glass hybrid materials designed (Basudeb et al., 2010), and several model simulations conducted (Fischer et al., 2012a,b; Goldschmidt et al., 2012). With respect to UCNPs, plasmonic enhancements of the UC emission by factors 3–4 are routinely obtained for Er^{III} (Schietinger et al., 2010); in some cases, the improvement can reach one order of magnitude (Basudeb et al., 2010). Moreover, amazing 30- to 110-fold enhancements are reported for Tm^{III}, which lead to a lowering of the threshold pumping power by a factor of at least 10 (Liu et al., 2011c).

3.4.6. *Photonic Enhancement of Photophysical Properties*

Another leverage to increase upconversion efficiency without having the disadvantage of plasmonics, namely, the introduction of an additional deactivation path resulting from light absorption by the metal particles, is to achieve large local fields by photonic crystals (Goldschmidt et al., 2012). Photonic crystals are analogue to semiconductors if electrons are replaced with photons. They feature a periodic nanostructure which affects the propagation of the photons and they have a photonic bandgap. The density of states is much larger near the bandgap which, according to Fermi's golden rule (Dirac, 1927), increases the transition probability. On the contrary, within the bandgap, emission is inhibited (Yablonovitch, 1987). A photonic, grating-like, architecture which is optimized for amplifying the local field with maximum effect at 1523 nm, a wavelength corresponding to the Er^{III} absorption, is depicted in Fig. 28. It consists of a material with refractive index 1.5 (typically glass or plastic) into which a structure with larger refractive index ($n=2$) is embedded. Varying the various sizes of the structure components allows one to tune the wavelength at which the local field is enhanced or decreased. Theoretical calculations on this structure show that absorption is increased at 1523 nm up to a factor 3–4, but Er^{III} emission at 980 and 800 nm is more enhanced, resulting in an increase in upconversion yield by a factor of approximately 3, while emissions in the visible are suppressed. Further optimization and practical implementation should follow (Herter et al., 2012).

3.5. Antireflection Coatings

In order to improve light collecttion by reducing reflection, a number of oxide nanostructures have been grown on bare c-Si cells. These structures include subwavelength gratings, porous layers, and one-dimensional nanostructures such as NRs, nanowires, or nanotips. One-dimensional zinc oxide nanostructures have received great attention in view of their high transparency,

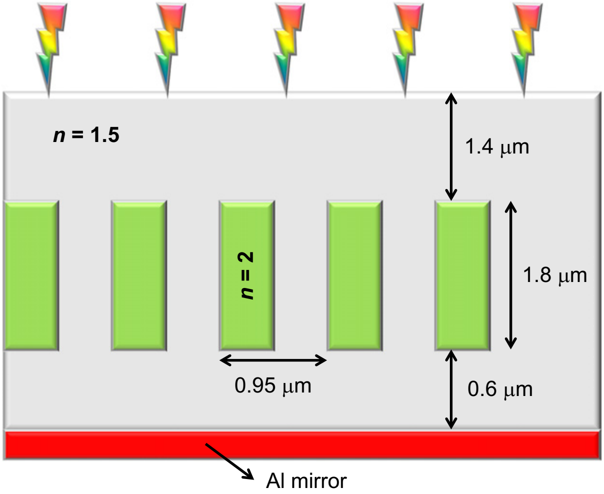

FIGURE 28 Sketch of a 2D waveguide structure optimized for maximum field enhancement at 1523 nm (absorption of $\mathrm{Er^{III}}$). *Redrawn after Herter et al. (2012).*

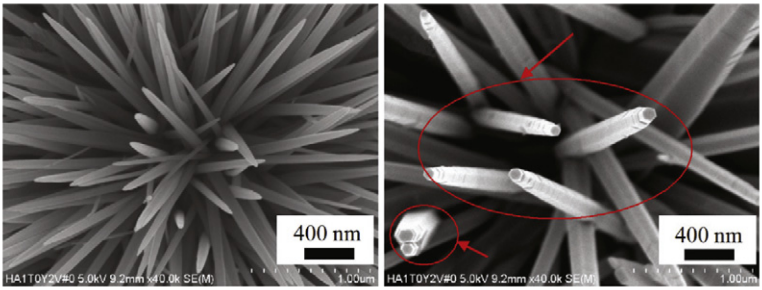

FIGURE 29 SEM images of the ZnO:Er nanotips grown on a c-Si cell for different deposition time: 60 min (left) and 90 min (right). *Reproduced with permission from Liu et al. (2012), © 2012 Elsevier B.V.*

appropriate refractive index ($n = 2$ at 632 nm) and easiness to grow on almost any kind of substrate while morphologies can be readily controlled. In this context, $\mathrm{Er^{III}}$-doped ZnO has been used to grow multiscaled hierachical antireflective layers on a c-Si cell: c-Si/SiN_x:H/ZnO/ZnO:Er where SiN_x:H is the conventional silicon nitride coating doped with hydrogen which functions as antireflective layer and, in addition, passivates the surface of the c-Si cell (Liu et al., 2012). The ZnO:Er material grows as nanotips, as shown in Fig. 29. In comparison with the cell coated with SiN_x:H only, the absolute conversion yield increases from 15.6% to 17.4% (+11.5 rel.%), mainly because of a 10% rise in the photocurrent.

3.6. Practical Implementation of Lanthanide Materials in Si Cells

Competition between solar panel producers is severe and most of the technology is protected by patents so that it is difficult to have a realistic information on the practical use of rare-earth materials in Si solar cells, especially that industry people include sometimes other elements into the term "rare earths," such as indium, titanium, germanium, for instance. There is, however, a number of recent patents mentioning lanthanide downshifting and/or upconverting layers, without much precision regarding their exact composition. Design of a-Si cells including an upconversion layer is described for both regular (Zhang et al., 2012e,g) and tandem (Zhang et al., 2012f) cells and the concept is extended to monocrystalline Si cells (Zhang et al., 2012d). The upconversion layer contains up to six elements and is plated both on the front and back surfaces of the solar cells (Zhang, 2012). Other cell fabrication methods include both an upconversion and a downshifting layer as shown in Fig. 30 (Cang et al., 2012). The latter authors note that the downshifting layer can equally be deposited onto the front face of the transparent glass. A similar design is described by Wang and Chen (2011) who use powdered molybdates doped with Yb^{III} and Er^{III} as upconversion materials and $Eu^{II/III}$-doped cerium phosphates as downshifting layers.

In some instances, lanthanide oxides are incorporated into solar cells to control properties other than luminescence. For instance, conduction between the semiconductor layer and the electrode can be enhanced in the following way. First, an antireflection film is formed on the surface of the semiconductor material followed by screen-printing of a conductive paste made up of silver, glass, an organic binder, and 1.5–4.5 volume % of Ln_2O_3 (Ln=La, Nd, Dy, Sm). The paste is then burnt, which removes the antireflective layer and brings the semiconductor substrate and the electrode into close contact (Takei, 2011).

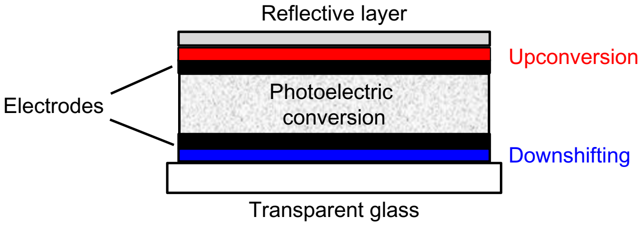

FIGURE 30 Scheme of a Si solar cell fitted with both downshifting and upconversion layers (Cang et al., 2012). A similar construction has been patented earlier by German researchers (Wehrspohn and Schweizer, 2009).

4. SOLAR CELLS WITH SEMICONDUCTORS OTHER THAN SILICON

The cells dealt with here belong to the category of thin-film cells and are made up of several thin layers (a few nanometer up to a few micrometer thick) of photovoltaic materials, electrodes, antireflection, and wavelength-converting materials. They are frequently tandem or multijunction cells. The photovoltaic material is a combination of elements from Groups12 (Zn, Cd) or 13 (Al, Ga, In) and 15 (P, As, Sb) or 16 (S, Se, Te) of the periodic table. More elaborate combinations including Group 11 elements (Cu, Ag, Au) also induce exploitable photoelectric properties in some materials such as Cu_2ZnSnS_4 which is cheap and nontoxic (Suryawanshi et al., 2013). One reason for substituting (or combining) a-Si with these group 12/16 (II/VI using the old groupnumbering of the periodic system) or 13/15 (III/V) elements is their lower bandgap and, therefore, better absorption in the NIR (Fig. 31). Bandgaps for some materials used in solar cells are listed in Table 5, and from these data, one can easily figure out that combining several semiconductor materials in one multijunction device allows one to cover a larger portion of the solar spectrum, henceforth achieving the largest yield of these cells.

The rich diversity of materials at disposition may be the reason why until now only a few attempts have been made to introduce rare earths into these devices. One example is a 100-μm thick vitroceramic plate doped with Yb^{III} and Er^{III} which has been coupled to a single-junction ultra-thin (3 μm) GaAs cell. The green upconverted light belongs to a spectral range where GaAs has a good light-to-electricity conversion (about 55%). When illuminated with a Ti-sapphire laser emitting at 890 nm, the photoresponse increases quadratically with the input power, a proof that upconversion is operating. Under 1-W illumination of a 0.039-cm^2 device (25.6 W cm^{-2}, corresponding to 256 suns), a conversion efficiency of 2.5% was reached, while no response from the cell is measured in the absence of

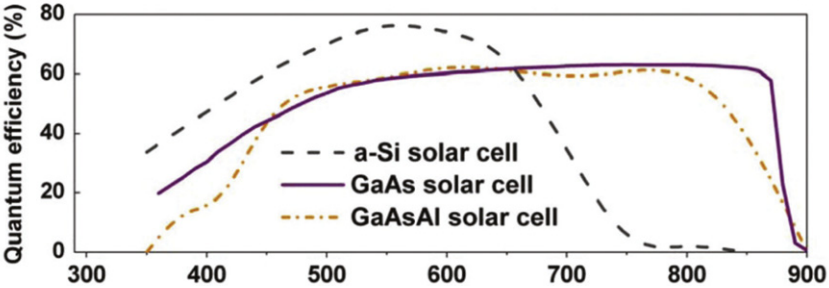

FIGURE 31 Comparison of quantum efficiencies of solar cells based on various semiconductor materials. *Reproduced with permission from Fang et al. (2011). © 2011 The Electrochemical Society.*

TABLE 5 Bandgaps E_g at 302 K and λ_{opt} (See Eq. (2)) for Selected Semiconductor Materials Used in Solar Cells

Material	Symbol	E_g (eV)	λ_{opt} (nm)	Material	Symbol	E_g (eV)	λ_{opt} (nm)
Silicon	c-Si	1.11	1117	Cadmium sulfide	CdS	2.42	512
Silicon	a-Si	1.7	729	Cadmium selenide	CdSe	1.73	717
Germanium	Ge	0.67	1851	Cadmium telluride	CdTe	1.49	832
Gallium phosphide	GaP	2.26	549	Indium phosphide	InP	1.35	919
Gallium arsenide	GaAs	1.43	867	Indium arsenide	InAs	0.36	3444

Data from Streetman and Banerjee (2000).

the upconverting layer (Gibart et al., 1996). In another, newer, work, layers of $Y_6W_2O_{15}$:Er(9 mol%),Yb(5 mol%) upconverting materials have been added to the rear of a GaAs cell, resulting in an increase in the spectral response around 973 nm; at this wavelength, the output power grows from 0 (without UC layer) to 0.339 μW with a 300-μm UC layer (Lin et al., 2012).

Cadmium telluride solar cells fitted with a cadmium sulfide layer are cheap and have reasonable conversion efficiency above 500 nm. As displayed in Fig. 12, about 19% of solar irradiance occurs in the range of 300–500 so that it is interesting to try to tap it. To this end, potassium magnesium fluoride crystal disks have been doped with samarium. The crystals contain both Sm^{II} and Sm^{III} and feature broad and fairly intense $4f^6$-$4f^55d^1$ absorption bands from Sm^{II} in the range of 250–480 nm in addition to the weak f-f transitions from Sm^{III}. Divalent samarium emits in the range of 660–720 nm with a maximum at 695 nm, while Sm^{III} has less intense emission bands between 550 and 650 nm. The combined quantum yields of $Sm^{II/III}$ ions reach 84%. When coupled to a 2-mm thick $KMgF_3$:Sm(0.8 mol%) disk via a refractive-index matching liquid, a commercial CdS/CdTe solar cell sees its short-circuit current increased by 5%, and since the open-circuit voltage and the FF are not affected, this figure corresponds to the increase in conversion yield. The authors calculated that the maximum increase in the latter could reach 22–23% for an optimized system and a unity quantum yield for samarium (Hong and Kawano, 2003). The study was subsequently completed by another group who measured all cell parameters and showed that the yield increases from 2.97% to 3.11% (+4.7 relative%). It was also extended to a-Si and m-Si cells for comparison: the same disk brought only 3% improvement in conversion efficiency. Other materials such as $Ca_xSr_{1-x}F_2$:Eu^{II},Tb^{III} or ethylene vinyl acetate doped with Eu^{II}, Tb^{III}, and Dy^{III} and coupled with the CdS/CdTe cell led to negligible improvements (1–1.7%) only. This is also the case of a borate glass doped with 1 mol% Sm_2O_3: a 3.2-nm layer on the top of a 300-nm layer of CdS buffer layer results in a 0.9% increase in the short-circuit current density of the CdTe cell, assuming a 50% quantum efficiency for the conversion of a blue into a red photon by Sm^{III} (Streudel et al., 2012). In this respect, organic downshifting compounds such as rhodamine 6G doped into PVB or PMMA or coumarin 153 doped into PVB perform much better, with relative increases in conversion yields reaching 11% and 5.6%, respectively (Kawano et al., 2009).

A light-focusing device has been designed which incorporates a concave parabolic surface coated with various rare-earth luminescent materials, including borides, fluorides, vanadates, silicates, chlorophosphates, or YAG doped with trivalent lanthanide ions or pairs of ions (including Mn^{II} and Pb^{II}) and which is proposed in connection with different cell types, including GaAs and AlGaAs. It is claimed that the conversion yield is substantially improved, but without quantifying the data (Zhou et al., 2011).

One of the main problems in multijunction cells resides in designing junctions generating no loss. To this end, lattices have to be matched. It turns out that the lattice spacing of rare-earth oxides, nitrides, or phosphides fairly well match those of silicon or SiGe materials, especially that fine tuning can be achieved by choosing the right R^{III} ion. For instance, the lattice of an equimolar Si/Ge material corresponds to the one of Nd_2O_3. The rare-earth materials are therefore helpful in realizing optimum junctions, as described in Fig. 32 (Clark et al., 2010).

Finally, it seems that some lanthanide nitrides, for example, GdN (Brewer et al., 2010) or LnB_6 (Brewer et al., 2011), could replace other semiconductor materials, but little information is disclosed until now on solar panels using such compounds (Cheung et al., 2012).

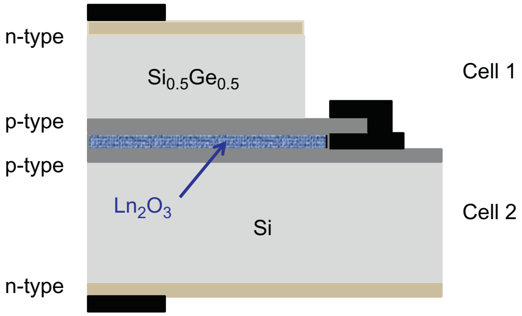

FIGURE 32 Scheme of a tandem $Si_{0.5}Ge_{0.5}$/Si solar cell with a rare-earth oxide layer as transition materials. *Redrawn after Clark et al. (2010).*

5. DYE-SENSITIZED SOLAR CELLS

5.1. Description and Relevant Parameters

DSSCs were initially proposed in 1991 (O'Regan and Grätzel, 1991) and are currently the subject of intense efforts to improve their relatively low efficiency compared to Si or III–V cells. Presently, best reported efficiencies are around 12% for single-junction cells (Heo et al., 2013; Kalyanasundaram, 2010b; Yella et al., 2011), between 15% and 16% for tandem cells (Liska et al., 2006) and near 10% for modules (Green et al., 2012).

DSSCs have the potential for competing with traditional silicon solar cells: they can be integrated into building facades and/or windows and outperform p-Si cells at incident angles larger than 55°. They also have better conversion yields under diffuse light conditions (hazy, foggy weather); Sony has demonstrated that a 10%-rated DSSC module produces as much electricity over 1 year as a 15%-rated Si module. Furthermore, stability may be comparable to one of the Si cells: a lifetime of 25–40 years (depending on the latitude) can be inferred from fast aging experiments conducted during 3 years (Harikisun and Desilvestro, 2011). It is presently estimated that DSSCs will become quite competitive if production costs can be lowered to the level of present production price of Si panels, 1–2 US$/W (Wikipedia (Engl.), 2012) and if practical modules with ≈12% efficiency can be built. This means that laboratory DSSCs, the parameters of which are usually determined on a <1-cm^2 cell whereas modules features 10–20 cm^2 areas, should achieve 15–16% yield, a goal which is probably reachable within the next few years.

DSSCs usually consist of multilayer cells (Fig. 33) built on a substrate glass coated with transparent conducting oxides such as ITO or FTO (Andrade et al., 2011). A few μm-thick mesoporous TiO_2 film made of 5–25 nm-sized

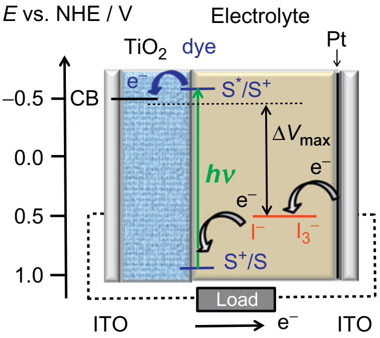

FIGURE 33 Scheme of a dye-sensitized solar cell. *Redrawn after Kalyanasundaram (2010b) and Gratzel (2003).*

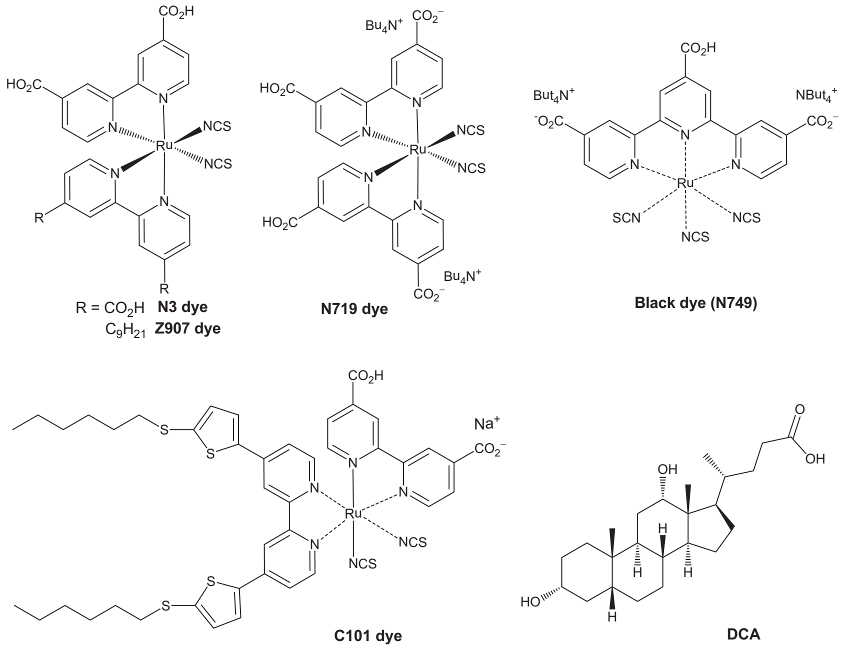

SCHEME 5 Ruthenium-based dyes and deoxycholic acid used to prevent aggregation.

TiO_2 nanoparticles coated with a dye (see, e.g., Scheme 5) plays the role of light harvester and electron donor. Typical characteristics of the dye-loaded TiO_2 electrode are a Brunauer-Emmett-Teller surface of 70–85 $m^2\,g^{-1}$ and a dye concentration in the range of 10^{-5}–10^{-7} mol cm^{-2}. Once the dye is excited, electrons are injected into the CB of TiO_2, a transfer which must be fast enough to successfully compete with decay to the ground state, by either fluorescence or nonradiative process. In fact, the large surface area, porosity, and electric contact of mesoporous titanium dioxide are particularly favorable for electron transfer and easy diffusion into the electrolyte.

The classical electrolyte, referred to as redox shuttle electrolyte, is the iodide/iodine redox couple, which regenerates the dye ground state by transferring an electron (Hamann and Ondersma, 2011). The voltage attainable by the cell corresponds to the difference between the Fermi level of TiO_2 and the redox potential of the electrolyte. Regeneration of the dye ground state unfortunately limits the attainable open-circuit potential V_{OC} to about 0.7–0.8 V, and this turned out to be a major cause for the relatively low efficiency of DSSCs. Hence, cobalt (III/II) polypyridine complexes have been proposed as alternatives. These complexes have less light absorption in the 350–450 nm range than the iodide electrolyte and their redox potential can be tuned by modifying the polypyridine ligands (reported range: 0.49–0.92 V, as compared to 0.31 V for I_3^-/I^-); this is of utmost importance in that the redox potential of the shuttle electrolyte should be matched to the ground state potential of the dye in order to regenerate it with minimum losses (Hamann, 2012). Grätzel's group recently came up with Co^{III}/Co^{II} tris(bipyridyl)-based redox electrolyte (coupled with a donor-π-bridge-acceptor zinc porphyrin) and reached a record efficiency of 12.3%, with $V_{OC} \approx 0.93$ V (Yella et al., 2011). Finally, the DSSC set-up is completed by Pt-coated ITO or FTO glass serving as a counter electrode (Fig. 33). In order to cut down the cost of the cells, efforts are now being made to replace the Pt electrode by poly(3,4-alkylthiophene) cathodes (Ahmad et al., 2012).

In addition to energy considerations, optimization of a solar cell requires a precise knowledge of the kinetic aspects of all the processes occurring in the cell: electron injection, excited state decay, recombination, regeneration, charge transport (Listorti et al., 2011). A recent study indicates that electron injection for the N719 dye proceeds on a sub-10 fs time scale, while fluorescence has a lifetime shorter than 30 fs (Bram et al., 2012). Furthermore, electron transport must be 100-fold faster than recombination if >99% of the photo-generated charge carriers are to be collected (Fig. 34). A difficult aspect of this kinetics is that it is heterogeneous, with rates varying strongly depending on the particle size and on the distance between the dye and the TiO_2 surface; impurities may also hamper the transfer. To date, few detailed studies are available on these aspects (Martiniani et al., 2012).

Light harvesting by the dye adsorbed on the TiO_2 surface can be increased by introducing larger TiO_2 particles (a few hundred nanometers in size) in the transparent TiO_2 film of or by printing them on the top of the transparent TiO_2 film as a scattering layer (SL). Alternatively, other metal oxide particles can be used as SL, for example, MgO, ZnO, Al_2O_3, or ZrO_2 aggregates (Chen and Mao, 2007), as well as various other microscopic or nanoscopic structures. The efficiency of the cell fitted with such a refractive layer can be increased by up to 10% (15–25% increase in photocurrent). Another improvement consists in co-adsorbing organic molecules such as deoxycholic acid (DCA, see Scheme 5) to break up dye aggregates.

The overall power conversion efficiency of a DSSC (written η in this section) is defined by Eq. (11), Section 2.3, with $P_{out} = V_{max} \times J_{max}$ being the maximum output power; the FF is given by Eq. (18), identical to the left part of Eq. (13), Section 3.1:

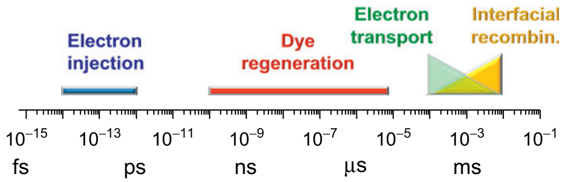

FIGURE 34 Time scale for DSSC kinetics.

$$\mathrm{FF} = \frac{V_{\max} \times J_{\max}}{V_{\mathrm{OC}} \times J_{\mathrm{SC}}} \tag{18}$$

where $V_{\max}$ (V) and $J_{\max}$ (mA cm^{-2}) are the voltage and current density at the point of the maximum power output in *J–V* curves; V_{OC} (V) is the open-circuit voltage, and J_{SC} is the short-circuit current density (usually given in mA cm^{-2}). Another parameter of interest is the incident photon-to-current conversion efficiency (IPCE/%) defined as:

$$\mathrm{IPCE} = \frac{J_{\mathrm{SC}}}{P_{\mathrm{in}}} \times \frac{1240}{\lambda} \times 100 \tag{19}$$

where λ is the wavelength of the incident light in nm and 1240 is the same unit conversion factor as in Eq. (2).

Four parameters determine the value of IPCE, the light-harvesting efficiency (LHE), the quantum yield of electron injection from the excited dye into the TiO_2 CB (ϕ_{inj}), the efficiency for dye regeneration (η_{reg}), and the collection efficiency of the photo-generated charge carriers (η_{coll}) itself determined by the time constants for transport (τ_{trans}) and recombination (τ_{rec}) of the electrons injected into the CB (Yella et al., 2011):

$$\mathrm{IPCE} = \mathrm{LHE} \times \Phi_{\mathrm{inj}} \times \eta_{\mathrm{reg}} \times \eta_{\mathrm{coll}} \tag{20}$$

$$\eta_{\mathrm{coll}} = \frac{1}{1 + \frac{\tau_{\mathrm{trans}}}{\tau_{\mathrm{rec}}}} = \frac{\tau_{\mathrm{rec}}}{\tau_{\mathrm{rec}} + \tau_{\mathrm{trans}}} \tag{21}$$

Much as for solar luminescent converters and silicon solar cells, lanthanides may play a role in improving the overall yield of DSSCs. Until now, however, few papers present quantitative and reliable data on the subject despite several review, feature, or perspective articles pointing to their potential in this respect (Abdel-Mottaleb, 2009; Bünzli and Eliseeva, 2010; Cates et al., 2012; Eliseeva and Bünzli, 2011; van Sark et al., 2010; Wang et al., 2011a,b). Lanthanides have been doped as ions, nanoparticles, or complexes into the TiO_2 mesoporous electrode, or provided in refractive layers or as additional, either down- or upconverting, layers in the devices. Moreover, Y^{III} and La^{III} have been shown to improve solar cell efficiency by simple treatment of the TiO_2 photoanode. Available quantitative data are gathered in Tables 6–8 in which we give improvements of short-circuit current, open voltage, FFs, and efficiency with respect to an adequate reference cell, whenever available. It is worth mentioning that in most papers, a reference and/or blank is either not appropriate or inexistent. A correct way of proceeding would be to compare the performances of the cell doped with luminescent lanthanide material with a cell doped at the same concentration with a similar but nonluminescent rare-earth compound (e.g., La^{III}, Gd^{III}, Lu^{III}, or Y^{III}) since adsorption of this material affects dye loading and aggregation; moreover, if dissociation occurs, Ln^{III} ions, which are p-dopants, may also modify the semiconductor bandgap.

TABLE 6 **Rare-Earth Materials as SL and Anode Modifiers in Dye-Sensitized Solar Cells; Effects Are Given for Conditions Leading to the Best Quantum Efficiency**

Nr	Rare-earth materials	Form under which provided	$TiCl_4$[a]	Dye	Cell area (cm^2)	ΔI_{SC} or ΔJ_{SC} (%)	ΔV_{OC} (%)	ΔFF (%)	$\Delta\eta$ (%)	η (%)	References
Scattering layer											
1	Cubic CeO_2	400 nm nanoparticles as scattering back layer	No	N719	0.15	19	0.7	−1.5	18	8.6	Yu et al. (2012c)
2	YAG:Ce	Scattering/downshifting layer on the top of TiO_2 electrode	n.a.	N719	n.a.	15	None	−1.5	13.5	7.9	Zhu et al. (2012)
Chemical modification of titanium oxide											
3	Y^{III} $[YCl_3(H_2O)_n]$	1 mol% in TiO_2 electrode	No	C101	0.16	17	2.5	2.5	22	9.0	Chandiran et al. (2011)
4	La^{III} $([La(NO_3)_3{\cdot}(H_2O)_n])$	1 mol% in TiO_2 electrode	Yes	N719	0.40	12	None	1	30	6.7	Zhang et al. (2010a)
5	La^{III} $[La(ac)_3(H_2O)_n]$[b]	Posttreatment of TiO_2 electrode with 1 mol% $La(ac)_3$ at pH 1 (HCl)	No	N719	1.03	23	−1	1.5	25	7.0	Yahav et al. (2011)
6	La_2O_3	8-μm layer dip-coated onto 12-μm layer of TiO_2	No	N719	1.0	49	3	7	41	9.7	Yu et al. (2012b)
7	$Ce^{III/IV}$ $[Ce(NO_3)_3(H_2O)_6]$	0.1%in TiO_2 electrode	No	N719	n.a.	12	−2	1	11	7.1	Zhang et al. (2012a)
8	$Ce^{III/IV}$ $[Ce(NO_3)_3(H_2O)_6]$	0.1% in TiO_2 electrode	Yes	N719	n.a.	8	−1	0	6	7.7	Zhang et al. (2012a)

Continued

TABLE 6 Rare-Earth Materials as SL and Anode Modifiers in Dye-Sensitized Solar Cells; Effects Are Given for Conditions Leading to the Best Quantum Efficiency—Cont'd

Nr	Rare-earth materials	Form under which provided	$TiCl_4$[a]	Dye	Cell area (cm^2)	ΔI_{SC} or ΔJ_{SC} (%)	ΔV_{OC} (%)	ΔFF (%)	$\Delta\eta$ (%)	η (%)	References
9	Nd^{III} TiO_2:Nd(5mol%) nanorods	2% TiO_2:Nd nanorods in TiO_2 electrode	Yes[c]	N719	0.2	22	−1	10	33	4.4	Yao et al. (2006)
10	Eu^{III} TiO_2:Eu(3 mol%)	Additional layer on TiO_2	Yes	BD	0.16	24	8	−3	38	3.4	Huang et al. (2010)
11	Gd^{III} $[Gd(NO_3)_3{\cdot}(H_2O)_6]$	TiO_2 dipped into 0.2 M Gd salt	Yes	N3	1.5	36[d]	3[d]	54[d]	35[d]	0.7[d]	Zalas et al. (2011)
12	Yb^{III} $YbCl_3$ in anh. ethanol	3 mol% doped into TiO_2	No	N719	0.16	7	−27	10	−28	4.4	Xu et al. (2006)
13	Er_2O_3	0.1 g Er_2O_3 in TiO_2 electrode	Yes	C101	0.05	27	n.a.	n.a.	25	6.1	Li and Gu (2012)
14	R^{III} (R = Sc, Y, La-Lu, except Tm)	Additional layer of TiO_2:R (0.05 wt%)	Yes	N3	0.13	14[e]	2[e]	12[e]	31[e]	8.9[e]	Zalas and Klein (2012)

Data are rounded to corresponding number of significant digits. Refer to Scheme 5 for chemical formulae of the dyes. Unless otherwise stated, data are for illumination corresponding to 1 sun (AM1.5G, 100 mW cm^{-2}).

[a] *Posttreatment with $TiCl_4$.*

[b] *Data with respect to TiO_2 without La^{III} and without $TiCl_4$ treatment.*

[c] *With Ti tetraisopropoxide.*

[d] *Tungsten-halogen lamp, 400 W m^{-2}.*

[e] *Data for Ce^{III}, see text for other R^{III} ions.*

TABLE 7 Rare-Earth Complexes as Dyes or Downshifting Materials for Dye-Sensitized Solar Cells; Effects Are Given for Conditions Leading to the Best Quantum Efficiency

Nr	Rare-earth materials	Form under which provided	Illum.[a]	Dye	Cell area (cm^2)	ΔI_{SC} or ΔJ_{SC} (%)	ΔV_{OC} (%)	ΔFF (%)	$\Delta\eta$ (%)	η (%)	References
Inorganic downshifting materials											
1	Sm^{III}	5% doped into colloidal TiO_2 electrode	1 sun	N719	0.2	31	1	5	37	5.8	Hafez et al. (2011)
2	Eu^{III}	5% doped into colloidal TiO_2 electrode	1 sun	N719	0.2	15.5	−4	8	22	5.2	Hafez et al. (2011)
3	$LaVO_4$:Dy (2 mol%)	luminescent UV-absorbing 300-nm thick coating of TiO_2 electrode	84 mW cm^{-2}	N3	0.2	−18	1	17	−5	3.7	Liu et al. (2006)
4	Y_2O_3:Eu(5 wt%)	Doped into TiO_2 electrode (3 wt%)	1 sun	N719	n.a.	1.7	10	1.3	14	6.5	Wu et al. (2010)
5	Y_2O_3:Eu(5 mol%), Gd(2 mol%)	Doped into TiO_2 electrode (4 wt%)	1 sun	N719	n.a.	3	8	6	19	6.4	Xie et al. (2012a)
6	TiO_2:Eu(0.07 mol %) nanorods [b]	Additional 4-μm thick layer on the top of TiO_2		N719	n.a.	7	−3	14	13	8.0	Hafez et al. (2010)

Continued

TABLE 7 Rare-Earth Complexes as Dyes or Downshifting Materials for Dye-Sensitized Solar Cells; Effects Are Given for Conditions Leading to the Best Quantum Efficiency—Cont'd

Nr	Rare-earth materials	Form under which provided	Illum.[a]	Dye	Cell area (cm^2)	ΔI_{SC} or ΔJ_{SC} (%)	ΔV_{OC} (%)	ΔFF (%)	$\Delta\eta$ (%)	η (%)	References
7	Gd_2O_3:Eu(6%)	Dispersed into TiO_2 photoanode	$\lambda < 420$ nm 24 mW cm^{-2}	N719	0.2	13	15	−0.7	29	1.9	Li et al. (2011a)
			1 sun(?)	N719	n.a.	12	3	2	17	7.0	Li et al. (2011a)
8	Gd_2O_3:Sm(3%)	Dispersed into TiO_2 photoanode	$\lambda < 420$ nm 24 mW cm^{-2}	N719	n.a.	12	13	0.7	27	1.9	Li et al. (2013)
			1 sun	N719	n.a.	5	4.5	2.4	13	6.7	Li et al. (2013)
Ln complexes as dyes											
9	[Lu(TBPor)PcBut]	SnO_2/[Lu(TBPor)(PcBut)], PDHEP, TiO_2/Al photoelectric cell	1.2 mW cm^{-2}	Complex	n.a.	[c]	n.a.	n.a.	n.a.	n.a.	Liu and Hu (2004)
10	[Sm(PcOct)(Pc)]	ITO/TiO_2:Sm(0.2%)/TiO_2/Al	50 mW cm^{-2}	Complex	1.0	0.52[d]	0.40[d]	0.33[d]	n.a.	0.14	Wang et al. (2008)
11	[$Sm_2(PcOct)_2(Nc)$]	ITO/TiO_2:Sm(0.2%)/TiO_2/Al	50 mW cm^{-2}	Complex	1.0	0.86[d]	0.44[d]	0.47[d]	n.a.	0.36	Wang et al. (2008)

12	$[Eu(DB8QB)_3]_n$	TiO_2 soaked into 0.5 mM complex solution in DMF	1 sun	Complex	0.2	4.8[d]	0.63[d]	0.75[d]	n.a.	2.3[c]	Xiao et al. (2010)
13	$[Eu(B8QDF)_3]_n$	TiO_2 soaked into 0.5 mM complex solution in DMF	1 sun	Complex	0.2	6.3[d]	0.64[d]	0.75[d]	n.a.	3.0[c]	Xiao et al. (2010)
14	$[Eu(C4)_3(BD2)]$	Doped into TiO_2 electrode	1 sun	Complex	n.a.	0.41[d]	0.49[d]	0.77[d]	n.a.	0.15	Oh et al. (2011)
Ln complexes as downshifting materials											
15	$[Eu(C4)_3(BPBA)]$	Doped with dye into TiO_2 electrode	1 sun	BD	n.a.	14	4	3	22	9.3	Oh et al. (2011)
16	$[Tb(HDPA)_3]$ × 4EtOH [c]	Cosensitizer 1:1 ratio with N719	1 sun	N719	n.a.	47	1	1	44	4.1	Wang et al. (2012e)
17	$[Dy(HDPA)_3]$ × 4EtOH	Cosensitizer 1:1 ratio with N719	1 sun	N719	n.a.	66	8	5	72	4.9	Wang et al. (2012e)

Data are rounded to the corresponding number of significant digits. Refer to Scheme 5 (dyes) and Scheme 7 (complexes) for chemical formulae

[a] *1 sun = AM1.5G (100 mW cm^{-2}).*

[b] *Data with respect to a bilayer solar cell (TiO_2 nanorods/TiO_2 nanoparticles) without Eu^{III}.*

[c] *J_{SC} = 0.69 mA cm^{-2}.*

[d] *Absolute values.*

TABLE 8 Rare-Earth Upconversion Materials for Dye-Sensitized Solar Cells; Effects Are Given for Conditions Leading to the Best Quantum Efficiency

Nr	Rare-earth materials	Form under which provided	Illum. [a]	Dye	Cell area (cm^2)	ΔI_{SC} or ΔJ_{SC} (%)	ΔV_{OC} (%)	ΔFF (%)	$\Delta\eta$ (%)	η (%)	References
1	TiO_2 doped with Er^{III}(8.5%), Yb^{III}(8.5%)[b]	Scattering layer	1 sun	N719	0.25	3	None	None	3	9.0	Han et al. (2009)
2	LaF_3:Er(2.5%), Yb(9%)	Doped TiO_2 UC layer	AM 1.0G	N719	n.a.	2	None	−3	−1	2.7	Shan and Demopoulos (2010)
3	β-$NaYF_4$:Er,Yb	External bifunctional layer at back of cell	1 sun	N719	0.16	9 [c]	1	−3	6[c]	7.4	Shan et al. (2011)
4	Colloidal TiO_2 doped with	2-layer anode	[d]	N719	1.0	136	40	13	265	0.15	Xie et al. (2011)
	Er^{III}, Yb^{III}	TiO_2/doped TiO_2 1/3	1 sun	N719	1.0	0.3	4	8.5	14[c]	7.3	
5	Colloidal TiO_2 doped with 7 wt % YOF:Er,Yb	2-layer anode TiO_2: doped TiO_2 1:3	1 sun	N719	n.a.	6.5	6	9.5	24	7.2	Wang et al. (2012d)
6	β-$NaYF_4$:Er,Yb/ graphene composite	Mixed with colloidal TiO_2	1 sun	N719	n.a.	3	2	0	4.4	2.8	Li et al. (2012b)
7	β-$NaYF_4$:Er(2 %), Yb(20%)	Core–shell $NaYF_4$: Er,Yb/TiO_2 NPs	1 sun	N719	n..a.	8	−2	18	23	4.3	Zhang et al. (2013)
8	β-$NaYF_4$:Er,Yb	Doped into TiO_2	1 sun	Z907	n.a.	10	n.a.	n.a.	3.7	2.8	Yuan et al. (2012)

9	β-$NaYF_4$:Er,Yb/ $NaYF_4$	Co-doped with dye into ZnO electrode	1 sun	BD	n.a.	−5.5	29	n.a.	12	1.8	Khan et al. (2011)
10	YF_3:Er(2%),Yb(18%)	7 wt% into TiO_2	1 sun	N719	n.a.	17	10	8	35	7.9	Wu et al. (2012b)
11	Y_2O_3:Er(10%) nanorods	5 wt% in TiO_2 electrode	[e]	N719	n.a.	50	28	19	205	0.17	Wang et al. (2012c)
			1 sun	N719	n.a.	10	5	2	20	7.0	
12	Lu_2O_3:Tm(0.4%), Yb(2%)	4 wt% into TiO_2	[d]	N719	n.a.	38	15	3	63	0.2	Li et al. (2011b)
			1 sun	N719	n.a.	9	2	0.6	10[c]	6.6	
13	Tm^{III},Yb^{III} (10/1)	Ln_2O_3 3.3 wt%/ TiO_2	1 sun	N719	n.a.	0.8	2	7	10	7.1	Xie et al. (2012b)

Data are rounded to significant digits. Refer to Scheme 5 for chemical formulae of the dyes. Unless otherwise stated, given percentages correspond to mol%.

[a] *1 sun = AM1.5G (100 mW cm^{-2}).*

[b] *See text.*

[c] *w.r.t. solar cell having a pure TiO_2 SL.*

[d] *$\lambda > 720$ nm, 60 mW cm^{-2}.*

[e] *$\lambda > 900$ nm, 33 mW cm^{-2}.*

5.2. Scattering Layer (Table 6)

The small size of TiO_2 nanoparticles provided as photoanode results in poor light-scattering properties, and a nonnegligible fraction of photons passes through the cell without being absorbed. One remedy consists in introducing a SL made up of TiO_2 mesoporous microspheres or Anatase nanoplatelets (Zhang et al., 2012c); with three 4-μm thick layers, the latter provided a 24% efficiency improvement for a cell based on N719, however, with an efficiency of only 6.5% (Shao et al., 2011). Cerium(IV) oxide is a well-known material with high refractive index, used in multilayer optical coatings. Hydrothermally prepared 400 nm sized NPs of cerium oxide have been introduced as a mirror-like scattering back layer with 1.5-μm thickness in a DSSC based on dye N719. Both one and two layers have been tested, and although the two-layer arrangement features a reflectance around 75%, the one-layer fitted cell displays the largest efficiency: 8.6% versus 7.3% for the reference uncoated cell; this is because the two CeO_2 layers reduce considerably the ability of the dye to diffuse into the TiO_2 electrode (Yu et al., 2012c). Similarly, a SL of 200–300 nm nanoparticles of $Y_3Al_5O_{12}$:Ce (% not given) on the top of the TiO_2 electrode leads to a 13.5% improvement in the overall efficiency of the N719 cell (Zhu et al., 2012). However, in this case, the authors also invoke the fact that CeO_2 is emissive, as shown in Fig. 35 so that both light reflection and wavelength downshifting contribute to the improvement. The IPCE curve is not shown to prove this hypothesis, but close examination of this curve in the preceding example (Yu et al., 2012c) demonstrates that the quantum efficiency at 550 nm is more enhanced than, for instance, at 500 nm, which substantiates the "bimodal" explanation in both cases.

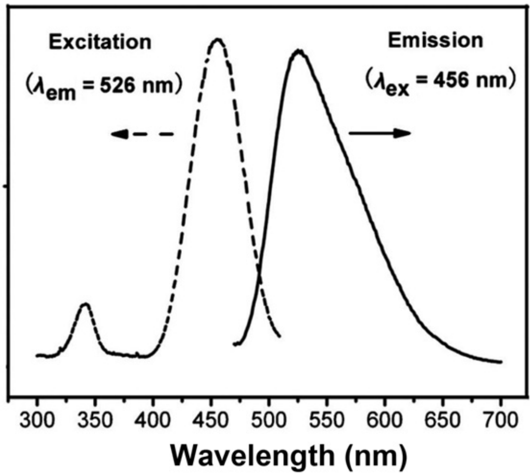

FIGURE 35 Excitation and emission spectra of $Y_3Al_5O_{12}$:Ce. *Reproduced with permission from Zhu et al. (2012); © Royal Society of Chemistry 2012.*

5.3. Titanium Oxide Modification (Table 6)

One of the major problems in DSSCs is charge recombination at the TiO_2/redox electrolyte interface. Electronic states below the CB of TiO_2 behave as efficient recombination centers on the nanoparticle surfaces thus slowing electron transport. To reduce these effects, a surface treatment generating several benefits is applied during which TiO_2 nanoparticles are coated with a thin layer of a wide bandgap semiconductor. First, the number of surface traps decreases. Second, an energy barrier is created which limits electron transfer and subsequent recombination into the electrolyte. Third, the TiO_2 CB is shifted downward with respect to the redox potential of the electrolyte, which favors electron transfer into the CB. Fourth, light scattering is also improved and, finally, the surface pH can be modified, and therefore, dye loading can be potentially increased. Typical coatings are metal oxides, carbonates, or titanates such as Al_2O_3, ZrO_2, MgO, $CaCO_3$, or $MTiO_3$ (M = Mg, Sr, Ba). Alternatively, another technique allows low-temperature (<150 °C) fabrication of the solar cells by electrodeposition of amorphous TiO_2 onto the nanoparticles. The best precursor for this posttreatment is $TiCl_4$: while the open-circuit voltage and FFs are hardly affected, the short-circuit current and therefore the cell efficiency goes up by about 20–28% (Sommeling et al., 2006; Zhao et al., 2011). A careful study of photoanodes with and without $TiCl_4$ posttreatment reveals that particle size increases by about 20%, which results in a 7.6% increase in dye adsorption; however, light absorption increases only marginally so that the increase in photocurrent is mainly due to increases in IPCE and in charge injection consecutive to a 100-mV lowering of the TiO_2 CB (Sommeling et al., 2006). $TiCl_4$ posttreatment is used by several authors and improvements in cell efficiencies of 15–25% are regularly reported.

Further improvement comes from simultaneous $TiCl_4$ treatment and doping of the TiO_2 electrode with metal ions. In one example, $TiCl_4$ treatment applied to an undoped TiO_2 electrode results in cell efficiency going up from 7.4% to 8.4% (+13.5%). Subsequent introduction of 0.5 mol% of aliovalent Nb^{V} into TiO_2 leads to a further improvement of the cell efficiency from 8.1% without $TiCl_4$ posttreatment to 8.7% with $TiCl_4$ treatment (+7.5%). The enhancement is attributed to better charge collection and electrode transparency (Chandiran et al., 2010). A similar enhancement is obtained with Sn^{IV}: when 11-μm-thick TiO_2 films are doped with 0.5 mol% SnO_2, the efficiency of a cell based on the N3 dye increases by 11.5%, from 7.45% to 8.3%, a consequence of both a negative shift of TiO_2 VB and a faster electron transport (Duan et al., 2012).

Trivalent Ga^{III} and Y^{III} ions have also been tested, with 0.2–2.0 mol% doping concentration range; they generate p-type doping in the electrode and the best results were obtained with 1 mol% concentration of the exogenous cation. The first ion increases the yield from 7.4% to 8.1% mainly because of an increase in the voltage and FF, while the photocurrent is slightly decreased.

On the other hand, yttrium performs much better, boosting the photocurrent by as much as +17% and the overall cell yield by +22%, to an absolute 9.0% (Table 6, entry 3). These data are obtained without $TiCl_4$ treatment, and the improvement is traced back to an increase in electron lifetime in the doped photoanode affording close to unity charge collection efficiency. When $TiCl_4$ treatment is further applied to the doped photoanodes, no clear improvement in their characteristics is recorded so that according to the authors, doping of Y^{III} can replace the somewhat cumbersome $TiCl_4$ posttreatment (Chandiran et al., 2011), which results in a ≈15–25% increase in η, see above. An earlier report reached a different conclusion (Zhang et al., 2010a). In this work, 1 mol% La^{III} is doped into the TiO_2 nanoparticles, followed by $TiCl_4$ treatment (Table 6, entry 4). With respect to the undoped, but similarly $TiCl_4$-treated electrode, the amount of oxygen vacancies on the La^{III}-doped TiO_2 surface increases, which leads to larger dye concentration and to a 13.5% larger cell efficiency. Here, dye N719 was used, whereas the work on Y^{III} was performed with the larger C101 dye (Chandiran et al., 2011) (Scheme 5), which may partly explain the different conclusions. We also note that Y^{III} has a more pronounced Lewis acidity character than La^{III}. As a matter of fact, Al^{III} is also reported to have beneficial effect on DSSCs efficiency (Ko et al., 2005) and an increase in efficiency from 10.42% to 10.75% (i.e., +3%) is documented for a cell based on the black dye (BD) when the electrode is treated by 0.01 M of $Al(OiPr)_3$. Magnesium *iso*-propyloxide has the same effect, but a much larger concentration of 0.15 M has to be used (Ozawa et al., 2012).

Less clear-cut conclusion is drawn in the report by Yahav et al. (Yahav et al., 2011). Here, the methodology differs in that the TiO_2 electrode is first treated with a lanthanum acetate solution (Table 6, entry 5). If the treatment is performed at neutral pH, the voltage increases, but this advantage is annihilated by a large decrease in photocurrent (≈−30%) so that the cell yield drops. On the other hand, acidic treatment at pH 1 is largely beneficial to the photocurrent, while the other parameters remain more or less constant and a +25% increase in η is achieved. A full set of comparative data is unfortunately not given for a dual treatment with $TiCl_4$ and $La(ac)_3$, but in this case, the photocurrent increases somewhat while the open-circuit voltage decreases. The increase in I_{SC} appears to be independent of the La^{III} concentration in the range of 0.01–0.4 mol%.

An amazing yield increase is generated when a thin layer of lanthanum sesquioxide is deposited onto a 12-μm thick TiO_2 film by dip-coating a solution of $La(NO_3)_3{\cdot}6H_2O$ in isopropanol, followed by heat treatment at 450 °C for ½ h (Table 6, entry 6). The coating results in a decrease in the electron transfer resistance, which reaches a minimum for an 8μm-thick layer. Remarkably, the concentration of the adsorbed N719 dye is little affected by the introduction of the La_2O_3 layer (±3–6%, that is at the limit of experimental errors). On the other hand, the 8μm-thick layer generates a huge increase in J_{SC} of 49% and a 41% improvement in the overall conversion yield, from 6.8% to 9.7%. No $TiCl_4$ posttreatment was used in this study (Yu et al., 2012b).

Cerium is an interesting element in view of its $Ce^{III/IV}$ redox properties exploited in catalysis and photocatalysis. When doped into TiO_2, CeO_2 induces the formation of an impurity band composed of $Ce^{III/IV}$(4f) and oxygen defect states which leads to a tailing of the CB. The resulting bandgap narrowing extends the photo-activity of TiO_2 into the visible (Chen et al., 2010). Therefore, Anatase photoanodes for DSSCs have been doped (0.05–0.9 mol%) with $Ce^{III/IV}$ by mixing cerium(III) nitrate hexahydrate with titanium isopropoxide and then proceeding with the usual fabrication of the nanoparticles (Table 6, entries 7 and 8). A doping concentration of 0.1% seems to be optimum in that it increases dye absorption from 1.39 to 1.43×10^{-7} mol cm^{-2} while reducing the average particle size from 13.1 to 12.3 nm; increasing the doping concentration further has the tendency to decrease dye absorption (1.31×10^{-7} mol cm^{-2} for Ce:Ti = 0.9%). In addition, there is a clear, although small, red shift of the absorption edge of TiO_2 translating into a reduction in the band gap from 3.23 to 3.15 eV. Solar cells with N719 dye were fabricated with an 8 μm nanocrystalline layer of the electrode fitted with a 4-μm SL (400 nm particle size). Some cells were subsequently treated with $TiCl_4$ before dye adsorption and others not in order to decipher the effect of this treatment. Several doping concentrations (0.1–0.9%) were also tested. In the end, the 0.1% doping concentration again gives the best results. The initial $TiCl_4$-untreated and undoped cell has a conversion yield of 6.4% which increases to 7.2% upon $TiCl_4$ treatment (+12%). Doping cerium leads to an increased yield reaching 7.1% for the untreated cell and of 7.65% for the $TiCl_4$-treated one. Therefore, the little amount of cerium introduced (0.1 mol%) results in an improvement of 6–11%, which entirely comes from a larger photocurrent, the open-circuit voltage having the tendency to slightly decrease while the FF remains almost constant (Zhang et al., 2012a). The authors conclude that the optimized performance of the cell arises from improved electron injection from the dye; we note, however, that part of it might simply be due to the larger dye concentration (+3%). This study also shows the cumulative effects of the $TiCl_4$ and Ln^{III} treatments.

Several other studies report modifications of TiO_2 films with other Ln^{III} ions leading to various results. For instance, Nd-doped TiO_2 NRs (20×2 nm^2) incorporated into a conventional TiO_2 anode boost the conversion yield by 33%, but the solar cell has very low final η of 4.4% only (Table 6, entry 9) (Yao et al., 2006). Similarly, a TiO_2:Eu (3 mol%)/TiO_2 double layer electrode increases the conversion yield by 56%, from 2.2% to 3.4% (Table 6, entry 10), and this is attributed to an increase in CB from 3.29 eV for the undoped TiO_2 to 3.34 eV in the doped one, reducing charge recombination (Huang et al., 2010). A comparable effect is induced by Gd^{III} doped into the TiO_2 electrode (% not specified) of a BD-based solar cell with a very low efficiency of

0.7% (Table 6, entry 11) (Zalas et al., 2011). Another investigation with a C101-based cell shows a TiO_2:Er_2O_3(0.1g) electrode, increasing the conversion efficiency by 25% (Table 6, entry 13) (Li and Gu, 2012). Finally, and surprisingly, Yb^{III} was found to have a dramatic detrimental effect on J_{SC} (down to −53%) and η (down to −48%) when doped (0.06–6 mol%) into TiO_2 (Table 6, entry 12) (Xu et al., 2006).

A systematic and reliable study is now available in which all of the rare-earth ions have been tested as modifiers of the TiO_2 photoelectrode together with $TiCl_4$ treatment (Table 6, entry 14). In the reported protocol, the TiO_2 electrodes are dipped during ½ h into an aqueous solution of $TiCl_4$ containing 0.2 M $Ln(NO_3)_3$, followed by sintering at 723 K during ½ h and subsequent immersion during 24 h into a 10^{-4} M solution of N3 dye. What is remarkable from the scientific point of view is that five cells have been fabricated for each tested R^{III} ion and that photoelectric measurements were repeated five times for each cell so that reported data are averages of 25 determinations (Zalas and Klein, 2012). The added coating contains about 0.05% of R^{III} ions, and their introduction in the modifying layer causes changes in several physicochemical properties of the materials as shown in Figs. 36 and 37. The R-containing layer acts as an energy barrier and/or as light SL and influences electron transport and dye adsorption ability. There is seemingly no systematic trend along the rare-earth series and only half

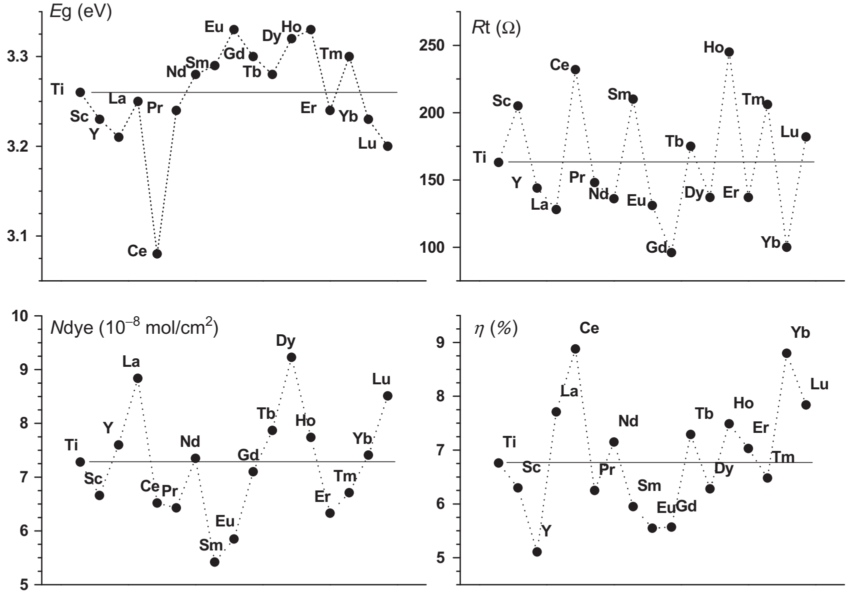

FIGURE 36 Clockwise from the top left: bandgap, total resistance, dye concentration, and conversion yields of DSSCs cells based on N3 dye and fitted with a coating layer TiO_2:R (0.05 wt%); data labeled Ti refer to an undoped photoanode. *Drawn from data reported in Zalas and Klein (2012).*

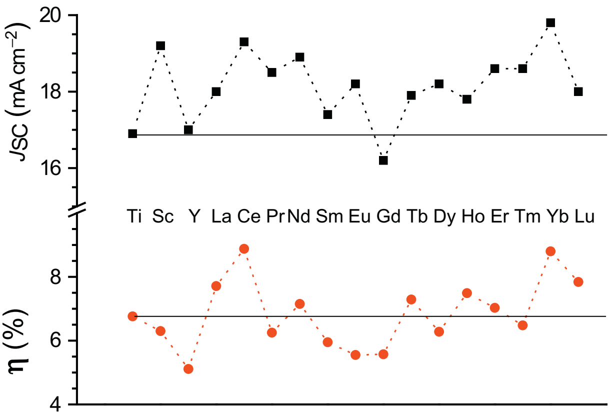

FIGURE 37 Photocurrent densities (top) and photoconversion yields (bottom) of N3-based solar cells fitted with a coating layer TiO_2:R (0.05 wt%); data labeled Ti refer to an undoped photoanode. *Drawn from data reported in Zalas and Klein (2012).*

of the ions have beneficial influence, La, Ce, Nd, Tb, Ho, Er, Yb, and Lu, with cerium and ytterbium (two ions having redox properties!), leading to the largest increase in photoconversion, 31% and 30%, respectively, the latter in complete contradiction with the previously cited work (Xu et al., 2006). It is noteworthy though that the photocurrent is larger for all doped photoanodes, except in the cases of Y^{III} (no improvement) and Gd^{III} (4% decrease).

What can be learned from these investigations is that results obtained by either adding a rare-earth containing coating or doping rare-earth ions into TiO_2 leads to contradictory results depending on the exact experimental procedure used. However, looking at the data reported in Table 6 for cells with yield above 7%, one realizes that (i) lanthanum leads to the best enhancements, 25% and 41% (entries 5 and 6), (ii) cerium is constantly beneficial (from +6% to +31%, entries 1, 2, 7, 8, and 14), (iii) yttrium may (entry 3, +22%) or may not (entry 14, −25%) be useful, and (iv) simultaneous or subsequent $TiCl_4$ treatment brings further benefits (compare entries 7 and 8). Completely opposite conclusions are reached for ZnO-based DSSCs (with N719 dye): La^{III}, Ce^{III}, Nd^{III} doping of ZnO decreases the yield (−11%, −94%, and −5%, respectively), while Sm^{III} and Gd^{III} increase it (11% and 45%, respectively). Since all photoconversion yields are smaller than 2% (Lu et al., 2011), these data are not discussed in details.

5.4. Inorganic Downshifting Materials (Table 7)

Downshifting technologies tested in DSSCs can be classified into three categories. The first is simple doping of luminescent Ln^{III} ions into TiO_2 nanoparticles, similar to the work described at the beginning of this section with nonluminescent ions. The second involves lanthanide-containing nanoparticles which are either doped into the photoanode or provided as an additional down-converting layer. The last category deals with lanthanide complexes with organic ligands, a promising avenue since it gave the best results to date, but remains little explored. The complexes are usually adsorbed onto the TiO_2 nanoparticles as described below, but one could also think of introducing them into the electrolyte or in an additional layer. Since the common dyes sketched in Scheme 5 have maximum IPCE in the range of 500–650 nm, Eu^{III} is the unavoidable ion because of its strong emission line around 615–620 nm and the availability of complexes with various ligands having large quantum yields, in the range of 75–85% (Bünzli and Eliseeva, 2013). On the other hand, europium may be sensitive to reduction and its cost is relatively high. Other ions have also been investigated, namely, Sm^{III} and Dy^{III}, but not Tb^{III} despite its main emission line at 540 nm which corresponds to a spectral range for which dyes usually have large IPCE. One reason could be that Tb^{III} has to be excited at shorter wavelengths than Eu^{III} that is in a range in which sun irradiance is very small.

To our knowledge, the first demonstration that mesoporous Anatase sensitizes the luminescence of Ln^{III} ions was made in 2002 on Eu^{III}-doped titania thin films (Frindell et al., 2002). The films have a well-ordered pore structure and two-phase walls made of amorphous titania and titania nanocrystallites. They were subsequently doped with various amounts of different Ln^{III} ions, and luminescence was observed for Nd^{III}, Sm^{III}, Eu^{III}, Er^{III}, and Yb^{III}, but not for Tb^{III} and Tm^{III}, which resulted in emission in the spectral range of 600–1540nm (Frindell et al., 2003). The nucleation and growth of the nanocrystallites is not affected by the Ln^{III} content (at least up to 8 mol%). The sensitization appears to go through TiO_2 defects: luminescence decays of the Eu^{III}-doped films are biexponential with a long component (0.5 ms for 8% Eu^{III} content) and a short 100-ns component corresponding to titania defects. Since the highest Ln^{III} excited state which could be populated is $Sm(^5G_{5/2})$ at around 18,000 cm^{-1}, this means that the energy of these defects is probably larger than about 19,000 cm^{-1}, otherwise too much back energy transfer would occur (Bünzli and Eliseeva, 2013). The situation is sketched in Fig. 38. Later, several papers studied in detail the spectroscopy of Eu^{III} doped into titania (see, for instance, Zeng et al., 2006).

For solar cell applications, the simplest use of Sm^{III} and Eu^{III} is their doping into the TiO_2 nanoparticles (Table 7, entries 1 and 2). Since this treatment increases the photocatalysis behavior of Anatase (Saif and Abdel-Mottaleb, 2007), the methodology was applied to DSSCs (Hafez et al., 2011). Doping was achieved from solutions containing 5 wt% of lanthanide and the authors report large increases in cell efficiency, +37% for Sm^{III} and +22% for Eu^{III}, with respect to an undoped photoanode. The larger increase generated by the Sm^{III} ions compared to Eu^{III} ions is ascribed to their shorter excited state lifetime, but inspection of the reported excitation spectra reveals

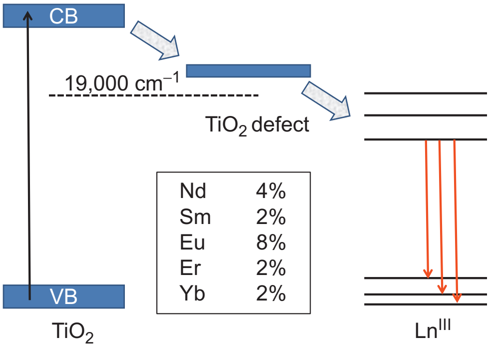

FIGURE 38 Sensitization of the luminescence of Ln^{III} ions by titania defects in Ln-doped thin films and maximum doping rate (mol%) attainable without generating self-quenching. *Redrawn from Frindell et al. (2002).*

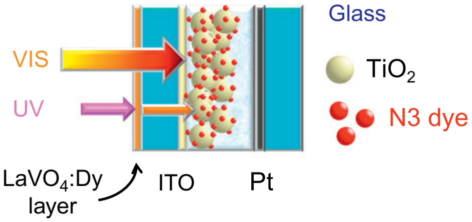

FIGURE 39 Scheme of the DSSC fitted with a UV-absorbing layer. *Redrawn from Liu et al. (2006).*

that Sm^{III} is mainly excited through the Anatase level (≈370 nm), while Eu^{III} is excited almost exclusively through its faint f-f transitions, which may as well explain the difference. The overall yields of the doped cells remain modest (5.8% and 5.2%), and no comparison with a nonluminescent ion is made so that one cannot decipher the "chemical" influence of the Ln^{III} ion as described above for Y^{III} and La^{III} (+20–30%!). In our opinion, energy-transfer processes contribute only little to the improvement of the solar cell characteristics.

The first documented attempt to use luminescent Ln^{III} ions to harvest the UV part of the solar spectrum dates back to 2006 when J.F. Liu and coworkers (Liu et al., 2006) coated a DSSC with an additional 300-nm thick UV-absorbing layer containing LaVO$_4$ nanocrystals doped with 2 mol% Dy^{III} (Table 7, entry 3; see Fig. 39).

According to the authors, the idea is to take advantage of the V-O CT band at 280 nm (!) to sensitize the Dy^{III} luminescence. The two main emission bands of Dy^{III} at 480 and 570 nm match reasonably well the long-wavelength absorption band of the N3 dye used in the experiments. However, when compared to a standard cell, the LaVO$_4$:Dy doped cell shows a decrease in efficiency from 3.9% to 3.7%. This may be due to light absorption by LaVO$_4$, which reduces UV-light absorption by the dye. However, downshifting occurs since a cell doped with $LaVO_4$ only has a lower yield of 3.0%. In summary, this attempt provides a UV-protective layer for the DSSC, increasing the lifetime of the dye: without protective layer, the cell yield is reduced by 50% after 12-h irradiation, compared to a 10% loss with the protective layer. The role of the Dy^{III} ions is to simply compensate the loss due to the removal of UV light by the protective layer. We also note that in reality, sunlight has very weak emission power below 320 nm so that the system chosen here is certainly not optimum. Despite this, the photophysical properties of thin films doped with $LaVO_4$:Dy(2 mol%) and spin-coated on ITO glass from 0.2 M solutions in PVA/citric acid have recently been investigated with the purpose of applying them to DSSCs (Wu et al., 2012a).

The red phosphor Y_2O_3:Eu is known for more than a century and still in use in fluorescent lamps, TV screens, computer displays, and OLEDs (Eliseeva and Bünzli, 2011). Various amounts (1–5 wt%) of Y_2O_3:Eu(3 wt%) have been doped into N719-based DSSCs (Table 7, entry 4). Excitation spectra of the Eu^{III} luminescence show excitation through the Eu-O CT state in the range of 220–280 nm (maximum at 250 nm), a domain in which there is no sun emission. Nevertheless, the authors find that the open-circuit voltage increases linearly with the phosphor content (Fig. 40), while short-circuit

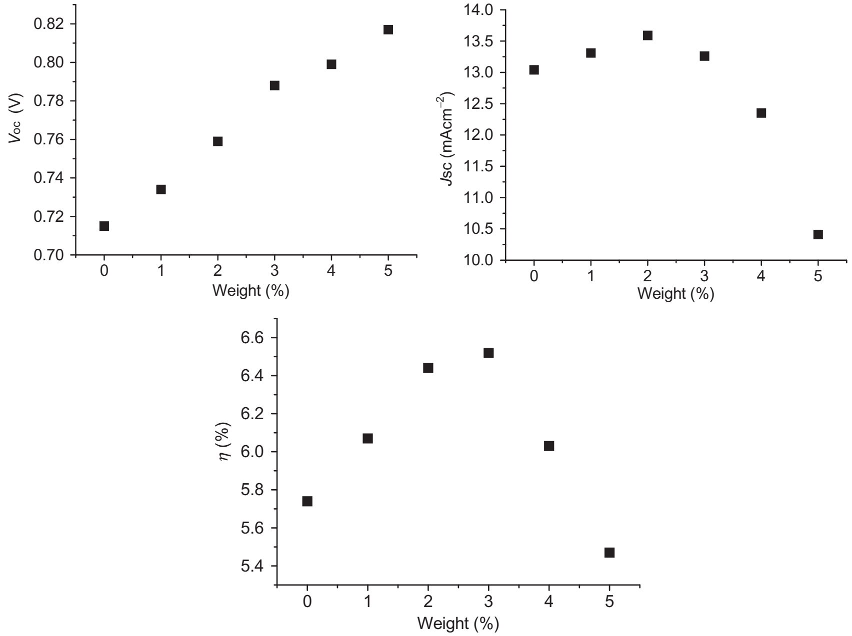

FIGURE 40 Effect of increasing quantities of Y_2O_3:Eu(3 wt%) doped into the TiO_2 electrode on the open-circuit voltage (left), short-circuit current density (middle), and overall cell efficiency (right). *Drawn from data in Wu et al. (2010).*

current variation is bell shaped with a maximum at 2 wt% displaying a modest 4% increase. With respect to the overall cell yield, the best doping amount is 3 wt% and translates into a 14% increase with respect to the undoped cell. No blank experiment is described in which luminescent Eu^{III} would be replaced by a nonluminescent (e.g., Gd^{III}) ion. In addition, no determination of the variation of dye concentration upon doping of the phosphor is available. We note, however, that the amount of Eu^{III} required to get the best yield is modest ($\approx$0.15 wt%) (Wu et al., 2010). In a similar work (Xie et al., 2012a), the anode has been doped with Y_2O_3:Eu(5 mol%), Gd(2 mol%). Here too, the excitation spectrum peaks around 254 nm and little downshifting can be expected, but due to p-doping by both ions, the conversion yield increases substantially (+19%) to reach 6.4% (Table 7, entry 5).

A similar improvement in cell yield (+13%) was obtained by adding a 4-μm thick layer of TiO_2 NRs doped with 0.07 mol% Eu^{III} (see Table 7, entry 6; Hafez et al., 2010). Here, the authors have compared four cell designs: (i) pure TiO_2 NRs (NR), (ii) pure TiO_2 nanoparticles (NP), (iii) bilayer NP/NR, and (iv) bilayer NP/Eu-NR. The amount of adsorbed N-719 dye increases from 2.1 to 3.6, 3.6, and 4.8×10^{-5} mol cm^{-2}, respectively, exemplifying the role of Eu^{III} ions. The introduction of the NR layer to the reference cell translates into an increase in cell yield from 5.8% to 7.1% (+22%), which is considerable. Adding Eu^{III} boosts the yield to 8% (+13 relative %). The authors invoke conversion of UV light into red light and give the argument that the IPCE at 250 nm amounts to 12% for the Eu-doped cell, compared to nil for the undoped one; furthermore, the same parameter increases from 89% at 575 nm to 94% upon doping with Eu^{III} (Hafez et al., 2010). Here again, we note that there is almost no sun emission below 300 nm and certainly no at 250 nm. We think that the beneficial effects recorded arise from a +33% increase in dye concentration (see above) and, also, from excitation of the Eu^{III} ion through its f-f transitions.

Another host material, Gd_2O_3, gives slightly better results when it contains 6 mol% of Eu^{III} and when the mole ratio Gd:Ti is 6% (see Table 7, entry 7; Li et al., 2011a). Under UV-irradiation ($\lambda < 420$ m), the cell yield increases from 1.5% to 1.9% upon doping Gd_2O_3:Eu into the TiO_2 electrode, the difference (0.4%) being consistent with the yield of a cell containing only the Eu phosphor. With full sunlight illumination, the undoped cell has $\eta = 6\%$ which can be increased up to 7% (+17%) when the phosphor is introduced into the electrode. The characteristic parameters of the cell vary similarly to the dependences shown in Fig. 40 for doping concentrations in the range of 0–12 mol%. The excitation spectrum contains the strong LMCT Eu-O band at 250 nm, along with f-f transitions from both Eu^{III} and Gd^{III}. However, LMCT and Gd^{III} should not play a large role in solar energy conversion since the corresponding excitation wavelengths are too short. The increased yield with respect to the preceding papers (17% vs. 13% and 14%) may be explained by the larger quantity of Eu^{III} ions introduced into the cell (0.36 as compared to 0.07 mol%).

Theoretically, one may also think of downconversion from Gd(^6P_J) to Eu(^5H_J), as observed in quantum-cutting (Wegh et al., 1999), but the Gd^{III} level absorbs in the range of 300–320 nm in which solar irradiance is faint. Another factor is the effect of ion doping on the electrode (see above). In this respect, a reference cell with Gd_2O_3 only would have clarified the relative contributions of ion doping and luminescence to the improved yield.

In these three works, the authors pretend relying on the Eu-O CT centered at 250 nm to excite Eu^{III}, which, in our opinion, is not reasonable since the solar spectrum has no emission intensity at this wavelength so that only the tails of the CT bands overlap with the solar spectrum in the range of 300–320 nm, meaning that very little light can be harvested (<0.1% of total solar emission!). Another contribution to Eu^{III} excitation is the $^5L_6 \leftarrow {}^5D_{0,1}$ transition centered at 395 nm, which is usually the strongest f-f absorption associated with this ion, together with several other weaker absorptions in the range of 360–460 nm corresponding to transitions to the ^5G_J ($J=2, 4, 6$) and $^5D_4$ levels.

A very similar work has been conducted with 50-nm Gd_2O_3 nanoparticles doped with Sm^{III} (see Table 7, entry 8; Li et al., 2013). The nanoparticles were prepared from the mixed nitrate $Gd_{0.97}Sm_{0.03}(NO_3)_3 \times nH_2O$ itself obtained by dissolving a mixture of Gd_2O_3 and Sm_2O_3 with mole ratio 97:3 in nitric acid followed by evaporation. A solution of the mixed salt was then treated by Na_2CO_3, and the collected precipitate was dried and calcined at 800 °C for 2 h. The X-ray diffraction pattern of the resulting powder is typical of gadolinium sesquioxide. The excitation spectrum of the nanoparticles displays the Sm(LMCT) band around 235 nm as well as f-f transitions from Gd^{III} and Sm^{III}. With respect to LMCT and Gd^{III}, the problematic is the same as for Gd_2O_3:Eu^{III}. Moreover, the main absorption band of Sm^{III} lies in the range of 400–425 nm (0.6% of sun irradiance), with much weaker ones in the range of 310–330 nm, so that the situation is not very favorable. Emission of Sm^{III} on the other hand occurs in the range of 560–750 nm, which is quite adequate for transferring energy to the dye. Under UV-irradiation ($\lambda < 420$ nm), the yield of the cell increases from 1.5% to 1.9% upon introducing Gd_2O_3:Sm(3 mol%) into the TiO_2 electrode (the doping amount is not given); therefore, an additional 0.4% of sunlight is converted, identical to the figure obtained with Gd_2O_3:Eu(6 mol%) (Li et al., 2011a); since the 300–420 nm spectral range represents 3.4% of the solar irradiance, it means that the overall efficiency of the Sm^{III} and Eu^{III} downconverters is about 12%. Under full 1-sun illumination, an additional 0.75% of sunlight is converted, leading to an improvement of 12.6% in the overall yield of the N-719 based cell, from 6.0% to 6.7%. This is due to increases in both photocurrent, which peaks at 6% doping concentration, and open-circuit voltage, which increases quasi linearly with the doping concentration (Fig. 41). The latter observation could point to ion doping into the TiO_2 electrode being responsible for the additional improvement seen in going from UV to full illumination (+0.75% vs. +0.4%). In fact,

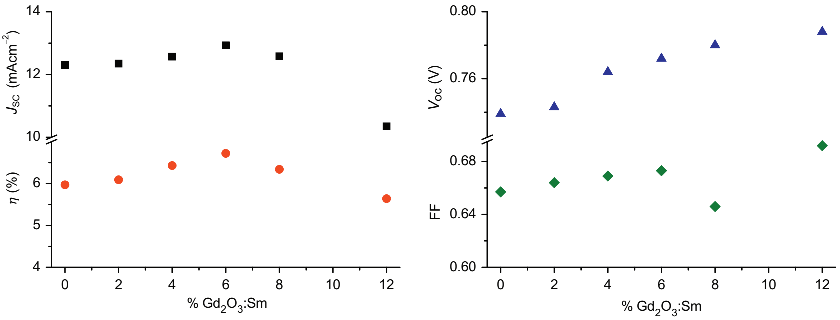

FIGURE 41 (Left) Current density and overall yield of a N-719-based solar cell versus the amount of Gd_2O_3:Sm (3 mol%) introduced into the TiO_2 electrode. (Right) Open-circuit voltage and fill factor. *Drawn after data reported by Li et al. (2013).*

a cell fabricated with TiO_2 doped with 6% pure Gd_2O_3 displays a relative improvement of 6.5% with respect to the reference undoped cell pointing to half of the total improvement effectively due to ion doping into TiO_2 (Li et al., 2013). The better improvement reached with the Eu^{III}-doped oxide (+1 absolute% under full illumination vs. 0.4% under UV-irradiation) is difficult to rationalize but could also stem from the influence of the Ln^{III} ions on the TiO_2 bandgap.

A very different strategy has been adopted by Zhu and coworkers (Zhu et al., 2012) who took advantage of the broad d-f emission of Ce^{III} around 530 nm. In fact, the lanthanide ion is doped into large YAG nanoparticles (200–300 nm) themselves incorporated into a 4-μm thick TiO_2 SL (Table 6, entry 2). An improvement of 13.5% is observed in the cell yield, attributed to energy transfer from Ce^{III} to N719 dye (Scheme 5). Despite the broad emission band which matches well the absorption spectrum of the dye, the increase is no better than those observed with narrow-emitting Eu^{III} ions, probably because the absorption band of Ce^{III}, centered at 450 nm interferes with the dye absorption.

5.5. Metal Complexes as Dyes or Downshifting Materials (Table 7)

In view of the comments made in the preceding section, one may hope that using coordination complexes rather than inorganic materials will improve light collection due to the antenna effect of the organic ligands. Until now, however, very few papers deal with downshifting materials or dyes based on lanthanide complexes with organic ligands and only three papers report full quantitative data (Oh et al., 2011; Wang et al., 2012e; Xiao et al., 2010). Other authors have simply concentrated on doped TiO_2 materials, for instance, by linking [Eu(tta)$_3$L] to the TiO_2 surface via the carboxylic groups

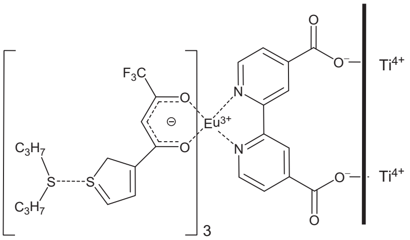

SCHEME 6 Tentative structure of the fixation of [Eu(tta)$_3$] on a TiO$_2$ electrode (Sirimanne and Cheng, 2009).

of L = 2,2′bipyridyl-4,4′dicarboxylic acid (Scheme 6); tta serves as the sensitizer, and the excitation spectrum displays the corresponding broad band between 320 and 420 nm (maximum at 375 nm) which can be further threefold enhanced if the system is immersed into dipropylsulfide during about 1 h (Sirimanne and Cheng, 2009).

With respect to DSSCs, three main types of ligands have been examined, macrocycles such as porphyrins and phthalocyanines, carboxylates, and 8-hydroxyquinolinates (Scheme 7) and the corresponding complexes have been used as either dyes or downshifting materials (Table 7). Interest for porphyrins comes from the fact that donor-acceptor-substituted zinc porphyrins can replace the Ru^{II}-based dyes and lead to DSSCs with efficiencies around 11% (Bessho et al., 2010). Moreover, the absorption spectrum can be extended in the NIR range by using more complex entities such as *N*-fused carbazole/zinc porphyrin/free-base porphyrin (Liu et al., 2011d).

Microwave-assisted synthesis easily provided the Lu^{III} complex [Lu(TBPor)(PcBut)], which was introduced into a photoelectric cell built from SnO$_2$ glass, [Lu(TBPor)(PcBut)] + PDHEP, and TiO$_2$/Al (Table 7, entry 9). Compared to other designs with or without the Lu complex or PDHEP, this cell produced a photocurrent density of 691 μA cm^{-2} under weak illumination of 1.2 mW cm^{-2} (Liu and Hu, 2004). No other parameter is reported. Samarium phthalocyanine double-decker and triple-decker complexes, [Sm(PcOct)(Pc)] and [Sm$_2$(PcOct)$_2$(Nc)], can function as dye in ITO/TiO$_2$-(TiO$_2$ Sm complex)/Al solar cells (entries 10 and 11). The overall yield remains, however, quite modest, 0.36% at most under 50 mW cm^{-2} illumination (Wang et al., 2008).

Much better results have been obtained with the 8-hydroxyquinolinate polymeric complexes [Eu(DB8QB)$_3$]$_n$ and [Eu(B8QDF)$_3$]$_n$ with molecular weight 20,500 and 28,000 Da, respectively (see entries 12 and 13; Xiao et al., 2010). In DMF solutions, these complexes have broad absorption bands with maxima around 310 and 400 nm for the first one and at 400 and 470 nm for the second compound. When adsorbed on TiO$_2$, the long-wavelength absorption band trails up to 700 nm. As could have been expected from the choice of chromophores, no Eu^{III} luminescence is seen upon excitation at

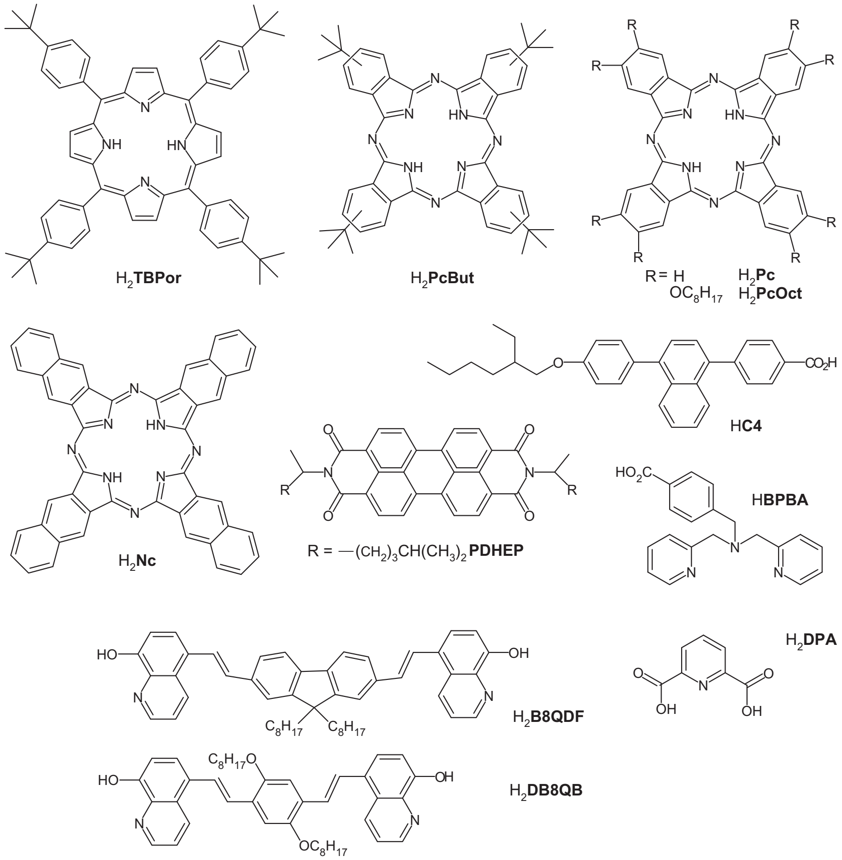

SCHEME 7 Ligands for Ln^{III} complexes used as downshifting materials in DSSCs and n-type photoconducting materials.

400 nm, but rather broad emission bands from the ligand are detected at 500 nm (DB8QB) and 460 nm (B8QDF) in DMF, which shift to 570 and 560 nm, respectively, for solid state samples. The bandgaps calculated from cyclic voltammetry data amount to 2.04 (DB8QB) and 1.90 (B8QDF) eV. Titanium dioxide anodes, preliminary treated with $TiCl_4$, were soaked into solutions of these polymers in DMF and cell parameters determined under AM1.5G illumination. The fluorene-derivatized polymer gave the best results, with an overall conversion efficiency of 3%.

When it comes to downshifting materials, only two attempts have been made so far. The group of H. K. Kim doped a DSSC cell with the $[Eu(C4)_3(BPBA)]$ complex (see Table 7, entries 14 and 15; Oh et al., 2011). The cell design is based on a FTO glass and comprises an 8μm-thick TiO_2 SL and a 8μm-thick layer of TiO_2 nanoparticles which were treated with

$TiCl_4$. Four cells were made by dipping the TiO_2 electrode for 12 h into solutions containing 0.2 mM of the Eu^{III} complex alone, or 0.2 mM BD (Scheme 5) or 0.2 mM BD+20 mM deoxycholic acid (BD-DCA), or 0.2 mM BD and 0.2 mM of the Eu complex (Bd-[Eu(C4)$_3$(BPBA)]). The cell with [Eu(C4)$_3$(BPBA)] alone has a low conversion efficiency of 0.15% only with the maximum of the IPCE spectrum located at 350 nm (absorption of the ligand). The BD cell has a conversion efficiency of 7.6% which increases to 8.5% by the addition of DCA (+12%). When DCA is replaced with the Eu^{III} complex, the efficiency reaches 9.3% (+ 22% with respect to BD and +9% with respect to BD-DCA). Both DCA and the Eu^{III} complex decrease the amount of adsorbed dye by 18% and 31%, respectively, but this has no direct correlation with the cell efficiency since when less Eu^{III} complex is provided (0.1 mM, leading to 25% decrease in dye concentration), the conversion yield is smaller (8.7%) compared to the one with 0.2 mM of [Eu(C4)$_3$(BPBA)]. Looking at the emission spectra, the authors note that naphthalene emission from $C4^-$ at 420 nm perfectly matches one of the absorption bands of the BD and indeed its emission intensity decreases in the presence of BD; on the other hand, emission of Eu^{III} at 620 nm is completely quenched so that both ligand and Eu^{III} probably transfer energy onto the BD, although no peak at 620 nm is seen on the IPCE curve. The contribution of Eu^{III} alone cannot be evaluated because this would require fabricating a cell with a reference complex featuring a nonluminescent lanthanide and this has not been done.

Much better improvements occur when [Ln(HDPA)$_3$] × 4EtOH complexes, Ln = Tb, Dy (Scheme 7) are provided as cosensitizers in a 1:1 ratio with N719 (see Table 7, entries 16 and 17; Wang et al., 2012e). With respect to a pure N719 cell, the current density increases substantially, +47% (Tb) and +66% (Dy), while the cell efficiency increases by 44% and 72%, respectively. The surface photovoltage spectra (SPS) reported in Fig. 42 (left) display the improvements obtained with the lanthanide complexes in the spectral range of 400–600 nm. The improvements are essentially due to much larger current densities as shown on the right part of the same figure. There are several reasons which could be invoked to explain the experimental data. First, the presence of the complex in the photoelectrode avoids aggregation of the N719 dye and therefore improves its efficiency. Second, electrons can be injected from the lanthanide complex into the CB of TiO_2 with a better yield than N719 alone. However, DPA absorbs light in the range of 250–290 nm (Chauvin et al., 2004), and therefore, it is not expected that the latter two processes will play a role here, despite the claim made by the authors. It is possible though that direct excitation of the Ln^{III} complexes occurs via the f-f transitions, but in view of the associated small molar absorption coefficients, the influence of this process should remain marginal. Unfortunately, no photophysical study of the complexes is available, nor have the authors fabricated reference cells with the complexes only and a composite one with a

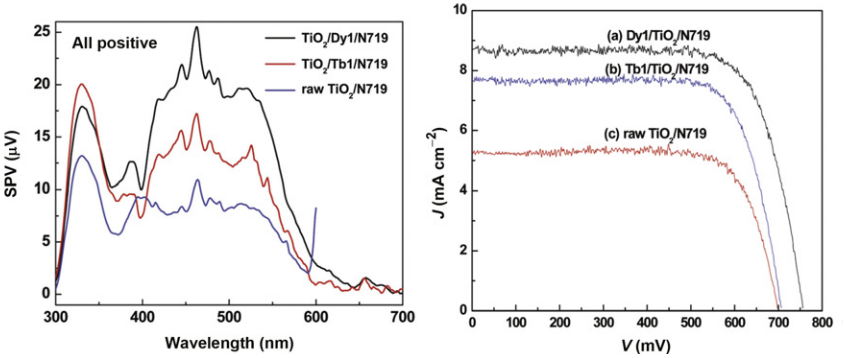

FIGURE 42 (Left) Surface photovoltage spectra (SPS) of the three photoanodes tested, with and without $[Ln(HDPA)_3] \times 4EtOH$ complexes. (Right) Current density versus voltage curves for the three cells tested. *Reproduced with permission from Wang et al. (2012e).*

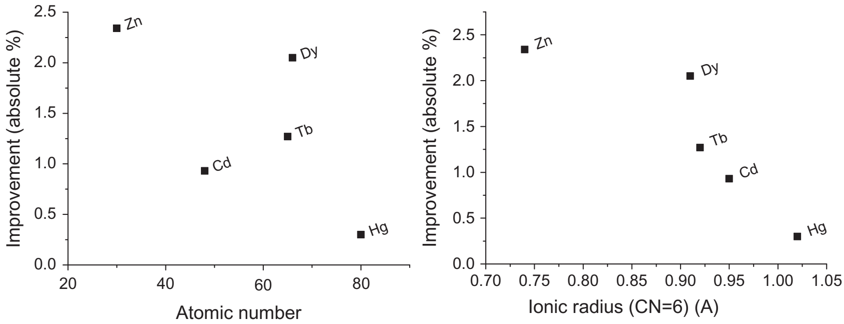

FIGURE 43 Absolute improvements in cell efficiency obtained by doping TiO_2 with M^{II} (M = Zn, Cd, Hg) or Ln^{III} (Ln = Tb, Dy) complexes. (Left): plot versus atomic number (authors' explanation); (right): plot versus ionic radii. *Drawn after data reported in Wang et al. (2010) and Wang et al. (2012e).*

nonluminescent lanthanide complex so that deciphering where the improvement is coming from is impossible. In a previous paper, the authors had tested in a similar way M^{II} (M = Zn, Cd, Hg) complexes with 2,6-bis[1-(2,6-dimethylphenylimino)ethyl]pyridine and reported large improvements, up to +105%, in the cell efficiency (Wang et al., 2010). From these two works, they conclude that the improvement is related to the atomic number of the metal (Wang et al., 2012e). Plots of the improvements, either absolute or relative, versus atomic numbers, however, results in quite scattered graphs so that in our mind the explanation is not valid. Better, although not totally satisfying, correlations are obtained when considering ionic radii for the coordination number 6 (Fig. 43). The main point, however, is that the starting cells in both reports have very low efficiencies, 2.2–2.9%, whereas cells based on N719 dye usually have $\eta = 9\%$. One may legitimately ask if improvements comparable to those reported in these two studies would be obtained by starting with such optimized N719 cells.

5.5.1. *Conclusion*

It is clear that downshifting is delicate, and putting it to work is challenging. Common organic dyes have large absorptivity in the visible and, in part, in the UV. Any downshifting system absorbing in the same wavelength range as organic dyes will lose the competition because even if the molar absorption coefficients were comparable, the yield of downshifting is never 100%. On the other hand, lanthanide complexes are far less photosensitive than organic dyes and this might be the very aspect to concentrate on. Indeed, practical DSSC devices are often coated with a UV filter, cutting all wavelengths smaller than 400 or 420 nm. That is 4.6% or 7.0% of the solar emission is available for DS materials; assuming an overall efficiency around 30% (light collection, energy transfer on the Ln^{III} ion, luminescence quantum yield, IPCE of the dye at the emitted wavelengths), it means that one may hope to add 1.5–2.0 absolute% to the overall cell efficiency, which is by no means negligible.

5.6. Upconverting Materials (Table 8)

From the theoretical studies described in Section 3.4, one may imagine that upconverting materials will also become useful for DSSCs since $E_g(TiO_2) \approx 3$ eV ($\approx$25,000 cm^{-1}) and $n \approx 2.6$ so that one expects conversion efficiency improvement upon building an upconverting layer into the cells. Ln^{III} ions most suitable for upconversion are Er^{III} and Tm^{III}, both of them lending themselves to sensitization by Yb^{III} which absorbs around 980 nm. As a matter of fact, some patents describe the principle, but without precise claim on efficiency improvement (Dai et al., 2011). Other articles establish a proof-of-principle, by using 980-nm laser illumination only; these are not described here and Table 8 contains only quantitative data obtained with real DSSC devices under one-sun illumination.

5.6.1. *Erbium-Based Upconverters*

Three different ways of introducing the upconverting materials into DSSCs are described: (i) addition of a scattering (SL, usually on the top) or upconverting (UC, usually at the bottom) layer, (ii) design of a two-layer anode doped with the dye, and (iii) introduction of the UC materials into the TiO_2 photoelectrode.

The first experimental attempt was made in 2009 by co-doping Er^{III} and Yb^{III} ions (8.5 mol% each) into a TiO_2 SL positioned on the top of the cell (Han et al., 2009). As can be seen from Table 8 (entry 1), a 3% improvement was recorded with respect to the same cell fitted with an undoped TiO_2SL.

In these systems, the conversion efficiency is going from 7.8% (no SL) to 8.7% (undoped SL) and 9.0% (doped SL), that is, the improvement due to upconversion is close to the experimental uncertainties in the measurement of η, while the SL itself brings a 12% improvement.

The upconversion ions can also be introduced into various matrices. For instance, a YAG disk was doped with 3% Yb^{III} and 0.5% Er^{III} and attached at the rear of a solar cell. Only limited quantitative parameters are given (not tabulated), but there is a clear increase in the photocurrent due to emission of Er^{III} in the visible under 500 mW illumination at 980 nm (Liu et al., 2011b).

Another attempt involved the insertion of an intermediate TiO_2 layer doped with LaF_3:Er^{III},Yb^{III} nanoparticles and loaded with the N719 dye (Shan and Demopoulos, 2010; see entry 2, Table 8). The solution used to prepare the lanthanide nanoparticles contained a mole ratio La:Er:Yb equal to 88.6:2.5:8.9. The reference cell fitted with a SL had $\eta = 2.7\%$ only (for undisclosed reasons). The doped layer has been introduced either (i) at the back of the regular TiO_2 layer ($\eta = 1.9\%$) or between the scattering and the dye-loaded layers ($\eta = 2.7\%$) or used alone ($\eta = 0.3\%$). With respect to a bilayer reference cell, the only improvement seen is with the second cell which displays a somewhat larger photocurrent, but the improvement is again close to experimental uncertainties. The fact that energy transfer to the N719 dye occurs is substantiated by the ratio of the upconverted luminescence bands at 540 and 660 nm, which decreases in the presence of the dye. Nevertheless, the conversion efficiency of the second cell is smaller than that of the reference cell. These deceptive results were attributed to the Ln-doped nanocrystals acting as recombination centers so that the authors proposed another material, one of the most studied and best rare-earth upconverting system, β-$NaYF_4$:Yb(18%),Er(2%) (Hehlen et al., 2001) and another cell design. The UC material produces a stronger green emission than red luminescence, which is favorable. A film containing hexagonal nanoplatelets (0.8 × 0.2 μm) of this compound was deposited at the rear of the Pt counter electrode. The open-circuit voltage and FF of cells fitted with different thicknesses of such an UC external layer do not vary much with the thickness and are comparable to those of the cell without the UC layer. On the other hand, the photocurrent and conversion efficiencies display bell-shaped variations (Fig. 44). The thickness giving the largest current and conversion yield is 14 μm for both the reference cell and the cell containing the UC layer. For this thickness, the cell conversion efficiency goes up to 6.9% for the former and to 7.4% for the latter, a 6% increase while the current increases by 8.9% (Table 8, entry 3). However, close comparison between the effect of the nanoplatelets with and without Yb^{III} and Er^{III} dopants clearly evidences that the main performance enhancements are due to the light-reflecting properties of the UC layer. The upconversion contribution is estimated to be only +1 relative% for both J_{SC} and η (Shan et al., 2011).

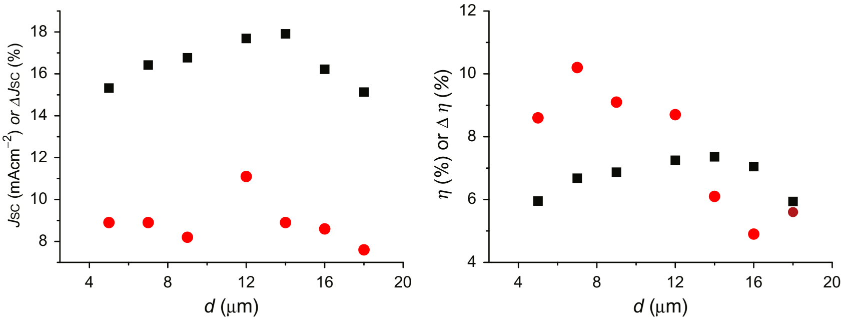

FIGURE 44 Absolute (black squares) and relative (red circles) variations of J_{SC} (left) and η (right) with respect to the thickness of an upconverting layer of β-$NaYF_4$:Yb(18%)/Er(2%) nanoplatelets. *Redrawn from data in Shan et al. (2011).*

An apparently better improvement was achieved by producing a TiO_2 colloid co-doped with Er^{III} and Yb^{III} (unspecified proportions) which was then mixed with nanocrystalline TiO_2 to produce the electrode (Table 8, entry 4). Under irradiation with wavelengths larger than 720 nm (60 mW cm^{-2}), this cell had a 2.6-fold larger conversion yield (0.15%) than a reference cell without upconverting layer ($\eta = 0.04\%$). Under full one-sun illumination, the conversion efficiency of the cells increased from 6.4% to 7.3% (+14%) (Xie et al., 2011). How much is really due to upconversion is not known since in view of the larger size of the doped TiO_2 nanocrystallites (68 nm vs. 19 nm), these will also act as light scattering particles; moreover, the doped Ln^{III} ions may act as p-dopants, see above, La^{III} (Yahav et al., 2011) and Y^{III} (Chandiran et al., 2011). These latter two facts may well create the largest effects responsible for the increase in cell efficiency, since the doped TiO_2 layer displays 0.15% yield only under NIR irradiation. A similar conclusion may be reached when the TiO_2 colloid is doped with YOF:Yb^{III},Er^{III}. The best conversion occurs for a doping concentration of 7 wt% (Table 8, entry 5) for which all four cell parameters sustain a marked increase. If the doping concentration is increased over 7%, only V_{OC} continues to increase, pointing to p-type doping effects (Wang et al., 2012d).

Entries 6–11of Table 8 are concerned with direct doping of the upconverting materials into the photoelectrode. Mixing the β-$NaYF_4$:Yb^{III},Er^{III} upconverter into graphene (entry 6) before doping it into colloidal TiO_2 does not bring much improvement, the conversion efficiency of the low performing cell (initial $\eta = 2.7\%$) being improved by only 0.1 absolute% (Li et al., 2012a). A better performance is achieved if the UCNPs are coated with a TiO_2 shell and the resulting core–shell nanoparticles used as photoelectrode after annealing at 480°C. The initial conversion yield of 3.5% with TiO_2 alone is increased to 4.3%, mainly due to increases in the photocurrent (+8 rel.%) and the FF (+18 rel%), while the open-circuit voltage slightly decreases

(−2 rel.%). A control experiments with an IR cut-off filter ($\lambda > 1100$ nm) leads to $\eta = 3.7\%$ so that one may infer than upconversion adds +0.6 absolute% to the yield. Another control experiment in which TiO_2 is mixed with the UCNPs results in a smaller yield, 2.2% (Zhang et al., 2013).

Experiments with other dyes, namely, Z907 (Yuan et al., 2012) and the BD associated with a ZnO photoelectrode (Khan et al., 2011) essentially parallel to the earlier data reported with N719, namely that the upconverter improves the absolute conversion yield by about 0.1–0.2 absolute% only (entries 8 and 9).

To date, the best results with an upconversion-modified electrode have been obtained by doping microcrystalline YF_3:Yb(20 mol%), Er(2 mol%) (Wu et al., 2012b), or Y_2O_3:Er(10 mol%) NRs (Wang et al., 2012c) into the TiO_2 electrode. In the first case, the optimum doping concentration was found to be 7 wt% (Fig. 45) and a 35% increase in cell efficiency was measured, from 5.8% without the upconversion layer to 7.9%. The improvement can be split into 17% increase in photocurrent, 10% rise in voltage, and 7% improvement in the FF (entry 10). As noted above, these improvements do not solely come from the upconverted light. Indeed, doping trivalent ions into the n-type semiconductor leads to a negative shift of the flat-band voltage (the voltage inducing zero charge in the semiconductor), pointing to a change in the Fermi level. At a doping concentration of 7 wt%, the flat-band voltage amounts to −0.65 V as compared to −0.44 V for pure TiO_2. The saturated photocurrent density is also larger in the doped anodes, 13.6 μA cm^{-2} for 7 wt% doping versus 10.1 μA cm^{-2} for pure Anatase. A clue on the real contribution of upconversion is given by the cell characteristics under

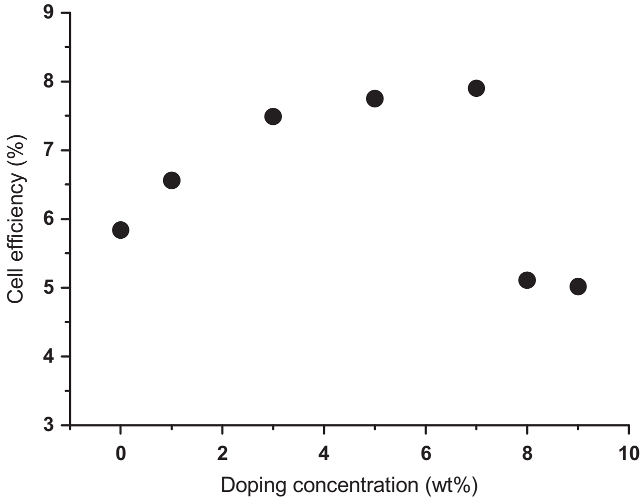

FIGURE 45 Influence of the doping concentration of $YF_{0.78}Yb_{0.20}Er_{0.02}$ in the photoanode of a N719-based DSSC. *Drawn from data reported in Wu et al. (2012b).*

illumination with $\lambda > 900$ nm (33 mW cm^{-2}): the undoped cell displays $\eta = 0.055\%$ only, compared to 0.255% for the 7 wt% doped photoanode, that is, upconversion really adds 0.2 absolute% to the conversion efficiency, and therefore contributes only 1/10th to the overall improvement in light-to-electricity conversion yield, the remaining 1.9% being attributable to +3-ion doping of TiO_2 (31 relative%, consistent with data in Table 6).

In the second study (entry 11), the efficiency of the Anatase photoelectrode under NIR illumination ($\lambda > 900$ nm) increases from a mere 0.06% to 0.17% upon doping with Y_2O_3:Er(10 mol%) NRs. The largest contribution stems from the increase in photocurrent density, from 0.22 to 0.44 mA cm^{-2} but V_{OC} increases also substantially, from 0.49 to 0.62 V. This is in line with data reported by Xie et al. (2011) for the two-layer anode (entry 4). However, under full 1-sun illumination, a spectacular increase in conversion efficiency is recorded: +1.2 absolute%. Again, since upconversion approximately adds 0.1% only, most of the improvement has to be credited to the p-dopant effect (+1.1 absolute% or 19 relative%, consistent with previous reports).

5.6.2. Thulium-Based Upconverters

Upconversion of thulium by energy transfer from Yb^{III} generates blue (476 nm) and red (653 nm) emission, both lying in favorable spectral range for absorption by organic dyes. The effect of Tm^{III} upconversion was tested with Lu_2O_3:Tm(0.4 mol%), Yb(2 mol%) dispersed at 4% into a TiO_2 colloid (entry 12) which in turn was deposited as a 4μm-thick layer on a 12 μm TiO_2 photoanode (Li et al., 2011b). With respect to a reference cell (16-μm thick photoanode), a noticeable improvement in η is seen when NIR illumination is used (>720 nm), from 0.12% to 0.19%. Under full sunlight illumination, the conversion yield increases from 6.0% to 6.6%. Smaller increase was expected from the data obtained under NIR irradiation. A clue to what may happen is given by the excitation spectrum of the 473-nm Tm^{III} emission which points to downshifting taking place as well since this spectrum displays a band at 320 nm with, as a consequence, excitation of the $^1G_4$ level and subsequent emission of blue light. In addition, the authors also remark that the Ln^{III} ions act as p-dopants so that the contribution of the UC process to the overall improvement cannot be deduced from the data presented in this paper but is probably rather small.

An interestingly simple procedure is used by Xie et al. (2012b) who prepare a TiO_2:Yb^{III},Tm^{III} powder (Yb^{III}:Tm^{III} ratio 10:1) and disperse it into a TiO_2 colloid; the electrode consists of a 10-μm layer of undoped titania and a 5-μm layer of doped titania onto which the N719 dye is adsorbed. A study of the cell performances versus doping concentration shows that J_{SC} increases up to 2.50 wt% and then decreases; this is explained by the formation of crystal defects at higher Ln^{III} concentrations. The best conversion yield, 7.1%, is obtained for 3.3 wt% doping, up 10 relative% from the cell without Ln^{III} ions (entry 13). In the absence of experiment with NIR light only, it is again difficult to decide which part of this improvement can be traced back to upconversion and which part arises from the p-type doping effect.

5.6.3. Conclusions

Considering the limited set of available data and accounting for major side effects such as p-type doping of TiO_2, it seems that in its present state of optimization, upconversion is not yet of much help in boosting the performance of DSSCs under 1-sun illumination. At most a few relative percent improvement is obtained with respect to reference cells without upconverting materials, but the reported results are often within experimental errors. This is understandable because the upconversion yield is usually small and depends on excitation power. For the archetype $NaYF_4$:Yb(18%),Er(2%) crystalline material, quantum efficiency is about 2.5×10^{-4} per W/cm^2 for the green emission (Hehlen et al., 2001), which translates to about 3×10^{-4} per W/cm^2 for both green and red emission or 3% for 100 mW/cm^2 irradiation at 980 nm. If one further considers that only about 6% of sunlight is available in the absorption range of Yb^{III} (950–1050 nm) and that molar absorption coefficients are small ($<10\ M^{-1}\ cm^{-1}$), the odds are difficult to overcome. The field is, however, in its infancy so that one may hope that more optimized systems will soon be at hand (see Sections 3.4.4–3.4.6). Moreover, concentrating sunlight to generate more surfacial power is an option since the upconversion quantum yield is proportional to the excitation power. Alternatively, photon upconversion upon irradiation with low-power noncoherent light sources is progressing, in particular with reference to organic compounds. Sensitized upconversion can indeed be obtained by annihilation of metastable triplet states of organic oligomers and yields up to 26% have been reported; but until now, excitation wavelengths shorter than 650 nm have to be used (Monguzzi et al., 2012), which is not of much help in DSSCs, and these organic materials are sensitive to oxygen quenching in addition to being photosensitive (Cates et al., 2012). Finally, metal-enhanced upconversion luminescence (plasmonics) might be as promising for solar energy conversion as it seems to be in bioanalyses (Fischer et al., 2012b; Goldschmidt et al., 2012; Zhong et al., 2011). For instance, incorporating core–shell Ag@TiO_2 NPs into a conventional TiO_2 photoanodes increases the yield of a N3-based DSSC from 7.8% to 9.0%, that is a relative 15% increase (Qi et al., 2011). Photonic crystals will also have to be considered (Section 3.4.6).

5.7. Upconverted DSSCs for Powering Nanobiological Devices

A futuristic vision in nanomedicine is to provide nanorobots for *in vivo* advanced diagnosis, medical therapies, and minimally invasive surgery. These nanorobots integrate embedded nanoelectronics and circuitry in order to sense their environment, both mechanically and chemically, for instance, for determining local temperature, pH, or concentrations of analytes in blood (Cavalcanti et al., 2008). As any machine, they of course require an adequate source of electrical energy. Solutions have been proposed for powering these nanomachines in a wireless way: nanogenerators driven by mechanical sources (ultrasonic waves, random mechanical actions, or muscle movement) or chemical nanogenerators converting chemical energy into electricity, for instance, in biofuel cells.

Both have their drawbacks so that an alternative way is being explored, taking advantage of the large transparency of biological tissues to NIR light: production of electricity from the conversion of NIR light by photovoltaic cells. To our knowledge, initial attempts have been made by the group of Zhigang Chen from Donghua University in Shanghai. In the first paper (Chen et al., 2009c), an unoptimized device is described which is made of a 980-nm semiconductor laser, a conventional DSSC consisting of a 8-μm-thick TiO_2 photoanode doped with the N3 dye (Scheme 5) and deposited on a transparent conductive oxide (TCO) glass, a 4-μm thick layer of $Na(Y_{1.5}Na_{0.5})F_6$: Yb(20%),Er(2%) upconverting NRs (0.2 × 1.0 μm), and a platinum counter-electrode deposited on TCO glass. When illuminated with the NIR laser, the NRs produce an intense green luminescence and a weaker red one; if collected through a TiO_2 layer deprived of N3 dye, the emission intensity is about 20-fold larger than when the titanium dioxide is coated with the organic dye, which demonstrates absorption of the upconverted light by the latter. The porosity of the NR layer allows for easy diffusion of the liquid electrolyte so that the resulting IPCE is about 80% in the range of 480–560 nm. Under 980-nm illumination with 1 W power, the 10-mm^2 device displays an overall laser-to-electricity conversion yield $\eta_{l-e} = 0.047\%$ ($V_{OC} = 600$ mV, $I_{SC} = 1.5$ mA, FF = 0.52) corresponding to a maximum output power of 470 μW. Moreover, the yield of upconversion has been estimated to be 0.45%, as compared to about 5% for the bulk material under 200 W cm^{-2} illumination, which leaves space for improvement. The device still worked when covered with 1–6 layers of 1-mm thick pig intestinal tissue, although the output power was eventually reduced to 20 μW. Definitively small, this power is, however, sufficient to energize devices fabricated with nanowires or nanotubes, for which the required power is 10 nW per nano item so that the six-layer covered photovoltaic cell could operate up to 2000 nanodevices under 1-W illumination. In biological and clinical studies, the accepted power limit for skin exposure to 980-nm light is set to 726 mW cm^{-2}. Operating the PV device at this power still results in an output power of 17 nW, enough to energize at least one nanodevice.

The upconversion properties of this initial photovoltaic device have now been considerably improved (Zhang et al., 2012b). First, hydrophilic nanophosphors $NaYF_4$(Yb20%),Er(2%) were prepared *via* one-step hydrothermal synthesis, and second, biological compatibility has been enhanced by replacing the

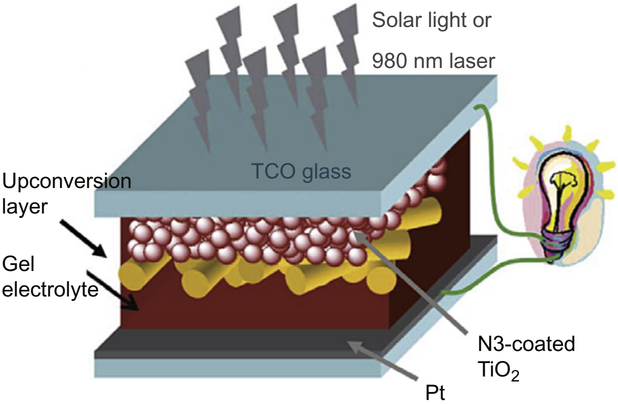

FIGURE 46 Schematic representation of the 980-nm driven upconverter photovoltaic device proposed for energizing nanorobots in clinical and biological applications. *Adapted with permission after Zhang et al. (2012b), © 2012 The Royal Society of Chemistry.*

liquid I_3^-/I_2 electrolyte with a stable succinonitrile-based gel electrolyte (Chen et al., 2007) made of 3-methoxypropionitrile containing 0.6 M 1-methyl-3-propylimidazolium iodide, 0.1 M iodide, and 0.5 M *N*-methylbenzimidazole (Fig. 46). Comparing the upconversion spectra obtained with and without N3 dye, the authors conclude that 93% of the upconverted light is absorbed by the organic dye. Under irradiation with a 980-nm laser delivering 1-W power, the yield of laser-to-electrical conversion is 0.09% almost double that of the initial PV device. Under 1-sun illumination (AM1.5G), the 0.16-cm^2 cell presents the following parameters: $V_{OC} = 0.604$ V, $I_{SC} = 1.61$ mA, FF = 0.54, $\eta = 3.3\%$. Without upconverting layer, the same cell has $\eta = 5.0\%$ (Chen et al., 2007), exemplifying the detrimental effect of this layer. With skin-safe 720 mW cm^{-2} illumination, the new device exhibits a maximum output power of 44.5 μW, corresponding to a $\eta_{l-e} = 0.039\%$; the output power reduces to 22.2 μW ($\eta_{l-e} = 0.019\%$) when the PV cell is covered with one 1-mm layer of chicken skin as model for biological tissue. This output power is large enough for the PV device to be effectively considered as power source for *in vivo* nanorobots (Zhang et al., 2012b).

5.8. Cerium Oxide as Photoanode

Owing to its nonstoichiometric structure and redox properties, Ce^{IV} oxide has many applications ranging from polishing powders to high-temperature automotive (Kilbourn, 1986) or solar fuel (Chueh et al., 2010) catalysts. Moreover, with a bandgap of 3.2 eV (387 nm), it is a UV-blocking material in cosmetics, particularly when coated with boron nitride as whitening agent and for reducing catalytic activity (Masui et al., 2000). On the other hand, the bulk material and large particles of CeO_2 do not have exploitable photovoltaic response, probably because the bandgap corresponds to an $O_{2p} \rightarrow Ce_{4f}$ ligand-to-metal transition. In 1997, Turkovic and Orel, who had been developing rechargeable, photosensitive galvanic cells proposed to replace TiO_2 with mesoporous CeO_2 or CeO_2/SnO_2 photoanode films. With the trinuclear complex initially used by Grätzel and O'Regan, $[Ru(bpy)_2(\mu\text{-}(CN)Ru(CN)(HL)_2]$ ($H_2L = 2,2'$-bipyridine-4,4'-dicarboxylic acid) as dye, the best results were obtained with $CeO_2/SnO_2(17\%)$: $V_{OC} = 100$ mV, $J_{SC} = 0.85$ mA cm^{-2} and maximal power of 85 nW cm^{-2} under sun illumination (91.7 mW cm^{-2}) and with a 0.6-μm layer thickness. Without dye, but with a layer thickness of only 0.3 μm, the cell power reached 10 nW cm^{-2} (Turkovic and Orel, 1997).

Yet, mesoporous CeO_2 particles with large pore volume are not very stable and their structure collapses upon steaming at mild temperature. *A priori*, these properties do not make cerium oxide a very good candidate as photovoltaic material. However, Corma et al. (2004) succeeded in fabricating hierarchically nanostructured CeO_2 nanoparticles by self-assembly of 5-nm nanoparticles, which are thermally stable and present a high surface area. Their reflectance spectrum extends more into the visible than the one of TiO_2, with a cutoff wavelength of 430 nm compared to 350 nm (Fig. 47). This corresponds to a bandgap of 3.0 eV which allows harvesting a larger portion of the solar spectrum. The unexpected reduction of the bandgap upon going from the bulk material to the nanostructured one is attributed to the presence of Ce^{III}/Ce^{IV} ions on the surface leading to oxygen vacancies the influence of which on the bandgap overcome the expected quantum size effect. In addition, charge recombination is about five times slower in nanostructured CeO_2 compared to standard P-25 TiO_2 as shown by the temporal profile of the voltage recorded after 355-nm excitation. Finally, the material can be doped (up to 30 mol%) with La_2O_3 or ZrO_2 without perturbing its structure, which results in modulation of its absorption spectrum with possible extension up to 600 nm.

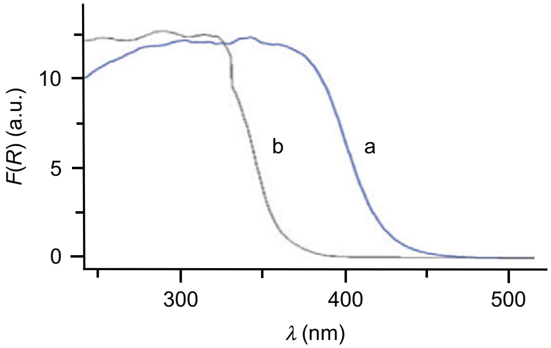

FIGURE 47 Diffuse reflectance spectra plotted as the Kubelka–Munk function F of the reflectance R of (a) CeO_2 and (b) TiO_2 nanoparticles. *Redrawn with permission from Corma et al. (2004), © 2004 Nature Publishing Group.*

A 1-cm^2 solar cell was prepared by depositing a suspension of La^{III}-doped CeO$_2$ onto a transparent ITO electrode followed by calcination at 300 °C and addition of LiI/I$_2$ and adding a platinized aluminum counter electrode. At 40 mW cm^{-2} irradiance (AM 1.5 spectrum), its efficiency was 1.4% (V_{OC} = 0.90 V, I_{SC} = 1.5 mA, FF = 0.41) but dropped to 0.9% under 1 sun illumination (V_{OC} = 0.82 V, I_{SC} = 3.4 mA, FF = 0.32). A patent was filed covering this finding and other photovoltaic applications of cerium oxide (Chane-Ching et al., 2005), but to our knowledge, no subsequent work has been conducted.

5.9. Cells with Light-Storage Capability for Night Operation

A cell design has been proposed for extending the DSSC operation during night. The cell is fitted with transparent glass layers containing a long-persistence phosphor. The latter absorbs UV-blue light and emits visible light in the dark, allowing solar cell operation in the absence of sun illumination (Guo, 2007, 2008). Commercial long-persistence phosphors are used in watch dials, emergency lighting devices, image storage, or detection of high-energy radiation. The best known, and commercially available, such material is SrAl$_2$O$_4$:Eu^{II},Dy^{III} discovered in the mid-1990s, but since then other materials displaying the same properties have been found, including aluminates, silicates, and stannates doped with various Ln^{III} ions, or simple oxysulfides, such as Y$_2$O$_2$S:Ln^{III},Mg^{II},Ti^{IV}, with Ln = Sm or Eu (Lei et al., 2010). The present patent covers the use of oxides, sulfides, and oxysulfides as afterglow materials in solar-powered street lamps. The most common material, SrAl$_2$O$_4$:Eu^{II},Dy^{III}, however, has less than 10% of the Eu^{III} ions associated with traps (Korthout et al., 2011), which may hamper its use as energy-storage material for solar cells.

6. PERSPECTIVES

If one counts the number of papers published since 2000 and dealing with improving the yield of solar cells with rare-earth materials, the total is over 200, a number which can certainly be doubled or even tripled if publications describing potential or prospective systems are taken into account. This prolific and inventive research effort has produced a wealth of spectroscopic data on lanthanide inorganic materials prone to either downconversion/downshifting or upconversion. Lanthanide complexes with organic ligands have attracted less attention despite that they appear to be highly useful in the design of efficient LSCs and as downshifting materials. What is real impact of all these investigations on photovoltaics? In order to get a synthetic picture, results obtained (or, better, claimed) with solar cells are summarized in Table 9, in terms of improvements made to these systems, expressed as the absolute percentage added to the conversion yield. We also assess the likely

TABLE 9 Summary of Claimed and Expected Future Improvements in Conversion Yields of Solar Cells (absolute%) Obtained by Providing Rare-Earth Containing Materials and Complexes in the Cell Architecture; Data Are for 1-Sun Illumination (AM1.5G) and For Cells Without LSC[a]

Process	Wavelength range to tap (nm)	Available portion of solar emission (%)	Most appropriate R ion(s)	Claimed/ demonstrated (%)	Feasible[b] (%)
Silicon cells					
DC/DS	300–500	18.6	Eu^{III} (Sm^{III})	1–2	3–5%
UC (m-Si)	900–1450	21	Yb^{III},Er^{III} Yb^{III}, Tm^{III}	0.3–0.4	1–2
UC (c-Si)	1450–1800	6.8	Er^{III}	0.6	1–1.5
Dye-sensitized cells					
DC/DS	300–400	4.6	Eu^{III} (Sm^{III})	1–1.5	1.5–2
UC[c]	1200–1800	12.4	Er^{III}; Yb^{III},Er^{III}; Yb^{III},Tm^{III}	0.2–0.4	1–2
SL	n.r	n.r.	Ce^{IV}	1–1.3	1.5
ET	n.r.	n.r.	Y^{III}, Ce^{III}, Yb^{III} (Ln^{III})[d]	1.5	1.5

[a] *Key: DC, downconversion; DS, downshifting; UC, upconversion; SL, scattering layer; ET, electrode treatment (p-doping of TiO_2); n.r., not relevant.*

[b] *Authors' estimate.*

[c] *Data reported in Table 8 reflect improvements due to both p-dopant effect and UC; here, only UC is taken into account.*

[d] *Several other ions depending on experimental conditions, see Section 5.3.*

enhancements that could be expected from a clever optimization of these materials taking into account both the specific properties of the rare-earth materials and the effective features and needs of the photovoltaic devices. These considerations have not always been fully integrated into the various studies published. Moreover, as mentioned already several times, parameters for solar cells including wavelength-converting layers are often not compared to adequate reference cells which makes it difficult to gain an unbiased opinion of the real advantage(s) introduced by these materials.

Table 9 does not include data for LSCs because comparisons are more difficult to conduct. Indeed, there are very few investigations which determine all necessary photovoltaic parameters when the LSC is linked to a solar cell so that a reliable image involving statistics on several systems cannot be established. In fact, the spectroscopic challenge is similar to the one encountered when adding wavelength-converting layers to solar cells. In particular, the conversion of UV light into visible light or UV–vis into NIR has to be tailored with respect to the type of solar cell, c-Si, m-Si, a-Si, or DSSC. In the case of an m-Si cell with initial 15% conversion yield, it is claimed that +2.6 absolute% could be added with a 1-layer LSC based on a Eu^{III} triazinyl complex (Katsagounos et al., 2011). Assuming conservatively that an LSC with 30–40% yield can be designed to harvest light in the 300–450 nm range (10.8% of solar irradiance) for m-Si and 300–500 nm range (18.6% of solar irradiance) for c-Si, one may hope to add 3–7 absolute% to these types of cells. For LSCs coupled to DSSCs, the expected maximum improvement would be smaller (1.5–2.5%) due to competition with dye absorption in the range of 300–400 nm.

In the case of single-crystal silicon cells, claimed (but not always unambiguously demonstrated) improvements are in the range of 1–2% for downshifting, mainly arising from Eu^{III} materials, and 0.3–0.6% for upconversion. These figures can likely be doubled for downshifting, particularly if other ways are exploited for harvesting UV-blue light, for instance, by resorting to 4f-5d transitions (Ce^{III}, Eu^{II}), which in our mind have been too little explored. In this case, Ce^{III}-to-Tb^{III} energy transfer could be taken advantage of in the case of m-Si and a-Si cells. Moreover, new nanophosphors such as spherical EuSe have ideal excitation (300–400 nm, max. at 350 nm; emission between 375 and 475 nm) could be helpful in the case of c-Si cells, possibly DSSCs (Wang et al., 2012a). Projections for upconversion are more difficult to formulate because despite the numerous efforts put forward, relatively few precise data sets are at hand. But taking into account both improved designs and syntheses of UNCPs and contributions of plasmonics and/or photonic materials, as well as concentration of sunlight (van Sark et al., 2013), one may hope that the demonstrated improvements will be tripled in a near future.

Finally, although heavily studied, downconversion materials have not yet been successfully introduced into solar cells despite their potential addition of up to 7 absolute % to the conversion yield (Abrams et al., 2011).

For DSSCs, it seems that downshifting has already met its limits with the addition of up to 1.5 absolute%, corresponding to an overall 30% efficiency of the process. It will be very difficult to surpass this achievement, or, even, to match it. Upconversion can certainly be improved along ways similar to those proposed for silicon cells, but owing to the different design of the cells we anticipate that the gain will be lower. Very important points for DSSCs are the large improvements (+1.5 absolute%) brought by Ce^{IV} containing SLs (helped by some downshifting) and by p-doping of the TiO_2 photoelectrode with various R^{III} ions. Interestingly, to our knowledge, no one has attempted combining these two effects which are simple (and cheap) to implement. On the other hand, it does not seem that using lanthanide complexes as substitute for ruthenium dyes or porphyrins has promising perspectives.

This comment brings us to an essential point: can the described beneficial effects be combined? The answer is not straightforward, owing to the peculiar requirements specific to each wavelength-converting/scattering/doping process. But some researchers are now tailoring materials with both downshifting and upconversion ability in order to combine both functions into a single nanophosphor or material (Richards et al., 2012). One such attempt is the fabrication of fluorinated silica glasses of composition $90SiO_2$–$5SnO_2$–$5LaF_3$ doped with 0.1% Eu^{III}, 0.1% Er^{III}, and 0.3% Yb^{III} in which the SnO_2 nanocrystals strongly absorb UV light and transfer energy onto Eu^{III} ions, leading to red emission while efficient IR-to-visible upconversion is mediated by the Yb^{III}/Er^{III} ions (Yanes et al., 2011). Another design implies the coating of Gd_2O_3:Yb(2%),Er(0.3%) nanoparticles with $[Eu(dbm)_3Phen]$ which results in a nanophosphor displaying upconverted green and red emission upon excitation at 976 nm and downshifted red emission when excited at 355 nm (into ligand levels) or 521 nm (into the $Er^{III2}H_{11/2}$ level). Although planned for luminescent security inks, the material could as well be applied to enhancing the yield of solar cells (Singh et al., 2011). If these and similar materials prove to be successful and if their performances can be optimized to meet the goals set in Table 9, once coupled with photovoltaic devices they might therefore be able to boost the conversion yields of silicon solar cells by as much as 5–8 absolute% and of dye-sensitized cells by *5.5-6.5 absolute%*. Given the difficulties described in the preceding sections though, it seems more reasonable to set these figures to 4–5% for Si cells and 3–5% for DSSCs. Another important point here is that the added absolute% in conversion yield will decrease if the semiconductor bandgap is better adjusted to the solar emission spectrum because the primary conversion process will efficiently compete with the wavelength-converting materials.

As far as other cell types are concerned (e.g., GaAs, mutijunction cells), too few data are at hand for any reliable estimate to be made although mutijunction cells will certainly continue to benefit from lattice-matching rare-earth inorganic compounds. Organic photovoltaic (OPV) cells have not been treated in a separate section in this review because there are presently very few papers describing the use of rare-earth containing materials for improving their performances: Ln^{III} complexes (Ln = Pr, Sm, Eu, Gd, Tb) have been tested as electron acceptors (Si et al., 2007), upconversion materials such as $NaYF_4$:Yb,Er (Wu et al., 2012c) and MoO_3:Yb,Er (Wang et al., 2012b) increase the photocurrent upon illumination at 975–980 nm, and Yb/Al/Se (Kaulachs et al., 2012) or Sm/Al (Yang et al., 2013) composite electrodes help increasing both the photocurrent and the power conversion efficiency. Given the relatively lower conversion efficiency of OPV, on may expect that lanthanide-based wavelength converting materials would be of help in improving their overall characteristics.

A final remark is aimed at scientists or engineers developing practical devices. Getting a high conversion yield is certainly satisfying and most desirable, but it is not the main point. Cost has to be considered if photovoltaics is to contribute substantially to electricity production in the future. More precisely, the cost per watt power is the ultimate parameter to optimize in order to reach "grid parity," that is the price of electricity produced by other means (nuclear energy, fossil fuels, wind, hydroelectricity). Presently, the matching cost is set to about 1 US$/W. This figure is now close to be reached for solar panels with 1-m^2 area (see, for instance, the MK series panels from GreenSun, http://www.greensun.biz/Products/). This is certainly encouraging for the development of wavelength converting materials and layers, provided they do not increase too much the cost, either because of the high price of the rare-earth containing materials or by too much added sophistication in the processing of the panels. An additional concern would be the rare-earth shortage which is much documented presently (Gschneidner, 2011). However, this shortage is artificial in that only few of the available rare-earth resources are presently exploited and the situation on the international rare-earth market may evolve quickly with the rapidly changing economic situation. As a conclusion, rare-earth wavelength converting materials for photovoltaics, as well as for photocatalysis (Cates et al., 2012; Walter et al., 2010) have a foreseeable bright future.

ACRONYMS AND ABBREVIATIONS

Ac	acetate
AM	air mass
a-Si	amorphous silicon
BD	black dye
bpy	2,2′-bipyridine
CB	conduction band
CET	cooperative energy transfer
c-Si	crystalline silicon
CT	charge transfer
Da	dalton
dbm	dibenzoylmethanate (1,3-diphenyl-1,3-propanedionate)
DC	downconversion (or quantum cutting)
DCA	deoxycholic acid
DPA	dipicolinate (2,6-pyridine-dicarboxylate)
dpbt	2-(*N*,*N*-diethylanilin-4-yl)-4,6-bis(3,5-dimethylpyrazol-1-yl)-1,3,5-triazine
dpepo	oxybis(2,1-phenylene)bis(diphenylphosphine oxide)
DS	downshifting
DSSC	dye-sensitized solar cell
EQE	external quantum efficiency (ratio of charges collected by the number of incident photons)
ESA	excited state absorption

ETU	energy-transfer upconversion
FF	fill factor
FTO	fluorinated tin oxide
G	global sun
G	area ratio of LSC to solar cell
GSA	ground state absorption
hfa	hexafluoroacetylacetonate (1,1,1,5,5,5-hexafluoro-2,4-pentanedionate)
IL	intermediate level
IOE	integrated optical efficiency
IPCE	incident photo-to-current conversion efficiency
IQE	internal quantum efficiency (= EQE corrected for reflection and absorption losses)
I_{SC}	short-circuit photocurrent (A)
ITO	indium tin oxide (90% In_2O_3, 10% SnO_2)
J_{SC}	short-circuit photocurrent density (A m^{-2})
LMCT	ligand-to-metal charge transfer
Ln	lanthanide (or lanthanoid) element
LSC	luminescent solar concentrator
lx	lux (unit of luminous flux per unit area: 1 lx = 1 lumen/m^2)
MEG	multiexciton generation
m-Si	multicrystalline silicon (or polycrystalline silicon or polysilicon)
NIR	near infrared
NP	nanoparticle
NR	nanorods
OPV	organic photovoltaic
ORMOSIL	organically modified silicate
PDHEP	*N*,*N*′-bis(1,5-dimethylhexyl)-3,4:9,10-perylenebis(dicarboxiimide)
PDMS	polydimethylsiloxane
phen	*o*-phenanthroline
PL	photoluminescence
PMMA	polymethylmethacrylate (poly(methyl)-2-methylpropenoate)
p-Si	polycrystalline silicon (see also m-Si)
PV	photovoltaic
PVA	polyvinyl alcohol
PVB	polyvinyl butyral (poly[(2-propyl-1,3-dioxane-4,6-diyl) methylene])
PVC	polyvinyl chloride
QD	quantum dot
QY	quantum yield
R	rare-earth element (Sc, Y, Ln)

SL	scattering layer
SPS	surface photovoltage spectra
STC	standard test conditions (25 °C, AM1.5G spectrum with 1000 W m^2 irradiance)
TCO	transparent conductive oxide
tfc	3-(trifluoromethylhydroxymethylene)-d-camphorate
TIR	total internal reflectance
TOPO	trioctylphosphine oxide
TPPO	triphenylphosphine oxide
tta	thenoyltrifluoroacetonate (4,4,4-trifluoro-1-(2-thienyl)-1,3-butanedionate)
UC	upconversion
UCNP	upconverting nanoparticle (or nanophosphor)
UV	ultraviolet
VB	valence band
V_{OC}	open-circuit voltage (V)
wt	weight
YAG	yttrium aluminum garnet ($Y_3Al_5O_{12}$)
ZBLAN	very stable glass containing $\underline{Z}$rF$_4$, $\underline{B}$aF$_2$, $\underline{L}$aF$_3$, $\underline{A}$lF$_3$, and $\underline{N}$aF

REFERENCES

Aarts, L., van der Ende, B.M., Meijerink, A., 2009. J. Appl. Phys. 106, Art. Nr. 023522.

Abdel-Mottaleb, M.S.A., 2009. Int. J. Nanomanufact. 4, 175.

Abrams, Z.R., Niv, A., Zhang, X., 2011. J. Appl. Phys. 109, Art. Nr. 114905.

Ahmad, S., Bessho, T., Kessler, F., Baranoff, E., Frey, J., Yi, C., Grätzel, M., Nazeeruddin, M.K., 2012. Phys. Chem. Chem. Phys. 14, 10631.

Ahrens, B., Loper, P., Goldschmidt, J.C., Glunz, S., Henke, B., Miclea, P.T., Schweizer, S., 2008. Phys. Stat. Sol. A 205, 2822.

Andrade, L., Ribeiro, H.A., Mendes, A., 2011. Encyclopedia of Inorganic and Bioinorganic Chemistry. John Wiley & Sons Ltd., Hoboken, http://dx.doi.org/10.1002/9781119951438.eibc0469.

Atwater, H.A., Polman, A., 2010. Nat. Mater. 9, 205.

Auzel, F., 2004. Chem. Rev. 104, 139.

Badescu, V., Badescu, A.M., 2009. Renew. En. 34, 1538.

Basudeb, K., Tirtha, S., ShivPrakash, S., Muthun, N., 2010. Trans. Ind. Ceram. Soc. 69, 171.

Bessho, T., Zakeeruddin, S.M., Yeh, C.Y., Diau, E.W.G., Grätzel, M., 2010. Angew. Chem. Int. Ed. 49, 6646.

Bram, O., Cannizzo, A., Chergui, M., 2012. Phys. Chem. Chem. Phys. 14, 7934.

Brewer, J.R., Gernhart, Z., Liu, H.Y., Cheung, C.L., 2010. Chem. Vap. Dep. 16, 216.

Brewer, J.R., Jacobberger, R.M., Diercks, D.R., Cheung, C.L., 2011. Chem. Mater. 23, 2606.

Bünzli, J.-C.G., 2013. In: de Bettencourt-Dias, A. (Ed.), Luminescence in Lanthanide Coordination Compounds and Nanomaterials. Wiley-Blackwell, Oxford, (Chapter 6) in press.

Bünzli, J.-C.G., Eliseeva, S.V., 2010. J. Rare Earths 28, 824.

Bünzli, J.-C.G., Eliseeva, S.V., 2013. In: Yam, V.W.-W. (Ed.), Comprehensive Inorganic Chemistry II, vol. 8. Elsevier B.V, Amsterdam, (Chapter 8.03) in press.

Cang, L., Wan, Z., Yan, T., Ding, W., Liu, W., Liu, Z., Chen, L. 2012. Solar cell with high photoelectric conversion efficiency and preparation method thereof, Pat. Nr. CN 102664213 A.

Carnall, W.T., 1979. In: Gschneidner Jr., K.A., Eyring, L. (Eds.), Handbook on the Physics and Chemistry of Rare Earths, vol. 3. North Holland Publishing Co., Amsterdam, pp. 172–208 (Chapter 24).

Catchpole, K.R., Polman, A., 2008. Appl. Phys. Lett. 93, Art. No.: 191113.

Cates, E.L., Chinnapongse, S.L., Kim, J., Kim, J.H., 2012. Environ. Sci. Technol. 46, 12316.

Cavalcanti, A., Shirinzadeh, B., Freitas, R.A., Hogg, T., 2008. Nanotechnology 19, Art. Nr. 015103.

Chan, E.M., Gargas, D.J., Schuck, P.J., Milliron, D.J., 2012. J. Phys. Chem. B 116, 10561.

Chandiran, A.K., Sauvage, F., Casas-Cabanas, M., Comte, P., Zakeeruddin, S.M., Grätzel, M., 2010. J. Phys. Chem. C 114, 15849.

Chandiran, A.K., Sauvage, F., Etgar, L., Graetzel, M., 2011. J. Phys. Chem. C 115, 9232.

Chane-Ching, J.Y., Corma, A., Garcia, H., 2005. Use of cerium oxide materials for photovoltaic applications, Pat. Nr. WO 2005/008786 A3.

Chapin, D.M., Fuller, C.S., Pearson, G.L., 1954. J. Appl. Phys. 25, 676.

Chatten, A.J., Bose, R., Farrell, D.J., Xiao, Y., Chan, N.L.A., Manna, L., Büchtemann, A., Quilitz, J., Debije, M.G., Barnham, K.W.J., 2010. In: Tsakalakos, L. (Ed.), Nanotechnology for Photovoltaics. CRC Press, Boca Raton, USA, pp. 323–329 (Chapter 9).

Chauvin, A.-S., Gumy, F., Imbert, D., Bünzli, J.-C.G., 2004. Spectrosc. Lett. 37, 517 erratum, 2007, 40, 193.

Chen, Y.C., Chen, T.M., 2011. J. Rare Earths 29, 723.

Chen, X., Mao, S.S., 2007. Chem. Rev. 107, 2891.

Chen, Z., Yang, H., Li, X., Li, F., Yi, T., Huang, C., 2007. J. Mater. Chem. 17, 1602.

Chen, D.Q., Wang, Y.S., Yu, Y.L., Huang, P., Weng, F.Y., 2008a. Opt. Lett. 33, 1884.

Chen, D.Q., Wang, Y.S., Yu, Y.L., Huang, P., Weng, F.Y., 2008b. J. Appl. Phys. 104, Art. Nr. 116105.

Chen, X.P., Huang, X.Y., Zhang, Q.Y., 2009a. J. Appl. Phys. 106, Art. Nr. 063518.

Chen, Z., Zhang, L., Sun, Y., Hu, J., Wang, D., 2009b. Adv. Funct. Mater. 19, 3815.

Chen, J., Luo, J., Qiu, J., Ye, S., Zhu, B., 2009a. Down-conversion light-emitting transparent microcrystalline glass for solar cells, comprises rare earth metal ions doped to oxyfluoride microcrystalline glass base body, Pat. Nr. CN101353229-A.

Chen, S.W., Lee, J.M., Lu, K.T., Pao, C.W., Lee, J.F., Chan, T.S., Chen, J.M., 2010. Appl. Phys. Lett. 97, Art. Nr. 012104.

Chen, Y.C., Huang, W.Y., Chen, T.M., 2011. J. Rare Earths 29, 907.

Chen, D., Wang, Y., Hong, M., 2012a. Nano Energy 1, 73.

Chen, Q.J., Zhang, W.J., Huang, X.Y., Dong, G.P., Peng, M.Y., Zhang, Q.Y., 2012b. J. Alloys Compd. 513, 139.

Chen, S., Zhou, G., Su, F., Zhang, H., Wang, L., Wu, M., Chen, M., Pan, L., Wang, S., 2012c. Mater. Lett. 77, 17.

Chen, X.B., Yang, G.J., Li, S., Yang, X.D., Liu, D.H., Chen, Y., Ding, F.L., Wu, Z.L., 2012d. Acta. Phys. Sin. 61, Art. Nr. 037804.

Cheng, C.L., Yang, J.Y., 2012. IEEE Electron Device Lett. 33, 697.

Cheng, Z.J., Pan, L.K., Su, F.F., Cao, M.L., Sun, Z., 2009. Surf. Rev. Lett. 16, 669.

Cheng, Y.Y., Fuckel, B., MacQueen, R.W., Khoury, T., Clady, R.G.C.R., Schulze, T.F., Ekins-Daukes, N.J., Crossley, M.J., Stannowski, B., Lips, K., Schmidt, T.W., 2012. Energy Environ. Sci. 5, 6953.

Cheung, C.L., Brewer, J.R., Deo, N., 2012. Crystalline nanostructures, Pat. Nr. US 8,247,070.

Chueh, W.C., Falter, C., Abbott, M., Scipio, D., Furler, P., Haile, S.M., Steinfeld, A., 2010. Science 330, 1797.

Chung, P., Chung, H.H., Holloway, P.H., 2007. J. Vac. Sci. Technol. A 25, 61.

Clark, A., Smith, R., Sewell, R., Semans, S., Srkun, F.E., Lebby, M., 2010. Passive rare earth tandem solar cell, Pat. Nr. US 20100122720 A1.

Corma, A., Atienzar, P., Garcia, H., Chane-Ching, J.Y., 2004. Nat. Mater. 3, 394.

Currie, M.J., Mapel, J.K., Heidel, T.D., Goffri, S., Baldo, M.A., 2008. Science 321, 226.

Dai, S.Y., Zhang, Y.X., Zhang, C.N., Hu, L.H., Kong, F.T., Xu, P., 2011. Application of up-conversion luminescent material on dye-sensitized solar cells, Pat. Nr. CN101582330 B.

de Boer, D.K.G., Ronda, C.R., Keur, W., Meijerink, A., 2011. Proc. SPIE 8108, Art. Nr. 81080E.

de Boer, D.K.G., Broer, D.J., Debije, M.G., Keur, W., Meijerink, A., Ronda, C.R., Verbunt, P.P.C., 2012. Opt. Express 20, A395.

De Vos, A., Szymanska, A., Badescu, V., 2009. Energy Conversion Manage. 50, 328.

de Wild, J., Meijerink, A., Rath, J.K., van Sark, W.G.J.H., Schropp, R.E.I., 2010a. Solar Energy Mater. Solar Cells 94, 1919.

de Wild, J., Rath, J.K., Meijerink, A., van Sark, W.G.J.H., Schropp, R.E.I., 2010b. Solar Energy Mater. Solar Cells 94, 2395.

de Wild, J., Meijerink, A., Rath, J.K., van Sark, W.G.J.H., Schropp, R.E.I., 2010c. Improved Photon Upconversion in Amorphous Silicon Solar Cells, In Proceedings of the 25th European Photovoltaic Solar Energy Conference, Valencia, Spain, 255.

de Wild, J., Meijerink, A., Rath, J.K., van Sark, W.G.J.H., Schropp, R.E.I., 2011. Energy Environ. Sci. 4, 4835.

Desmet, L., Ras, A.J.M., de Boer, D.K.G., Debije, M.G., 2012. Opt. Lett. 37, 3087.

Dexter, D.L., 1957. Phys. Rev. 108, 630.

Diaw, D., 1998. Solar Energy Mater. Solar Cells 53, 379.

Dirac, P.A.M., 1927. Proc. R. Soc. Lond. A 114, 243.

Duan, Y., Fu, N., Liu, Q., Fang, Y., Zhou, X., Zhang, J., Lin, Y., 2012. J. Phys. Chem. C 116, 8888.

Earp, A.A., Smith, G.B., Franklin, J., Swift, P., 2004a. Solar Energy Mater. Solar Cells 84, 411.

Earp, A.A., Smith, G.B., Swift, P.D., Franklin, J., 2004b. Solar Energy 76, 655.

Eilers, J.J., van Wijngaarden, J.T., Krämer, K., Güdel, H.U., Meijerink, A., 2010. Appl. Phys. Lett. 96, Art. Nr. 151106.

Eliseeva, S.V., Bünzli, J.-C.G., 2011. New J. Chem. 35, 1165.

Fang, Y.C., Kao, P.C., Chu, S.Y., 2011. J. Electrochem. Soc. 158, J120.

Fischer, S., Goldschmidt, J.C., Loper, P., Bauer, G.H., Bruggemann, R., Krämer, K., Biner, D., Hermle, M., Glunz, S.W., 2010. J. Appl. Phys. 108, Art. Nr. 044912.

Fischer, S., Hallermann, F., Eichelkraut, T., von Plessen, G., Krämer, K.W., Biner, D., Steinkemper, H., Hermle, M., Goldschmidt, J.C., 2012a. Opt. Express 20, 271.

Fischer, S., Steinkemper, H., Krämer, K.W., Goldschmidt, J.C., 2012b. Proc. SPIE 8438, Art. Nr. 843806.

Fischer, S., Steinkemper, H., Loper, P., Hermle, M., Goldschmidt, J.C., 2012c. J. Appl. Phys. 111, Art. Nr. 013109.

Frindell, K.L., Bartl, M.H., Popitsch, A., Stucky, G.D., 2002. Angew. Chem. Int. Ed. 41, 959.

Frindell, K.L., Bartl, M.H., Robinson, M.R., Bazan, G.C., Popitsch, A., Stucky, G.D., 2003. J. Solid State Chem. 172, 81.

Fukuda, T., Kato, S., Kin, E., Okaniwa, K., Morikawa, H., Honda, Z., Kamata, N., 2009. Opt. Mater. 32, 22.

Giannini, V., Fernandez-Dominguez, A.I., Heck, S.C., Maier, S.A., 2011. Chem. Rev. 111, 3888.

Giaume, D., Buissette, V., Lahlil, K., Gacoin, T., Boilot, J.P., Casanova, D., Beaurepaire, E., Sauviat, M.P., Alexandrou, A., 2005. Prog. Solid State Chem. 33, 99.

Gibart, P., Auzel, F., Guillaume, J.C., Zahraman, K., 1996. Jpn. J. Appl. Phys. I 35, 4401.

Goetzberger, A., Greubel, W., 1977. Appl. Phys. 14, 123.

Goldschmidt, J.C., Loper, P., Fischer, S., Janz, S., Peters, M., Glunz, S.W., Willeke, G., Lifshitz, E., Krämer, K., Biner, D., 2008. Advanced upconverter systems with spectral and geometric concentration for high upconversion efficiencies. In: IEEE Proceedings, Conf.on Optoelectronic and Microelectronic Materials and Devices (COMMAD 2008), 307.

Goldschmidt, J.C., Peters, M., Gutmann, J., Steidl, L., Zentel, R., Blasi, B., Hermle, M., 2010. Proc. SPIE 7725, Art. Nr. 77250S.

Goldschmidt, J.C., Fischer, S., Loper, P., Krämer, K.W., Biner, D., Hermle, M., Glunz, S.W., 2011. Solar Energy Mater. Solar Cells 95, 1960.

Goldschmidt, J.C., Fischer, S., Steinkemper, H., Herter, B., Rist, T., Wolf, S., Blasi, B., Hallermann, F., von Plessen, G., Krämer, K.W., Biner, D., Hermle, M., 2012. Proc. SPIE 8256, Art. Nr. 825602.

Graffion, J., Cattoen, X., Man, M.W.C., Fernandes, V.R., Andre, P.S., Ferreira, R.A.S., Carlos, L.D., 2011. Chem. Mater. 23, 4773.

Gratzel, M., 2003. J. Photochem. Photobiol. C: Photochem. Rev. 4, 145.

Green, M.A., Pillai, S., 2012. Nat. Phot. 6, 130.

Green, M.A., Emery, K., Hishikawa, Y., Warta, W., Dunlop, E.D., 2012. Prog. Photovolt. 20, 606.

Gschneidner Jr., K.A., 2011. Mater. Matters 6, 32.

Guo, C., 2007. A solar cell with visible light response, Pat. Nr. CN200979886.

Guo, C., 2008. Visible light responding solar cell for e.g. storing solar energy, has transparent glasses provided with rare earth luminescent material membrane layers, where rare earth luminescent material is oxide, sulfide or oxy-sulfide, Pat. Nr. CN200979886-Y.

Gutmann, J., Peters, M., Blasi, B., Hermle, M., Zappe, H., Goldschmidt, J.C., 2011. Proc. SPIE 8111, Art. Nr. 81110K.

Hafez, H., Wu, J.H., Lan, Z., Li, Q.H., Xie, G.X., Lin, J.M., Huang, M.L., Huang, Y.F., Abdel-Mottaleb, M.S., 2010. Nanotechnology 21, 415201.

Hafez, H., Saif, M., Abdel-Mottaleb, M.S.A., 2011. J. Power. Sources 196, 5792.

Hamann, T.W., 2012. Dalton Trans. 41, 3111.

Hamann, T.W., Ondersma, J.W., 2011. Energy Environ. Sci. 4, 370.

Han, C.H., Lee, H.S., Lee, K.W., Han, S.D., Singh, I., 2009. Bull. Kor. Chem. Soc. 30, 219.

Harikisun, R., Desilvestro, H., 2011. Solar Energy 85, 1179.

Hehlen, M.P., Phillips, M.L.F., Cockroft, N.J., Güdel, H.U., 2001. Up-conversion phosphors. In: Buschow, K.H.J., Cahn, R.W., Flemings, M.C., Ilschner, B., Kramer, E.J., Mahajan, S. (Eds.), Encyclopedia of Materials: Science and Technology. Elsevier Science Ltd., Oxford, pp. 9456–9458.

Henke, B., Ahrens, B., Johnson, J.A., Miclea, P.T., Schweizer, S., 2009. Proc. SPIE 7411, 74110E–74111E.

Herb, J., 2012. Commercialization of New Lattice-Matched Multi-Junction Solar Cells Based on Dilute Nitrides. Report Nr. NREL/SR-5200-54721, http://www.nrel.gov/docs/fy12osti/54721.pdf.

Herter, B., Wolf, S., Fischer, S., Peters, M., Blasi, B., Goldschmidt, J.C., 2012. Proc. SPIE 8438, Art. Nr. 84381D.

Hong, B.C., Kawano, K., 2003. Solar Energy Mater. Solar Cells 80, 417.

Huang, X.Y., Zhang, Q.Y., 2009. J. Appl. Phys. 105, Art. Nr. 053521.

Huang, X.Y., Zhang, Q.Y., 2010. J. Appl. Phys. 107, Art. Nr. 063505.

Huang, X.Y., Yu, D.C., Zhang, Q.Y., 2009. J. Appl. Phys. 106, Art. Nr. 113521.

Huang, J.H., Hung, P.Y., Hu, S.F., Liu, R.S., 2010. J. Mater. Chem. 20, 6505.

Huang, X.Y., Ji, X.H., Zhang, Q.A., 2011. J. Am. Cer. Soc. 94, 833.

Hyldahl, M.G., Bailey, S.T., Wittmershaus, B.P., 2009. Solar Energy 83, 566.

Iso, Y., Takeshita, S., Isobe, T., 2012. J. Electrochem. Soc. 159, J72.

Ivanova, S., Pellé, F., 2009. J. Opt. Soc. Am. B: Opt. Phys. 26, 1930.

Jin, T., Inoue, S., Machida, K., Adachi, G., 1997. J. Electrochem. Soc. 144, 4054.

Kalyanasundaram, K., 2010a. Dye-sensitized Solar Cells. EPFL Press, Lausanne.

Kalyanasundaram, K., 2010b. Photochemical and photoelectrochemical approaches to energy conversion. In: Kalyanasundaram, K. (Ed.), Dye-Sensitized Solar Cells. EPFL Press, Lausanne, pp. 1–44 (Chapter 1).

Kanesato, M., Sugaya, K., Segawa, M., 2010. Fluorescent resin composition and solar battery module using the same, Pat. Nr. EP 2 080 785 B1.

Katsagounos, G., Stathatos, E., Arabatzis, N.B., Keramidas, A.D., Lianos, P., 2011. J. Lumin. 131, 1776.

Kaulachs, I., Muzikante, I., Gerca, L., Shlihta, G., Shipkovs, P., Grehovs, V., Kalnachs, J., Roze, M., Rozite, G., Ivanova, A., 2012. Chem. Phys. 405, 46.

Kawano, K., Arai, K., Yamada, H., Hashimoto, N., Nakata, R., 1997a. Solar Energy Mater. Solar Cells 48, 35.

Kawano, K., Hashimoto, N., Nakata, R., 1997b. Mater. Sci. Forum 239–241, 311.

Kawano, K., Hong, B.C., Sakamoto, K., Tsuboi, T., Seo, H.J., 2009. Opt. Mater. 31, 1353.

Khan, A.F., Yadav, R., Mukhopadhya, P.K., Singh, S., Dwivedi, C., Dutta, V., Chawla, S., 2011. J. Nanopart. Res. 13, 6837.

Kilbourn, B.T., 1986. J. Less-Common Met. 126, 101.

Klampaftis, E., Ross, D., McIntosh, K.R., Richards, B.S., 2009. Solar Energy Mater. Solar Cells 93, 1182.

Ko, K.H., Lee, Y.C., Jung, Y.J., 2005. J. Colloid Interface Sci. 283, 482.

Korthout, K., Van den Eeckhout, K., Botterman, J., Nikitenko, S., Poelman, D., Smet, P.F., 2011. Phys. Rev. B 84, Art. Nr. 085140.

Kozlowska, A., Nakielska, M., Sarnecki, J., Lipinska, L., Jeremiasz, O., Podniesinski, D., Malag, A., 2011. Opt. Appl. 41, 359.

Krämer, K.W., Biner, D., Frei, G., Güdel, H.U., Hehlen, M.P., Luthi, S.R., 2004. Chem. Mater. 16, 1244.

Lahoz, F., 2008. Opt. Lett. 33, 2982.

Lahoz, F., Perez-Rodriguez, C., Hernandez, S.E., Martin, I.R., Lavin, V., Rodriguez-Mendoza, U.R., 2011. Solar Energy Mater. Solar Cells 95, 1671.

Lakowicz, J.R., 2005. Anal. Biochem. 337, 171.

Le Donne, A., Acciarri, M., Narducci, D., Marchionna, S., Binetti, S., 2009. Prog. Photovolt. 17, 519.

Lei, B.F., Yue, S., Zhang, Y.Z., Liu, Y.L., 2010. Chin. Phys. Lett. 27, Art. Nr. 037201.

Levitt, J.A., Weber, W.H., 1977. Appl. Optics 16, 2684.

Li, F., Gu, Y., 2012. Mater. Sci. Semicond. Proc. 15, 11.

Li, W., Xianping, F., 2008. Rare Met. Mater. Eng. 37, 80.

Li, Q.B., Lin, J.M., Wu, J.H., Lan, Z., Wang, J.L., Wang, Y., Peng, F.G., Huang, M.L., Xiao, Y.M., 2011a. Chin. Sci. Bull. 56, 3114.

Li, Q., Lin, J., Wu, J., Lan, Z., Wang, Y., Peng, F., Huang, M., 2011b. Electrochim. Acta 56, 4980.

Li, Y., Wang, G., Pan, K., Jiang, B., Tian, C., Zhou, W., Fu, H., 2012a. J. Mater. Chem. 22, 20381.

Li, Z.Q., Li, X.D., Liu, Q.Q., Chen, X.H., Sun, Z., Liu, C., Ye, X.J., Huang, S.M., 2012c. Nanotechnology 23, Art. Nr. 025402.

Li, Q., Lin, J., Wu, J., Lan, Z., Wang, Y., Peng, F., Huang, M., 2013. J. Lumin. 134, 59.

Lin, H., Zhou, S.M., Teng, H., Li, Y.K., Li, W.J., Hou, X.R., Jia, T.T., 2010. J. Appl. Phys. 107, Art. Nr. 043107.

Lin, H.Y., Chen, H.N., Wu, T.H., Wu, C.S., Su, Y.K., Chu, S.Y., 2012. J. Am. Cer. Soc. 95, 3172.

Liska, P., Thampi, K.R., Gratzel, M., Bremaud, D., Rudmann, D., Upadhyaya, H.M., Tiwari, A.N., 2006. Appl. Phys. Lett. 88, Art. Nr. 203103.

Listorti, A., O'Regan, B., Durrant, J.R., 2011. Chem. Mater. 23, 3381.

Liu, M.O., Hu, A.T., 2004. J. Organomet. Chem. 689, 2450.

Liu, J.F., Yao, Q.H., Li, Y.D., 2006. Appl. Phys. Lett. 88, Art. Nr. 173119.

Liu, X., Ye, S., Qiao, Y., Dong, G., Zhu, B., Chen, D., Lakshminarayana, G., Qiu, J., 2009a. Appl. Phys. B: Laser Opt. 96, 51.

Liu, X., Teng, Y., Zhuang, Y., Xie, J., Qiao, Y., Dong, G., Chen, D., Qiu, J., 2009b. Opt. Lett. 34, 3565.

Liu, G.X., Zhang, R., Xiao, Q.L., Zou, S.Y., Peng, W.F., Cao, L.W., Meng, J.X., 2011a. Opt. Mater. 34, 313.

Liu, M., Lu, Y.L., Xie, Z.B., Chow, G.M., 2011b. Solar Energy Mater. Solar Cells 95, 800.

Liu, N., Qin, W.P., Qin, G.S., Jiang, T., Zhao, D., 2011c. Chem. Commun. 47, 7671.

Liu, Y., Lin, H., Dy, J.T., Tamaki, K., Nakazaki, J., Nakayama, D., Uchida, S., Kubo, T., Segawa, H., 2011d. Chem. Commun. 47, 4010.

Liu, B., Qiu, S., Hu, R., Liao, Y., Chen, N., Du, G., 2012. Appl. Surf. Sci. 259, 705.

Liu, J., Wang, K., Zheng, W., Huang, W., Li, C. H., You, X. Z., 2013. Prog. Photovolt: Res. Appl., 21, 668.

Lo, W.S., Kwok, W.M., Law, G.L., Yeung, C.T., Chan, C.T.-L., Yeung, H.L., Kong, H.K., Chen, C.H., Murphy, M.B., Wong, K.L., Wong, W.T., 2011. Inorg. Chem. 50, 5309.

Lohse, S.E., Murphy, C.J., 2012. J. Am. Chem. Soc. 134, 15607.

Lu, L.L., Li, R.J., Peng, T.Y., Fan, K., Dai, K., 2011. Renew. En. 36, 3386.

MacDougall, S.K.W., Ivaturi, A., Marques-Hueso, J., Chen, D., Wang, Y., Richards, B.S., 2012. Proc. SPIE 8438, Art. Nr. 84380Y.

Machida, K., Li, H., Ueda, D., Inoue, S., Adachi, G., 2000. J. Lumin. 87–89, 1257.

Malta, O.L., Brito, H.F., Menezes, J.F.S., Gonçalves e Silva, F.R., Donega, C.D., Alves, S., 1998. Chem. Phys. Lett. 282, 233.

Marchionna, S., Meinardi, F., Acciarri, M., Binetti, S., Papagni, A., Pizzini, S., Malatesta, V., Tubino, R., 2006. J. Lumin. 118, 325.

Marques-Hueso, J., Chen, D.Q., MacDougall, S.K.W., Wang, Y.S., Richards, B.S., 2011. Proc. SPIE 8111, Art. Nr. 811102.

Martiniani, S., Anderson, A.Y., Law, C., O'Regan, B.C., Barolo, C., 2012. Chem. Commun. 48, 2406.

Masui, T., Yamamoto, M., Sakata, T., Mori, H., Adachi, G., 2000. J. Mater. Chem. 10, 353.

Mawyin, J.A., Chawda, S.G., Halada, G.P., Clayton, C.R., Tonucci, R.J., Fortmann, C.M., 2008. J. Non-Cryst. Solids 354, 2492.

McIntosh, K.R., Lau, G., Cotsell, J.N., Hanton, K., Batzner, D.L., Bettiol, F., Richards, B.S., 2009. Prog. Photovolt. 17, 191.

Meijer, J.-M., Aarts, L., van der Ende, B.M., Vlugt, T.J.H., Meijerink, A., 2010. Phys. Rev. B 81, Art. Nr. 035107.

Meseguer, F.J., Cusso, F., Jaque, F., Sanchez, C., 1981. J. Lumin. 24–25 (Part 2), 865.

Misra, V., Mishra, H., 2008. J. Chem. Phys. 128, Art Nr. 244701.

Monguzzi, A., Tubino, R., Hoseinkhani, S., Campione, M., Meinardi, F., 2012. Phys. Chem. Chem. Phys. 14, 4322.

Moudam, O., Rowan, B.C., Alamiry, M.A.H., Richardson, P., Richards, B.S., Jones, A.C., Robertson, N., 2009. Chem. Commun. 2009, 6649.

Munz, P., Bucher, E., 1982. Rare Earths Modern Sci. Technol. 3, 547.

Muthu, P., Calander, N., Gryczynski, I., Gryczynski, Z., Talent, J.M., Shtoyko, T., Akopova, I., Borejdo, J., 2008. Biophys. J. 95, 3429.

Oh, J.H., Song, H.M., Eom, Y.K., Ryu, J.H., Ju, M.J., Kim, H.K., 2011. Bull. Kor. Chem. Soc. 32, 2743.

Ohwaki, J., Wang, Y.H., 1994. Jpn. J. Appl. Phys. Lett. 2:Lett 33, L334.

O'Regan, B.C., Grätzel, M., 1991. Nature 353, 737.

Ozawa, H., Okuyama, Y., Arakawa, H., 2012. Dalton Trans. 41, 5137.

Pala, R.A., White, J., Barnard, E., Liu, J., Brongersma, M.L., 2009. Adv. Mater. 21, 3504.

Passlick, C., Henke, B., Csaszar, I., Ahrens, B., Miclea, P.T., Johnson, J.A., Schweizer, S., 2010. Proc. SPIE 7772, Art. Nr. 777201.

Peng, Y.J., Liu, J., Zhang, K., Luo, H., Li, J.H., XU, B., Han, L.X., Li, X.J., Yu, X.B., 2011. Appl. Phys. Lett. 99, Art. Nr. 121110.

Piper, W.W., DeLuca, J.A., Ham, F.S., 1974. J. Lumin. 8, 344.

Qi, J., Dang, X., Hammond, P.T., Belcher, A.M., 2011. ACS Nano 5, 7108.

Reisfeld, R., 1983. J. Less-Common Met. 93, 243.

Reisfeld, R., 1987. Inorg. Chim. Acta 140, 345.

Reisfeld, R., 2010. Opt. Mater. 32, 850.

Richards, B.S., 2006a. Solar Energy Mater. Solar. Cells 90, 2329.

Richards, B.S., 2006b. Solar Energy Mater. Solar Cells 90, 1189.

Richards, B.S., Shalav, A., 2005. Synt. Met. 154, 61.

Richards, B.S., Shalav, A., 2007. IEEE Trans. Electron. Dev. 54, 2679.

Richards, B.S., Aruna, I., MacDougall, S.K.W., Marques-Hueso, J., 2012. Proc. SPIE 8438, Art. Nr. 843802.

Rodriguez, V.D., Tikhomirov, V.K., Mendez-Ramos, J., Yanes, A.C., Moshchalkov, V.V., 2010. Solar Energy Mater. Solar Cells 94, 1612.

Rodriguez, V.D., Mendez-Ramos, J., Tikhomirov, V.K., del-Castillo, J., Yanes, A.C., Moshchalkov, V.V., 2011. Opt. Mater. 34, 179.

Rowan, B.C., Wilson, L.R., Richards, B.S., 2008. IEEE J. Quantum Electron. 14, 1312.

Saif, M., Abdel-Mottaleb, M.S.A., 2007. Inorg. Chim. Acta 360, 2863.

Sanguineti, A., Monguzzi, A., Vaccaro, G., Meinardi, F., Ronchi, E., Moret, M., Cosentino, U., Moro, G., Simonutti, R., Mauri, M., Tubino, R., Beverina, L., 2012. Phys. Chem. Chem. Phys. 14, 6452.

Santan-Alonso, A., Yanes, A.C., Mendez-Ramos, J., del-Castillo, J., Rodriguez, V.D., 2011. Opt. Mater. 33, 587.

Schietinger, S., Aichele, T., Wang, H.Q., Nann, T., Benson, O., 2010. Nano Lett. 10, 134.

Schuller, J.A., Barnard, E.S., Cai, W., Jun, Y.C., White, J.S., Brongersma, M.L., 2010. Nat. Mater. 9, 193.

Schulze, T.F., Cheng, Y.Y., Fueckel, B., MacQueen, R.W., Danos, A., Davis, N.J.L.K., Tayebjee, M.J.Y., Khoury, T., Clady, R.G.C.R., Ekins-Daukes, N.J., Crossley, M.J., Stannowski, B., Lips, K., Schmidt, T.W., 2012. Aust. J. Chem. 65, 480.

Schweizer, S., Henke, B., Ahrens, B., Passlick, C., Miclea, P.T., Wenzel, J., Reisacher, E., Pfeiffer, W., Johnson, J.A., 2010. Proc. SPIE 7725, 77250X–77251X.

Sewell, R.H., Clark, A., Smith, R., Semans, S., Jamora, A., Vosters, G., 2009. IEEE Photovoltaic Specialist Conference, 2448.

Shalav, A., Richards, B.S., Trupke, T., Corkish, R.P., Gäme, K.W., Güdel, H.U., Green, M.A., 2003. The application of up-converting phosphors for increased solar cell conversion efficiencies. In: 3rd World Conference on Photovoltaic Energy Conversion, Osaka, May 11-18, 2003, A-C, 248.

Shalav, A., Richards, B.S., Krämer, K., Güdel, H.U., 2005a. Improvements of an up-conversion NaYF4: Er3+ phosphor/silicon solar cell system for an enhanced response in the near-infrared. In: Conference Record of the Thirty-First IEEE Photovoltaic Specialists Conference - 2005, Lake Buena Vista, Florida, Jan 3-7, 2005, 114.

Shalav, A., Richards, B.S., Trupke, T., Krämer, K.W., Güdel, H.U., 2005b. Appl. Phys. Lett. 86, Art. Nr. 013505.

Shalav, A., Richards, B.S., Green, M.A., 2007. Solar Energy Mater. Solar Cells 91, 829.

Shan, G.B., Demopoulos, G.P., 2010. Adv. Mater. 22, 4373.

Shan, G.B., Assaaoudi, H., Demopoulos, G.P., 2011. ACS Appl. Mater. Interface 3, 3239.

Shao, W., Gu, F., Gai, L., Li, C., 2011. Chem. Commun. 47, 5046.

Shockley, W., Queisser, H.J., 1961. J. Appl. Phys. 32, 510.

Sholin, V., Olson, J.D., Carter, S.A., 2007. J. Appl. Phys. 101, Art. Nr. 123114.

Shpaisman, H., Niitsoo, O., Lubomirsky, I., Cahen, D., 2008. Solar Energy Mater. Solar Cells 92, 1541.

Si, Z., Li, B., Wang, L., Yue, S., Li, W., 2007. Solar Energy Mater. Solar Cells 91, 1168.

Singh, S.K., Singh, A.K., Rai, S.B., 2011. Nanotechnology 22, Art. Nr. 275703.

Sirimanne, P.M., Cheng, Y.B., 2009. J. Lumin. 129, 563.

Slooff, L.H., Bende, E.E., Burgers, A.R., Budel, T., Pravettoni, M., Kenny, R.P., Dunlop, E.D., Buchtemann, A., 2008. Phys. Stat. Sol. Rap. Res. Lett. 2, 257.

Sommeling, P.M., O'Regan, B.C., Haswell, R.R., Smit, H.J.P., Bakker, N.J., Smits, J.J.T., Kroon, J.M., van Roosmalen, J.A.M., 2006. J. Phys. Chem. B 110, 19191.

Song, P., Jiang, C., 2012. AIP Adv. 2, Art. Nr. 042130.

Streetman, B.G., Banerjee, S., 2000. Solid State Electronic Devices. Prentice Hall, New Jersey.

Strek, W., Bednarkiewicz, A., Deren, P.J., 2001. J. Lumin. 92, 229.

Streudel, F., Dyrba, M., Schweizer, S., 2012. Proc. SPIE 8438, Art. Nr. 843803.

Strümpel, C., McCann, M., Beaucarne, G., Arkhipov, V., Slaoui, A., Svrcek, V., del Canizo, C., Tobias, I., 2007. Solar Energy Mater. Solar Cells 91, 238.

Suryawanshi, M.P., Agawane, G.L., Bhosale, S.M., Shin, S.W., Patil, P.S., Kim, J.H., Moholkar, A.V., 2013. Mater. Technol.: Adv. Perform. Mater. 28, 98.

Sytko, V., Pershina, M., 1995. Proc. SPIE 2531, 272.

Takei, M., 2011. Conductive paste for solar cell, Pat. Nr. JP20100099623 20100423 (A).

Tan, T.T.Y., 2012. Rare Earth Nanotechnology. Pan Stanford Publishing, Singapore.

Tanner, P.A., Mak, C.S.K., Kwok, W.M., Phillips, D.L., Joubert, M.F., 2002. J. Phys. Chem. B 106, 3606.

Teng, Y., Zhou, J.J., Liu, X.F., Ye, S., Qiu, J.R., 2010. Opt. Express 18, 9671.

Teotonio, E.E.S., Fett, G.M., Brito, H.F., Faustino, W.M., de Sa, G.F., Felinto, M.C., Santos, R.H.A., 2008. J. Lumin. 128, 190.

Thomann, I., Pinaud, B.A., Chen, Z., Clemens, B.M., Jaramillo, T.F., Brongersma, M.L., 2011. Nano Lett. 11, 3440.

Timmerman, D., Izeddin, I., Stallinga, P., Yassievich, I.N., Gregorkiewicz, T., 2008. Nat. Phot. 2, 105.

Ting, Chu-Chi, Tsai, C.H., 2009. The optical and electrical properties of Eu(3+)-Y(3+) codoped ITO transparent conductive electrodes as luminescent solar concentrators. In: Brebbia, C.A., Mammoli, A.A. (Eds.), WIT Transactions on Ecology and the Environment: Energy and Sustainability II121, 79–89.

Trupke, T., Green, M.A., Wurfel, P., 2002a. J. Appl. Phys. 92, 1668.

Trupke, T., Green, M.A., Wurfel, P., 2002b. J. Appl. Phys. 92, 4117.

Trupke, T., Shalav, A., Richards, B.S., Wurfel, P., Green, M.A., 2006. Solar Energy Mater. Solar Cells 90, 3327.

Turkovic, A., Orel, Z.C., 1997. Solar Energy Mater. Solar Cells 45, 275.

Ueda, J., Tanabe, S., 2009. J. Appl. Phys. 106, Art. Nr. 043101.

van der Ende, B.M., Aarts, L., Meijerink, A., 2009a. Phys. Chem. Chem. Phys. 11, 11081.

van der Ende, B.M., Aarts, L., Meijerink, A., 2009b. Adv. Mater. 21, 3073.

van Sark, W.G.J.H., 2005. Appl. Phys. Lett. 87, Art. Nr. 151117.

van Sark, W.G.J.H., 2008. Thin Solid Films 516, 6808.

van Sark, W.G.J.H., 2013. Renew. En. 49, 207.

van Sark, W.G.J.H., Barnham, K.W.J., Slooff, L.H., Chatten, A.J., Buchtemann, A., Meyer, A., McCormack, S.J., Koole, R., Farrell, D.J., Bose, R., Bende, E.E., Burgers, A.R., Budel, T., Quilitz, J., Kennedy, M., Meyer, T., Donega, C.D.M., Meijerink, A., Vanmaekelbergh, D., 2008. Opt. Express 16, 21773.

van Sark, W.G.J.H., Meijerink, A., Schropp, R.E.I., 2010. Proc. SPIE 7772, Art. Nr. 777206.

van Sark, W.G.J.H., de Wild, J., Rath, J.K., Meijerink, A., El Schropp, R., 2013. Nanoscale Res. Lett. 8, Art. Nr. 81.

van Wijngaarden, J.T., Scheidelaar, S., Vlugt, T.J.H., Reid, M.F., Meijerink, A., 2010. Phys. Rev. B 81, Art. Nr. 155112.

Vergeer, P., Vlugt, T.J.H., Kox, M.H.F., den Hertog, M.I., van der Eerden, J.P.J.M., Meijerink, A., 2005. Phys. Rev. B 71, Art. Nr. 014119.

Walter, M.G., Warren, E.L., McKone, J.R., Boettcher, S.W., Mi, Q., Santori, E.A., Lewis, N.S., 2010. Chem. Rev. 110, 6446.

Wang, C., Chen, Y., 2011. Solar cell with fluorescent powder, Pat. Nr. CN 202004034 U.

Wang, L., Li, Y., 2006. Nano Lett. 6, 1645.

Wang, Q., Li, Y., Yan, X.Z., Rathi, M., Ropp, M., Galipeau, D., Jiang, J.Z., 2008. Appl. Phys. Lett. 93, Art. Nr. 073303.

Wang, Y.H., Xie, L.C., Zhang, H.J., 2009. J. Appl. Phys. 105, Art. Nr. 023528.

Wang, X., Yang, Y., Fan, R., Jiang, Z., 2010. New J. Chem. 34, 2599.

Wang, G., Peng, Q., Li, Y., 2011a. Acc. Chem. Res. 44, 322.

Wang, H.Q., Batentschuk, M., Osvet, A., Pinna, L., Brabec, C.J., 2011b. Adv. Mater. 23, 2675.

Wang, T., Zhang, J., Ma, W., Luo, Y., Wang, L., Hu, Z., Wu, W., Wang, X., Zou, G., Zhang, Q., 2011c. Solar Energy 85, 2571.

Wang, X., Wang, T., Tian, X., Wang, L., Wu, W., Luo, Y., Zhang, Q., 2011d. Solar Energy 85, 2179.

Wang, C., Xu, L., Li, X., Lin, Q., 2012a. Chemphyschem 13, 3765.

Wang, H.Q., Stubhan, T., Osvet, A., Litzov, I., Brabec, C.J., 2012b. Solar Energy Mater. Solar Cells 105, 196.

Wang, J.L., Wu, J.H., Lin, J.M., Huang, M.L., Huang, Y.F., Lan, Z., Xiao, Y.M., Yue, G.T., Yin, S., Sato, T., 2012c. ChemSusChem 5, 1307.

Wang, J., Lin, J., Wu, J., Huang, M., Lan, Z., Chen, Y., Tang, S., Fan, L., Huang, Y., 2012d. Electrochim. Acta 70, 131.

Wang, X., Yang, Y.L., Wang, P., Li, L., Fan, R.Q., Cao, W.W., Yang, B., Wang, H., Liu, J.Y., 2012e. Dalton Trans. 41, 10619.

Weber, W.H., Lambe, J., 1976. Appl. Optics 15, 2299.

Weber, A.S., Grady, A.M., Koodali, R.T., 2012. Catal. Sci. Technol. 2, 683.

Wegh, R.T., Donker, H., Oskam, K.D., Meijerink, A., 1999. Science 283, 663.

Wehrspohn, R.B., Schweizer, S., 2009. Solar cell assembly with an optically-active glass ceramic, Pat. Nr. WO 2009033466 A1.

Wikipedia (Engl.), 2012. On line document, http://en.wikipedia.org/wiki/Photovoltaic_system.

Wilson, L.R., Rowan, B.C., Robertson, N., Moudam, O., Jones, A.C., Richards, B.S., 2010. Appl. Optics 49, 1651.

Wu, J.H., Xie, G.X., Lin, J.M., Lan, Z., Huang, M.L., Huang, Y.F., 2010. J. Power. Sources 195, 6937.

Wu, D.D., Ma, Y.Q., Zhang, X., Qian, S.B., Zheng, G.H., Wu, M.Z., Li, G., Sun, Z.Q., 2012a. J. Rare Earths 30, 325.

Wu, J.H., Wang, J.L., Lin, J.M., Lan, Z., Tang, Q.W., Huang, M.L., Huang, Y.F., Fan, L.Q., Li, Q.B., Tang, Z.Y., 2012b. Adv. Energy Mater. 2, 78.

Wu, J.L., Chen, F.C., Chang, S.H., Tan, K.S., Tuan, H.Y., 2012c. Org. Electron. 13, 2104.

Xiao, L.F., Liu, Y., Tan, S., Feng, X., Xiu, Q., Zhang, L.R., Guo, L.H., Zhang, H.L., Zhong, C.F., 2010. J. Polym. Sci. Part A: Polym. Chem. 48, 1943 (erratum 3215).

Xie, F., Baker, M.S., Goldys, E.M., 2006. J. Phys. Chem. B 110, 23085.

Xie, L.C., Wang, Y.H., Zhang, H.J., 2009. Appl. Phys. Lett. 94, Art. Nr. 061905.

Xie, G.X., Lin, J.M., Wu, J.H., Lan, Z., Li, Q.H., Xiao, Y.M., Yue, G.T., Yue, H.F., Huang, M.L., 2011. Chin. Sci. Bull. 56, 96.

Xie, G., Wu, J., Lin, J., Li, Q., Lan, Z., Xiao, Y., Yue, G., Ye, H., Huang, M., 2012a. Energy Sources. Part A: Recovery Utilization Environ. Eff. 34, 1534.

Xie, G.X., Wei, Y.L., Fan, L.Q., Wu, J.H., 2012b. J. Phys. Conf. Ser. 339, Art. Nr. 012010.

Xu, W.W., Dai, S.Y., Hu, L.H., Liang, L.Y., Wang, K.J., 2006. Chin. Phys. Lett. 23, 2288.

Xue, F.M., Ma, Y., Fu, L.M., Hao, R., Shao, G.S., Tang, M.X., Zhang, J.P., Wang, Y., 2010. Phys. Chem. Chem. Phys. 12, 3195.

Yablonovitch, E., 1987. Phys. Rev. Lett. 58, 2059.

Yahav, S., Rühle, S., Greenwald, S., Barad, H.N., Shalom, M., Zaban, A., 2011. J. Phys. Chem. C 115, 21481.

Yanes, A.C., del-Castillo, J., Mendez-Ramos, J., Rodriguez, V.D., 2011. J. Nanopart. Res. 13, 7295.

Yang, B.B., Zhang, D.D., Lee, S.T., Li, Y.Q., Tang, J.X., 2013. Appl. Phys. Lett. 102, Art Nr. 073301.

Yao, Q.H., Liu, J.F., Peng, Q., Wang, X., Li, Y.D., 2006. Chem. Asian J. 1, 737.

Ye, S., Zhu, B., Luo, J., Chen, J.X., Lakshminarayana, G., Qiu, J.R., 2008a. Opt. Express 16, 8989.

Ye, S., Zhu, B., Luo, J., Teng, Y., Chen, J.X., Lakshminarayana, G., Qian, G.D., Qiu, J.R., 2008b. Appl. Phys. Lett. 93, 181110–181111.

Ye, S., Jiang, N., He, F., Liu, X., Zhu, B., Teng, Y., Qiu, J.R., 2010. Opt. Express 18, 639.

Yella, A., Lee, H.W., Tsao, H.N., Yi, C.Y., Chandiran, A.K., Nazeeruddin, M.K., Diau, E.W.G., Yeh, C.Y., Zakeeruddin, S.M., Grätzel, M., 2011. Science 334, 629.

Yeo, J.H., Im, S.H., Mandal, T.N., Lim, C.S., Chang, J.A., Lee, Y.H., Kim, H.J., Sarkar, A., Nazeeruddin, Md.K., Grätzel, M., Seok, S.I., 2013. Nat. Photon. 7, 486.

Yi, G.S., Chow, G.M., 2007. Chem. Mater. 19, 341.

Yu, D.C., Huang, X.Y., Ye, S., Peng, M.Y., Zhang, Q.Y., 2012a. Solar Energy Mater. Solar Cells 101, 303.

Yu, H., Xue, B.F., Liu, P.R., Qiu, J.X., Wen, W., Zhang, S.Q., Zhao, H.J., 2012b. ACS Appl. Mater. Interface 4, 1289.

Yu, H., Bai, Y., Zong, X., Tang, F., Lu, G.Q.M., Wang, L., 2012c. Chem. Commun. 48, 7386.

Yuan, C., Chen, G., Prasad, P.N., Ohulchanskyy, T.Y., Ning, Z., Tian, H., Sun, L., Agren, H., 2012. J. Mater. Chem. 22, 16709.

Zalas, M., Klein, M., 2012. Int. J. Photoenergy 2012, Art. Nr. 927407.
Zalas, M., Walkowiak, M., Schroeder, G., 2011. J. Rare Earths 29, 783.
Zeng, Q.G., Ding, Z.J., Zhang, Z.M., 2006. J. Lumin. 118, 301.
Zhang, Y., 2012. Solar cell efficiently using solar infrared and visible light to generate power, Pat. Nr. CN 102646743 A.
Zhang, Q.Y., Yang, C.H., Pan, Y.X., 2007. Appl. Phys. Lett. 90, Art. Nr. 021107.
Zhang, Q., Wang, J., Zhang, G., Su, Q., 2009. J. Mater. Chem. 19, 7088.
Zhang, J., Zhao, Z., Wang, X., Yu, T., Guan, J., Yu, Z., Li, Z., Zou, Z., 2010a. J. Phys. Chem. C 114, 18396.
Zhang, X.D., Jin, X., Wang, D.F., Xiong, S.Z., Geng, X.H., Zhao, Y., 2010b. Phys. Status Solidi (c) 7, 1128.
Zhang, J., Peng, W., Chen, Z., Chen, H., Han, L., 2012a. J. Phys. Chem. C 116, 19182.
Zhang, L., Tian, Q., Xu, W., Kuang, X., Hu, J., Zhu, M., Liu, J., Chen, Z., 2012b. J. Mater. Chem. 22, 18156.
Zhang, Q., Myers, D., Lan, J., Jenekhe, S.A., Cao, G., 2012c. Phys. Chem. Chem. Phys. 14, 14982.
Zhang, Y., Liu, Y., Liu, J., 2012d. Solar cell having microcrystalline silicon intrinsic layer and high photoelectric conversion efficiency, Pat. Nr. CN 102479834.
Zhang, Y., Liu, Y., Liu, J., 2012e. Solar cell with high photoelectric conversion efficiency and capable of adjusting amount of transmitting light, Pat. Nr. CN 102479833 A.
Zhang, Y., Mei, C., Liu, J., 2012f. Solar cell having high- and low-temperature amorphous silicon intrinsic layers and high photoelectric conversion efficiency, Pat. Nr. CN 102479836 A.
Zhang, Y., Mei, C., Liu, J., 2012g. Solar cell with high photoelectric conversion efficiency, Pat. Nr. CN 102479832 A.
Zhang, J., Shen, H., Guo, W., Wang, S., Zhu, C., Xue, F., Hou, J., Su, H., Yuan, Z., 2013. J. Power. Sources 226, 47.
Zhao, Y., Li, X., Li, Q., Deng, C., 2011. J. Mater. Chem. Technol. 27, 764.
Zhong, L., Luu, Q.A., Paudel, H.P., Bayat, K., Baroughi, M.F., May, P.S., Smith, S., 2011. MRS Online Proc. Library 1342, v04.
Zhou, J.J., Zhuang, Y.X., Ye, S., Teng, Y., Lin, G., Zhu, B., Xie, J.H., Qiu, J.R., 2009. Appl. Phys. Lett. 95, Art. Nr. 141101.
Zhou, J.J., Teng, Y., Liu, X.F., Ye, S., Xu, X.Q., Ma, Z.J., Qiu, J.R., 2010a. Opt. Express 18, 21663.
Zhou, J.J., Teng, Y., Ye, S., Liu, X.F., Qiu, J.R., 2010b. Opt. Mater. 33, 153.
Zhou, J., Teng, Y., Liu, X., Ye, S., Ma, Z., Qiu, J., 2010c. Phys. Chem. Chem. Phys. 12, 13759.
Zhou, J., Teng, Y., Ye, S., Zhuang, Y., Qiu, J., 2010d. Chem. Phys. Lett. 486, 116.
Zhou, M., Huang, J., Wang, L., 2011. Light focusing device and manufacturing method thereof, and solar cell system comprising the condensing device, Pat. Nr. CN 102253481 A.
Zhou, J.J., Teng, Y., Ye, S., Lin, G., Qiu, J.R., 2012. Opt. Mater. 34, 901.
Zhu, G., Wang, X., Li, H., Pan, L., Sun, H., Liu, X., Lv, T., Sun, Z., 2012. Chem. Commun. 48, 958.
Zou, W.Q., Visser, C., Maduro, J.A., Pshenichnikov, M.S., Hummelen, J.C., 2012. Nat. Phot. 6, 560.
Zucchi, G., Murugesan, V., Tondelier, D., Aldakov, D., Jeon, T., Yang, F., Thuéry, P., Ephritikhine, M., Geffroy, B., 2011. Inorg. Chem. 50, 4851.

This page intentionally left blank

Chapter 262

R_5T_4 Compounds: An Extraordinary Versatile Model System for the Solid State Science

Yaroslav Mudryk*, Vitalij K. Pecharsky*,† and Karl A. Gschneidner, Jr.*,†
*Ames Laboratory US DOE, Iowa State University, Ames, Iowa, USA
†Department of Materials Science and Engineering, Iowa State University, Ames, Iowa, USA

Chapter Outline

Handbook on the Physics and Chemistry of Rare Earths, Vol. 44.
http://dx.doi.org/10.1016/B978-0-444-62711-7.00262-0

1. INTRODUCTION

With the exception of the compounds of 4*f* elements with 3*d* magnetic transition metals (Fe, Co, Ni), which are in the spotlight due to their useful magnetic (e.g., $Nd_2Fe_{14}B$ and $SmCo_5$ magnets, $Tb_{\sim0.3}Dy_{\sim0.7}Fe_2$, also known as Terfenol-D) and hydrogen absorption properties ($LaNi_5$-based alloys for nickel–metal–hydride rechargeable batteries), vast majority of rare earths intermetallic compounds remain an extended family of materials with a rich basic science but little potential for applications. Intermetallic compounds formed by rare earth metals with group 14 elements were among those that were nearly exclusively studied for their interesting fundamental science. The study of the $Gd_5Si_xGe_{4-x}$ system and discovery of other rare earth-based systems with 5:4 stoichiometries substantially changed the status quo. Soon after the giant magnetocaloric effect (GMCE) was reported in $Gd_5Si_2Ge_2$ in 1997 (Pecharsky and Gschneidner, 1997a), a number of other, both fundamentally interesting and potentially useful phenomena have been discovered in the R_5T_4 alloys, where R is the rare earth element and T is a *p*-element from groups 13, 14, and/or 15 of the periodic table. Among those are colossal magnetostriction, spontaneous generation of voltage, pressure enhancement of magnetocaloric effect, unconventional magnetic glass state, spin-flop transition, magnetic deflagration, short-range order magnetic correlations (Griffiths-like phase), and this list is incomplete since science of the R_5T_4 materials remains an active field. Several brief reviews containing information about both chemistry and physics of these extraordinarily interesting compounds have been already published (Miller, 2006; Mudryk et al., 2011; Pecharsky and Gschneidner, 2005, 2007), but a comprehensive review covering most of the available science of these materials is lacking.

In addition to rich physics, R_5T_4 compounds are known for their versatile and interesting structural chemistry. The overall 5:4 molar ratio of *f* metals to *p* elements in these compounds is quite stable, and no statistically significant deviations from the 5:4 stoichiometry have been reported. When one of the components is taken in excess, it is mainly done to compensate for the excessive weight loss of that component due to evaporation (usually R, but sometimes T) during alloy preparation, but the resulting intermetallic phase maintains the 5:4 stoichiometry. For example, one can prepare single-phase Er_5Si_4 compound by starting at the $Er_{5.05}Si_4$ composition, but this does not mean the existence of measurable homogeneity region based of Er_5Si_4.

On the other hand, the R_5T_4 phases form a great variety of solid solutions, and a large number of studies reporting the pseudobinary R_5T_4 systems have been published. For the most part, the substitutions have been performed on the T side, for example, Si was substituted for Ge, Ge for Sb, etc. With a few exceptions (i.e., Yb_5Si_4–Yb_5Ge_4 or Lu_5Si_4–Lu_5Ge_4 systems), these solid solutions are limited: the binary end members have different crystal structures, and quite often an intermediate ternary compound is formed with a closely related crystal structure but unique and interesting properties. Pressure-, temperature-, and magnetic-field-dependent polymorphism is a common structural phenomenon observed in these systems in both binary and intermediate ternary compounds. It is well documented that high-temperature annealing can also affect the crystallography of intermetallic compounds, and in some systems heat-treated and as-cast phase diagrams of pseudobinary R_5T_4 systems are substantially different.

Given the fact that the R_5T_4 compounds have been discovered with all rare earth elements except Eu (Eu_5As_4 is an exception but neither the silicide nor the germanide form at the 5:4 stoichiometry) and Pm (not studied), a large range of solid solutions can be created by substitutions on the R side. Such systems are less studied than those with *p*-element substitutions of the T atoms, in part because most of them are expected to be continuous solid solution systems (at least, at room temperature). For example, no intermediate phase is expected to form in the Gd_5Si_4-Tb_5Si_4 pseudobinary system, because both Gd_5Si_4 and Tb_5Si_4 belong to the same structure type. The ground state of the alloys in these systems, however, may be different from their room temperature structure. The alloys formed by two or more rare earth elements that have opposite signs of their second-order Stevens parameters (Stevens, 1952) may be of particular interest in this regard.

This chapter is focused on the composition–structure–property relationships in pseudobinary R_5T_4 systems as they are known to date, covering most of the available literature through the end of 2012.

2. CRYSTALLOGRAPHY

The R_5T_4 compounds were discovered in 1966, when G.S. Smith, A.G. Tharp, and Q. Johnson (Smith et al., 1966) published a short note reporting compositions and lattice parameters of six germanides and three silicides with the 5:4 stoichiometry. A detailed investigation of the crystal structure of samarium germanide, Sm_5Ge_4, performed using single-crystal X-ray diffractometry quickly followed (Smith et al., 1967a). This compound, as well as other 12 rare earth germanides with the 5:4 stoichiometry (Smith et al., 1967b), was found to crystallize in its own unique crystal structure with space group *Pnma* and a relatively large unit cell (unit cell volume varies from 796 for Lu_5Ge_4 to 1019 Å^3 for La_5Ge_4) containing a total 20 rare earth and 16 germanium atoms distributed among 6 crystallographic sites. The alloys with Eu, Yb, and Pm were not studied at that time. The crystal structures of the rare earths silicides with 5:4 compositions were also reported but the situation here is more complex. Out of eleven reported R_5Si_4 compounds (Ho_5Si_4 and Tm_5Si_4 were not reported), four, formed by light lanthanides La, Ce, Nd, and Pr, crystallize in the tetragonal Zr_5Si_4 type. Six compounds (R = Sm, Gd, Tb, Dy, Er, and Y) are characterized by an orthorhombic unit cell similar to the one adopted by the related germanides (i.e., Sm_5Ge_4 type). Nearly simultaneously, Holtzberg et al. (1967) published a study on R_5T_4 compounds where they argued that germanides and silicides are not isostructural even though they adopt the same space group symmetry and have similar lattice parameters, which was later confirmed by Iglesias and Steinfink (1972). At that time, Lu_5Si_4 compound was thought to be a special case crystallizing in a monoclinic crystal structure with space group symmetry $P2_1/a$, which is considered a simple distortion of the Sm_5Ge_4 type with $\gamma = 92.1°$ (Smith et al., 1967b).

The layered structure of Sm_5Ge_4 was first analyzed by Smith et al. (1967a), who described it as a stacking of three types of atomic networks (layers) along the *b*-axis (the longest axis of the unit cell). They identified (i) layer *G* containing Ge atoms only, (ii) layer *S* containing samarium atoms, and (iii) layer *C*—a combination of both types of atoms (Figs. 1–3). The layers are grouped as *-GSCSG-* (*G*, germanium layer; *S*, samarium layer; and *C*, combined germanium–samarium layer) blocks, and this sequence is being repeated along the *b*-axis. The importance of these five-layer blocks (or slabs), which are essentially two-dimensional assemblies of atoms because their extent in the *ac*-plane is much greater (i.e., they are infinite in the *ac*-plane assuming an ideal crystal) than their thickness along the *b*-axis (1/2 of the unit cell dimension *b*, or approximately 0.7 nm), was not realized until systematic studies of the physical behaviors of these materials started in the late 1990s. The layers *G* and *S* are similar to those found in the tetragonal $CuAl_2$–C16 type, while the networks of *C* and *S* types occur in the U_3Si_2 type of structure. Therefore, in a formal sense, the Sm_5Ge_4-type structure is a hybrid of the $CuAl_2$ and U_3Si_2 networks, as was pointed out by Smith et al. (1967a).

The lattice parameters and atomic positions of Sm_5Ge_4 are summarized in Table 1. Six (three rare earths and three Ge) nonequivalent atomic

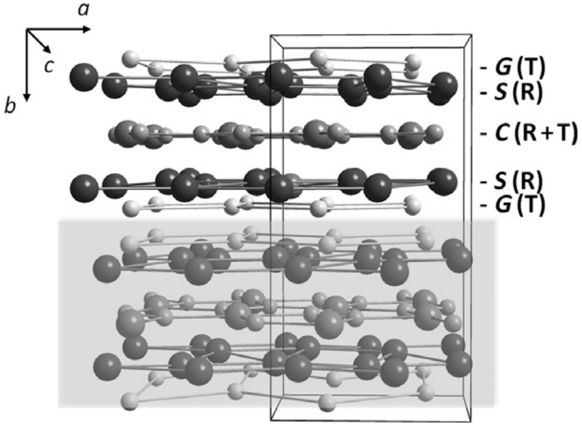

FIGURE 1 Crystal structure of Sm_5Ge_4. Large spheres represent rare earth (R) atoms; small spheres represent Ge (T) atoms. The shaded area highlights the slab that consists of five atomic layers or networks. Atom connectivity is shown for clarity and does not represent actual chemical bonds.

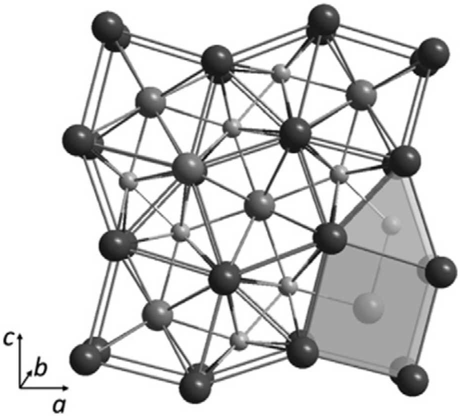

FIGURE 2 Projection of the slab along the *b*-axis. Only *S* and *C* layers are shown for clarity. The highlighted areas represent main building blocks of the slab (distorted cubes and trigonal prisms connected via rectangular faces) and are not the actual polyhedra.

positions combine 36 atoms in one unit cell, resulting in $Z=4$. The coordinates of atoms listed in Table 1 are taken from a recent study by Ahn et al. (2007) (X-ray powder diffraction method); they differ insignificantly from those reported first by Smith et al. (1967a) (X-ray single crystal diffraction method).

The study by Holtzberg et al. (1967) was mainly focused on the physical properties of newly discovered R_5T_4 compounds; however, it also provided new insight into crystallography of this series of alloys. Their study was performed on the R_5Si_4 and R_5Ge_4 binary compositions containing heavy

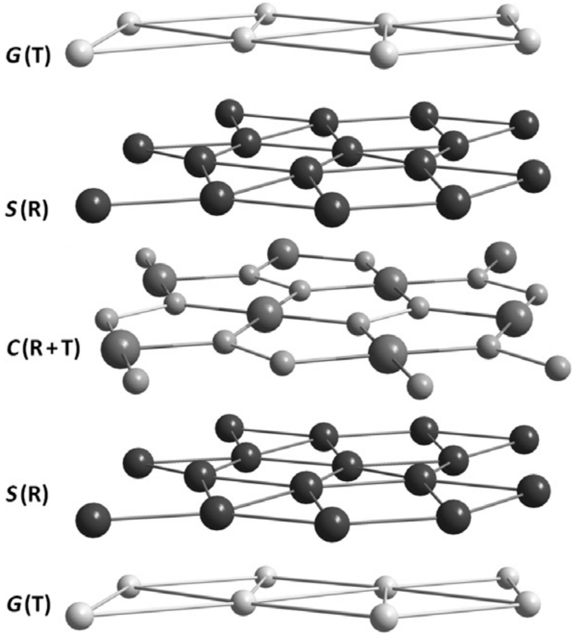

FIGURE 3 Expanded view of atomic networks (layers) of the R_5T_4 layered compounds. Large spheres represent rare earth atoms; small spheres represent T atoms. The T–T distances of the *G* layer are too long for direct bonding and are shown for clarity of presentation only.

TABLE 1 Atomic Coordinates of the Prototype Sm_5Ge_4-Type Crystal Structure

Atom	Wycoff position	*x/a*	*y/b*	*z/c*
Sm1	4(c)	0.2909	¼	0.0011
Sm2	8(d)	−0.0187	0.1000	0.1862
Sm3	8(d)	0.3808	0.8853	0.1647
Ge1	4(c)	0.178	¼	0.362
Ge2	4(c)	0.929	¼	0.905
Ge3	8(d)	0.222	0.952	0.474

The X-ray powder diffraction data used in the Rietveld refinement were collected at ambient conditions. The space group is *Pnma* (no. 62), and the lattice parameters are: $a=7.7726(6)$ Å, $b=14.947(1)$ Å, and $c=7.8611(6)$ Å.
After Ahn et al. (2007).

TABLE 2 Lattice Parameters and Characteristic Temperatures of R_5Si_4 and R_5Ge_4 Compounds (R = Gd, Tb, Dy, Ho, and Er) as Reported by Holtzberg et al. (1967)

Compound	*a* (Å)	*b* (Å)	*c* (Å)	θ_p (K)	T_C (K)	T_N (K)
Gd_5Si_4	7.498	14.752	7.752	349	336	
Tb_5Si_4	7.413	14.625	7.699	216	225	
Dy_5Si_4	7.373	14.536	7.675	133	140	
Ho_5Si_4	7.338	14.449	7.625	69	76	
Er_5Si_4	7.289	14.371	7.591	20	25	
Gd_5Ge_4	7.701	14.832	7.787	94		15, 47
Tb_5Ge_4	7.634	14.701	7.707	80		30
Dy_5Ge_4	7.603	14.640	7.680	43		40
Ho_5Ge_4	7.565	14.582	7.635	16		21
Er_5Ge_4	7.536	14.506	7.600	10		7

The lattice parameters are reported with ±0.005 Å accuracy.

lanthanides (R = Gd, Tb, Dy, Ho, and Er) by means of metallographic, X-ray powder diffraction, and magnetic measurements (Table 2). The most interesting part of this work included the investigation of the pseudobinary $Gd_5Si_xGe_{4-x}$ system and several unusual if not unique observations were made. First, Holtzberg et al. (1967) reported that the silicide and the germanide do not form a continuous $Gd_5Si_xGe_{4-x}$ solid solution, and in the region of the diagram with $\sim 1 < x < 2$ another phase with a more complex (than either the silicide or the germanide) X-ray powder diffraction pattern was observed. Consequently, it became logical to assume that the end members (Gd_5Ge_4 and Gd_5Si_4) have different crystal structures. Second, the silicides have relatively high ferromagnetic ordering temperatures: Gd_5Si_4, for example, has the Curie temperature (T_C) of 336 K, which is by 43 K higher than the T_C of pure Gd. The increase in magnetic exchange interactions between Gd atoms induced by alloying with nonmagnetic Si (in fact dilution) was quite surprising and not understood. The magnetism of the germanides, especially Gd_5Ge_4, did not fit the theory as well: while all R_5Ge_4 compounds were found to be antiferromagnetic, they all have positive Weiss constants (θ_p), and Gd_5Ge_4 has a particularly high value of $\theta_p = 94$ K (Table 2). Moreover, two antiferromagnetic transitions were observed in gadolinium germanide. In addition, the magnetic ordering temperature of the $Gd_5Si_xGe_{4-x}$ alloys in the Ge-rich part of the diagram was found to be very sensitive to the Si content (the $Gd_5Si_xGe_{4-x}$ system will be discussed in detail later). The reported antiferromagnetic ordering temperatures (T_N) of other R_5Ge_4 phases were also a bit unusual—in particular, the high T_N of Dy_5Ge_4 compared to the other R_5Ge_4 compounds.

Even though a number of interesting features was observed in R_5T_4 compounds, especially in the $Gd_5Si_xGe_{4-x}$ system, this family of compounds did not attract much attention of researchers over the next three decades. It is fair to say that no significant effort directed toward a systematic investigation of the R_5T_4 compounds existed before the discovery of the giant magnetocaloric effect in $Gd_5Si_2Ge_2$ by Pecharsky and Gschneidner (1997a). The research on 5:4 systems exploded in the twenty-first century, and nearly 400 papers (the prevailing majority of them in the peer-reviewed literature) devoted to the investigation of R_5T_4 compounds have been published so far. While it is nearly impossible to cover all of this research in this chapter, the important structural features and physical properties of these interesting intermetallic compounds are systematically reviewed below. It is important to note that both the properties and structure of these compounds are extremely sensitive to the purity of starting materials, particularly rare earths, and sometimes even very careful research efforts performed in the best research labs do not really report intrinsic properties of an alloy being examined. Many published results should be carefully scrutinized, especially when purity of starting elements used for the sample preparation is either "commercial grade 99.9% pure rare earth metal" or not reported in the corresponding article.

Structurally, the R_5T_4 compounds can be separated in two major groups: compounds formed by slabs, or layered, and compounds without the slabs, or nonlayered. The nonlayered group mainly constitutes the compounds of light lanthanide elements with group 14 elements and is essentially limited to the Zr_5Si_4 type of crystal structure. The term "nonlayered" should not be taken literally, of course, because practically all intermetallic structures can be represented as a stacking of various atomic nets. However, in case of R_5T_4 compounds the typical layer is not a single atomic net, but a group of five nets stacked on top of each other (Fig. 3). Such group is commonly called a "slab," and this slab substructure repeats itself along the longest (b) axis of the unit cell. The R_5T_4 compounds without the slabs will be called "nonlayered," and those that contain the slabs will be referred to as "layered" (strictly speaking, the names "slab" and "nonslab" structures would be more appropriate but we will use the definitions commonly used in literature). Several different layered structures have been reported to exist in the R_5T_4 series of compounds, and one can safely predict that a few others may be found in the future.

The first 5:4 layered crystal structure was discovered by Smith et al. (1967a) in the Sm_5Ge_4 compound. The -*GSCSG*- sequence of atomic nets is a hybrid combination of the atomic networks characteristic for the $CuAl_2$ and U_3Si_2 types of crystal structure. Essentially, this -*GSCSG*- sequence, or slab, may be considered as a separate structural entity because, as shown in many studies, it is well preserved in a number of related crystal structure types and practically does not change during the massive crystallographic transformations that are typical among R_5T_4 compounds (Pecharsky and Gschneidner, 2001). One may argue that such extraordinary stability of these slabs is one of the reasons why R_5T_4 systems experience these transitions in the first place—the slabs resist any deformations (with a few exceptions) and the relative movements of the slabs with respect to each other remains the only structural degree of freedom that is allowed to change with the change of the external stimuli, such as temperature, hydrostatic pressure, shear stress, and magnetic field. The nature of such extraordinary slab stability in the absence of strong covalent bonding (the prevailing bonding mechanism in R_5T_4 is indeed metallic) is not fully understood at this point. However, it is in the origin of many interesting phenomena observed in the R_5T_4 compounds and the slab structure is a key to their understanding.

In the R_5T_4-related literature, there are often referrals to the interslab/intraslab T atoms and bond distances. Sometimes they are also called interlayer/intralayer distances, when the whole *GSCSG* sequence is considered as one layer. This ambiguity in the definition of a "layer" is, unfortunately, well rooted now in the R_5T_4 literature reflecting the peculiarity of the crystal structure of these compounds. The "inner" *C* net atoms (both rare earths and T) are always considered as intra-, while the T atoms from the "outer" *G* net are considered interslab. The atomic bonds connecting *G–G* layers from the neighboring slabs are typically called interslab T—T bonds, and their length is, probably, the most important crystallographic parameter of the layered structures indicative of both crystallographic and physical nature of the R_5T_4 compounds.

The rare earth atoms from the *S* net can form intraslab bonds with the atoms from the *C* and *G* nets of the same slab or interslab bonds with the atoms of *S* and *G* nets from the neighboring slabs. Given that most rare earth atoms are located in the *S* net, one may expect that the bonds connecting this atomic net with other atoms are most important in determining the magnetic behavior of R_5T_4 compounds. Somehow surprisingly, no clear correlation between *S–S* bond length and magnetism has been found; moreover, the *S* atoms were found to be less relevant in determining the magnetic ground state of compounds compared to the rare earth atoms from the *C* net and T atoms from the *G* net.

Coordination polyhedra of atoms in the Sm_5Ge_4 structure are shown in Fig. 4. Only the shorter (<3.9 Å) R–R distances are taken into account while plotting the polyhedra for atoms Sm2 and Sm3. It is easy to note that Sm2 and Sm3 polyhedra are almost identical and so are the polyhedra for the Ge1 and Ge2. It is also clear that the coordination environment of the intraslab atoms (*C* network, Sm1, Ge1, and Ge2) is more symmetrical compared to the atoms from the outer *S* and *G* networks.

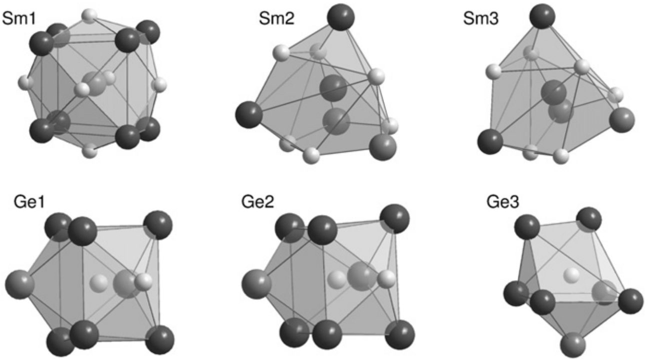

FIGURE 4 Coordination polyhedra of six nonequivalent atomic positions in the Sm_5Ge_4 structure.

Based on the study of the Gd_5Si_4–Gd_5Ge_4 pseudobinary system Holtzberg et al. (1967) suggested that 5:4 germanides and silicides do not share the same type of crystal structure, because they do not form a continuous solid solution and there is an additional intermediate phase with different crystal structure in the middle region of the Gd_5Si_4–Gd_5Ge_4 phase diagram. Iglesias and Steinfink (1972) calculated the crystal structure of Gd_5Si_4 using the X-ray single crystal diffraction method and found that despite its strong similarity to the germanides its crystal structure differs from the one of Sm_5Ge_4. Pecharsky and Gschneidner (1997d), and numerous studies published afterward confirmed that the Gd_5Si_4 and alloys from Gd_5Si_4 side of the quasibinary Gd_5Si_4–Gd_5Ge_4 phase diagram indeed adopt crystal structure that is different from the one of the Gd_5Ge_4 and Gd_5Ge_4-based alloys, which crystallize in the original Sm_5Ge_4-type structure. The analyses of many parameters such as bond lengths, lattice parameters, electronic structure, magnetic ground state, etc. confirm the individuality of the Gd_5Si_4 type. For example, as pointed out by Iglesias and Steinfink (1972), the coordination polyhedron of the interslab Si atom (*G* net) has changed from a distorted pentagonal bipyramid, as described for Sm_5Ge_4, into a trigonal prism of rare earth atoms with two rectangular faces capped by another rare earth atom and Si. Contrary, in the Sm_5Ge_4 type the interslab Ge atom is not bonded to any other Ge atom. Most decisively, the fact that these two crystal structures exist and even coexist in the same compound, transforming into each other depending on the external thermodynamic parameters, indicates that they are two distinct structure types. However, in older handbooks and papers the compounds with Gd_5Si_4 type of crystal structure are sometimes listed with the Sm_5Ge_4 prototype crystal structure.

It is not at all surprising that compounds with the Gd_5Si_4 and Sm_5Ge_4 types of structure were sometimes considered to be crystallographically the same. They have same space group *Pnma*, very similar lattice parameters and atomic positions, and occur in similar systems of the related elements such as Si and Ge. As mentioned above, the easiest and, at the same time, the most reliable way to figure out what type of structure, Gd_5Si_4 or Sm_5Ge_4, exists in a given alloy, is to calculate the interatomic distance between T atoms belonging to the *G* net (T atoms occupying the eightfold atomic site). As shown by Iglesias and Steinfink (1972), Pecharsky and Gschneidner (1997d), and a number of later research papers (Choe et al., 2000, 2003a,b; Morellon et al., 2000) this atomic position is mostly affected by the structural change from Gd_5Si_4 to Sm_5Ge_4 structure. If distance between these T atoms is close to the sum of the T atoms radii, indicating the presence of the covalent-like bonds, then the Gd_5Si_4 type is present. If no bonds between the *G* networks of the neighboring slabs occur, than most likely (there are a few exclusions discussed below) the structure type is Sm_5Ge_4.

These interslab (interlayer) T—T bonds have surprisingly strong influence of the physical properties and ground states of the R_5T_4 compounds. Essentially, the magnetism of these compounds is defined by the presence or absence of atomic bonds that are formed by mainly nonmagnetic elements like Si and Ge, despite the fact that RKKY exchange interactions are carried through the metallic R—R bonds (Pecharsky and Gschneidner, 2001). It is particularly well highlighted during the magnetostructural transitions when the change in crystal structure is accompanied by the change in magnetic ordering. For example, Gd_5Ge_4, which has the Sm_5Ge_4 structure in the absence of applied magnetic field, orders antiferromagnetically at 125 K (Pecharsky and Gschneidner, 1997a,d). Application of a strong enough magnetic field at low temperatures not only induces ferromagnetic order in this compound, but also changes its crystal structure to the Gd_5Si_4 type with the interslab Ge—Ge bond distance of 2.7 Å (Pecharsky et al., 2003a). The difference between the two polymorphs of Gd_5Ge_4 and their powder diffraction patterns are shown in Table 3 and Fig. 5.

The Gd_5Si_4 structure type is also commonly known as the O(I) type and the Sm_5Ge_4 type is often denoted as the O(II) type. Another common structure type observed in the R_5T_4 systems is the M phase, or $Gd_5Si_2Ge_2$ type that adopts monoclinic $P112_1/a$ space group symmetry. The overwhelming majority of R_5T_4 compounds adopt one of these three structure types at room temperature.

The occurrence of a monoclinic phase with lattice parameters close to those of other R_5Si_4 compounds and a probable space group symmetry $P2_1/a$ were reported for Lu_5Si_4 by Smith et al. (1967b).[1] Holtzberg et al. (1967) suggested the existence of the intermediate phase with a crystal structure different from O (I) and O(II) in the $Gd_5Si_xGe_{4-x}$ pseudobinary system. Thirty years later, Pecharsky and Gschneidner (1997b) reported the discovery of the giant magnetocaloric effect in $Gd_5Si_2Ge_2$, and also determined the crystal structure of this compound (Pecharsky and Gschneidner, 1997a,d). They found that $Gd_5Si_2Ge_2$

---

[1] A later study by Gschneidner et al. (2000b) showed that Lu_5Si_4 prepared using high purity Lu crystallizes in the Gd_5Si_4 structure type.

TABLE 3 **Crystallographic Parameters of the O(II)-Sm_5Ge_4 and O(I)-Gd_5Si_4 Structural Polymorphs of the Gd_5Ge_4 Compound Measured at $T=25$ K in Different Magnetic Fields (H)**

O(II)-Gd_5Ge_4: $a=7.6841(2)$ Å, $b=14.7839(5)$ Å, $c=7.7639(3)$ Å; $T=25$ K, $H=0$ kOe				O(I)-Gd_5Ge_4: $a=7.5399(3)$ Å, $b=14.8050(5)$ Å, $c=7.8125(3)$ Å; $T=25$ K, $H=35$ kOe			
Atom	x/a	y/b	z/c	*Atom*	x/a	y/b	z/c
Gd1	0.2936(5)	0.25	−0.0005(5)	Gd1	0.3481(6)	0.25	0.0076(5)
Gd2	−0.0294(2)	0.1013(1)	0.1773(3)	Gd2	0.0146(3)	0.0964(1)	0.1843(3)
Gd3	0.3794(3)	0.8830(1)	0.1642(3)	Gd3	0.3216(3)	0.8787(1)	0.1757(3)
Ge1	0.1786(8)	0.25	0.3663(9)	Ge1	0.2360(9)	0.25	0.3640(9)
Ge2	0.9188(9)	0.25	0.8850(9)	Ge2	0.9723(9)	0.25	0.8937(9)
Ge3	0.2186(6)	0.9564(3)	0.4636(6)	Ge3	0.1503(9)	0.9568(3)	0.4758(7)

Space group is *Pnma* for both structures. Gd1, Ge1, and Ge2 atoms form the *C* network of the slab, Gd2, and Gd3 are parts of the *S* network, and Ge3 belongs to the *G* network. The Ge3—Ge3 bonds are present in the O(I) structure but not in the O(II) structure.

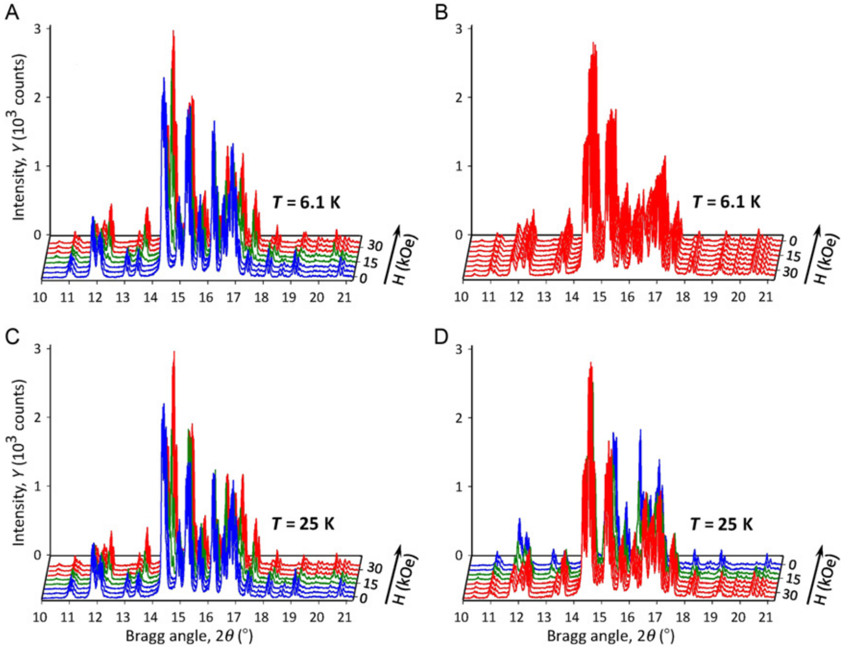

FIGURE 5 The X-ray powder diffraction patterns of the Gd_5Ge_4 at 6.1 and 25 K collected during increasing (A and C) and decreasing (B and D) magnetic field. The patterns were collected using Mo $K\alpha$ radiation.

adopts crystal structure that must be similar to the one reported for Lu_5Si_4 by Smith et al. (1967b), with the monoclinic space group $P112_1/a$ and lattice parameters being intermediate between those for pure germanide and silicide phases. Each of the eightfold sites of the orthorhombic structures (Table 3) splits into pairs of nonequivalent fourfold sites in the monoclinic structure. Choe et al. (2000) performed the X-ray single crystal diffraction study of the $Gd_5Si_2Ge_2$ and parameters of the room temperature crystal structure are listed in Table 4.

The T sites are occupied by a statistical mixture of Si and Ge atoms. It is easy to notice that the Si/Ge ratio is not the same in all positions. In $Gd_5Si_2Ge_2$ structure, the intraslab atomic sites (T1 and T2) have lower concentration of germanium, while the interslab sites (T3 and T4) contain more than 50% of germanium. This preferential occupation tendency is observed among all $Gd_5Si_xGe_{4-x}$ compounds, regardless of the actual type of crystal structure (Choe et al., 2003b; Misra and Miller, 2006). In case of the orthorhombic structures, the T3 (eightfold site) is richer in germanium compared to the fourfold T1 and T2 sites.[2] This indicates that the slab structure itself

TABLE 4 Atomic Positions, Occupations, and Equivalent Thermal Displacement Parameters in the Crystal Structure of $Gd_5Si_2Ge_2$ at 292 K

Atom	*x/a*	*y/b*	*z/c*	Occupancy[a]	$U_{eq.}$, Å^2
Gd1	0.17534(11)	0.75355(6)	0.50562(11)	1	0.0064(2)
Gd2(2A)	0.01731(11)	0.40100(6)	0.18203(11)	1	0.0077(2)
Gd3(2B)	0.00515(11)	0.90165(6)	0.81942(11)	1	0.0075(2)
Gd4(3A)	0.66997(11)	0.37795(5)	0.82256(11)	1	0.0060(2)
Gd5(3B)	0.35660(10)	0.88136(6)	0.16328(11)	1	0.0064(2)
T1	0.2913(3)	0.74793(19)	0.8691(4)	0.461(7) Ge	0.0074(8)
T2	0.0477(3)	0.7483(2)	0.1082(4)	0.429(7) Ge	0.0090(9)
T3(3A)	0.8460(3)	0.45898(16)	0.5294(3)	0.575(7) Ge	0.0083(8)
T4(3B)	0.2068(3)	0.95794(17)	0.4639(3)	0.570(8) Ge	0.0083(8)

The data are taken from Choe et al. (2000), however, the atom names are changed in accordance with their relationship to the atomic positions of the orthorhombic structure types reported in Table 1. Space group (SG) is $P112_1/a$, lattice parameters: $a=7.589(2)$ Å, $b=14.827(3)$ Å, $c=7.7862(2)$ Å, $\gamma=93.262(4)°$.

[a] *All T sites are fully occupied with Si and Ge atoms. In this table, only Ge occupations are listed; Si occupations are 1—occupancy (Ge).*

---

[2] Note that both Choe et al. (2003b) and Misra and Miller (2006) use different notation for the interslab and intraslab T atoms.

prefers the smaller (Si) atoms inside and larger (Ge) atoms on the slab surface. Since Ge and Si are isoelectronic, it is safe to assume that the atomic positions of the outer layer of the slab (*G* net) are located in the atomic environment that can accommodate larger atoms more freely. This supports the notion that the intraslab environment is more rigid and resists expansion.

The monoclinic (M) $Gd_5Si_2Ge_2$ type is often considered as an intermediate structure between O(I) Gd_5Si_4 and O(II) Sm_5Ge_4 types, partially because its lattice parameters have values intermediate between those of two orthorhombic structures, but mainly because of the interslab bonding. The structure is constructed from the same 3^2434 (rare earth atomic networks, *S*) slabs, but contrary to the Sm_5Ge_4 type, where no T—T (Ge3–Ge3) interslab bonding exists, and the Gd_5Si_4 type, where all interslab T atoms form short T—T bonds, in the $Gd_5Si_2Ge_2$ structure 50% percent of the interslab T atoms are connected as short pairs. In $Gd_5Si_2Ge_2$, the T3–T3 atoms (see Table 4) from neighboring slabs are connected ($d_{T3-T3}=2.614$ Å) while the T4–T4 atoms are not—$d_{T4-T4}=3.488$ Å (Choe et al., 2000). When the monoclinic structure transforms into the O(I) Gd_5Si_4 through massive shear movements of the slabs along the *a*-direction, the T4–T4 atoms reconnect and the nonequivalent fourfold T3 and T4 positions of the M structure become the same eightfold T3 position of the O(I) structure. Interestingly, no breaking of the monoclinic T3—T3 bonds that would result in the transition from the M phase into the O(II) Sm_5Ge_4-type phase has been reported so far. Also, the polymorphic transformation involving the O(II) structure rarely results in the partial formation of the T–T dimers and occurrence of the $Gd_5Si_2Ge_2$ structure. Instead, the O(I) structure is often the end result of such transformation, except for a few nonconventional cases, when crystallographic transformations typical for a particular chemical composition only occur.

Figure 6 schematically illustrates the crystallographic relationships between the O(II), O(I), and M structures. The O(I) phase may transform into either O(II) or M phase by breaking all or half of the interslab T—T bonds, respectively. It is important to note that the interslab surfaces with or without T–T dimers alternate along the *b*-axis, creating the monoclinic distortion. There is a clear correlation between the crystal structure type and magnetic properties of R_5T_4 compounds (Morellon et al., 1998a; Pecharsky and Gschneidner, 1997d, 2001; Rao, 2000).

Application of the Zintl–Klemm formalism to these crystal structures reveals another interesting tendency—change of the electron concentration depending on the presence of the T—T bonds (Choe et al., 2000, 2003a). Indeed, when Gd atoms are considered as 3+ ions and group 14 elements as 4− ions, then the charge-balanced formula of the Gd_5Si_4 compound can be written as $\left[\left(Gd^{3+}\right)_5\left({T_2}^{6-}\right)_2\left(3e^-\right)\right]$ with three electrons assigned to the conduction band, because all Si(*T*) atoms in this structure form covalently bonded T_2 dimers each using one electron for such chemical bonding. When some of these bonds are

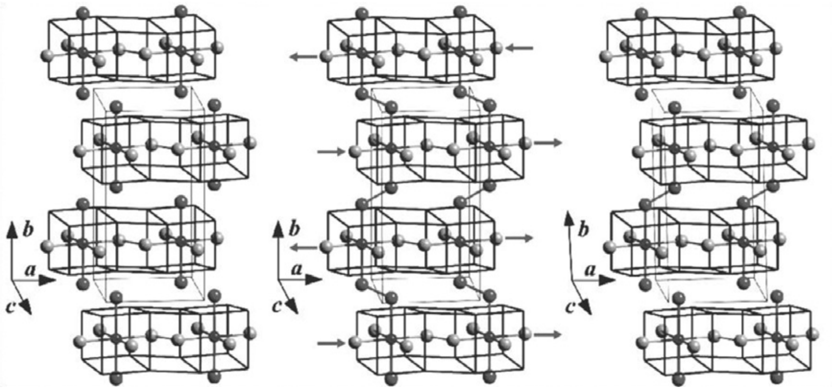

FIGURE 6 The schematic of relationships between main crystallographic types observed in the $Gd_5(Si_xGe_{4-x})$ system (Pecharsky and Gschneidner, 2001). From left to right: O(II)-Sm_5Ge_4 type with all inteslab T—T bonds "broken," O(I)-Gd_5Si_4 type with all T—T interslab bonds present, and M-$Gd_5Si_2Ge_2$ type with half of the interslab T—T bonds formed. The rare earth atoms located in the corners of the prisms are not shown for clarity.

broken, the dimers change into a pair of T^{4-} monomers. Therefore, for the $Gd_5Si_2Ge_2$, the charge-balanced formula is $\left[\left(\mathrm{Gd}^{3+}\right)_5\left(\mathrm{T}_2{}^{6-}\right)_{1.5}\left(\mathrm{T}^{4-}\right)\left(2\mathrm{e}^-\right)\right]$, and for the Gd_5Ge_4 – $\left[\left(\mathrm{Gd}^{3+}\right)_5\left(\mathrm{T}_2{}^{6-}\right)\left(\mathrm{T}^{4-}\right)_2\left(1\mathrm{e}^-\right)\right]$. As a result, the number of electrons potentially associated with the conduction band drops indicating possible changes in physical properties. It would be fair to admit that this approach oversimplifies complex chemical and magnetic interactions occurring in the R_5T_4 systems, and, obviously, does not take into account crystallographic changes induced by the variation of external thermodynamic parameters, such as temperature, hydrostatic pressure, and magnetic field. However, it became useful in analyses of the effect of tetravalent element substitutions by, for example, trivalent elements like Ga on the crystal structure of R_5T_4 alloys (Mozharivskyj et al., 2003).

One intrinsic structural feature of the monoclinic phase, which was not observed in either of the orthorhombic structures, is the intrinsic presence of the nonmerohedral twinning. The original X-ray single crystal diffraction study of the $Gd_5Si_2Ge_2$ (Choe et al., 2000) showed a considerable number of Bragg reflections with noninterger indices, all multiples of 1/9, along the *b*-axis only. The nonmerohedral twinning for which only a small fraction of reflections from two twin components superimpose, while the rest (majority) of the reflections remain separate, was indeed found to be very common in compounds with the M-type crystal structure, for example, in $Gd_5Si_{1.5}Ge_{2.5}$ (Choe et al., 2003a). The microstructural investigation of $Gd_5Si_2Ge_2$ by Meyers et al. (2002a) revealed a twin law, which transforms one twin component into the other, as follows:

$$\begin{aligned} a' &= a \\ b' &= b + a\left(\frac{2b}{a}\right)\cos\gamma \cong b - 0.2229a \cong b - \frac{2}{9}a \\ c' &= -c \end{aligned}$$

When the monoclinic phase transforms into O(I) phase, for example, via cooling below the transition temperature, the twinning disappears, but after the system returns to the previous condition, where *M* is the stable phase, the twinning reappears.

While the $Gd_5Si_2Ge_2$ type may be considered as the intermediate structure between Gd_5Si_4 and Sm_5Ge_4 types, the closet structural relative to these orthorhombic types was first discovered in Pu–Rh system. Chebotarev and Beznosikova (1976) reported the existence of the crystal structure very similar to those of Sm_5Ge_4 and Gd_5Si_4 in the Pu_5Rh_4 and Pu_5Ir_4 compounds. Cromer (1977) also analyzed and published the crystal structure of Pu_5Rh_4, and the corresponding type of crystal structure was named after this compound. Its space group, axial dimensions, and Wyckoff sites are the same for the three orthorhombic structures and the same -*GSCSG*- sequence of atomic networks maintains the slab structure for the Pu_5Rh_4. The main difference between these structure types is in the positional parameters of atoms, particularly in their locations along the *a*-axis (i.e., the values of the *x* parameters, Table 5). Such difference leads to a slightly different coordination environment with different number of nearest neighbors and modified interatomic distances. Clearly, from the crystallographic point of view it is more appropriate to call the Pu_5Rh_4 as an intermediate structure between Sm_5Ge_4 and Gd_5Si_4, even though the monoclinic structure is often present in the pseudobinary R_5T_4 diagrams. At the same time, Mozharivskyj et al. (2003) reported the Pu_5Rh_4 type of crystal structure in Gd_5GaGe_3 alloy, which on the Gd_5Ge_4–$Gd_5Ge_{1.8}Ga_{2.2}$ pseudobinary phase diagram occupies a middle position between the compounds with O(II) and O(I) crystal structures (the $Gd_5Ga_xGe_{4-x}$ solid solution is terminated at $x > 2.2$).

The first-principles calculations performed by Paudyal et al. (2010a) confirm the stability of the Pu_5Rh_4 structure in the Gd_5Ge_4-based alloys. It is more typical, however, for this structure type to be present in the compounds formed by the rare earths elements and the 4*d* and 5*d* transition metal elements; for example, in the R_5Pt_4 series of intermetallic compounds (Le Roy et al., 1978). Such compounds are not in the scope of this chapter, and, therefore, the Pu_5Rh_4 type will be rarely mentioned. However, it is important to note that the R_5T_4 compounds with layered structures are formed by rare earth elements with many other elements from the periodic table and the slabs are, indeed, stable structural elements commonly occurring in many intermetallic compounds.

According to Mozharivskyj et al. (2003), the interslab T3—T3 bond distances in Pu_5Rh_4 type indicate that T atoms are connected in this structure similar to the O(I) Gd_5Si_4, which agrees with calculated ferromagnetic type of

TABLE 5 Comparison of Positional Parameters of R_5T_4 Orthorhombic Structures with Space Group *Pnma* (Cromer, 1977)

	Wyckoff position	Sm_5Ge_4	Pu_5Rh_4	Gd_5Si_4
R1 *x*	4c	0.2880	0.322	0.3560
y		0.25	0.25	0.25
z		−0.0024	0.11	0.0113
R2 *x*	8d	0.3795	0.342	0.3164
y		0.6157	0.622	0.6223
z		0.1612	0.162	0.1795
R3 *x*	8d	−0.0253	0.001	0.0289
y		0.3996	0.410	0.4028
z		0.1781	0.180	0.1827
T1 *x*	4c	0.1761	0.190	0.2411
y		0.25	0.25	0.25
z		0.3667	0.356	0.3746
T2 *x*	4c	0.4132	0.459	0.4787
y		0.25	0.25	0.25
z		0.6115	0.607	0.5986
T3 *x*	8d	0.2206	0.194	0.1435
y		0.5449	0.534	0.5395
z		0.4688	0.451	0.4716

Equivalent atoms have been chosen and reordered. The Sm_5Ge_4 type was reported by Smith et al. (1967a), Gd_5Si_4 type by Iglesias and Steinfink (1972), and Pu_5Rh_4 type by Chebotarev and Beznosikova (1976).

exchange interactions in both compounds (Paudyal et al., 2010a). However, these bonds are also longer: d_{T3-T3} is 2.93 Å in Gd_5GaGe_3 (Pu_5Rh_4 type) versus 2.74 Å in $Gd_5Ga_2Ge_2$ (Gd_5Si_4 type). This again indicates the intermediate position of the Pu_5Rh_4 structure compared to O(II) and O(I) types.

The Pu_5Rh_4 type of structure has been observed in the R_5T_4 compounds when the 14 group element (e.g., Ge) was substituted by the 13 group element (Ga). With the inclusion of the 15 group element as T element, for example, with As or Sb, R_5T_4 compositions tend to crystallize in a more symmetric crystal structure, which is closely related to Sm_5Ge_4 and essentially maintains the same slab structure. The new orthorhombic structure type was originally reported for Eu_5As_4 adopting space group symmetry *Ccmb* with the following

TABLE 6 Atomic Positions for the $Tm_5Sb_2Si_2$ (Kozlov et al., 2004)

Atom	Wyckoff cite	*x*/*a*	*y*/*b*	*z*/*c*	U_{eq}, $Å^2 \times 10^{-3}$
Tm1	4a	0	0	0	28
Tm2	16g	0.1291	0.1650	0.3355	35
Sb	8d	0.2049	0	0	35
Si	8f	0	0.3608	0.1380	29

lattice parameters: $a = 8.021$ Å, $b = 15.802$ Å, and $c = 8.058$ Å (Wang et al., 1978). Two nonequivalent eightfold atomic positions R2 and R3 from the *S* networks are combined into one 16-fold site, and the fourfold intraslab T1 and T2 positions (*C* network) are also combined into one eightfold site. Kozlov et al. (2004) reported an ordered superstructure to the Eu_5As_4 type, $Tm_5Si_2Sb_2$, in which antimony atoms occupy interslab T position and silicon atoms are located intraslab (Table 6). Space group symmetry was determined as *Cmca* with lattice parameters $a = 14.768$ Å, $b = 7.723$ Å, $c = 7.741$ Å, and both the unit cell orientation and the origin of the unit cell are modified compared to the Eu_5As_4 and other R_5T_4 slab structures; however, this is essentially the same -*GSCSG*- slab stacking motif occurring along the longest axis of the unit cell. There are practically no bonds between Sb atoms meaning that all T—T interslab bonds are "destroyed" in this structure type.

A series of $R_5Sb_2Si_2$ and $R_5Sb_2Ge_2$ compounds adopting $Tm_5Sb_2Si_2$ structure type has been reported by Kozlov et al. (2004). Recent work by Chernyshov et al. (2006) indicates the presence of a limited ternary solid solution of the $Tm_5Sb_2Si_2$ structure in the $Gd_5Sb_xGe_{4-x}$ pseudobinary system indicating that Ge and Sb can form a statistical mixture while occupying the T sites in the $Tm_5Sb_2Si_2$ crystal structure. Such mixed occupancy has been also observed for the alloys with the Sm_5Ge_4 structure type which exist at $x < 2$ in the same system. However, even in this structure type there is a strong tendency for larger Sb atoms to occupy the interslab position only (Chernyshov et al., 2009). A similar situation occurs in the $Gd_5Sb_xSi_{4-x}$ system (Svitlyk et al., 2010), where Eu_5As_4 type of structure was reported at $x > 2$. Crystallographic analysis shows strong preference of Sb atoms to occupy the interslab positions and no more than 6% of Sb is accommodated inside the slabs. Therefore, the solid solution alloys with the *Cmca* structure are at least partially ordered superstructures of Eu_5As_4, and using the $Tm_5Sb_2Si_2$ type for the description of their crystal structure may also be an appropriate choice. References to both structure types can be found in literature.

Apparently, the majority of layered R_5T_4 compounds crystallize in four major structure types: O(I)-Gd_5Si_4, M-$Gd_5Si_2Ge_2$, O(II)-Sm_5Ge_4, and $Tm_5Sb_2Si_2$ (or

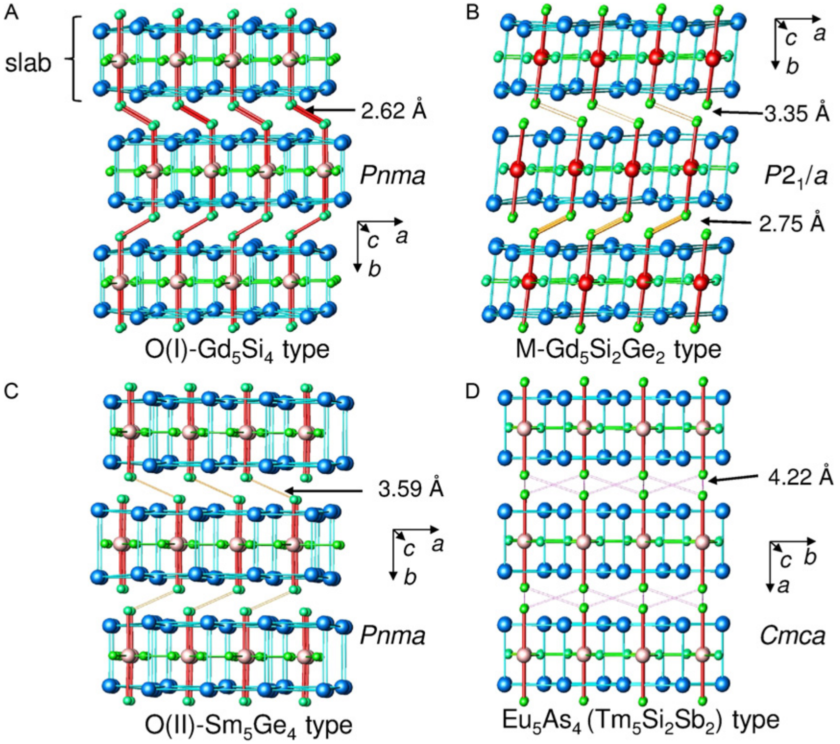

FIGURE 7 Crystal structure types that are most common in the R_5T_4 compounds. The large light spheres indicate positions of the interslab R atoms, while the large dark spheres mark the rest of the R atoms. Small gray spheres represent T atoms (T = Si, Ge, Sn, Ga, or Sb). The interslab T–T distances are the only interslab distances shown.

Eu_5As_4). They all have the distinct slab structure, and, apart from space group symmetry, the main difference between them lays in the presence or absence of the interslab T—T bonds (Fig. 7). The compounds with Pu_5Rh_4 structure are relatively rare among R_5T_4, even though this structure becomes much more common among R_5M_4 phases, where M is transition metal.

In addition to the above mentioned structures, there are a few peculiar cases of the layered (slab) intermetallics when R_5T_4 alloys either (a) crystallize in their unique structure types at nonambient conditions or (b) adopt other known structure types at particular chemical compositions.

The low-temperature crystal structure of Ho_5Ge_4 is an example of the former case (Singh et al., 2009). The Ho_5Ge_4 compound adopts the O(II)-Sm_5Ge_4 structure at room temperature. The X-ray powder diffraction measurements, which were later confirmed by neutron diffraction experiments (Ritter et al., 2009), showed that the paramagnetic–antiferromagnetic transition in Ho_5Ge_4 at 23 K is accompanied by lattice deformation in the crystallographic *ac*-plane (and not in the *ab*-plane, see Fig. 7, as in the majority of known cases). The new crystal structure is monoclinic with the $P12_1/m1$ space group and the monoclinic angle is $\beta=90.57°$ (Table 7).

A number of interesting crystal structures has been observed during chemical substitution of the Gd_5Si_4 phase by Bi. Svitlyk et al. (2009a) reported that in addition to the Gd_5Si_4 structure type observed in the $Gd_5Si_{3.904}Bi_{0.096}$, and Eu_5As_4 type observed for the $Gd_5Si_{2.416}Bi_{1.584}$ compositions, at higher bismuth concentrations new layered crystal structures appear with the unit cell doubled along the long axis. The slabs are preserved in those structures but their stacking along the long axis becomes more complicated allowing two new tetragonal crystal structure types. The $Gd_5Si_{1.93}Bi_{2.07}$ compound crystallizes with the space group $I4_1/acd$, and lattice parameters $a=7.9858$ Å, $c=30.700$ Å; $Gd_5Si_{1.58}Bi_{2.42}$ adopts space group $P4_2bc$, and has lattice parameters $a=8.0296$ Å, $c=30.883$ Å. The atomic parameters for these new crystal structures are presented in Table 8.

Another layered crystal structure was observed in the $Gd_{5-x}Y_xGe_4$ system by Misra and Miller (2008). Despite the fact that both end members of this pseudobinary system crystallize in the Sm_5Ge_4 structure type, for the composition range of $3.6 \leq x \leq 4.2$ a monoclinic $U_2Mo_3Si_4$-type structure occurs as a majority phase (Table 9). This type of structure, which is rarely observed in the R_5T_4 systems, is also built by stacking the typical -*GSCSG*- slabs. Interestingly, the unit cell volume of this structure is half of the other main structural types containing slabs. This happens because the longest axis of these types (usually *b*-axis) is two times shorter in $U_2Mo_3Si_4$ type where all lattice dimensions are quite similar to each other. There are no direct bond distances between the interslab germanium atoms, which makes it more similar to the orthorhombic O(II)-Sm_5Ge_4 structure than to the another monoclinic structure type, M-$Gd_5Si_2Ge_2$, where half of the interslab T atoms are connected with each other.

Smith et al. (1966) reported that the crystal structure of Nd_5Si_4 (Table 10) was different from the majority of other R_5Si_4 and R_5Ge_4 compounds, and soon after Smith et al. (1967b) found that a few additional R_5Si_4 compounds formed by light lanthanide elements (R = La, Ce, Pr) crystallize in the Zr_5Si_4 tetragonal structure type (Pfeifer and Schubert, 1966). No tetragonal phases were observed among R_5Ge_4 compounds (Smith et al., 1967b). Apparently, as shown by Le Roy et al. (1978), Zr_5Si_4 type has same structural features (distorted cubes and trigonal prisms) as layered structure types, for example, Pu_5Rh_4, but instead of the whole slabs stacked alternately—an essential feature of all previously discussed structures—only fragments of the slabs are arranged alternately. The absence of slabs dictates a substantially different behavior of Zr_5Si_4 type compounds when compared to slab-based structures—the shift of slabs with respect to each other, which typically results in change of interslab bonding and physical properties in the layered R_5T_4 compounds, cannot occur in the nonslab phases, and their physics is not as interesting compared to their layered relatives.

TABLE 7 Crystallographic Data of Ho_5Ge_4 at 293 and 15 K

T = 293 K; SG *Pnma*; a = 7.5789(2) Å, b = 14.5876(4) Å, c = 7.6478(2) Å, β = 90°				T = 15 K, SG $P12_1/m1$; a = 7.5661(2) Å, b = 14.5589(3) Å, c = 7.6226(2) Å, β = 90.572(2)°			
Atom	x/a	y/b	z/c	*Atom*	x/a	y/b	z/c
Ho1	−0.0295(2)	0.6001(1)	0.1787(2)	Ho1A	−0.0328(4)	0.6021(2)	0.1793(4)
				Ho1B	0.4691(4)	0.5998(2)	0.3212(4)
Ho2	0.3787(2)	0.1173(1)	0.1625(2)	Ho2A	0.3827(4)	0.1167(2)	0.1640(4)
				Ho2B	0.8771(4)	0.1173(2)	0.3370(4)
Ho3	0.2100(3)	1/4	0.4998(3)	Ho3A	0.2122(5)	1/4	0.4982(7)
				Ho3B	0.7120(6)	1/4	−0.0030(7)
Ge1	0.2175(5)	0.0454(2)	0.4671(5)	Ge1A	0.2210(8)	0.0445(4)	0.4695(9)
				Ge1B	0.7223(8)	0.0471(4)	0.026(1)
Ge2	0.0801(7)	1/4	0.1149(7)	Ge2A	0.085(1)	1/4	0.111(2)
				Ge2B	0.583(1)	1/4	0.386(1)
Ge3	0.3347(6)	1/4	0.8647(7)	Ge3A	0.338(1)	1/4	0.858(1)
				Ge3B	0.832(1)	1/4	−0.364(1)

TABLE 8 Atomic and Isotropic Thermal Displacement Parameters for New Crystal Structures Observed in the $Gd_5Si_{4-x}Bi_x$ System (Svitlyk et al., 2009a)

Atom	Site	*x/a*	*y/b*	*z/c*	Occupancy	*U* (Å^2)
$Gd_5Si_{1.93}Bi_{2.07}$ (*I*4_1/*acd*)						
Gd1	32g	0.3331	0.9178	0.06149	1	0.0163
Gd2	8a	0	0.25	0.375	1	0.0116
Bi/Si1	16d	0	0.25	0.97841	0.938/0.062	0.0135
Bi/Si2	16f	0.3658	$x+0.25$	0.125	0.098/0.902	0.011
$Gd_5Si_{1.58}Bi_{2.42}$ (*P*4_2*bc*)						
Gd1	8c	0.6754	0.1615	0.06388	1	0.043
Gd2	8c	0.6692	0.1583	0.93612	1	0.046
Gd3	8c	0.1693	0.1699	0.3137	1	0.026
Gd4	8c	0.1604	0.1652	0.1864	1	0.026
Gd5	4a	0	0	0.9987	1	0.034
Gd6	4b[a]	0	0.5	0.2478	1	0.024
Bi1	4a	0	0	0.1033	1	0.033
Bi2	4a	0	0	0.8965	1	0.035
Bi3	4b	0	0.5	0.3511	1	0.039
Bi4	4b	0	0.5	0.1459	1	0.024
Bi/Si5	8c	0.6409	0.8666	0.9974	0.211/0.789	0.037
Bi/Si6	8c	0.1422	0.8647	0.2470	0.211/0.789	0.025

[a] *4a in Svitlyk et al. (2009a).*

Figure 8 shows the crystal structure of Nd_5Si_4 highlighting the similarities in coordination polyhedra between Sm_5Ge_4 and Zr_5Si_4 structure types, particularly the similar environment of the R1 atoms and of the T atoms (see also Fig. 4).

3. $Gd_5Si_xGe_{4-x}$ PSEUDOBINARY SYSTEM

The $Gd_5Si_xGe_{4-x}$ is the most studied pseudobinary system of the R_5T_4 intermetallic alloys. Over 200 publications report the crystallography and physical properties of the $Gd_5Si_xGe_{4-x}$ alloys—half of all published papers about

TABLE 9 Crystallographic Data for the $Gd_1Y_4Ge_4$ Alloy Crystallizing in the $U_3Mo_2Si_4$ Type of Crystal Structure (Misra and Miller, 2008)

Atom	Wyckoff cite	*x*/*a*	*y*/*b*	*z*/*c*	Occupancy[a]	U_{eq} (Å^2)
M1	4e	0.7007(1)	0.3219(1)	0.0571(1)	0.32(1)	0.011(1)
M2	4e	0.2658(1)	0.3373(1)	0.2776(1)	0.13(1)	0.009(1)
M3	2a	0	0	0	0.09(1)	0.009(1)
Ge1	4e	0.4112(2)	0.0312(1)	0.1807(2)	1	0.010(1)
Ge2	4e	0.0083(2)	0.6300(1)	0.1286(2)	1	0.011(1)

Space group $P2_1/c$; $a=8.0067(9)$ Å, $b=7.7540(10)$ Å, $c=7.6174(8)$ Å, $\beta=113.04(1)°$.

[a] *All M sites are fully occupied by a mixture of Gd and Y atoms. Only Gd occupations are listed.*

TABLE 10 Crystallographic Data for the Nd_5Si_4 Alloy Crystallizing in the Zr_5Si_4 Type of Crystal Structure (Yang et al., 2002a)

Atom[a]	Wyckoff cite	*x*/*a*	*y*/*b*	*z*/*c*
Nd1	4a	0.3129	0.3129	0
Nd2	8b	0.3696	0.0114	0.4542
Nd3	8b	0.1300	−0.0155	0.8742
Si1	8b	0.1871	0.1638	0.6945
Si2	8b	0.2864	0.9349	0.0627

Space group $P4_12_12$; $a=7.8694$ Å, $c=14.8077$ Å.

[a] *All sites are fully occupied.*

R_5T_4. The majority of interesting physical phenomena, among them giant magnetocaloric effect (GMCE), giant magnetostriction (GMS), giant magnetoresistance (GMR), magnetic glass state (kinetic arrest), magnetic deflagration, spontaneous generation of voltage (SGV), were first observed, reported, and explained during the investigation of the $Gd_5Si_xGe_{4-x}$ alloys. The current understanding of the relationships between magnetism and structure in R_5T_4 compounds, as well as in some other systems exhibiting magnetostructural transitions, was mainly developed through the studies of the composition–structure–property relationships of the $Gd_5Si_xGe_{4-x}$ compounds. Therefore, the knowledge of crystallography and properties of the $Gd_5Si_xGe_{4-x}$ alloys is essential for understanding the behavior of all R_5T_4 slab structures with and without Gd.

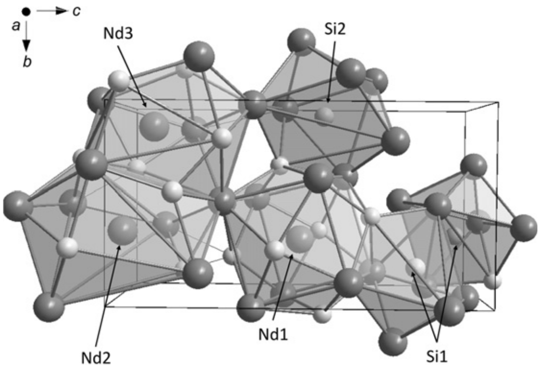

FIGURE 8 Coordination polyhedra in the Nd_5Si_4 compound of the Zr_5Si_4 structure type. Only atoms included in polyhedra are shown for clarity.

In addition, $Gd_5Si_xGe_{4-x}$ attracts so much attention because it is the only R_5T_4 system that can show many of the above mentioned phenomena near room temperature, which makes those phenomena not only fundamentally interesting but also potentially useful for practical applications. The high magnetic ordering temperature of the Gd_5Si_4 and silicon rich $Gd_5Si_xGe_{4-x}$ alloys had been noted long time ago by Holtzberg et al. (1967), but this finding did not spark much attention from the researchers. However, the discovery of the giant magnetocaloric effect in $Gd_5Si_2Ge_2$ (Pecharsky and Gschneidner, 1997b) became an open invitation for other scientists to look closer at this system, especially when it was shown that the magnetocaloric machines using $Gd_5Si_2Ge_2$ or materials with similar properties may become competitors to the commonly used vapor pressure refrigeration systems on the industrial scale (Zimm et al., 1998). This discovery was a major milestone for the whole magnetic refrigeration research field. A reader interested in the magnetic refrigeration may find a few informative reviews about the magnetocaloric effect elsewhere (Franco et al., 2012; Gschneidner and Pecharsky, 2000b; Guttfleisch et al., 2012; Miller, 2006; Pecharsky and Gschneidner, 2005; Smith et al., 2012; Yu, et al., 2010).

It is well established by now that the change in the crystal structure of the $Gd_5Si_xGe_{4-x}$ and R_5T_4 alloys in general occurs in accord with the change in the magnetic ground state (or *vice versa*) and can be induced by: (1) change in x (chemistry), (2) cooling and/or heating through the magnetic ordering temperature, (3) application of the magnetic field above H_{CR} or demagnetization from high-field state, and (4) application of hydrostatic pressure. In addition, the crystal structure may be altered by such factors as: (1) heat treatment of the alloys near the phase boundaries, (2) varying the purity of the starting materials, and (3) application of shear stress during mechanical grinding (observed in Er_5Si_4, Cao et al., 2013). Such extraordinary sensitivity of these compounds to the external thermodynamic stimuli makes the $Gd_5Si_xGe_{4-x}$

and other R_5T_4 systems an excellent playground for the study of the composition–structure–property relationships, as well as making them promising candidates for use in future technological applications. For example, the fact that the magnetostructural response in these compounds may be triggered by a number a various factors (temperature, magnetic field, pressure) without an external source of power makes them interesting for multifunctional sensors.

The interslab T—T bond length is a crucial structural parameter influencing magnetism of Gd_5T_4 phases (Choe et al., 2000; Rao, 2000). While the situation is different in other R_5T_4 systems, in $Gd_5Si_xGe_{4-x}$ the ferromagnetic state is always associated with the O(I)-Gd_5Si_4 type of crystal structure, and, therefore, with shorter T—T bonds (Pecharsky and Gschneidner, 2007; Pecharsky et al., 2003a). The physical phenomena occurring at the magnetostructural transition are, in effect, caused by the breaking and formation of single pair of the essentially nonmagnetic tetralide atoms.

Haskel et al. (2007) established the role of the Ge atoms in bridging ferromagnetic interactions in the $Gd_5Si_2Ge_2$ and $Gd_5Si_{0.5}Ge_{3.5}$ using the X-ray magnetic circular dichroism (XMCD) spectroscopy. The induced magnetic polarization of the Ge electrons caused by hybridization of the Gd 5*d* and Ge 4*p* conduction bands plays a primary role in supporting three-dimensional ferromagnetism of the $Gd_5Si_xGe_{4-x}$ alloys enabling long-range exchange interactions between Gd 4*f* moments in adjacent slabs. Breaking of the Ge(Si)—Ge(Si) interslab bonds weakens such interactions and effectively destroys long-range ferromagnetic order.

As shown by the high pressure XMCD studies (see Section 3.7), the role of Si atoms on the onset of ferromagnetism in $Gd_5Si_xGe_{4-x}$ is also significant. In addition to the well-established presence of chemical pressure exerted on the system due to smaller size of Si atoms compared to Ge atoms, there must be additional ways for the Si to promote the formation of the O(I)-FM phase, which are not completely known at this point. A plausible scenario includes the involvement of the 3*p* Si bands in the *p*–*d* hybridization necessary to support the three-dimensional ferromagnetism in $Gd_5Si_xGe_{4-x}$, decreasing the total energy of Si-substituted alloys in the ferromagnetic state. This is partially supported by the fact that the magnetic ordering temperature and, consequently, magnetic exchange interactions in Gd_5Si_4 are stronger than in pure Gd.

3.1. Phase Equilibria

The early study by Holtzberg et al. (1967) reported a tentative $Gd_5Si_xGe_{4-x}$ phase diagram. The authors observed an existence of an intermediate phase with crystal structure different from those of Gd_5Si_4 and Gd_5Ge_4. Later, during investigation of the giant magnetocaloric effect in $Gd_5Si_xGe_{4-x}$, Pecharsky and Gschneidner (1997d) refined the pseudobinary phase diagram of $Gd_5Si_xGe_{4-x}$ system. They determined the crystal structure of the intermediate phase, and found that it crystallizes in its own structure type, $Gd_5Si_2Ge_2$. In addition to the intermediate monoclinic phase, the alloys from the Ge-rich side of the diagram were found to crystallize in the O(II)-Sm_5Ge_4 type, while the alloys from the Si rich part adopt the O(I)-Gd_5Si_4 type of crystal structure. The magnetic phase diagram of $Gd_5Si_xGe_{4-x}$ system was constructed in the same study. It was immediately pointed out that the distinct magnetic behavior of alloys from the three different regions in the system correlates with the crystal structure of the alloys from the respective regions (Pecharsky and Gschneidner, 1997d).

The recent and the most complete $Gd_5Si_xGe_{4-x}$ pseudobinary phase diagram was constructed by Pecharsky et al. (2002a). The crystal structure, lattice parameters, and magnetic ordering temperatures were determined for the total of 27 alloys with different x. Most alloys were analyzed as-cast, but those with the monoclinic crystal structure at room temperature were also heat treated at 1300 °C for 1 h in Ta crucibles under high vacuum using an induction furnace. The heat treatment does not have a significant effect on the values of lattice parameters of the monoclinic $Gd_5Si_xGe_{4-x}$, although it was found that annealing may affect the phase content of the alloys at compositions near the phase boundaries. The main features of the 1997 phase diagram were confirmed, such as the existence of three distinct magnetic–crystallographic regions, and the strong compositional variation of the magnetic ordering temperature, particularly in the Ge-rich region. The location of the O(II)–M boundary was corrected. The resulting room temperature crystallographic phase diagram is shown in Fig. 9 (Pecharsky et al., 2002a). The lattice parameters and unit cell volume values from the studies by Holtzberg et al. (1967) and Pecharsky and Gschneidner (1997d) are shown for comparison, and they all are in good agreement with each other.

It is important to remember that the phase diagram shown in Fig. 9 is drawn for the ambient conditions. Morellon et al. (1998a) were first to show that the $Gd_5Si_{1.8}Ge_{2.2}$ compound, which has the monoclinic structure at room temperature (RT), transforms into the orthorhombic Gd_5Si_4-type structure below ~230 K. The $Gd_5Si_{0.4}Ge_{3.6}$ alloy, which has O(II)-Sm_5Ge_4 structure at room temperature also transforms into the O(I)-Gd_5Si_4 below ~80 K (Morellon et al., 2000). Similar temperature-induced transformations occur in other $Gd_5Si_xGe_{4-x}$ samples with $0<x\leq 2$ (Choe et al., 2000; Liu et al., 2001a; Mudryk et al., 2008). Therefore, at different temperatures this phase diagram will look differently. For example, at liquid nitrogen temperature (~80 K) the monoclinic phase does not exist in the $Gd_5Si_xGe_{4-x}$ system, and only two phase regions, Ge-rich O(II) and Si-rich O(I), can be observed (Liu et al., 2001a,b). The structure types and lattice parameters of $Gd_5Si_xGe_{4-x}$ alloys with $x=0.0$, 0.4, 0.6, 0.8, 1.2, 1.4, 1.6, 1.84, 2.4, 3.2, and 4.0 determined at room temperature and at 80 K are listed by Liu et al. (2001b).

The phase boundaries may slightly shift after heat treatment. The location of the O(I)–M boundary is especially sensitive to annealing, and the 5:2:2

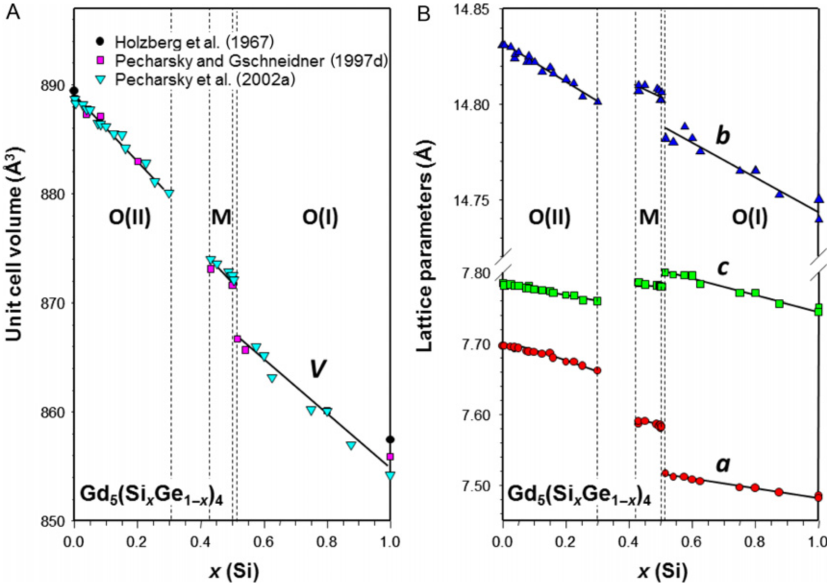

FIGURE 9 The room temperature crystallographic phase diagram of the $Gd_5Si_xGe_{4-x}$ system: (A) unit cell volume as a function of concentration; (b) lattice parameters as functions of concentration (Pecharsky et al., 2002a). The lines are guides for the eye. *Figure (A) after Holtzberg et al. (1967), Pecharsky and Gschneidner (1997d), and Pecharsky et al. (2002a).*

composition may adopt either the monoclinic or the orthorhombic crystal structure depending on the heat treatment regime. The as-cast $Gd_5Si_2Ge_2$, prepared from the high-purity Gd, usually contains the monoclinic phase as a majority phase and a minor amount of O(I)-Gd_5Si_4 type phase (Pecharsky et al., 2002b). The high-temperature heat treatment typically results in the pure monoclinic phase while the low-temperature treatment (below 650 °C) promotes the formation of the Gd_5Si_4-type structure (Mozharivskyj et al., 2005; Pecharsky et al., 2002a) and may even lead to a partial decomposition of $Gd_5(Si_xGe_{1-x})_4$ into a mixture of $Gd(Si_xGe_{1-x})$ and $Gd_5(Si_xGe_{1-x})_3$ phases (Gschneidner et al., 2000a; Pecharsky et al., 2002a). Pecharsky et al. (2003d) showed that the high-temperature polymorph (γ phase) of $Gd_5Si_{2.09}Si_{1.91}$ has nearly identical X-ray powder diffraction pattern at 690 K as the low-temperature orthorhombic structure (α phase) at 240 K. Apparently, once the γ phase is formed by heat treatment at ~750 K, the $Gd_5Si_{2.09}Ge_{1.91}$ paramagnetic phase exists in the orthorhombic Gd_5Si_4 type of crystal structure and undergoes a second-order phase transition from PM to FM state at T_C without structural transformation. The Curie temperature in this case is by 14 K higher than the T_C of the first-order transformation from the paramagnetic monoclinic phase (β phase) to the ferromagnetic α phase at the same composition (Pecharsky et al., 2003d). Fu et al. (2007) found that the low-temperature heat treatment of phase-pure monoclinic $Gd_5Si_2Ge_2$ powder (150 °C/2 h and 400 °C/0.5 h) promotes the β to γ structural transformation in the paramagnetic state producing a mixture of the orhthorhombic and monoclinic phases, both existing at the same $Gd_5Si_2Ge_2$ stoichiometry. At the same time, annealing of bulk $Gd_5Si_2Ge_2$ alloy at 400 °C for both 0.5 and 10 h does not change the crystal structure and it remains monoclinic. Since a powdered sample is more prone to oxidation compared with a bulk sample of the same chemical composition, Fu et al. (2007) explained the observed difference in structural behavior by higher concentration of interstitial impurities (O and N) in the powdered samples. However, stress induced by grinding may be related to this difference as well. The detailed high-temperature single-crystal investigation of the monoclinic phase stability complemented by tight-binding linear-muffin-tin-orbital electronic structure calculations using the atomic sphere approximation method (TB-LMTO ASA) was performed by Mozharivskyj et al. (2005). The study found that the presence of interstitial impurities, such as O or N, may impede shear movement of the slabs, consequently slowing the transitions and making them irreversible.

In order to prevent the formation of the γ phase, a high-temperature heat treatment is commonly performed on $Gd_5Si_xGe_{4-x}$ with $x \sim 2$. The optimal annealing regime for the formation of the single-phase monoclinic structure with the highest magnetocaloric effect was found to be heat treatment at 1300 °C for 1 h (Pecharsky et al., 2003b). Several studies showed that longer annealing times even at optimal temperatures are detrimental to the phase purity and magnetocaloric properties of the $Gd_5Si_2Ge_2$ (Belo et al., 2012a; Pecharsky et al., 2003b).

Isothermal cross-section of the ternary Gd–Si–Ge phase diagram (Gd-rich corner) at 900 °C was constructed by Zhuang et al. (2006a). Samples were arc-melted using the “commercial grade” Gd metal, heat treated in evacuated quartz tubes at 900 °C for 10 days, and quenched in liquid nitrogen. All three crystal structures, O(I), M, and O(II), were observed along the Gd_5Si_4–Gd_5Ge_4 tie-line (denoted in the paper as γ, δ, and β, respectively). The homogeneity range of monoclinic $Gd_5Si_xGe_{4-x}$ phase was reported to be from 13.3 to 22 at.% Si, corresponding to $1.2 \leq x \leq 1.98$.

Purity of the starting rare earth metal, gadolinium, particularly the presence of interstitial impurities such as oxygen, carbon, and nitrogen, is a very important factor affecting both the phase composition and properties of $Gd_5Si_2Ge_2$ (Gschneidner and Pecharsky, 1999; Gschneidner et al., 2000a; Mozharivskyj et al., 2005). The carbon addition drastically decreases the magnetocaloric effect in $Gd_5Si_2Ge_2$ (Pecharsky and Gschneidner, 1997c), and preparation route that reduces carbon concentration in the alloys made from commercial gadolinium by prolonged melting in the Ta crucible in vacuum allowing release of C and O in the form of CO and CO_2 gases was developed by Gschneidner et al. (2000a). Overall it is difficult, though not impossible, to obtain the single-phase monoclinic $Gd_5Si_2Ge_2$ using the commercial purity gadolinium.

Meyers et al. (2002b) observed that various contaminants and secondary phases (i.e., $Gd(Si_xGe_{1-x})$, $Gd_5(Si_xGe_{1-x})_3$, and Ta_2Si as a result of reaction with Ta crucible) form during synthesis of large batches (approximately 1 kg total) of $Gd_5Si_{1.95}Ge_{2.05}$ from "commercial grade" Gd. Gama et al. (2004) prepared a $Gd_5Si_2Ge_2$ sample from the commercial grade Gd and found only a second-order transition at 299 K in the as-cast sample. However, after the sample was annealed at 1600 °C for 48 h two transitions, a second-order at 299 K, and a first order at 274 K were observed and GMCE of 18 J/Kg K was reported for 0–7 T magnetic field change in the heat-treated sample, meaning that a substantial amount of the monoclinic phase has formed during the heat treatment.

The O(II) phase is separated from the M phase on the $Gd_5Si_xGe_{4-x}$ diagram by a wide ($1.2 \leq x \leq 1.72$) two-phase region compared to the narrow O(I)–M boundary ($\Delta x = 0.05$). This two-phase region is less important for practical application since phase transitions here occur well below room temperature, and therefore, it was not studied as rigorously as the region near the $Gd_5Si_2Ge_2$ stoichiometry. There is not much change in the values of the lattice parameters of the annealed and as-cast alloys in the vicinity of this two-phase region, indicating no major change in the x in the 5:4 phases due to heat treatment.

The study of rapidly solidified melt-spun ribbons of $Gd_5Si_2Ge_2$ showed an interesting dependence of their phase composition on the wheel speed (Fu et al., 2006). The crystal structure of the ribbons prepared at 20 m/s wheel speed is mostly monoclinic and they exhibit a first-order transition at 273 K on the DSC curves. Higher wheel speeds promote the formation of the orthorhombic phase instead of the monoclinic, and a second-order transformation is observed around 290 K in materials prepared at wheel speeds of 30, 40, and 50 m/s. Exothermic peaks located at ~250–300 °C are attributed to the crystallization of an amorphous phase. Similar study performed on a $Gd_5Si_2Ge_2$ material prepared using lower purity Gd than the one used by Fu et al. (2006) showed that Gd_5Si_4-type orthorhombic phase forms in the rapidly solidified ribbons at wheels speeds of 25 and 40 m/s (Zhang et al., 2007). The rapid solidification, however, at least produces single-phase 5:4 material while the as-cast alloy prepared from the same starting materials consists of a mixture of both $Gd_5Si_2Ge_2$ polymorhps (O(I) and M), $Gd_5(Si_xGe_{1-x})_3$, and $Gd(Si_xGe_{1-x})$ phases.

3.1.1. *Coupled Magnetic and Structural Diagram*

The particularly interesting property of this series of compounds is strong coupling of their magnetic and crystallographic lattices. The close relationship between the crystal structure and magnetic properties in the $Gd_5Si_xGe_{4-x}$ system was originally observed by Holtzberg et al. (1967) and highlighted in the refined magnetic phase diagram of $Gd_5Si_xGe_{4-x}$ (Pecharsky and Gschneidner, 1997a,d). However, a detailed investigation of low-temperature crystal structure and magnetic behavior of many compounds was needed to establish a clear correspondence between a particular magnetic state and one of three crystal structure types in $Gd_5Si_xGe_{4-x}$ alloys. Soon, it was discovered that the structural transformation from the $P112_1/a$ monoclinic structure into the *Pnma* O(I) structure was observed at 240 K in the $Gd_5Si_{1.8}Ge_{2.2}$ phase, which is also the temperature of the transition from the paramagnetic to the ferromagnetic state (Morellon et al., 1998a). Further systematic studies of numerous $Gd_5Si_xGe_{4-x}$ alloys clearly showed the intimate relationship between the magnetic behavior of the alloys and their room temperature crystal structure, particularly with presence or absence of interslab T—T bonds (Pecharsky and Gschneidner, 1997d), which is the only substantial difference between three different types of crystal structure observed in the $Gd_5Si_xGe_{4-x}$ system. Breaking of at least half of the interslab T_2 dimers during O(I) to M structural transformation usually causes the transition from the ferromagnetic ordering into the paramagnetic state (Choe et al., 2000, 2003a). In the O(II) type of structure with all interslab T—T bonds broken, the FM state does not occur at all, and the magnetic ordering is antiferromagnetic only (Morellon et al., 2000). Multiple studies confirmed that crystallography of the $Gd_5Si_xGe_{4-x}$ system changes with temperature in accord with its magnetic state and *vice versa*, and the combined magnetostructural x–T diagram can be constructed for the $Gd_5Si_xGe_{4-x}$ system. Pecharsky and Gschneidner (2007) presented the most recent version of this diagram, as shown in Fig. 10. It is worth to note that Gd_5Ge_4 ($x=0$) remains in the O(II) structure at low temperatures after cooling in zero magnetic field, and its transformation into FM O(I) polymorphic modification (Pecharsky et al., 2003a) is "kinetically arrested" (Roy et al., 2006); this interesting phenomenon will be discussed below in more detail. First-principles calculations confirm that the antiferromagnetic O(II)-Sm_5Ge_4-type structure is a ground state in Gd_5Ge_4 (Paudyal et al., 2007).

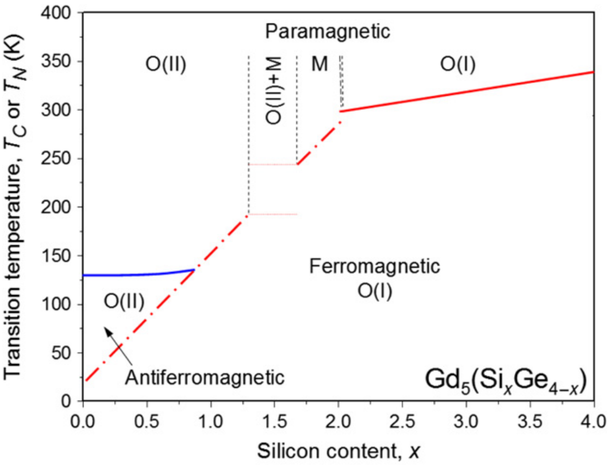

FIGURE 10 Combined magnetic and structural diagram of the $Gd_5Si_xGe_{4-x}$ pseudobinary system. Thick solid lines indicate temperature-dependent boundaries of the second-order phase transitions, while the thick dash-dotted lines indicate those of the first-order transitions. Thin horizontal lines indicate constant temperatures of FM-O(I)→PM-M (upper line) and FM-O(I)→PM-O(II) (lower line) transformations in the O(II)+M two-phase region.

While it is widely accepted and confirmed by numerous magnetic measurements that the O(I) structure in $Gd_5Si_xGe_{4-x}$ alloys is coupled to the FM state, recent neutron diffraction experiments performed on the samples with $0 \leq x \leq 0.9$ failed to observe any long-range ferromagnetic ordering in these samples in the absence of the applied magnetic field (Ryan et al., 2010). At the same time, a clear removal of long-range AFM state was confirmed when the O(II) to O(I) structural transition occurrs. Therefore, the magnetic part of the x–T $Gd_5Si_xGe_{4-x}$ diagram presented in Fig. 10 may not be strictly valid in the complete absence of applied magnetic field.

3.2. Magnetic Properties, Magnetocaloric Effect, and First-Order Transitions

The GMCE observed originally in $Gd_5Si_2Ge_2$ occurs in other $Gd_5Si_xGe_{4-x}$ compounds, however, in the Si-rich alloys, which exhibit highest magnetic ordering temperatures, only the conventional magnetocaloric effect is present (Gschneidner et al., 1999).[3] Yet, the extraordinary sensitivity of the magnetic phase transition temperature to the Si/Ge content, originally noted by Holtzberg et al. (1967), means that in the $Gd_5Si_xGe_{4-x}$ system the temperature of the giant magnetocaloric effect is tunable in the wide range from ~30 to ~276 K by adjusting the Si/Ge ratio (Pecharsky and Gschneidner, 1997a, 1998). Alloying with a small amount (~0.33 at.%) of Ga raises the Curie temperature to ~290 K and preserves GMCE, while alloying with some other elements, both magnetic and nonmagnetic (Fe, Co, Ni, Cu, Al, etc.) tends to increase Curie temperature but destroys the giant magnetocaloric effect (Pecharsky and Gschneidner, 1997c; Provenzano et al., 2004). Usually, in the $Gd_5Si_xGe_{4-x}$ system the magnetocaloric effect increases as the magnetic ordering temperature decreases, particularly in the alloys with the room temperature O(II) crystal structure (Pecharsky and Gschneidner, 1997a, 1998). While these materials are not suitable for use in magnetocaloric refrigerators operating at ambient conditions, there is still a wide range of applications where they may prove to be useful, that is, for the liquefaction of H_2, natural gas, and propane (Gschneidner et al., 1999).

---

[3] The name "giant magnetocaloric effect (GMCE)" was coined by Pecharsky and Gschneidner (1997a) to designate an unusually large magnetocaloric effect observed during a magnetic field-induced first order magnetic phase transition in $Gd_5Si_2Ge_2$. It was later shown by Morellon et al. (1998a) that in the $Gd_5Si_xGe_{4-x}$ family, the magnetic ordering–disordering transformation coincides with a structural transformation. Today, it is broadly accepted that the giant magnetocaloric effect originates from the enhancement of the conventional magnetocaloric effect, borne by the magnetic-field-induced changes in the magnetic sublattices, by the entropy difference between different polymorphic modifications of a crystalline material that are associated with different magnetic states of the system. Hence, the giant magnetocaloric effect results from coupled magnetostructural transformations that are triggered by varying external magnetic fields (Pecharsky et al., 2003a).

The occurence of GMCE in $Gd_5Si_xGe_{4-x}$ alloys (and in any other magnetic system) is always associated with a first order of the phase transition that can be induced reversibly by magnetic field (Gschneidner and Pecharsky, 2000b; Gschneidner et al., 1999; Liu et al., 2006; Tegus et al., 2002a). Typically, the order of a transition is clearly seen from heat capacity measurements of a given material, but presence of thermal hysteresis in temperature dependence of material's magnetization is a good indication of the first order of the transition as well. $Gd_5Si_2Ge_2$ shows a sharp first-order peak on its heat capacity data at T_C (Fig. 11A; Pecharsky and Gschneidner, 1997b) and similar first-order heat capacity peaks have been observed for every other studied $Gd_5Si_xGe_{4-x}$ compound with $x \leq 2$. On the other hand, in the Si-rich region ($x > 2$, no GMCE) the heat capacity at the transition shows a textbook λ-shaped anomaly that reflects the second order of the transition (Gschneidner et al., 1999). This changeover from the first to the second order of the transition with raising x is shown in Fig. 11B. Despite not showing the GMCE, the Si-rich alloys with $x > 2$ remain interesting materials for certain applications due to their high T_C and large magnetization. For example, high magnetization and T_C that may be easily tuned between 40 and 45 °C are desired properties for materials potentially suitable for a hypothermal treatment of inoperable tumors (Ahmad and Shaheen, 2009; Ahmad et al., 2005).

The first-order transitions usually show relatively sharp peaks in the heat capacity data even in high magnetic fields at which the second-order

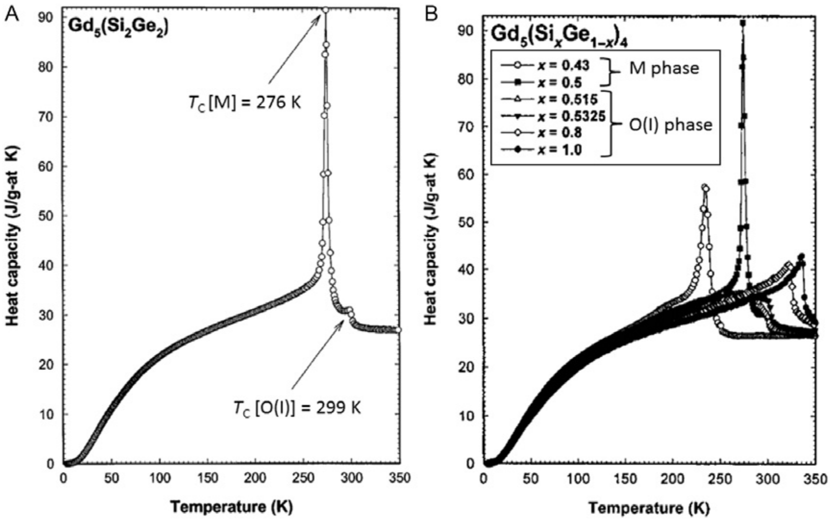

FIGURE 11 (A) Heat capacity of $Gd_5Si_2Ge_2$ measured as a function of temperature in zero magnetic field. In addition to the main peak associated with the paramagnetic M to ferromagnetic O(I) magnetostructural transition, the purely magnetic transition of the minor O(I) phase is seen at 299 K. (B) Heat capacities of selected $Gd_5Si_xGe_{4-x}$ alloys measured as functions of temperature in zero magnetic field. The samples with room temperature M crystal structure show strong first-order transitions, but the samples with O(I) crystal structure show second-order λ-shaped peaks.

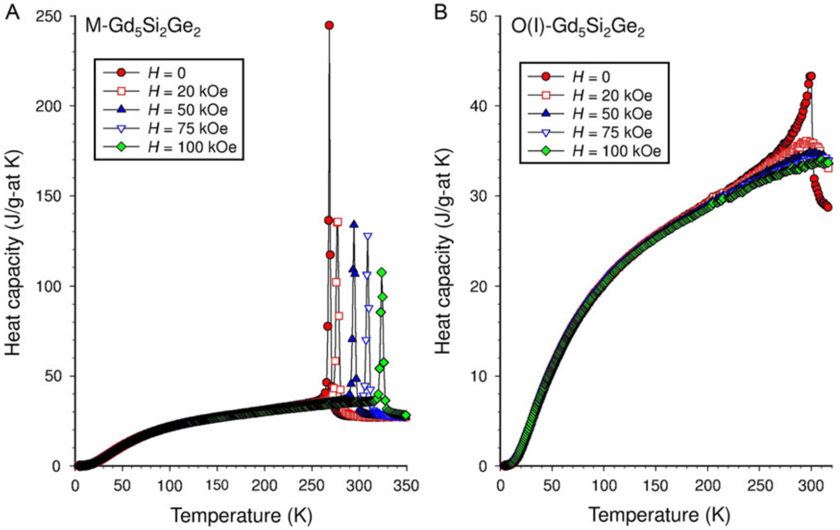

FIGURE 12 Heat capacity of the first-order M-$Gd_5Si_2Ge_2$ (A) and the second-order O(I)-$Gd_5Si_2Ge_2$ (B) materials measured as a function of temperature in applied magnetic fields of 0, 20, 50, 75, and 100 kOe.

transitions become broad. As shown in Fig. 12A, in $Gd_5Si_2Ge_2$ the first order of the transition is clearly seen even in magnetic fields as high as 100 kOe contrary to the second-order behavior shown in Fig. 12B.

Heat capacity measurements of Gd_5Ge_4 in 0, 5, 20, 30, 40, 50, 80, and 110 kOe applied magnetic fields have been carried out by Sharath Chandra et al. (2009). In magnetic fields higher than 30 kOe, a strong anomaly that corresponds to the O(I)-FM → O(II)-AFM transition is observed above ~45 K and it moves toward higher temperatures as the applied field increases. Magnetic contribution to the total heat capacity was calculated by subtracting the heat capacity of La_5Ge_4 from that of Gd_5Ge_4. In addition to a large peak at T_C, a small anomaly in heat capacity is seen at ~15 K in low fields, which disappears in high magnetic fields. Sharath Chandra et al. (2009) suggested that this anomaly indicates the "freezing boundary" of Gd_5Ge_4 (see Section 3.6). The magnetic entropy of Gd_5Ge_4 decreases with applied magnetic field following the field-induced transition into a fully ordered ferromagnetic state.

Calorimetric measurements performed using a differential scanning calorimeter (DSC), developed by Marcos et al. (2003), also show the presence of a large peak at the first-order AFM-O(II)–FM-O(I) transition in $Gd_5Si_{0.4}Ge_{3.6}$ alloy, and much weaker effect at T_N, which is the second-order PM–AFM transition (Fig. 13). A linear increase in the temperature of the first-order transition with applied magnetic field was observed, $dT_C/dH = 0.41 \pm 0.01$ K/kOe. The peaks associated with the first-order transition become considerably stronger

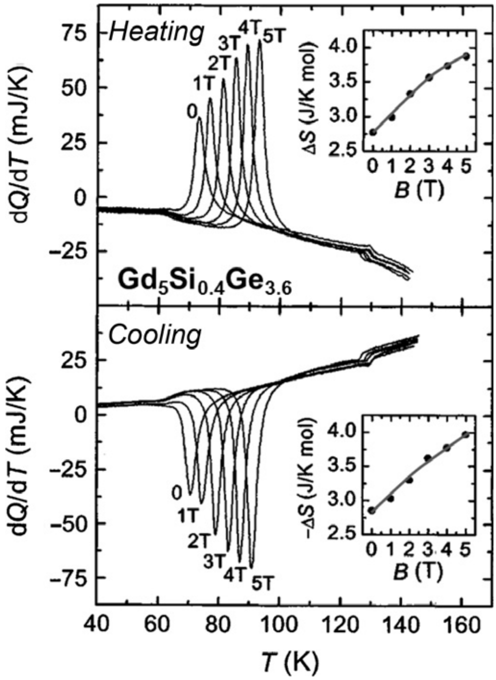

FIGURE 13 DSC curves measured on a $Gd_5Si_{0.4}Ge_{3.6}$ sample for different applied magnetic fields. Insets show the entropy change as a function of the magnetic field (Marcos et al., 2003).

when magnetic field increases, as the entropy change at the transformation increases: from $\Delta S = 2.85$ J/mol K for $H = 0$ kOe to $\Delta S = 3.96$ J/mol K for $H = 50$ kOe (see insets of Fig. 13). Using the same experimental setup as Marcos et al. (2003), Casanova et al. (2004b) studied the variation of the transition field with the transition temperature dH_t/dT_t in $Gd_5Si_xGe_{4-x}$ alloys for $0 \leq x \leq 2$. Two distinct behaviors of dH_t/dT_t were observed. For $x \leq 0.8$, two different values of dH_t/dT_t corresponding to low-field (AFM–FM) and high-field (PM–FM) regimes exist, while a single value of dH_t/dT_t is found for $0.96 \leq x \leq 2$ compositional range, where only the PM–FM transition is present. The emergence of two field regimes in the Ge-rich region is due to the fact that in high magnetic fields (over 10 T) the magnetostructural transition overlaps with the second-order PM–AFM transition giving rise to a unique PM-O(II)–FM-O(I) transformation (Casanova et al., 2004b).

In addition to the magnetic ordering temperature(s), T_C or T_N, other major parameters describing magnetocaloric effect are: magnetic entropy change, $-\Delta S_M$; adiabatic temperature change, ΔT_{ad}; and relative cooling power, RCP (Gschneidner and Pecharsky, 2000b). For characterization of the magnetocaloric properties of a given material, the maximum value of each parameter (except the ordering temperature) is usually reported for a certain magnetic

TABLE 11 **The Magnetic Ordering Temperatures and Magnetocaloric Properties (for the Magnetic Field Change from 0 to 50 kOe) of the $Gd_5Si_xGe_{4-x}$ Phases (Gschneidner and Pecharsky, 2000b)**

Composition	Crystal structure[a]	T_C (K)	T_N (K)	$-\Delta S_M$ (J/Kg K)	ΔT_{ad} (K)	Relative cooling power (J/Kg)
Gd_5Si_4	O(I)	336	–	8.8	8.8	635
$Gd_5Si_{2.5}Ge_{1.5}$	O(I)	313	–	9.6	8.5	630
$Gd_5Si_2Ge_2$	M	276	–	18.7	15.0	448
$Gd_5Si_{1.72}Ge_{2.28}$	M	246	–	39.2	18.8	549
$Gd_5Si_{0.33}Ge_{3.67}$	O(II)	68	128	36.1	11.2	758
Gd_5Ge_4[b]	O(II)	–	125	16.0	7.2	432

[a] *At room temperature.*
[b] *Gd_5Ge_4 remains in the O(II) structure at low temperatures in zero magnetic field but transforms into O(I) structure when a magnetic field is applied (Pecharsky et al., 2003a). It exhibits GMCE due to this field-induced transition.*

field change. $-\Delta S_M$ and RCP are extensive parameters usually quoted per unit of either volume or mass. It is more common in literature to report magnetic entropy change per unit of mass (g or kg) though the volumetric units are better from an engineer's point of view. The magnetic and magnetocaloric properties of several $Gd_5Si_xGe_{4-x}$ alloys with different crystal structures from each part of the phase diagram (Fig. 9) are summarized in Table 11 and magnetocaloric properties of monoclinic alloys are also shown in Fig. 14. Obviously, the alloys with M and O(II) room temperature structures show much larger MCE compared to the O(I) phases. It is worth to note here that the actual MCE values for a given $Gd_5Si_xGe_{4-x}$ composition may vary significantly depending on the sample preparation routine and quality of the starting materials. As shown by Pecharsky et al. (2003b), almost a twofold increase in the magnetocaloric effect in $Gd_5Si_2Ge_2$ occurs when the sample is optimally heat treated at 1300 °C compared to other annealing protocols (i.e., annealing at lower temperatures). Effect of cooling rate on the magnetic entropy change of $Gd_5Si_xGe_{4-x}$ alloys with $x = 1.7$ and 2.0 was studied by Yan et al. (2004). They found that a slow cooling has detrimental effect on MCE, especially for the $Gd_5Si_2Ge_2$ compound; both higher Ge content and higher cooling rate are favorable for the formation of the monoclinic phase.

The magnetocaloric effect (change of materials temperature with applied magnetic field) can be directly measured using a properly designed experimental setup. Huang et al. (2005) performed direct ΔT_{ad} measurements on $Gd_5Si_2Ge_2$, $Gd_5Si_{3.2}Ge_{0.8}$, and Gd_5Si_4 for the 0–13 kOe magnetic field

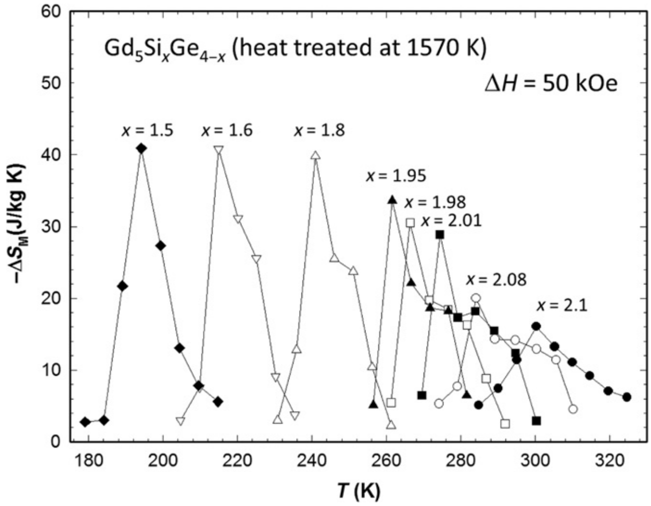

FIGURE 14 Magnetocaloric effect (for a magnetic field change from 0 to 50 kOe) calculated for the selected monoclinic $Gd_5Si_xGe_{4-x}$ alloys using the magnetization data (Pecharsky et al., 2003c). For the details of calculating magnetocaloric effect from heat capacity or magnetization data refer to Gschneidner and Pecharsky (2000b).

change, and reported the maximum ΔT_{ad} values of 2.2, 2.6, and 2.9 K, respectively. The low ΔT_{ad} for the first-order transition in $Gd_5Si_2Ge_2$ indicates that 13 kOe is below the critical field needed to complete the PM → FM transformation in this compound at the temperature of the measurement.

Differential scanning calorimetry may also be used to measure the entropy change for a magnetic-field-induced first-order transition. In the study by Casanova et al. (2005a), the $Gd_5Si_{0.2}Ge_{3.8}$ sample was used to directly measure the entropy change at $T = 50$, 55, 60, and 65 K and in magnetic fields up to 50 kOe. An unusual increase in $-\Delta S_M$ with cycling has been observed in this work, at least when the number of cycles was small, on the order of $\sim 10^2$ cycles.

The magnetocaloric effect as a function of temperature for the $Gd_5Si_{0.15}Ge_{3.85}$ alloy, which adopts the O(II)-Sm_5Ge_4 structure at room temperature is shown in Fig. 15. It is interesting to note that since the sample undergoes two transitions, first-order magnetostructural at $T_C = 40$ K, and second-order magnetic ordering at $T_N = 128$ K, there are two peaks in both ΔS_M and ΔT_{ad} graphs. However, the magnetocaloric effect exhibited at the low-temperature first-order transition is much stronger when compared to the high-temperature one.

Gschneidner et al. (1996) observed that the value of magnetic entropy change determined for the isostructural series of $Dy_{1-x}Er_xAl_2$ alloys decreases with the temperature increase. This fact was explained by the increase in the lattice heat capacity so more energy is required to heat the sample itself, that is, there is an entropy loss (see also Gschneidner et al., 2005). Casanova et al.

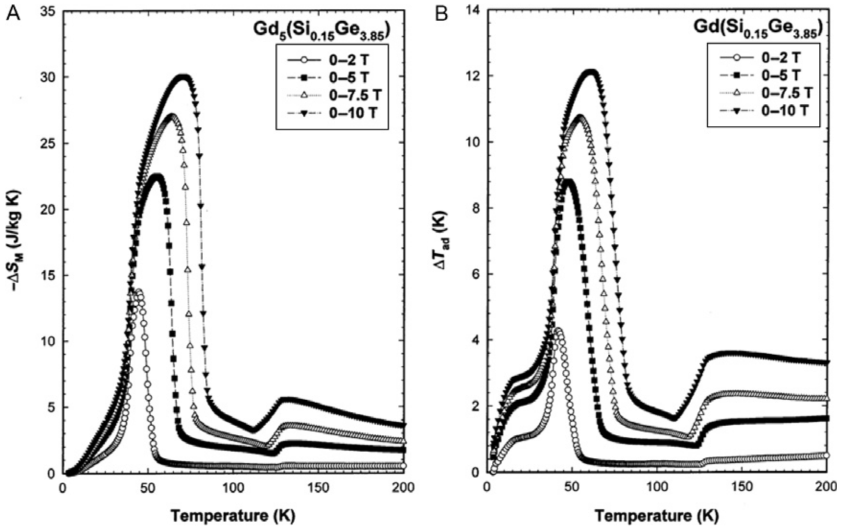

FIGURE 15 The magnetocaloric effect in $Gd_5Si_{0.15}Ge_{3.85}$ calculated using heat capacity data for four magnetic field changes: $\Delta H = 0$–20, 0–50, 0–75, and 0–100 kOe: (A) $-\Delta S_M$ and (B) ΔT_{ad} (Gschneidner and Pecharsky, 2000a).

(2002a) have shown that such universal dependence can also be applied to the $Gd_5Si_xGe_{4-x}$ system. The maximum entropy change during the first-order transition in $Gd_5Si_xGe_{4-x}$ scales well with the temperature of the transition, regardless of whether that temperature is modified by chemical substitution or change in magnetic field. The amount of the magnetic entropy change decreases with the temperature increase between ~100 and ~300 K. Somewhat unexpectedly, it was reported that ΔS_M also decreases when temperature decreases below ~100 K (Casanova et al., 2002a, 2003). It is important to note, however, that the MCE of a particular compound obtained by different methods or in different laboratories may vary substantially.

The formation of a particular polymorphic modification in the paramagnetic state of $Gd_5Si_2Ge_2$ due to heat treatment and/or purity of starting materials has a profound effect on its magnetocaloric properties: when this compound crystallizes in the monoclinic $Gd_5Si_2Ge_2$ structure it is a first-order giant magnetocaloric material, but when the sample is crystallizing in the orthorhombic Gd_5Si_4 structure, it is a second-order material and does not exhibit either GMCE or other interesting phenomena, such as GMS, GMR or SGV (the difference in MCE for the $Gd_5Si_{2.09}Ge_{1.91}$ composition is shown in Fig. 16, below). The M to O(I) transition occurs in the former case but not in the latter. As shown by Hadimani et al. (2008a) by means of the Arrott plot method the estimated magnetic ordering temperature of O(I) $Gd_5Si_2Ge_2$ phase is ~300 K in any case. However, when the structural M to O(I) transition occurs, the PM monoclinic phase forms below this temperature and from

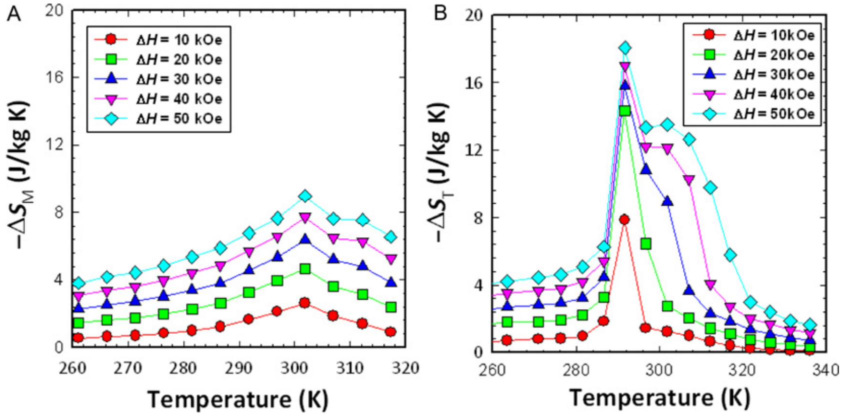

FIGURE 16 Magnetocaloric effect in the $Gd_5Si_{2.09}Ge_{1.91}$ compounds with the room temperature crystal structure being: (A) orthorhombic Gd_5Si_4 type and (B) monoclinic $Gd_5Si_2Ge_2$ type (Pecharsky et al., 2002b).

the $M(T)$ plot, the observed T_C is equal to 269 K; similar effect was observed for the $Gd_5Si_{1.95}Ge_{2.05}$ composition. At the same time, for the typical second-order $Gd_5Si_{2.7}Ge_{1.3}$ compound the $T_C = 304$ K determined by the Arrott method agrees well with the $T_C = 307$ K determined from the $M(T)$ plot by the inflection point method (Hadimani et al., 2008b). The magnetic-field-induced first-order PM→FM phase transition occurs in the $Gd_5Si_xGe_{4-x}$ alloys for $0.41 \leq x \leq 0.51$ even above the projected T_C of the O(I) phase, which is possible due to the broadening of the second-order magnetic ordering transition of the O(I) structure (Hadimani et al., 2009b).

The competition between orthorhombic and monoclinic structures in $Gd_5Si_2Ge_2$ has been analyzed employing the first-principles electronic structure calculations coupled to the magnetothermodynamic modeling (Paudyal et al., 2006). The calculated temperature dependences of magnetization and total energy are in excellent agreement with experimental results. The mechanism of the magnetostructural transformation in $Gd_5Si_2Ge_2$ is illustrated in Fig. 17. The O(I) phase is stable at low temperatures, but it has higher $T_C^{O(I)}$ than the M phase, which is stable at high temperatures but its calculated T_C^M is around 210 K. The energy crossover occurs at the temperature of the first-order transition, the measured T_C of the material, which is $T_C^M < T_C < T_C^{O(I)}$. It is easy to see from Fig. 17 that the change in magnetization at the transition in such case is theoretically discontinuous, and experimentally is much sharper compared to a classical second-order scenario.

It is equally easy to note that the free energy difference between M and O(I) phases is relatively small near T_C and extrinsic factors (such as interstitial impurities) may easily shift the temperature of the crossover or lift the free energy

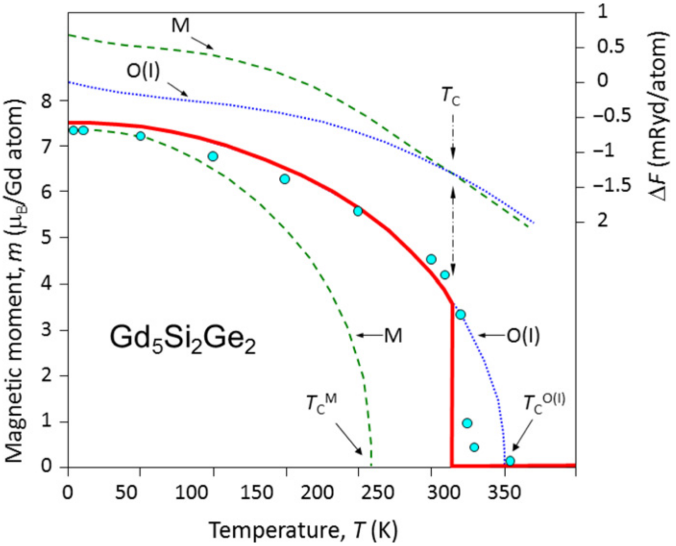

FIGURE 17 Magnetization (lower part of the plot, dashed and dotted lines) and Helmholtz free energies (upper part of the plot, solid and dash-dotted lines) of M and O(I) polymorphic modifications of $Gd_5Si_2Ge_2$ calculated from first principles coupled to magnetothermodynamic models (Pecharsky et al., 2009). The thick solid line is predicted magnetization of $Gd_5Si_2Ge_2$ in the case of first-order structural M→O(I) transformation. The full circles represent experimentally measured values of the spontaneous magnetization of $Gd_5Si_2Ge_2$ as a function of temperature.

curve of the M phase enough to prevent its formation from the O(I) phase, which would remain the only thermodynamically stable phase in $Gd_5Si_2Ge_2$.

The fact that the same compound may order magnetically either simultaneously with a structural transition or without it allows one to estimate the contribution from the structural entropy (~9 J/Kg K, Fig. 16) to the total entropy change observed during the magnetostructural transition in $Gd_5Si_2Ge_2$. This is relatively easy to do because with the same chemicalcomposition and nearly the same transition temperatures, the difference between the magnetic entropy change values of two polymorphs comes only from the changes in the crystal structure (Gschneidner et al., 2012).

The influence of the first-order ferromagnetic-paramagnetic phase transition on the MCE was theoretically investigated by von Ranke et al. (2004). A simple phenomenological modeling was used to estimate the influence of external parameters (i.e., magnetic field, pressure, volume deformation) on the magnetic entropy change. Monte Carlo calculations of the magnetocaloric effect in $Gd_5Si_xGe_{4-x}$ alloys with $x > 0.5$ (no first-order structural transition) were performed by Nóbrega et al. (2005) and showed good agreement with available experimental data. Basso et al. (2006) applied a temperature-dependent Preisach model to describe hysteresis in a material with magnetic-field-induced temperature transformation, namely in $Gd_5Si_{0.328}Ge_{3.672}$.

Another factor that affects the measured entropy change is the history dependence often observed in samples undergoing first-order transitions, particularly those with a substantial thermal or magnetic hysteresis. This was illustrated by the Hall probe measurements of the monoclinic $Gd_5Si_{2.09}Ge_{1.91}$ sample, which was exposed to two different paths: in one case in order to achieve the transition the temperature was increased first, followed by the increase in magnetic field; in the other case the sample was magnetized first and then heated up (Kuepferling et al., 2008). The Hall imaging showed that the final phase compositions (the ratios of M and O(I) structures) in two cases were different, and so were the measured MCE values (refer to Section 3.6 for more information explaining the history dependence).

Guimarães et al. (2010) applied the acoustic detection method for the measurement of magnetocaloric effect in several $Gd_5Si_xGe_{4-x}$ materials ($x=2$, 2.5, 3.0, 3.5, and 4.0) prepared in the form of both pellets and powders (pellets were made out of powders by compression under 0.6 GPa). For the second-order samples with $2.0<x\leq 4.0$, good agreement between the MCE of powders and pellets was observed. For the sample with the $Gd_5Si_2Ge_2$ composition, the measured MCE properties of the powder and the pellet were different (pellet has smaller MCE) indicating that a significant fraction of the high-volume monoclinic phase have transformed into the low-volume O(I) phase during the compression.

As was mentioned earlier, the purity of the starting rare earth metal has significant influence on the MCE of $Gd_5Si_xGe_{4-x}$ alloys. Thuy et al. (2001) were able to obtain GMCE ($\Delta S_M=-20$ J/Kg K) in as-cast $Gd_5Si_2Ge_2$ prepared using commercial grade Gd metal. The reported T_C was 279 K, and $\theta_p=305$ K. The sample was reported to be single phase based on the X-ray powder diffraction data; it was not clearly specified whether the compound's crystal structure was monoclinic or orthorhombic, though based on the presence of GMCE one may suggest that it was indeed monoclinic in the paramagnetic state. More information regarding sample preparation and X-ray powder diffraction analysis were provided in a second study of several other GMCE $Gd_5Si_xGe_{4-x}$ alloys ($x=0.33$, 1.01, 1.72, 2.0) made from commercial grade Gd by Thuy et al. (2002). These alloy were prepared with the 3 at.% Gd excess, and a small amount of impurity phase has been observed on their X-ray diffraction patterns.

$Gd_{1-x}(Si_{0.5}Ge_{0.5})_x$ series of alloys, $x=0.38$, 0.41, 0.45, 0.47, 0.5, was studied by Manivel Raja et al. (2008). Essentially, the authors studied the composition range between $Gd_5(Si_{0.5}Ge_{0.5})_3$ and $Gd_1(Si_{0.5}Ge_{0.5})_1$ phases, and expectedly found that the alloy with $x=0.45$ (closest to the $Gd_5(Si_{0.5}Ge_{0.5})_4$ composition) shows the largest MCE. Interestingly, in agreement with Thuy et al. (2002), they found that Gd-rich alloys ($x\geq 0.45$) contain the monoclinic 5:4 phase, but Gd-depleted samples contain the orthorhombic O(I) 5:4 phase.

Wu and Lu (2004) confirmed that the presence of GMCE in $Gd_5Si_xGe_{4-x}$ alloys with $x \sim 2$ is strongly dependent on the purity of the starting Gd metal. They found an increase in magnetic entropy change values in the materials made from purified Gd metal compared to the materials made from the "as-received" Gd metal obtained from the same commercial vendor. Alves et al. (2004) were able to obtain GMCE (19 J/Kg K for $\Delta H = 70$ kOe at $T_C = 274$ K) in $Gd_5Si_2Ge_2$ alloy prepared from low-purity Gd by using the high-temperature heat treatment of the cast alloy at 1650 °C for 48 h. However, a significant amount of the O(I) structure magnetically ordering at 299 K through a second-order transition was still present in the sample after annealing. Zhang et al. (2005) observed more than a twofold increase of the magnetic entropy change in $Gd_5Si_2Ge_2$ alloy prepared from low-purity commercial grade Gd after annealing at 1200 °C for 1 h.

Wu et al. (2005a) prepared a series of $Gd_5Si_{1.95}Ge_{2.05}O_x$ alloys ($x = 0.05$, 0.10, 0.15, 0.40, and 0.50), in which oxygen was added as Gd_2O_3, and the magnetocaloric effect was compared with the parent GMCE alloy $Gd_5Si_{1.95}Ge_{2.05}$. High amounts of oxygen ($x \geq 0.15$) lead to the decomposition of the 5:4 phase into the 1:1 and 5:3 phases. Even the lowest amount of added oxygen ($x = 0.05$) destroys GMCE by stabilizing the orthorhombic γ phase, and decreasing the amount of the monoclinic β phase that undergoes a first-order transition.

Hydrogen absorption has similar effect. Carvalho et al. (2007) studied the effect of hydrogen on the structural and magnetic properties of $Gd_5Si_{1.9}Ge_{2.1}H_x$ alloy ($0 < x < 2.5$) and found that even the smallest measured amount of hydrogen ($x = 0.09$) changes the PM → FM transition from first to second order stabilizing the O(I) Gd_5Si_4-type crystal structure. Hydrogen absorption expands the lattice along the a- and b-axes but shrinks it along the c-direction. Total volume expansion measured at $x(H) = 2.5$ is 1.7%.

Usually, it is much easier to obtain a pure monoclinic phase at room temperature when the composition is slightly shifted from the ideal $Gd_5Si_2Ge_2$ composition toward the Ge side of the $Gd_5Si_xGe_{4-x}$ pseudobinary diagram. However, the temperature of the magnetic ordering lies below the room temperature. Chernyshov et al. (2002) studied magnetic, magnetocaloric, and magnetoelastic properties of a $Gd_5Si_{1.95}Ge_{2.05}$ sample and found that simultaneous magnetostructural transition occurs at 262 K in zero magnetic field.

Magnetocaloric effect (magnetic entropy change) was determined for the $Gd_5Si_{1.8}Ge_{2.2}$ sample using the high-field (up to 230 kOe) isothermal magnetization measurements (Casanova et al., 2002b). The authors established that the Maxwell relations can be used to calculate MCE in first-order transition systems such as $Gd_5Si_xGe_{4-x}$ ($x \leq 2$) as long as the Maxwell relation is evaluated within the transition region only and the applied field is high enough to complete the transition. The value of the critical field (H_{cr}) needed to start the PM → FM transition is $H_{cr} = 170$ kOe at 307 K, and a linear behavior of $H_{cr}(T)$ was found, with $dT/dH_{cr} = 0.45 \pm 0.02$ K/kOe.

Tegus et al. (2002a) synthesized single crystals of $Gd_5Si_{1.65}Ge_{2.35}$ and $Gd_5Si_{1.7}Ge_{2.3}$ by means of traveling floating zone method. Magnetic measurements in small applied magnetic field of 0.5 kOe show that the crystals order magnetically at 222 and 241 K, respectively. Application of 50 kOe magnetic field increases T_C of both compounds by 18 K. The magnetic moment in ordered state is 7.6 μ_B/Gd at 5 K. The value of magnetic entropy change peaks above -30 J/Kg K for both compounds for $\Delta H = 0$–50 kOe. The measured MCE is practically identical when the magnetic field is applied along any of the three principal crystallographic axes of these monoclinic crystals.

Zhuo et al. (2003) measured magnetocaloric properties of three Ge-rich $Gd_5Si_xGe_{4-x}$ alloys with $x = 0.33$, 0.6, 0.75. The Néel temperature of these alloys is nearly same ($T_N = 133 \pm 1$ K) but T_C changes quickly with x and is equal to 67, 92, and 108 K, respectively. The MCE at T_N is small (3 J/Kg K for 0–70 kOe field change). The magnetic entropy change at T_C reaches a saturation plateau at about -45 J/Kg K for a magnetic field change above $\Delta H = 0$–20 kOe, and for larger field changes (0–50 and 0–70 kOe), the maximum value of ΔS_M remains the same but the width of the MCE peak substantially increases. The width of the "flat" MCE peak is ~20 K for the 0 to 70 kOe field change. Mudryk et al. (2008) reported a similar value of the maximum magnetic entropy change (-44 J/Kg K for a magnetic field change from 0 to 50 kOe) for the $Gd_5Si_{0.5}Ge_{3.5}$ alloy, $T_C = 77$ K.

Matsumoto et al. (2004) measured magnetic entropy change for several $Gd_5Si_xGe_{4-x}$ alloys ($x = 0.33$, 0.6, 0.9, 1.01, and 2.0) and in the Ge-rich alloys obtained similar maximum $-\Delta S_M$ values (~40 J/mol K) for the magnetic field change from 0 to 50 kOe; the maximum $-\Delta S_M$ also reached a plateau value above $\Delta H = 0$–20 kOe magnetic field change.

3.2.1. Phase Composition and MCE in Doped $Gd_5Si_2Ge_2$ Alloys

Lewis et al. (2004) compared the magnetic entropy change of $Gd_5Si_{1.5}Ge_{2.5}$ and of the same specimen coated with 100 nm layer of Fe and Al and found some enhancement of the magnetocaloric effect as a result of coating. Pecharsky and Gschneidner (1997c) and Provenzano et al. (2004) independently showed that iron doping (substitution of Ge by Fe) essentially transforms the first-order transition observed in $Gd_5Si_2Ge_2$ (Pecharsky and Gschneidner, 1997b) into a second-order one (no M-to-O(I) transition) with smaller and wider peak of magnetic entropy change and negligible hysteresis loss calculated from the $M(H)$ data. The temperature of the transition increases from ~275 K to ~300 K (Pecharsky and Gschneidner, 1997c) or higher (~305 K according to Provenzano et al., 2004). The Provenzano et al. (2004) study also claims that the monoclinic structure becomes the stable phase at low temperatures in the iron-doped $Gd_5Ge_{1.9}Si_2Fe_{0.1}$ alloy. However, the follow-up temperature- and magnetic-field-dependent X-ray powder diffraction study by Her et al. (2005) of the $Gd_5Ge_{1.8}Si_2Fe_{0.2}$ and

$Gd_5Ge_{1.95}Si_2Fe_{0.05}$ alloys shows that the low-temperature phase is indeed orthorhombic, and the monoclinic phase forms at and continues to form above T_C. Due to increase in Fe content only part of the low-temperature O(I) matrix transforms into the M phase, and the magnetostructural transition is incomplete; the volume fraction of the impurity phases increases with Fe doping as well. The volume change at T_C for $Gd_5Ge_{1.95}Si_2Fe_{0.05}$ is equal to 1.2%.

A series of $Gd_5Ge_{1.9}Si_2M_{0.1}$ alloys (M = Cu, Co, Ga, Mn, Al, Bi, Sn) was prepared and studied by Shull et al. (2006) in order to investigate the effect of metal doping on the magnetocaloric properties of $Gd_5Si_2Ge_2$. The obtained result is similar to the one reported by Pecharsky and Gschneidner (1997c)—most metal additions (except Sn and Bi) promote the formation of the orthorhombic phase at the expense of the monoclinic phase effectively destroying the first-order PM → FM transition, and, therefore, GMCE. According to Pecharsky and Gschneidner (1997c), small level doping by Ga for both Si and Ge preserves the first-order of this transition in $Gd_5Si_{1.985}Ge_{1.985}Ga_{0.03}$. However, Aksoy et al. (2008) observed the reduction of the magnetocaloric effect in $Gd_5Si_{2-x}Ge_{2-x}Ga_{2x}$ alloys with Ga substitution from $2x = 0.03$ and higher, and found that the stability of the orthorhombic phase increases with x. Raj Kumar et al. (2008) obtained similar result (a decrease of MCE and an increase in the O(I) phase concentration at the expense of the M phase) with Ga doping in their study of a series of $Gd_5Si_2(Ge_{1-x}Ga_x)_2$ alloys with $x = 0$, 0.01, 0.02, 0.03. The Curie temperatures of the Ga-substituted alloys correspond to the second-order transition of the O(I) phase (~299 K). It is worth to note here that the parent $Gd_5Si_2Ge_2$ alloy in this study contained a significant amount of the O(I) phase and its magnetic entropy change was already relatively low, −7 J/Kg K. Both the 5:3 and 1:1 minor phases were observed by SEM in the Ga-doped alloys. Magnetocaloric properties of the $Gd_5Si_2Ge_{1.9}Ga_{0.1}$ sample, which according to the X-ray powder diffraction analysis contained ~81% of the 5:4 major phase, ~4% of the 1:1 phase, and ~15% of the 5:3 phase, were studied by means of heat capacity and direct magnetocaloric measurements (Palacios et al., 2010a). The sample undergoes a second-order transition at $T_C = 296.8$ K. The MCE parameters for the 0 to 50 kOe magnetic field change are $\Delta S_M = 6.93$ J/Kg K and $\Delta T_{ad} = 8$ K.

Zhang et al. (2007) confirmed the formation of the Gd_5Si_4 structure after doping $Gd_5Si_2Ge_2$ phase with Mn, Co, and Fe, and found that Ni doping also produces the same effect. The substitution of Si by Fe, however, does not suppress the structural transition in $Gd_5Si_{2-x}Fe_xGe_2$ alloys but instead promotes the formation of the 5:3 phase (Podmiljšak et al., 2008, 2009a). Iron was mainly found in the grain-boundary phases and the main effect of its substitution is the change of the Si/Ge ratio in the 5:4 matrix. This, probably, holds true for other transition metal substitutions: when during substitution the $Gd_5Si_2Ge_2$-based matrix becomes Si-rich the O(I) orthorhombic structure forms, in agreement with the $Gd_5Si_xGe_{4-x}$ phase diagram (Fig. 9), but when it becomes enriched in Ge, the monoclinic structure remains stable.

Podmiljšak et al. (2009b) carried out an extensive study of how the Si-for-Fe, Ge-for-Fe, and (Si,Ge)-for-Fe substitutions affect the phase composition and magnetocaloric properties of $Gd_5Si_2Ge_2$. They found that the Fe substitution promotes the formation of the secondary $Gd_5(Si,Ge,Fe)_3$ phase, which orders magnetically at ~110 K (Podmiljšak et al., 2009b,c). The T_C of the 5:4 phase increases when Fe replaces Ge but rapidly decreases when Fe replaces Si.

A study of the effect that the Fe substitution has on microstructure and magnetism of $Gd_5Si_2Ge_2$ has been also carried out by Raj Kumar et al. (2009). The study confirmed that Fe does not dissolve in the 5:4 matrix and suppresses the structural first-order transition in $Gd_5Si_2Ge_2$, effectively promoting the formation of the O(I) phase. As a result, the MCE is significantly reduced in Fe-doped alloys even though the magnetic hysteresis nearly disappears. Microstructure and magnetocaloric effect of the $Gd_5Si_xGe_{3.9-x}Fe_{0.1}$ alloys ($1.8 \leq x \leq 2.1$) were investigated by Rajkumar et al. (2010). Monoclinic 5:4 phase was observed in all alloys as a main phase; while the alloys with $x=1.8$, 1.9, 1.95, and 2 ordered via a first-order transition at T_C, the alloy with $x=2.1$ exhibited a second-order of the transition with no magnetic hysteresis in basic agreement with the $Gd_5Si_xGe_{4-x}$ phase diagram but in contradiction with its mostly monoclinic crystal structure (as judged by room temperature XRD experiments). Consequently, the GMCE has been observed in all investigated alloys except the one with $x=2.1$. The 5:3 phase was observed as a minor impurity in all alloys; in addition the 1:1 phase was detected in the sample with $x=2.1$. The iron does not dissolve in the main matrix but forms the minor FeSi phase.

Yucel et al. (2006) studied the effect of Mn doping on the phase composition and magnetic properties of $Gd_5Si_2Ge_2$, making a series of $Gd_5Si_{2-z}Ge_{2-z}Mn_{2z}$ alloys with $z=0.01$, 0.025, 0.04, 0.05, 0.07, and 0.10. The second-order PM to FM transition was observed in the as-cast alloys with no GMCE. Crystal structure, magnetic and magnetocaloric properties of the $Gd_5Si_{2.05-x}Si_{1.95-x}Mn_{2x}$ alloys ($x=0$, 0.3, 0.08) annealed at 900 °C for 1 week have been reported by Yüzüak et al. (2010a). All heat-treated samples crystallized in the $Gd_5Si_2Ge_2$ monoclinic structure; Gd_5Si_3 phase was reported as a minor phase. The Curie temperature was determined as 295 K for $x=0$, 0.03, and 299 K for $x=0.08$. The best magnetocaloric effect was obtained for the sample with $x=0.03$: $\Delta S_M = -11.6$ J/Kg K, RCP = 220.1 J/Kg ($\Delta H = 0$–50 kOe).

Phase composition and magnetocaloric properties of $Gd_5Si_{2-x}Ge_{2-x}Nb_{2x}$ alloys ($2x=0$, 0.05, 0.1, 0.15, 0.2) annealed at 1200 °C for 1 h have been investigated by Prabahar et al. (2010). Monoclinic phase was a majority phase but the samples with $2x=0.05$ and 0.1 contained the O(I) phase as well. Nb addition results in formation of $Nb_5(Si,Ge)_3$ and α-Nb phases. However, at low concentrations Nb is beneficial for MCE because it prevents the formation of the $Gd_5(Si,Ge)_3$ phase, and a maximum $\Delta S_M = -9.6$ J/Kg K was obtained at $T_C = 293$ K for $2x = 0.1$ alloy (for a field change from 0 to 20 kOe).

Li et al. (2006) reported the enhancement of magnetocaloric effect in $Gd_5Si_{1.95}Ge_{2.05}$ by Sn doping. Among five $Gd_5Si_{1.95-x}Ge_{2.05-x}Sn_{2x}$ samples ($2x = 0$, 0.01, 0.03, 0.05, 0.10) the sample with $2x = 0.03$ has the largest MCE, $\Delta S_M = -28.9$ J/Kg K for 0–20 kOe magnetic field change. Zhang et al. (2008b) studied the effect of Sn doping on the phase formation of $Gd_5Si_{2-x}Ge_{2-x}Sn_{2x}$ alloys ($x \leq 0.25$) and found that the Sn addition enhances the stability of the monoclinic phase in alloys made from the "commercial grade" Gd. Nearly single-phase monoclinic samples were obtained even in as-cast tin-doped alloys. Aghababyan and Harutyunyan (2009) prepared a series of $Gd_5Si_{2-x}Ge_{2-x}Sn_{2x}$ samples ($2x = 0$, 0.01, 0.03, 0.05, 0.10) and measured the temperature dependence of their dynamic magnetic susceptibility. They observed that the magnetic ordering temperatures of tin-doped alloys are nearly the same (varying from 275 to 278 K) but are ~15 K higher than the T_C of their un-doped $Gd_5Si_2Ge_2$ (262 K).

Zhuang et al. (2006b) prepared a series of $Gd_5Si_{2-x}Ge_{2-x}Pb_{2x}$ alloys ($2x = 0$, 0.01, 0.03, 0.05, 0.10) and measured their magnetic and magnetocaloric properties. Largest MCE (27.5 J/Kg K for $\Delta H = 0$–20 kOe) was observed at 274 K for the $Gd_5Si_{1.975}Ge_{1.975}Pb_{0.05}$. All samples were prepared by arc-melting and annealed at 900 °C for 5 days.

Yüzüak et al. (2010b) reported the maximum $\Delta S_M = -13.6$ J/Kg K and maximum $\Delta T_{ad} = 13$ K for the magnetic field change from 0 to 50 kOe in the $Gd_5Si_{1.925}Ge_{2.025}In_{0.05}$ sample. The sample was prepared by arc-melting followed by annealing at 1173 K for 1 week. According to the electron microscopy and X-ray powder diffraction analysis the main phase is a $Gd_5Si_2Ge_2$-type monoclinic structure but with $T_C = 298$ K. The Arrot plots confirm the first order of the transition. The $Gd_5(Si,Ge)_3$ minor phase is present in the studied specimen.

The effect of boron doping on the MCE of $Gd_{5.1}Ge_2Si_2$ has been investigated by Zhang et al. (2008a). When Ge was nominally substituted with B, that is, when the alloy compositions were designed to be $Gd_{5.1}Ge_{2-x}Si_2B_x$, the Curie temperature increased but when Si was substituted with B in a similar fashion, the temperature of magnetic ordering was decreasing. The MCE decreased with boron doping in both cases.

Scaling analysis of the magnetocaloric effect in $Gd_5Si_2Ge_{1.9}X_{0.1}$ alloys (X = Al, Cu, Ga, Mn, Fe, Co) has been performed by Franco et al. (2010). In alloys doped with Al, Cu, Ga, and Mn the first-order transition is fully suppressed and the universal curve can be constructed using a single reference temperature. Moreover, all the magnetic energy curves for all compositions undergoing second-order transition fit onto the same universal curve constructed using the phenomenological scaling model (Franco et al., 2006). In the Fe-doped sample, the first-order character almost disappeared but the presence of weak hysteresis makes the scaling procedure more complicated (two reference temperatures were needed). In the Co-doped alloy, there is a significant thermal hysteresis, which makes the scaling results inconclusive.

Unlike the majority of studies, which examined the effect of doping on the T element side, Prabahar et al. (2011) investigated the effect of doping Zr to replace Gd. A series of $Gd_{5-x}Zr_xSi_2Ge_2$ alloys ($x=0$, 0.05, 0.1, 0.15, and 0.2) has been prepared by arc-melting followed by annealing at 1200 °C for 2 h. The Zr substitution results in the formation of the O(I) orthorhombic phase in all Zr-containing samples; therefore the MCE observed in these samples is lower compared to the un-doped $Gd_5Si_2Ge_2$. Interestingly, the Curie temperature increases for the $x=0.05$ alloy (295 K) compared to the pure $Gd_5Si_2Ge_2$ (278 K) because, as shown above, the T_C of the second-order transition is always higher than the T_C of the first-order transformation for the same composition. However, further increase of Zr content reduces the T_C due to a trivial dilution effect (substitution of the magnetic Gd atoms with the nonmagnetic Zr atoms).

3.3. Anomalous Electrical Resistivity and Magnetoresistance

In 1998, a series of experiments performed on the $Gd_5Si_{1.8}Ge_{2.2}$ compound with the room temperature monoclinic structure established the existence of strong coupling between magnetism and crystal structure in $Gd_5Si_xGe_{4-x}$ and led to discovery of a number of interesting and potentially useful phenomena occurring in this system, such as giant magnetostriction and giant magnetoresistance (Morellon et al., 1998a,b). The $Gd_5Si_{1.8}Ge_{2.2}$ undergoes PM-M$\leftrightarrow$FM-O(I) magnetostructural transition at $T_C=240$ K. A strong decrease of the electrical resistivity ($\Delta\rho/\rho=-20\%$) was observed at T_C on cooling, and the resistivity increased during heating above T_C. The thermal hysteresis was ~5 K. In the ferromagnetic state, the application of magnetic field induces a small (−4% at 120 kOe) and negative magnetoresistance effect. However, above and near T_C the material undergoes a first-order field-induced phase transition to the FM state at certain critical field H_{CR}, which is different for each measuring temperature, and a GMR effect (magnetoresistance $\Delta\rho/\rho=[\rho(H,T)-\rho(0,T)]/\rho(0,T)\approx-20\%$) is observed as shown in Fig. 18 (Morellon et al., 1998b). An even stronger GMR effect, $\Delta\rho/\rho=-50\%$, was observed in the $Gd_5Si_{0.4}Ge_{3.6}$ alloy, which undergoes AFM-O(II)–FM-O(I) transformation at $T_C=81$ K (Morellon et al., 2001a).

Levin et al. (1999) performed magnetic-field- and temperature-dependent measurements of the electrical resistivity of $Gd_5Si_2Ge_2$ prepared using high-purity Gd, and observed a similar behavior around T_C. The resistivity sharply decreases below T_C and reversibly increases when the samples were heated above T_C. A large thermal hysteresis of ~15 K was observed in both $H=0$ kOe and $H=40$ kOe measurements. Application of 40 kOe magnetic field shifts both the T_C and the resistivity anomaly by 24–30 K depending on the sample (Levin et al., 1999). The anomalous behavior of the electrical

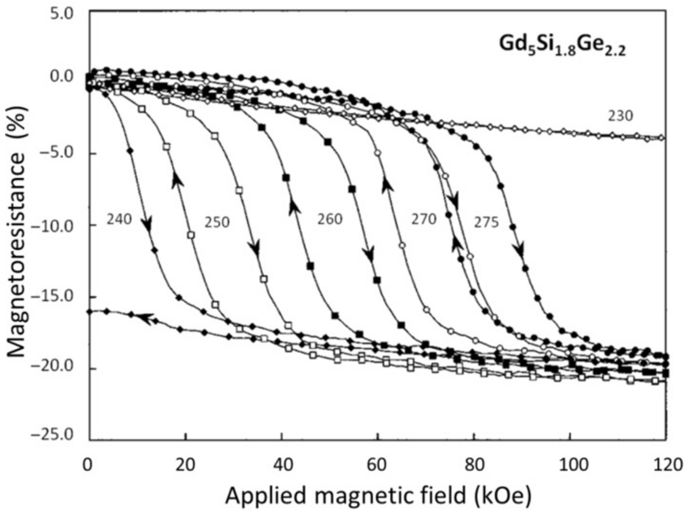

FIGURE 18 Isothermal magnetoresistance of $Gd_5Si_{1.8}Ge_{2.2}$ measured as a function of applied magnetic field (Morellon et al., 1998b). The temperatures, at which the isothermal loops were measured, are shown in K.

resistance was also observed in the $Gd_5Si_{1.5}Ge_{2.5}$ alloy with room temperature monoclinic crystal structure (Levin et al., 2000a). The measurements indicate that the magnetostructural transition in this alloy can be induced by both temperature and magnetic field. Interestingly, the temperature dependence of the electrical resistance in $Gd_5Si_{1.5}Ge_{2.5}$ indicates a similar in magnitude but positive $\Delta\rho/\rho = \sim 25\%$ on cooling below T_C, contrary to the negative discontinuity observed during cooling in $Gd_5Si_{1.8}Ge_{2.2}$ (Morellon et al., 1998b) and $Gd_5Si_2Ge_2$ (Levin et al., 1999). This difference in behaviors of similar compositions with same crystal structures in both the paramagnetic and ferromagnetic states is difficult to explain unless one assumes strong macroscopic (extrinsic) effects that may be specimen dependent.

Levin et al. (2001a) performed extensive cycling experiments on a $Gd_5Si_{1.95}Ge_{2.05}$ sample using electrical resistivity, heat capacity, and magnetization measurements. They found that the effects of cycling on the magnetic properties and heat capacity of the studied sample are minor and basically are limited to the decrease of the transition temperature by 2 K. At the same time, much stronger influence of thermal cycling on the electrical transport properties has been observed: (1) electric resistivity of high-temperature phase (β) was lower compared to the electric resistivity of the low-temperature phase (α) during the first few cycles, but after 20 cycles the electrical resistivity of the β phase became larger than the one of the α phase; (2) the transition temperature decreased by almost ~7 K. These findings allowed Levin et al. (2001a) to speculate that a different, high electrical resistivity β'' phase forms after extensive cycling in $Gd_5Si_{1.95}Ge_{2.05}$, however, this suggestion has not been confirmed. Hadimani et al. (2009a) measured electrical resistivity and magnetization of a $Gd_5Si_{1.8}Ge_{2.2}$ single-crystal and polycrystalline $Gd_5Si_{2.09}Ge_{1.91}$ sample. The irreversible increase in the magnetic coercivity was observed in the $M(H)$ loops of $Gd_5Si_{1.8}Ge_{2.2}$ single crystal after the cycling had been performed. The signatures of the first-order transition were clearly seen on the temperature dependences of both magnetic and electrical properties. Cycling through this transition shows a gradual increase of the electrical resistivity values for the polycrystalline $Gd_5Si_{2.09}Ge_{1.91}$ sample. The annealing of the cycled specimen above room temperature can partially reduce its electrical resistivity back. By holding the $Gd_5Si_{2.09}Ge_{1.91}$ sample at 360 K for 25 h, Hadimani and Jiles (2010) were able to recover 45% of the electrical resistivity increase that had occurred due to cycling through the first-order phase transition.

The magnetostructural transition in $Gd_5Si_xGe_{4-x}$ is strongly anisotropic and changes in lattice dimensions are significantly different along all three major crystallographic directions because the slab movement occurs along the *a*-axis in the *ac*-plane, while there is very little change along the *b*-axis (see Section 3.4). It should not come as a surprise that such anisotropy strongly reflects upon the physical properties of these compounds, especially when there is a possibility to measure a particular property (magnetization, resistivity, etc.) along one of the crystallographic axes using oriented single crystals. However, it does not necessarily mean that the effect observed along the *b*-axis at the transition point will always be weaker when compared with the *a*- or *c*-axes. For example, the negative magnetoresistance measured in $Gd_5Si_2Ge_2$ single crystal is strongly anisotropic, but MR effect observed along the *c*-axis ($\Delta\rho/\rho = -14.5\%$) is ~60% weaker compared to the one observed along the *a*-axis ($\Delta\rho/\rho = -24\%$), while the MR effect observed along the *b*-axis ($\Delta\rho/\rho = -21\%$) is comparable to the one measured for the *a*-direction (Tang et al., 2004a).

Temperature- and field-dependent electrical resistivity measurements were performed on polycrystalline Gd_5Ge_4 by Levin et al. (2001b). These measurements were accompanied by the field-dependent heat capacity measurements and electronic structure calculations. The zero magnetic field electrical resistivity shows intriguing metal-insulator-like transition at $T_N = 130$ K (Fig. 19). Both the Fermi-liquid behavior of the electrical resistivity of Gd_5Ge_4 and its electronic heat capacity indicate a presence of a narrow conduction band at low temperatures. Among the models that were used to explain the electrical resistivity behavior above T_N, the hopping conductivity model provided the best description for the observed results. In an applied magnetic field of 20 kOe, a sharp transition became apparent in the $\rho(T)$ data at 29 K. The initial isothermal application of magnetic field to Gd_5Ge_4 at 5 K resulted in a sharp first-order like increase in electrical resistivity of the sample above 20 kOe, which was later associated with the AFM-O(II) → FM-O(I) transition

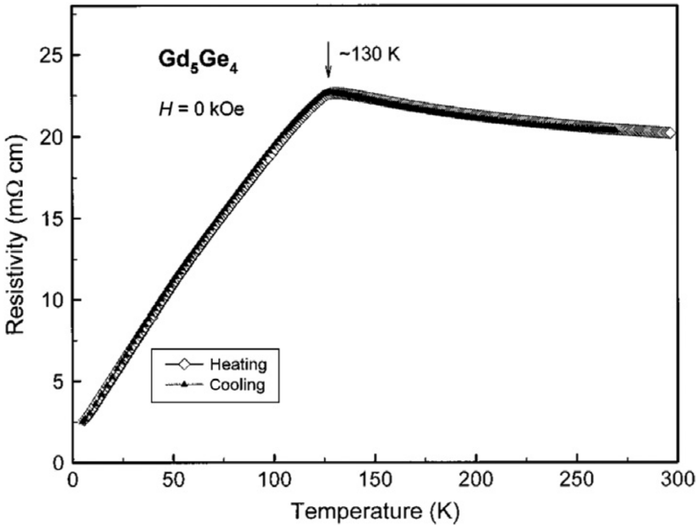

FIGURE 19 Temperature dependence of the electrical resistivity of polycrystalline Gd_5Ge_4.

(Pecharsky et al., 2003a). However, the sample did not return into a low electrical resistivity state during demagnetization and remained in high resistivity state during subsequent magnetic cycling showing the behavior consistent with the formation of the kinetically arrested "magnetic glass" state (see Section 3.6).

The electrical resistivity as a function of temperature of Gd_5Ge_4 in magnetic fields of 0, 10, 20, and 40 kOe has been measured by Xue et al. (2009). The temperature-dependent magnetoresistance was calculated from the measured electrical resistivity data. Large positive magnetoresistance $\Delta\rho/\rho = [\rho(H,T) - \rho(0,T)]/\rho(0,T)$ (up to 50% for 40 kOe applied magnetic field) was observed above 50 K; at low temperatures negative −30% magnetoresistance was observed around 25 K.

High-resolution electrical resistivity measurements were performed on the $Gd_5Si_{0.4}Ge_{3.6}$ compound in order to study the evolution of its anomalous electrical transport behavior through more than 50 thermal cycles between 10 and 300 K (Sousa et al., 2003). The electrical resistivity initially showed a sharp peak at $T_C \sim 80$ K, but after cycling the peak disappeared and was replaced by a rather monotonous increase in resistivity on heating up to the AFM ordering temperature ($T_N = 128$ K). Above T_N the resistivity starts to decrease on further heating and this part of $\rho(T)$ behavior is not affected by the thermal cycling. Thermal hysteresis associated with the first-order transition at T_C slowly decreases through the cycling and becomes negligible after ~50 cycles are performed. However, the electrical resistivity even for the same composition is sample dependent, and one of the $Gd_5Si_{0.4}Ge_{3.6}$ specimens studied in this work had higher $T_C = 87$ K and clear multistep behavior in the vicinity of the first-order transition. Analysis of the anomalous resistivity behavior of $Gd_5Si_{0.4}Ge_{3.6}$ after a moderate number of cycles (13–28 thermal cycles) was performed by Correia et al. (2004). Even more detailed investigation of this sample was performed by Sousa et al. (2005) who found that during the initial electrical resistivity measurements the magnetostructural transition takes place in three closely spaced steps. Further thermal cycling results in appearance of an additional reproducible anomaly ~4 K below the main transition, which remains stable after many cycles (>30).

Stankiewicz et al. (2000) studied the magnetic field and temperature dependences of Hall resistivity in $Gd_5Si_{1.8}Ge_{2.2}$ polycrystalline material. A clear correspondence between magnetization and Hall resistivity data has been observed. A sharp dip in the value of the Hall coefficient exists at the temperature of the magnetostructural transition (~235 K, on heating).

3.4. Linear Thermal Expansion Studies and Magnetostriction

In addition to the GMR effect, Morellon et al. (1998a) observed the occurrence of a large volume contraction, $\Delta V/V = -0.4\%$, in $Gd_5Si_{1.8}Ge_{2.2}$ at its transition temperature $T_C = 240$ K using linear thermal expansion measurements. As shown by magnetostriction measurements, a large volume magnetostriction of $\omega = (4.5 \pm 0.2) \times 10^{-3}$ can be achieved above H_{CR} at $T > T_C$. The behavior of magnetostriction is similar to the behavior of magnetoresistance in the sense that it is reversible, significant hysteresis is present, and the value of H_{CR} is a linear function of temperature. The higher was the measurement temperature the higher H_{CR} was required to start the transition.

It is easy to deduce that occurrence of a number of different phenomena (GMCE, GMR, GMS) at the same T_{CR} and H_{CR} must be caused by same process related to the first-order nature of the magnetostructural transitions in accordance with the $Gd_5Si_xGe_{4-x}$ magnetostructural phase diagram. The unit cell volume change observed during the temperature-dependent X-ray powder diffraction experiment on $Gd_5Si_{1.8}Ge_{2.2}$ (Morellon et al., 1998a) was comparable with the value of the measured magnetostriction indicating that the GMS and GMR effects observed in this alloy must be directly related to this structural transformation. Casanova et al. (2002a) have shown that magnetovolume effects observed in $Gd_5Si_xGe_{4-x}$ are of the same nature as the volume changes caused by the Si/Ge chemical substitution. Magnetostructural transitions occur in all GMCE alloys from the $Gd_5Si_xGe_{4-x}$ system, which are characterized by strong first-order transitions at T_C. In fact, the presence of magnetostructural coupling underpins nearly all extraordinary phenomena observed in R_5T_4 systems.

The giant magnetostriction effect becomes colossal when an oriented single crystal is used instead of a polycrystalline material. Thermal expansion measurements of the $Gd_5Si_{1.95}Ge_{2.05}$ single-crystal oriented along the a-axis showed sudden and strong (more than −8000 ppm) change in strain due to first-order structural transformation (Han et al., 2002). An applied magnetic field shifts the temperature of this transformation by about 0.49 K/kOe. Linear thermal expansion measurements performed on a polycrystalline $Gd_5Si_{1.95}Ge_{2.05}$ sample showed much smaller change at T_C: ~1300 ppm (Chernyshov et al., 2002). As noted above, the structural transformation in $Gd_5Si_xGe_{4-x}$ alloys is strongly anisotropic, and the change along the a crystallographic direction is a few times higher and of the opposite sign than the change along the c-direction. The change along the b-direction is quite small when compared with the other two. Using temperature-dependent X-ray powder diffraction Morellon et al. (2000) have found that when $Gd_5Si_{0.4}Ge_{3.6}$ alloy undergoes magnetostructural transition [O(II)–O(I)] on cooling at $T_C = 81$ K, its lattice dimensions change as follows: $\Delta a/a = -1.6\%$, $\Delta b/b = +0.3\%$, $\Delta c/c = +0.7\%$. Using high-resolution X-ray powder diffraction Mudryk et al. (2008) found that for a sample of nearly the same composition, $Gd_5Si_{0.5}Ge_{3.5}$, the difference between the lattice strains along different crystallographic directions ($T_C = 77$ K) is even higher: $\Delta a/a = -1.86\%$, $\Delta b/b = +0.07\%$, $\Delta c/c = +0.63\%$. The resulting unit cell volume change is $\Delta V/V = -1.16\%$, which qualifies it as colossal magnetostriction that one may expect to observe in a bulk sample with completely random orientation of crystallites. However, if a bulk polycrystalline sample is textured along the b- or c-direction, as it often happens in real specimens, the measured strain would be much lower than the one measured along the a-axis of an oriented single crystal. For example, Hadimani et al. (2011) observed that linear strain observed in the $Gd_5Si_2Ge_2$ crystal oriented at 20° angle to the a-axis (i.e., not completely aligned) is still three times larger than the liner strain measured for bulk $Gd_5Si_{2.09}Si_{1.91}$ polycrystalline sample. Somewhat surprisingly, Han et al. (2003a) observed significant spontaneous LTE strain of ~3000 ppm at $T_C = 255$ K of a Brigman-grown $Gd_5Si_2Ge_2$ single-crystal oriented along the b-axis. LTE measurements of two $Gd_5Si_{2.09}Ge_{1.91}$ polycrystalline samples, one made from high-purity Gd and another made from commercial grade Gd, showed that the T_C of the latter sample was 13 K lower compared to the former one, but the strain observed at T_C in the latter sample was about three times higher than in the sample made from high-purity Gd (Han et al., 2003b), which suggests that the grains in the specimen obtained from the commercial purity Gd were primarily oriented along the a-axis during the LTE measurements.

Magnetostriction and LTE measurements were performed on a Bridgman-grown $Gd_5Si_2Ge_2$ single crystal by Han et al. (2004). They confirmed that the giant magnetostriction in $Gd_5Si_2Ge_2$ occurs only as a result of the MST. For example, at 15 K (~250 K below the transition) practically no magnetostriction was observed, as expected for a Gd-based material (4f charge density of Gd is spherically symmetrical). A thorough linear thermal expansion study of the $Gd_5Si_2Ge_2$ single crystal (Magen et al., 2005) shows that macroscopic changes of the crystal's dimensions agree very well with the calculated changes in lattice parameters for the M to O(I) transformation, that is, $\Delta a/a = -0.94\%$, $\Delta b/b = +0.13\%$, and $\Delta c/c = +0.22\%$.

Anomalous volume expansion of ~0.8% was observed during thermal expansion measurements performed on a polycrystalline bulk $Gd_5Si_2Ge_2$ sample prepared using Ames Laboratory Gd, which generally has 99.9 at.% or better purity with respect to all other elements in the periodic table (Nersessian et al., 2003, 2004), also in agreement with crystallographic data. The study found a substantial decrease in the amount of strain produced at the transition (1300 vs. 8000 ppm) when a composite made out of a ball-milled $Gd_5Si_2Ge_2$ (35 vol.%) and vinyl ester resin (65 vol.%) was tested. Magnetic-field-induced strain for the composite results in a volume strain of 1650 ppm (Nersessian et al., 2004).

Nazih et al. (2003) carried out LTE measurements on a $Gd_5Si_{1.72}Ge_{2.28}$ single crystal along all three major crystallographic axes. They obtained the following values of the step-like changes at $T_C = 240$ K (on heating): $(\Delta L/L)_a = 0.68\%$, $(\Delta L/L)_b = -0.2\%$, and $(\Delta L/L)_c = 0.21\%$. The calculated volume change $\Delta V/V$ is positive and amounts to 0.27%. Using the Clausius–Clapeyron relation Nazih et al. (2003) estimated a hydrostatic pressure dependence $dT_C/dP = 3.2 \pm 0.2$ K/kbar but suggested that the pressure effect is strongly anisotropic.

LTE results were reported for polycrystalline $Gd_5Si_2Ge_2$ and $Gd_5Si_{0.6}Ge_{3.4}$ alloys by Kamiya et al. (2004) and Kamiya et al. (2005). For $Gd_5Si_2Ge_2$, the LTE was measured in magnetic fields of 0, 10, 20, 30, 40, and 50 kOe. However, these measurements of LTE by the capacitance method were problematic because some of the specimens were too brittle, and some disintegrated when the magnetic field was applied.

Magen et al. (2003b) studied the magnetoelastic behavior of Gd_5Ge_4 by means of linear thermal expansion and magnetostriction measurements in the temperature range from 5 to 300 K and in applied magnetic fields up to 120 kOe. Zero magnetic field measurements indicated no anomaly in LTE data on cooling but an anomaly on heating at 16 K. LTE measurements in applied magnetic fields of $H = 20$, 50, and 120 kOe have been performed indicating a clear presence of a first-order $O(I) \leftrightarrow O(II)$ structural transition ($T_C \sim 50$ K for 50 kOe data), which has been confirmed afterward by temperature- and magnetic-field-dependent X-ray powder diffraction studies (Mudryk et al., 2005a; Pecharsky et al., 2003a). The temperature of this transition increases with the magnetic field at a rate of ~0.5 K/kOe, similar to other $Gd_5Si_xGe_{4-x}$ compounds. The magnetostriction isotherms indicate a reversible first-order transition with ~7 kOe hysteresis above 20 K. Below 20 K the magnetoelastic behavior starts to show significant irreversibility effects associated with the "magnetic glass" kinetic phenomena discussed in Section 3.6.

According to the temperature- and magnetic-field-dependent X-ray powder diffraction measurements by Mudryk et al. (2005a), the following LTE coefficients were obtained for Gd_5Ge_4 in the paramagnetic state: 0.69, 1.18, and $1.03 \times 10^{-5}\ K^{-1}$ along the *a*-, *b*-, and *c*-axes, respectively. It is interesting to note that the normal thermal expansion is the smallest along the *a*-axis while the structural transformations in R_5T_4 alloys usually result in the largest shift in that same direction. In Gd_5Ge_4, the relative changes in lattice parameters during the magnetic-field-induced structural O(II) → O(I) transformation are $\Delta a/a = -1.9\%$, $\Delta b/b = +0.1\%$, and $\Delta c/c = +0.6\%$ (Mudryk et al., 2005a). The resulting contraction of the unit cell volume is $\Delta V/V = -1.2\%$.

The temperature dependence of lattice parameters of Gd_5Si_4 was studied by Altounian and Liu (2007) using temperature-dependent X-ray powder diffraction. They found that the lattice expands evenly and almost linearly above and below $T_C = 336$ K, but small anisotropic shifts in lattice parameters were observed around T_C. Between 325 and 345 K, the *a*-parameter remains almost the same when accounting for the regular thermal expansion ($a_{325K} = 7.4834(1)$ Å vs. $a_{345K} = 7.4846(2)$ Å), while the *b* parameter contracts slightly ($b_{325K} = 14.7476(3)$ Å vs. $b_{345K} = 14.7452(4)$ Å) and the *c* parameter expands by ~0.08% ($c_{325K} = 7.7493(2)$ Å vs. $c_{345K} = 7.7560(1)$ Å).

3.5. Thermoelectricity and Spontaneous Generation of Voltage

The spontaneous generation of an electrical signal (voltage) at the magnetostructural transition, or SGV effect, has been observed in several $Gd_5Si_xGe_{4-x}$ alloys with $x = 0.33$, 1.5, 1.95, and 2 (Levin et al., 2001c). Majority of the measurements were performed on the $Gd_5Si_{1.95}Ge_{2.05}$ sample, which undergoes the O(I)-FM ↔ M-PM transition at 266 K during heating and at 249 K during cooling in zero magnetic field. When the sample temperature is changed at 1.5 K/min rate across the transition distinct voltage signals of 8 μV (cooling) and −6 μV (heating) are observed with their peaks located at the above mentioned transition temperatures. When the temperature sweep is performed in applied magnetic field (i.e., 20 kOe) the temperature at which the SGV occurs is 12 K higher compared to the zero magnetic field measurement. This is expected because the magnetic field raises the first-order transition temperatures of $Gd_5Si_xGe_{4-x}$ alloys. In most measurements, observed SGV signals were not single peaks but contained a number of relatively random spikes occurring as the transition was approached. In all cases, however, a strongest peak could be clearly distinguished as the peak of the transition. When the sample's temperature was changed at a higher rate (e.g., 3 K/min), the recorded electric signal was stronger.

An identical effect was observed when the sample was isothermally magnetized or demagnetized near the transition temperature (Levin et al., 2001c) indicating that the occurrence of a magnetostructural transition is the origin of the SGV phenomena in $Gd_5Si_xGe_{4-x}$. In other measured $Gd_5Si_xGe_{4-x}$ samples, the SGV is also observed around the temperature of magnetostructural transition (MST). Thus, this phenomenon is expected to occur in all R_5T_4

systems undergoing first-order transitions and, probably, in many other metallic and nonmetallic systems with structural transitions. The nonequilibrium first-order phase transition process results in a noneven distribution of latent heat (expelled or absorbed, depending on the direction of the transformation) across the specimen during the transition. The created thermal gradient generates a thermoelectric response, which, apparently, is the basis for the observed SGV effects. It is safe to suggest that the SGV signal occurs in $Gd_5Si_xGe_{4-x}$ samples when the transition is triggered by other thermodynamic variables, for example by applied hydrostatic pressure.

Zou et al. (2006) studied the SGV effect using both polycrystalline and single-crystalline $Gd_5Si_2Ge_2$. The experiments showed the presence of reversible and repeatable SGV signals along all crystallographic directions in response to the changes in temperature and applied magnetic field. The magnitude of the response is anisotropic and depends on the sweep rate (see Fig. 20). Usually the higher sweep rate (both temperature and magnetic field)

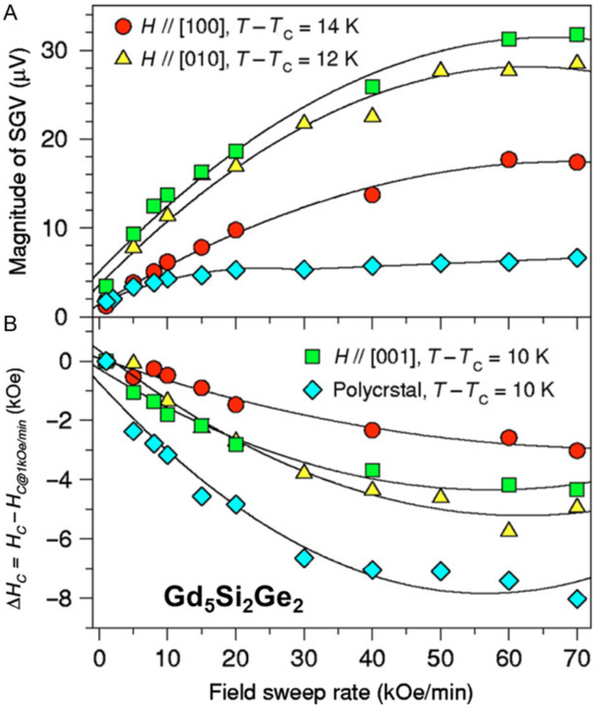

FIGURE 20 The magnitude of SGV (A) and the change of the critical field of SGV compared with the critical field at 1 kOe/min sweep rate (B) as functions of the magnetic-field sweep rate in $Gd_5Si_2Ge_2$ (Zou et al., 2006).

the stronger is SGV signal. The signal for the polycrystalline sample is about three times weaker than for the single crystal.

Temperature-dependent measurements of thermopower of $Gd_5Si_xGe_{4-x}$ alloys were performed on a $Gd_5Si_{0.4}Ge_{3.6}$ sample [undergoes O(II)-AFM-O(I)-FM transformation at $T_C = 78$ K] by Sousa et al. (2002). A sharp change in thermopower has been observed at T_C, and a shallow minimum in Seebeck coefficient versus temperature-dependence occurs between T_C and T_N reaching −23 μV/K at ~95 K. The first derivative of such dependence clearly displays critical features at both T_C and T_N. Contrary to the electrical resistivity measurements (e.g., Morellon et al., 2001a), thermal cycling does not have much effect on thermoelectric behavior. In addition to $Gd_5Si_{0.4}Ge_{3.6}$, Pinto et al. (2005) also reported temperature-dependent thermopower of Gd_5Ge_4 and $Gd_5Si_{1.8}Ge_{2.2}$ samples. Distinct steps were observed in Seebeck coefficient versus temperature curves at the temperatures of magnetostructural transition measured for both $Gd_5Si_{0.4}Ge_{3.6}$ and $Gd_5Si_{1.8}Ge_{2.2}$. A Gaussian distribution, typical for the first-order transformations, was observed in the first derivative of the temperature-dependent thermopower plots in the vicinity of T_C.

Temperature dependences of electrical resistivity and thermopower were measured on bulk polycrystalline $Gd_5Si_xGe_{4-x}$ samples ($x = 1.7$, 2.0, 2.2, and 2.3) annealed at 1573 K for 1 h (Raj Kumar et al., 2011). A noticeable change in thermopower (−8 μV/K) was obtained at the temperature of the magnetostructural transition (273 K) for the $Gd_5Si_2Ge_2$ compound.

3.6. Kinetics of Magnetostructural Transitions in $Gd_5Si_xGe_{4-x}$

Ideally, first-order transitions occur momentarily when at a certain critical point one phase is replaced by another. In reality, mainly due to macroscopic effects, such as strain, imperfections of the crystal lattice, compositional inhomogeneity, etc., these transitions develop over a certain temperature (or magnetic field, or pressure) range, and instead of having only a single critical parameter (T_{CR}, H_{CR}, or P_{CR}) they may be characterized by, for example, H_{CR1} of the start and H_{CR2} of the end of a magnetic-field-induced transition. In the region $H_{CR1} < H < H_{CR2}$, a system exists in the so-called phase separated state, where the low-field and high-field phases coexist at proportions that depend on the magnetic field value. Moreover, first-order transitions usually exhibit thermal (pressure, magnetic field) hysteresis, and the critical parameters of the transition during heating (demagnetization) are different from those of the same transition during cooling (magnetization). As a result, instead of having a single-phase transition boundary on the ideal *H–T* diagram, real $Gd_5Si_xGe_{4-x}$ specimens typically have complex *H–T* diagrams similar to the one shown in Fig. 21, which was constructed for $Gd_5Si_{1.5}Ge_{2.5}$ using magnetization measurements (Levin et al., 2000b, 2001d).

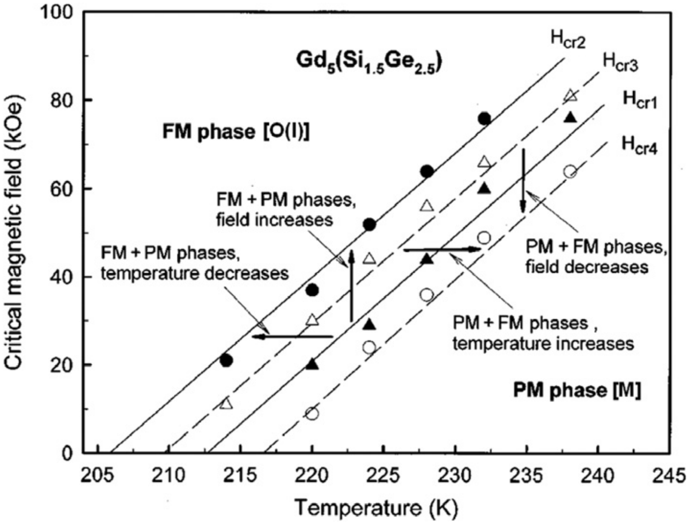

FIGURE 21 Magnetic field (*H*)–temperature (*T*) diagram of $Gd_5Si_{1.5}Ge_{2.5}$ (Levin et al., 2000b, 2001d). Critical magnetic fields are determined from the isothermal magnetization measurements and represent the start and the end of the field-induced magnetic PM-M↔FM-O(I) transformation.

The dc magnetic field increases the PM↔FM transition temperature in $Gd_5Si_{1.5}Ge_{2.5}$ by ~0.36 K/kOe (Levin et al., 2001d). Both field and temperature-induced transitions are characterized by large hysteresis, indicating the formation of the magnetically and structurally heterogeneous system in $Gd_5Si_{1.5}Ge_{2.5}$ near the transition where O(I)-FM and M-PM phases coexist. Teng et al. (2002) provided a phenomenological description of the PM↔FM first-order transition for $Gd_5Si_xGe_{4-x}$ alloys with $0.96 < x < 2.0$ using the Landau–Devonshire theory. They reasonably reproduced the field-driven magnetic transitions as well as thermal and magnetic hystereses.

The dynamic of the first-order magnetostructural transition in $Gd_5Si_{0.2}Ge_{3.8}$ compound was studied by means of high-sensitivity DSC measurements (Casanova et al., 2004a). The study found that the entropy change associated with the transition is different for the thermally and field-induced processes due to the work done by the magnetic field during field sweep. The study reports the “jerky” character of calorimetric curves, which is explained by the avalanche-type dynamics. Such avalanches occur as a result of nucleation and growth of domains of the new structure taking place during a first-order transition. The structure of the avalanches becomes repetitive after a material is cycled a few times through the transition, and can be characterized by power-law distribution (Casanova et al., 2004a).

Pérez-Reche et al. (2006) detected acoustic emission occurring when $Gd_5Si_2Ge_2$ undergoes magnetostructural transition from M-PM to O(I)-FM state. The acoustic emission spectra confirm the presence of the avalanches but there is no characteristic scale for the size of these avalanches. The analysis of results shows that thermal fluctuations are irrelevant for the transformation process indicating athermal character of the M↔O(I) transition. Guimarães et al. (2009) propose to use acoustic detection of the adiabatic temperature change for the determination of the magnetocaloric effect, and tested this method on Gd and $Gd_{5.09}Si_{1.88}Ge_{2.03}$ samples. The measurements were reproducible and with an appropriate calibration the ΔT results obtained for Gd were consistent with those obtained by direct measurements. The measurements performed on the $Gd_{5.09}Si_{1.88}Ge_{2.03}$ alloy clearly identified a two-phase nature of the sample and allowed distinguishing between first- and second-order transitions.

The Bridgman-grown single crystal was used to study magnetic relaxation in $Gd_5Si_2Ge_2$ by Leib et al. (2004). The dynamics of the first-order transformation is different from the magnetization reversal that may be observed in conventional magnetic relaxation experiments. The measured variations of magnetic moment with time are consistent with a thermal activation process with a single energy barrier, which must be overcome in order to proceed with transformation from one polymorph into another. The study found that magnetization curves took as long as 300 s to approach its asymptotic values. The energy barrier was estimated to be 4.2 ± 0.2 eV (Leib et al., 2004).

A particularly complex kinetic behavior is observed at low temperatures in Gd_5Ge_4. When cooled in zero or low ($<\sim 10$ kOe) magnetic field, this compound remains in the AFM-O(II) state ($T_N = 125$ K) down to at least ~2 K even though the AFM–FM transition may be expected at ~25 K from the linear extrapolation of the AFM–FM phase boundary of the $Gd_5Si_xGe_{4-x}$ phase diagram shown in Fig. 10. Application of magnetic field at or above H_{CR} triggers a sharp metamagnetic-like magnetostructural transformation from the AFM-O(II) into FM-O(I) phase (the actual value of H_{CR} depends on many factors including temperature, thermal history, purity of the rare earth metal used in sample preparation, etc., but normally lies in the range between 10 and 16 kOe). However, after the Gd_5Ge_4 sample is isothermally demagnetized from the FM state, the second magnetization curve is much different from the first one and is more typical of a conventional ferromagnetically ordered material (Fig. 22, Levin et al., 2002). Figure 23 shows the structural low-temperature diagram of Gd_5Ge_4, determined using X-ray powder diffraction (XRPD) experiments performed as a function of temperature and applied magnetic field (Mudryk et al., 2005a). The H–T phase diagram of Gd_5Ge_4: (a) indicates structural phase coexistence (phase separation) over an extended range of temperatures and magnetic fields, (b) is history dependent, and (c) shows correspondence between magnetism and crystal structure similar to other $Gd_5Si_xGe_{4-x}$ alloys. It should be noted here that the transition range observed using the XRPD method is typically broader than the range of transition observed in magnetization measurements (Mudryk et al., 2005a, 2008).

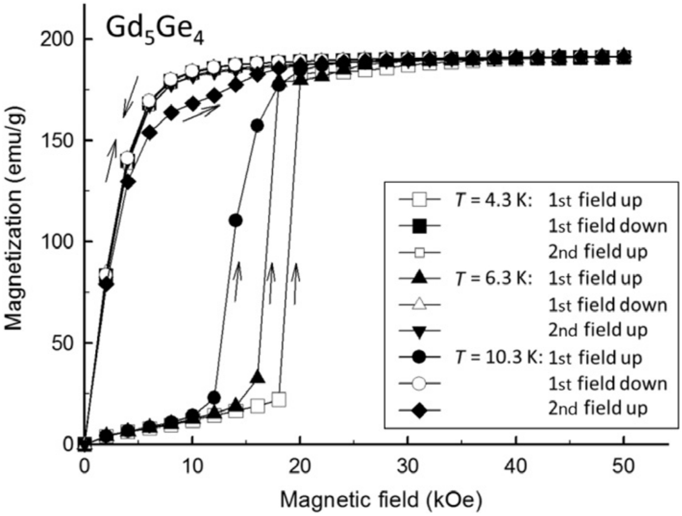

FIGURE 22 Isothermal magnetization of polycrystalline Gd_5Ge_4 measured at 4.3, 6.3, and 10.3 K. The sample was cooled to the temperature of the measurement in zero magnetic field. The second magnetization curve coincides with the first demagnetization curve (Levin et al., 2002).

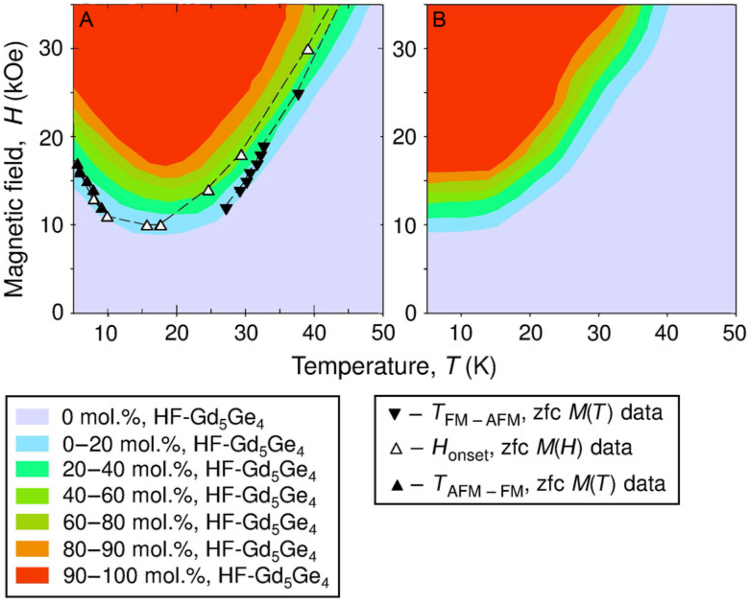

FIGURE 23 Magnetic field (H)–temperature (T) structural diagram for (a) zero-field cooled Gd_5Ge_4; (B) field cooled Gd_5Ge_4. Zero-field cooled magnetization data measured during warming of a polycrystalline Gd_5Ge_4 are shown for comparison (measured by Tang et al., 2004b). High-field (HF) Gd_5Ge_4 corresponds to O(I) crystal structure. *After Mudryk et al. (2005a).*

This is not surprising because larger quantities of material are typically used in these XRPD experiments (Holm et al., 2004), while magnetic measurements utilize much smaller (and more homogeneous) quantities of material producing, therefore, sharper transitions.

Chattopadhyay et al. (2004) noted that distinct metastable behavior in Gd_5Ge_4 is evidenced by large magnetic relaxation present in H–T region were the field-induced AFM to FM transition occurs. The magnetization was still changing with time at certain combinations of applied magnetic field and temperature (e.g., $T=5$ K, $H=18.5$ kOe), 50 min after both the magnetic field and temperature were stable.

Interestingly, in ZFC Gd_5Ge_4 the H_{CR} required to initiate the transformation in zero-field cooled sample has three types of behavior: below ~13–15 K, dH_{CR}/dT is negative, above ~23–25 K it is positive, and between ~15 and ~25 K it remains nearly constant (Fig. 23). This reflects the presence of the so-called freezing boundary, which is shown in the detailed phase diagram of the system in Fig. 24. In essence, the state below the freezing boundary is a unique magnetically and crystallographically ordered state that behaves much as a magnetic glassy state (Roy et al., 2006). Here, when Gd_5Ge_4 is cooled in zero or low magnetic fields, the AFM-O(II) Gd_5Ge_4 lattice becomes "frozen" or kinetically arrested. Thus, when the AFM-O(II)–FM-O(I) boundary is crossed, the system is retained in a nonequilibrium state and in order to transform it into the thermodynamically stable ferromagnetic state it needs to be moved out of the frozen region by changing magnetic field and/or

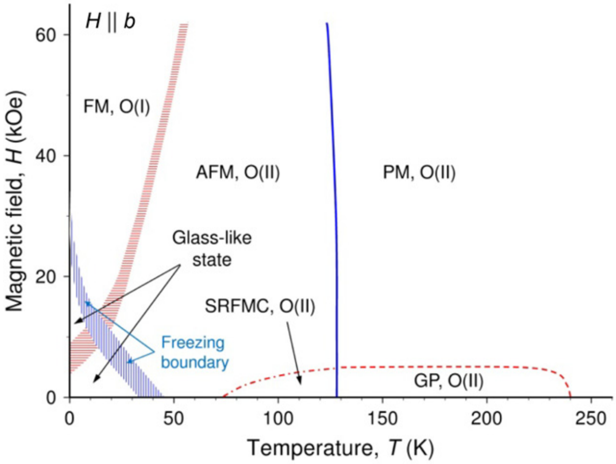

FIGURE 24 The magnetic field (H)–temperature (T) phase diagram of a Gd_5Ge_4 single crystal with the magnetic field vector parallel to the b-axis. The diagram maps the kinetically arrested state below the freezing boundary, short-range FM correlations (SRFMC) below T_N (~130 K), and a Griffiths-like state (GP) above T_N.

temperature (Roy et al., 2007). The dynamics of this transformation is typical of glasses, especially when the system is near the freezing boundary; however, this phenomenon should not be confused with spin-glasses where the spin configuration is frozen at random on a microscopic scale. In fact, using Hall probe microscopy Chattopadhyay et al. (2008) provided visual evidence that the magnetic glass state in Gd_5Ge_4 is clearly heterogeneous and contains equilibrium ferromagnetic clusters randomly distributed in a kinetically arrested antiferromagnetic matrix. Energy fluctuations (introduced for example through thermal cycling) lead to the formation of additional FM clusters from the AFM matrix similar to glass recrystallization process.

When Gd_5Ge_4 is cooled in magnetic fields above a certain H_{CR}, the "freezing" effect is not observed (Fig. 25) because when the AFM-O(II)–FM-O(I) boundary is approached from the "warm" side of the phase diagram this is the boundary that is first crossed by the material. At high temperatures, where the freezing region has no effect on magnetic behavior, the $M(H)$ curves from the first, second, and subsequent cycles become identical, and the transformation dynamics becomes typical as in the other alloys from the $Gd_5Si_xGe_{4-x}$ system experiencing a first-order magnetostructural transition, for example, the H–T phase diagram becomes similar to the one shown in Fig. 21. As shown in the Section 3.7, the kinetic arrest may also be removed by application of hydrostatic pressure.

Hardy et al. (2004) reported that their Gd_5Ge_4 sample already had a sizeable ferromagnetic component as follows from their virgin ZFC $M(H)$ curve

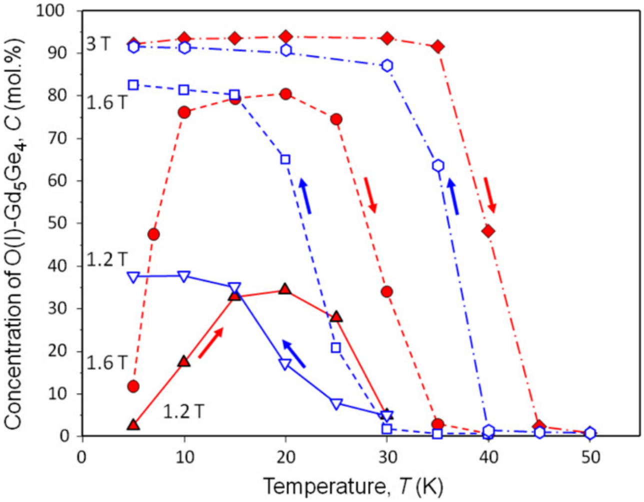

FIGURE 25 The irreversibility of the O(I)-FM Gd_5Ge_4 phase content observed while comparing the ZFC and FC sets of X-ray powder diffraction measurements performed as a function of temperature in different magnetic fields (Mudryk et al., 2005a).

measured at $T=2$ K. They suggested that a microstructure as well as purity of starting Gd metal could have stabilized the high-field FM phase. Interestingly, this study also pointed out strong similarities between the kinetic behaviors (in M vs. H measurements) of Gd_5Ge_4 and manganite compound $Pr_{0.6}Ca_{0.4}Mn_{0.96}Ga_{0.04}O_3$ at 3.25 K. Similarly, formation of some amount of the FM phase in the Gd_5Ge_4 sample in a zero magnetic field was observed by Xue et al. (2009) in their isothermal magnetization measurements. Therefore, the H–T phase diagram of Gd_5Ge_4 constructed by Xue et al. (2009) reflects the presence of an extended AFM+FM phase separated regions, which do not necessarily occur due to the kinetic arrest but, perhaps, due to peculiarities of the sample preparation, the purity of Gd being likely the most important factor. Ouyang et al. (2011) prepared Gd_5Ge_4 alloy using commercial 99.9 wt.% pure Gd metal and confirmed that it contains a significant fraction of low-field FM component clearly visible in the $M(H)$ curves. Moreover, the field-induced AFM→FM transformation, which is sharp in high-purity samples, especially at low temperatures (Fig. 22), becomes unusually sluggish in this sample although broad magnetic hysteresis indicates that this transformation is still a first-order one. The pulse field measurements indicate interesting developments in the transition dynamics as a function of the magnetic field sweep rate.

Levin (2009) studied magnetic properties of a series of $Gd_5Si_xGe_{4-x}$ alloys, $x=0.02$, 0.06, 0.1, 0.2, 0.3, 0.4, and showed that even very small substitution of Ge atoms with Si ($x=0.06$) quickly promotes the formation of the FM phase and a phase separated AFM+FM state exists in ZFC samples even without application of magnetic field. This work also confirms that as the Si concentration increases further ($0.1 \leq x \leq 0.4$) the $Gd_5Si_xGe_{4-x}$ alloys are ferromagnets below T_C.

The glassy nature of Gd_5Ge_4 is manifested through time dependence of magnetization of the oriented single crystals when it is measured inside the region (low temperature, low fields) delineated by the freezing boundary. For example, the character of the magnetostructural transition in Gd_5Ge_4 is influenced by magnetic-field step size during the magnetization measurements. The dynamics of both the magnetization and demagnetization processes is associated with approaching true equilibrium states, which becomes easier with a reduction of the magnetic field step. Small but frequent discontinuities in magnetization, that is multistep behavior, are commonly observed in Gd_5Ge_4 samples during slow measurements (Ouyang et al., 2007a). When the rate of field sweep is very high, for example, in pulse field measurements the large magnetocaloric effect observed in the $Gd_5Si_xGe_{4-x}$ alloys starts to play a defining role, especially when the heat exchange between the sample and environment is low (Ouyang et al., 2008). In such a case, the magnetic glass state may not be observed in Gd_5Ge_4 due to the fact that the sample's temperature rises above the freezing boundary as a result of MCE and the kinetic arrest is thus removed. The same study reports the increase of H_{CR} with higher sweep rates below 20 K.

Another interesting kinetic phenomenon observed in Gd_5Ge_4 is magnetic deflagration. Deflagration commonly defines a slow burning process, for example in a combustion engine, in contrast to an explosion. Recently, the concept of deflagration has been applied to the spontaneous magnetization process happening in some classes of magnetic materials (e.g., manganites and molecular magnets). It was found that the energy released by a magnetic transition initiated locally in a specific part of a material may "ignite" the nearby regions causing the propagation of the magnetic transformation process in striking similarity to chemical oxidation (burning) reaction. Casanova et al. (2005b) have found that the low-temperature magnetostructural transition in Gd_5Ge_4 dissipates heat differently depending on whether the transition is reversible or not. They observed that when the transition is reversible (above the "freezing boundary," Fig. 24) the heat exchanged by the sample is mostly the latent heat of the first-order transition. However, when this transition is irreversible, the heat dissipation value strongly increases with the lowering temperature (i.e., with the sample being moved further into the metastable frozen state), reaching 237 J/Kg at 4 K. In a follow-up study, Velez et al. (2010) revealed that the released heat is sufficient to initiate magnetic deflagration, which originates from the metastable state of Gd_5Ge_4 at low temperatures. Essentially, when a kinetically arrested AFM Gd_5Ge_4 specimen is moved into a certain point of the *H*–*T* diagram where its thermodynamically stable modification is the FM-O(I) phase (e.g., at $T=2$ K and $H=\sim 20$ kOe), the application of a weak heat pulse to one end of the sample (sample dimensions in the experiment were $4\times 1\times 1\ \mathrm{mm}^3$) triggers the avalanche-like magnetostructural transformation at a speed 0.1–1 m/s that transforms the whole Gd_5Ge_4 sample into FM phase. The process is driven by the conductance of the heat released by the structural transformation of the metastable phase and the kinetics of the transformation agrees well with the deflagration theory (Velez et al., 2010). Investigation of the deflagration process in a single crystal of Gd_5Ge_4 found that this process is anisotropic, particularly with respect to the applied magnetic field vector (Vélez et al., 2012). The deflagration was induced by controlled pulses of surface acoustic waves. The measured data show that the thermal diffusivity in Gd_5Ge_4 is anisotropic, following $\kappa_a > \kappa_b > \kappa_c$.

Interestingly, the development of a field-induced magnetostructural transition in Gd_5Ge_4 (and, likely, in other $Gd_5Si_xGe_{4-x}$ alloys) is affected by the actual size of the polycrystalline particles. Magnetometry and scanning Hall probe imaging studies show that the critical field H_{CR} for the AFM-O(II) → FM-O(I) transition in Gd_5Ge_4 can be reduced by 20% when small fragments (~100 μm) removed from the bulk sample are measured as compared to the parent bulk sample (Moore et al., 2006). It is believed that the fragmentation reduces the strain energy constraining the nucleation of the FM phase within the AFM matrix at the onset of the field-induced transformation. Hall imaging shows that the macroscopic domain size is on the order of 30–100 μm, so a single fragment extracted from the bulk sample would contain up to 3–5 domains only. The nucleation process in this case would proceed virtually stress-free. On the other hand, when the sample is powdered the material's behavior is opposite to fragmentation, with broad transition loops and depressed saturation magnetization (Moore et al., 2006).

Because in $Gd_5Si_xGe_{4-x}$ alloys strain produced during the structural transition in bulk alloy affects the path of the transition, and, consequently, the critical parameters, such as H_{CR}, one may expect to see the evolution of the H–T diagram when the material is cycled through the transition multiple times. As noted above, cycling has a profound effect on the electrical resistivity of $Gd_5Si_xGe_{4-x}$ compounds, for example for $Gd_5Si_{0.4}Ge_{3.6}$ (Sousa et al., 2003). Cycling through the structural transition in the presence of stress-controlling boundaries results in the so-called training effect. Microstructure of cycled materials changes compared to the microstructure of virgin samples in order to minimize strain energy as was experimentally observed by Manekar et al. (2006) in Gd_5Ge_4. It is important to note that training may not necessary involve the change in a crack structure (not observed by Manekar et al., 2006), but creates changes at lower length scales, below ~20 μm. Using the same scanning Hall probe setup, Perkins et al. (2007) were able to show the formation of separated phase clusters during the magnetostructural transition in Gd_5Ge_4. In addition, they showed that microstructural features have a strong influence on both nucleation and growth of the emerging phase (O(I)-FM in case of magnetization) ultimately controlling the macroscopic properties (such as magnetization) of this material. Comparing the development of reversible (at 35 K) and irreversible (at 6 K) transitions, significant differences in the nucleation rate but not in the growth rate have been observed in Gd_5Ge_4.

Localized magnetic relaxation measurements were performed using a scanning Hall probe technique in Gd_5Ge_4 at 6, 10, and 35 K (Moore et al., 2008). The characteristic time for bulk relaxation at 6 K is ~38 min. Contrary to bulk magnetization relaxation measurements, sharp steps were observed in local magnetization during the relaxation experiments at 10 and 35 K but not at 6 K.

Yuan et al. (2010) observed very small (~7 Oe) exchange bias effect in Gd_5Ge_4 polycrystalline specimen in the hysteresis loops measured at 5 K between ±3000 Oe. The authors of the study believe that the observed effect originates from exchange coupling between FM clusters and AFM matrix in the kinetically arrested state. The exchange bias field decreases with temperature and is history dependent.

3.7. Pressure Effects

Because magnetostructural transitions in $Gd_5Si_xGe_{4-x}$ system are characterized by a large volume change, it is expected that they will be substantially affected by application of an external pressure, for example, hydrostatic pressure. Indeed, the transition temperature of $Gd_5Si_{1.8}Ge_{2.2}$ is dependent on the applied pressure, increasing at a rate of $dT_C/dP = 3.79$ K/kbar (Morellon et al., 1998a), though the actually reported rate somewhat varies in different studies. An *in situ* X-ray synchrotron powder diffraction experiment directly confirmed the polymorphic transformation from the monoclinic β-$Gd_5Si_2Ge_2$ (M) to the orthorhombic α-$Gd_5Si_2Ge_2$ (O(I)) when hydrostatic pressure was applied at room temperature (Mudryk et al., 2005b). The transition occurs between 10 and 20 kbar at 298 K. It was shown that in the $Gd_5Si_xGe_{4-x}$ system the application of hydrostatic pressure may induce magnetostructural transition similar to those induced by the chemical substitution, temperature, and/or magnetic field changes.

Magnetic and magnetocaloric properties of $Gd_5Si_2Ge_2$ under hydrostatic pressures up to 9.2 kbar were investigated by Carvalho et al. (2005). The study confirmed that the magnetic ordering temperature of M-$Gd_5Si_2Ge_2$ increases with pressure, but reported a higher rate of 6.1 K/kbar than quoted by Morellon et al. (1998a) (see above). Since the orthorhombic (γ-phase) $Gd_5Si_2Ge_2$ was also present in the prepared sample, the pressure dependence of the T_C of this phase was estimated to be 0.9 K/kbar—a much lower value because this transition is a second-order one. Above 6 kbar only a single transition was observed because both the first-order and the second-order phase transformations merge at this pressure. Morellon et al. (2004a) reported dT_C/dP equal to 0.3 K/kbar for the O(I)-$Gd_5Si_{3.2}Ge_{0.8}$ phase and ~3 K/kbar for M-$Gd_5Si_{1.8}Ge_{2.2}$ and O(II)-$Gd_5Si_{0.4}Ge_{3.6}$. Morellon et al. (2004a) also observed a moderate effect of hydrostatic pressure on the PM → AFM transition in O(II)-$Gd_5Si_{0.4}Ge_{3.6}$, $dT_N/dP = 0.7$ K/kbar. Magnetization measurements at 4 K indicate that the saturation magnetization does not change with pressure; but the near room temperature MCE strongly decreases with pressure when the order of the magnetic transition changes from first to second (Carvalho et al., 2005).

Magen et al. (2003a) studied the effect of the applied hydrostatic pressure on the phase transitions in Gd_5Ge_4 using LTE and magnetization measurements. They found that ferromagnetic order can arise in this compound when the applied pressure initiates the transition from the high-volume O(II) phase into the low-volume O(I) phase. As the pressure goes up, the phase separated state (mixture of AFM-O(II) + FM-O(I)) occurs first, and above 10 kbar the entire volume of the sample is in the O(I) structure below the T_C (10 kbar) = 53 K. According to their estimates, the rate of temperature change for the first-order transition ($dT_C/dP = \sim 4.9$ K/kbar) is about seven times higher than the pressure dependence of the second-order transition temperature ($dT_N/dP = \sim 0.7$ K/kbar). The compressibility of Gd_5Ge_4 at low pressure is equal to $-(1/V)dV/dP = 1.85(1)$ Mbar^{-1}.

Carvalho et al. (2008) also performed a pressure-dependent magnetization study of Gd_5Ge_4, and obtained $dT_C/dP = 45$ K/GPa (~4.5 K/kbar), in good agreement with Magen et al. (2003a). However, they did not detect any change in T_N with applied pressure. The magnetic entropy change as a function of both temperature and applied pressure was obtained from isothermal magnetization data ($\Delta H = 0$–50 kOe). Two MCE peaks, at 11 and 43 K were observed. When the pressure increases the low temperature peak moves toward lower temperatures and eventually disappears; the temperature of the second $-\Delta S_M$ peak moves toward higher temperatures and its magnitude fluctuates between 20 and 25 J/Kg K (Carvalho et al., 2008). The pressure–temperature (P–T) phase diagram shows the presence of an FM + AFM phase separated state similar to the H–T diagram. The total entropy change values obtained using different measurement protocols are different reflecting the complex transition kinetics in Gd_5Ge_4.

The effect of applied hydrostatic pressure ($P = 0$, 2.2, 3.7, and 8.7 kbar) on the magnetocaloric effect in Gd_5Ge_4 has also been studied by Arnold et al. (2009a) in the range of temperatures between 16 and 100 K. The $-\Delta S_M$ value for a 0 to 50 kOe magnetic field change was ~24 J/Kg K in zero applied pressure, in agreement with other studies. The maximum $-\Delta S_M$ values measured under the applied pressure are lower compared to the results reported by Carvalho et al. (2008). Because the applied pressure promotes the formation of the FM phase, and consequently increases the initial low-field magnetization in Gd_5Ge_4, the sharp metamagnetic transitions at H_{CR} observed at $P = 0$ become much smoother at $P = 2.2$ and 3.7 kbar. At $P = 8.7$ kbar, the magnetization curves have typical FM shape indicating pressure-induced formation of the FM phase in the majority of the samples. The MCE decreases significantly at low applied pressures: the maximum $-\Delta S_M$ drops almost twofold at $P = 2.2$ kbar (12.3 J/Kg K) compared to the $P = 0$ result (24 J/Kg K). As the applied pressure increases, the removal of the magnetic inhomogeneity state becomes complete in Gd_5Ge_4 (Tseng et al., 2008a), and the MCE starts to modestly increase again (Arnold et al., 2009a).

Effect of the hydrostatic pressure on the magnetic transitions in $Gd_5Si_xGe_{4-x}$ system has been carefully studied using X-ray magnetic circular dichroism (XMCD) spectroscopy (Tseng et al., 2007). In particular, the differences and similarities between the chemical pressure, induced by Si substitution and external hydrostatic pressure were observed and analyzed with the help of other research tools such as temperature-dependent X-ray powder diffraction and magnetization measurements. A clear correspondence between the P–T and x–T diagrams of the $Gd_5Si_xGe_{4-x}$ system was reported. However, it was also found that a similar volume change results in ~3 times larger increase in T_C with Si substitutions than with hydrostatic pressure (Fig. 26).

Apparently, Si doping is more effective in the stabilization of the FM state in these alloys than just compressing the lattice that also promotes the formation of the low-volume phase. On the other hand the XMCD pressure study of the $Gd_5Si_xGe_{4-x}$ with low $x = 0.1$, 0.2, and 0.3 showed that Si in small concentrations leads to the emergence of ferromagnetism when compared to unsubstituted Gd_5Ge_4, as expected (Tseng et al., 2008a). However, both magnetization and X-ray powder diffraction measurements indicated the presence

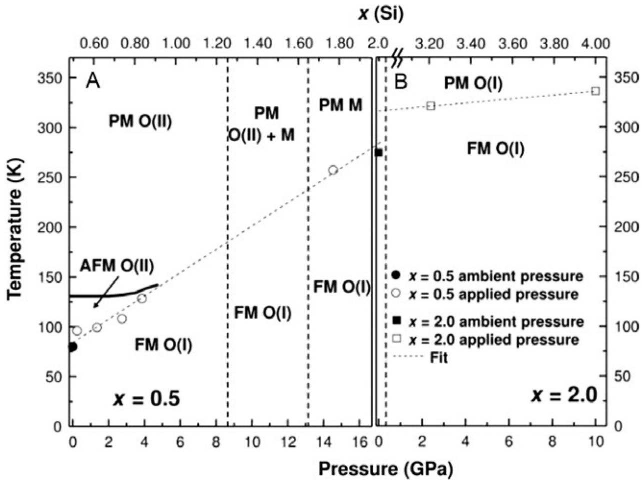

FIGURE 26 The correspondence between compositional and pressure magnetic phase diagrams in the $Gd_5Si_xGe_{4-x}$ system. Only relevant parts of the phase diagram are shown. Data points indicate the observed T_C for the $Gd_5Si_{0.5}Ge_{3.5}$ (A) and $Gd_5Si_2Ge_2$ (B) samples for different pressures as measured by XMCD (Tseng et al., 2007).

of the magnetically and structurally inhomogeneous (phase separated) state with both AFM-O(II) and FM-O(I) phases coexisting over an extended temperature range (tens of Kelvin). Application of a magnetic field, while increasing the content of the FM-O(I) phase, could not completely remove this inhomogeneity. The strong irreversibility between ZFC and FC data and reduced low-temperature magnetization were also strong indications of the magnetic frustration present in these low-Si specimens. At the same time, the application of hydrostatic pressure (at 17 K, $P=2$, 3, and 5 GPa for $x=0.3$, 0.2, and 0.1, respectively) results in the removal of the magnetically inhomogeneous state as can be judged by the restoration of the saturation magnetization values measured by XMCD (Tseng et al., 2008a). Similarly, XMCD data collected at the Gd L_3 absorption edge at $T=35$ K for pressures from 0 to ~15 GPa for $Gd_5Si_{0.15}Ge_{3.85}$ and $Gd_5Si_{0.5}Ge_{3.5}$ samples show that the former sample has reduced saturation magnetization at ambient pressure indicative of competing AFM and FM interactions. Above 6 GPa saturation magnetizations of both samples become nearly identical indicating stabilization of the FM state (Haskel et al., 2008). Pressure dependence of the magnetic ordering temperature has also been studied by XMCD for $Gd_5Si_{1.5}Ge_{2.5}$, and the two distinct regions with two different dT_C/dP rates were observed (Tseng et al., 2008b): below 7.2 GPa, the rate is 1.5 K/kbar, comparable to 1.2 K/kbar reported for the $Gd_5Si_{0.5}Ge_{3.5}$ sample (Tseng et al., 2007), while the rate in the high-pressure range (0.15 K/kbar) is comparable to the one measured for the $Gd_5Si_2Ge_2$ sample (0.2 K/kbar, Tseng et al., 2007).

The application of hydrostatic pressure to the $Gd_5Si_2Ge_2$ sample indicates that T_C is 336 K at 10 GPa and given the linear increase of the Curie temperature with pressure, even higher T_C values may be reached at higher pressures. At the same time, this is the maximum Curie temperature that may be achieved by Si substitution ($T_C = 336$ K for Gd_5Si_4) proving that despite its lower impact on T_C, hydrostatic pressure provides a valuable method of transition temperature manipulation in $Gd_5Si_xGe_{4-x}$ alloys in addition to chemical substitutions (Tseng et al., 2007).

Another interesting effect observed in the pressure-dependent XMCD measurements is the variation of the dT_C/dP rate with sample composition (for low-Si substitutions) and with the range of the applied pressures. For example, the rate is higher (typically over 3 K/kbar) below 1 GPa as determined for the $Gd_5Si_xGe_{4-x}$ alloys with $0 < x \leq 2$ using magnetic susceptibility data (Morellon et al., 2004a); but when measured up to 14.55 GPa, lower $dT_C/dP = 1.2$ K/kbar rate was observed from XMCD data for $Gd_5Si_{0.5}Ge_{3.5}$ (Tseng et al., 2007). During the measurements of the barocaloric effect in $Gd_5Si_2Ge_2$ (Yuce et al., 2012), a 3.2 to 3.8 K/kbar rate was observed in pressure-dependent calorimetric measurements at relatively low pressures (0–2.9 kbar). The fact that the barocaloric effect in $Gd_5Si_2Ge_2$ reaches its maximum near 3 kbar and that both the latent heat and the structural entropy of the M-PM - O(I)-FM transition are expected to decrease as pressure increases indicates that $Gd_5Si_xGe_{4-x}$ compounds show a stronger response to the applied pressure when compression is low, that is, when the pressure is moderate (Yuce et al., 2012).

The variation of T_C with pressure for Gd_5Si_4 was found to be linear, with dT_C/dP equal to 2.9 K/GPa (Parviainen, 1980).

3.8. Magnetocrystalline Anisotropy

Interestingly, even when long-range ferromagnetism is destroyed, short-range ferromagnetic order may still be present in the O(II) structure. The X-ray resonant magnetic scattering study of Gd_5Ge_4 antiferromagnetic phase (Tan et al., 2005) complimented by the magnetization studies of the Gd_5Ge_4 single crystals along three major crystallographic axis (Levin et al., 2004; Ouyang et al., 2006a) indicate that the Gd moments are primarily aligned along the *c*-axis in the low-field AFM state (Fig. 27). The alignment of the moments within a single slab unit is nearly collinear so the slabs are practically ideally ferromagnetic. However, the slabs themselves are magnetically aligned antiparallel with respect to each other (Gd moments in each consequent slab are rotated ~180° with respect to the previous slab, see Fig. 27) so the ground state becomes antiferromagnetic (Tan et al., 2005). Therefore, the prevailing magnetic interactions in the magnetically ordered slabs are ferromagnetic, which explains both the highly positive Weiss temperature (θ_p) observed in Gd_5Ge_4 and other antiferromagnetic R_5T_4 alloys, and the ease of the transition

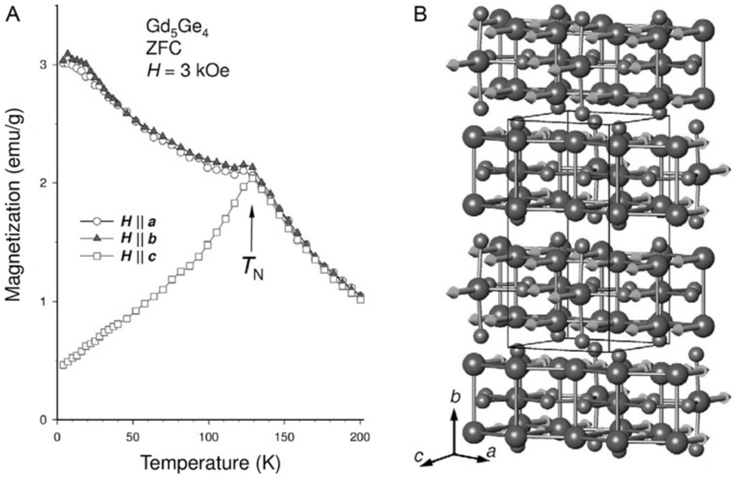

FIGURE 27 (A) Magnetization of the Gd_5Ge_4 single crystal with the magnetic vector applied along three major crystallographic directions. (B) Schematic low-field magnetic structure of Gd_5Ge_4.

into the ferromagnetic state by R_5T_4 compounds at proper conditions even with the minor external stimuli.

This peculiar magnetic structure results in a number of interesting magnetic effects observed in a Gd_5Ge_4 single crystal. For example, a weak but distinct and reversible spin-flop transition is observed when a magnetic field of 8.4 kOe is applied along the *c*-axis of Gd_5Ge_4 (Levin et al., 2004). Ouyang et al. (2007b) examined the angular dependence of the spin-flop transition and found that when the magnetic field vector is tilted away from the *c*-axis toward the *b*-axis, the spin-flop transition remains first-order in nature. When the field vector is tilted away from the *c*-axis toward the *a*-axis, the first-order spin-flop transition is only observed at $0<\theta<20°$ indicating that the Gd moments "flip" from the *c*-axis to the *a*-axis during the spin-flop transformation. Presence of such 90° flop was confirmed at $T=9$ K, $H=9$ kOe by means of the X-ray resonant magnetic scattering experiment performed on the Gd_5Ge_4 single crystals (Tan et al., 2008). No magnetostriction effects were observed at the transition. Both magnetic sublattices, before and after the spin-flop transformation have intraslab FM correlations and interslab AFM correlations.

A neutron diffraction study of the magnetic structure (in the AFM state) of a series of $Gd_5Si_xGe_{4-x}$ alloys ($x=0$, 0.1, 0.3, 0.5, 0.7, and 0.9) was performed in a zero magnetic field by Ryan et al. (2010). The magnetic structure with *Pnma* magnetic space group identified by Tan et al. (2005) was confirmed. As shown in Table 12, the Gd magnetic moments of all three symmetrically independent sites are primarily oriented along the *c*-direction with zero spin component along the *b*-axis. A small but definite *a* component was

TABLE 12 Gd Moments in Gd_5Ge_4 Determined from Neutron Diffraction Data Measured at 10 K (Ryan et al., 2010)

	Gd moments (μ_B)			
Gd site	*a*	*b*	*c*	Total
4c	0.9 ± 1.2	0	6.7 ± 0.3	6.8 ± 0.4
8d1	0.3 ± 1.0	0	6.6 ± 0.3	6.6 ± 0.4
8d2	2.3 ± 0.9	0	6.2 ± 0.2	6.6 ± 0.4

obtained at least for one of the three Gd sites, the 8*d*2 position. The magnetic structure of the FM state in these alloys was not determined; in fact the study did not observe any long-range ferromagnetic order even in alloys with relatively high amounts of Si although the transition from O(II) to O(I) crystal structure was clearly seen. The magnetic moments in the AFM-O(II) phase are confined in the *ac*-plane and are strictly perpendicular to the *b*-direction while in the FM state they are most likely oriented along the *b*-axis (the easy magnetization direction of Gd_5Ge_4, Ouyang et al., 2006a). Based on the study by Ryan et al. (2010) one may speculate that the magnetic moment rotation toward the *b*-direction followed by the setting of the long-range FM state does not occur spontaneously when the O(I) phase forms out of the O(II) phase through a temperature-induced transformation in the absence of magnetic field, and at least a very small (a few Oe) applied field is needed for the occurrence of the FM order in $Gd_5Si_xGe_{4-x}$ alloys with $x \leq 0.9$. Complex dynamics of the displacive structural O(II)–O(I) transition described above is probably responsible for this unusual behavior.

Despite the fact that Gd magnetic moments align along the *c*-axis in the antiferromagnetic state, the easy magnetization direction of Gd_5Ge_4 is the *b*-axis (Ouyang et al., 2006a) since the ferromagnetic order is set quickly and is the most stable along this direction. Similarly, magnetic force microscopy (MFM) and vibrating sample magnetometry (VSM) measurements preformed on a single crystal of the monoclinic $Gd_5Si_2Ge_2$ phase also indicate the *b*-axis as the easy axis in $Gd_5Si_2Ge_2$ (Leib et al., 2002a). The MFM study of the $Gd_5Si_{1.95}Ge_{2.05}$ single crystal confirms this observation (Leib et al., 2002b). The same authors performed an MFM study on a polycrystalline $Gd_5Si_{2.09}Ge_{1.91}$ showing that the domain appearance during the PM → FM first-order transformation is sharper in the single crystal than in a polycrystalline sample. The values of magnetic anisotropy coefficients for $Gd_5Si_2Ge_2$, $K_0 = 0.78 \pm 0.03 \times 10^4$ J/m^3, $K_1 = 4.1 \pm 0.2 \times 10^4$ J/m^3 are similar to those of iron (Leib et al., 2002a). Essentially, these materials have uniaxial magnetic anisotropy, which agrees with nearly tetragonal crystal structure ($a \approx c << b$).

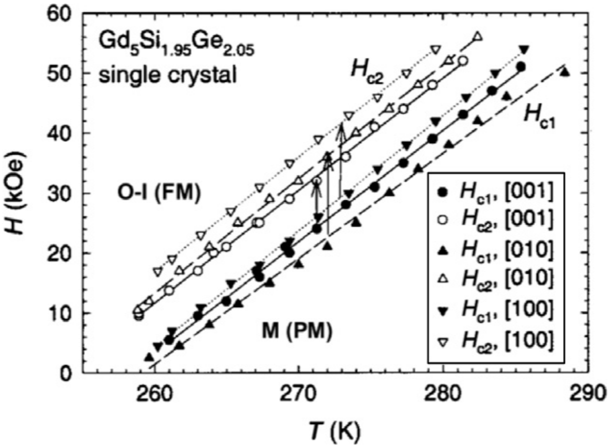

FIGURE 28 Critical magnetic field as a function of temperature of the $Gd_5Si_{1.95}Ge_{2.05}$ single crystal with the magnetic field applied along three major crystallographic directions.

According to Tegus et al. (2002a), the magnetocrystalline anisotropy in monoclinic $Gd_5Si_xGe_{4-x}$ alloys with $x=1.65$ and 1.7 is observed only in low applied magnetic field (0.05 T) and is practically negligible in higher magnetic fields, such as 50 kOe. The magnetic measurements of a high-quality oriented single crystal of $Gd_5Si_2Ge_2$ (Magen et al., 2005), showed small but measurable magnetic anisotropy, and the easy magnetization axis determined using the M(*H*) data collected at 5 K is the *a*-axis. This result is in disagreement with the magnetic measurements of Leib et al. (2002a) and the neutron diffraction study by Palacios et al. (2010b).

Magnetic *H*–*T* diagrams were constructed for the $Gd_5Si_{1.95}Ge_{2.05}$ single crystal along three major crystallographic directions using isothermal magnetization measurements (Tang et al., 2003). Magnetocaloric effect was calculated along all three major axes as well. A small anisotropy affecting the location of the phase boundaries on the *H*–*T* diagrams was observed (Fig. 28). Direction-dependent differences in the shape of the MCE peak were also found.

Neutron diffraction determination of the magnetic structure of $Gd_5Si_2Ge_2$ and doped $Gd_5Si_2Ge_{1.9}M_{0.1}$ (M = Ga, Cu) compounds confirms the collinear ferromagnetic alignment of Gd magnetic moments along the *b*-axis below T_C (Palacios et al., 2010b). The magnetic structure is independent of whether the magnetic ordering occurred via a first-order transition ($Gd_5Si_2Ge_2$) or a second-order transition ($Gd_5Si_2Ge_{1.9}Ga_{0.1}$).

3.9. Short-Range Correlations

In the paramagnetic state, the magnetic susceptibility of Gd_5Ge_4 measured in an 8 kOe applied magnetic field obeys the Curie–Weiss law with $\theta_p = 94$ K and effective moment $p_{\mathrm{eff}} = 7.8\ \mu_B$/Gd (Levin et al., 2004). However, when the magnetic susceptibility of Gd_5Ge_4 is examined in paramagnetic state using magnetic fields below 5 kOe, a clear signature of the so-called Griffith-phase behavior is observed in the inverse magnetic susceptibility plots in the region between T_N and the characteristic temperature $T_G > T_N$ (Ouyang et al., 2006b); T_G is approximately $2T_N$ for O(II) R_5T_4 structures (Pereira et al., 2010). Essentially, short-range order magnetic correlations in the paramagnetic state lead to dynamic ferromagnetically ordered clusters that enhance the magnetic susceptibility of Gd_5Ge_4 and other R_5T_4 systems (Pereira et al., 2010). This effect is most pronounced when the magnetic field is low, $H \sim 10$ Oe, and when the measurements are performed in magnetic field applied along the *b*-axis (Ouyang et al., 2006b). Ouyang (2010) carried out an extensive investigation of the Griffiths-like behavior in $Gd_5Si_xGe_{4-x}$ alloys with $x = 0$, 0.5, 1.012, 1.5, and 3.5 using temperature-dependent ac magnetic susceptibility and low-field (10 Oe) dc magnetization measurements. Substantial deviations from the Curie–Weiss behavior indicative of the short-range magnetic clustering were observed in all samples with $x < 2$. These short-range FM correlations are characterized by unusually slow relaxation dynamics above the magnetic ordering temperature, which is observed in time-dependent magnetic relaxation measurements and are also manifested in the frequency dependence of ac susceptibility. Ouyang (2010) argues that the low-field region of the $Gd_5Si_xGe_{4-x}$ x–T diagram should include the area of the Griffiths-like phase between the long-range magnetically ordered state and the truly paramagnetic region; the T_G for $x < 2$ can be derived from the linear extrapolation of T_C's of the alloys with $x > 2$.

Casanova et al. (2005c) reported the presence of short-range competing FM and AFM correlations in $Gd_5Si_xGe_{4-x}$ Ge-rich alloys for $x = 0$, 0.2, and 0.4 in high magnetic fields (~140–150 kOe) at temperatures slightly below T_N but greater than ~80 K. In this area of H–T diagram, the magnetic-field-induced AFM–FM transition proceeds through an intermediate state, which the authors mark as a short-range correlation (SRC) region. By using pulse magnetic fields as high as 400 kOe, Wu et al. (2011) studied the same region ($85\ \mathrm{K} < T < 105\ \mathrm{K}$) of the Gd_5Ge_4 H–T diagram and concluded that the intermediate state is paramagnetic. As a result, during high-field (> 100 kOe) isothermal magnetization measurements in this range of temperatures, Gd_5Ge_4 undergoes two transitions: (1) second-order AFM–PM transition and (2) first-order PM–FM transition. Wu et al. (2011) also suspect the presence of short-range magnetic correlations in this intermediate region between the AFM and FM states. Appearance of the Griffiths-like phase in Gd_5Ge_4 at $T_G = 240$ K was observed in the same work using ac magnetic susceptibility measurements. Isofield temperature-dependent magnetization measurements of a Gd_5Ge_4 sample in 80, 100, 120, 140, 180, and 220 kOe applied magnetic fields confirms the presence of an additional magnetically inhomogeneous region immediately below (in terms of temperature) the first-order magnetostructural

AFM–FM phase transition at $H \geq 100$ kOe (Pérez et al., 2011). Pérez et al. (2011) also examined the low-field short-range magnetic correlations (Griffiths-like phase) in Gd_5Ge_4 using ac magnetic susceptibility measurements. The T_G in their experiments was found to be 225 K, in fair agreement with other reports. Frequency dependence of *ac* magnetic susceptibility was observed both at T_G and in the low-temperature region (<80 K). The anomaly at T_G becomes suppressed by dc field of 200 Oe.

3.10. Targeted Chemical Modification of Gd_5Ge_4

The complexity of the exchange interactions in the $Gd_5Si_xGe_{4-x}$ system has been exemplified through substitutional doping of Gd_5Ge_4 with nonmagnetic rare earth elements (Mudryk et al., 2010). By adding small amounts of La and Lu (≤5%), the effects of chemical pressure and trivial dilution were minimized so the main difference between La- and Lu-substituted alloys was in the atomic positions where these added atoms were located: Lu atoms prefer the interslab 4*c* sites while La atoms occupy the intraslab 8*d* sites. Such seemingly subtle difference, however, has a drastic influence on the magnetism of the doped alloys—the La substitution does not have any meaningful effect on the properties compared with the parent Gd_5Ge_4, while in the Lu-substituted alloys the ferromagnetic state is practically destroyed (at least below 70 kOe) with 5% Lu substitution (Fig. 29).

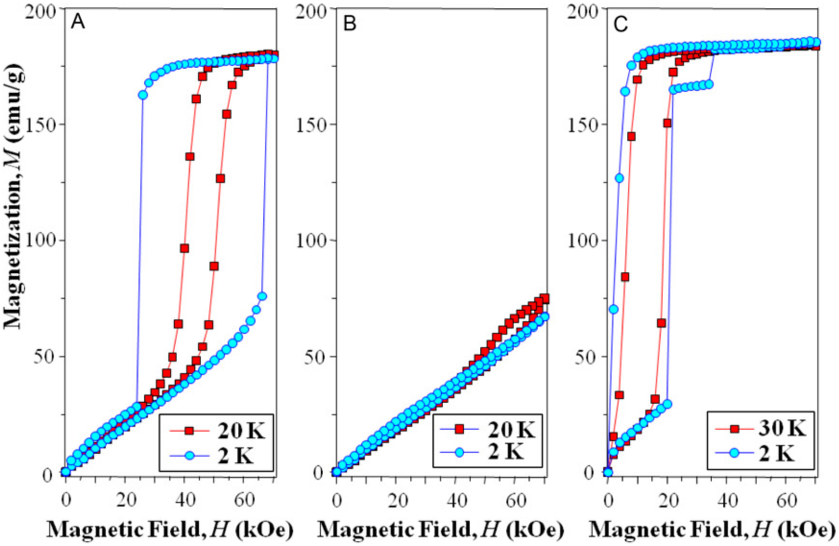

FIGURE 29 Isothermal magnetization of (A) $Gd_{4.875}Lu_{0.125}Ge_4$, (B) $Gd_{4.75}Lu_{0.25}Ge_4$, and (C) $Gd_{4.75}La_{0.25}Ge_4$ alloys. The magnetic properties of the La-substituted alloy are similar to those of the pure Gd_5Ge_4 (see Figure 22).

These results show that the interslab position (the 4*c* site) occupied by the rare earth atoms plays a key role in setting the ferromagnetic interactions in Gd_5Ge_4 compound compared to the remaining two eightfold sites. The critical role of this particular location in the crystal lattice has been also confirmed by first-principles calculations (Mudryk et al., 2010; Paudyal et al., 2010b). The study of the $Gd_{4.875}Lu_{0.125}Ge_4$ sample (2.5% Lu substitution, Fig. 29A) shows that even such a small (overall) quantity of Lu placed selectively in the 4*c* site of Gd_5Ge_4 crystal structure increases the critical field of the AFM–FM transformation by ~35 kOe (Mudryk et al., 2013). Similar nearly impurity level substitutions by other nonmagnetic rare earth elements (Sc and Y) show that the Y substitution produces the same effect as the Lu substitution (Paudyal et al., 2010b), but the effect of chemical pressure becomes substantial even at a low level scandium substitutions. Apparently, Sc promotes the FM state but with significantly lower efficiency when compared to Si. Both Sc and Y prefer the intraslab 4*c* location in the Gd_5Ge_4 structure. As the amount of substitution increases (more Gd is replaced by nonmagnetic R), the effects of chemical dilution become dominant.

3.11. Microstructure and Formation of Thin Plates

The surface structure of the Gd_5Si_4, $Gd_5Si_2Ge_2$, and Gd_5Ge_4 compounds was first studied by Szade et al. (1999) using single crystals of these compounds grown by Czochralski method from a levitated melt. The Berg-Barrett X-ray topography examination has confirmed that the prepared plate-like materials were single crystals and also has shown the presence of large stresses in the crystals. Somewhat unexpectedly, they also observed a regular system of thin channels or lines, which grew independently from the stress structure. The reported width of the linear features is about 2 μm, and Auger spectroscopy indicated the increase of gadolinium and oxygen contents in the vicinity of the lines. Meyers et al. (2002b) observed widespread presence of similar linear features in the $Gd_5Si_{1.95}Ge_{2.05}$ sample; the chemical composition of the lines determined by energy dispersive spectroscopy (EDS) was close to $Gd_5(Si,Ge)_3$. Gama et al. (2004) observed the linear features of a $Gd_5Si_2Ge_2$ sample prepared using the "commercial grade" Gd.

Ugurlu et al. (2005a) performed a detailed microstructural characterization of the oriented $Gd_5Si_2Ge_2$ single crystals by means of scanning electron microscopy (SEM) and transmission electron microscopy (TEM). The presence of a second phase consisting of extremely thin (~250 nm) yet long (hundreds of microns) plates growing in specific directions was confirmed. These plates can be observed in a form of linear features reported in other studies as well. The orientation of the plates is reminiscent of Widmanstätten precipitation, though conditions of its formation are atypical. TEM indicates that the structure of the plates is hexagonal with parameters $a = b = 8.53$ Å and $c = 6.40$ Å. In agreement with EDS, these results point on the $Gd_5Si_1Ge_2$

composition for the plates. Ugurlu et al. (2006a) determined the orientation relationship between $Gd_5Si_xGe_{4-x}$ matrix and $Gd_5Si_xGe_{3-x}$ plates as $\left[\bar{1}010\right]\left(1\bar{2}11\right)_p//[010]\left(10\bar{2}\right)_m$. $Gd_5Si_2Ge_2$, $Gd_5Si_{0.33}Ge_{3.67}$, and Gd_5Ge_4 compounds were studied. High-resolution TEM revealed a series of regularly spaced risers and terraces aligned along an irrational interface habit plane. The study proposed a displacive–diffusional transformation as a possible mechanism of the thin plate's formation.

Interestingly, when Fu et al. (2005) performed a microscopy study of the $Gd_5Si_2Ge_{2.2}$ sample they also observed the regular line features but reported the decrease of Gd content at the lines compared with the 5:2:2 matrix indicating that they are not the $Gd_5(Si,Ge)_3$ phases. High-temperature optical microscopy did not detect changes in microstructure of $Gd_5Si_2Ge_{2.2}$ up to 1400 °C, and the authors suggested that the linear features form during solidification. Cao et al. (2010) report that the thermal annealing of the Gd_5Ge_4 single crystal at 1200 °C induces dissolution of the plates, which according to their data have 5:3 stoichiometry, into the 5:4 matrix.

Ugurlu et al. (2005b), reported that thin plates exist not only in $Gd_5Si_xGe_{4-x}$ but also in other $R_5Si_xGe_{4-x}$ systems (R = Tb, Dy, Er) and confirmed that the chemical composition of thin plates is enriched in rare earths compared with the 5:4 matrix, upholding the 5:3 stoichiometry. At the same time, Ugurlu et al. (2006b) confirmed the stability of the thin plates: they found that temperature changes in the range between −70 and 850 °C do not have any effect on their morphology, even when the monoclinic matrix underwent both the low-temperature reversible ($\beta \leftrightarrow \alpha$) and high-temperature irreversible ($\beta \rightarrow \gamma$) structural transformations. Podmiljšak et al. (2007) suggested that quick cooling prevents formation of the Widmanstätten-like structure in $Gd_5Si_xGe_{4-x}$, based on the fact that they do not see it in the smaller arc-melted buttons that supposedly cool faster, but found it in all larger arc-melted buttons. This suggestion has been supported by Cao et al. (2010) who found that rapid solidification occurring after the laser surface melting experiment suppresses precipitation of the thin plates in the $Ho_5Si_{3.2}Ge_{0.8}$ sample. Presence of long straight lines in the SEM picture of $Gd_5Si_{2.1}Ge_{1.8}Fe_{0.1}$, which were too thin for an accurate estimation of composition, was reported by Rajkumar et al. (2010).

Detailed microstructural study of the Gd_5Ge_4 sample that underwent multiple cycling through a first-order AFM–FM transition has been performed by Manekar et al. (2006). They observed a change in microstructure at length scales below 20 μm through the so-called training effect, and came to the conclusion that the linear features (or "herringbone structure") belong to a kinetically arrested phase embedded into the stable matrix.

The most comprehensive study of the linear features in $Gd_5Si_xGe_{4-x}$ alloys used microscopy (optical, SEM, and TEM) and bulk characterization methods such as X-ray diffraction, magnetization, and heat capacity measurements to analyze and explain the discrepancies in the published reports about the nature of thin plates (Chumbley et al., 2008). The authors came to the conclusion that the difficulties in the phase identification of these features are caused by the fact that the majority of microscopy studies strongly overestimate their actual volume fraction (found to be a few percent maximum), sometimes by a factor of ten. Because the features are thinner than they appear in SEM pictures, it is easy to obtain erroneous EDS data by scanning the sample area that belongs not only to the plates but to the matrix and other potential impurities. Chumbley et al. (2008) assert that the true composition of the second phase is $Gd_5(Si,Ge)_3$, and its volume fraction is $1.0 \pm 0.5\%$ in the majority of the analyzed samples.

Moore et al. (2009) established that despite their minuscule concentrations these microstructural features play a significant role in the development of metamagnetic transitions in R_5T_4 alloys. In particular, they studied the magnetic-field-induced metamagnetic M-PM - O(I)-FM transformation in $Gd_5Si_2Ge_2$ using high-resolution scanning Hall probe imaging and found that the $Gd_5(Si,Ge)_3$ platelets act as nucleation centers for the FM phase when the magnetic field increases above the critical value. The mechanism of such seeding is interesting because the $Gd_5(Si,Ge)_3$ phase is paramagnetic at the studied temperature (280 K). Most likely, the $Gd_5(Si,Ge)_3$ mesoscopic phase is responsible for the variation of local strain energies at the phase boundaries and, therefore, for the distribution of critical fields across the sample volume. At the same time, the platelets do not have any influence on the return FM-to-PM transformation, thus indirectly confirming the theory that strain at the 5:4 matrix—5:3 platelet interfaces is indeed responsible for seeding the nucleation of the low-volume ferromagnetic matrix phase when the magnetic field increases.

Transmission electron microscopy and selected area diffraction (SAD) investigation of the optimally prepared single-phase $Gd_5Si_2Ge_2$ sample confirmed the presence of intrinsic microstructural twinning in the room temperature monoclinic structure (Meyers et al., 2002a, 2003). The twinning provides a mechanism for stress relief during the $M \leftrightarrow O(I)$ reversible phase transformation. Interestingly, ion milling of $Gd_5Si_2Ge_2$ at room temperature causes the irreversible structural transformation into the high-temperature orthorhombic polymorph. The structure remains monoclinic for all samples which were thinned by ion milling using a liquid nitrogen cold stage (Meyers et al., 2003).

Du et al. (2008) studied the magnetostructural transition in $Gd_5Si_{1.85}Ge_{2.15}$ using TEM and HRTEM. They confirmed that the $O(I)\text{-FM} \leftrightarrow \text{M-PM}$ transition is diffusionless and displacive by nature.

3.12. Spectroscopy

X-ray photoemission spectroscopy (XPS) measurements were performed on Gd_5Si_4, $Gd_5Si_2Ge_2$, and Gd_5Ge_4 compounds and compared with the magnetic susceptibility and electrical resistivity measurements by Szade and Skorek

(1999). All compounds show a characteristic feature on their XPS data at ~2 eV, which may be attributed to the Gd 5*d*-Si(Ge) *sp* covalently bonded states. The spectra indicate stronger Gd—Ge bonding compared to the Gd—Si bonding. The large shift of core levels (including Gd 4*f*) was observed for Gd–Ge (+0.5 eV for Gd and −0.8 eV for Ge; the experimental error for most XPS lines is ±0.1 eV). In Gd–Si compounds, the Gd binding energy levels do not shift with respect to those of the pure element but the Si ones are shifted by −0.5 eV (2*p*) and −0.3 (2*s*), Szade and Neumann (1999). Since the Gd—Si bonding is supposed to be quite strong (as may be judged, for example, from the high melting points of gadolinium silicides), this result means that the simple charge-transfer bonding is not applicable here, and the model involving *p*–*d* hybridization is needed in order to explain the complex properties of $Gd_5Si_xGe_{4-x}$ compounds. Resonant photoemission from a Gd_5Si_4 sample has been studied in the photon energy range of Gd 4*d*–4*f* threshold, but analysis of the Si states was not possible due to overlap with Gd states (Szade et al., 2002).

X-ray absorption and ultraviolet photoemission spectroscopy was used by Bondino et al. (2007) for the experimental investigation of the electronic structure of $Gd_5Si_2Ge_2$. The Gd core levels show similarity with Gd metallic compounds and differences from Gd ionic compounds. The Gd 5*d* itinerant electrons appear to be responsible for the magnetic exchange interaction between Gd 4*f* local moments. A comparison of the spectra measured above and below the structural transition did not show any clear changes in the 0 to 4 eV binding energy region. Instead, variations are observed at energies between 4.5 and 6.5 eV, and are associated with changes in the energy distribution of Ge(Si) *s* states.

Lee et al. (2004) measured reflectance difference (RD) spectra for the *a*–*b* and *b*–*c* planes of $Gd_5Si_2Ge_2$ in the photon energy range of 1.5–5.5 eV. For the *b*–*c* plane of $Gd_5Si_2Ge_2$ (and $Tb_5Si_{1.8}Ge_{2.2}$, which was also measured in this study), one strong peak appeared at 3.2 eV, a small peak at 1.7 eV, and a weak shoulder at 4.1 eV. For the *a*–*b* plane, a weak shoulder was observed at 2.8 eV together with two peaks at 1.7 and 3.8 eV. Park et al. (2006) obtained complex dielectric functions of $Gd_5Si_2Ge_2$ single crystal using spectroscopic ellipsometry in nearly same photon energy range (1.5–5.0 eV). The reflectance difference spectra were derived from these functions and compared with the ones obtained directly by reflectance difference spectroscopy. These RD spectra were found to agree well with each other.

The atomic excitations in Gd_5Ge_4 and $Gd_5Si_2Ge_2$ compounds were studied by electron energy loss spectroscopy (EELS). The spectra mainly reveal the excitations in Gd, like $4f \rightarrow 4f$ (at 4–8 eV), $5p \rightarrow 5d$ (23–27 eV), and $5p \rightarrow 5d$ plus $5d \rightarrow$ continuum (~35 eV), Tyszka et al. (2005).

Electron spin resonance (ESR) measurements were carried out on $Gd_{5.09}Ge_{2.03}Si_{1.88}$ samples, both as-cast and annealed, by Pires et al. (2005). Distinct signatures of two coexisting phases were clearly seen in the ESR spectra around room temperature (268 K < T < 315 K). Pires et al. (2006) reported an ESR study of Gd_5Si_4, Gd_5Ge_4, and $Gd_{5.09}Ge_{2.03}Si_{1.88}$ samples at temperatures between 105 and 405 K. The paramagnetic effective g values were determined and a negative paramagnetic g_{eff} shift was found for the Si containing samples but it was positive for Gd_5Ge_4. The values of the exchange parameter (j) between 4f spins and conduction electrons were calculated from the g shifts and were found to be positive and of the same order of magnitude for Gd_5Si_4 and $Gd_{5.09}Ge_{2.03}Si_{1.88}$ samples and negative and one order of magnitude smaller for Gd_5Ge_4.

Ouyang et al. (2009) performed an electron spin resonance study of the high-quality Gd_5Ge_4 sample (prepared at Ames Laboratory using 99.92 at.% pure Gd) across the field-induced AFM→FM transition. The measured ESR data were compared with the results of magnetization measurements and a reasonable correlation between these two methods has been found. The frequency-resonance field curve of the AFM state exhibits nearly the same slope as that of the FM state. The g value derived from this curve for the FM state assuming perfectly parallel alignment of all spins is 1.93, close to that of noninteracting Gd^{3+} ions ($g = 1.992$).

Skorek et al. (2002) compared the results of their TB-LMTO ASA calculations with the experimentally measured XPS and ultraviolet photoemission spectroscopy (UPS) data. The LSDA approach to the exchange-correlation potential in the von Barth–Hedin form with the nonlocal correction of Langreth, Mehl, and Hu was applied in these calculations. The authors found good correlation between the measured spectra and calculated electronic structure and were able to relate the details of the calculated structure with temperature-dependent XPS spectra. The energy gaps were observed for both Gd_5Si_4 and Gd_5Ge_4, but in the former case the gap is located below the Fermi level while in the latter case the gap is responsible for the semiconductor-like behavior above T_N (see Fig. 19). The 5 at.% substitution of titanium for Si or Ge resulted in a relative increase in photoemission intensity in the vicinity of the Fermi level for Ti-doped compounds. The chemical shifts of the most pronounced photoemission levels for Gd_5Si_4, $Gd_5Si_2Ge_2$, Gd_5Ge_4, $Gd_5Si_{3.8}Ti_{0.2}$, and $Gd_5Ge_{3.8}Ti_{0.2}$ are listed in Table 13.

3.13. First-Principles Calculations

A substantial amount of research effort has been directed toward determination of the electronic structure of $Gd_5Si_xGe_{4-x}$ compounds from first-principles calculations. The complex crystal structure of these alloys and the presence of Si/Ge statistical mixture in all T positions (except for the binary Gd_5Si_4 and Gd_5Ge_4 end members) complicate the band structure and density of states (DOS) calculations, as well as the estimations of exchange interactions. Nevertheless, the overall progress in understanding the electronic structure of R_5T_4 compounds is quite good.

TABLE 13 **Chemical Shifts of the Most Pronounced Photoemission Levels for Gd_5Si_4, $Gd_5Si_2Ge_2$, Gd_5Ge_4, $Gd_5Si_{3.8}Ti_{0.2}$, and $Gd_5Ge_{3.8}Ti_{0.2}$ Compounds (Skorek et al., 2002)**

	Gd 4*f*	Gd 3$d_{5/2}$	Si 2*p*	Si 2*s*	Ge 3*d*	Ge 3*s*	Ge 3$p_{1/2}$	Ti 2$p_{3/2}$
Pure Elements	8.1	1187.0	99.3	150.2	29.4	181.2	125.7	453.9
Gd_5Si_4	+0.1	+0.3	−0.5	−0.25	–	–	–	–
$Gd_5Si_{3.8}Ti_{0.2}$	+0.3	+0.2	−0.1	−0.4	–	–	–	+0.5
Gd_5Ge_4	+0.5	–	–	–	−0.85	−0.7	−0.9	–
$Gd_5Ge_{3.8}Ti_{0.2}$	+0.6	+0.2	–	–	−0.7	−0.4	−0.4	+0.8
$Gd_5Si_2Ge_2$	+0.3	–	−0.4	−0.35	−0.8	−0.7	−0.8	–

The binding energies for pure elements are shown in the first row. All data are in electron volts (eV).

Harmon and Antonov (2002) applied both local spin density approximation (LSDA) and so-called LSDA + U[4] approaches and found that the U_{eff} parameter strongly influences the results of the electronic structure calculations in $Gd_5Si_2Ge_2$. Based on the LSDA + U calculations they predicted that the magneto-optical spectra can be used for detecting the structural transition in $Gd_5Si_2Ge_2$. Soon after, using the same LSDA + U method they also calculated XMCD spectra for $Gd_5Si_2Ge_2$ and theoretically found that the XMCD measurements may also be used to study the magnetostructural transition in $Gd_5Si_2Ge_2$, particularly at Gd M_4 and N_4 edges (Harmon and Antonov, 2003).

Samolyuk and Antropov (2002) performed TB-LMTO calculations using local density (LDA) and generalized gradient (GGA) approximations on Gd_5Ge_4, $Gd_5Si_2Ge_2$, and Gd_5Si_4 compounds. Total energy calculations confirmed that the orthorhombic $Gd_5Si_2Ge_2$ has lower energy than the monoclinic one. They also have shown that the total energy is sensitive to the distribution of Si and Ge atoms within the lattice in $Gd_5Si_xGe_{4-x}$ alloys. Temperature dependences of free energy and magnetic moment were calculated for $Gd_5Si_2Ge_2$ by Samolyuk and Antropov (2003), but the calculated transition temperature ($T_m = 61$ K) was much lower than the one experimentally observed in $Gd_5Si_2Ge_2$ ($T_C = 276$ K, Pecharsky and Gschneidner, 1997b). Such difference is related to both the underestimation of the magnetic

---

[4] LSDA + U method enables proper treatment of the localized 4f electrons of Gd by supplementing conventional LSDA with an additional intra-atomic Coloumb correlation term (U) and exchange interaction term (J) of multiband Hubbard type less a so-called double-counting term to subtract the electron–electron interactions already included in LSDA (Paudyal et al., 2006).

exchange parameters and simplifications used in the description of the free energy. Pecharsky et al. (2003d) were able to model the effect of applied magnetic field on the transition temperature of $Gd_5Si_2Ge_2$ obtaining the value of $dT_m/dH = 0.26$ K/kOe, slightly lower than the experimentally observed rates ~0.4–0.5 K/kOe.

Rhee (2003) performed electronic band structure calculations of $Gd_5Si_2Ge_2$ compound using full-potential linear-augmented-plane-wave (FP-LAPW) methods within the local density approximation. The optical conductivity spectra were plotted for all three diagonal components. The off-diagonal component was also calculated but found to be negligibly small. The optical anisotropy is significant in the 0 to 2 eV range, but it becomes much weaker at higher photon energies (2–6 eV).

Samolyuk and Antropov (2005) applied the multiple-scattering formalism in LSDA + U to analyze the electronic structure of $Gd_5Si_2Ge_2$ and pure Gd metal. The thermodynamic properties were analyzed within the pair cluster approximation. The calculated T_C (through second-order transition) was 230 K for the orthorhombic (α) $Gd_5Si_2Ge_2$ and 180 K for the monoclinic (β) $Gd_5Si_2Ge_2$. However, in this model a first-order transition occurs at 206 K due to a crossover in free energy dependences of α and β phases. Interestingly, Hadimani et al. (2008a) experimentally proved by using the Arrott plot method that the α phase would order at a higher temperature (301 K) than the experimentally observed $T_C = 269$ K, if it did not undergo a first-order transition.

Altounian and Liu (2007) performed LMTO ASA calculations with LSDA given by von Barth and Hedin. They found that anisotropic thermal expansion observed in Gd_5Si_4 at T_C is related to the valence electron distribution at the magnetic transition when the electrons are transferred from Gd to Si atoms changing the strength of the Gd—Si bond and producing magnetovolume effect.

The LSDA + U method implemented in the TB-LMTO scheme with $U = 6.7$ eV and $J_0 = 0.7$ eV was employed to perform the first-principles electronic structure calculations for Gd_5Ge_4 compound (Paudyal et al., 2007). When the total energy was plotted against the value of the shear atomic displacement modeled along a-axis, a clear crossover of energy curves was obtained confirming the intrinsic nature of the structural transition in Gd_5Ge_4. The antiferromagnetic Sm_5Ge_4-type O(II) crystal structure was confirmed as a ground state. The 5d FM exchange splitting was found to be much larger in the O(I) structure compared to O(II). The origin of magnetic ordering in $Gd_5Ge_4$was further analyzed by Paudyal et al. (2008) using the same calculation method. The evaluation of 4f–5d exchange interaction energies showed that the short-range interactions in Gd_5Ge_4 are ferromagnetic but the long-range antiferromagnetic order prevails in the O(II) structure, supporting the experimental observations (e.g., see Tan et al., 2005). The calculated increase in 4f–5d interactions in O(I) structure agrees with its ferromagnetic state.

Tan et al. (2008) reported the magnetic anisotropic energies in Gd_5Ge_4 calculated using FP-LAPW. They concluded that easy plane (*ac*) anisotropy in Gd_5Ge_4 arises mainly from the dipolar interactions.

By performing the first-principles calculations ($LSDA+U$) of the formation energy as a function of a shear displacement of neighboring slabs, Paudyal et al. (2010a) found four closely related crystal structure types that may be stable in the Gd_5Ge_4 compound. When the lattice parameter a and, consequently, the interatomic interslab Ge3–Ge3 distance increases, the structures became stable in the following order: O(I)-Gd_5Si_4, Pu_5Rh_4, O(II)-Sm_5Ge_4, and $Tm_5Si_2Sb_2$. The modeling of the slab exchange interactions using the Heisenberg approach shows that O(I)-Gd_5Si_4, Pu_5Rh_4, and $Tm_5Sb_2Si_2$ structures have positive effective Gd–Gd exchange interactions indicating ferromagnetic ground state, while the O(II)-Sm_5Ge_4 structure supports antiferromagnetic ground state (Paudyal et al., 2010a).

3.14. Miscellaneous

Thermal conductivity and thermal diffusivity of $Gd_5Si_2Ge_2$ was measured by Fujieda et al. (2004). The thermal conductivity of $Gd_5Si_2Ge_2$ decreases during cooling of the high-temperature phase (α), shows a minimum at $T_C \approx 275$ K, and then starts to increase slowly upon further cooling down to ~50 K. Below 50 K a sharp decrease in thermal conductivity was observed. The absolute values are in the ~4–6 W/mK range. A strong anomaly in thermal diffusivity is observed at T_C.

Sambandam et al. (2005) attempted to grow the $Gd_5Si_2Ge_2$ thin film on the PECVD Si_3N_4 coated Si substrate. The study found that Si_3N_4 is unsuitable as a diffusion barrier for $Gd_5Si_xGe_{4-x}$ thin film preparation process and dissolution of $Gd_5Si_2Ge_2$ films into silicon nitride and Si upon annealing at 1150 °C was observed.

The elastic stiffness and compliance constants of the monoclinic $Gd_5Si_2Ge_2$ phase were determined by Svitelskiy et al. (2006). Using the pulse-echo ultrasonic technique the study measured the speeds of sound waves propagating in six directions of $Gd_5Si_2Ge_2$. The value of bulk modulus of $Gd_5Si_2Ge_2$ is equal to 68.5 GPa, and its Debye temperature, calculated from the measured elastic properties is $\theta_D = 250$ K.

Phase equilibria in the Gd–Si binary system were studied by means of both experiment and theoretical modeling by Huang et al. (2007). The study confirmed that Gd_5Si_4 is a line compound that forms by peritectic reaction from liquid (40.66 at.% Si) and Gd–Si phase at 1770 °C. Modeling gives the formation temperature at 1774 °C, in excellent agreement with the experiment.

The effect of ball milling on the crystal structure, magnetization, and MCE of $Gd_5Si_2Ge_2$ and $Gd_5Si_2Ge_{1.9}Fe_{0.1}$ alloys, and on the $Gd_5Si_2Ge_2$/0.1 wt.% Fe mixture was studied by Rajkumar et al. (2008). Both magnetization and MCE decrease with milling time. Giovanna do Couto et al. (2011) carried out a comparative study of magnetic and magnetocaloric properties of bulk and ball-milled $Gd_5Si_2Ge_2$ samples. Even a relatively short (4 h) milling time resulted in a significant decrease of MCE from $\Delta S_M = -20$ J/Kg K to $\Delta S_M = -4$ J/Kg K for bulk and ball-milled samples, respectively ($\Delta H = 0$–50 kOe). Both loss of the $M \rightarrow O(I)$ structural transition and appearance of super paramagnetic behavior of small particles were observed in the ball-milled samples.

The effect of annealing at different temperatures (650, 750, and 850 °C for 4 days) on the lattice parameters, microstructure, thermal behavior, and magnetic properties of Gd_5Si_4 has been investigated by Yazdani and Bonder (2011). The authors report a significant change in the lattice parameters of Gd_5Si_4 as a function of annealing temperature. The properties of the Gd_5Si_4 material ball-milled both in a dry argon atmosphere and with liquid ethanol were also investigated.

The powder metallurgy processing was applied to the $Gd_{5.09}Ge_{2.03}Si_{1.88}$ material to evaluate its effect on magnetic and magnetocaloric properties as well (Trevizoli et al., 2008). The study found that after pulverization and sintering the GMCE may be preserved in this material if large enough particles (>106 μm) are used for sintering. The first-order transition disappears when finer powders are used.

The effect of aging on the magnetocaloric properties of first-order $Gd_5Si_{1.9}Ge_{2.1}$ was studied by Canepa et al. (2008). The specimen was exposed to air and water for prolonged periods of time, up to 1 year; a clear but relatively slow degradation of MCE was observed.

4. OTHER $R_5Si_xGe_{4-x}$ SYSTEMS

The $R_5(Si,Ge)_4$ compounds have been discovered with all rare earth elements except Eu (neither the silicide nor the germanide form at the 5:4 stoichiometry) and Pm (not studied), The diagram summarizing the current state of knowledge regarding the formation and crystallography of $R_5Si_xGe_{4-x}$ compounds is shown in Fig. 30.

As can be seen from this figure, the phase digrams of the $R_5Si_xGe_{4-x}$ systems are well studied for the ambient conditions (except for the Tm system). The available information about their properties is summarized below.

4.1. $Y_5Si_xGe_{4-x}$

Both Y_5Si_4 and Y_5Ge_4 were discovered by Smith et al. (1967b) and reported to crystallize in the Sm_5Ge_4 type of crystal structure. Schmidt et al. (1972) constructed the binary phase diagram of the Y-Ge system, confirming the Sm_5Ge_4 structure for Y_5Ge_4. They also reported that Y_5Ge_4 forms by peritectic reaction from Y_5Ge_3 and liquid at 1900 °C. A few years later a binary Y–Si diagram was reported by Button et al. (1990), who found that Y_5Si_4 also

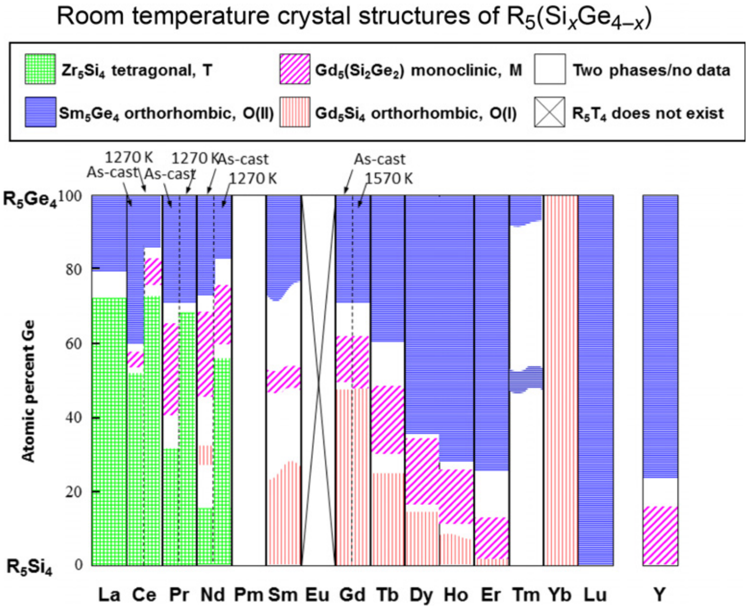

FIGURE 30 Room temperature crystallography of $R_5Si_xGe_{4-x}$ phases. Terminal compositions that have been established with a few mol.% accuracy are shown as straight lines, while curved boundaries designate the same known with a lower accuracy, typically to ~10–25 mol.%.

forms peritectically at 1836 °C from Y_5Si_3 and liquid; Sm_5Ge_4 type of crystal structure was confirmed as well.

The pseudobinary Y_5Si_4–Y_5Ge_4 phase diagram has been recently investigated by Pecharsky et al. (2004a). Contrary to the earlier literature the crystal structure of Y_5Si_4 was found to be monoclinic $Gd_5Si_2Ge_2$ type with the following lattice parameters: $a = 7.4722(5)$ Å, $b = 14.613(1)$ Å, $c = 7.6592(5)$ Å, and $\gamma = 93.399(4)°$ (SG $P112_1/a$). It is possible that Y_5Si_4 adopts the monoclinic structure only when the highest purity yttrium metal is used for the sample preparation. The crystal structure of Y_5Ge_4 was confirmed as Sm_5Ge_4-type: $a = 7.6317(3)$ Å, $b = 14.695(1)$ Å, $c = 7.6963$ (2) Å (SG *Pnma*); Misra and Miller (2008) reported the Sm_5Ge_4 type of crystal structure for the Y_5Ge_4 compound as well. Two solid solutions exist in the $Y_5Si_xGe_{4-x}$ system: in a narrow Si-rich region the alloys with $3.5 \leq x \leq 4.0$ have monoclinic crystal structure, while the alloys with $0 \leq x \leq 3.0$ adopt the orthorhombic structure. The dependence of the lattice parameters of $Y_5Si_xGe_{4-x}$ samples with x at room temperature is shown in Fig. 31; the monoclinic angle γ is not shown as it remains practically the same (~93.4°) for all of the monoclinic alloys.

The heat capacity measurements of the $Y_5Si_xGe_{4-x}$ alloys indicate that no phase transitions occur in any of them down to 2 K (Pecharsky et al., 2004a). The electronic specific heat constant γ is close to 2 mJ/g-at K^2 for the whole

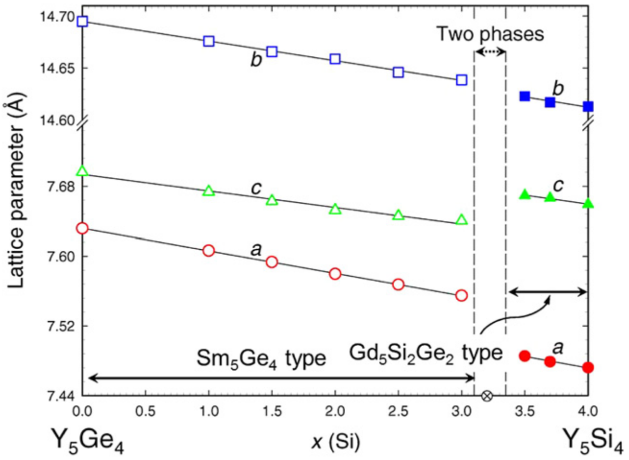

FIGURE 31 The unit cell parameters of single-phase $Y_5Si_xGe_{4-x}$ alloys as functions of Si concentration. The location of the two-phase sample is shown as ⊗.

series, while Debye temperature (θ_D) rises from 240 to 330 K as the concentration of Si increases from $x=0$ to $x=4$.

4.2. $La_5Si_xGe_{4-x}$

Binary La_5T_4 compounds were reported by Smith et al. (1967b). The same study reported the tetragonal Zr_5Si_4-type nonlayered crystal structure for the La_5Si_4 and Sm_5Ge_4-type structure for La_5Ge_4. These results were later confirmed by Gschneidner et al. (2000b) who performed a study of crystal structure, heat capacity, and magnetic susceptibility of several $La_5Si_xGe_{4-x}$ alloys as a part of a broader investigation of R_5T_4 systems. According to Gschneidner et al. (2000b) both La_5Si_4 and $La_5Si_2Ge_2$ (and, probably, the intermediate compositions as well) crystallize with the Zr_5Si_4 structure (SG $P4_12_12$), while La_5Ge_4 and La_5SiGe_3 adopt the Sm_5Ge_4-type structure.

The heat capacity study of these four $La_5Si_xGe_{4-x}$ alloys reveal that similarly to the $Y_5Si_xGe_{4-x}$ system the electronic specific heat constant γ is essentially constant (3.0 ± 0.5 mJ/mol K^2) and the Debye temperature increases with the Si content from 198 ± 10 for La_5Ge_4 to 239 ± 27 K for La_5Si_4. The magnetic susceptibility of La_5Ge_4 is nearly constant, $0.34 \pm 0.02 \times 10^{-6}$ emu/g Oe, between 5 and 300 K indicating that it is a Pauli paramagnet (Gschneidner et al., 2000b).

Yang et al. (2002a) reported a crystallographic investigation of La_5Si_4 compound also confirming its tetragonal Zr_5Si_4-type crystal structure with lattice parameters $a=8.0467$ Å and $c=15.4476$ Å. Yang et al. (2003a) verified the orthorhombic Sm_5Ge_4 type of crystal structure for La_5Ge_4 with lattice parameters $a = 8.0761$ Å, $b = 15.5209$ Å, and $c = 8.1725$ Å.

Guloy and Corbett (2005) reported the same crystal structures for the end members of the La_5Si_4–La_5Ge_4 system prepared by the sintering reactions of the elements at 1100–1300 °C for 10–15 days as well as by arc-melting. They also studied the crystal structure of arc-melted and sintered samples for the $La_5Ge_3Si_x$ series of alloys, where $0.2 < x \leq 1$. In most cases, a mixture of Mn_5Si_3- and Sm_5Ge_4-type phases were observed but by using a special preparation procedure they obtained a single-phase Mn_5Si_3-type compound for the $La_5Ge_3Si_{0.75}$ composition. Interestingly, the La_5Ge_3Si compound has been observed crystallizing in both tetragonal and orthorhombic modifications, depending on the preparation. The α-La_5Si_4 sample obtained after annealing at 1100 °C crystallizes in the Sm_5Ge_4 type, while the β-La_5Si_4 compound, which is a quenched high-temperature phase observed in as-cast alloy, belongs to the Zr_5Si_4 type of crystal structure.

Liu and Altounian (2012) reported a systematic investigation of the La_5Si_4–La_5Ge_4 that confirmed and completed the structural information about this pseudobinary system (Fig. 32).

Alloys with $0 \leq x \leq 0.8$ crystallize in the orthorhombic Sm_5Ge_4-type structure, while for $1.2 \leq x \leq 4$ the tetragonal Zr_5Si_4-type occurs. The $x = 1.0$ sample was found to be a two-phase alloy containing both α- and β-La_5Si_4 (not shown in Fig. 32). Note that due to a rotation of basis vectors the longest (*b*) axis of the orthorhombic structure becomes the *c*-axis of the tetragonal structure. The unit cell volume (not shown) continuously decreases in a linear fashion when the large Ge atoms are replaced by the small Si atoms. Contrary to what was observed in the R_5T_4 systems (T = Si, Ge) with yttrium and the

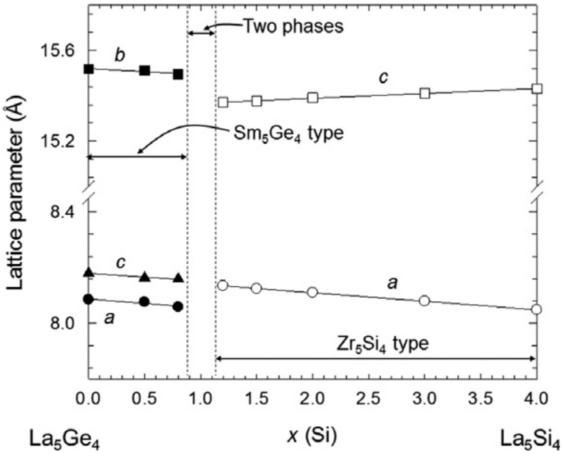

FIGURE 32 Dependence of lattice parameters on the Si concentration in the $La_5Si_xGe_{4-x}$ system.

heavy lanthanides, in the light lanthanides an increase in Si concentration leads to the destruction of the layered (slab) structure and formation of the nonlayered Zr_5Si_4 type.

Liu and Altounian (2012) also calculated the compositional dependence of the Wigner–Seitz volume (WSV) and found that the WSV of the La atoms decreases when the amount of Ge increases. The study suggests that when the WSV of the La1 atom decreases below a certain value the crystal structure changes from Zr_5Si_4 type to Sm_5Ge_4 type.

4.3. $Ce_5Si_xGe_{4-x}$

Ce_5Si_4 and Ce_5Ge_4 compounds were discovered by Smith et al. (1967b). As with other light lanthanides, the silicide crystallizes in the tetragonal Zr_5Si_4-type crystal structure while the germanide adopts the orthorhombic Sm_5Ge_4 type. The phase diagram of the Ce–Si system has been investigated by Bulanova et al. (2002). The study confirms the tetragonal crystal structure for Ce_5Si_4 and reports that it forms by peritectic reaction from Ce–Si and liquid at 1500 °C. Vejpravová et al. (2006) studied the crystal structure (reporting the same Zr_5Si_4 type) and magnetic behavior of Ce_5Si_4, which orders antiferromagnetically at $T_N = 5.6$ K. The magnetic susceptibility obeys Curie–Weiss law in the paramagnetic region with $p_{eff} = 2.6 \pm 0.1$ μ_B/Ce and $\theta_p = -4 \pm 1$ K.

Malik et al. (2009) investigated basic magnetic properties of Ce_5Ge_4 (Sm_5Ge_4-type structure) and reported that this compound orders ferromagnetically at $T_C = 12$ K. However, the value of the calculated paramagnetic Weiss temperature was clearly negative, −20 K, and a magnetization value at 6 K and 90 kOe is only 0.8 μ_B/Ce atom, much lower than g_J value of 2.14 μ_B expected for the trivalent cerium ion in the ferromagnetic state. At the same time, the effective paramagnetic moment, p_{eff}, is 2.44 μ_B/Ce atom, close to the theoretical $g_J[J(J+1)]^{1/2}$ value of 2.54 μ_B for the free Ce^{3+} ion. The maximum magnetic entropy change is −9 J/Kg K for 0–90 kOe magnetic field change. Heat capacity measurements show that the magnetic transition in Ce_5Ge_4 is of second order (Nirmala et al., 2010).

The phase compositions and crystal structures of compounds in the $Ce_5Si_xGe_{4-x}$ system were studied on the arc-melted alloys annealed at 1000 °C for 1 week by Zhang et al. (2009). Two solid solutions were clearly identified: a Ce_5Si_4-based solid solution ($1.15 < x \leq 4$) with the Zr_5Si_4-type structure and a Ce_5Ge_4-based solid solution ($0 \leq x < 0.65$) with the Sm_5Ge_4-type structure. In addition, an intermediate phase with the $Gd_5Si_2Ge_2$-type monoclinic structure was observed near the $x = 1.05 \pm 0.05$ composition (SG $P112_1/a$, $a = 7.9305(2)$ Å, $b = 15.2713(6)$ Å, $c = 8.0609(1)$ Å, $\gamma = 93.452(7)°$); however, this compound was not obtained as a single-phase alloy, but as a mixture of either M + O(II) or M + T.

The phase boundaries shift slightly due to annealing. Zhang et al. (2010) reported the results of investigation of the phase relationships, crystal structures, magnetic and magnetocaloric properties of the as-cast $Ce_5Si_xGe_{4-x}$ alloys, and found that the composition of the monoclinic phase in the non-heat-treated samples is closest to $Ce_5Si_{1.75}Ge_{2.25}$. However, a single-phase alloy with the monoclinic crystal structure has not been obtained. The tetragonal structure in the as-cast alloys exists for $1.85 \leq x \leq 4.0$, and the orthorhombic structure exists for $0 \leq x \leq 1.6$. The temperature dependence of the lattice parameters and unit cell volume on the Si concentration is shown in Fig. 33. Magnetic properties of the as-cast $Ce_5Si_xGe_{4-x}$ alloys were measured by Zhang et al. (2010) and are summarized in Table 14. All samples order magnetically at low temperatures and their inverse magnetic susceptibilities follow the Curie–Weiss law in the paramagnetic state.

It is interesting to note that unlike the R_5T_4 systems with heavy lanthanides, in the $Ce_5Si_xGe_{4-x}$ system the Ce_5Ge_4 and other germanium-rich alloys with the Sm_5Ge_4-type structure order ferromagnetically, while Ce_5Si_4 and silicon-rich alloys with the tetragonal Zr_5Si_4 structure adopt antiferromagnetic ground state. The magnetic phase transitions in all alloys appear to be second-order ones.

4.4. $Pr_5Si_xGe_{4-x}$

Pr_5Si_4 and Pr_5Ge_4 compounds were discovered by Smith et al. (1967b). Similarly to most of the other R_5T_4 compounds formed by light lanthanides, the silicide crystallizes in the nonlayered tetragonal Zr_5Si_4-type structure, while the germanide adopts the orthorhombic Sm_5Ge_4 type. Thuy et al. (2001) prepared the $Pr_5Si_2Ge_2$ compound and found it to be isostructural with the monoclinic $Gd_5Si_2Ge_2$. They also reported that $Pr_5Si_2Ge_2$ orders

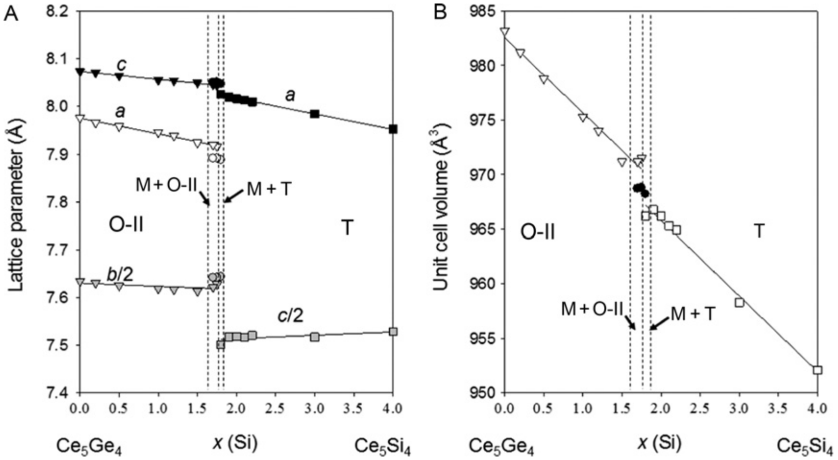

FIGURE 33 Lattice parameters (A) and unit cell volume (B) of the as-cast alloys from the pseudobinary Ce_5Si_4–Ce_5Ge_4 system plotted as a function of Si content (Zhang et al., 2010).

TABLE 14 The Magnetic and Magnetocaloric Properties of the As-Cast $Ce_5Si_xGe_{4-x}$ Alloys (Zhang et al., 2010)

Composition	Structure[a]	T_C/T_N[b] (K)	θ_p (K)	p_{eff} (μ_B/Ce)	M_S (μ_B/Ce)	$-\Delta S_M$ (J/Kg K), $\Delta H = 20$ kOe	$-\Delta S_M$ (J/Kg K), $\Delta H = 50$ kOe
Ce_5Si_4	T	3.8[b]	−8.2	2.35	0.909	3.0	8.8
Ce_5Si_3Ge	T	4.8[b]	−13.4	2.39	0.916	3.1	7.6
$Ce_5Si_{2.2}Ge_{1.8}$	T	4.9[b]	−14.2	2.35	0.857	2.5	6.2
$Ce5Si_{1.75}Ge_{2.25}$	M, O(II)	11.5	13.5	2.30	1.053	3.1	6.6
Ce_5SiGe_3	O(II)	11.5	50.3	2.25	1.254	4.5	9.9
Ce_5Ge_4	O(II)	11.5	48.7	2.00	1.200	5.6	11.6

[a] *The symbols: T, tetragonal Zr_5Si_4 type; M, monoclinic $Gd_5Si_2Ge_2$ type; and O(II), orthorhombic Sm_5Ge_4 type.*

[b] *Values that denote the Néel temperature.*

ferromagnetically at $T_C = 48$ K and its magnetic susceptibility follows the Curie–Weiss law in the paramagnetic state.

Phase relationships in the pseudobinary Pr_5Si_4–Pr_5Ge_4 system were first studied on the as-cast arc-melted alloys using X-ray powder diffraction (Yang et al., 2002b). The study confirmed the presence of the intermediate phase with the monoclinic $Gd_5Si_2Ge_2$ structure in the concentration range of $1.4 \leq x \leq 2.35$. The Pr_5Ge_4-based solid solution adopts the Sm_5Ge_4-type structure for $0 \leq x \leq 1.1$. The Si-rich alloys adopting the Zr_5Si_4-type structure form a solid solution for $2.65 \leq x \leq 4.0$. The variation of the lattice parameters and unit cell volume in the $Pr_5Si_xGe_{4-x}$ system plotted as a function of the Si content is shown in Fig. 34. Similar to other solid solutions with the Zr_5Si_4-type crystal structure, the a parameter increases, while the c parameter decreases when larger Ge atoms are substituted for the smaller Si atoms.

The phase boundaries in the $Pr_5Si_xGe_{4-x}$ system change substantially after the heat treatment. While the as-cast $Pr_5Si_2Ge_2$ crystallizes with the monoclinic crystal structure (α), annealing the sample at 1000 °C for 1 week followed by quenching in water changes the crystal structure to tetragonal (β), $a = 7.9725$ Å, c = 14.8855 Å (Yang et al., 2002c). Both polymorphs order ferromagnetically at 38 (α-phase) and 50 K (β-phase) showing significant irreversibility in the ordered state between low-field (500 Oe) ZFC and FC $M(T)$ data. The magnetic transitions are clearly seen in the temperature-dependent electrical resistivity data; however, in both cases the transitions appear to be of second order. Canted magnetic structure is expected for both structural modifications based on $M(H)$ data (Yang et al., 2002c). The neutron diffraction examination of magnetic and crystal structures of both $Pr_5Si_2Ge_2$ polymorphs has been reported by Wang et al. (2007). The study confirms the Curie temperatures ($T_C = 52$ K for the tetragonal phase and 40 K for the

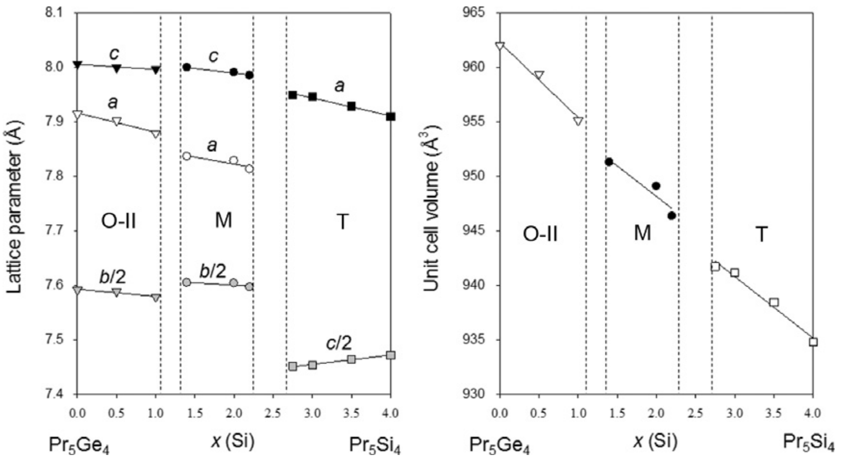

FIGURE 34 Lattice parameters and unit cell volume as a function of Si concentration for as-cast Pr_5Si_4–Pr_5Ge_4 alloys (Yang et al., 2002b).

monoclinic) and a second order of the magnetic transition for both Zr_5Si_4- and Sm_5Ge_4-type structures; no structural transition was observed between 300 and 4 K though small magnetovolume effects are present at T_C. No spin-reorientation transition occurs below T_C. In the magnetically ordered state, magnetic moments are mainly oriented along the *c*-axis in the Zr_5Si_4 structure, and they lie in the *ab* plane (with the larger *a* component) in the $Gd_5Si_2Ge_2$ structure. In both polymorphs, the lattice contraction at T_C occurs in the direction of the largest net magnetic moment component, while there is an increase in lattice parameter along other crystallographic directions.

Investigation of the $Pr_5Si_xGe_{4-x}$ system using alloys annealed at 1000 °C for 1 week showed that such heat treatment indeed transforms the monoclinic crystal structure observed in the as-cast alloys into the tetragonal one. Consequently, only two phase regions, the Pr_5Ge_4-based solid solution with the orthorhombic Sm_5Ge_4 type for $0 \le x \le 1$, and the Pr_5Si_4-based solid solution with the tetragonal Zr_5Si_4 type for $1.2 \le x \le 4.0$, exist in this system when the samples are heat treated (Yang et al., 2003b).

Yang et al. (2003c) performed magnetic measurements on the as-cast $Pr_5Si_xGe_{4-x}$ alloys and found that the magnetic ordering temperature increases from 41 to 47 K with the increase of Si concentration in the O(II) region of the phase diagram but remains nearly the same (38 K) in the monoclinic alloys. On the contrary, in the solid solution region with the tetragonal crystal structure the Curie temperature decreases from 47 to 38 K with the increase in *x*(Si).

Magnetic properties and temperature dependences of electrical resistivity at 0 and 50 kOe magnetic fields have been reported for the Pr_5Ge_4 compound by Yang et al. (2003d). Two magnetic transitions at 25 and 41 K were observed in 500 Oe applied magnetic field. There is an irreversibility between ZFC and FC $M(T)$ data below 25 K but not between 25 and 41 K. The transitions appear to be of second order. Only one broad magnetic transition is observed in 50 kOe applied magnetic field. This magnetic behavior is reflected in the electrical resistivity data, which also show two transitions in zero magnetic field but only one in $H = 50$ kOe. A significant magnetoresistance of 25% at 24 K and 15% at 40 K is probably caused by magnetic-field-induced changes to the magnetic structure.

The existence of two different magnetic structures in Pr_5Ge_4, one below 25 K and another between 25 and 42 K, has been shown by temperature-dependent neutron diffraction experiments (Rao et al., 2004). However, they observed that the crystal structure maintains the Sm_5Ge_4 type from room temperature down to 1.6 K. In fact, two magnetic sublattices of Pr_5Ge_4 experience long-range ordering differently: at 42 K only the praseodymium atoms occupying the 4(*c*) site order magnetically, inducing small magnetic moments on the 8(*d*) sites. Below 25 K both Pr 4(*c*) and Pr 8(*d*) sublattices become magnetically ordered. The Pr moments on the 4(*c*) site align along the *b*-axis. At 9 K, the absolute values of 4(*c*) Pr magnetic moment is 2.66(7) μ_B, while the 8(*d*) Pr moments are 2.6(1) μ_B. According to Rao et al. (2004) lower than $g_J = 3.2\ \mu_B/Pr^{3+}$ values of magnetic moments indicate crystalline electric field effect in Pr_5Ge_4, and, likely, in other $Pr_5Si_xGe_{4-x}$ alloys.

Temperature-dependent neutron diffraction study of $Pr_5Si_{1.5}Ge_{2.5}$ shows that the ferromagnetic ordering in this compound occurs through a second-order transition at $T_C=32$ K, and, similar to Pr_5Ge_4, the room temperature crystal structure (in this case monoclinic $Gd_5Si_2Ge_2$ type) is preserved down to $T=4$ K (Magen et al., 2004a). However, unlike Pr_5Ge_4 only one magnetic transition (at T_C) is observed so the Pr atoms located both outside [8(*d*)] and inside [4(*c*)] the slabs order simultaneously in $Pr_5Si_{1.5}Ge_{2.5}$. The net magnetic moment is primarily aligned along the *a*-axis but significant canting is also observed. It is important to note that while in the $Gd_5Si_xGe_{4-x}$ system the magnetic ordering of the monoclinic phase is always coupled with a structural transformation into the Gd_5Si_4-type phase (O(I)), in $Pr_5Si_xGe_{4-x}$ (and some other $R_5Si_xGe_{4-x}$ systems) the monoclinic $Gd_5Si_2Ge_2$-type structure may order ferromagnetically without structural transition.

Magnetic and electrical transport properties of Pr_5Si_4 were studied by Pinguet et al. (2003). This compound is a ferromagnet with weak magnetocrystalline anisotropy. The Curie temperature is 40 K and the saturation moment measured at $T=5$ K and $H=30$ kOe is 2.14 μ_B/Pr. Pr_5Si_4 is a hard ferromagnet with ~80% remanence. In the paramagnetic state, it follows the Curie–Weiss law with $p_{eff}=3.5\ \mu_B$/Pr and $\theta_p=39$ K. The electrical resistivity of Pr_5Si_4 is metallic and follows the $(\rho/\rho_{300})_T=(\rho/\rho_{300})_0+AT^{\alpha}$ law below T_C: $(\rho/\rho_{300})_0=0.48$, $A=4.4\times10^{-6}\ \mu\Omega/K$, $\alpha=2.8$.

4.5. $Nd_5Si_xGe_{4-x}$

The end members of this pseudobinary system, Nd_5Si_4 and Nd_5Ge_4, were first discovered and their crystal structures determined by Smith et al. (1967b). Nd_5Ge_4 adopts the Sm_5Ge_4-type crystal structure (SG *Pnma*, $a=7.86$ Å, $b=15.06$ Å, $c=7.93$ Å). Similarly to the R_5Si_4 compounds with R = La–Pr, Nd_5Si_4 crystallizes in the tetragonal Zr_5Si_4-type crystal structure (SG $P4_12_12$, $a=7.78$ Å, $c=14.78$ Å). However, Al-Shahery and McColm (1984) indicate that under certain conditions an unspecified orthorhombic crystal structure may be observed for this composition.

The investigation of $Nd_5Si_xGe_{4-x}$ as-cast alloys showed that they may crystallize in four different crystal structure types depending on the composition (Gschneidner et al., 2000b; Yang et al., 2002d). The Nd_5Ge_4-based solid solution adopts the Sm_5Ge_4-type structure (O(II)) for $0\leq x\leq 1.1$; the monoclinic $Gd_5Si_2Ge_2$-type phase (M) forms for $1.35\leq x\leq 2.2$; the orthorhombic Gd_5Si_4-type structure (O(I)) exists in a narrow range of concentrations ($2.6\leq x\leq 2.9$); and the samples in the Nd_5Si_4-based solution crystallize with the tetragonal Zr_5Si_4-type structure for $3.3\leq x\leq 4.0$ (Yang et al., 2002d).

The concentration dependence of lattice parameters of as-cast $Nd_5Si_xGe_{4-x}$ alloys is shown in Fig. 35. However, similar to the $Pr_5Si_xGe_{4-x}$ system, annealing (1000 °C/1 week) of the arc-melted alloys changes the observed phase boundaries, extending the silicide-based solid solution

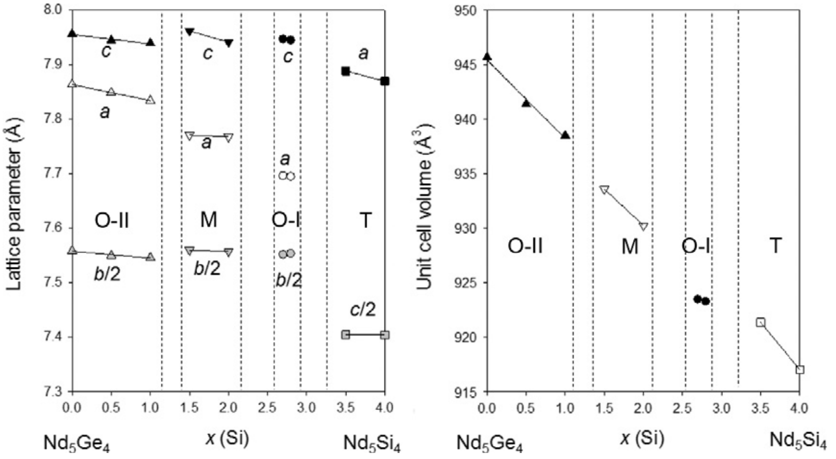

FIGURE 35 Lattice parameters and unit cell volume as a function of Si concentration for the as-cast Nd_5Si_4–Nd_5Ge_4 alloys (Yang et al., 2002d).

($1.7 \leq x \leq 4.0$) with the tetragonal crystal structure at the expense of the other crystal structure. In this case, the Gd_5Si_4-type solid solution does not form in the heat-treated $Nd_5Si_xGe_{4-x}$ alloys (Yang et al., 2003b).[5] Unlike the praseodymium system, the monoclinic phase was observed in the annealed neodymium-based alloys for $0.95 \leq x \leq 1.5$. Finally, the germanide-based solution with the Sm_5Ge_4 structure is also affected by the heat treatment and exists over a narrower range of concentrations: $0 \leq x \leq 0.7$.

An early neutron diffraction experiment determined that Nd_5Ge_4 has a canted magnetic structure with magnetic moments primarily confined in the *ac*-plane of the crystal lattice (Schobinger-Papamantellos and Niggli, 1981). The moments are ferromagnetically aligned along the *a*-axis, but show a minor AFM component along the *c*-axis. A single magnetic ordering transition was detected by this neutron diffraction experiment at $T_N = 52$ K (the compound was considered a ferrimagnet). A more recent neutron diffraction study of Nd_5Ge_4 essentially confirmed this magnetic structure reporting zero net magnetization along the *b*- and *c*-directions and a significant net magnetic moment along the *a*-direction (Cadogan et al., 2002). The magnetic structure of Nd_5Si_4 was investigated by neutron diffraction experiment in the same work, and was described as antiferromagnetic in the tetragonal basal plane (*ab*) and ferromagnetic along the *c*-axis ($T_C = 66$ K). The Nd magnetic moment components of Nd_5Ge_4 and Nd_5Si_4 compounds are presented in Table 15.

---

[5] Interestingly, the O(I)-Gd_5Si_4-type structure is stable after annealing (600 °C/2 weeks) when a small amount of Si is substituted by Ag (instead of Ge) in $Nd_5Ag_{0.5}Si_{3.5}$ (Stepień-Damm et al., 1995).

TABLE 15 Crystal Structures (at $T=295$ K) and Nd Magnetic Moment Components of Nd_5Si_4 (at $T=12$ K) and Nd_5Ge_4 ($T=11$ K) Compounds Determined by Cadogan et al. (2002) and of $Nd_5Si_{1.45}Ge_{2.55}$ (Both Nuclear and Magnetic Structures Determined at $T=4$ K) Reported by Magen et al. (2004a)

Atom	x	y	z	μ_x (μ_B)	μ_y (μ_B)	μ_z (μ_B)	Total moment (μ_B)
Nd_5Si_4 ($P4_12_12$, $a=7.8760(8)$ Å, $c=14.8010(18)$ Å)							
Nd1(4a)	0.1901	0.1901	0	0.36(4)	0.36(4)	2.34(6)	2.39(6)
Nd2(8b)	0.0142	0.1326	0.6192	0.33(4)	0.43(4)	2.41(6)	2.47(6)
Nd3(8b)	0.9861	0.3667	0.2025	1.38(4)	0.58(4)	2.35(6)	2.79(6)
Si1(8b)	0.0529	0.2810	0.8070	–	–	–	–
Si2(8b)	0.2826	0.3270	0.6926	–	–	–	–
Nd_5Ge_4 ($Pnma$, $a=7.8684(9)$ Å, $b=15.1207(16)$ Å, $c=7.9628(9)$ Å)							
Nd1(4c)	0.2888	0.25	0.0020	1.84(4)	0	0.16(6)	1.85(6)
Nd(8d)	0.1197	0.1161	0.3429	2.79(4)	1.01(4)	1.12(6)	3.17(6)
Nd(8d)	0.9757	0.0991	0.8176	2.47(4)	0.14(4)	1.20(6)	2.75(6)
Ge1(4c)	0.9159	0.25	0.1032	–	–	–	–
Ge2(4c)	0.1801	0.25	0.6373	–	–	–	–
Ge3(8d)	0.2197	0.9567	0.5305	–	–	–	–
$Nd_5Si_{1.45}Ge_{2.55}$($P112_1/a$, $a=7.7674(7)$ Å, $b=15.0967(9)$ Å, $c=7.9324(3)$ Å, $\gamma=93.859(5)°$)							
Nd1(4e)	0.333	0.2430	0.0057	2.3(1)	0.1(2)	0.9(1)	2.5(1)
Nd2(4e)	−0.0043	0.1002	0.1820	2.4(2)	1.9(2)	1.7(1)	3.7(2)
Nd3(4e)	0.0291	0.3974	0.1791	2.7(2)	0.6(2)	0.2(1)	2.8(1)
Nd4(4e)	0.358	0.8853	0.1665	1.6(2)	1.8(2)	1.6(1)	3.0(1)
Nd5(4e)	0.326	0.6223	0.1818	2.6(2)	1.0(2)	0.2(1)	2.8(1)
[a]T1(4e)	0.950	0.2526	0.9013	–	–	–	–
[a]T2(4e)	0.215	0.2513	0.3681	–	–	–	–
[a]T3(4e)	0.208	0.9573	0.4735	–	–	–	–
[a]T4(4e)	0.143	0.5444	0.474	–	–	–	–

[a] *T = 36.25% Si + 63.75% Ge.*

The $Nd_5Si_{1.45}Ge_{2.55}$ compound crystallizes in the monoclinic structure at room temperature and orders ferromagnetically at $T_C = 56$ K (Magen et al., 2004a). Similarly to the $Pr_5Si_{1.5}Ge_{2.5}$ monoclinic phase it preserves the same crystal structure down to 4 K, demonstrating the existence of the monoclinic ferromagnetic phase in the $Nd_5Si_xGe_{4-x}$ system. Overall, the magnetic structure of $Nd_5Si_{1.45}Ge_{2.55}$ is similar to the one reported for Nd_5Ge_4 by Cadogan et al. (2002), that is, the net magnetization is mainly oriented along the *a*-axis and a strong magnetic moment canting is observed for *b*- and *c*-axis. The magnetic coupling along the *c*-axis is essentially antiferromagnetic. Only one magnetic ordering transition occurs in $Nd_5Si_{1.45}Ge_{2.55}$.

On the other hand, neutron diffraction investigation of $Nd_5Si_{2.4}Ge_{1.6}$ alloy prepared using high-purity neodymium metal (99.8+at.% pure with respect to all other elements in the periodic table) from Ames Laboratory shows that both magnetic and structural transitions occur at $T_C = 68$ K in this sample (Magen et al., 2004b). The transformation from room temperature $Gd_5Si_2Ge_2$-type structure into the O(I) Gd_5Si_4-type structure is intimately coupled with magnetic ordering; the transition is accompanied by a strong volume change estimated as $\Delta V/V = -0.61\%$. The changes in lattice parameters are anisotropic and mainly occur along the *a*-axis: $\Delta a/a = -0.85\%$, $\Delta b/b = +0.05\%$, $\Delta c/c = -0.02\%$. Similar to the transitions occurring in the $Gd_5Si_xGe_{4-x}$ system the temperature of the transition changes with applied magnetic field with a rate of 0.11(1) K/kOe. The structural transition, however, was not complete and both room temperature and low-temperature structures coexist at 4 K. The magnetic moments of the orthorhombic phase are almost collinearly aligned along the *a*-axis and show small AFM canting in the *b*- and *c*-directions. It is important to note that the $Nd_5Si_{2.4}Ge_{1.6}$ composition is supposed to be a multiphase alloy according to the diagram provided by Yang et al. (2002d) (Fig. 35). However, according to Magen et al. (2004b) an alloy of this composition prepared using the high-purity Nd was single phase with the monoclinic $Gd_5Si_2Ge_2$-type crystal structure. Therefore, apparent phase boundaries in R_5T_4 systems (i.e., those established using samples prepared from rare earth metals with commercial purity) are different from the true phase boundaries established when using alloys prepared from the high-purity rare earth metals. In addition, purity affects the nature of the phase transitions occurring in the R_5T_4 systems as it was well documented in the $Gd_5Si_xGe_{4-x}$ system. It is also important to emphasize that it does not mean that the monoclinic $Nd_5Si_xGe_{4-x}$ compound prepared from high-purity components will necessary show magnetostructural coupling. The relatively low value of the magnetocaloric effect observed in the monoclinic $Nd_5Si_2Ge_2$ sample prepared using high-purity Nd suggests that this compound orders magnetically via a second-order phase transition (Gschneidner et al., 2000b). In fact, Wang et al. (2008) showed that the magnetostructural transition in the $Nd_5Si_xGe_{4-x}$ alloys can be observed in alloys made from commercial purity metals, yet it occurs in the narrow concentration range: $2.25 < x < 2.5$.

Basic magnetic properties of Nd_5Si_4 measured by Boulet et al. (2001) show $T_C = 67$ K, $\mu_s = 1.4\ \mu_B$/Nd, and a remanence of 57% (hard magnetic material). The Curie–Weiss fit of the magnetic susceptibility in the paramagnetic region gives $\theta_p = 76$ K and $p_{eff} = 3.5\ \mu_B$/Nd. A systematic study of magnetic properties of $Nd_5Si_xGe_{4-x}$ alloys by Gschneidner et al. (2000b) shows that in general the magnetic ordering (and paramagnetic Weiss) temperatures decrease almost linearly from 71 ($\theta_p = 74$) to 55 K ($\theta_p = 52$) when the germanium concentration increases. However, the Curie temperature of an Nd_5Si_3Ge alloy with the O(I) Gd_5Si_4 type of crystal structure does not follow this trend as it orders at $T_C = 124$ K. The changes in crystal structure due to heat treatment consequently affect the magnetic properties, especially when the structure changes from O(I) Gd_5Si_4 to tetragonal (T) Zr_5Si_4. For example, β-$Nd_5Si_{2.8}Ge_{1.2}$ (T polymorphic modification, $T_C = 77$ K) orders magnetically at much lower temperature compared to α-$Nd_5Si_{2.8}Ge_{1.2}$, which adopts the O(I) polymorphic modification and has $T_C = 122$ K. At the same time, the difference in magnetic ordering temperatures between monoclinic $Nd_5Si_2Ge_2$ ($T_C = 66$ K) and tetragonal $Nd_5Si_2Ge_2$ ($T_C = 74$ K) is not that large (Yang et al., 2003e).

Tsutaoka et al. (2010) performed magnetic and electrical resistivity measurements on an Nd_5Ge_4 single crystal and identified two critical temperatures: $T_C = 53$ K and $T_t = 39$ K. According to their study T_t is the temperature at which magnetic moments align along the *a*-axis. At 2 K, a typical FM magnetization curve is observed when a magnetic field is applied along the *a*-axis, and a metamagnetic transition occurs at $H = 30$ kOe applied along the *c*-axis. When the magnetic field is applied along the *b*-axis the magnetization increases linearly with the applied magnetic field suggesting strong AFM coupling along this direction. A magnetic moment $\mu_s = 2.3\ \mu_B$/Nd is obtained for the *a*-direction in 70 kOe applied magnetic field. The electrical resistivity of Nd_5Ge_4 was measured along the *a*-axis. It shows typical metallic behavior with a rapid decrease in ρ below T_C.

4.6. $Sm_5Si_xGe_{4-x}$

The Sm_5Ge_4 and Sm_5Si_4 compounds were first reported together with other R_5Si_4 and R_5Ge_4 compounds by Smith et al. (1967b). In fact, the crystal structure of Sm_5Ge_4 (Smith et al., 1967a) became a prototype crystal structure for the large class of the layered R_5T_4 materials (i.e., the O(II) structure) and is characterized, among other features, by the absence of short interslab T—T bonds. Another interesting observation made by Smith et al. (1967b) was that Sm_5Si_4 also crystallizes with the orthorhombic structure type while R_5T_4

compounds formed by other light lanthanides (R = La–Nd) adopt the tetragonal Zr_5Si_4-type structure.

The number of studies of the $Sm_5Si_xGe_{4-x}$ alloys is limited, probably, due to difficulties in preparation of high-quality samarium-based intermetallics related to the high vapor pressure of Sm and the high melting temperature (>1600 °C) of the Sm_5T_4 phases. However, Ahn et al. (2007) presented a systematic investigation of phase relationships and crystal structures in this pseudobinary system complemented by thorough measurements of the magnetic and thermodynamic properties. Samples were prepared in sealed Ta crucibles. Similar to the $Gd_5Si_xGe_{4-x}$ system there are three distinct phase regions in the $Sm_5Si_xGe_{4-x}$ system: Si-rich solid solution with the O(I) Gd_5Si_4-type structure (Sm_5Si_4 and Sm_5Si_3Ge alloys), intermediate $Sm_5Si_2Ge_2$ composition with the monoclinic $Gd_5Si_2Ge_2$-type structure, and the Ge-rich solid solution with the O(II) Sm_5Ge_4-type structure (Sm_5SiGe_3 and Sm_5Ge_4 alloys). Magnetic properties of $Sm_5Si_xGe_{4-x}$ alloys are summarized in Table 16 below.

The alloys with O(I) and M crystal structures order ferromagnetically while the alloys adopting the O(II)-type structure are antiferromagnetic. As commonly observed in the Sm compounds, here the inverse susceptibility in the paramagnetic region cannot be described by linear Curie–Weiss law due to a number of interrelated factors including crystalline electric field (CEF) splitting, the low level excited states of J multiplet, and the Van Vleck transition between different J multiplets. Both effective paramagnetic and saturation moments are much lower in $Sm_5Si_xGe_{4-x}$ alloys compared to what is expected based on the Hund's rule. The energy separation between $J = 7/2$ and $J = 5/2$ states obtained from the fitting of the magnetic susceptibility data is also lower than expected for free Sm^{3+} ions (~1350 K, Van Vleck, 1932).

TABLE 16 The Magnetic Properties of $Sm_5Si_xGe_{4-x}$ Alloys (Ahn et al., 2007)

Compound	T_C, T_N[a] (K)	θ_p (K)	p_{eff} (μ_B/Sm)	μ_s at 1.8 K (μ_B/Sm)	μ_s near T_C (μ_B/Sm)	Δ (K)[b]
Sm_5Si_4	220	220	0.34	0.025	0.1	776
Sm_5Si_3Ge	210	212	0.29	0.02	0.08	824
$Sm_5Si_2Ge_2$	125	120	0.36	0.02	0.05	1000
Sm_5SiGe_3	90[a]	70	0.31	0.024	0.018	1030
Sm_5Ge_4	90[a]	60	0.35	0.018	0.018	1030

[a] *For AFM compounds.*
[b] *Energy separation between J = 7/2 and J = 5/2 states.*

Another interesting observation is that the behavior of $M(H)$ loops at high temperatures but below T_C is typical for a hard ferromagnet with significant coercivity, while at 1.8 K the M versus H dependence is close to linear.

The measured temperature dependences of heat capacity suggest that the magnetic ordering transitions are of second order since the heat capacity plots exhibit λ-type peaks for all compounds except $Sm_5Si_2Ge_2$, whose transition appears to be of first order. The low-temperature X-ray diffraction data (Ahn et al., 2007) show that a coupled magnetostructural transition from paramagnetic M structure into ferromagnetic O(I) structure occurs in $Sm_5Si_2Ge_2$ at T_C. The structural transition is incomplete: ~60% of the powder transformed to the O(I) phase at the lowest temperature of the measurement (5 K). A significant change in lattice dimensions during this transition occurs along the a-axis ($\Delta a/a = -0.6\%$) yet the changes along the b- and c-axes are negligible: $\Delta b/b = -0.02\%$, $\Delta c/c = 0.01\%$.

4.7. $Tb_5Si_xGe_{4-x}$

4.7.1. Crystallography and Magnetism

The existence, crystal structure, and lattice parameters of the end members of the $Tb_5Si_xGe_{4-x}$ pseudobinary system, Tb_5Si_4 and Tb_5Ge_4 were originally reported by Smith et al. (1966, 1967b). Holtzberg et al. (1967) confirmed the crystal structure of the Tb_5Si_4 and Tb_5Ge_4 compounds (both were believed to crystallize in the Sm_5Ge_4 type) and reported lattice parameters similar to those of Smith et al. (1967b). In addition, Holtzberg et al. measured basic magnetic properties of both the silicide and germanide compounds. In line with the trend observed for all other measured R_5Si_4 and R_5Ge_4 compounds, Tb_5Si_4 orders ferromagnetically at a relatively high $T_C = 225$ K, while Tb_5Ge_4 is antiferromagnetic below $T_N = \sim 30$ K (later studies showed that this temperature is actually much higher). At the same time, the paramagnetic Curie temperatures determined from the Curie–Weiss fits of reciprocal magnetic susceptibility plots are clearly positive for silicide and germanide, 216 and 80 K, respectively (Holtzberg et al., 1967).

Spichkin et al. (2001) studied the crystal structure, magnetic, and magnetocaloric properties of Tb_5Si_4 as part of an investigation of the $Gd_xTb_{5-x}Si_4$ system. The silicide is isostructural with Gd_5Si_4 and has lattice parameters $a = 7.4234(5)$ Å, $b = 14.621(1)$ Å, $c = 7.6938(6)$ Å and unit cell volume $V = 835.1(2)$ Å^3. The magnetic properties of Tb_5Si_4 agree with those reported by Holtzberg et al., 1967: $T_C = 223.2$ K, $\theta_p = 227$ K, paramagnetic moment $p_{eff} = 9.76\ \mu_B$, and saturation moment $\mu_s = 9.06\ \mu_B$ at 5 K (moments are reported per Tb atom). The magnetocaloric properties were calculated from the isothermal magnetization data and the values of the maximum magnetic entropy change were observed as $-\Delta S_M = 4.5$ J/Kg K and $-\Delta S_M = 9$ J/Kg K for the magnetic field changes of $\Delta H = 20$ and 50 kOe, respectively. The zero-field heat capacity of Tb_5Si_4 indicates that the magnetic transition is of second order.

Crystal structure and magnetocaloric properties of Tb_5Si_4, $Tb_5Si_2Ge_2$, and Tb_5Ge_4 samples were examined by Morellon et al. (2001b). The crystal structures of the binary compounds have been reported as orthorhombic (SG *Pnma*), and the measured lattice parameters agree with those reported by Holtzberg et al. (1967) and Spichkin et al. (2001). The study discovered that ternary $Tb_5Si_2Ge_2$ compound crystallizes in the $Gd_5Si_2Ge_2$ monoclinic structure type (SG$P112_1/a$) with lattice parameters $a = 7.5088(6)$ Å, $b = 14.653(1)$ Å, $c = 7.7147(7)$ Å, and $\gamma = 93.00(1)°$. The reported magnetic and magnetocaloric properties of these alloys are presented in Table 17.

It appears that the $Tb_5Si_2Ge_2$ compound is a GMCE material while the binary compounds show only moderate magnetocaloric effect. The temperature dependence of magnetic entropy change for the Tb_5Ge_4 compound is unusual, because it exhibits two maxima which are practically equal in their magnitude, one at $T_N = 95$ K, and another at 60 K, which corresponds to a change in magnetic structure (see below).

Thuy et al. (2001) reported similar magnetic properties for $Tb_5Si_2Ge_2$: $T_C = 110$ K and $-\Delta S_M = 22.5$ J/Kg K for $\Delta H = 50$ kOe. On the other hand Tegus et al. (2002c) reported much lower magnetic ordering temperature, $T_C = 76$ K, for their $Tb_5Si_2Ge_2$ sample. In addition, while they confirm the monoclinic $Gd_5Si_2Ge_2$-type crystal structure for this compound, the lattice parameters determined by Tegus et al. (2002c) are larger (by ~0.1 Å in general) compared to those reported by Morellon et al. (2001b) indicating that their sample must be Ge-rich (more Ge results in lower T_C) despite the same nominal 5:2:2 composition used in the two studies. Interestingly, Tegus et al. (2002c) reported that there is a first-order transition above the magnetic ordering temperature in $Tb_5Si_2Ge_2$ as they observed strong magnetic hysteresis in $M(H)$ data taken at 90 K. The calculated magnetic entropy change is $\Delta S_M = -19.5$ J/Kg K for the $\Delta H = 50$ kOe.

TABLE 17 Magnetic Ordering Temperatures and Maximum Magnetocaloric Effect ($-\Delta S_M$) for $Tb_5Si_xGe_{4-x}$ Compounds (Morellon et al., 2001b)

			Maximum $-\Delta S_M$ (J/Kg K)		
Compound	T_C (K)	T_N (K)	$\Delta H = 20$ kOe	$\Delta H = 50$ kOe	$\Delta H = 120$ kOe
Tb_5Si_4	225		5.2	9.8	17.2
$Tb_5Si_2Ge_2$	110		10.4	21.8	36.4
Tb_5Ge_4		95	1.0	3.7	13.1

The monoclinic crystal structure of $Tb_5Si_2Ge_2$ was confirmed by Huang et al. (2002) and the observed Curie temperature, $T_C = 101$ K, is between the values reported by Morellon et al. (2001b) and Thuy et al. (2001) (110 K) and that of Tegus et al. (2002c) (76 K). The discrepancies in the magnetic ordering temperature values reported in several independent studies indicate that T_C in $Tb_5Si_xGe_{4-x}$ is sensitive to the actual chemical composition of the sample, particularly to the Si/Ge ratio (or x). The purity of the starting rare earth metal used in the sample preparation also, probably, plays a role. It is worth to note that the $Tb_5Si_2Ge_2$ samples from Morellon et al. (2001b) (prepared using the commercial quality Tb) and Huang et al. (2002) (prepared using high-purity Tb from Ames Laboratory, which was 99.67 at.% pure with respect to all other elements in the periodic table) have similar lattice parameters yet their T_C's are ~9 K apart. Huang et al. (2002) also studied the crystal structure and MCE of Tb_5Si_4 and Tb_5Si_3Ge. The results obtained for the Tb_5Si_4 sample are practically identical to those of Spichkin et al. (2001) (see above). The Tb_5Si_3Ge alloy has orthorhombic O(I)-Gd_5Si_4 crystal structure with $T_C = 209.6$ K. According to heat capacity measurements the orthorhombic alloys have second-order magnetic transitions while $Tb_5Si_2Ge_2$ shows a first-order transition in the $C_p(T)$ data, a scenario similar to the $Gd_5Si_xGe_{4-x}$ system. Consequently, the MCE is the largest for the monoclinic phase as well. Tocado et al. (2005) determined MCE of $Tb_5Si_2Ge_2$ from heat capacity data measured in 0 and 50 kOe applied magnetic fields; the direct measurement of MCE have been performed as well. The heat capacity data generally agree with those reported by Huang, et al., 2002: a large first-order like heat capacity peak is observed at 105 K. The maximum ΔT_{ad} (at 109 K) is 6.5 K for the direct measurement and 7.8 K for the heat capacity data (Tocado et al., 2005).

Thuy (2002) and Thuy et al. (2002) studied the $Tb_5Si_xGe_{4-x}$ alloys with $x = 2$, 3, and 4 but these alloys were prepared using commercial purity Tb. They reported monoclinic crystal structure for the Tb_5Si_3Ge compound, however, the measured $T_C = 215$ K is in good agreement with the value obtained by Huang et al. (2002), and the calculated MCE for this compound is typical for a second-order material. The magnetic ordering temperatures for $Tb_5Si_2Ge_2$ and Tb_5Si_4 were 116 and 223.2 K, respectively. The temperature dependences of magnetization (measured at $H = 1$ kOe) and electrical resistivity ($H = 0$ kOe) for $Tb_5Si_xGe_{4-x}$ samples with $x = 2.4$, 3.0, and 4.0 were measured by Yao et al. (2003). A sharp first-order like anomaly and strong thermal hysteresis were observed around T_C for the $Tb_5Si_{2.4}Ge_{1.6}$ sample. Kupsch et al. (2005) confirmed that the $Tb_5Si_{2.4}Ge_{1.6}$ sample undergoes transformation from the monoclinic ($Gd_5Si_2Ge_2$ type, $P112_1/a$) structure into the orthorhombic (O(I)-Gd_5Si_4 type, $Pnma$) structure between 100 and 150 K. A large effective shift (0.84 Å) of the adjacent slabs with respect to each other along the a crystallographic direction has been observed. Similarly to $Gd_5Si_2Ge_2$, this magnetostructural transition results in the GMCE observed in $Tb_5Si_{2.4}Ge_{1.6}$ at $T_C = 150$ K: $\Delta S_M = -29$ J/Kg K for $\Delta H = 50$ kOe.

The first preliminary $Tb_5Si_xGe_{4-x}$ x–T magnetostructural phase diagram was constructed by Ritter et al. (2002) based on both macroscopic (LTE, ac susceptibility, electrical resistivity) and microscopic (neutron powder diffraction) experiments. As-cast samples with $x = 0$, 0.8, 1.2, 1.6, 2.0, 2.4, 2.8, 3.2, and 4.0 were prepared for this investigation. The samples with $1.6 \leq x \leq 2.4$ crystallized in the monoclinic $Gd_5Si_2Ge_2$ type of crystal structure (at room temperature), while other samples had orthorhombic crystal structures: O(I) in the Si-rich side of the diagram and O(II) in the Ge-rich side. The reported diagram was similar to the $Gd_5Si_xGe_{4-x}$ in several aspects: (1) the magnetic ordering temperature decreases with increasing concentration of Ge; (2) the PM→FM magnetic transition is observed in alloys with $x \geq 1.6$, while in Ge-rich alloys the ordering is antiferromagnetic: (3) a strong coupling between magnetism and crystal structure was observed. According to Ritter et al. (2002) the PM→FM magnetic transition in the samples with $1.6 \leq x \leq 2.4$ occurs simultaneously with the M to O(I) structural transition though later studies showed that this is not true for all $Tb_5Si_xGe_{4-x}$ alloys with room temperature monoclinic crystal structure. Although Ritter et al. (2002) did not observe a partial decoupling of the magnetic and structural transitions, they pointed out two other notable differences between $Gd_5Si_xGe_{4-x}$ and $Tb_5Si_xGe_{4-x}$ systems: (1) samples with the O(II) crystal structure do not undergo crystallographic transformation and remain antiferromagnetically ordered even at temperatures as low as 2 K, (2) spin-reorientation transitions were observed in both the AFM and the FM ordered states.

A high-resolution neutron powder diffraction study of $Tb_5Si_2Ge_2$ compound complemented by temperature- and magnetic-field-dependent LTE and magnetoresistance experiments further underscored the differences between the $Gd_5Si_xGe_{4-x}$ and $Tb_5Si_xGe_{4-x}$ systems (Morellon et al., 2003). The most important result of this study was a discovery of a ferromagnetically ordered $Tb_5Si_2Ge_2$ phase crystallizing in the $Gd_5Si_2Ge_2$ monoclinic structure. This phase exists over a narrow temperature range, between $T_C = 114$ K and $T_{str} = \sim 105$ K (on cooling, Morellon et al., 2003), but the very fact of the presence of ferromagnetic order in the monoclinic R_5T_4 structure has profound implications on the theoretical understanding of the R_5T_4 systems. For $Gd_5Si_xGe_{4-x}$ alloys, it holds true that breaking even a half of the interslab T—T bonds destroys long-range ferromagnetic interactions but it appears that this may not be common for other lanthanides; moreover, complete coupling of the magnetic and crystallographic sublattices seems to be mostly constrained to the Gd-based compounds.

Using pressure-dependent XMCD experiment Tseng et al. (2011) showed that the $4f$–$5d$ hybridization is stronger in $Tb_5Si_xGe_{4-x}$ compared to the $Gd_5Si_xGe_{4-x}$. The less stable $4f^8$ configuration of Tb compared to the $4f^7$ configuration of Gd may explain why $4f$–$5d$ hybridization becomes stronger in the Tb-containing alloys. While in gadolinium alloys the presence of the Gd-5*d*–T-*p* hybridization is critical for the FM exchange interactions (Haskel et al., 2007), there are, probably, alternative ways for the FM order to settle in the R_5T_4 alloys with R other than Gd even though the 5*d*–3(4)*p* hybridization remains important. The presence of single-ion anisotropy is also an crucial factor influencing the magnetism of Tb compounds.

The practical implications from the existence of such an intermediate phase are substantial as well. When the structural and magnetic transitions are not fully coupled and are occurring at different temperatures the sharp metamagnetic-like transitions, observed in $Gd_5Si_2Ge_2$, are not seen in $Tb_5Si_2Ge_2$ when the magnetic field is applied around T_C. As shown by Morellon et al. (2003), both magnetostriction and magnetoresistance curves still indicate the presence of first-order transition manifested by strong hysteresis. However, the field-induced transitions are quite sluggish. The magnitudes of the field-induced effects (both magnetostrictive and magnetoresistive) are smaller than the magnitudes of the same effects measured during the temperature change across the transition. For example, the maximum volume magnetostriction in $Tb_5Si_2Ge_2$ amounts to $\Delta V/V = -0.14\%$ at 105 K and 120 kOe, while the spontaneous volume magnetostriction is $\Delta V/V = -0.6\%$ (Morellon et al., 2003). Neutron powder diffraction experiments indicate that the magnetic field is a very inefficient driving force for inducing the FM-M→FM-O(I) structural transition in $Tb_5Si_2Ge_2$ transition: at 105 K only 50% of the monoclinic phase is transformed into the Gd_5Si_4-type structure by application of a 50 kOe magnetic field. The magnetic structure of the M-FM phase is mostly collinear along the *a*-axis, with reduced magnetic moments on the Tb atomic positions that are located near the broken interslab T—T bonds.

The influence of increasing Si concentration and applied hydrostatic pressure on the magnetic properties of $Tb_5Si_xGe_{4-x}$ alloys ($x = 1.6$, 1.94, 2.5, and 2.8) has been studied by Tseng et al. (2011). The full O(I)-FM state was observed only in the $x = 2.8$ sample ($T_C = 206$ K). $Tb_5Si_{1.6}Ge_{2.4}$ displays canted AFM component in the magnetically ordered state ($T_C = 105$ K), while two other alloys show clear signs of phase separated FM [M + O(I)] state. The magnetic ordering temperatures for the $Tb_5Si_{1.94}Ge_{2.06}$ and $Tb_5Si_{2.5}Ge_{1.5}$ alloys are 111 and 145 K, respectively. Both chemical substitution of Ge by Si and applied pressure transform the AFM-O(II) state of $Tb_5Si_{1.6}Ge_{2.4}$ into the FM-O(I) state. However, applied hydrostatic pressure modifies the electronic 4*f* and 5*d* states of Tb, which is not seen with Si doping (Tseng et al., 2011).

The magnetic and structural transformations in $Tb_5Si_2Ge_2$ can become coupled by application of external (e.g., hydrostatic) pressure. It is well known that the first-order and second-order transitions respond to applied pressure differently. For example, in the $Gd_5Si_xGe_{4-x}$ system the pressure rate of the T_C of magnetostructural transformations is by an order of magnitude higher than the same for purely magnetic transitions (see Section 3.7). Thus, it may be expected that in $Tb_5Si_2Ge_2$ and similar systems the temperature of the structural transformation increases faster with applied pressure than the temperature of the magnetic transition. At some P value in the P–T phase diagram, a tricritical point should exist at which both temperatures coincide, and above which only the coupled magnetostructural transformation occurs. This hypothesis has been experimentally proved by Morellon et al. (2004b), who performed magnetization, LTE, and neutron diffraction measurements of a $Tb_5Si_2Ge_2$ sample at selected applied pressures. The magnetization measurements indicate that dT_C/dP is $+0.54(3)$ K/kbar below 8 kbar (in the range where transitions are decoupled) but the temperature of the structural transition changes at 2.64(6) K/kbar rate, as determined from the LTE measurements. The tricritical point is at ~8.6 kbar (see Fig. 36); above this pressure the coupled M-PM→O(I)-FM transformation occurs in $Tb_5Si_2Ge_2$. Accordingly, the M-FM phase is not seen on the neutron powder diffraction patterns collected at 9 kbar as a function of temperature.

The coupling of magnetic and structural transformations results in a significant (~40%) enhancement of the magnetocaloric effect observed in $Tb_5Si_2Ge_2$. The maximum magnetic entropy change (for $\Delta H = 50$ kOe) is -13.4 J/Kg K for $P = 0$ kbar but increases to -22.1 J/Kg K at $P = 9$ kbar. Since the MCE enhancement takes place due to addition of the structural transformation it is reasonable to argue that the difference $|\Delta S(0\ \text{kbar}) - \Delta S(9\ \text{kbar})| = 8.7$ J/Kg K is the structural contribution to the total (not purely magnetic) entropy change (Gschneidner et al., 2012; Morellon et al., 2004b). Gomes and de Oliveira (2008) theoretically analyzed the influence of applied pressure on the MCE of $Tb_5Si_2Ge_2$ using a model of interacting spins where the effective exchange interaction parameter was self-consistently calculated in terms of the electronic structure of the compound. Even though

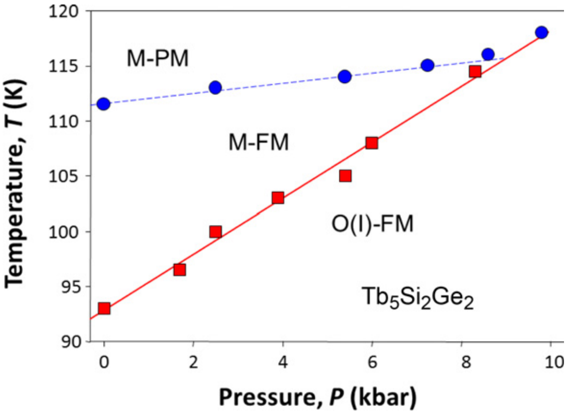

FIGURE 36 Pressure–temperature phase diagram of $Tb_5Si_2Ge_2$. The dashed and solid lines represent the second- and first-order transitions, respectively. *After Morellon et al. (2004b).*

the performed calculations did not account for the effect of the pressure-induced coupling, an increase with applied pressure of both T_C and MCE was observed.

Alternatively, the decoupling of magnetic and crystallographic transitions in the $Tb_5Si_xGe_{4-x}$ system can be diminished by changing the chemical composition, namely by increasing the Si concentration. Garlea et al. (2005) performed temperature-dependent single-crystal neutron scattering measurements using the $Tb_5Si_{2.2}Ge_{1.8}$ single crystal prepared at Ames Laboratory using tri-arc pulling technique, and no intermediate magnetic-only ordering transformation of the monoclinic phase has been detected. The temperature step of the experiment was 5 K so any difference in structural and magnetic transition temperatures in this sample, if any, must be smaller than 5 K. The macroscopic magnetic properties of the $Tb_5Si_{2.2}Ge_{1.8}$ single crystal as well as the magnetic and structural behavior of a powdered sample prepared from the same crystal were studied by Zou et al. (2007). The study found excellent agreement between the temperature of the structural transformation $T_{str} = \sim 108$ K, determined by temperature-dependent X-ray powder diffraction measurements, and magnetic ordering temperature $T_C = 110$ K, determined from Arrott plots. While a minor decoupling ($T_C \neq T_{str}$) is still a possibility in the Si-rich $Tb_5Si_xGe_{4-x}$ alloys, the transition behaves as a coupled magnetostructural one in applied magnetic fields over 10 kOe (in $Tb_5Si_{2.2}Ge_{1.8}$), and it is clear that the extent of decoupling is composition dependent in the $Tb_5Si_xGe_{4-x}$ system.

The magnetostriction measurements performed on a $Tb_5Si_{2.2}Ge_{1.8}$ single crystal along the a-axis indicate that the magnetostriction behavior around the ordering transition is more complex than in the $Gd_5Si_2Ge_2$ even when the magnetic and structural transitions appear to be coupled (Ring et al., 2006). They observed large field hysteresis in the measurements performed in the 100 to 116 K temperature range but the multistep shape of magnetostriction curves in this region was not observed in $Gd_5Si_2Ge_2$. The same study also noted a different magnetostriction behavior in $Tb_5Si_{2.2}Ge_{1.8}$ below and above the spin-reorientation temperature of ~70 K. Additional LTE and magnetostriction measurements were performed on a $Tb_5Si_{2.2}Ge_{1.8}$ single crystal along the a-direction (Ring et al., 2007, strain gauge method). Large strains up to 1500 ppm occur when a magnetic field is applied to the sample in the paramagnetic range above T_C as a result of a field induced M to O(I) transformation but the observed strain is much smaller in the ferromagnetic state. At $T = 108.6$ K, the field-induced transition is irreversible. The transition temperature increases with the application of magnetic field.

The magnetic and structural transitions in $Tb_5Si_2Ge_2$ may become coupled due to thermal hysteresis. The heat capacity measurements performed by Tocado et al. (2005) showed two transitions on cooling but only one on heating. The thermal hysteresis associated with the first-order transition is ~9 K, so during heating the temperature of this transition will coincide with the temperature of the magnetic only transformation, which is not influenced by the hysteresis.

Yüzüak et al. (2007) studied the effect of doping on the magnetocaloric properties of $Tb_5Si_2Ge_2$ compound. A series of $Tb_5Si_{2-x}Ge_{2-x}M_{2x}$ alloys ($0 \leq 2x \leq 0.1$; M = Fe, Pb, Mn) were prepared by arc-melting of commercial grade materials followed by annealing at 900 °C for 24 h. The crystal structure of the main phase is monoclinic and the concentration of Tb_5Ge_3-type impurity phase increases with x. Manganese addition decreases the unit cell volume of $Tb_5Si_2Ge_2$ (Yüzüak et al., 2010c) but significantly increases the magnetocaloric effect in $Tb_5Si_2Ge_2$ from 13 to 21 J/Kg K ($\Delta H = 0$–50 kOe), and changes T_C from 111 to 125 K (for $2x = 0.1$). It is plausible to suggest that such enhancement occurs due to coupling of the magnetic and structural transitions in $Tb_5Si_2Ge_2$ induced by chemical pressure. The maximum $-\Delta S_M$, refrigerant capacity, and RCP of $Tb_5Si_{1.975}Ge_{1.975}Fe_{0.05}$ are 13.3 J/Kg K, 462 J/Kg, and 512 J/Kg, respectively, for $\Delta H = 0$–50 kOe (Yüzüak et al., 2009). The MCE decreases when $Tb_5Si_2Ge_2$ is doped by Pb (Yüzüak et al., 2007).

Yüzüak et al. (2007) reported that in the $Tb_5Si_{2-x}Ge_{2-x}Fe_{2x}$ alloys the Fe addition does not produce any significant change in MCE though it decreases the hysteresis loss, as the transition at T_C becomes clearly second order; but T_C itself is not affected. However, Pereira et al. (2011) report a significant increase in MCE and Curie temperature with Fe substitution in the $Tb_5Si_2Ge_{2-x}Fe_x$ series of alloys, which is similar to the effect of Mn substitution on the magnetic properties of $Tb_5Si_{2-x}Ge_{2-x}Mn_{2x}$ alloys (Yüzüak et al., 2010c). The study confirmed that Fe addition indeed induces the coupling of magnetic and crystallographic transitions. Iron addition promotes the formation of the $Tb_5(Si,Ge)_3$ phase because, similar to the $Gd_5Si_xGe_{4-x}$ alloys, it cannot be incorporated into the 5:4 matrix. The presence of this phase creates external pressure at the grain boundaries, and such pressure, as shown by Morellon et al. (2004b), forces the magnetostructural coupling in $Tb_5Si_2Ge_2$. The MCE in the $Tb_5Si_2Ge_{2-x}Fe_x$ series is largest for $x = 0.15$, with maximum entropy change over -30 J/Kg K for 0–50 kOe magnetic field change at ~120 K (Pereira et al., 2011).

The single-ion anisotropy of Tb has a serious impact on the magnetic properties of $Tb_5Si_xGe_{4-x}$ alloys. While the spin-reorientation transitions are rare in the $Gd_5Si_xGe_{4-x}$ system, the variety of competing magnetic structures created by nonspherically shaped atomic orbitals of Tb and many other rare earths causes a number of spin-reorientation transitions to occur in non-Gd-based compounds. Araújo et al. (2005) identified two critical transition temperatures in $Tb_5Si_2Ge_2$ in the magnetically ordered O(I)-FM state: $T_{SR1} = 57$ K (same as reported by Ritter et al., 2002), and $T_{SR2} = 40$ K. Erratic reorientations between T_{SR1} and T_{SR2} were observed. The authors also showed that a simple phenomenological modeling based on approximate magnetic anisotropy energy gives a satisfactory description of the spin-reorientation process. The temperature dependence of Seebeck coefficient measured for $Tb_5Si_2Ge_2$ between 10 and 300 K also shows two anomalies in the magnetically ordered state in addition to the one at T_C that may correspond to two spin-reorientation transitions reported by Pereira et al. (2007). High-resolution measurements of Seebeck coefficient and electrical resistivity in the vicinity of the magnetostructural transition of $Tb_5Si_2Ge_2$ confirmed the temperature splitting between magnetic and structural transitions (Pereira et al., 2008a). The structural transition occurs with a large thermal hysteresis: T_{str} is 97 K on cooling and 107 K on heating. The magnetic transition occurs at $T_C = 112$ K, thus it is easy to see that the splitting is larger during cooling than during heating. Pereira et al. (2008a) also analyzed the magnetic critical behavior of electrical resistivity and obtained a mean field exponent $\alpha \sim 0.59$ for $T > T_C$. A different exponent, $\alpha \sim 1.06$, was obtained below T_{str}.

4.7.2. Anisotropy

The magnetic structures and associated anisotropy phenomena are more interesting in the $Tb_5Si_xGe_{4-x}$ system compared to $Gd_5Si_xGe_{4-x}$ because in addition to the anisotropic crystal structure, the complexity of magnetic interactions increases due to the presence of the single-ion anisotropy. The transitions between different magnetic configurations occur with a change of the external thermodynamic conditions. Evolution of the magnetic structure of monoclinic $Tb_5Si_{2.2}Ge_{1.8}$ and $Tb_5Si_{2.5}Ge_{1.5}$ compounds with temperature was investigated by means of neutron powder diffraction and the detailed description of both crystallographic and magnetic sublattices is presented by Garlea et al. (2005). The magnetic structures are quite complex as the magnetic moments of the Tb atoms, with a few exceptions, are mostly canted. Below the magnetic ordering temperature (~120 K) the magnetic components (projections of magnetic moments on particular crystallographic axes) are antiferromagnetically aligned along the *b*- and *c*-directions, but all are directed (with slight canting) along the *a*-axis, so the net moment is ferromagnetic. The moments on the intraslab Tb atoms have the smallest canting. Below the spin-reorientation transition at 75 K the arrangement of magnetic moments along the *c*-axis changes to ferromagnetic and the magnetic moment projection along this direction increases; consequently, the moment canting along the *a*-direction increases too. The moment alignment along the *b*-axis remains antiferromagnetic. Both magnetic structures of $Tb_5Si_{2.2}Ge_{1.8}$ are shown in Fig. 37. These results indicate that the *a*-axis is the easy magnetization direction in $Tb_5Si_xGe_{4-x}$ alloys (at least in the alloys with monoclinic crystal structure at room temperature).

An investigation of the magnetic properties of a $Tb_5Si_{2.2}Ge_{1.8}$ single crystal confirms that the *a*-axis is the easy axis (Zou et al., 2007). Overall, the magnetic properties of this compound are extremely anisotropic and are in agreement with the magnetic structure determined by neutron diffraction

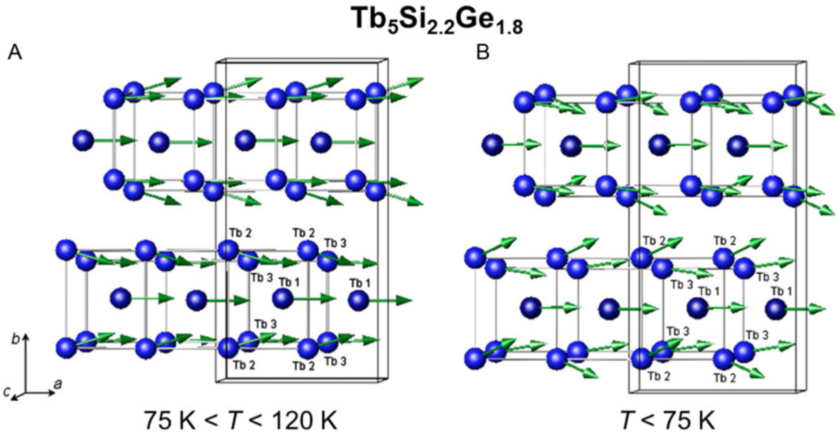

FIGURE 37 Magnetic structure of $Tb_5Si_{2.2}Ge_{1.8}$ at temperatures above (A) and below (B) the spin-reorientation transition. The nonmagnetic (Si/Ge) atoms are excluded for clarity.

studies. When magnetization is measured along the *a*-axis, $Tb_5Si_{2.2}Ge_{1.8}$ behaves similarly to the $Gd_5Si_xGe_{4-x}$ alloys with $x \leq 2$ showing a sharp first-order transition at the point of the PM→FM transformation ($T_{C\{H\|a\}} = 118$ K). Isothermal magnetization of the single-crystal oriented along the *a*-axis measured just above T_C shows a sharp metamagnetic step and presence of hysteresis, which correspond to the coupled magnetostructural transformation. When the magnetic field is applied along the *c*-axis, the PM→FM metamagnetic transition also occurs but is not as sharp as observed along the *a*-axis. Furthermore, the critical field H_{CR} is ~36 kOe higher along the *c*-axis than along the *a*-axis and the rate of change dH_{CR}/dT is also much higher for the *c*-axis when compared with the *a*-axis: 5.4 ± 0.3 kOe/K versus 2.64 ± 0.02 kOe/K, respectively. The *b*-axis, which is the hard axis in $Tb_5Si_{2.2}Ge_{1.8}$, shows predominantly antiferromagnetic behavior (a small ferromagnetic component can be seen in high magnetic fields), and no characteristic metamagnetic transitions indicative of the PM→FM magnetostructural transitions have been observed along this axis. The stark difference between the magnetic behaviors along three major crystallographic directions is clearly seen in the temperature-dependent magnetization measurements (see Fig. 38).

The magnetocaloric effect calculated from the $M(H)$ isotherms using the Maxwell relation is also anisotropic. Along the *a*- and *c*-axes a maximum entropy change for $\Delta H = 0$–50 kOe is ~−40 J/Kg K, however, MCE along the *a*-axis shows a wide 20 K plateau while a single sharp peak is observed along the *c*-axis (Zou et al., 2007). Consequently, the cooling power should be significantly larger with the magnetic field applied along the *a*-direction. The MCE along the *b*-axis is almost nonexistent for the same field change (−3.6 J/Kg K). As a result, the MCE of a $Tb_5Si_{2.2}Ge_{1.8}$ powder is −26 J/Kg K, an

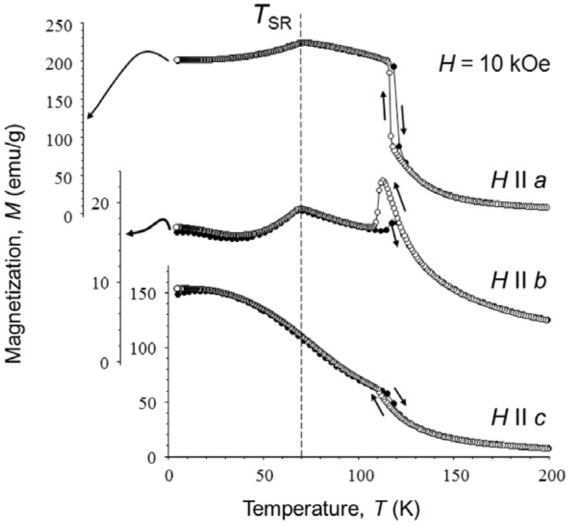

FIGURE 38 Temperature dependence of magnetization of the $Tb_5Si_{2.2}Ge_{1.8}$ single crystal measured along the three major crystallographic directions in 10 kOe applied magnetic field (Zou et al., 2008).

averaged value over all three directions. This value is smaller compared to the $Gd_5Si_xGe_{4-x}$ alloys, where MCE is practically isotropic (Tegus et al., 2002a). On the other hand, it is almost twice the value obtained for $Tb_5Si_2Ge_2$ at ambient conditions (−13.4 J/Kg K) and is comparable to the MCE in the same $Tb_5Si_2Ge_2$compound when the magnetostructural coupling is induced by an applied pressure of 8.6 kbar (−22.1 J/Kg K). This alone provides a valid argument that the magnetic and structural transitions are coupled in high magnetic fields in $Tb_5Si_{2.2}Ge_{1.8}$ but not in $Tb_5Si_2Ge_2$.

It is worth to note that the T_C of the $Tb_5Si_{2.2}Ge_{1.8}$ powder obtained by Zou et al. (2007) is equal to 110 K, or 8 K lower than the T_C of the single crystal. The authors suggest that both intrinsic (anisotropy) and extrinsic (induced stress and compositional inhomogeneities) factors may be responsible for such a difference. The T_C of the powdered sample as determined by magnetization measurements corresponds to the temperature of the M to O(I) structural transformation observed by temperature-dependent X-ray powder diffraction measurements. This structural change from the $Gd_5Si_2Ge_2$ structure type into the Gd_5Si_4 structure type is accompanied by substantial discontinuous changes in the lattice parameters and unit cell volume: $\Delta a/a = -1.0\%$, $\Delta b/b = -0.08\%$, $\Delta c/c = 0.16\%$, and $\Delta V/V = -0.74\%$. The large spontaneous striction observed along the a-axis clearly makes $Tb_5Si_{2.2}Ge_{1.8}$ a giant magnetostrictive material. However, the application of magnetic field brings a complication, which is similar to the one observed for $Tb_5Si_2Ge_2$ by Morellon et al., 2003: while the changes in the lattice dimensions during the field-induced magnetostructural transition are identical to those shown above, the transition itself is broad and largely incomplete. Only 40% of the structural M to O(I) transformation is completed at 40 kOe at T = 112 K (just above the $T_C = 110$ K of $Tb_5Si_{2.2}Ge_{1.8}$ powder) so the change in the bulk dimensions is expected to be much smaller for the field-induced transition than for the temperature-induced change (Zou et al., 2007).

As expected from the complex nature of the spin-reorientation transitions in $Tb_5Si_xGe_{4-x}$ alloys (Garlea et al., 2005; Ritter et al., 2002), the magnetic behavior along the three major crystallographic directions is different not only at T_C but also near T_{SR}. This can be seen both in the $M(T)$ (Fig. 38) and $M(H)$ dependences measured with magnetic field along the different axes of the $Tb_5Si_{2.2}Ge_{1.8}$ single crystal (Zou et al., 2008). The critical fields for steps in $M(H)$ curves that correspond to the spin-reorientation transitions and the characteristic shape of these steps clearly vary from one axis to another for the $M(H)$ data collected at the same temperature using the same measurement protocol.

The anisotropic behavior of $Tb_5Si_{2.2}Ge_{1.8}$ is summarized in Fig. 39, which shows three H–T magnetic phase diagrams constructed for each crystallographic direction (Zou et al., 2008). Since no field-induced transitions were observed in $M(H)$ data for H||c measurements between 1.8 and 70 K, the phase boundary line for the spin-reorientation transition along the c-direction is rather tentative. It is clear that the phase boundaries between the paramagnetic and magnetically ordered states are considerably different from each other.

The magnetic anisotropy is also present in the paramagnetic state because both the parameters (p_{eff} and θ_p) obtained using the Curie–Weiss fits of the high-field $\chi_{dc}^{-1}(T)$ data and the characteristics of the Griffiths-like phase behavior (see below) are also different for each direction. According to Zou et al. (2007), the effective paramagnetic moments, p_{eff}, are 10.15, 10.05, and 10.09 μ_B/Tb for a-, b-, and c-axes respectively, while the corresponding values of θ_p are 117.3, 80.9, and 105.8 K.

The electrical properties of the $Tb_5Si_xGe_{4-x}$ alloys also show a significant anisotropy in the presence of an applied magnetic field. For example, the SGV effect, which is essentially a thermoelectric response to the nonequilibrium distribution of the latent heat released at the transition within a solid (see also Section 3.5), in the $Tb_5Si_{2.2}Ge_{1.8}$ single crystal may be isotropic or anisotropic depending on whether the magnetostructural transition is induced thermally or magnetically (Zou et al., 2009a). The voltage signal is similar along all three major crystallographic directions upon heating or cooling across the T_C in a zero magnetic field. However, isothermal magnetization at 120 K results in a strong SGV response only when the magnetic field is applied along the a-axis of $Tb_5Si_{2.2}Ge_{1.8}$, but not along the b- or c-axes (at least for $H \leq 40$ kOe). This observation agrees with the fact that sharp, first-order like field-induced magnetic transformations were observed only along the a-axis in $Tb_5Si_{2.2}Ge_{1.8}$ (Zou et al., 2007).

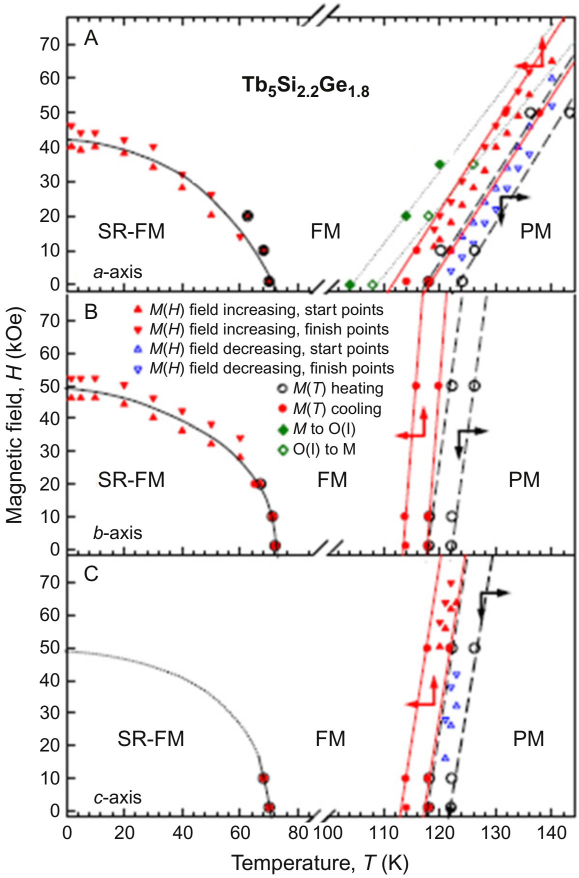

FIGURE 39 The H–T phase diagram of $Tb_5Si_{2.2}Ge_{1.8}$ with magnetic applied along the *a*, *b*, and *c*-axes of the unit cell. The lines are guides to the eye. Arrows placed between the boundaries indicate phase separated regions for the corresponding directions of the temperature and magnetic field changes. *After Zou et al. (2008).*

The measurements of the electrical transport properties of the $Tb_5Si_{2.2}Ge_{1.8}$ single crystal reveal other interesting anisotropic effects that may be dubbed as “from 5% to 160% magnetoresistance in 90°”. Essentially, a colossal positive magnetoresistance (CMR) of 160% is observed in $Tb_5Si_{2.2}Ge_{1.8}$ when both the magnetic field and electrical current vectors were applied along the *a*-axis, but only minor decreases in the electrical resistivity of −5% and −8% were observed when magnetic field and electrical current vectors were applied along the *b*- and *c*-axes, respectively (Zou et al., 2009b). Again the peculiarities of the anisotropic H–T phase diagram discussed above, particularly the location of the PM–FM boundary play a role in this effect. Specifically, the presence of the phase separated state that can be manipulated by the applied magnetic field is responsible for the CMR. In addition, the scattering by interphase boundaries that have a particular orientation relationship due to the monoclinic–orthorhombic distortion of the lattice also leads to large anisotropic effects observed in the electrical transport measurements. Cycling through the transition substantially decreases the MR value from 160% to 90% after just one cycle, falling further down to ~20%, the value observed during the 30th cycle. Such reduction of MR effect is related to an increase of temperature-independent component of the electrical resistivity due to an increase of incoherent phase boundaries and stress build up.

The magnetic structure of the Tb_5Ge_4 compound that orders antiferromagnetically at 92 K (Tian et al., 2009) is similar to the magnetic structure of Gd_5Ge_4: the individual magnetic moments of Tb atoms are ferromagnetically aligned within the slab (in *ac*-plane) but the slabs themselves are magnetically antiparallel with respect to each other as they are stacked along the *b*-axis. However, the moments are completely confined to the *ac*-plane in the temperature region between T_N and $T_{SR} = \sim 55$ K; below T_{SR} a small *b*-axis component exists for the canted Tb2 and Tb3 (8*d* sites) moments (Ritter et al., 2002). The anisotropy of the Tb_5Ge_4 magnetic structure is seen in the temperature dependences of dc magnetic susceptibility measured with the magnetic field applied along the three major crystallographic axes of Tb_5Ge_4 (Tian et al., 2009). All three $\chi^{-1}(T)$ curves follow the Curie–Weiss law above ~160 K and the effective paramagnetic moment (9.7 μ_B/Tb atom) is essentially the same for all directions. However, the paramagnetic Weiss temperature (θ_p) is practically the same and is equal to ~25 K for the *a*- and *c*-axes reflecting prevailing FM interactions occurring in the *ac*-plane but is negative (−50 K) for the *b*-axis, along which the interactions are AFM (Tian et al., 2009). This is different from Gd_5Ge_4 where θ_p's are decisively positive for all directions (Ouyang et al., 2006b).

The magnetic structure of Tb_5Si_4 is largely noncollinear and the *a*-axis is the easy magnetization direction (Ritter et al., 2002). This compound also undergoes a spin-reorientation transition at low temperatures (~80 K), and a second strong ferromagnetic component develops along the *c*-axis.

4.7.3. Short-Range Correlations (Griffiths-like Phase)

The deviation of the temperature dependence of reciprocal magnetic susceptibility from the Curie–Weiss law in the paramagnetic region may be associated with a variety of magnetic phenomena, both intrinsic (superparamagnetism, Van-Fleck effect) and extrinsic (ferromagnetic impurities). However, as was shown for Gd_5Ge_4 (see Section 3.9), the behavior of the reciprocal magnetic susceptibility of layered R_5T_4 alloys below a characteristic temperature T_G may be well described in terms of the effect discovered by Griffiths (1969)

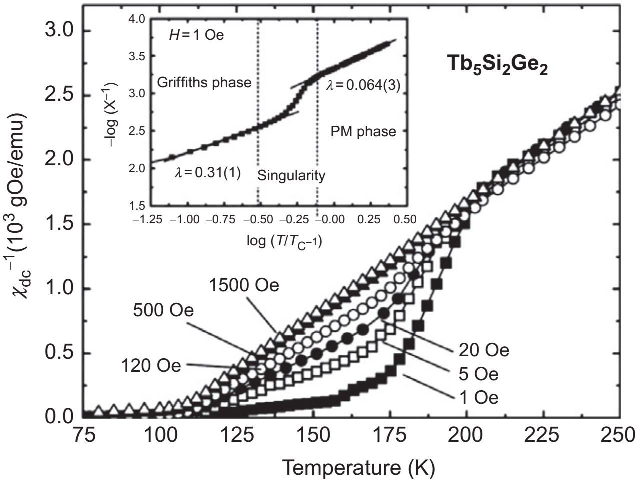

FIGURE 40 Temperature dependence of $\chi^{-1}(T)$ of $Tb_5Si_2Ge_2$ as a function of applied magnetic field, measured on heating. The inset shows fits of data collected at 1 Oe. *After Magen et al. (2006a).*

in highly diluted systems of *d*-elements. The study of the Griffiths-like phase in $Tb_5Si_2Ge_2$ by means of low-field temperature-dependent magnetization and small angle neutron scattering (SANS) spectroscopy described the main properties of this phase (Magen et al., 2006a). The presence of this phase in the range of temperatures between $T_C = 110$ K and $T_G \sim 200$ K was manifested by significant negative deviations from linearity in the $\chi^{-1}(T)$ plots in magnetic fields below 500 Oe (see Fig. 40). As expected for the Griffiths phase, the low-field magnetic susceptibility can be characterized by the $\chi^{-1}(T) \equiv (T - T_C)^{1-\lambda}$ dependence, where $0 \leq \lambda < 1$. Moreover, according to Magen et al. (2006a), even in higher magnetic fields (1500 Oe), where the $\chi^{-1}(T)$ plot appears to be linear, there are substantial differences in λ between a true paramagnetic region above T_G ($\lambda = 0.04$) and in the $T_C < T < T_G$ region ($\lambda = 0.25$). This shows that the short-range FM clustering above T_C, which is responsible for the Griffiths-like behavior, exists even in higher magnetic fields but is masked by an increasingly stronger signal from the paramagnetic matrix.

These short-range magnetic clusters were observed in the SANS experiment as well, and it was found that the correlation length of magnetic interactions (ξ) is suppressed by the applied magnetic field but increases with cooling (Magen et al., 2006a). The authors suggest that the presence of local structural disorder is responsible for the nucleation of magnetic clusters and appearance of a Griffiths-like phase in $Tb_5Si_2Ge_2$. It is safe to suggest that the mechanism of this effect is similar for other R_5T_4 phases crystallizing in either the monoclinic $Gd_5Si_2Ge_2$ or orthorhombic Sm_5Ge_4 type of crystal structure, because a universal (x, T) phase diagram can be constructed at least for R = Gd, Tb, Dy, and Ho (Pereira et al., 2010). Essentially, T_G may be viewed as the potential “pure” (not affected by a first-order transition) ordering temperature of the O(I) structure for a given chemical composition, and may be interpolated from the region were the second-order only O(I)-PM to O(I)-FM transition occurs (Ouyang, 2010; Pereira et al., 2010).

The Griffiths-like phase has been observed for a $Tb_5Si_{2.2}Ge_{1.8}$ single crystal in magnetic fields up to 1000 Oe (Zou et al., 2008). The T_G was estimated to be near 200 K. The study also found that the Griffiths-like behavior in $Tb_5Si_{2.2}Ge_{1.8}$ single crystal is anisotropic and shows a correlation with θ_p values determined using the Curie–Weiss fit of high-field $M(T)$ data: a strongest deviation from $\chi^{-1}(T)$ linearity and a largest λ value in 10 Oe field is observed along the a-axis, which also has the highest value of $\theta_p = 117.3$ K. When the magnetic field is applied along the b-axis ($\theta_p = 80.9$ K), the Griffiths-like phase appearance is minimal. At the same time, the anomalous thermal hysteresis observed in $Tb_5Si_{2.2}Ge_{1.8}$ at T_C in magnetic fields $H \leq 1000$ Oe around T_C is most pronounced along the b-axis. A sharp magnetic peak around T_C is observed on cooling but not on heating. It is believed that the presence of such peak is related to the existence of short-range FM clustering least masked by the matrix along the b-axis; the thermal history dependence for such peak indicates that the magnetic and structural transitions may not be fully coupled in low magnetic fields in $Tb_5Si_{2.2}Ge_{1.8}$ (Zou et al., 2008).

Presence of diffuse scattering in the neutron diffraction investigation of an antiferromagnetic Tb_5Ge_4 single crystal indicates three-dimensional short-range correlations both above and below T_N (Tian et al., 2009). The shape of the observed diffuse scattering peak is somewhat unconventional showing a squared-Lorentzian peak shape. The results support the presence of a clustered magnetic state in Tb_5Ge_4 but the nature of the diffuse scattering is apparently AFM, which is different from the FM clustering model proposed for the Griffiths-like phase in Gd_5Ge_4 (Ouyang et al., 2006b).

4.7.4. *Miscellaneous*

Reflectance difference spectra for the b–c plane of $Tb_5Si_{2.2}Ge_{1.8}$ Bridgeman-grown single crystal were obtained in the photon energy range of 1.5–5.5 eV. At fixed photon energy, the angle-dependent RD spectra have a sinusoidal form. The energy-dependent RD spectra of $Tb_5Si_{2.2}Ge_{1.8}$ (b–c plane) are similar to those of $Gd_5Si_2Ge_2$ (b–c plane) showing one strong peak at 3.2 eV, a minor peak at 1.7 eV, and a weak shoulder at 4.1 eV (Lee et al., 2004).

Ugurlu et al. (2005b) observed thin plates similar to those found in the $Gd_5Si_xGe_{4-x}$ alloys in the Tb_5Si_4, Tb_5Ge_4, and $Tb_5Si_{2.25}Ge_{1.75}$ samples, whose room temperature crystal structures are O(I)-Gd_5Si_4, O(II)-Sm_5Ge_4, and M-$Gd_5Si_2Ge_2$, respectively. While they could not identify the chemical composition of these plates accurately, the EDS results indicate that the plates are enriched in both Tb and oxygen compared to the matrix.

The electronic structure and magnetic properties of $Tb_5Si_{2.2}Ge_{1.8}$ have been studied from first-principles electronic structure calculations (scalar relativistic version of LSDA + U approach implemented in the TB-LMTO method) by Paudyal et al. (2011). The calculations showed that the FM-O(I) structure has lower total energy, and, therefore, is a more stable phase than the FM-M structure in this compound. Also, the splitting of the 5d bands of Tb is larger in the orthorhombic structure indicating higher 5d contribution to the rare earth magnetic moments. These results provide theoretical support for the fact that $Tb_5Si_{2.2}Ge_{1.8}$ undergoes a structural-only transformation in the ferromagnetic state, even though the monoclinic structure here may support the FM order.

4.8. $Dy_5Si_xGe_{4-x}$

The crystal structure of Dy_5Si_4 and Dy_5Ge_4 compounds has been determined by Smith et al. (1967b). Both compounds were originally reported to crystallize in the Sm_5Ge_4 type of crystal structure, though Holtzberg et al. (1967) already noted that germinides and silicides have different crystal structures. Later it was found that the silicide adopts the Gd_5Si_4-type structure. According to Holtzberg et al. (1967) Dy_5Si_4 ordered ferromagnetically at $T_C = 140$ K while $Dy_5Ge_4$is an antiferromagnetic compound with $T_N = 40$ K. Paramagnetic Curie temperatures are both positive: $\theta_p = 133$ K for Dy_5Si_4 and 43 K for Dy_5Ge_4. The variation of T_C with pressure for Dy_5Si_4 was found to be linear with dT_C/dP equal to 3.0 K/GPa (Parviainen, 1980).

The $Dy_5Si_xGe_{4-x}$ system in many aspects is similar to $Gd_5Si_xGe_{4-x}$ but the phase boundaries are shifted toward the Si-rich side. There are three phase regions: (1) extensive germanium-based solid solution occurring for $0 \leq x < 2.6$ with AFM type of ordering, (2) intermediate monoclinic structure at $2.6 < x < 3.2$, and (3) silicon-based solid solution at $3.2 < x \leq 4.0$ with the Gd_5Si_4-type crystal structure and relatively high (compared to two other regions) magnetic ordering temperatures (Gschneidner et al., 2000b; Ivtchenko et al., 2000). The Dy_5Si_3Ge compound with room temperature monoclinic crystal structure undergoes a first-order transition, which is accompanied by a relatively large magnetocaloric effect > -20 J/Kg K (Gschneidner et al., 2000b; Ivtchenko et al., 2000).

Dy_5Si_3Ge has a number of interesting and unique properties. Most of R_5T_4 compounds with room temperature monoclinic $Gd_5Si_2Ge_2$-type structure typically order ferromagnetically and the magnetic transition may or may not be coupled with the M to O(I) structural transition depending on chemical composition or applied pressure. Dy_5Si_3Ge, which also adopts the M-type crystal structure at room temperature, at first orders antiferromagnetically at $T_N = 74$ K, then undergoes an AFM–FM transition at $T_C = 62$ K (Nirmala et al., 2007b). The ordering temperature is magnetic-field dependent: the slope of dT_C/dH is equal to ~0.45 K/kOe. The transition into the ferromagnetic state is followed by a partial structural M to O(I) transition, which is occurring a few degrees below T_C indicating a slight decoupling between the crystallographic and magnetic lattices. Therefore, Dy_5Si_3Ge is the only known R_5T_4 compound where the monoclinic crystal structure exists in all three magnetic states: paramagnetic, antiferromagnetic, and ferromagnetic. Interestingly, the magnetostructural decoupling is not clearly seen on the heat capacity data—only one first-order like peak is observed at T_C when data are collected during warming in zero magnetic field (Nirmala et al., 2011). Only 47% of the monoclinic phase transforms into orthorhombic phase even when the sample is cooled down to 5 K yet low-temperature M(H) loops reveal the magnetic behavior typical for a hard ferromagnet (Nirmala et al., 2007b). The application of magnetic field increases the amount of the orthorhombic phase but even a 40 kOe magnetic field is not strong enough to complete the structural transition. The M to O(I) structural transition is characterized by large anisotropic change in lattice parameters and unit cell volume, which are typical for this type of transition: $\Delta a/a = -1.0\%$, $\Delta b/b = -0.2\%$, $\Delta c/c = 0.2\%$, and $\Delta V/V = 0.7\%$ (Nirmala et al., 2007b).

The saturation magnetization at 70 kOe is 9.7 μ_B/Dy ($g_J J = 10\ \mu_B$) indicating that: (a) the material is 100% FM at 1.8 K and 70 kOe, (b) the magnetic structure at these conditions is nearly collinear, and (c) crystal field effects are small. Coercivity decreases with the temperature increase and becomes zero at 50 K (Nirmala et al., 2007b). In fact, there are reasons to suspect that the FM phase with the monoclinic crystal structure is a soft magnet while the FM phase with orthorhombic crystal structure is a hard phase; however, since both phases are present in the magnetically ordered Dy_5Si_3Ge alloy in nearly 1:1 ratio, and, consequently, are affecting each other's coercivity via microstructure, it is more appropriate to consider this material as a composite. Such structurally phase separated materials containing an intimately coupled mixture of hard and soft magnetic phases may have a substantial practical potential for future development of permanent magnets.

In the paramagnetic region, Dy_5Si_3Ge follows the Curie–Weiss law. The paramagnetic temperature θ_p is 76 K and the effective magnetic moment p_{eff} is 11.1 μ_B/Dy. Electrical resistivity versus temperature of Dy_5Si_3Ge shows a strong history dependence and thermal hysteresis (Nirmala et al., 2011).

The $Dy_5Si_2Ge_2$ composition crystallizes in the orthorhombic Sm_5Ge_4-type structure ($a = 7.527$ Å, $b = 14.574$ Å, and $c = 7.628$ Å) and orders antiferromagnetically at $T_N = 56$ K via a second-order transition (Nirmala et al., 2005). Below 20 K, however, it shows a sharp field induced AFM to FM metamagnetic-like transition. According to the measured $M(H)$ loops (Nirmala et al., 2007a) this transition is reversible but shows significant hysteresis. Its critical field is temperature dependent though the rate of this dependence is smaller above 10 K than at lower temperatures. Above 20 K the metamagnetic-like transition becomes smooth with no measurable hysteresis. Neutron diffraction experiment shows that magnetic moments in

$Dy_5Si_2Ge_2$ arrange spirally along the a-axis and the net structure is a canted AFM. The averaged Dy magnetic moment in the ordered state is 7.6(1) μ_B, much lower than the 10 μ_B value expected for the Dy^{3+} free ion; thus, a significant CEF presence was suggested for this compound (Nirmala et al., 2005). The temperature dependence of heat capacity of $Dy_5Si_2Ge_2$ has been measured in applied magnetic fields of 0, 50, and 90 kOe and reveals a typical second-order transition at T_N (Nirmala et al., 2007a). The maximum magnetic entropy change is relatively low (~ -8 J/mol K), yet it remains nearly constant over a broad temperature range 30–50 K when calculated for a 0 to 90 kOe magnetic field change.

Dy_5Si_4 alloy with the O(I) crystal structure, Dy_5Si_3Ge alloy with the M structure, and $Dy_5Si_{2.5}Ge_{1.5}$ alloy with the O(II) structure were found to share another common characteristic with the $Gd_5Si_xGe_{4-x}$—the microstructural thin plate features (Ugurlu et al., 2005b). The composition of these plates was also proposed to have the $Dy_5(Si_xGe_{3-x})$ stoichiometry.

4.9. $Ho_5Si_xGe_{4-x}$

Both Ho_5Ge_4 and Ho_5Si_4 compounds were discovered by Smith et al. (1967b). The germanide crystallizes in the Sm_5Ge_4-type crystal structure while the silicide adopts the Gd_5Si_4 type. Their magnetic properties were first reported by Holtzberg et al. (1967), who found that similarly to other R_5T_4 (T = Si, Ge) compounds formed by the heavy lanthanides the silicide orders ferromagnetically and the germanide is antiferromagnetic. Formation of the Ho_5Si_4 compound was investigated by Eremenko et al. (1995), and it was reported that it forms by peritectic reaction $L + Ho_5Si_3 \rightarrow Ho_5Si_4$ at 1850 °C. Schobinger-Papamantellos and Niggli (1979) performed a neutron diffraction study of the magnetic structure of Ho_5Ge_4 without knowing that it undergoes a structural deformation at $T_N = 23$ K (discovered much later by Singh et al., 2009). They reported a canted alignment of magnetic moments and a presence of two coexisting magnetic structures. The variation of T_C with pressure for Ho_5Si_4 was found to be linear with dT_C/dP equal to 1.8 K/GPa (Parviainen, 1980).

$Ho_5Si_2Ge_2$ orders antiferromagnetically at $T_N = 25$ K (Thuy et al., 2001, 2003), which is related to the fact that this compound adopts the orthorhombic Sm_5Ge_4 type of crystal structure ($a = 7.501$ Å, $b = 14.510$ Å, and $c = 7.599$ Å). A metamagnetic transition is observed in $M(H)$ data measured for $Ho_5Si_2Ge_2$ below T_N; interestingly, the critical field decreases with increasing temperature. High magnetic field measurements (up to 380 kOe) performed at 4.2 K show that magnetization approaches very slowly the estimated saturation value of 10.18 μ_B/Ho. In the paramagnetic region, the magnetic susceptibility of $Ho_5Si_2Ge_2$ follows the Curie–Weiss law ($\theta_p = 17$ K, $p_{eff} = 9.7$ μ_B/Ho). A second transition at 15 K was observed during heat capacity measurements of $Ho_5Si_2Ge_2$ (Thuy et al., 2003). However, another study, while confirming the two transitions at ~25 and 15 K, reports that $Ho_5Si_2Ge_2$ magnetically orders at higher temperature, $T_N = 35$ K, based on a series of magnetization, electrical resistivity and heat capacity measurements (Prokleška et al., 2006, 2007). Two nearby compositions, $Ho_5Si_{1.5}Ge_{2.5}$ and $Ho_5Si_{2.5}Ge_{1.5}$, also order antiferromagnetically at 37 and 34 K, respectively (Prokleška et al., 2006). It is worth to note that in these alloys T_N is seen only as a weak shoulder on the $M(T)$ data and becomes largely smeared in high magnetic fields but is clearly visible in the heat capacity and electrical resistivity data.

A preliminary study of the magnetic properties of $Ho_5Si_xGe_{4-x}$ alloys ($x = 0$, 0.5, 1.5, 2.0, 2.5, 3.5, 4.0) indicates the presence of multiple magnetic transitions in both Ho_5Si_4 and Ho_5Ge_4 (Prokleška et al., 2007). Ho_5Ge_4 showed two broad transitions: $T_N = 23$ K and another transition at 16 K. Ho_5Si_4, in addition to the first magnetic ordering transition at ~70 K showed two low-temperature transformations seen in both $C_p(T)$ and $\rho(T)$ data at 23 and 16 K, Prokleška et al. (2007). However, as noted by Ritter et al. (2009) these low-temperature transitions may occur due to presence of impurities, namely HoSi. In fact, the neutron diffraction study did not reveal any spin-reorientation transitions in Ho_5Si_4 (Ritter et al., 2009). Yet another study (Singh et al., 2010a) confirmed that the single-phase Ho_5Si_4 sample prepared by using high-purity Ho metal (99.68 at.% with respect to all other elements in the periodic table) indeed shows a spin-reorientation transition around 15 K in addition to the main ordering transition at $T_C = 76$ K. The magnetocaloric effect in Ho_5Si_4 has been determined using heat capacity data measured in 0, 20, and 50 kOe applied magnetic fields. The magnetic entropy change was found to be −6.6 J/Kg K and −14.8 J/Kg K for the magnetic field changes $\Delta H = 20$ kOe and $\Delta H = 50$ kOe, respectively. The adiabatic temperature change for the same magnetic field changes was 2.6 and 6.1 K, respectively (Singh et al., 2010a).

A study of structural and magnetic behavior of $Ho_5Si_xGe_{4-x}$ performed by Pereira et al. (2008b) also shows discrepancies with the previous results. While the magnetic ordering transition temperatures generally agree with those reported by Prokleška et al. (2007), only one spin-reorientation transition (at ~15–18 K, depending on composition) is observed in all studied $Ho_5Si_xGe_{4-x}$ samples, though as noted above, some of these transitions, that is, in Ho_5Si_4, may not be intrinsic and occur due to impurity phases (Ritter et al., 2009). According to Pereira et al. (2008b) the Ho_5Si_4 compound (with O(I) crystal structure) behaves like a normal ferromagnet below $T_C = 77$ K with a clear saturation ($\mu_s = 8.9\ \mu_B$/Ho at 10 K), and the same is true for Ho_5Si_3Ge. Two alloys, Ho_5Si_3Ge and $Ho_5Si_{3.5}Ge_{0.5}$ crystallize in the monoclinic structure, while Ho_5Ge_4, Ho_5SiGe_3, and $Ho_5Si_2Ge_2$ have the O(II)-type crystal structure at room temperature. No thermal hysteresis is observed around T_C (or T_N) in agreement with the linear thermal expansion measurements suggesting second order for the magnetic transitions for all $Ho_5Si_xGe_{4-x}$ alloys except Ho_5Ge_4, which shows a small step at T_N. The structural and magnetic properties of $Ho_5Si_xGe_{4-x}$ alloys determined by Pereira et al. (2008b) are summarized in Table 18.

TABLE 18 **Crystallographic Parameters and Magnetic Data for the $Ho_5Si_xGe_{4-x}$ System (Pereira et al., 2008b)**

x(Si)	Crystal structure	a (Å)	b (Å)	c (Å)	γ (°)	T_C, T_N[a] (K)	μ_s[b] (μ_B/Ho)	p_{eff} (μ_B/Ho)	θ_p (K)
0	O(II)	7.565	14.549	7.636	–	25[a]	6.5	8.9	21
1	O(II)	7.531	14.537	7.610	–	30[a]	6.5	10.2	15
2	O(II)	7.517	14.535	7.601	–	31[a]	6.6	11.3	15
3	M	7.428	14.498	7.624	93.003	49	7.8	10.1	32.7
3.5	M	7.425	14.486	7.605	93.084	57	8.4	9.9	33.9
4	O(I)	7.340	14.470	7.639	–	77	8.9	10.0	40

[a] *Antiferromagnetic compounds.*
[b] *T = 10 K and H = 50 kOe.*

Temperature- and magnetic-field-dependent X-ray powder diffraction studies show that Ho_5Ge_4 undergoes a magnetostructural transition at $T_N = 23$ K (Singh et al., 2009). The transition, however, is unique and has not been observed in any other R_5T_4 compound. No shear displacements of the slabs occur during the transformation, and the volume change is quite small: $\Delta V/V = 0.1\%$. Essentially, the monoclinic distortion occurs in the *ac*-plane simultaneously with the onset of the antiferromagnetic ordering resulting in a new crystal structure type (see Table 7 in the “Crystallography” Section 2) with the space group $P12_1/m1$. Interestingly, Singh et al. (2009) found that this distortion can be predicted from first-principles calculations, which means that this unique monoclinic crystal structure is indeed thermodynamically stable in Ho_5Ge_4.

Heat capacity data confirm the presence of the first-order transition at T_N in zero magnetic field; however, the first-order heat capacity peak broadens substantially in applied magnetic fields and practically flattens out at 50 kOe. The reason for this phenomenon may lay in the fact that according to powder diffraction data, application of a magnetic field actually induces a reverse monoclinic–orthorhombic transformation in Ho_5Ge_4 (Singh et al., 2009), which, however, requires high magnetic fields (above 30 kOe) for its completion. The same set of heat capacity data indicates a spin-reorientation transition at 16 K, which shifts to lower temperatures in applied magnetic field.

A neutron diffraction study of $Ho_5Si_xGe_{4-x}$ with $x = 0$, 2, 3, and 4 confirmed that Ho_5Ge_4 undergoes a structural transformation below 25 K, while other alloys preserve their room temperature crystal structures down to 2 K (Ritter et al., 2009). However, the neutron diffraction data suggest that the long-range magnetic order sets in Ho_5Ge_4 at ~30 K, above the temperature of the structural transformation, so the monoclinic distortion occurs when the material is already in the AFM state. In addition to the main magnetic structure with $\mathbf{k} = (0\ 0\ 0)$, a second magnetic phase appears at 17 K with a propagation vector $\mathbf{k} = (0\ 0\ ½)$. Application of a magnetic field induces ferromagnetic order in Ho_5Ge_4, which may be concomitant with the reappearance of the orthorhombic structure. The magnetic moments in the magnetic structure of $Ho_5Ge_4$are essentially restricted to the *ac*-plane.

Ho_5Si_4 has a noncollinear FM magnetic structure below T_C, with the magnetic moments mainly oriented along the *a*-axis but shows weak AFM coupling along the *b*- and *c*-directions (Ritter et al., 2009). Ho_5Si_3Ge (monoclinic $Gd_5Si_2Ge_2$-type structure, $T_C = 50$ K) orders ferromagnetically with $\mathbf{k} = (0\ 0\ 0)$. It shows an FM moment orientation along the *a*-axis and an AFM canting along the *c*-axis. Similar to Ho_5Ge_4, a second magnetic phase appears at 16 K. Initially, this second phase is incommensurate, but it becomes commensurate below 8 K with a propagation vector $\mathbf{k} = (0\ 0\ ¼)$. $Ho_5Si_2Ge_2$ has the most complex magnetic structure among the $Ho_5Si_xGe_{4-x}$ compounds: in addition to the main AFM magnetic structure appearing at $T_N \sim 30$ K ($\mathbf{k} = (0\ 0\ 0)$), two additional magnetic phases with propagation vectors $\mathbf{k} = (0\ 0\ ¼)$ and $\mathbf{k} = (½\ 0\ 0)$ occur at 15 and 12 K, respectively.

Structural, magnetic, and thermodynamic properties of the monoclinic $Ho_5Si_{3.2}Ge_{0.8}$ phase ($Gd_5Si_2Ge_2$ type) have been examined in detail by Singh et al. (2010b). The temperature-dependent X-ray powder diffraction experiment confirmed that the crystal structure of $Ho_5Si_{3.2}Ge_{0.8}$ remains monoclinic below $T_C = 50$ K, in the ferromagnetic state. Two additional anomalies in $M(T)$ curves, probably associated with changes in magnetic structure (see Ritter et al., 2009), occur at 23 and 7 K. Even though the magnetostructural transition and possible related kinetic arrest phenomena are absent in $Ho_5Si_{3.2}Ge_{0.8}$, a significant magnetic frustration that may be described in terms of spin-glass behavior was observed in this compound. Metastability of the low-temperature magnetization data, frequency dependence of the ac magnetic susceptibility, and strong magnetic relaxation behavior were found to coexist with the long-range ferromagnetic order in the extended temperature range below T_C. Above T_C, a Griffiths-like phase behavior was also observed in $Ho_5Si_{3.2}Ge_{0.8}$. The magnetocaloric effect is moderate ($\Delta T_{ad} = 1.3$ K for the $\Delta H = 20$ kOe) and exhibits a plateau-like behavior between ~20 and 50 K (Singh et al., 2010b).

4.10. $Er_5Si_xGe_{4-x}$

The Er_5Si_4 and Er_5Ge_4 intermetallic compounds were discovered by Smith et al. (1967b) together with other R_5T_4 compounds. The silicide, Er_5Si_4, crystallizes in the O(I) Gd_5Si_4 type of crystal structure while the germanide, Er_5Ge_4, adopts the Sm_5Ge_4-type orthorhombic crystal structure. Holtzberg et al. (1967) determined that Er_5Si_4 orders ferromagnetically at 25 K, and Er_5Ge_4 orders antiferromagnetically at 7 K. According to the Er–Si phase diagram (Luzan et al., 1996), Er_5Si_4 forms peritectically from liquid and Er_5Si_3 at 1875 °C.

4.10.1. Er_5Si_4 ($x=4$)

Er_5Si_4 is one of most studied layered R_5T_4 compounds (after $Gd_5Si_2Ge_2$ and Gd_5Ge_4) due to a number of specific physical phenomena which are only characteristic of this compound. In particular, the structural-only transition at $T_{str} \sim 220$ K of the room temperature O(I) Gd_5Si_4-type structure into the low-temperature monoclinic M $Gd_5Si_2Ge_2$-type structure is not accompanied by a change of magnetic state (Er_5Si_4 remains paramagnetic both below and above the transition). This transformation, however, is extraordinarily sensitive to external influence, such as hydrostatic pressure, magnetic field, or even mechanical grinding, the last two being quite unexpected.

The presence of the "high-temperature"[6] O(I) to M structural transition in Er_5Si_4 during cooling was first reported by Pecharsky et al. (2003e); the structural and thermodynamic details of this transition including an established twin law for the monoclinic deformation were carefully investigated by Mozharivskyj et al. (2004), and the structural transition in the polycrystalline Er_5Si_4 was studied by Mudryk et al. (2012). Despite the nonmagnetic character of this transition, it can be seen as a step in the temperature dependence of magnetization, especially when the inverse dc susceptibility (H/M) is plotted. Moreover, since this is a first-order transition there is also a sizeable thermal hysteresis associated with this transition clearly visible in the magnetic data (Pecharsky et al., 2003e). The temperature dependence of heat capacity of this structural-only transition is manifested as a broad Δ-type peak with a width of $\sim$30 K. The magnetic ordering in Er_5Si_4 occurs at $T_C = 30$ K, is a typical second-order transition, and is not coupled with a structural transformation. Therefore, in zero magnetic field the monoclinic crystal structure supports both paramagnetic and ferromagnetic states. Thus, in addition to the fact that the polymorphic temperature sequence is opposite in Er_5Si_4 compared to the Gd_5T_4 or Tb_5T_4 systems (i.e., the low-temperature structure is monoclinic in Er_5Si_4 and the high-temperature structure is orthorhombic), the magnetic and structural transitions appear to be substantially decoupled with almost 200 K interval between them. Due to this reverse sequence, the net magnetostriction on cooling is positive ($\Delta V/V = 0.68\%$) though the values of the anisotropic lattice strains are comparable to those observed during the magnetostructural transitions for other R_5T_4 phases: the largest change along the a-axis ($\Delta a/a = 0.99\%$) is accompanied by a smaller change of the opposite

---

[6] The term "high-temperature" is used here as a reference point to the magnetic-only transition that occurs at much lower temperatures.

sign along the *c*-axis ($\Delta c/c = -0.4\%$) and a minor change of lattice dimensions along the *b*-axis ($\Delta b/b = 0.23\%$), as determined by Mudryk et al. (2012).

It is worth to note that no structural transition has been observed in Er_5Si_4 during the temperature-dependent neutron diffraction investigation of its magnetic and crystal structure (Cadogan et al., 2004). Possible explanation for this discrepancy is that the purity of the starting Er metal used for the preparation of Er_5Si_4 could be lower in this study since the stability of the orthorhombic phase increases when interstitial impurities are present, similar to the stabilization of the O(I) phase by interstitials in $Gd_5Si_2Ge_2$. The magnetic structure of O(I) Er_5Si_4 in the magnetically ordered state is characterized by the ferromagnetic alignment of Er moments along the *b*-axis and a strong AFM component in the *ac*-plane (Cadogan et al., 2004).

The most interesting fact about the high-temperature transition is that despite of being a structural-only transition occurring in the paramagnetic state, the temperature shows a weak but clear dependence on the applied magnetic field! At first, Pecharsky et al. (2004b) reported that the heat capacity peak associated with this transition slightly shifts to lower temperatures ($dT/dH = -0.058$ K/kOe) in applied magnetic fields exceeding 40 kOe. Afterward the shift in the transition temperature was observed in the magnetic measurements, both in polycrystalline (Mudryk et al., 2011) and single-crystalline (Mudryk et al., 2012) samples, see Figs. 41 and 42.

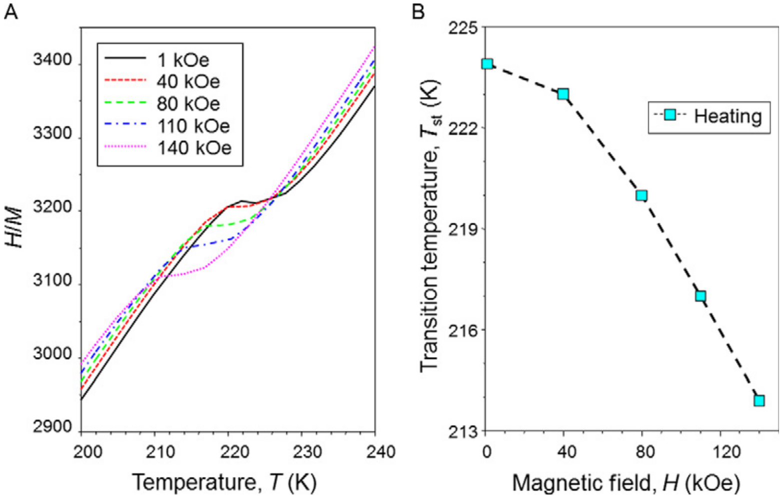

FIGURE 41 Magnetic field dependence of the structural-only M to O(I) transition in polycrystalline Er_5Si_4 occurring in the paramagnetic region. (A) Inverse dc susceptibility measured in magnetic fields 1, 40, 80, 110, and 140 kOe; (B) transition temperature as a function of applied magnetic field. *After Mudryk et al. (2011).*

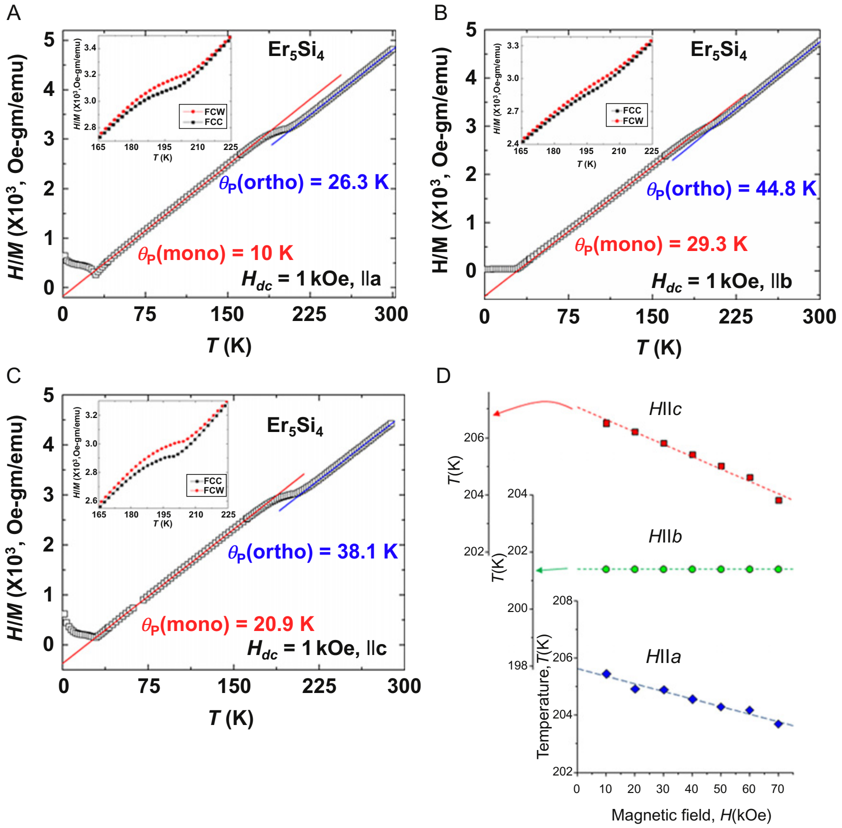

FIGURE 42 (A–C) Inverse dc magnetic susceptibility of single-crystalline Er_5Si_4 measured with magnetic field applied along the three major crystallographic directions. The insets show the dc susceptibility data in the immediate vicinity of the high-temperature transition. (D) magnetic field dependencies of the structural transition temperature determined along the three major crystallographic directions.

It is easy to see that the critical temperatures obtained from the Curie–Weiss fits are different for two different polymorphs. In addition, Fig. 42D clearly indicates that the magnetic field dependence is anisotropic: the transition temperature changes with field only when the magnetic field is applied within the *ac*-plane but is not affected when the field is perpendicular to it. This behavior may be understood in terms of strong magnetocrystalline anisotropy and large value of Er effective magnetic moment: 9.71 and 9.63 μ_B/Er, for O(I) and M polymorphs, respectively (Pecharsky et al., 2004b). Even though the magnetic moments in paramagnetic state are noninteracting they still tend to align with the applied magnetic field. This field-induced rotation of the moments along the *a*- and *c*-axes may induce greater strain compared to the *b*-axis. The strain generates pressure that leads to the structural transformation.

Of course, in order to support this scenario the compound should have an extraordinary strong dependence of its transition temperature to the applied pressure. Several studies confirm that this is, indeed, the case in Er_5Si_4. The high-temperature PM-O(I) - PM-M transition shifts to lower temperatures with applied hydrostatic pressure at the incredibly high rate of $dT_{s1}/dP = \sim -30$ K/kbar (Magen et al., 2006b; Marcano et al., 2012). Moreover, the application of hydrostatic pressure forces the re-entrance of the orthorhombic structure in the low-temperature ferromagnetic state. This is understandable since the orthorhombic phase is the low-volume phase. The temperature at which this FM-M to FM-O(I) transformation occurs increases at a rate of $dT_{s2}/dP = 6$ K/kbar. Above ~6 kbar both transitions merge, yielding a stable O(I) phase throughout the whole range of measured temperatures (2–300 K). For example, no structural transition is detected in the LTE measurements performed at applied pressure of $P = 9$ kbar (Magen et al., 2006b). The Curie temperature of the emergent O(I) Er_5Si_4 phase is slightly higher (~35 K) compared to the T_C of M Er_5Si_4 (~32 K).

The higher Curie temperature of the O(I) phase compared to T_C of the M phase points to the enhancement of the ferromagnetic interactions due to the formation of additional interslab Si—Si bonds. Arnold et al. (2009b) showed that such enhancement leads to an increase in the magnetocaloric effect measured around T_C with the application of applied pressure. In particular, setting the pressure to 1.4 kbar increases the magnetic entropy change from −14.9 to −20.1 J/Kg K for $\Delta H = 50$ kOe. Further increase in hydrostatic pressure does little to increase the maximum $|\Delta S_M|$ value but shifts the peak position of the $|\Delta S_M|(T)$ curve toward 36 K, the T_C of the O(I) phase. The mechanism of such increase is different from the one observed in $Tb_5Si_2Ge_2$ by Morellon et al. (2004b). The formation of interslab Si—Si bonds leading to higher exchange interactions is the reason for the increase in MCE of Er_5Si_4, not the coupling of the crystal and magnetic lattices as observed in $Tb_5Si_2Ge_2$.

Study of the magnetic properties of single-crystalline Er_5Si_4 under applied hydrostatic pressure showed that the magnetic behavior is largely anisotropic (Marcano et al., 2012). However, the overall response to the applied pressure–the enhancement of the ferromagnetic interactions due to the formation of the interslab Si—Si bonds, manifested as the increase in T_C, is seen along all three crystallographic directions. At the same time, the spin-reorientation transitions observed in $M(H)$ data when magnetic field was applied along *a*- or *c*-directions are largely preserved, even if modified, under different pressures reflecting similarity of the magnetic structures of both the O(I) and M polymorphs (see below). Interestingly, the major increase of MCE due to the application of hydrostatic pressure occurs when the magnetic field is applied along the *c*-axis and, to a lesser degree, along the *a*-axis, while there is almost no enhancement along the easy magnetization axis *b* (Marcano et al., 2012).

The application of a strong magnetic field is also affecting the ground state of Er_5Si_4. The analysis of $C_p(T)$ data measured in magnetic fields ranging from 0 to 100 kOe showed that a magnetostructural transformation may occur in this compound near 18 K in magnetic fields of 75 kOe and above (Pecharsky et al., 2004b). Magnetization and magnetostriction measurements performed in ultra-high pulsed magnetic fields (up to 450 kOe) confirmed that the field-induced transformation in Er_5Si_4 indeed proceeds through a magnetostructural transition, though the lowest critical field observed was $H_{cr}=50$ kOe for the $T=5$ K measurements (Magen et al., 2006c). The critical field value rapidly increases with the temperature increase reaching ~250 kOe for $T=80$ K. Since the phase volume is decreasing during the transition it was safe to assume that the reversible M to O(I) transition is occurring as it happens with the application of the hydrostatic pressure. The analysis of neutron diffraction patterns measured at $T=2$ K in $H=0$ and 50 kOe applied magnetic fields confirmed that while in zero field the sample has the single-phase monoclinic structure, the majority (~61 vol.%) phase at 50 kOe is O(I) (Magen et al., 2006c). The interesting fact about this transformation is that the magnetic-field-induced structural transition occurs without a change in the magnetic state as both phases are ferromagnetic and have similar magnetic structures (Magen et al., 2006c; Ritter et al., 2006).

The magnetic structures of both the monoclinic and orthorhombic Er_5Si_4 polymorphs are characterized by the easy magnetization axis *b*, along which the moments are oriented with a canted ferromagnetic alignment. Apparently, magnetic moment canting is stronger in the monoclinic structure while in the O(I) structure the moments are fully aligned along the *b*-axis in the Er 4*c* positions with a slight canting of the moments located on the Er atoms in the 8*d* sites (Magen et al., 2006c). A weak AFM component is observed in the *ac*-plane. There is a minor spin-reorientation process that occurs in monoclinic Er_5Si_4 at 15 K, which leads to a small increase in the values of canting angles (Ritter et al., 2006).

It is hard to say whether the magnetic-field-induced FM-M to FM-O(I) transformation can be completed by sufficiently high magnetic field. However, since the high-temperature transition is also affected (its temperature is lowered) by the applied magnetic field, it is safe to assume that the stable structure above ~250 kOe is O(I) over the whole temperature range between 2 and 300 K, so in this case the influence of the 250 kOe magnetic field on the crystal structure of Er_5Si_4 is comparable to the effect of 6 kbar hydrostatic pressure.

Another unusual property of Er_5Si_4 is also related to high sensitivity of its crystal structure to external factors. Hence, Cao et al. (2013) observed that simple mechanical hand grinding using mortar and pestle at ambient conditions results in a partial structural transformation from the orthorhombic into the monoclinic phase. The same result is obtained when the grinding is performed in a glove box filled with high-purity argon gas. When the powder is annealed at 500 °C for 20 min (stress relieving annealing), the reversible M to O(I) transformation occurs indicating that the stress induced during the grinding is indeed the cause of the O(I) to M transformation. This observation is fascinating because it shows that the shear stress produced during the mechanical treatment has the effect opposite to the application of hydrostatic pressure, which actually promotes the formation of the low-volume orthorhombic phase.

4.10.2. $Er_5Si_xGe_{4-x}$: *Alloys with* $x<4$

Addition of Ge removes the structural instability observed in the Er_5Si_4 alloy. As shown by Pecharsky et al. (2004b), the main part of the $Er_5Si_xGe_{4-x}$ diagram ($0 \leq x < 3.5$) consists of the Er_5Ge_4-based solid solution with the O(II) Sm_5Ge_4-type crystal structure. The monoclinic $Gd_5Si_2Ge_2$-type alloys form in a narrow region of the phase diagram: $3.5 \leq x \leq 3.8$. Er_5Si_4 is the only compound with the O(I) Gd_5Si_4-type structure at room temperature in this system; no ternary $Er_5Si_xGe_{4-x}$ compound crystallizing in this structure type has been observed. According to heat capacity measurements both $Er_5Si_{3.5}Ge_{0.5}$ (M structure) and Er_5Ge_4 (O(II) structure) order magnetically via second-order transitions (Pecharsky et al., 2004b). Ritter et al. (2006) confirm that no structural transformations are observed in $Er_5Si_{3.5}Ge_{0.5}$ or Er_5Ge_4 using temperature-dependent neutron diffraction data. The magnetic transitions of $Er_5Si_xGe_{4-x}$ alloys with the O(II) structure appear to be antiferromagnetic in low magnetic fields but clear ferrimagnetic signatures have been observed in $H \geq 20$ kOe. The magnetic structure of $Er_5Si_{3.5}Ge_{0.5}$ is similar to that of the monoclinic Er_5Si_4. The magnetic structure of Er_5Ge_4 has not been fully determined, but according to Ritter et al. (2006) the compound adopts a complex incommensurate antiferromagnetic structure at $T_N = 14$ K. Basic magnetic properties of the $Er_5Si_xGe_{4-x}$ alloys are listed in Table 19.

TABLE 19 Basic Magnetic Properties of the $Er_5Si_xGe_{4-x}$ Alloys (Pecharsky et al., 2004b)

x(Si)	Crystal structure	T_C, T_N[a] (K)	p_{eff} (μ_B/Ho)	θ_p (K)
0	O(II)	14[a]	9.56	14.8
1.95	O(II)	17[a]	9.56	13.9
3	O(II)	17[a]	9.57	5.3
3.5	M	28	9.55	15.9
4	M[b]	30	9.63	19.6
4	O(I)[b]		9.71	30.3

[a] *Antiferromagnetic ordering.*
[b] *Structural transition in* Er_5Si_4 *occurs at* ~200 K.

Electrical and thermal transport properties of $Er_5Si_xGe_{4-x}$ alloys with $x=2$, 3.6, 3.8, and 4 were measured by Lue et al. (2008). All samples are orthorhombic at room temperature, and no sign of high-temperature structural transition around 200 K was detected in the measurements, indicating that the formation of the monoclinic crystal structure was suppressed in these alloys, probably due to interstitial impurities. Anomalies corresponding to magnetic ordering at T_C were observed in temperature dependences of electrical resistivity, Seebeck coefficient and thermal conductivity for all alloys except $Er_5Si_2Ge_2$; however, a broad peak in thermal conductivity at 25 K occurs in this compound. In general, when the Si content increases, the thermal conductivity also increases while the electrical resistivity decreases (Lue et al., 2008).

4.11. $Tm_5Si_xGe_{4-x}$

The formation of Tm_5Ge_4 with Sm_5Ge_4-type crystal structure was originally reported by Smith et al. (1967b). The investigation of the Tm–Ge binary system (Eremenko et al., 1989) confirmed this crystal structure for the Tm_5Ge_4 compound, which was found to form peritectically from liquid and Tm_5Ge_3 at 1776 °C. Somewhat surprisingly, no reports on the existence of the silicide Tm_5Si_4 can be found in literature. Overall, information about $Tm_5Si_xGe_{4-x}$ alloys is quite limited. Just about the only composition studied is $Tm_5Si_2Ge_2$, which also crystallizes in the Sm_5Ge_4-type crystal structure (Kim et al., 2010). A single crystal was grown by Bridgeman method and studied by X-ray diffraction, EDS, XPS, magnetic, electrical resistivity, and heat capacity measurements. Thulium was found to be nearly trivalent in this compound but 4*f* states were split by the crystalline electric field. $Tm_5Si_2Ge_2$ orders magnetically at 8 K with antiferromagnetic alignment of magnetic moments along the *b*-axis; however, there is a possibility of ferromagnetic coupling in the *ac*-plane. A metamagnetic-like transition was observed when a magnetic field was applied along the *b*-axis in ~5 kOe field at 2 K. The magnetization data presented in the same manuscript also show that the *b*-axis is an easy magnetization axis while the magnetization in the *ac*-plane is much lower and does not show any saturation in 50 kOe applied magnetic field. The low-temperature electrical resistivity shows $-\log T$ dependence indicating a Kondo effect. Thus, a competition between Kondo effect and magnetic order occurs in $Tm_5Si_2Ge_2$ (Kim et al., 2010).

4.12. $Yb_5Si_xGe_{4-x}$

Both Yb_5Si_4 and Yb_5Ge_4 binary compounds were first reported in 2003. The investigations of the Yb–Si binary system (Palenzona et al., 2003) and Yb–Ge binary system (Pani and Palenzona, 2003) reveal the existence of the phases with R_5T_4 stoichiometry; both compounds were reported to crystallize in the O(II) Sm_5Ge_4 type of crystal structure. In the same year, Černý and Alami-Yadri

(2003) determined the crystal structure of Yb_5Si_4. They also assigned Sm_5Ge_4 as a structure prototype but noted that the coordination of some of the Si atoms is different from the typical Sm_5Ge_4 coordination and similar to the Gd_5Si_4 type of crystal structure. According to Palenzona et al. (2003) Yb_5Si_4 forms by peritectic reaction from YbSi and liquid at approximately 1680 °C. On the other hand, Yb_5Ge_4 melts congruently at 1640 °C and it has the highest melting temperature among all other Yb–Ge binary compounds (Pani and Palenzona, 2003).

Systematic study of the crystallography, magnetic properties, and heat capacity of the $Yb_5Si_xGe_{4-x}$ pseudobinary system has been carried out by Ahn et al. (2005). Somewhat surprisingly, all studied $Yb_5Si_xGe_{4-x}$ alloys ($x=0$, 1, 2, 3, and 4) crystallize in the same Gd_5Si_4-type crystal structure. The lattice parameters in the system linearly decrease with the increase in Si content. However, comparison of the lattice parameters and unit cell volumes of the binary compounds with those of other R_5Si_4 and R_5Ge_4 compounds shows positive deviation from the normal lanthanide contraction[7] indicating that some or all of the Yb atoms in Yb_5T_4 compounds may be in the Yb^{2+} valence state. Since inverse magnetic susceptibility of all $Yb_5Si_xGe_{4-x}$ follow the Curie–Weiss law in the paramagnetic region, the effective magnetic moments were calculated and were found to be between 2.73 and 2.84 μ_B/Yb. Since the theoretical p_{eff} for pure Yb^{2+} state is zero, and for the Yb^{3+} state it is equal to 4.54 μ_B, it is clear that $Yb_5Si_xGe_{4-x}$ alloys are mixed-valence systems. Analysis of the magnetic and crystallographic data (see Ahn et al., 2005 for the details) suggested that 12 out of 20 Yb atoms are in the divalent state and, most likely, this is achieved byYb^{2+} occupying the 4*c* and one of the 8*d* atomic sites of the O(I)-type crystal structure, while the trivalent ytterbium atoms occupy another 8*d* site. Mössbauer spectroscopy gives a different ratio for Yb^{2+}/Yb^{3+}: 51.6(0.3)/48.4(0.3), which is both compositionally (valid for all $Yb_5Si_xGe_{4-x}$ compositions) and temperature independent (Voyer et al., 2006). This indicates that Yb atoms with a certain valence state cannot be completely assigned to a particular atomic site, and therefore, at least some of the Yb ions must exist in the intermediate valence state.

According to magnetization data, $Yb_5Si_xGe_{4-x}$ alloys order antiferromagnetically and the Néel temperature slightly increases from 2.4 for Yb_5Si_4 to 3.2 K for Yb_5Ge_4 (Ahn et al., 2005). The temperature dependence of the hyperfine field gives slightly lower T_N ranging between ~1.5 and 1.7 K (Voyer et al., 2006). However, the ternary compositions exhibit two distinct orderings of the Yb^{3+} sublattice, though the temperature difference between these two orderings is small (~0.1 K). There is also an unusual increase in T_N between $x=3$ and 3.5, though there is no change in the crystal structure. Except Yb_5Si_3Ge, which shows slightly positive $\theta_p=2$ K, all other compositions have negative values of their paramagnetic temperatures

---

[7] An exception: A small negative deviation was observed for the *a* lattice parameter in Yb_5Ge_4 (Ahn et al., 2005).

(Ahn et al., 2005). The $M(H)$ curves measured at 1.8 and 10 K in magnetic fields up to 70 kOe indicate gradual saturation below 1 μ_B/Yb and a metamagnetic-like spin-flop transformation at ~13 kOe. The heat capacity data collected in 0, 10, and 20 kOe applied magnetic fields show an upturn below 9 K, while the C_p values measured at 50 and 70 kOe are enhanced compared to zero-field and low-field data (Ahn et al., 2005).

Electron microscopy study of Yb_5Ge_4 shows the presence of 5:3 platelets, which typically form in other R_5T_4 systems as well (Qian et al., 2009). However, in most R_5T_4 compounds studied to date, the platelets, or linear features, exhibit a characteristic criss-cross pattern, while in Yb_5Ge_4 they are parallel to each other.

4.13. $Lu_5Si_xGe_{4-x}$

According to Smith et al. (1967b) Lu_5Ge_4 crystallizes in the Sm_5Ge_4-type crystal structure, while Lu_5Si_4 has a monoclinic crystal structure with space group $P2_1/a$, which indicates the possibility of adopting the $Gd_5Si_2Ge_2$ type of crystal structure discovered later. However, Gschneidner et al. (2000b) prepared Lu_5Ge_4, Lu_5SiGe_3, $Lu_5Si_2Ge_2$, and Lu_5Si_4 alloys from high-purity Lu metal and found that all synthesized alloys crystallize in the orthorhombic Sm_5Ge_4-type structure. Temperature dependences of heat capacity were measured for all prepared samples and both the electronic specific heat coefficient γ and the Debye temperature θ_D were determined using the fitting of the low-temperature C/T versus T^2 plots. The Debye temperature increases with the Si concentration (215 ± 4 for Lu_5Ge_4, 262 ± 30 K for Lu_5Si_4), while γ remains constant, 1.2 ± 0.3 mJ/mol K^2 (Gschneidner et al., 2000b).

An orthorhombic crystal structure with the lattice parameters $a = 7.386$ Å, $b = 14.262$ Å, and $c = 7.456$ Å has been reported by Thuy et al. (2003) for $Lu_5Si_2Ge_2$. No transitions were observed in the measured heat capacity data.

5. R_5T_4 SYSTEMS: SUBSTITUTIONS OF THE RARE EARTHS

Chemical similarity of the lanthanide elements leads to common occurrence of series of isostructural intermetallic compounds encompassing several or, in some cases, all rare earth elements with a great variety of stoichiometries and crystal structures. As shown above, the $R_5Si_xGe_{4-x}$ compounds are formed by the majority of the rare earth elements, Sc and Eu being two exceptions. However, $R_5Si_xGe_{4-x}$ are not cookie-cutter systems, and it is clear that each R brings something unique, both structurally and magnetically, to the whole picture. Therefore, while the vast majority of R_5T_4 studies are focused on the chemical variations of the T atoms, one may expect some interesting science to emerge from the combinations of two different lanthanides within the same layered crystal structure. As was shown for the $Yb_5Si_xGe_{4-x}$ system (Ahn et al., 2005), R atoms of different size may have specific preferences for particular atomic sites, which indicates the possibility of having multiple sublattices of different rare earth atoms existing within the same crystal structure.[8] At the same time, these structures should remain sensitive to external stimuli. Consequently, their physical behavior is expected to be more complex compared to the alloys with single R, and proper interpretation of the measurement results may become complicated. This could be one of the reasons why the number of investigations of such $(R'_xR_{1-x})_5T_4$ systems is relatively small.

In addition, several investigations on the substitution of R atom by non-R atoms (e.g., Ca, Mg, Zr) have been carried out. Most of the studies are focused on T = Si, Ge. It should be noted that a significant number of ternary R_5T_4 compounds has been prepared during exploratory studies of either various ternary systems or isostructural series of compounds. Compounds for which only crystallographic data are available are not discussed here since the scope of this review covers composition–structure–property relationships in pseudobinary R_5T_4 systems.

5.1. $(R'_xR_{1-x})_5T_4$ Systems with T = Si, Ge

5.1.1. $(Gd_{1-x}R_x)_5Si_4$ Systems

The substitution of Gd by other rare-earth elements in the Gd_5Si_4 compound is relatively well studied due to its high Curie temperature, 336 K. Having the magnetic ordering temperature in the near room temperature range, such $(Gd_{1-x}R_x)_5Si_4$ systems with a small amount of R added were deemed promising for some practical applications, mostly as potential magnetocaloric materials.

In 1991, Elbicki and coworkers studied the effect of Y and La substitution on the magnetism and crystal structure of Gd_5Si_4 (Elbicki et al., 1991). They found that Y substitution induces a gradual change of T_C in $Gd_{5-x}Y_xSi_4$ alloys [$\sim$60 K/x(Y)], and all alloys in the studied compositional range $0 \leq x(Y) \leq 2.0$ retain the orthorhombic O(I) crystal structure. This observation was confirmed later by Misra and Miller (2008). On the contrary, in the $Gd_{5-x}La_xSi_4$ series an abrupt change of T_C ($\sim$90 K) was observed between x(La) = 0.5 and x(La) = 1.0. The X-ray analysis showed that the crystal structure of the $Gd_{5-x}La_xSi_4$ alloys also changes from the orthorhombic at x(La) = 0.5 to the tetragonal at x(La) = 1.0. Therefore, the observed anomaly in compositional dependence of T_C could be clearly associated with this particular crystallographic change. Such intimate relationship between magnetism and crystallography is in the foundation for the majority of interesting phenomena observed in R_5T_4 compounds and is the key to understanding their fascinating physical properties. The authors (Elbicki et al., 1991) also noted that the

---

[8] Strictly speaking, these alloys are not necessarily superstructures as some statistical distribution of atoms of different kind is still expected in each particular atomic site similar to the Si/Ge distribution between the inter- and intraslab T positions.

temperature dependence of magnetization in Gd_5Si_4 and substituted alloys does not follow the Brillouin function for $J=S=7/2$ calculated from simple molecular-field theory. Misra and Miller (2008) observed that the $Gd_{5-x}Y_xSi_4$ solid solution with the Gd_5Si_4-type crystal structure extends at least up to $x=4$. Y_5Si_4 crystallizes in the monoclinic $Gd_5Si_2Ge_2$ type (Pecharsky et al., 2004a) therefore there should be a two-phase region in the $Gd_{5-x}Y_xSi_4$ system between $x=4$ and 5.

Spichkin et al. (2001) studied the crystallographic and magnetic properties of the $Gd_{5-x}Tb_xSi_4$ ($x=0$, 0.5, 1, 1.5, 2, 2.5, 5) and $Gd_{5-x}Pr_xSi_4$ ($x=0.5$, 0.75, 1.0) solid solutions. Substitution of Gd by Tb or Pr does not change the crystal structure in the studied range of concentrations—it remains the O(I) Gd_5Si_4 type. As expected, the lattice parameters increase with the increase in Pr concentration and decrease when Gd is replaced by Tb in the linear fashion obeying Vegard's law.

No noticeable differences in magnetic behavior were detected between as-cast and heat-treated alloys. The prepared alloys order ferromagnetically via second-order transitions, as confirmed by heat capacity measurements. The magnetic ordering temperature decreases much faster when Gd is replaced by Pr (T_C of $(Gd_4Pr_1)Si_4$ is 291.5 K) compared to the change in T_C due to Tb substitution (T_C of $(Gd_4Tb_1)Si_4$ is 318 K), which is expected based on the de Gennes factor. The calculated paramagnetic Curie temperature of the alloys also shows linear dependence on the de Gennes factor for both Tb- and Pr-based solid solutions (Fig. 43). The maximum magnetocaloric effect remains nearly constant through the $Gd_{5-x}Tb_xSi_4$ system varying between −8 and −9.5 J/Kg K (for $\Delta H=50$ kOe). On the other hand, the reduction of MCE due to Pr substitution is substantial: maximum ΔS_M for $(Gd_4Pr_1)Si_4$ alloy is only −6.1 J/Kg K for the same 50 kOe magnetic field

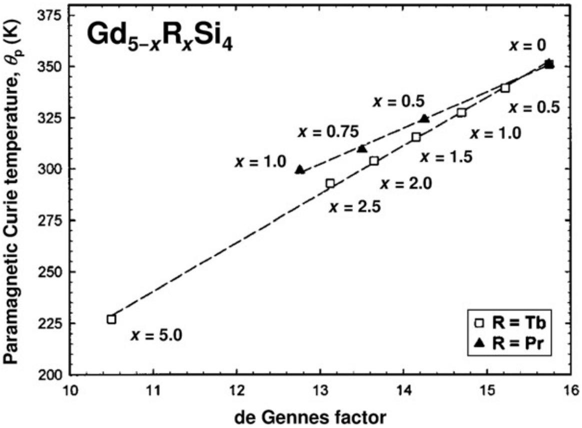

FIGURE 43 The paramagnetic Curie temperature of $Gd_{5-x}R_xSi_4$ alloys, R = Pr, Tb, as a function of de Gennes factor (Spichkin et al., 2001).

change. This may be due a strong reduction of the saturation magnetization in the Pr-substituted alloys. The analysis of ac magnetic susceptibility and dc magnetization data suggests the existence of complex magnetic structures in magnetic fields below 5 kOe.

The magnetic and magnetocaloric properties of $Gd_{5-x}Dy_xSi_4$ alloys were studied by Xie et al. (2004). The room temperature XRD analysis showed the presence of a continuous solid solution with the orthorhombic crystal structure (the study claims Sm_5Ge_4-type structure, but most likely it was actually the Gd_5Si_4 type that was observed). A linear decrease in T_C from 338 for Gd_5Si_4 to 140 K for Dy_5Si_4 occurs with the increase of x(Dy). The magnetic transitions in all measured $Gd_{5-x}Dy_xSi_4$ alloys are of second order. The magnetic entropy change, ΔS_M, was determined for the magnetic field change of 9.5 kOe and its maximum value is approximately the same for all alloys (varying between -2.24 and -2.52 J/Kg K) though pure Dy_5Si_4 shows a slightly larger value: $\Delta S_M = -2.72$ J/Kg K. Direct measurements of MCE were carried out for the $Gd_{5-x}Dy_xSi_4$ alloys with $x = 0$, 0.5, 1, and 2 using an electromagnet with magnetic field of 19.2 kOe (Shimotomai and Ido, 2006). The maximum measured temperature rise was found to be 3.1 K for Gd_5Si_4, and similar values were obtained for $x = 0.5$ and 1 (the $x = 2$ sample with $T_C = 253$ K was out of the measurement range of the apparatus).

The $Gd_{5-x}Ho_xSi_4$ system is also characterized by a continuous solid solution in the entire range of concentrations (Zhou et al., 2008). The crystal structure belongs to the Gd_5Si_4 type. The lattice parameters and unit cell volume linearly decrease with increasing x(Ho), essentially following Vegard's law.

Investigation of the crystal structure, magnetic and thermodynamic properties of alloys in the erbium-rich part of the $Gd_{5-x}Er_xSi_4$ system ($x = 0.75$, 0.9) has been carried out by Singh et al. (2008). The room temperature crystal structure of these samples corresponds to the Gd_5Si_4 type, and the compositional dependence of the lattice parameters (when plotted together with the binary compounds) appears to follow Vegard's law. No first-order transition was detected in gadolinium substituted silicides according to both magnetization and heat capacity measurements. Competition of FM and AFM interactions is clearly observed in magnetization data and is manifested via the presence of two magnetic transitions: the AFM-like magnetic ordering transition is observed at $T_N = 61$ and 101 K for $x = 0.9$ and 0.75, respectively, and the FM-like transition occurs in the magnetically ordered state at $T_C = 27$ and 46 K, respectively. The values of saturation magnetization at 5 K and 70 kOe are 7.34 and 7.14 μ_B/R^{3+} for the $x = 0.9$ and 0.75, respectively; $\sim$1.4 μ_B lower than expected from Hund's rule. The magnetization measurements show strong relaxation with logarithmic time dependence. However, no significant frequency dependence of the *ac* susceptibility has been observed so the magnetic frustration of the complex magnetic state with competing anisotropic exchange interactions is responsible for the observed relaxation behavior rather than the traditional spin-glass behavior (Singh et al., 2008).

5.1.2. $(Gd_{1-x}R_x)_5Ge_4$ Systems

Yang et al. (2003a) reported the results of a crystallographic investigation of the Gd_5Ge_4–La_5Ge_4 system using X-ray powder diffraction. However, only one ternary alloy, $Gd_3La_2Ge_4$, has been prepared and analyzed during this study; two other alloys studied were Gd_5Ge_4 and La_5Ge_4. Investigation of the crystal structure revealed an unexpected result: while both binary compounds crystallize with the same Sm_5Ge_4-type structure, the intermediate ternary composition has the $Gd_5Si_2Ge_2$ monoclinic structure. Thus, no continuous solid solution exists between two isostructural R_5Ge_4 compounds in the $Gd_{5-x}La_xGe_4$ pseudobinary system. A more detailed investigation of this system may reveal further changes of crystallography, but this remains to be seen.

The pseudobinary $Gd_{5-x}Y_xGe_4$ system where Gd was substituted by another nonmagnetic rare earth element, yttrium, was investigated in great detail showing some unique crystallographic properties (Misra and Miller, 2008). Both Gd_5Ge_4 and Y_5Ge_4 crystallize in the Sm_5Ge_4 type of crystal structure but there is no continuous solid solubility between these two binary compounds. Instead, for the composition range of $3.6 \leq x \leq 4.2$, a monoclinic $U_2Mo_3Si_4$-type structure (space group $P2_1/c$, see Section 2 for atomic positions) occurs, which is rare in the R_5T_4 systems. This composition-driven transformation from Sm_5Ge_4 type to the $U_2Mo_3Si_4$ type of structure and back does not result in significant changes in the interslab bonding and magnetic interactions. The Gd and Y atoms statistically occupy all three rare earths atomic sites that exist in both crystal structures. However, there is a clear preference for Y to occupy the interslab 4*c* (2*a* in the $U_2Mo_3Si_4$ type of structure) and one of the 8*d* (4*e*) sites (Misra and Miller, 2008) opening opportunities for a targeted chemical substitution of specific atomic sites by a particular type of rare earth atom. Magnetic measurements of $Gd_{5-x}Y_xGe_4$ alloys show a decrease in the strength of exchange interaction (dilution effect) when Gd is substituted by Y. However, it is worth to note that the initial drop in θ_p value—+69 K for Gd_4YGe_4 versus ~+130 K for Gd_5Ge_4—is much larger than the decrease in the paramagnetic Curie temperature (31 K for GdY_4Ge_4) with further increase in x(Y). This is different from the linear decrease in T_C observed in $Gd_{5-x}Y_xSi_4$ system (Elbicki et al., 1991; Misra and Miller, 2008) and is related to the fact that the interslab 4*c* position plays a special role for magnetic interslab exchange in the Sm_5Ge_4-type structures (see Section 3.10). The samples with $x=1$ and 2 show antiferromagnetic-like transition at 92 and 57 K, respectively. The samples with larger Y content do not show a clear magnetic ordering transition, but ferrimagnetic type ordering (as suggested by Misra and Miller, 2008) occurs at 31, 24, 20, and 15 K for $x=3.0$, 3.4, 3.6, and 4.0, respectively.

No binary R_5T_4 compounds with R = Eu are known. However, it was shown that Eu can partially substitute Gd in the pseudobinary $Gd_{5-x}Eu_xGe_4$

system resulting in interesting crystal chemistry and unconventional magnetic properties (Yao et al., 2012a,b). Since Eu ions (Eu^{2+}, Eu^{3+} and any mixed valent Eu) are larger than Gd^{3+}, an expansion of the crystallographic lattice is expected. On the other hand, the reduction of the VEC number, which in R_5T_4 systems leads to the formation of the interslab T—T bonds and transformation into the Gd_5Si_4-type structure with lower unit cell volume, should occur if at least some of the europium atoms are divalent or mixed valent. An experimental study shows that both of these phenomena indeed occur in the $Gd_{5-x}Eu_xGe_4$ system for $x<2$ (at larger x, the Gd_5Si_4-structure solid solution decomposes, Yao et al., 2012b). According to single-crystal X-ray diffraction data the samples with $x=0$ and 0.25 crystallize in the O(II) Sm_5Ge_4-type structure (no interslab T—T bonds), the sample with $x=0.5$ adopts the room temperature M $Gd_5Si_2Ge_2$-type structure (half of the interslab T—T bonds formed), and the O(I) Gd_5Si_4-type (all interslab T–T dimers exist) solid solution is formed for $1\leq x<2$. Similarly to the $Gd_5Si_xGe_{4-x}$ system, this gradual formation of the interslab T–T dimers results in strengthening of the magnetic exchange interactions. Even the sample with $x=0.25$ shows a PM-O(II)–FM-O(I) magnetostructural transition at 97 K, indicating a greater stability of the low-temperature FM-O(I) phase compared to the binary Gd_5Ge_4. Further increase in Eu concentration leads to a sharp increase in T_C, even though the samples with $x\geq 1$ show a magnetic (second order) transition only. The $Gd_{4.5}Eu_{0.5}Ge_4$ sample with the monoclinic room temperature crystal structure undergoes a magnetostructural PM-M–FM-O(I) transition at 132 K. The $Gd_{3.5}Eu_{1.5}Ge_4$ sample was reported to have the highest $T_C=191$ K in the system, while the magnetic ordering temperature of the sample with $x=2$ drops to 96 K. Obviously, in the $Gd_{5-x}Eu_xGe_4$ system the transition from the O(II) to M and O(I) structure cannot be explained by the effect of chemical pressure as in the $Gd_5Si_xGe_{4-x}$ system because the unit cell volume is increasing with Eu substitution. Thus, this system provides a solid confirmation for the validity of the valence electron concentration effects in R_5T_4 systems.

5.1.3. $(Gd_{1-x}R_x)_5(Si,Ge)_4$ Systems

Magnetic and electrical transport properties of several quaternary $Gd_{5-x}Dy_xSi_2Ge_2$ samples were investigated. The $Gd_{5-x}Dy_xSi_2Ge_2$ alloys with $x\leq 3.5$ adopt a monoclinic $Gd_5Si_2Ge_2$-type crystal structure, while the alloys with $x\geq 4.5$ crystallize in the orthorhombic Sm_5Ge_4 type (Nirmala et al., 2007c,d). The magnetic ordering temperature drops quickly with x(Dy): $T_C=210$ K was observed for $Dy_{0.5}Gd_{4.5}Si_2Ge_2$, and for $Dy_{3.5}Gd_{1.5}Si_2Ge_2$ T_C is equal to ~80 K (Nirmala et al., 2007c,d). The Dy substitution also leads to a loss of a first-order character typical for pure $Gd_5Si_2Ge_2$. The maximum magnetic entropy changes for a field change of 55 kOe are −8.8, −13.9, and −6.9 J/Kg K for $x=0.5$, 3.0, and 5.0, respectively. Another transition at 21 K is clearly seen in the temperature dependences of electrical resistivity and heat capacity of

$Dy_{0.5}Gd_{4.5}Si_2Ge_2$ (Nirmala et al., 2006). In other measured $Gd_{5-x}Dy_xSi_2Ge_2$ samples, the temperature dependences of electrical resistivity show a single anomaly at T_C, below which it falls steeply (Nirmala et al., 2007d). The temperature dependence of the thermoelectric power of $Dy_{0.5}Gd_{4.5}Si_2Ge_2$, on the other hand, shows an anomaly at 46 K. A negative magnetoresistance of $\sim -25\%$ is observed in $Dy_{0.5}Gd_{4.5}Si_2Ge_2$ at 50 K in an applied magnetic field of 100 kOe. The field dependence of magnetoresistance at this temperature (well below T_C) was practically linear (Nirmala et al., 2006).

Aghababyan and Harutyunyan (2012) also studied the magnetocaloric properties of $Gd_{5-x}Dy_xSi_2Ge_2$ alloys for $x=0$, 0.5, 1.0, 1.5, 2.0. While the study confirmed that in this range of concentrations the crystal structure is $Gd_5Si_2Ge_2$-type monoclinic, the change of T_C with Dy concentration is smaller than reported by Nirmala et al. (2007d). For example, Nirmala et al. (2007d) reports that the $Gd_{3.5}Dy_{1.5}Si_2Ge_2$ composition has T_C of 201 K, while Aghababyan and Harutyunyan (2012) obtained $T_C=231$ K. The maximum magnetic entropy change values, measured by Aghababyan and Harutyunyan (2012) for a magnetic field change of 10 kOe, gradually decreases from -8.1 for a ternary $Gd_5Si_2Ge_2$ to -7.5 J/Kg K obtained for $Gd_3Dy_2Si_2Ge_2$.

Substitution of Gd by Tb was studied by Deng et al. (2007) in the $(Gd_{1-x}Tb_x)_5Si_{1.72}Ge_{2.28}$ series of alloys with $0 \leq x \leq 0.1$. X-ray diffraction and magnetization measurements show that in this range of concentrations the studied alloys form a solid solution with the $Gd_5Si_2Ge_2$-type crystal structure and a gradual decrease of the magnetic ordering temperature with x(Tb) was observed. The first order of the magnetic transition and the giant magnetocaloric effect are retained. The magnetocaloric effect in the $(Gd_{1-x}Tb_x)_5Si_2Ge_2$ series of alloys was theoretically studied by Gomes et al. (2009) and is in good agreement with the experimental results (which are only known for the end members).

Substitution of Gd by Er was investigated in the $(Gd_{1-x}Er_x)_5Si_{1.7}Ge_{2.3}$ series of alloys for $0 \leq x \leq 0.2$ (Chen et al., 2011). A strong and linear decrease in the magnetic ordering temperature was observed: T_C is 229 K for $x=0$ but drops rapidly to 135 K for $x=0.2$. A decrease in the magnetic hysteresis was reported for Er-substituted alloys but it is accompanied by a smaller value of the magnetic entropy change. The monoclinic $Gd_5Si_2Ge_2$-type crystal structure was observed in all samples.

5.1.4. $(R'_xR_{1-x})_5T_4$ Systems without Gd

$(R'_xR_{1-x})_5T_4$ pseudobinary systems that do not contain gadolinium have rarely been studied systematically until recently even though there are a number of earlier studies in which ternary $(R'_xR_{1-x})_5T_4$ compounds with layered crystal structure have been prepared. They are typically reported to crystallize in the Sm_5Ge_4-type crystal structure even though many of them, particularly silicides, probably have the Gd_5Si_4-type crystal structure. A significant number of $(R'_xR_{1-x})_5T_4$ compounds were discovered in systems with Sc. For example, $Sc_3Pr_2Si_4$, $Sc_{1.26}Pr_{3.74}Si_4$, and $Sc_{3.96}Nd_{1.04}Si_4$ were reported to crystallize in the Sm_5Ge_4 type (Kotur et al., 1997); however, analysis of Si—Si atomic bonding indicates that assignment to the Gd_5Si_4 type would be more appropriate for these compounds.

The crystallography of $Nd_{5-x}Er_xSi_4$ and $Nd_{5-x}Er_xGe_4$ pseudobinary systems was investigated by Misra et al. (2009a). In the silicide system, the end members crystallize in different structure types at room temperature: Er_5Si_4 adopts the Gd_5Si_4-type structure, while Nd_5Si_4 belongs to the tetragonal Zr_5Si_4 type. Somewhat predictably, two solid solution regions with different crystal structures exist in $Nd_{5-x}Er_xSi_4$: alloys with $x \leq 1.0$ have the tetragonal crystal structure, while the alloys in the compositional range $2.0 \leq x \leq 5.0$ exhibit the Gd_5Si_4 orthorhombic structure. The crystallographic properties of the $Nd_{5-x}Er_xGe_4$ alloys are similar to those of the $Gd_{5-x}Y_xGe_4$ system studied by Misra and Miller (2008). While the binary compounds, Er_5Ge_4 and Nd_5Ge_4, adopt the same Sm_5Ge_4-type crystal structure no continuous solid solution was observed. Instead, in the region of concentrations of $3.2 \leq x \leq 4.0$ the monoclinic $U_2Mo_3Si_4$-type structure occurs as the majority phase (Misra et al., 2009a). According to X-ray single crystal diffraction experiment, the smaller Er atoms tend to occupy the interslab 4*c* sites and to a slightly lesser degree one of the 8*d* sites (also preferentially occupied by Y in $Gd_{5-x}Y_xGe_4$, Misra and Miller, 2008), indicating that such preference is a particular property of most if not all R_5T_4 compounds with or without slab structure. Nd_4ErGe_4 undergoes an AFM-like ordering typical for other R_5Ge_4 compounds at $T_N = 23$ K. The Er-rich sample does not show a clear magnetic ordering transition but analysis of the low-temperature M(T) upturns indicates ferromagnetic-like ordering at 6, 12, and 11 K for $x = 2$, 3, 4, respectively. The magnetic ordering state of these alloys is confirmed by a saturation of the magnetization curves measured as a function of the applied magnetic field below these characteristic temperatures.

Unexpected and interesting results were obtained when Tb was gradually replaced by La in the $Tb_{5-x}La_xSi_2Ge_2$ system (Fig. 44, Belo et al., 2012b). When La substitutes for Tb at low concentrations ($x < 1$), the monoclinic $Gd_5Si_2Ge_2$ type of crystal structure of the ternary $Tb_5Si_2Ge_2$ compound is retained and the lattice dimensions increase due to much larger atomic radii of the La atoms compared to Tb. At the same time, the extent of the monoclinic distortion, the γ angle, decreases from 93.010(4)° to 92.109(4)° for $x = 0$ and 0.75, respectively. The effect of dilution of Tb by nonmagnetic La on the magnetic properties of these alloys is counterintuitive: the magnetic ordering temperature (T_C) *increases* with the increase in the La content for the monoclinic solid solution (see Fig. 44). At the same time, θ_p behaves erratically: it remains nearly the same, 94.0 versus 95.7 K, for $x = 0$ and 0.75, respectively, but is noticeably smaller for $x = 0.5$, 83.8 K. A similar lack of a clear trend is also reported for the effective paramagnetic and saturation magnetic moments. However, there are two characteristic magnetic temperatures that show a clear decrease with the rise in x(La): T_G, which indicates the onset of the Griffiths-like behavior, decreases from 208 to 195 K for $x = 0$ and 0.75, respectively, and the temperature of a spin-reorientation

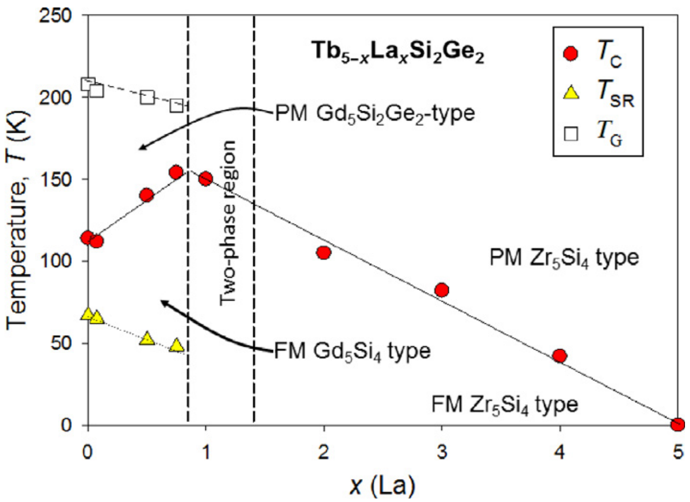

FIGURE 44 Magnetic and crystallographic phase diagram of $Tb_{5-x}La_xSi_2Ge_2$. *After Belo et al. (2012b).*

transition occurring in the magnetically ordered state also decreases from 67 to 48 K for the same range of concentrations. The magnetic ordering transition in $Tb_{5-x}La_xSi_2Ge_2$ alloys with $x<1$ is fully coupled with the structural $M \leftrightarrow O(I)$ transformation.

In the $Tb_4LaSi_2Ge_2$ sample ($x=1$) coexistence of two phases, monoclinic with the $Gd_5Si_2Ge_2$ structure type and tetragonal with the Zr_5Si_4-type crystal structure was observed. The samples with $x \geq 2$ crystallize with the tetragonal structure only. This $La_5Si_2Ge_2$-based solid solution predictably shows an increase in lattice dimensions and decrease in both T_C and θ_p with increasing La concentration. Neither the appearance of the Griffiths-like behavior nor the spin-reorientation transition were detected in the alloys with the Zr_5Si_4 crystal structure indicating dominance of one kind of magnetic exchange interactions in the alloys with nonlayered crystal structure compared to various competing mechanisms in compounds with slab structure.

5.2. $(R_{1-x}M_x)_5T_4$: Substitutions of R Sites by non-R Elements

5.2.1. *Substitutions by Ca*

An interesting change in crystal structure has been observed by Wu et al. (2005b) in $La_{5-x}Ca_xGe_4$ and $Ce_{5-x}Ca_xGe_4$ systems when trivalent La and nearly trivalent Ce (Zhang et al., 2010) were substituted by the divalent Ca atoms in narrow ranges of concentrations: $3.4 \leq x \leq 3.8$ and $3.0 \leq x \leq 3.3$, respectively. Both binary germanides crystallize in the Sm_5Ge_4-type structure with broken interslab T—T bonds; furthermore, the Gd_5Si_4 type of structure with strong interslab T—T bonds does not form in either $La_5Si_xGe_{4-x}$ or $Ce_5Si_xGe_{4-x}$. Yet, the Ca-substituted germanides crystallize in the Gd_5Si_4-type structure since the interslab Ge–Ge dimers ($d \sim 2.6$ Å) are, indeed, present in the studied samples. The effect of chemical pressure may not be the most relevant factor here because the effective ionic radius of divalent Ca (0.99 Å) is only slightly lower than the ionic radius of trivalent La (1.04 Å) and is similar to the ionic radius of trivalent Ce (1.01 Å).[9] Most likely it is the change in VEC that affects the crystal structure. As was shown also for the $Gd_5Ga_xGe_{4-x}$ system (Mozharivskyj et al., 2003, also see Section 2), application of the Zintl–Klemm formalism to electron count in R_5T_4 compounds leads to a prediction of the T–T dimers formation, and, consequently, allows derivation of the possible structure type for a given VEC value. Lower VEC is associated with the increased number of dimers and stability of the Gd_5Si_4-type structure. Therefore, reduction of VEC caused by replacement of the trivalent lanthanides with the divalent Ca may also lead to the formation of the Gd_5Si_4-type structure, as was experimentally verified by Wu et al. (2005b).

5.2.2. *Substitutions by Mg*

The Yb_4MgGe_4 has been synthesized by Tobash and Bobev (2006) and was found to crystallize in the Gd_5Si_4-type structure—the same as the binary Yb_5Ge_4. Similarly to Yb_5Ge_4 and other $Yb_5Si_xGe_{4-x}$ alloys (Ahn et al., 2005) Yb_4MgGe_4 is also an inhomogeneous mixed-valence system where Yb atoms in one of the 8*d* sites are trivalent while the other two sites are expected to be occupied by divalent Yb atoms based on the analysis of their nearest neighbor environments. Interestingly, Mg mainly prefers the intraslab 4*c* site for the substitution, but it also can be found (up to 28%) in the trivalent 8*d* site. Magnetic susceptibility of Yb_4MgGe_4 shows no magnetic transition and a modified Curie–Weiss fit gives a paramagnetic Curie temperature $\theta_p = -11$ K, an effective magnetic moment $p_{eff} = 2.3\ \mu_B$/Yb, and a temperature-independent parameter $\chi_0 = 9 \times 10^{-4}$ emu/mol.

A systematic study of the Mg substitution for the rare earth element in the $R_{5-x}Mg_xGe_4$ systems (for $1.0 < x < 2.3$) with R = Gd–Tm, Lu, and Y has been reported by Tobash et al. (2009). Several compositions from the $Ho_{5-x}Mg_xGe_4$ system were studied while only one compound from the other systems was reported. Interestingly, all these ternary germanides crystallize in the Gd_5Si_4-type crystal structure even though the parent binary R_5Ge_4 compounds usually adopt the Sm_5Ge_4-type structure. As noted above, the change in VEC results in the formation of the interslab Ge—Ge bonds, and the presence of such bonds differentiates Gd_5Si_4-type structure from the Sm_5Ge_4 type.

---

[9] Here and below, the values of atomic, metallic, and ionic radii are taken from Teatum et al. (1968).

TABLE 20 **Lattice Parameters and Basic Magnetic Properties of Selected $R_{5-x}Mg_xGe_4$ Compounds (Tobash et al., 2009)**

Compound	a (Å)	b (Å)	c (Å)	T_N (K)	θ_p (K)	p_{eff} (μ_B/R^{3+})
$Y_{3.49}Mg_{1.51}Ge_4$	7.085(2)	14.465(4)	7.718(2)	Pauli paramagnet		
$Gd_{3.55}Mg_{1.45}Ge_4$	7.1574(9)	14.623(2)	7.7801(9)	110	42	8.30
$Tb_{3.52}Mg_{1.48}Ge_4$	7.128(5)	14.512(11)	7.732(6)	70	19	9.97
$Dy_{3.50}Mg_{1.50}Ge_4$	7.0845(14)	14.425(3)	7.687(2)	31	8	10.85
$Ho_{3.62}Mg_{1.38}Ge_4$	7.0710(11)	14.419(2)	7.6627(12)	23	6	10.75
$Er_{3.41}Mg_{1.59}Ge_4$	7.0214(5)	14.3063(10)	7.6350(5)		3	9.92
$Tm_{3.51}Mg_{1.49}Ge_4$	7.0128(9)	14.270(2)	7.5998(9)		1	8.15
$Lu_{3.60}Mg_{1.40}Ge_4$	6.9750(8)	14.224(2)	7.5619(9)	Pauli paramagnet		

Consequently, as a result of the structural change a strong contraction (up to 6%) in the *a* and *b* crystallographic directions occurs due to Mg substitution when compared with the R_5Ge_4, while the change in the *c*-direction is the smallest. In the $Ho_{5-x}Mg_xGe_4$ solid solution, the change in lattice parameters is linear and monotonic. The magnetic ordering temperature (T_N) for the $Ho_{5-x}Mg_xGe_4$ solid solution increases from 17.4 to 24.2 K as the Mg content decreases from $x=2.06$ to 1.23. The T_N for R=Er, Tm could not be determined due to potentially very low magnetic ordering temperatures, and compounds with R=Y and Lu are Pauli paramagnets. Compositions, lattice parameters and basic magnetic properties of selected $R_{5-x}Mg_xGe_4$ compounds are presented in Table 20.

5.2.3. Substitutions by Zr and Hf

The metallic radii of Gd (1.802 Å) and Zr (1.602 Å) are quite different and they are not isoelectronic elements. Considering that Gd_5Si_4 and Zr_5Si_4 crystallize in different structure types a continuous solid solution between them is not expected. The study of $Gd_{5-x}Zr_xSi_4$ system shows that the Zr_5Si_4-based solution has a wider stability range ($1 \leq x \leq 5$) than the Gd_5Si_4-type solution, which exists only in a narrow range of concentrations for $x \leq 0.25$ (Yao et al., 2011). The lattice parameters and unit cell volume substantially decrease when Zr substitutes for Gd. Interestingly, the plotted dependence of the unit cell volume versus composition x indicates a weak negative deviation from Vegard's rule for the Zr_5Si_4-based solid solution. Even though the Zr_5Si_4-type structure is not layered, it was found that the larger atoms tend to avoid the inner-slab position when Zr substitutes for Gd both in the

$Gd_{5-x}Zr_xSi_4$ and $Gd_{5-x}Zr_xGe_4$ systems (Yao and Mozharivskyj, 2011). It is important to note, however, that the effect of VEC may also play a role in the distribution of substituting atoms among different atomic sites. The discussed site occupation preferences were observed in many M_5T_4 systems (including non-rare earths) and are compiled in a paper presented by Yao and Mozharivskyj (2011).

The $Gd_{5-x}Zr_xGe_4$ system is somewhat similar to $Gd_{5-x}Zr_xSi_4$, but the Gd_5Ge_4-based solid solution with the Sm_5Ge_4-type structure exists over a larger composition range ($0 \leq x \leq 1.49$, Yao and Mozharivskyj, 2011), compared to the Gd_5Si_4-based solid solution in the silicide system. The Zr_5Ge_4-based solid solution with the Zr_5Si_4-type structure occurs for $x \geq 1.77$.

Magnetic measurements show that the Curie temperature of $Gd_{5-x}Zr_xSi_4$ alloys is barely changed by Zr substitution in the Gd_5Si_4-type region, but it drops by ~100 K when the crystal structure changes to the Zr_5Si_4 type, and then gradually decreases due to a dilution effect (Yao et al., 2011). The $Gd_{5-x}Hf_xSi_4$ pseudobinary system is nearly identical to $Gd_{5-x}Zr_xSi_4$ (Yao and Mozharivskyj, 2011). The Gd_5Si_4-type solid solution exists over a narrow range of concentrations ($x \leq 0.41$), while the alloys for $x \geq 0.7$ adopt the Zr_5Si_4-type structure.

5.2.4. *Substitutions by Li*

The structural investigation of Tm_4LiGe_4 compound shows that it crystallizes in the ordered superstructure of the Sm_5Ge_4 type (Pavlyuk et al., 1990).

The Yb_4LiGe_4 compound (Xie et al., 2008) can be characterized as an ordered version of the Gd_5Si_4 type because the interslab Ge–Ge distance in this compound indicates the presence of the dimers ($d_{Ge3-Ge3} = 2.603(2)$ Å). These phases deserve special mentioning due to strict preferences in the occupation of R atomic sites: Li exclusively occupies the interslab 4*c* site, while the rare earth atoms are located in the 8*d* positions. The R_4LiGe_4 compounds were reported for all lanthanides except Eu (Fornasini et al., 2012).

6. R$_5$T$_4$ SYSTEMS CONTAINING Sn

R_5T_4 compounds containing Sn have not been studied as well as the silicides and germanides, but also draw significant attention due to the magnetostructural transitions and physical phenomena that are associated with them. Binary R_5Sn_4 easily hydrolyze when left at ambient atmospheric conditions and this fact also complicates their investigation. Two pseudobinary $R_5Sn_xSi_{4-x}$ systems with R = Nd and Gd have been studied so far; in addition, the effect of substitution of Si by Sn on the magnetic properties and crystal structure of GMCE compound $Gd_5Si_2Ge_2$ was investigated.

6.1. R_5Sn_4 Compounds

The crystal structure, lattice parameters, and basic magnetic properties of R_5Sn_4 compounds are summarized in Table 21. All known R_5Sn_4 compounds crystallize in the Sm_5Ge_4-type structure, except Yb_5Sn_4, which was found to adopt the Gd_5Si_4-type structure. While the compounds with R = Ce, Nd, Gd–Er are relatively well studied (see Table 21), little or no information is available about the R_5Sn_4 compounds formed by other rare earths.

The Y_5Sn_4 compound was observed during the investigation of the Y–Sn system (Schmidt and McMasters, 1968). It forms by peritectic reaction at 1790 ± 10 °C. The Sm_5Ge_4 type of crystal structure has been suggested for this compound. The Yb_5Sn_4 compound forms peritectically at 1160 °C, and

TABLE 21 Basic Crystallographic and Magnetic Properties of R_5Sn_4 Compounds (Sm_5Ge_4-Type Structure,[a] SG *Pnma*)

R	*a* (Å)	*b* (Å)	*c* (Å)	T_C, T_N (K)	Reference
Y	8.05	15.29	8.05	–	Schmidt and McMasters (1968)
La	8.435(1)	16.194(2)	8.630(1)	–	Guloy and Corbett (2005)
Ce	8.337	16.05	8.480	8.2	Borzone et al. (1982) and Givord et al. (1992)
Pr	8.270	15.94	8.429	–	Fornasini and Merlo (1971)
Nd	8.2093(6)	15.8504(13)	8.3797(7)	36	Wang et al. (2005)
Sm	8.126	15.67	8.290	–	Fornasini and Merlo (1971)
Gd	8.047(3)	15.545(5)	8.199(3)	82	Wang et al. (2002) and Ryan et al. (2003)
Tb	8.0086(3)	15.4369(7)	8.1390(4)	84 (54[a])	Zhong et al. (2011)
Dy	7.9865(5)	15.3693(9)	8.0930(5)	22[b]	Zhong et al. (2011)
Ho	7.9628(2)	15.3001(4)	8.0534(2)	15[b]	Zhong et al. (2011)
Er	7.9366(1)	15.2330(3)	8.0140(2)	8[b]	Zhong et al. (2011)
Yb[c]	7.822	15.813	8.280	–	Palenzona and Cirafici (1976)

[a] *Spin-reorientation transition.*
[b] *Néel temperature, T_N.*
[c] *Yb_5Sn_4 was reported to crystallize in the Gd_5Si_4-type structure.*

adopts the Gd_5Si_4 type of crystal structure (Palenzona and Cirafici, 1976) similar to Yb_5Si_4 and Yb_5Ge_4 (Ahn et al., 2005). Compounds with R = Sc, Eu, Tm, and Lu have not been reported.

6.1.1. R_5Sn_4 Compounds with R = La, Ce, Pr, Nd, and Sm

The formation and crystal structure of R_5Sn_4 compounds with R = La, Pr, and Sm has been reported (Fornasini and Merlo, 1971), but to the best of our knowledge no information about their physical properties is available. Guloy and Corbett (2005) synthesized the La_5Sn_4 compound and confirmed that it crystallizes in the Sm_5Ge_4-type structure.

Magnetic structure of Ce_5Sn_4 was studied by neutron diffraction and magnetization measurements (Givord et al., 1992). The study confirmed the orthorhombic Sm_5Ge_4-type crystal structure both above (at 16.6 K) and below (at 1.8 K) the magnetic ordering transition, which occurs at $T_C = 8.2$ K. The paramagnetic Curie temperature and effective paramagnetic moment were found to be −16 K and 2.63 μ_B/Ce atom, respectively, suggesting antiferromagnetic interactions and the trivalent state of cerium in this compound. Examination of the magnetic structure by neutron diffraction shows that Ce_5Sn_4 is a noncollinear ferromagnet with ferromagnetic component aligned along the *a*-axis. Two other directions, however, exhibit AFM interactions, in agreement with negative θ_p.

The magnetic structure of Nd_5Sn_4 has been determined by using neutron diffraction (Wang et al., 2005). A complex canted antiferromagnetic structure is observed below the magnetic ordering temperature of $T_C = 36$ K with magnetic moments essentially confined in the *ac*-plane. The Nd magnetic moments are higher in the 8*d* atomic sites (2.44 and 2.63 μ_B per Nd) than in the interslab 4*c* site (1.76 μ_B).

6.1.2. Gd_5Sn_4

Gd_5Sn_4 undergoes a low-temperature magnetostructural PM–FM transition and the nature of the transition was first studied in Gd_5Sn_4 by means of magnetization measurements and ^{119}Sn Mössbauer spectroscopy (Ryan et al., 2003). The temperature of the coupled magnetic and structural transition has been identified as 82 K, based on magnetic susceptibility data. The transition can be induced by both the change in temperature and applied magnetic field. The $M(H)$ curve collected at 5 K confirms the ferromagnetic state of Gd_5Sn_4 with a saturation moment of 6.8 μ_B/Gd. Another magnetic transition, probably reflecting the presence of a magnetic impurity, was observed in the sample at ~130 K (Ryan et al., 2003). The Mössbauer spectrum of Gd_5Sn_4 at 9 K is dominated by two well-split magnetic sextets. A characteristic change is observed in both temperature and magnetic-field-dependent spectra when the material proceeds through the first-order transition. The temperature dependence of the magnetic entropy change forms a plateau for a magnetic field change above $\Delta H = \sim 30$ kOe with a maximum height of the plateau at ~ -35 J/Kg K. The width of the plateau increases with the increase in ΔH, while the maximum value remains stable, a behavior indicative of the first-order nature of the transition. Ryan et al. (2003) also suggests that the sample used in their study is magnetically inhomogeneous below 130 K.

The temperature-dependent X-ray powder diffraction study of Gd_5Sn_4 was carried out by Yang et al. (2004) in the temperature range between ~80 and 298 K. The investigation did not show any change of crystal structure at T_C, even though a notable dip in lattice parameters and unit cell volume was observed at the point of magnetic ordering. However, Wang et al. (2004) using temperature-dependent X-ray synchrotron diffraction data showed that Gd_5Sn_4 (and Si-doped $Gd_5Si_{0.4}Sn_{3.6}$) actually change their crystal structure at T_C from the room temperature O(II) Sm_5Ge_4 type into the low-temperature O(I) Gd_5Si_4 type. The diffraction pattern collected at 20 K shows that the transition is incomplete, and 13% of the room temperature structure (6% according to Mössbauer spectroscopy, Ryan et al., 2003) is still present. The Bragg peaks of impurity phases, Gd_5Sn_3 and $Gd_{11}Sn_{10}$, were present as well. The contraction of the lattice along the *a*-axis during the transition is smaller than in Gd_5Ge_4, but still large (~1%) especially when compared to negligible expansions observed along the *b*- and *c*-axes.

6.1.3. R_5Sn_4 Compounds with $R = Tb$, Dy, Ho, and Er

Scarce and often contradictory information regarding the formation of R_5Sn_4 compounds with heavy lanthanides was available in the literature until recently. Bulanova et al. (1998) reported the formation of Ho_5Sn_4 by a peritectic reaction from liquid and Ho_5Sn_3 at 1720 ± 13 °C yet its crystal structure has not been determined. According to Eremenko et al. (1992), Dy_5Sn_4 also forms by peritectic reaction from liquid and Dy_5Sn_3 at 1712 ± 11 °C, and its crystal structure was identified as Sm_5Ge_4 type.

Zhong et al. (2011) studied the crystallographic and magnetic properties of R_5Sn_4 compounds with $R = $ Tb, Dy, Ho, and Er. The study found that all compositions crystallize in the Sm_5Ge_4-type structure but are difficult to obtain as single-phase materials. The $R_{11}Sn_{10}$ and R_5Sn_3 impurity phases are present in all prepared samples; annealing at 1300 °C for 24 h decreases the amount of impurities but their concentrations are still relatively high, varying between 9% and 17% depending on the sample. The lattice parameters and magnetic ordering temperatures of R_5Sn_4 compounds for $R = $ Gd–Er are listed in Table 21. It is noted that according to Zhong et al. (2011), Tb_5Sn_4 orders ferromagnetically at ~84 K and its magnetic ordering temperature is nearly the same as Gd_5Sn_4 (Ryan et al., 2003). In addition, Tb_5Sn_4 exhibits a spin-reorientation transition (AFM like) at 54 K. Ho_5Sn_4, Dy_5Sn_4, and Er_5Sn_4 order antiferromagnetically at 22, 15, and 8 K, respectively.

6.2. $R_5Sn_xSi_{4-x}$ Systems

6.2.1. $Gd_5Sn_xSi_{4-x}$

The replacement of Si atoms by much larger isoelectronic Sn atoms can be expected to produce the similar effect as the replacement of Si by Ge. The atomic radius of Sn is larger than Ge, therefore a stronger chemical pressure effect should be observed in the Gd_5Sn_4 side of the phase diagram compared to the $Gd_5Si_xGe_{4-x}$ system (faster increase in T_C with Si addition). In addition, the O(I) phase has a narrower stability range due to a larger expansion of the unit cell volume so that the low-volume phase may be replaced with a larger volume phase at smaller x. The investigation of the $Gd_5Sn_xSi_{4-x}$ pseudobinary system (Wang et al., 2002) indicates that the Gd_5Si_4-based solid solution[10] is indeed slightly narrower ($0 \leq x \leq 1.2$) compared to the $Gd_5Si_xGe_{4-x}$ system. The monoclinic phase with room temperature $Gd_5Si_2Ge_2$ structure type exists for $2.8 \leq x \leq 3.2$, and the Gd_5Sn_4-based solid solution with room temperature O(II) Sm_5Ge_4-type structure occurs for $x \geq 3.6$. An extensive two-phase region containing both M and O(I) structures was found by Wang et al. (2002) for $1.6 \leq x \leq 2.4$.

A separate study of the $Gd_5Sn_xSi_{4-x}$ pseudobinary system over the $0 \leq x \leq 3$ range of concentrations using X-ray single crystal diffraction (Mozharivskyj et al., 2006) shows a notable discrepancy with the results obtained by Wang et al. (2002). While the Gd_5Si_4-type solid solution was found by Mozharivskyj et al. (2006) to exist in a range of concentrations ($0 \leq x \leq 1.5$) similar to the one reported by Wang et al. (2002) (see above), they did not observe a $Gd_5Si_2Ge_2$-type phase in the $Gd_5Sn_xSi_{4-x}$ system. Instead, the Pu_5Rh_4-type structure with slightly elongated interslab T—T bonds ($d_{T\text{–}T} = 3.04$ Å) was obtained for the $Gd_5Sn_2Si_2$ alloy. According to Mozharivskyj et al. (2006) a further increase in the Sn concentration results in the formation of alloys with the Ti_5Ga_4 structure, a filled version of the Mn_5Si_3 type. The composition of these alloys is not a 5:4 stoichiometry due to a partial occupation of Si in the $2a$ site of the Ti_5Ga_4 structure (i.e., $Gd_5Si_{0.7}Sn_3$). Ti_5Ga_4 is not a layered (slab) structure, yet it is interesting to note that a further increase in Sn concentration leads to the binary Gd_5Sn_4, which has a layered Sm_5Ge_4-type structure again. Apparently, more detailed studies are needed on the Sn-rich side of the $Gd_5Sn_xSi_{4-x}$ diagram. However, as noted by many authors in the past, the Sn-rich alloys are quite air sensitive, which complicates further research of bulk samples.

Similarly to the $Gd_5Si_xGe_{4-x}$ system, the Curie temperature of $Gd_5Sn_xSi_{4-x}$ alloys gradually decreases with x(Sn) for the O(I) structure, but the alloys with M and O(II) crystal structures reported by Wang et al. (2002) show the opposite trend (a slow increase of T_C with Sn addition), which is remarkably different from the $Gd_5Si_xGe_{4-x}$ alloys. ^{119}Sn Mössbauer

---

[10] Wang et al. (2002) assigns Sm_5Ge_4-type structure for the Gd_5Si_4-based solid solution.

spectroscopy shows large transferred hyperfine fields (~370 kOe) at the Sn sites. In addition, a first-order magnetostructural transformation was reported for the alloys with Sm_5Ge_4-type structure, including binary Gd_5Sn_4. The presence of a structural transformation was confirmed by temperature-dependent X-ray synchrotron diffraction studies for the $Gd_5Si_{0.4}Sn_{3.6}$ alloy, as well as for the binary Gd_5Sn_4 (Wang et al., 2004). At T_C, the re-forming of the interslab Sn–Sn occurs resulting in a structural change from the O(II) Sm_5Ge_4 type into the low-temperature O(I) Gd_5Si_4 type.

A magnetocaloric effect has been measured for the $Gd_5Si_2Sn_2$ compound by Campoy et al. (2004). The study points on the difficulties in preparing single-phase material; the annealing lowers the Curie temperature from 230 (as-cast alloy) to 210 K (1400 °C/20 h + 1000 °C/5 d). The observed maximum entropy change for $\Delta H = 50$ kOe is moderate, −4.2 J/Kg K. The crystal structure and magnetocaloric properties of $Gd_5Sn_xSi_{4-x}$ alloys with $x = 1.2$, 1.4, and 1.6 were reported by Zhang et al. (2006). In agreement with Wang et al. (2002), the sample with $x = 1.2$ was single-phase alloy with the Gd_5Si_4-type structure, while two other samples were two-phase alloys containing both Gd_5Si_4 and $Gd_5Si_2Ge_2$ structures. The Curie temperature decreases from 302 for $x = 1.2$ to 276 K for $x = 1.6$, while the maximum magnetic entropy change for a field change of 1.8 T is the largest for $x = 1.4$, $\Delta S_M = -2.3$ J/Kg K. The moderate to low values of MCE are in agreement with the X-ray diffraction analysis performed by Zhang et al. (2006), which did not observe any crystallographic transition in the studied samples.

It is worth to add, that when Sn replaces Si in the $Gd_5Ge_2(Si_{1-x}Sn_x)_2$ compound, the crystal structure remains monoclinic for $x = 0.23$ but changes to O(II) for $x = 0.40$ (Campoy et al., 2007). Two nonequivalent hyperfine sites for the Sn atoms were observed by using ^{119}Sn Mössbauer spectroscopy. According to the magnetization measurements both samples order ferromagnetically, $x = 0.23$ at 218 K, and $x = 0.4$ at 172 K. The measured magnetocaloric effect is larger in the sample with the O(II) room temperature crystal structure than for the sample with the monoclinic crystal structure: the maximum ΔS_M is −33 versus −23 J/Kg K, respectively ($\Delta H = 50$ kOe). The X-ray powder diffraction data collected at 100 K show a Gd_5Si_4-type structure for both samples indicating that the crystallographic transformation occurs at T_C (Campoy et al., 2010). ^{155}Gd Mössbauer spectra obtained at 4.2 K can be numerically resolved as two quadrupolar patterns with relative area ratios 87:13 for $x = 0.23$, and 79:21 for $x = 0.40$, which approximately corresponds to the nonequivalent distribution of Gd atoms between two interslab 8*d* and single intraslab 4*c* sites (80:20) of the Gd_5Si_4-type structure (Campoy et al., 2010).

6.2.2. $Nd_5Sn_xSi_{4-x}$

An investigation of the $Nd_5Sn_xSi_{4-x}$ pseudobinary system shows that except for the binary Nd_5Si_4 compound, which adopts the tetragonal Zr_5Si_4-type structure, all other synthesized samples in this system ($0<x\leq 3.5$) crystallize in the Sm_5Ge_4-type crystal structure (Wang et al., 2003). Within the orthorhombic $Nd_5Sn_xSi_{4-x}$ solid solution the lattice parameters and unit cell volume increase linearly with x(Sn) while T_C gradually decreases from ~120 K for $x=0.5$ to ~33 K for $x=4$. The saturation magnetic moment measured at 5 K also decreases with x(Sn) from ~1.6 μ_B/Nd for $x=3.5$ to ~0.8 μ_B/Nd for $x=0.5$ and both values are well below the $g_J=3.27\ \mu_B$ value expected for the Nd^{3+} ion. The samples with $x=1.5$ and 4 were reported to have metamagnetic-like jumps in their $M(H)$ curves. Mössbauer spectroscopy, however, shows no indication of a first-order transition in $Nd_5Sn_xSi_{4-x}$ triggered by either the applied magnetic field or temperature. The transferred hyperfine fields in the $Nd_5Sn_xSi_{4-x}$ measured at 9 K are in the range of 100–160 kOe, much smaller compared with the ~370 kOe of $Gd_5Sn_xSi_{4-x}$ (Wang et al., 2003).

6.3. $R_5Sn_xGe_{4-x}$

Only limited information is available for the $R_5Sn_xGe_{4-x}$ systems. Guloy and Corbett (2005) synthesized the La_5Ge_3Sn compound, and determined that its crystal structure belongs to the Sm_5Ge_4 type with lattice parameters $a=8.156(1)$ Å, $b=15.630(2)$ Å, and $c=8.292(1)$ Å.

Qian et al. (2009) reported that the Gd_5Ge_3Sn compound crystallizes in the Sm_5Ge_4 type of crystal structure. A microstructural investigation revealed a large number of linear features in the Gd_5Ge_3Sn alloy.

7. R_5T_4 SYSTEMS WHERE T INCLUDES A GROUP 13 OR 15 ELEMENT

The Eu_5As_4 compound is one of the few R_5T_4 compounds where T sites are completely occupied by a group 15 element (Wang et al., 1978). Its crystal structure is closely related to Sm_5Ge_4 and other structure types containing -*GSCSG*- slabs (see Section 2), and its ternary variant, $Tm_5Sb_2Si_2$-type structure, is commonly observed in ternary R_5T_4 compounds containing Sb (Kozlov et al., 2004). The high-temperature β-Yb_5Sb_4 phase, whose crystal structure may represent a supercell ($a=8.13$ Å, $b=15.97$ Å, $c=24.39$ Å) to the Sm_5Ge_4-type structure (Bodnar and Steinfink, 1967) is another example of the R_5T_4 phase with a slab-based structure[11] that does not contain any of the group 14 elements (Si, Ge, Sn, or Pb). However, in most cases the slab-based structures containing group 13 or group 15 elements form in ternary alloys such as pseudobinary $R_5T^{14}{}_{1-x}T^{13}{}_x$ or $R_5T^{14}{}_{1-x}T^{15}{}_x$ since binary $R_5T_4^{13}$, $R_5T_4^{15}$ compounds do not exist with trivalent lanthanides.

Such pseudobinary systems have been mainly studied with Ga and Sb. The investigations of ternary alloys with other group 13 or group 15 elements is

---

[11] The actual crystal structure of the β-Yb_5Sb_4 phase has not been reported.

limited, either because of concerns about their safe handling (i.e., T = As) or because such alloys do not readily form slab structures (i.e., T = In). However, they are interesting systems to explore because their substitution enables gradual variation of the valence electron concentration and thus the effect of VEC on the crystal structure and properties can be determined. The $Gd_5Ga_xGe_{4-x}$ system was, in fact, the model system in which the dependence of the crystal structure (more specifically, formation of the interslab T—T bonds) has been explained using the Zintl–Klemm formalism (Mozharivskyj et al., 2003).

7.1. Substitutions by Ga

The investigations of the $R_5(Ga_xT_{1-x})_4$ pseudobinary systems are basically limited to the system with R = Gd (see below). In addition, Guloy and Corbett (2005) synthesized the La_5Ge_3Ga alloy, and the crystal structure determination showed that it adopts the Gd_5Si_4-type structure (in accord with the decrease in VEC) with lattice parameters $a = 7.910(1)$ Å, $b = 15.294(2)$ Å, and $c = 8.252(1)$ Å.

7.1.1. $Gd_5Ga_xGe_{4-x}$

The initial crystallographic study of the $Gd_5Ga_xGe_{4-x}$ system ($0 \leq x \leq 3$) showed that the increase in Ga concentration leads to strongerinterslab T–T dimers, resulting in the gradual transition from the Sm_5Ge_4 type, adopted by the gadolinium germanide, to the Pu_5Rh_4-type crystal structure, and, finally to the formation of the Gd_5Si_4-type structure (Mozharivskyj et al., 2003). The Gd_5Ge_4-based solid solution extends to $x = 0.6$ and a two-phase region ($Sm_5Ge_4 + Pu_5Rh_4$) occurs for $0.7 \leq x \leq 0.9$. The single Pu_5Rh_4-type phase was observed in a Gd_5GaGe_3 sample, and for the $1.2 \leq x \leq 2.2$ region there is a solid solution with the Gd_5Si_4-type structure. However, Mozharivskyj et al. (2003) argue that the precise value for Ga concentration where Pu_5Rh_4 transforms into Gd_5Si_4 cannot be defined, and such transition is continuous. At higher concentrations of Ga, the $Gd_5(Ga_xGe_{1-x})_4$ phase decomposes into a mixture of $Gd_3(Ga_xGe_{1-x})_2$ and $Gd(Ga_xGe_{1-x})$ phases.

The continuous transition from the Pu_5Rh_4 structure to the Gd_5Si_4 structure is manifested by a smooth compositional dependence of the lattice parameters above $x = 0.9$, and therefore the only indication of this structural change is the shortening of the T—T interslab bonds. However, a step-like change in lattice parameters is observed above $x = 0.6$. The a-parameter contracts accommodating the formation of the interslab T—T bonds, while the c-parameter increases, and a slight gradual expansion is observed along the b-axis.

Since the sizes (metallic radii) of the Ga (1.411 Å) and Ge (1.369 Å) atoms are similar, the observed structural evolution may be controlled by a change in the valence electron concentration. Specifically, when the VEC value (calculated using the Zintl–Klemm formalism) is between 31 and 30.4 e$^-$/formula, the Sm_5Ge_4-type structure is stable, but further decrease in VEC promotes the formation of the interslab T–T dimers, and for VEC values between 28.8 and 30, the Pu_5Rh_4 and Gd_5Si_4 type structures are observed (Mozharivskyj et al., 2003). TB-LMTO calculations show lower population of the T—T antibonding states when Ga substitutes Ge.

Temperature-dependent crystallographic, magnetic, and heat capacity behaviors of $Gd_5Ga_{0.7}Ge_{3.3}$ and Gd_5GaGe_3 compounds have been studied by Misra et al. (2009b). Both X-ray powder and X-ray single crystal diffraction properties were employed for the identification of structural phase transitions. The $Gd_5Ga_{0.7}Ge_{3.3}$ compound shows a unique sequence of crystallographic transformations: at first, its room temperature O(II) Sm_5Ge_4-type crystal structure changes to the monoclinic M $Gd_5Si_2Ge_2$-type at 165 K, which exists in the narrow range of temperatures $150 < T < 165$ K. Below 150 K the O(I) Gd_5Si_4-type structure occurs. While it is common to have an O(II)–O(I) transition in the R_5T_4 alloys, the presence of the intermediate monoclinic phase so far has been reported only for the $Gd_5Ga_{0.7}Ge_{3.3}$ alloy. However, it is worth to note that the monoclinic phase was observed in a tiny ($\sim 10^2$ μm) single crystal. Magnetization and heat capacity measurements performed on a bulk sample show a second-order magnetic ordering transition at ~195 K, while the sequence of structural transformations observed in the small $Gd_5Ga_{0.7}Ge_{3.3}$ single-crystal is hardly noticeable in bulk measurements, except for a change of slope of $M(T)$ curve around 165 K. Misra et al. (2009b) suggest that the contraction of the interslab T—T bonds in $Gd_5Ga_{0.7}Ge_{3.3}$ occurs gradually, contrary to what was observed in $R_5Si_xGe_{4-x}$ alloys where structural change is always sharp; therefore, no clear first-order phase transition can be observed. The maximum magnetocaloric effect for $Gd_5Ga_{0.7}Ge_{3.3}$ is $\Delta S_M = -14$ J/Kg K at ~170 K for $\Delta H = 50$ kOe. The heat capacity peak at the magnetic ordering transition of Gd_5GaGe_3 at $T_C = 190$ K is, however, more typical for a first-order transition and does not become smeared with the application of magnetic field, although it is broad even in zero field. The Gd_5GaGe_3 alloy appears to exhibit a structural transition at 523 K from the room temperature Pu_5Rh_4 type (interslab $d_{T-T} = 2.837$ Å) to the high-temperature Gd_5Si_4 type (interslab $d_{T-T} = 2.521$ Å).

The $Gd_5Ge_{3.8}Ga_{0.2}$ alloy with the O(II) Sm_5Ge_4 type of crystal structure was characterized by magnetic and electrical transport measurements (Bhattacharyya et al., 2009) and showed magnetic metastability and training effects similar to the parent Gd_5Ge_4 compound. However, such a small substitution of Ge by Ga already promotes the temperature-induced transition into the FM-O(I) state without applied magnetic field, indicating that the VEC influence may reflect upon the low-temperature properties even when it is not affecting the room temperature crystal structure.

SEM examination of the Gd_5GaGe_3 compound by Qian et al. (2009) revealed the presence of the 5:3 thin plates, which are commonly observed in the $R_5(Si,Ge)_4$ samples. Therefore, a decrease in VEC does not have effect on the thin plate formation.

7.1.2. $Gd_5Ga_xSi_{4-x}$

Characterization of structural and magnetic properties of $Gd_5Ga_xSi_{4-x}$ alloys showed that the Gd_5Si_4-based solid solution exists up to x(Ga) ~ 1 (Wang et al., 2010). Above this concentration, the Gd_5Si_4-type structure can be observed in the multiphase $Gd_5Ga_{1.5}Si_{2.5}$ alloy, but not in the annealed $Gd_5Ga_2Si_2$. No other R_5T_4 layered structure types were observed in this pseudobinary system. The Ga atoms preferentially occupy the interslab T sites of the Gd_5Si_4-type structure. Temperature dependences of the dc magnetization were measured for $Gd_5Ga_{0.63}Si_{3.37}$ and $Gd_5Ga_{0.81}Si_{3.19}$ compounds. The former compound has $T_C = 310$ K and the latter has $T_C = 286$ K. The θ_p values obtained via the Curie–Wess fits (308 and 283 K, respectively) agree well with the magnetic ordering temperatures (Wang et al., 2010).

7.2. Substitutions by Sb

Except for the Yb_5Sb_4 binary compound (Bodnar and Steinfink, 1967), the R_5T_4 alloys containing antimony usually adopt the layered crystal structure in ternary alloys in which only some of the tetralide atoms are substituted by Sb. Alternatively, ternary $R_5(Sb,T)_4$ compounds with slab-based structures may form when Ga is used instead of Ge or Si. This was observed for the Ho_5GaSb_3 compound, which crystallizes in the Sm_5Ge_4-type structure with the lattice parameters $a = 7.9667(8)$ Å, $b = 15.128(2)$ Å, $c = 7.9616(8)$ Å (Antonyshyn et al., 2009). Such cases may not be rare in nature but they are not well studied at this point.

According to the Zintl–Klemm formalism, antimony brings five electrons to the formula unit, so its substitution into the alloys is not expected to result in the formation of the interslab T—T bonds. In fact, ternary $R_5Sb_xSi_{4-x}$ and $R_5Sb_xGe_{4-x}$ alloys with high concentrations of x(Sb) crystallize in the $Tm_5Si_2Sb_2$-type crystal structure (Kozlov et al., 2004), which is an ordered superstructure variant of the Eu_5As_4 type (Wang et al., 1978). This crystal structure is formed by the stacking of the same -*GSCSG*- slabs as other layered structures (see Section 2) but is more symmetrical and characterized by the complete absence of inteslab T—T bonds. Moreover, even when $Gd_5Sb_{0.5}Ge_{3.5}$ with the O(II) Sm_5Ge_4 room temperature crystal structure undergoes a magnetostructural transition at $T_C = 40$ K with a substantial volume change (−0.5%), the formation of interslab T–T dimers does not occur and this compound remains in a slightly modified version of the Sm_5Ge_4-type crystal structure (Chernyshov et al., 2009).

Kozlov et al. (2004) reported the discovery of 11 isostructural ternary compounds with $R_5Sb_2T_2$ stoichiometry (T = Si, Ge) adopting the $Tm_5Sb_2Si_2$-type crystal structure: compounds for R = Y, Dy–Tm were observed with both Si and Ge, while a terbium compound was reported with Si only. The alloys were heat treated at 670 K for 2 weeks. No ternary phase containing Gd was found in this study. The investigation of the Y–Sb–Si system (the alloys were annealed at 670 K for 30 days) did not indicate any extended homogeneity region for the $Y_5Sb_2Si_2$ compound (Kozlov and Pavlyuk, 2004).

7.2.1. $Gd_5Sb_xGe_{4-x}$

Using high-purity Gd metal Chernyshov et al. (2006) observed the ternary phase with the $Tm_5Sb_2Si_2$-type structure in the $Gd_5Sb_xGe_{4-x}$ system, and showed that it exists in the extended range of concentrations, approximately from $x = 2$ to $x = 2.7$. Moreover, the study observed that a Gd_5Ge_4-based solid solution with the Sm_5Ge_4-type crystal structure occurs when Sb substitutes Ge at least up to $x = 1$. Interestingly, the alloys with higher Sb concentration and $Tm_5Sb_2Si_2$-type crystal structure order magnetically at much higher temperatures than alloys with the O(II) room temperature crystal structure: T_C for $Gd_5Sb_{2.1}Ge_{1.9}$ is 200 K while T_C for Gd_5SbGe_3 is 37 K only. At the same time, the $Gd_5Sb_{2.1}Ge_{1.9}$ alloy orders via a second-order transition, while the transitions observed in alloys with $x = 0.7$ and 1 are typical first-order ones. A characteristic increase of the transition temperature with application of a magnetic field is clearly seen in magnetic, electrical resistivity, and heat capacity measurements of the $Gd_5Sb_{0.7}Sb_{3.3}$ polycrystalline alloy (Chernyshov et al., 2006).

The first-order transition occurring in the $Gd_5Sb_xGe_{4-x}$ alloys with $x \leq 1$, has been studied in detail using temperature- and magnetic-field-dependent X-ray powder diffraction as well as by means of ac magnetic susceptibility, magnetization, and heat capacity measurements of a $Gd_5Sb_{0.5}Ge_{3.5}$ oriented single crystal; the experimental results were complemented by first-principles calculations (Chernyshov et al., 2009). The study reports a strong coupling of the magnetic and crystallographic lattices along all three major crystallographic directions. The a-axis appears to be the easy magnetization direction, but the overall magnetic anisotropy in this compound is weak. Sharp metamagnetic transitions are seen in the $M(H)$ data measured at temperatures just above T_C (40 K), and it is worth noting that both thermal and magnetic hystereses associated with this compound are small. Another, weaker transition is observed in the heat capacity data at 63 K; however, this transition is not seen in either magnetization or ac susceptibility data indicating that its origin is nonmagnetic. Since the temperature of the main first-order transition increases in magnetic field, and the temperature of the weaker second-order transition is field independent, the crossover occurs in magnetic fields above 20 kOe and only the stronger transition is seen in $C_p(T)$ data collected in 50, 75, and 100 kOe applied magnetic fields.

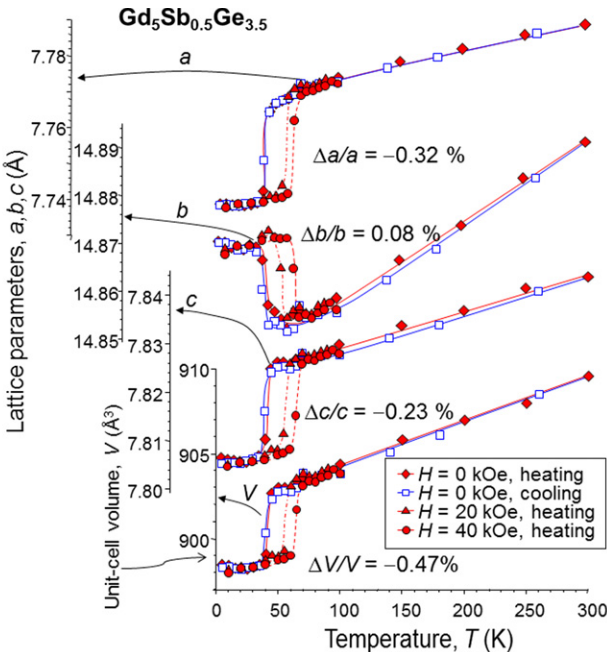

FIGURE 45 Temperature dependencies of the lattice parameters and unit cell volume of $Gd_5Sb_{0.5}Ge_{3.5}$ in 0, 20, and 40 kOe applied magnetic fields. Zero magnetic field data are shown for both heating and cooling (Chernyshov et al., 2009).

While the first-order transition in $Gd_5Sb_{0.5}Ge_{3.5}$ appears to be similar to the magnetostructural transitions observed in other R_5T_4 alloys, for example in $Gd_5Si_2Ge_2$, there is one important difference. Despite a large volume change at the transition ($\Delta V/V = -0.47\%$) and an intimate coupling of magnetic and crystallographic lattices, $Gd_5Sb_{0.5}Ge_{3.5}$ maintains the same O(II) Sm_5Ge_4-type crystal structure below and above T_C. No formation of interslab T—T bonding and no shear movement of the slabs occur during the transition. Instead, an almost uniform slab contraction within the *ac*-plane is detected as shown in Fig. 45. First-principles calculations confirm that in the Sb-substituted alloys the Sm_5Ge_4-type structure can support the ferromagnetic ground state (Chernyshov et al., 2009).

Interestingly, SEM examination did not detect the 5:3 thin plates in the $Gd_5Sb_{0.7}Ge_{3.3}$ alloy, even though they are commonly present in other R_5T_4 alloys (including Ga substituted), and the fact that Gd_5Sb_3 is a stable phase in the Gd–Sb system (Qian et al., 2009).

7.2.2. $Gd_5Sb_xSi_{4-x}$

The phase relationships and magnetic properties of alloys in the $Gd_5Sb_xSi_{4-x}$ pseudobinary system in the range of antimony concentrations up to $x = 3.5$

have been reported by Svitlyk et al. (2010). With the increase in x(Sb) the crystal structure of the alloys transforms from the Gd_5Si_4 type ($x \leq 0.38$) to the Sm_5Ge_4 type ($1.21 \leq x \leq 1.79$), and, finally to the Eu_5As_4 type of crystal structure ($2.27 \leq x \leq 3.1$). Above $x = 3.1$ the ternary $Gd_5Sb_xSi_{4-x}$ solid solution decomposes. There is a clear preference for the larger Sb atoms to occupy the interslab T site while smaller Si atoms are located inside the slabs. All $Gd_5Sb_xSi_{4-x}$ alloys order ferromagnetically. The Curie temperature first drops when the crystal structure changes from Gd_5Si_4 to Sm_5Ge_4 type, but after that it increases with the increase in Sb concentration, reaching room temperature ($T_C = 295$ K) for the Gd_5SiSb_3 sample. All magnetic phase transitions appear to be of second order. Interestingly, the alloys with the Eu_5As_4-type crystal structure show large values of the effective paramagnetic moment per Gd atom, 8.45 and 8.71 for $x = 2.5$ and 3, respectively.

7.3. Other Elements (Bi, P, and Pb)

Since it is hard to cover all possible combinations of T elements that may lead to the formation of the slab-based structures, only the studied pseudobinary systems are described below.

7.3.1. *$Gd_5Bi_xSi_{4-x}$*

Because Si and Bi have much different metallic sizes (1.319 and 1.70 Å, respectively) and different number of valence electrons, extended solid solutions are not expected in this pseudobinary system. According to Svitlyk et al. (2009a), the upper limit of Bi substitution into the Gd_5Si_4-based solid solution is $x = 0.096(8)$. Further increase in Bi content results in a variety of layered crystal structures with different accommodations of -*GSCSG*- slabs. The $Gd_5Si_{2.42}Bi_{1.58}$ sample adopts the Eu_5As_4-type structure, while two other compositions reported by Svitlyk et al. (2009a), $Gd_5Si_{1.93}Bi_{2.07}$ and $Gd_5Si_{1.58}Bi_{2.42}$ adopt their own tetragonal structure types (see Section 2).

7.3.2. *$Gd_5P_xSi_{4-x}$*

Phase transformations in the $Gd_5Si_{4-x}P_x$ system were investigated in order to explore the effect of increasing valence electron concentration on the crystallographic behavior of the R_5T_4 alloys (Svitlyk et al., 2009b). The atomic (metallic) radii of P (1.28 Å) is smaller than that of Si (1.319 Å) but since the increase of VEC is known to prevent the occurrence of the interslab T–T dimers (i.e., in $Gd_5Sb_{0.5}Ge_{3.5}$) the increased concentration of phosphorous causes the formation of the high-volume O(II) Sm_5Ge_4-type structure in this system. In fact, the Gd_5Si_4-based solid solution exists over a limited range of concentrations, for $x \leq 0.25$. A small homogeneity region for alloys adopting the Sm_5Ge_4-type structure was found for $1.0 < x < 1.25$. The two-phase region containing both O(I) and O(II) structures exists between $x = 0.25$ and $x = 1$, and above $x = 1.25$ and up to $x = 2$, a mixture of O(II)-type $Gd_5Si_{4-x}P_x$ phase and GdP was observed. Because the O(II) phase is a high-volume phase, the unit cell volume of the $Gd_5Si_{2.75}P_{1.25}$ sample ($V = 856.0(4)$ Å^3) is larger than the unit cell volume of the binary Gd_5Si_4 compound ($V = 853.74(8)$ Å^3). The $Gd_5Si_{2.75}P_{1.25}$ phase orders magnetically at $T_C = 184$ K (Svitlyk and Mozharivskyj, 2009). The phase transition appears to be of second order and MCE is moderate: maximum $\Delta S_M = -7.8$ J/Kg K for $\Delta H = 50$ kOe.

7.3.3. $La_5Pb_xGe_{4-x}$

Guloy and Corbett (2005) have prepared La_5Pb_4 and La_5Ge_3Pb and showed that they have the Sm_5Ge_4-type structure. The same study also reports the crystal structure of the La_5Ge_3In compound, which due to the decrease in VEC crystallizes in the Gd_5Si_4 type.

8. CONCLUSIONS AND OUTLOOK

As one can conclude from reading this book chapter, the fundamental science of R_5T_4 compounds is alive; interesting and important chemical and physical phenomena are abundant. Some of the effects are well studied and may soon be developed for technological applications (e.g., giant magnetocaloric effect, colossal magnetostriction, and giant magnetoresistance) while the exploration of others (e.g., magnetic deflagration, spontaneous generation of voltage, and role of microstructure in controlling magnetostructural transformations) has just begun. It is fair to say that at this point we already have a substantial understanding of the composition–structure–property relationships of layered R_5T_4 systems, and in many cases one can predict the occurrence of interesting physical effects based on the knowledge of the alloy's composition and crystal structure. In addition, the appearance of a certain physical phenomenon may serve as a reliable projection for the occurrence (or absence) of several others. For example, the presence of GMCE in any of the $Gd_5Si_xGe_{4-x}$ alloys, regardless of composition, is a solid indicator that colossal magnetostriction and giant magnetoresistance also exist near T_C. Multifunctionality is what makes these alloys special and warrants further exploration of effects associated with the magnetostructural transitions. The exceptional compositional and structural diversity of the layered R_5T_4 systems coupled with a unique contribution that every rare earth element brings to the fascinating behavior of this family of intermetallic compounds holds a promise for future discoveries of novel physical effects.

Continuing investigations of these materials are important for transformative advances in energy related materials science and this is true not only because of their potential applications in energy conversion systems of the future. In fact, the intrinsic brittleness of alloys, hysteresis effects, and chemical reactivity of powders are well-known problems that may be limiting the widespread application of R_5T_4-based materials. However, better understanding of the behaviors of these systems should lead to a better control over other materials systems that exhibit structural phase transformations coupled with spin ordering–disordering effects. For example, the realization that the presence of the magnetostructural first-order phase transition is a necessary requirement for the occurrence of GMCE in $Gd_5Si_2Ge_2$ had already triggered rapid development of other intermetallic systems where the coupling of magnetic and structural transformations results in a highly desired strong magnetocaloric effect. $LaFe_{13-x}Si_x$-based materials (Shen et al., 2009), transition metal pnictides (Tegus et al., 2002b), and Ni–Mn–Sn Heusler alloys (Krenke et al., 2005) are a few well-known examples.

The avenues for the fundamental investigations of R_5T_4 systems are open in many directions. The complexity of the crystal structure provides numerous opportunities for the manipulation of the extraordinary behaviors of these compounds. Rapid development of density functional theory and first-principles calculation methods adds an element of control and even prediction to the experimental research and a significant progress in uncovering basic science of R_5T_4 materials is expected to come from the area of first-principles calculation in the near future. Much can be learned from both novel and traditional experimental techniques such as spectroscopy and neutron diffraction; a successful preparation of thin films may increase the technological value of these compounds tremendously.

We believe that some of the information presented in this book chapter will be refined in coming years, which is a good sign indeed, and much will be added to their interesting physics and chemistry. Over the past two decades knowledge gained during the studies of these systems provided a valuable addition to the rich and exciting science of rare earths—yet the story of the layered R_5T_4 systems is far from being complete.

ABBREVIATIONS

AFM	antiferromagnetic
ASA	atomic sphere approximation
B	magnetic induction
C	heat capacity
CEF	crystalline electric field
d	interatomic distance
DOS	density of states
DSC	differential scanning calorimetry
EDS	energy dispersive spectroscopy
EELS	electron energy loss spectroscopy
ESR	electron spin resonance
FC	in-field cooling
FM	ferromagnetic

FP-LAPW	full-potential linear-augmented-plane-wave
GGA	generalized gradient approximation
g_J	Landé factor
GMCE	giant magnetocaloric effect
GMR	giant magnetoresistance
GMS	giant magnetostriction
H	magnetic field strength
H_{CR}	critical magnetic field
HRTEM	high-resolution transmission electron microscopy
J	total electronic angular momentum
K	magnetic anisotropy coefficient
L	orbital electronic angular momentum
LSDA	local spin density approximation
LTE	linear thermal expansion
M	magnetization
MCE	magnetocaloric effect
MFM	magnetic force microscopy
MR	magnetoresistance
MST	magnetostructural transition
P	pressure
PECVD	plasma-enhanced chemical vapor deposition
p_{eff}	effective magnetic moment
PM	paramagnetic
ppm	parts per million
RCP	relative cooling power
RD	reflectance difference (spectra)
RKKY	Ruderman–Kittel–Kasuya–Yosida
S	spin angular momentum, entropy
SAD	selected area diffraction
SANS	small angle neutron scattering
SEM	scanning electron microscopy
SG	space group
SGV	spontaneous generation of voltage
SRC	short-range correlations (magnetic)
T	temperature
TB-LMTO	tight-binding linear-muffin-tin-orbital
T_C	Curie temperature
TEM	transmission electron microscopy
T_G	Griffiths temperature
T_N	Néel temperature
UPS	ultraviolet photoemission spectroscopy
V	unit cell volume
VEC	valence electron concentration
VSM	vibrating sample magnetometry

WSV	Wigner–Seitz volume
XMCD	X-ray magnetic circular dichroism
XPS	X-ray photoemission spectroscopy
XRD	X-ray diffraction
$\boldsymbol{Z}$	number of formula units per unit cell
ZFC	zero-field cooled heating
$\boldsymbol{\Delta S_M}$	magnetic entropy change
$\boldsymbol{\Delta T_{ad}}$	adiabatic temperature change
$\boldsymbol{\kappa}$	thermal diffusivity
$\boldsymbol{\mu_B}$	Bohr magneton
$\boldsymbol{\mu_s}$	saturation magnetic moment
$\boldsymbol{\theta_D}$	Debye temperature
$\boldsymbol{\theta_p}$	paramagnetic Curie–Weiss temperature
$\boldsymbol{\rho}$	electrical resistivity
$\boldsymbol{\omega}$	volume magnetostriction

REFERENCES

Aghababyan, E.V., Harutyunyan, N.P., 2009. J. Contemp. Phys. (Armenian Acad. Sci.) 44, 197.

Aghababyan, E.V., Harutyunyan, N.P., 2012. J. Contemp. Phys. (Armenian Acad. Sci.) 47, 142.

Ahmad, S.N., Shaheen, S.A., 2009. J. Appl. Phys. 106, 064701.

Ahmad, S.N., Akin, Y., Shaheen, S.A., 2005. J. Appl. Phys. 97, 10Q902.

Ahn, K., Tsokol, A.O., Mozharivskyj, Yu., Gschneidner Jr., K.A., Pecharsky, V.K., 2005. Phys. Rev. B 72, 054404.

Ahn, K., Pecharsky, V.K., Gschneidner Jr., K.A., 2007. Phys. Rev. B 76, 014415.

Aksoy, S., Yucel, A., Elerman, Y., Krenke, T., Acet, M., Moya, X., Mañosa, L., 2008. J. Alloys Compd. 460, 94.

Al-Shahery, G.Y.M., McColm, I.J., 1984. J. Less-Common Met. 98, L5.

Altounian, Z., Liu, X.B., 2007. J. Appl. Phys. 101, 09D507.

Alves, C.S., Gama, S., Coelho, A.A., Plaza, E.J.R., Calvalho, A.M.G., Cardoso, L.P., Persiano, A.C., 2004. Mater. Res. 7, 535.

Antonyshyn, I., Zhak, O., Oryshchyn, S., Babizhetsky, V., Hoch, C., Aksel'rud, L., 2009. Z. Naturforsch. 64b, 909.

Araújo, J.P., Pereira, A.M., Braga, M.E., Pinto, R.P., Teixeira, J.M., Correia, F.C., Sousa, J.B., Morellon, L., Algarabel, P.A., Magen, C., Ibarra, M.R., 2005. J. Phys. Condens. Matter 17, 4941.

Arnold, Z., Skorokhod, Y., Kamarad, J., Magen, C., Algarabel, P.A., 2009a. J. Appl. Phys. 105, 07A934.

Arnold, Z., Magen, C., Morellon, L., Algarabel, P.A., Kamarad, J., Ibarra, M.R., Pecharsky, V.K., Gschneidner Jr., K.A., 2009b. Phys. Rev. B 79, 144430.

Basso, V., LoBue, M., Sasso, C.P., Bertotti, G., 2006. J. Appl. Phys. 99, 08K907.

Belo, J.H., Pereira, A.M., Ventura, J., Oliveira, G.N.P., Araújo, J.P., Tavares, P.B., Fernandes, L., Algarabel, P.A., Magen, C., Morellon, L., Ibarra, M.R., 2012a. J. Alloys Compd. 529, 89.

Belo, J.H., Pereira, A.M., Belo, J.H., Pereira, A.M., de la Cruz, C., dos Santos, A.M., Gonçalves, J.N., Amaral, V.S., Morellon, L., Ibarra, M.R., Algarabel, P.A., Magen, C., 2012b. Phys. Rev. B 86, 014403.

Bhattacharyya, A., Giri, S., Majumdar, S., 2009. J. Phys. Condens. Matter 21, 336007.

Bodnar, R.E., Steinfink, H., 1967. Inorg. Chem. 6, 327.

Bondino, F., Brinkman, A., Zangrando, M., Carbone, F., van der Marel, D., Schlagel, D.L., Lograsso, T.A., Gschneidner Jr., K.A., Pecharsky, V.K., Parmigiani, F., 2007. J. Phys. Condens. Matter 19, 186219.

Borzone, G., Borsese, A., Ferro, R., 1982. J. Less-Common Met. 85, 195.

Boulet, P., Weitzer, F., Hiebl, K., Noël, H., 2001. J. Alloys Compd. 315, 75.

Bulanova, M.V., Eremenko, V.N., Petjukh, V.M., Sidorko, V.R., 1998. J. Phase Equil. 19, 136.

Bulanova, M.V., Zheltov, P.N., Meleshevich, K.A., Saltykov, P.A., Effenberg, G., 2002. J. Alloys Compd. 345, 110.

Button, T.W., McColm, I.J., Ward, J.M., 1990. J. Less-Common Met. 159, 205.

Cadogan, J.M., Ryan, D.H., Altounian, Z., Wang, H.B., Swainson, I.P., 2002. J. Phys. Condens. Matter 14, 7191.

Cadogan, J.M., Ryan, D.H., Altounian, Z., Liu, X., Swainson, I.P., 2004. J. Appl. Phys. 95, 7076.

Campoy, J.C.P., Plaza, E.J.R., Carvalho, A.M.G., Coelho, A.A., Gama, S., von Ranke, P.J., 2004. J. Magn. Magn. Mater. 272–276, 2375.

Campoy, J.C.P., Plaza, E.J.R., Nascimento, F.C., Coelho, A.A., Pereira, M.C., Fabris, J.D., Raposo, M.T., Cardoso, L.P., Persiano, A.I.C., Gama, S., 2007. J. Magn. Magn. Mater. 316, 368.

Campoy, J.C.P., dos Santos, A.O., Cardoso, L.P., Paesano Jr., A., Raposo, M.T., Fabris, J.D., 2010. Hyperfine Inter. 195, 191.

Canepa, F., Cirafici, S., Napoletano, M., Cimberle, M.R., Tagliafico, L., Scarpa, F., 2008. J. Phys. D: Appl. Phys. 41, 155004.

Cao, Q., Chumbley, L.S., Qian, Z., 2010. Intermetallics 18, 1021.

Cao, Q., Chumbley, L.S., Mudryk, Y., Zou, M., Pecharsky, V.K., Gschneidner Jr., K.A., 2013. J. Alloys Compd. 556, 127.

Carvalho, A.M.G., Alves, C.S., de Campos, A., Coelho, A.A., Gama, S., Gandra, F.C.G., von Ranke, P.J., Oliveira, N.A., 2005. J. Appl. Phys. 97, 10M320.

Carvalho, A.M.G., Alves, C.S., Colucci, C.C., Bolanho, M.A., Coelho, A.A., Gama, S., Nascimento, F.C., Cardoso, L.P., 2007. J. Alloys Compd. 432, 11.

Carvalho, A.M.G., Coelho, A.A., Gama, S., von Ranke, P.J., Alves, C.S., 2008. J. Appl. Phys. 104, 063915.

Casanova, F., Batlle, X., Labarta, A., Marcos, J., Mañosa, L., Planes, A., 2002a. Phys. Rev. B 66, 212402.

Casanova, F., Batlle, X., Labarta, A., Marcos, J., Mañosa, L., Planes, A., 2002b. Phys. Rev. B 66, 100401(R).

Casanova, F., Batlle, X., Labarta, A., Marcos, J., Mañosa, L., Planes, A., 2003. J. Appl. Phys. 93, 8313.

Casanova, F., Labarta, A., Battle, X., Vives, E., Marcos, J., Mañosa, L., Planes, A., 2004a. Eur. Phys. J. B 40, 427.

Casanova, F., Labarta, A., Battle, X., Marcos, J., Mañosa, L., Planes, A., de Brion, S., 2004b. Phys. Rev. B 69, 104416.

Casanova, F., Labarta, A., Batlle, X., Pérez-Reche, F.J., Vives, E., Mañosa, L., Planes, A., 2005a. Appl. Phys. Lett. 86, 262504.

Casanova, F., Lambarta, A., Batlle, X., 2005b. Phys. Rev. B 72, 172402.

Casanova, F., de Brion, S., Labarta, A., Batlle, X., 2005c. J. Phys. D: Appl. Phys. 38, 3343.

Černý, R., Alami-Yadri, K., 2003. Acta Cryst. E59, i1.

Chattopadhyay, M.K., Manekar, M.A., Pecharsky, A.O., Pecharsky, V.K., Gschneidner Jr., K.A., Moore, J., Perkins, G.K., Bugoslavsky, Y.V., Roy, S.B., Chaddah, P., Cohen, L.F., 2004. Phys. Rev. B 70, 214421.

Chattopadhyay, M.K., Roy, S.B., Morrison, K., Moore, J.D., Perkins, G.K., Cohen, L.F., Gschneidner Jr., K.A., Pecharsky, V.K., 2008. Eur. Phys. Lett. 83, 57006.

Chebotarev, N.T., Beznosikova, A.V., 1976. In: Blank, H., Lindner, R. (Eds.), Plutonium 1975 and Other Actinides. American Elsevier, New York, p. 115.

Chen, X., Chen, Y., Tang, Y., 2011. J. Alloys Compd. 509, 9604.

Chernyshov, A.S., Filippov, D.A., Ilyn, M.I., Levitin, R.Z., Pecharskaya, A.O., Pecharsky, V.K., Gschneidner Jr., K.A., Snegirev, V.V., Tishin, A.M., 2002. Phys. Met. Metallogr. 93, S19.

Chernyshov, A.S., Mudryk, Ya., Pecharsky, V.K., Gschneidner Jr., K.A., 2006. J. Appl. Phys. 99, 08Q102.

Chernyshov, A.S., Mudryk, Ya., Paudyal, D., Pecharsky, V.K., Gschneidner Jr., K.A., Schlagel, D.L., Lograsso, T.A., 2009. Phys. Rev. B 80, 184416.

Choe, W., Pecharsky, V.K., Pecharsky, A.O., Gschneidner Jr., K.A., Young, V.G., Miller, G.J., 2000. Phys. Rev. Lett. 84, 4617.

Choe, W., Miller, G.J., Meyers, J., Chumbley, S., Pecharsky, A.O., 2003a. Chem. Mater. 15, 1413.

Choe, W., Pecharsky, A.O., Wörle, M., Miller, G.J., 2003b. Inorg. Chem. 42, 8223.

Chumbley, L.S., Ugurlu, O., McCallum, R.W., Dennis, K.W., Mudryk, Y., Gschneidner Jr., K.A., Pecharsky, V.K., 2008. Acta Mater. 56, 527.

Correia, F.C., Araújo, J.P., Sousa, J.B., Braga, M.E., Morellon, L., Algarabel, P.A., Ibarra, M.R., 2004. J. Magn. Magn. Mater. 272–276, 2370.

Cromer, D.T., 1977. Acta Cryst. B33, 1993.

Deng, J.Q., Zhuang, Y.H., Li, J.Q., Zhou, K.W., 2007. J. Alloys Compd. 428, 28.

Du, Z.W., Liu, A.S., Shao, B.L., Zhang, Z.Y., Zhang, X.S., Sun, Z.M., 2008. Mater. Char. 59, 1241.

Elbicki, J.M., Zhang, L.Y., Obermeyer, R.T., Wallace, W.E., Sankar, S.G., 1991. J. Appl. Phys. 69, 5571.

Eremenko, V.N., Meleshevich, K.A., Buyanov, Y.I., Martsenyuk, P.S., 1989. Sov. Powder Metall. Met. Ceram. 28, 543.

Eremenko, V.N., Bulanova, M.V., Martsenjuk, P.S., 1992. J. Alloys Compd. 189, 229.

Eremenko, V.N., Listovnichii, V.E., Luzan, S.P., Buyanov, Yu.I., Martsenyuk, P.S., 1995. J. Alloys Compd. 219, 181.

Fornasini, M.L., Merlo, F., 1971. Atti Accad. Naz. Lincei, Cl. Sci. Fis. Mat. Nat., Rend. 50, 186.

Fornasini, M.L., Palenzona, A., Pani, M., 2012. Intermetallics 31, 114.

Franco, V., Blázquez, J.S., Conde, A., 2006. Appl. Phys. Lett. 89, 222512.

Franco, V., Conde, A., Provenzano, V., Shull, R.D., 2010. J. Magn. Magn. Mater. 322, 218.

Franco, V., Blázquez, J.S., Ingale, B., Conde, A., 2012. Annu. Rev. Mater. Res. 42, 305.

Fu, H., Zhang, T., Chen, Y., Tu, M., 2005. J. Chin. Rare Earth Soc. 23, 409.

Fu, H., Zu, X.T., Shen, T.D., 2006. Therm. Acta 445, 53.

Fu, H., Zu, X.T., He, X., He, W.S., Shen, T.D., 2007. J. Alloys Compd. 431, 89.

Fujieda, S., Hasegawa, Y., Fujita, A., Fukamichi, K., 2004. J. Appl. Phys. 95, 2429.

Gama, S., Alves, C.S., Coelho, A.A., Ribeiro, C.A., Persiano, A.I.C., Silva, D., 2004. J. Magn. Magn. Mater. 272–276, 848.

Garlea, V.O., Zarestky, J.L., Jones, C.Y., Lin, L.-L., Schlagel, D.L., Lograsso, T.A., Tsokol, A.O., Pecharsky, V.K., Gschneidner Jr., K.A., Stassis, C., 2005. Phys. Rev. B 72, 104431.

Giovanna do Couto, G., Svitlyk, V., Jafelicci Jr., M., Mozharivskyj, Y., 2011. Solid State Sci. 13, 209.

Givord, F., Lejay, P., Muñoz, A., Schweizer, J., 1992. J. Magn. Magn. Mater. 116, 419.

Gomes, M.B., de Oliveira, N.A., 2008. J. Magn. Magn. Mater. 320, e153.

Gomes, M.B., de Oliveira, N.A., von Ranke, P.J., Troper, A., 2009. J. Magn. Magn. Mater. 321, 4006.

Griffiths, R.B., 1969. Phys. Rev. Lett. 23, 17.

Gschneidner Jr., K.A., Pecharsky, V.K., 1999. J. Appl. Phys. 85 (8), 5365.

Gschneidner Jr., K.A., Pecharsky, V.K., 2000a. Mater. Sci. Eng. A 287, 301.

Gschneidner Jr., K.A., Pecharsky, V.K., 2000b. Annu. Rev. Mater. Sci. 30, 387.

Gschneidner Jr., K.A., Pecharsky, V.K., Gailloux, M.J., Takeya, H., 1996. Adv. Cryog. Eng. 42, 465.

Gschneidner Jr., K.A., Pecharsky, V.K., Pecharsky, A.O., Zimm, C.B., 1999. Mater. Sci. Forum 315–317, 69.

Gschneidner Jr., K.A., Pecharsky, A.O., Pecharsky, V.K., Lograsso, T.A., Schlagel, D.L., 2000a. In: Bautista, R.G., Mishra, B. (Eds.), Rare Earth and Actinides: Science, Technology and Applications IV. TMS, Warrendale, PA, p. 63.

Gschneidner Jr., K.A., Pecharsky, V.K., Pecharsky, A.O., Ivtchenko, V.V., Levin, E.M., 2000b. J. Alloys Compd. 303–304, 214.

Gschneidner Jr., K.A., Pecharsky, V.K., Tsokol, A.O., 2005. Rep. Prog. Phys. 68, 1479.

Gschneidner Jr., K.A., Mudryk, Y., Pecharsky, V.K., 2012. Scripta Mater. 67, 512.

Guimarães, A.O., Soffner, M.E., Mansanares, A.M., Coelho, A.A., Carvalho, A.M.G., Pires, M.J.M., Gama, S., da Silva, E.C., 2009. Phys. Rev. B 80, 134406.

Guimarães, A.O., Soffner, M.E., Mansanares, A.M., Coelho, A.A., Carvalho, A.M.G., Pires, M.J.M., Gama, S., da Silva, E.C., 2010. J. Appl. Phys. 107, 073524.

Guloy, A., Corbett, J.D., 2005. J. Solid State Chem. 178, 1112.

Guttfleisch, O., Willard, M.A., Brück, E., Chen, C.H., Shankar, S.G., Liu, J.P., 2012. Adv. Mater. 23, 821.

Hadimani, R.L., Jiles, D.C., 2010. J. Appl. Phys. 107, 09C501.

Hadimani, R.L., Melikhov, Y., Snyder, J.E., Jiles, D.C., 2008a. J. Appl. Phys. 103, 033906.

Hadimani, R.L., Melikhov, Y., Snyder, J.E., Jiles, D.C., 2008b. J. Magn. Magn. Mater. 320, e696.

Hadimani, R.L., Melikhov, Y., Snyder, J.E., Jiles, D.C., 2009a. IEEE Trans. Magn. 45, 4368.

Hadimani, R.L., Melikhov, Y., Snyder, J.E., Jiles, D.C., 2009b. J. Appl. Phys. 105, 07A927.

Hadimani, R.L., Bartlett, P.A., Melikhov, Y., Snyder, J.E., Jiles, D.C., 2011. J. Magn. Magn. Mater. 323, 532.

Han, M., Paulsen, J.A., Snyder, J.E., Jiles, D.C., Lograsso, T.A., Schlagel, D.L., 2002. IEEE Trans. Magn. 38, 3252.

Han, M., Jiles, D.C., Lee, S.J., Snyder, J.E., Lograsso, T.A., Schlagel, D.L., 2003a. IEEE Trans. Magn. 39, 3151.

Han, M., Jiles, D.C., Snyder, J.E., Lo, C.C.H., Leib, J.S., Paulsen, J.A., Pecharsky, A.O., 2003b. J. Appl. Phys. 93, 8486.

Han, M., Jiles, D.C., Snyder, J.E., Lograsso, T.A., Schlagel, D.L., 2004. J. Appl. Phys. 95, 6945.

Hardy, V., Majumdar, S., Crowe, S.J., Lees, M.R., Paul, D.McK., Hervé, L., Maignan, A., Hébert, S., Martin, C., Yaicle, C., Hervieu, M., Raveau, B., 2004. Phys. Rev. B 69, 020407(R).

Harmon, B.N., Antonov, V.N., 2002. J. Appl. Phys. 91, 9815.

Harmon, B.N., Antonov, V.N., 2003. J. Appl. Phys. 93, 4678.

Haskel, D., Lee, Y.B., Harmon, B.N., Islam, Z., Lang, J.C., Srajer, G., Mudryk, Ya., Gschneidner Jr., K.A., Pecharsky, V.K., 2007. Phys. Rev. Lett. 98, 247205.

Haskel, D., Tseng, Y.C., Souza-Neto, N.M., Lang, J.C., Sinogeikin, S., Mudryk, Ya, Gschneidner Jr., K.A., Pecharsky, V.K., 2008. High Pres. Res. 28, 185.

Her, J.L., Koyama, K., Watanabe, K., Provenzano, V., Fu, A., Shapiro, A.J., Shull, R.D., 2005. Mater. Trans. 46, 2011.

Holm, A.P., Pecharsky, V.K., Gschneidner Jr., K.A., Rink, R., Jirmanus, M.N., 2004. Rev. Sci. Instrum. 75, 1081.

Holtzberg, F., Gambino, R.J., McGuire, T.R., 1967. J. Phys. Chem. Solids 28, 2283.

Huang, H., Pecharsky, A.O., Pecharsky, V.K., Gschneidner Jr., K.A., 2002. Adv. Cryog. Eng. 48, 11.

Huang, J.H., Qiu, J.F., Liu, J.R., Jin, P.Y., Xu, L.Z., Zhang, J.X., 2005. In: First IIF-IIR International Conference on Magnetic Refrigeration at Room Temperature, Montreux, Switzerland, 27–30 September, 2005, p. 179.

Huang, M., Schlagel, D.L., Schmidt, F.A., Lograsso, T.A., 2007. J. Alloys Compd. 441, 94.

Iglesias, J.E., Steinfink, H., 1972. J. Less-Common Met. 26, 45.

Ivtchenko, V.V., Pecharsky, V.K., Gschneidner Jr., K.A., 2000. Adv. Cryog. Eng. 46, 405.

Kamiya, K., Numazawa, T., Koen, T., Okano, T., Matsumoto, K., Nimori, S., 2004. IEEE Trans. Appl. Supercond. 14, 1734.

Kamiya, K., Numazawa, T., Koen, T., Okano, T., Matsumoto, K., 2005. Adv. Cryog. Eng. 50, 11.

Kim, J.H., Kim, S.J., Lee, C.I., Jung, M.A., Oh, H.J., Rhyee, J.-S., Jo, Y., Mitani, H., Miyazaki, H., Kimura, S., Kwon, Y.S., 2010. Phys. Rev. B 81, 104401.

Kotur, B.Ya., Banakh, O.E., Černý, R., Espejel, P., 1997. J. Alloys Compd. 260, 157.

Kozlov, A.Yu., Pavlyuk, V.V., 2004. J. Alloys Compd. 370, 192.

Kozlov, A.Yu., Pavlyuk, V.V., Davydov, V.M., 2004. Intermetallics 12, 151.

Krenke, T., Duman, E., Acet, M., Wasserman, E.F., Moya, X., Mañosa, L., Planes, A., 2005. Nat. Mater. 4, 450.

Kuepferling, M., Basso, V., Sasso, C.P., Giudici, L., Moore, J.D., Morrison, K., Cohen, L.F., 2008. IEEE Trans. Magn. 44, 3233.

Kupsch, A., Levin, A.A., Meyer, D.C., 2005. Cryst. Res. Technol. 1/2, 42.

Lee, S.J., Park, J.M., Snyder, J.E., Jiles, D.C., Schlagel, D.L., Lograsso, T.A., Pecharsky, A.O., Lynch, D.W., 2004. Appl. Phys. Lett. 84, 1865.

Leib, J.S., Lo, C.C.H., Snyder, J.E., Jiles, D.C., Pecharsky, V.K., Schlagel, D.S., Lograsso, T.A., 2002a. IEEE Trans. Magn. 38, 2447.

Leib, J., Snyder, J.E., Lo, C.C.H., Paulsen, J.A., Xi, P., Jiles, D.C., 2002b. J. Appl. Phys. 91, 8852.

Leib, J., Snyder, J.E., Lograsso, T.A., Schlagel, D., Jiles, D.C., 2004. J. Appl. Phys. 95, 6915.

Le Roy, J., Moreau, J.-M., Paccard, D., Parthé, E., 1978. Acta Cryst. B34, 3315.

Levin, E.M., 2009. Phys. Rev. B 80, 144401.

Levin, E.M., Pecharsky, V.K., Gschneidner Jr., K.A., 1999. Phys. Rev. B 60 (11), 7993.

Levin, E.M., Pecharsky, V.K., Gschneidner Jr., K.A., Tomlinson, P., 2000a. J. Magn. Magn. Mater. 210, 181.

Levin, E.M., Pecharsky, V.K., Gschneidner Jr., K.A., 2000b. Phys. Rev. B 62, R14625.

Levin, E.M., Pecharsky, A.O., Pecharsky, V.K., Gschneidner Jr., K.A., 2001a. Phys. Rev. B 63, 064426.

Levin, E.M., Pecharsky, V.K., Gschneidner Jr., K.A., Miller, G.J., 2001b. Phys. Rev. B 64, 235103.

Levin, E.M., Pecharsky, V.K., Gschneidner Jr., K.A., 2001c. Phys. Rev. B 63, 174110.

Levin, E.M., Gschneidner Jr., K.A., Pecharsky, V.K., 2001d. J. Magn. Magn. Mater. 231, 135.

Levin, E.M., Gschneidner Jr., K.A., Pecharsky, V.K., 2002. Phys. Rev. B 65, 214427.

Levin, E.M., Gschneidner Jr., K.A., Lograsso, T.A., Schlagel, D.L., Pecharsky, V.K., 2004. Phys. Rev. B 69, 144428.

Lewis, L.H., Yu, M.H., Welch, D.O., Gambino, R.J., 2004. J. Appl. Phys. 95, 6912.

Li, J.Q., Sun, W.A., Jian, Y.X., Zhuang, Y.H., Huang, W.D., Liang, J.K., 2006. J. Appl. Phys. 100, 073904.

Liu, X.B., Altounian, Z., 2012. J. Alloys Compd. 540, 1.

Liu, Q.L., Rao, G.H., Liang, J.K., 2001a. Rigaku J. 18, 46.

Liu, Q.L., Rao, G.H., Yang, H.F., Liang, J.K., 2001b. J. Alloys Compd. 325, 50.

Liu, G.J., Sun, J.R., Lin, J., Xie, Y.W., Zhao, T.Y., Zhang, H.W., Shen, B.G., 2006. Appl. Phys. Lett. 88, 212505.

Lue, C.S., Sivakumar, K.M., Kuo, Y.K., 2008. J. Phys. Chem. Solids 69, 269.

Luzan, S.P., Listovnichii, V.E., Buyanov, Yu.I., Martsenyuk, P.S., 1996. J. Alloys Compd. 239, 77.

Magen, C., Arnold, Z., Morellon, L., Skorokhod, Y., Algarabel, P.A., Ibarra, M.R., Kamarad, J., 2003a. Phys. Rev. Lett. 91, 207202.

Magen, C., Morellon, L., Algarabel, P.A., Marquina, C., Ibarra, M.R., 2003b. J. Phys. Condens. Matter 15, 2389.

Magen, C., Ritter, C., Morellon, L., Algarabel, P.A., Ibarra, M.R., 2004a. J. Phys. Condens. Matter 16, 7427.

Magen, C., Morellon, L., Algarabel, P.A., Ibarra, M.R., Ritter, C., Pecharsky, A.O., Gschneidner Jr., K.A., Pecharsky, V.K., 2004b. Phys. Rev. B 70, 224429.

Magen, C., Morellon, L., Algarabel, P.A., Ibarra, M.R., Arnold, Z., Kamarad, J., Lograsso, T.A., Schlagel, D.L., Pecharsky, V.K., Tsokol, A.O., Gschneidner Jr., K.A., 2005. Phys. Rev. B 72, 024416.

Magen, C., Algarabel, P.A., Morellon, L., Araújo, J.P., Ritter, C., Ibarra, M.R., Pereira, A.M., Sousa, J.B., 2006a. Phys. Rev. Lett. 96, 167201.

Magen, C., Morellon, L., Arnold, Z., Algarabel, P.A., Ritter, C., Ibarra, M.R., Kamarad, J., Tsokol, A.O., Gschneidner Jr., K.A., Pecharsky, V.K., 2006b. Phys. Rev. B 74, 134427.

Magen, C., Ritter, C., Morellon, L., Algarabel, P.A., Ibarra, M.R., Tsokol, A.O., Gschneidner Jr., K.A., Pecharsky, V.K., 2006c. Phys. Rev. B 74, 174413.

Malik, S.K., de Almeida, R.L., Quezado, S., Morozkin, A.V., Nirmala, R., 2009. Physica B 404, 3063.

Manekar, M., Chattopadhyay, M.K., Kaul, R., Pecharsky, V.K., Gschneidner Jr., K.A., 2006. J. Phys. Condens. Matter 18, 6017.

Manivel Raja, M., Gopalan, R., Rajkumar, D.M., Balamuralikrishnan, R., Chandrasekaran, V., Suresh, K.G., Hono, K., 2008. J. Phys. D: Appl. Phys. 41, 055008.

Marcano, N., Algarabel, P.A., Rodríguez-Fernández, J., Magén, C., Morellón, L., Singh, N.K., Schlagel, D.L., Gschneidner Jr., K.A., Pecharsky, V.K., Ibarra, M.R., 2012. Phys. Rev. B 85, 024408.

Marcos, J., Casanova, F., Batlle, X., Labarta, A., Planes, A., Mañosa, L., 2003. Rev. Sci. Instrum. 74, 4768.

Matsumoto, K., Okano, T., Kouen, T., Abe, S., Numazawa, T., Kamiya, K., Nimori, S., 2004. IEEE Trans. Appl. Supercond. 14, 1738.

Meyers, J., Chumbley, S., Choe, W., Miller, G.J., 2002a. Phys. Rev. B 66, 012106.

Meyers, J.S., Chumbley, L.S., Laabs, F., Pecharsky, A.O., 2002b. Scripta Mater. 47, 509.

Meyers, J.S., Chumbley, S., Laabs, F., Pecharsky, A.O., 2003. Acta Mater. 51, 61.

Miller, G.J., 2006. Chem. Soc. Rev. 35, 799.

Misra, S., Miller, G.J., 2006. J. Solid State Chem. 179, 2290.

Misra, S., Miller, G.J., 2008. J. Am. Chem. Soc. 130, 13900.

Misra, S., Poweleit, E.T., Miller, G.J., 2009a. Z. Anorg. Allg. Chem. 635, 889.

Misra, S., Mozharivskyj, Y., Tsokol, A.O., Schlagel, D.L., Lograsso, T.A., Miller, G.J., 2009b. J. Solid State Chem. 182, 3031.

Moore, J.D., Perkins, G.K., Bugoslavsky, Y., Chattopadhyay, M.K., Roy, S.B., Chaddah, P., Pecharsky, V.K., Gschneidner Jr., K.A., Cohen, L.F., 2006. Appl. Phys. Lett. 88, 072501.

Moore, J.D., Perkins, G.K., Morrison, K., Ghivelder, L., Chattopadhyay, M.K., Roy, S.B., Chaddah, P., Gschneidner Jr., K.A., Pecharsky, V.K., Cohen, L.F., 2008. J. Phys. Condens. Matter 20, 465212.

Moore, J.D., Morrison, K., Perkins, G.K., Schlagel, D.L., Lograsso, T.A., Gschneidner Jr., K.A., Pecharsky, V.K., Cohen, L.F., 2009. Adv. Mater. 21, 3780.

Morellon, L., Algarabel, P.A., Ibarra, M.R., Blasco, J., García-Landa, B., Arnold, Z., Albertini, F., 1998a. Phys. Rev. B 58 (22), R14721.

Morellon, L., Stankiewicz, J., García-Landa, B., Algarabel, P.A., Ibarra, M.R., 1998b. Appl. Phys. Lett. 73 (23), 3462.

Morellon, L., Blasco, J., Algarabel, P.A., Ibarra, M.R., 2000. Phys. Rev. B 62, 1022.

Morellon, L., Algarabel, P.A., Magen, C., Ibarra, M.R., 2001a. J. Magn. Magn. Mater. 237, 119.

Morellon, L., Magen, C., Algarabel, P.A., Ibarra, M.R., Ritter, C., 2001b. Appl. Phys. Lett. 79, 1318.

Morellon, L., Ritter, C., Magen, C., Algarabel, P.A., Ibarra, M.R., 2003. Phys. Rev. B 68, 024417.

Morellon, L., Arnold, Z., Algarabel, P.A., Magen, C., Ibarra, M.R., Skorokhod, Y., 2004a. J. Phys. Condens. Matter 16, 1623.

Morellon, L., Arnold, Z., Magen, C., Ritter, C., Prokhnenko, O., Skorokhod, Y., Algarabel, P.A., Ibarra, M.R., Kamarad, J., 2004b. Phys. Rev. Lett. 93, 137201.

Mozharivskyj, Y., Choe, W., Pecharsky, A.O., Miller, G.J., 2003. J. Am. Chem. Soc. 125, 15183.

Mozharivskyj, Y., Pecharsky, A.O., Pecharsky, V.K., Miller, G.J., Gschneidner Jr., K.A., 2004. Phys. Rev. B 69, 144102.

Mozharivskyj, Y., Pecharsky, A.O., Pecharsky, V.K., Miller, G.J., 2005. J. Am. Chem. Soc. 127, 317.

Mozharivskyj, Yu., Tsokol, A.O., Miller, G.J., 2006. Z. Kristallogr. 221, 493.

Mudryk, Ya., Holm, A.P., Gschneidner Jr., K.A., Pecharsky, V.K., 2005a. Phys. Rev. B 72, 064442.

Mudryk, Ya., Lee, Y., Vogt, T., Gschneidner Jr., K.A., Pecharsky, V.K., 2005b. Phys. Rev. B 71, 174104.

Mudryk, Ya., Paudyal, D., Pecharsky, V.K., Gschneidner Jr., K.A., 2008. Phys. Rev. B 77, 024408.

Mudryk, Y., Paudyal, D., Pecharsky, V.K., Gschneidner Jr., K.A., Misra, S., Miller, G.J., 2010. Phys. Rev. Lett. 105, 066401.

Mudryk, Y., Pecharsky, V.K., Gschneidner Jr., K.A., 2011. Z. Anorg. Allg. Chem. 637, 1948.

Mudryk, Ya., Singh, N.K., Pecharsky, V.K., Schlagel, D.L., Lograsso, T.A., Gschneidner Jr., K.A., 2012. Phys. Rev. B 85, 094432.

Mudryk, Y., Pecharsky, V.K., Gschneidner Jr., K.A., 2013. J. Appl. Phys. 113, 17E104.

Nazih, M., de Visser, A., Zhang, L., Tegus, O., Brück, E., 2003. Solid State Commun. 126, 255.

Nersessian, N., Or, S.W., Carman, G.P., Choe, W., Radousky, H.B., Pecharsky, V.K., Pecharsky, A.O., 2003. In: Lagoudas, D.C. (Ed.), Proc. of SPIE, vol. 5053. SPIE, Bellingham, WA, USA, p. 25.

Nersessian, N., Or, S.W., Carman, G.P., McCall, S.K., Choe, W., Radousky, H.B., McElfresh, M.W., Pecharsky, V.K., Pecharsky, A.O., 2004. Appl. Phys. Lett. 84, 4801.

Nirmala, R., Sankaranarayanan, V., Sethupathi, K., Morozkin, A.V., Cai, Q., Chu, Z., Yang, J.B., Yelon, W.B., Malik, S.K., 2005. J. Appl. Phys. 97, 10M314.

Nirmala, R., Sankaranarayanan, V., Sethupathi, K., Morozkin, A.V., Yamamoto, Y., Hori, H., 2006. Physica B 373, 120.

Nirmala, R., Morozkin, A.V., Malik, S.K., 2007a. Phys. Rev. B 75, 094419.

Nirmala, R., Mudryk, Ya., Pecharsky, V.K., Gchneidner Jr., K.A., 2007b. Phys. Rev. B 76, 104417.

Nirmala, R., Kundaliya, D.C., Shinde, S.R., Joshi, A.G., Morozkin, A.V., Malik, S.K., 2007c. J. Appl. Phys. 101, 123901.

Nirmala, R., Sankaranarayanan, V., Sethupathi, K., Morozkin, A.V., Joshi, A.G., Malik, S.K., 2007d. J. Magn. Magn. Mater. 309, 212.

Nirmala, R., Morozkin, A.V., Lamsal, J., Yelon, W.B., Malik, S.K., 2010. J. Appl. Phys. 107, 09E308.

Nirmala, R., Paudyal, D., Pecharsky, V.K., Gschneidner Jr., K.A., Nigam, A.K., 2011. J. Appl. Phys. 109, 07A923.

Nóbrega, E.P., de Oliveira, N.A., von Ranke, P.J., Troper, A., 2005. Phys. Rev. B 72, 134426.

Ouyang, Z.W., 2010. J. Appl. Phys. 108, 033907.

Ouyang, Z.W., Pecharsky, V.K., Gschneidner Jr., K.A., Schlagel, D.L., Lograsso, T.A., 2006a. Phys. Rev. B 74, 024401.

Ouyang, Z.W., Pecharsky, V.K., Gschneidner Jr., K.A., Schlagel, D.L., Lograsso, T.A., 2006b. Phys. Rev. B 74, 094404.

Ouyang, Z.W., Pecharsky, V.K., Gschneidner Jr., K.A., Schlagel, D.L., Lograsso, T.A., 2007a. Phys. Rev. B 76, 134406.

Ouyang, Z.W., Pecharsky, V.K., Gschneidner Jr., K.A., Schlagel, D.L., Lograsso, T.A., 2007b. Phys. Rev. B 76, 134415.

Ouyang, Z.W., Nojiri, H., Yoshii, S., Rao, G.H., Wang, Y.C., Pecharsky, V.K., Gschneidner Jr., K.A., 2008. Phys. Rev. B 77, 184426.

Ouyang, Z.W., Nojiri, H., Yoshii, S., Rao, G.H., Wang, Y.C., 2009. Phys. Rev. B 80, 054401.

Ouyang, Z.W., Xia, Z.C., Wang, Y.C., Rao, G.H., 2011. J. Appl. Phys. 109, 023901.

Palacios, E., Wang, G.F., Burriel, R., Provenzano, V., Shull, R.D., 2010a. J. Phys. Confer. Series 200, 092011.

Palacios, E., Rodríguez-Velamazán, J.A., Wang, G.F., Burriel, R., Cuello, G., Rodríguez-Carvajal, J., 2010b. J. Phys. Condens. Matter 22, 446003.

Palenzona, A., Cirafici, S., 1976. J. Less-Common. Met. 46, 321.

Palenzona, A., Manfrinetti, P., Brutti, S., Balducci, G., 2003. J. Alloys Compd. 348, 100.

Pani, M., Palenzona, A., 2003. J. Alloys Compd. 360, 151.

Park, J.M., Lynch, D.W., Lee, S.J., Schlagel, D.L., Lograsso, T.A., Tsokol, A.O., Snyder, J.E., Jiles, D.C., 2006. Phys. Rev. B 73, 035110.

Parviainen, S., 1980. Phys. Stat. Sol. 60, K13.

Paudyal, D., Pecharsky, V.K., Gschneidner Jr., K.A., Harmon, B.N., 2006. Phys. Rev. B 73, 144406.

Paudyal, D., Pecharsky, V.K., Gschneidner Jr., K.A., Harmon, B.N., 2007. Phys. Rev. B 75, 094427.

Paudyal, D., Pecharsky, V.K., Gschneidner Jr., K.A., 2008. J. Phys. Condens. Matter 20, 235235.

Paudyal, D., Mudryk, Ya., Pecharsky, V.K., Gschneidner Jr., K.A., 2010a. Phys. Rev. B 82, 144413.

Paudyal, D., Mudryk, Y., Pecharsky, V.K., Misra, S., Miller, G.J., Gschneidner Jr., K.A., 2010b. J. Appl. Phys. 107, 09A908.

Paudyal, D., Mudryk, Y., Pecharsky, V.K., Gschneidner Jr., K.A., 2011. Phys. Rev. B 84, 014421.

Pavlyuk, V.V., Bodak, O.I., Zavodnik, V.E., 1990. Dopov. Akad. Nauk. Ukr. SSR B 29.

Pecharsky, V.K., Gschneidner Jr., K.A., 1997a. Appl. Phys. Lett. 70 (24), 3299.

Pecharsky, V.K., Gschneidner Jr., K.A., 1997b. Phys. Rev. Lett. 78 (23), 4494.

Pecharsky, V.K., Gschneidner Jr., K.A., 1997c. J. Magn. Magn. Mater. 167, L179.

Pecharsky, V.K., Gschneidner Jr., K.A., 1997d. J. Alloys Compd. 260, 98.

Pecharsky, V.K., Gschneidner Jr., K.A., 1998. Adv. Cryog. Eng. 43, 1729.

Pecharsky, V.K., Gschneidner Jr., K.A., 2001. Adv. Mater. 13, 683.

Pecharsky, V.K., Gschneidner Jr., K.A., 2005. In: Planes, A., Mańosa, L., Saxena, A. (Eds.), Magnetism and Structure in Functional Materials. Springler-Verlag, Berlin, p. 199.

Pecharsky, V.K., Gschneidner Jr., K.A., 2007. Pure Appl. Chem. 79, 1383.

Pecharsky, A.O., Gschneidner Jr., K.A., Pecharsky, V.K., Schindler, C.E., 2002a. J. Alloys Compd. 338, 126.

Pecharsky, V.K., Pecharsky, A.O., Gschneidner Jr., K.A., 2002b. J. Alloys Compd. 344, 362.

Pecharsky, V.K., Holm, A.P., Gschneidner Jr., K.A., Rink, R., 2003a. Phys. Rev. Lett. 91, 197204.

Pecharsky, A.O., Gschneidner Jr., K.A., Pecharsky, V.K., 2003b. J. Appl. Phys. 93, 4722.

Pecharsky, A.O., Gschneidner Jr., K.A., Pecharsky, V.K., 2003c. J. Magn. Magn. Mater. 267, 60.

Pecharsky, V.K., Samolyuk, G.D., Antropov, V.P., Pecharsky, A.O., Gschneidner Jr., K.A., 2003d. J. Solid State Chem. 171, 57.

Pecharsky, V.K., Pecharsky, A.O., Mozharivskyj, Y., Gschneidner Jr., K.A., Miller, G.J., 2003e. Phys. Rev. Lett. 91, 207205.

Pecharsky, A.O., Pecharsky, V.K., Gschneidner Jr., K.A., 2004a. J. Alloys Compd. 379, 127.

Pecharsky, A.O., Gschneidner Jr., K.A., Pecharsky, V.K., Schlagel, D.L., Lograsso, T.A., 2004b. Phys. Rev. B 70, 144419.

Pecharsky, V.K., Gschneidner Jr., K.A., Mudryk, Ya., Paudyal, D., 2009. J. Magn. Magn. Mater. 321, 3541.

Pereira, A.M., Magen, C., Araújo, J.P., Algarabel, P.A., Morellon, L., Braga, M.E., Pinto, R.P., Ibarra, M.R., Sousa, J.B., 2007. J. Magn. Magn. Mater. 310, e580.

Pereira, A.M., Magen, C., Braga, M.E., Pinto, R.P., Fermento, R., Algarabel, P.A., Morellon, L., Ibarra, M.R., Araújo, J.P., Sousa, J.B., 2008a. J. Non-Cryst. Solids 354, 5298.

Pereira, A.M., Sousa, J.B., Araujo, J.P., Magen, C., Algarabel, P.A., Morellon, L., Marquina, C., Ibarra, M.R., 2008b. Phys. Rev. B 77, 134404.

Pereira, A.M., Morellon, L., Magen, C., Ventura, J., Algarabel, P.A., Ibarra, M.R., Sousa, J.B., Araújo, J.P., 2010. Phys. Rev. B 82, 172406.

Pereira, A.M., dos Santos, A.M., Magen, C., Sousa, J.B., Algarabel, P.A., Ren, Y., Ritter, C., Morellon, L., Ibarra, M.R., Araújo, J.P., 2011. Appl. Phys. Lett. 98, 122501.

Pérez, N., Casanova, F., Bartolomé, F., García, L.M., Labarta, A., Batlle, X., 2011. Phys. Rev. B 83, 184411.

Pérez-Reche, F.-J., Casanova, F., Vives, E., Mañosa, L., Planes, A., Marcos, J., Batlle, X., Labarta, A., 2006. Phys. Rev. B 73, 014110.

Perkins, G.K., Moore, J.D., Chattopadhyay, M.K., Roy, S.B., Chaddah, P., Pecharsky, V.K., Gschneidner Jr., K.A., Cohen, L., 2007. J. Phys. Condens. Matter 19, 176213.

Pfeifer, H.U., Schubert, K., 1966. Z. Metallkd. 57, 884.

Pinguet, N., Weitzer, F., Hiebl, K., Schuster, J.C., Noël, H., 2003. J. Alloys Compd. 348, 1.

Pinto, R.P., Sousa, J.B., Correia, F.C., Araújo, J.P., Braga, M.E., Pereira, A.M., Morellon, L., Algarabel, P.A., Magen, C., Ibarra, M.R., 2005. J. Magn. Magn. Mater. 290–291, 661.

Pires, M.J.M., Carvalho, A.M.G., Gama, S., da Silva, E.C., Coelho, A.A., Mansanares, A.M., 2005. Phys. Rev. B 72, 224435.

Pires, M.J.M., Mansanares, A.M., da Silva, E.C., Carvalho, A.M.G., Gama, S., Coelho, A.A., 2006. Phys. Rev. B 73, 144404.

Podmiljšak, B., McGuiness, P.J., Škulj, I., Markoli, B., Dražič, G., Kobe, S., 2007. In: Second IIF-IIR International Conference on Magnetic Refrigeration at Room Temperature, Potoroz, Slovenia, 11–13 April 2007, p. 145.

Podmiljšak, B., Škulj, I., Markoli, B., McGuiness, P.J., Žužek Rožman, K., Kobe, S., 2008. IEEE Trans. Magn. 44, 4529.

Podmiljšak, B., Škulj, I., Markoli, B., Žužek Rožman, K., McGuiness, P.J., Kobe, S., 2009a. J. Magn. Magn. Mater. 321, 300.

Podmiljšak, B., McGuiness, P.J., Mattern, N., Ehrenberg, H., Kobe, S., 2009b. IEEE Trans. Magn. 45, 4364.

Podmiljšak, B., McGuiness, P.J., Miklavič, B., Žužek Rožman, K., Kobe, S., 2009c. J. Appl. Phys. 105, 07A941.

Prabahar, K., Raj Kumar, D.M., Manivel Raja, M., Chandrasekaran, V., 2011. J. Magn. Magn. Mater. 323, 1755.

Prahabar, K., Raj Kumar, D.M., Manivel Raja, M., Palit, M., Chandrasekaran, V., 2010. Mater. Sci. Eng. B 172, 294.

Prokleška, J., Vejpravová, J., Daniš, S., Sechovský, V., 2006. Physica B 378–380, 1111.

Prokleška, J., Vejpravová, J., Sechovský, V., 2007. J. Magn. Magn. Mater. 316, 313.

Provenzano, V., Shapiro, A.J., Shull, R.D., 2004. Nature 429, 853.

Qian, Z., Chumbley, L.S., Misra, S., Miller, G., Pecharsky, V.K., Gschneidner Jr., K.A., Ahn, K., Chernyshov, A.S., Singh, N.K., 2009. Acta Mater. 57, 3374.

Raj Kumar, D.M., Manivel Raja, M., Goplan, R., Balamuralikrishnan, R., Singh, A.K., Chandrasekaran, V., 2008. J. Alloys Compd. 461, 14.

Raj Kumar, D.M., Manivel Raja, M., Gopalan, R., Sambasiva Rao, A., Chandrasekaran, V., 2009. J. Magn. Magn. Mater. 321, 1300.

Raj Kumar, D.M., Manivel Raja, M., Prabahar, K., Chandrasekaran, V., Poddar, A., Ranganathan, R., Suresh, K.G., 2011. J. Magn. Magn. Mater. 323, 1750.

Rajkumar, D.M., Manivel Raja, M., Goplan, R., Chandrasekaran, V., 2008. J. Magn. Magn. Mater. 320, 1479.

Rajkumar, D.M., Manivel Raja, M., Gopalan, R., Singh, A.K., Chandrasekaran, V., Suresh, K.G., 2010. Intermetallics 18, 518.

Rao, G.H., 2000. J. Phys. Condens. Matter 12, L93.

Rao, G.H., Huang, Q., Yang, H.F., Ho, D.L., Lynn, J.W., Liang, J.K., 2004. Phys. Rev. B 69, 094430.

Rhee, J.Y., 2003. J. Kor. Phys. Soc. 43, 621.

Ring, A.P., Ziebler, H.L., Lograsso, T., Schlagel, D., Snyder, J.E., Jiles, D.C., 2006. J. Appl. Phys. 99, 08R104.

Ring, A.P., Lograsso, T., Schlagel, D., Snyder, J.E., Jiles, D.C., 2007. J. Appl. Phys. 101, 09C527.

Ritter, C., Morellon, L., Algarabel, P.A., Magen, C., Ibarra, M.R., 2002. Phys. Rev. B 65, 094405.

Ritter, C., Magen, C., Morellon, L., Algarabel, P.A., Ibarra, M.R., Pecharsky, V.K., Tsokol, A.O., Gschneidner Jr., K.A., 2006. J. Phys. Condens. Matter 18, 3937.

Ritter, C., Magen, C., Morellon, L., Algarabel, P.A., Ibarra, M.R., Pereira, A.M., Araujo, J.P., Sousa, J.B., 2009. Phys. Rev. B 80, 104427.

Roy, S.B., Chattopadhyay, M.K., Chaddah, P., Moore, J.D., Perkins, G.K., Cohen, L.F., Gschneidner Jr., K.A., Pecharsky, V.K., 2006. Phys. Rev. B 74, 012403.

Roy, S.B., Chattopadhyay, M.K., Banerjee, A., Chaddah, P., Moore, J.D., Perkins, G.K., Cohen, L.F., Gschneidner Jr., K.A., Pecharsky, V.K., 2007. Phys. Rev. B 75, 184410.

Ryan, D.H., Elouneg-Jamróz, M., van Lierop, J., Altounian, Z., Wang, H.B., 2003. Phys. Rev. Lett. 90, 117202.

Ryan, D.H., Cadogan, J.M., Cranswick, L.M.D., Gschneidner Jr., K.A., Pecharsky, V.K., Mudryk, Y., 2010. Phys. Rev. B 82, 224405.

Sambandam, S.N., Bethala, B., Sood, D.K., Bhansali, S., 2005. Surf. Coat. Technol. 200, 1335.

Samolyuk, G.D., Antropov, V.P., 2002. J. Appl. Phys. 91, 8540.

Samolyuk, G.D., Antropov, V.P., 2003. J. Appl. Phys. 93, 6882.

Samolyuk, G.D., Antropov, V.P., 2005. J. Appl. Phys. 97, 10A310.

Schmidt, F.A., McMasters, O.D., 1968. J. Less-Common Met. 15, 1.

Schmidt, F.A., McMasters, O.D., Carlson, O.N., 1972. J. Less-Common Met. 26, 53.

Schobinger-Papamantellos, P., Niggli, A., 1979. J. Phys. 40, C5.

Schobinger-Papamantellos, P., Niggli, A., 1981. J. Phys. Chem. Solids 42, 583.

Sharath Chandra, L.S., Pandya, S., Vishwakarma, P.N., Jain, D., Ganesan, V., 2009. Phys. Rev. B 79, 052402.

Shen, B.G., Sun, J.R., Hu, F.X., Zhang, H.W., Cheng, Z.H., 2009. Adv. Mater. 21, 4545.

Shimotomai, S., Ido, H., 2006. J. Appl. Phys. 99, 08Q109.

Shull, R.D., Provenzano, V., Shapiro, A.J., Fu, A., Lufaso, M.W., Karapetrova, J., Kletetschka, G., Mikula, V., 2006. J. Appl. Phys. 99, 08K908.

Singh, N.K., Pecharsky, V.K., Gschneidner Jr., K.A., 2008. Phys. Rev. B 77, 054414.

Singh, N.K., Paudyal, D., Mudryk, Y., Pecharsky, V.K., Gschneidner Jr., K.A., 2009. Phys. Rev. B 79, 094115.

Singh, N.K., Paudyal, D., Pecharsky, V.K., Gschneidner Jr., K.A., 2010a. J. Appl. Phys. 107, 09A921.

Singh, N.K., Paudyal, D., Mudryk, Ya., Pecharsky, V.K., Gschneidner Jr., K.A., 2010b. Phys. Rev. B 81, 184414.

Skorek, G., Deniszczyk, J., Szade, J., 2002. J. Phys. Condens. Matter 14, 7273.

Smith, G.S., Tharp, A.G., Johnson, Q., 1966. Nature 210, 1148.

Smith, G.S., Johnson, Q., Tharp, A.G., 1967a. Acta Cryst. 22, 269.

Smith, G.S., Tharp, A.G., Johnson, Q., 1967b. Acta Cryst. 22, 940.

Smith, A., Bahl, C.R.H., Bjork, R., Engelbrecht, K., Nielsen, K.K., Pryds, N., 2012. Adv. Energy Mater. 2, 1288.

Sousa, J.B., Braga, M.E., Correia, F.C., Carpintero, F., Morellon, L., Algarabel, P.A., Ibarra, R., 2002. J. Appl. Phys. 91, 4457.

Sousa, J.B., Braga, M.E., Correia, F.C., Carpinteiro, F., Morellon, L., Algarabel, P.A., Ibarra, M.R., 2003. Phys. Rev. B 67, 134416.

Sousa, J.B., Pereira, A.M., Correia, F.C., Teixeira, J.M., Araújo, J.P., Pinto, R.P., Braga, M.E., Morellon, L., Algarabel, P.A., Magen, C., Ibarra, M.R., 2005. J. Phys. Condens. Matter 17, 2461.

Spichkin, Y.I., Pecharsky, V.K., Gschneidner Jr., K.A., 2001. J. Appl. Phys. 89, 1738.

Stankiewicz, J., Morellon, L., Algarabel, P.A., Ibarra, M.R., 2000. Phys. Rev. B 61, 12651.

Stepeń-Damm, J., Zaplatynsky, O.V., Prots', Yu.M., Slamakha, P.S., Bodak, O.I., 1995. J. Alloys Compd. 221, 91.

Stevens, K.W.H., 1952. Proc. Phys. Soc. LXV A65, 209.

Svitelsky, O., Suslov, A., Schlagel, D.L., Lograsso, T.A., Gschneidner Jr., K.A., Pecharsky, V.K., 2006. Phys. Rev. B 74, 184105.

Svitlyk, V., Mozharivskyj, Y., 2009. Solid State Sci. 11, 1941.

Svitlyk, V., Campbell, B.J., Mozharivskyj, Y., 2009a. Inorg. Chem. 48, 10364.

Svitlyk, V., Miller, G.J., Mozharivskyj, Y., 2009b. J. Am. Chem. Soc. 131, 2367.

Svitlyk, V., Cheung, Y.Y.J., Mozharivskyj, Y., 2010. J. Magn. Magn. Mater. 322, 2558.

Szade, J., Neumann, M., 1999. J. Phys. Condens. Matter 11, 3887.

Szade, J., Skorek, G., 1999. J. Magn. Magn. Mater. 196–197, 699.

Szade, J., Skorek, G., Winiarski, A., 1999. J. Cryst. Growth 205, 289.

Szade, J., Skorek, G., Neumann, M., Schneider, B., Fangmeyer, F., Matteucci, M., Paolucci, G., Goldoni, A., 2002. Surf. Sci. 497, 29.

Tan, L., Kreyssig, A., Kim, J.W., Goldman, A.I., McQueeney, R.J., Wermeille, D., Sieve, B., Lograsso, T.A., Schlagel, D.L., Budko, S.L., Pecharsky, V.K., Gschneidner Jr., K.A., 2005. Phys. Rev. B 71, 214408.

Tan, L., Kreyssig, A., Nandi, S., Jia, S., Lee, Y.B., Lang, J.C., Islam, Z., Lograsso, T.A., Schlagel, D.L., Pecharsky, V.K., Gschneidner Jr., K.A., Canfield, P.C., Harmon, B.N., McQueeney, R.J., Goldman, A.I., 2008. Phys. Rev. B 77, 064425.

Tang, H., Pecharsky, A.O., Schlagel, D.L., Lograsso, T.A., Pecharsky, V.K., Gschneidner Jr., K.A., 2003. J. Appl. Phys. 93, 8298.

Tang, H., Pecharsky, V.K., Samolyuk, G.D., Zou, M., Gschneidner Jr., K.A., Antropov, V.P., Schlagel, D.L., Lograsso, T.A., 2004a. Phys. Rev. Lett. 93, 237203.

Tang, H., Pecharsky, V.K., Gschneidner Jr., K.A., Pecharsky, A.O., 2004b. Phys. Rev. B 69, 064410.

Teatum, E.T., Gschneidner, K.A., Waber, J.T., 1968. Los Alamos National Laboratory Report No. LA-4003. Clearinghouse for Federal Scientific and Technical Information, Springfield, VA.

Tegus, O., Brück, E., Zhang, L., Dagula, W., Buschow, K.H.J., de Boer, F.R., 2002a. Physica B 319, 174.

Tegus, O., Brück, E., Buschow, K.H.J., de Boer, F.R., 2002b. Nature 415, 150.

Tegus, O., Dagula, O., Brück, E., Zhang, L., de Boer, F.R., Buschow, K.H.J., 2002c. J. Appl. Phys. 91, 8534.

Teng, B., Tu, M., Chen, Y., Tang, J., 2002. J. Phys. Condens. Matter 14, 6501.

Thuy, N.P., 2002. Solid State Sci. Technol. (Malaysia) 10, 1.

Thuy, N.P., Tai, L.T., Hien, N.T., Nong, N.V., Vinh, T.Q., Thang, P.D., Nguyen, T.P., Molinié, P., 2001. In: APPC 2000: Proceedings of the 8th Asia-Pacific Physics Conference, Taipei, Taiwan, 7–10 August 2000, 354–359.

Thuy, N.P., Nong, N.V., Hien, N.T., Tai, L.T., Vinh, T.Q., Thang, P.D., Brück, E., 2002. J. Magn. Magn. Mater. 242–245, 841.

Thuy, N.P., Chen, Y.Y., Yao, Y.D., Wang, C.R., Lin, S.H., Ho, J.C., Nguyen, T.P., Thang, P.D., Klaasse, J.C.P., Hien, N.T., Tai, L.T., 2003. J. Magn. Magn. Mater. 262, 432.

Tian, W., Kreyssig, A., Zarestky, J.L., Tan, L., Nandi, S., Goldman, A.I., Lograsso, T.A., Schlagel, D.L., Gschneidner Jr., K.A., Pecharsky, V.K., McQueeney, R.J., 2009. Phys. Rev. B 80, 134422.

Tobash, P.H., Bobev, S., 2006. J. Am. Chem. Soc. 128, 3532.

Tobash, P.H., Bobev, S., Thompson, J.D., Sarrao, J.L., 2009. Inorg. Chem. 48, 6641.

Tocado, L., Palacios, E., Burriel, R., 2005. J. Magn. Magn. Mater. 290–291, 719.

Trevizoli, P.V., Alves, C.S., Mendes, M.A.B., Carvalho, A.M.G., Gama, S., 2008. J. Magn. Magn. Mater. 320, 1582.

Tseng, Y.C., Haskel, D., Lang, Y.C., Sinogeikin, S., Mudryk, Ya., Pecharsky, V.K., Gschneidner Jr., K.A., 2007. Phys. Rev. B 76, 014411.

Tseng, Y.C., Haskel, D., Souza-Neto, N.M., Mudryk, Ya., Pecharsky, V.K., Gschneidner Jr., K.A., 2008a. Phys. Rev. B 78, 214433.

Tseng, Y.C., Haskel, D., Lang, J.C., Mudryk, Ya., Pecharsky, V.K., Gschneidner Jr., K.A., 2008b. J. Appl. Phys. 103, 07B301.

Tseng, Y.-C., Ma, H.-J., Yang, C.-Y., Mudryk, Y., Pecharsky, V.K., Gschneidner Jr., K.A., Souza-Neto, N.M., Haskel, D., 2011. Phys. Rev. B 83, 104419.

Tsutaoka, T., Tokunaga, T., Tanaka, A., Narumi, Y., Kindo, K., 2010. J. Phys. Confer. Ser. 200, 1.

Tyszka, B., Szade, J., Skorek, G., Neumann, M., 2005. J. Alloys Compd. 400, 51.

Ugurlu, O., Chumbley, L.S., Schlagel, D.L., Lograsso, T.A., 2005a. Acta Mater. 53, 3525.

Ugurlu, O., Chumbley, L.S., Schlagel, D.L., Lograsso, T.A., Tsokol, A.O., 2005b. Scripta Mater. 53, 373.

Ugurlu, O., Chumbley, L.S., Schlagel, D.L., Lograsso, T.A., 2006a. Acta Mater. 54, 1211.

Ugurlu, O., Chumbley, L.S., Fisher, C.R., 2006b. J. Mater. Res. 21, 2669.

Van Vleck, J.H., 1932. The Theory of Electric and Magnetic Susceptibilities. Oxford University Press, London.

Vejpravová, J., Prokleška, J., Daniš, S., Sechovský, V., 2006. Physica B 378–380, 784.

Velez, S., Hernandez, J.M., Fernandez, A., Macià, F., Magen, C., Algarabel, P.A., Tejada, J., Chudnovsky, E.M., 2010. Phys. Rev. B 81, 064437.

Vélez, S., Hernandez, J.M., García-Santiago, A., Tejada, J., Pecharsky, V.K., Gschneidner Jr., K.A., Schlagel, D.L., Lograsso, T.A., Santos, P.V., 2012. Phys. Rev. B 85, 054432.

von Ranke, P.J., de Oliveira, N.A., Gama, S., 2004. J. Magn. Magn. Mater. 277, 78.

Voyer, C.J., Ryan, D.H., Ahn, K., Gschniedner Jr., K.A., Pecharsky, V.K., 2006. Phys. Rev. B 73, 174422.

Wang, Y., Calvert, L.D., Gabe, E.J., Taylor, J.B., 1978. Acta Cryst. B34, 1962.

Wang, H.B., Altounian, Z., Ryan, D.H., 2002. Phys. Rev. B 66, 214413.

Wang, H.B., Elouneg-Jamróz, M., Ryan, D.H., Altounian, Z., 2003. J. Appl. Phys. 93, 8304.

Wang, H.B., Altounian, Z., Ryan, D.H., 2004. J. Phys. Condens. Matter 16, 3053.

Wang, H.B., Altounian, Z., Ryan, D.H., Cadogan, J.M., Swainson, I.P., 2005. J. Appl. Phys. 97, 10M506.

Wang, Y.C., Yang, H.F., Huang, Q., Duan, L.B., Lynn, J.W., Rao, G.H., 2007. Phys. Rev. B 76, 064425.

Wang, H.B., Altounian, Z., Ryan, D.H., Cadogan, J.M., Swainson, I.P., Cranswick, L.M.D., 2008. J. Appl. Phys. 103, 07B330.

Wang, H., Misra, S., Wang, F., Miller, G.J., 2010. Inorg. Chem. 49, 4586.

Wu, W., Lu, D., 2004. J. Rare Earths 22, 654.

Wu, W., Tsokol, A.O., Gschneidner Jr., K.A., Sampaio, J.A., 2005a. J. Alloys Compd. 403, 118.

Wu, L.-M., Kim, S.-H., Seo, D.-K., 2005b. J. Am. Chem. Soc. 127, 15683.

Wu, Y.Y., Xia, Z.C., Ouyang, Z.W., Huang, Y., Li, L., 2011. J. Appl. Phys. 109, 083911.

Xie, K., Sun, Z., Zhu, Y., Yang, S., Song, X., 2004. J. Alloys Compd. 372, 49.

Xie, Q., Kubata, C., Wörle, M., Nesper, R., 2008. Z. Anorg. Allg. Chem. 634, 2469.

Xue, Y., Chen, Z., Zhang, X., Su, Y., Cao, S., Zhang, J., 2009. J. Supercond. Nov. Magn. 22, 637.

Yan, A., Handstein, A., Kerschl, P., Nenkov, K., Müller, K.-H., Gutfleisch, O., 2004. J. Appl. Phys. 95, 7064.

Yang, H.F., Rao, G.H., Chu, W.G., Liu, G.Y., Ouyang, Z.W., Liang, J.K., 2002a. J. Alloys Compd. 334, 131.

Yang, H.F., Rao, G.H., Chu, W.G., Liu, G.Y., Ouyang, Z.W., Liang, J.K., 2002b. J. Alloys Compd. 339, 189.

Yang, H.F., Rao, G.H., Liu, G.Y., Ouyang, Z.W., Feng, X.M., Liu, W.F., Chu, W.G., Liang, J.K., 2002c. J. Phys. Condens. Matter 14, 9705.

Yang, H.F., Rao, G.H., Liu, G.Y., Ouyang, Z.W., Liu, W.F., Feng, X.M., Chu, W.G., Liang, J.K., 2002d. J. Alloys Compd. 346, 190.

Yang, H.F., Rao, G.H., Liu, G.Y., Ouyang, Z.W., Liu, W.F., Feng, X.M., Chu, W.G., Liang, J.K., 2003a. J. Alloys Compd. 361, 113.

Yang, H.F., Rao, G.H., Liu, G.Y., Ouyang, Z.W., Liu, W.F., Feng, X.M., Chu, W.G., Liang, J.K., 2003b. J. Alloys Compd. 348, 150.

Yang, H.F., Rao, G.H., Liu, G.Y., Ouyang, Z.W., Liu, W.F., Feng, X.M., Chu, W.G., Liang, J.K., 2003c. J. Magn. Magn. Mater. 263, 146.

Yang, H.F., Rao, G.H., Liu, G.Y., Ouyang, Z.W., Feng, X.M., Liu, W.F., Chu, W.G., Liang, J.K., 2003d. Phys. Stat. Sol. A 198, 156.

Yang, H.F., Rao, G.H., Liu, G.Y., Ouyang, Z.W., Liu, W.F., Feng, X.M., Chu, W.G., Liang, J.K., 2003e. Physica B 325, 293.

Yang, H.F., Rao, G.H., Liu, G.Y., Ouyang, Z.W., Liu, W.F., Feng, X.M., Chu, W.G., Liang, J.K., 2004. J. Alloys Compd. 368, 248.

Yao, J., Mozharivskyj, Y., 2011. Z. Anorg. Allg. Chem. 637, 2039.

Yao, Y.D., Lee, S.F., Lee, M.D., Wu, K.T., Cheng, D.G., Thuy, N.P., Hien, N.T., Tai, L.T., Vinh, T.Q., Nong, N.V., 2003. Physica B 327, 324.

Yao, J., Lyutyy, P., Mozharivskyj, Y., 2011. Dalton Trans. 40, 4275.

Yao, J., Wang, P., Mozharivskyj, Y., 2012a. Chem. Mater. 24, 552.

Yao, J., Wang, P.L., Mozharivskyj, Y., 2012b. J. Alloys Compd. 534, 74.

Yazdani, A., Bonder, M.J., 2011. J. Magn. Magn. Mater. 323, 1658.

Yu, B.F., Liu, M., Egolf, P.W., Kitanowski, A., 2010. Intern. J. Refriger. 33, 1029.

Yuan, S., Ge, J., Cao, S., Yu, L., Wu, A., Xu, J., 2010. J. Appl. Phys. 107, 09E105.

Yuce, S., Barrio, M., Emre, B., Stern-Taulats, E., Planes, A., Tamarit, J.-L., Mudryk, Y., Gschneidner Jr., K.A., Pecharsky, V.K., Mañosa, L., 2012. Appl. Phys. Lett. 101, 071906.

Yucel, A., Elerman, Y., Aksoy, S., 2006. J. Alloys Compd. 420, 182.

Yüzüak, E., Yücel, A., Elerman, Y., 2007. In: Second IIF-IIR International Conference on Magnetic Refrigeration at Room Temperature, Potoroz, Slovenia, 11–13 April 2007, 81.

Yüzüak, E., Emre, B., Yücel, A., Elerman, Y., 2009. J. Alloys Compd. 476, 929.

Yüzüak, E., Dincer, I., Elerman, Y., 2010a. J. Rare Earths 28, 477.

Yüzüak, E., Dincer, I., Elerman, Y., 2010b. Chin. Phys. B 19, 037502.

Yüzüak, E., Emre, B., Elerman, Y., Yücel, A., 2010c. Chin. Phys. B 19, 057501.

Zhang, T., Chen, Y., Fu, H., Teng, B., Tang, Y., Tu, M., 2005. Chin. Sci. Bull. 50, 1811.

Zhang, E., Chen, Y., Zhang, T., Tang, Y., Tu, M., 2006. J. Magn. Magn. Mater. 305, 410.

Zhang, T., Chen, Y., Tang, Y., Du, H., Ren, T., Tu, M., 2007. J. Alloys Compd. 433, 18.

Zhang, A., Hou, X., Zhang, P., Hu, X.H., Xu, H., Ni, J.S., Zhou, B.X., Zhao, T., 2008a. Rare Met. Mater. Eng. 37, 1597.

Zhang, T., Chen, Y., Tang, Y., Ren, T., Tu, M., 2008b. Mater. Char. 59, 1518.

Zhang, H., Mudryk, Ya., Zou, M., Pecharsky, V.K., Gschneidner Jr., K.A., Long, Y., 2009. J. Alloys Compd. 487, 98.

Zhang, H., Mudryk, Ya., Cao, Q., Pecharsky, V.K., Gschneidner Jr., K.A., Long, Y., 2010. J. Appl. Phys. 107, 013909.

Zhong, X.C., Zou, M., Zhang, H., Liu, Z.W., Zeng, D.C., Gschneidner Jr., K.A., Pecharsky, V.K., 2011. J. Appl. Phys. 109, 07A917.

Zhou, Y.F., Hao, Y.M., Hu, Z.B., 2008. Key Eng. Mat. 368–372, 632.

Zhuang, Y.H., Huang, W.D., Li, J.Q., Jian, Y.X., Huang, J.L., 2006a. J. Alloys Compd. 414, 78.

Zhuang, Y.H., Li, J.Q., Huang, W.D., Sun, W.A., Ao, W.Q., 2006b. J. Alloys Compd. 421, 49.

Zhuo, Y., Chahine, R., Bose, T.K., 2003. IEEE Trans. Magn. 39, 3358.

Zimm, C., Jastrab, A., Sternberg, A., Pecharsky, V., Gschneidner Jr., K., Osborne, M., Anderson, I., 1998. Adv. Cryog. Eng. 43, 1759.

Zou, M., Tang, H., Schlagel, D.L., Lograsso, T.A., Gschneidner Jr., K.A., Pecharsky, V.K., 2006. J. Appl. Phys. 99, 08B304.

Zou, M., Mudryk, Y., Pecharsky, V.K., Gschneidner Jr., K.A., Schlagel, D.L., Lograsso, T.A., 2007. Phys. Rev. B 75, 024418.

Zou, M., Pecharsky, V.K., Gschneidner Jr., K.A., Schlagel, D.L., Lograsso, T.A., 2008. Phys. Rev. B 78, 014435.

Zou, M., Pecharsky, V.K., Gschneidner Jr., K.A., Schlagel, D.L., Lograsso, T.A., 2009a. J. Alloys Compd. 488, 550.

Zou, M., Pecharsky, V.K., Gschneidner Jr., K.A., Mudryk, Ya., Schlagel, D.L., Lograsso, T.A., 2009b. Phys. Rev. B 80, 174411.

Index

Note: Page numbers followed by "*f*" indicate figures, and "*t*" indicate tables.